

AUGUST 2017

**AJNR**

VOLUME 38 • PP 1463-1661

# AJNR

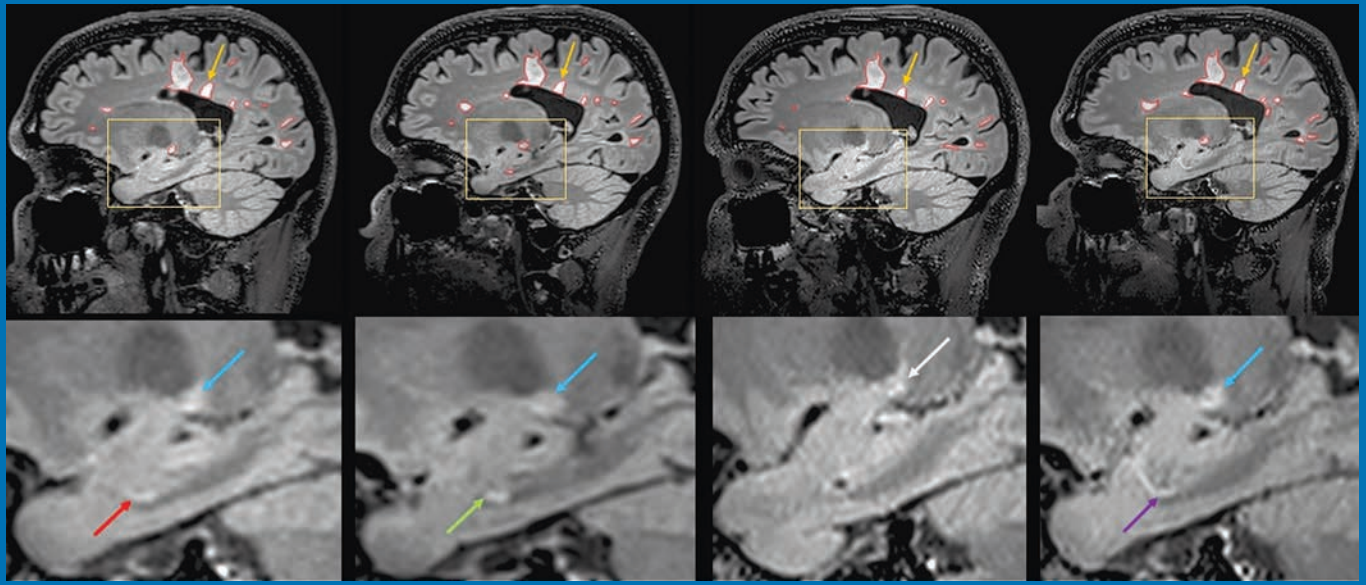
## AMERICAN JOURNAL OF NEURORADIOLOGY

AUGUST 2017  
VOLUME 38  
NUMBER 8  
WWW.AJNR.ORG

THE JOURNAL OF DIAGNOSTIC AND  
INTERVENTIONAL NEURORADIOLOGY

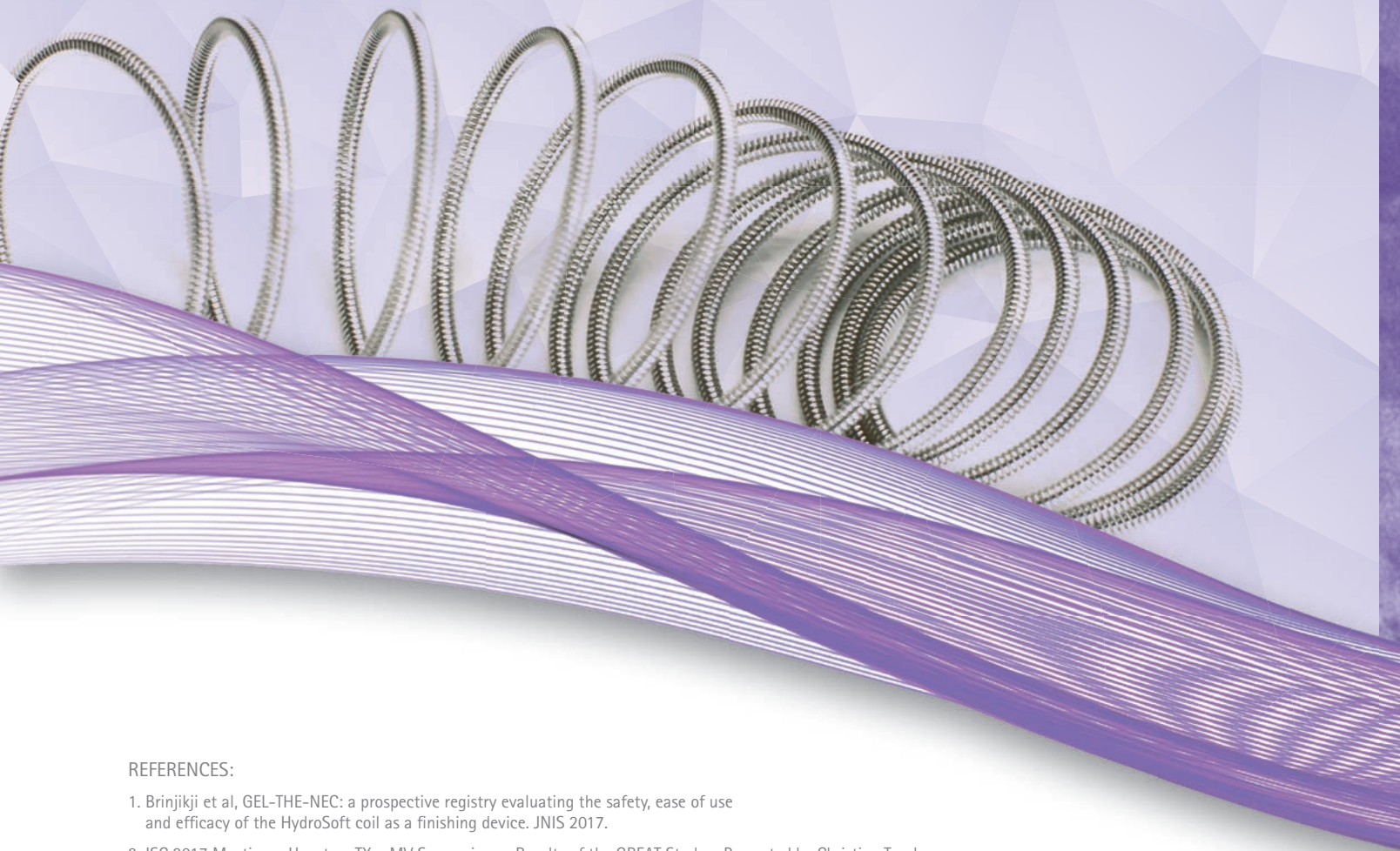
MRI systematic biases due to site differences in MS  
<sup>11</sup>C-Methionine-PET in differentiating necrosis from  
recurrent metastatic disease  
Conscious sedation versus general anesthesia for  
stroke thrombectomy

Official Journal ASNR • ASFNR • ASHNR • ASPNR • ASSR



# A Complete Coil Portfolio

MicroVention's comprehensive portfolio features clinically proven Hydrogel coils, which can be used exclusively or in combination with our trusted Platinum coils to treat a wide range of aneurysms and neurovascular lesions.



## REFERENCES:

1. Brinjikji et al, GEL-THE-NEC: a prospective registry evaluating the safety, ease of use and efficacy of the HydroSoft coil as a finishing device. JNIS 2017.
2. ISC 2017 Meeting – Houston, TX – MV Symposium – Results of the GREAT Study – Presented by Christian Taschner, MD, Department of Neuroradiology, Medical Centre – University of Freiburg, Germany

## INDICATIONS FOR USE:

The HydroCoil® Embolic System (HES) and MicroPlex Coil System (MCS) are intended for the endovascular embolization of intracranial aneurysms and other neurovascular abnormalities such as arteriovenous malformations and arteriovenous fistulae. The HES and MCS are also intended for vascular occlusion of blood vessels within the neurovascular system to permanently obstruct blood flow to an aneurysm or other vascular malformation and for arterial and venous embolizations in the peripheral vasculature.

The device should only be used by physicians who have undergone pre-clinical training in all aspects of HES/MCS procedures as prescribed by MicroVention.

MICROVENTION, MicroPlex and HydroCoil are registered trademarks of MicroVention, Inc. Refer to Instructions for Use, contraindications and warnings for additional information. Federal (USA) law restricts this device for sale by or on the order of a physician.

## Breakthrough Hydrogel Technology

- Less Retreatment Compared to Platinum<sup>1,2</sup>
- Less Recurrence Compared to Platinum<sup>1,2</sup>
- High Progressive Occlusion<sup>1,2</sup>

For more information or a product demonstration,  
contact your local MicroVention representative:



**MicroVention, Inc.**  
**Worldwide Headquarters**

1311 Valencia Avenue  
Tustin, CA 92780 USA  
MicroVention UK Limited  
MicroVention Europe, S.A.R.L  
MicroVention Deutschland GmbH  
[microvention.com](http://microvention.com)

**PH +1.714.247.8000**

PH +44 (0) 191 258 6777  
PH +33 (1) 39 21 77 46  
PH +49 211 210 798-0

## Smooth and stable.

Target Detachable Coils deliver consistently smooth deployment and exceptional microcatheter stability. Designed to work seamlessly together for framing, filling and finishing. Target Coils deliver the high performance you demand.

For more information, please visit [www.strykerneurovascular.com/Target](http://www.strykerneurovascular.com/Target) or contact your local Stryker Neurovascular sales representative.



**Target**<sup>®</sup>  
DETACHABLE COILS



TIGERTRIEVER

The brain at your fingertips

 **Rapid Medical**

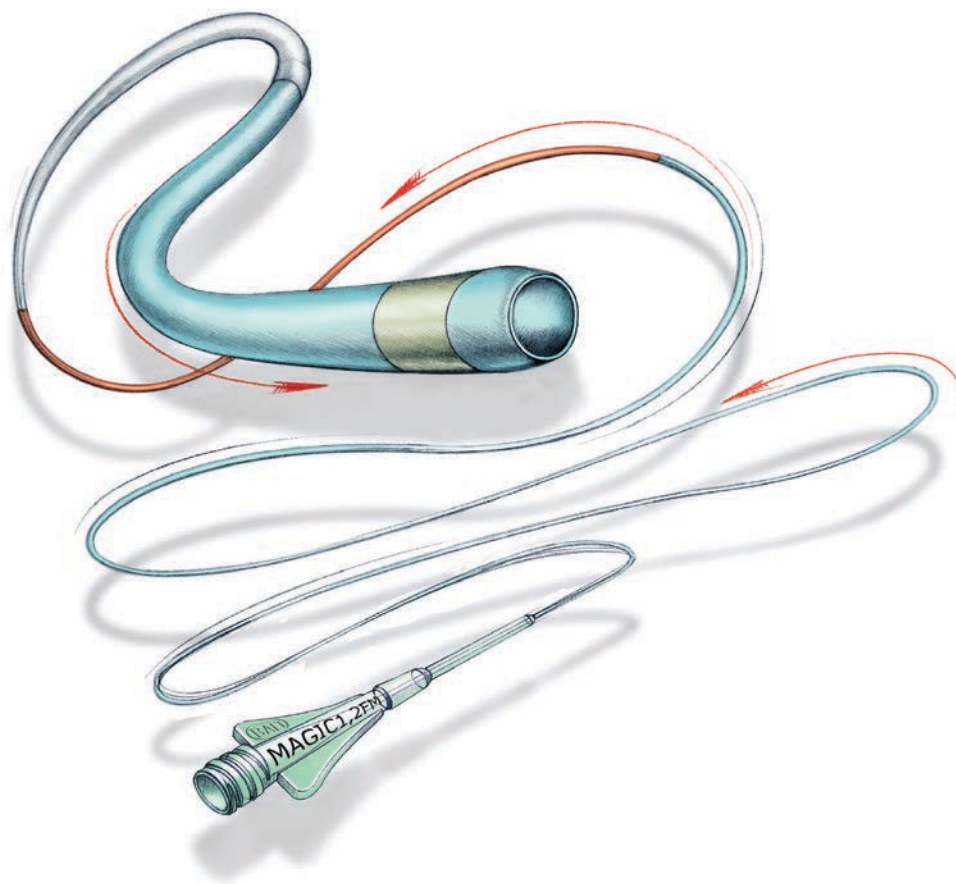
// [www.rapid-medical.com](http://www.rapid-medical.com)

# Magic<sup>®</sup>



## FLOW-DEPENDENT MICROCATHETER SERIES

Now available through Balt USA



[ordermagics@balt-usa.com](mailto:ordermagics@balt-usa.com)

MAGIC catheters are designed for general intravascular use. They may be used for the controlled, selective regional infusion of therapeutic agents or embolic materials into vessels.<sup>1</sup>

Federal (USA) law restricts this device to sale, distribution by or on the order of a physician. Indications, contraindications, warnings and instructions for use can be found in the product labeling supplied with each device.

1. Magic Catheters IFU - Ind 19



BALT USA  
18 Technology Drive #169, Irvine, CA 92618  
P 949.788.1443 F 949.788.1444

© 2017 BALT USA MKTG-068 Rev. B

# ASNR 56<sup>th</sup> Annual Meeting & The Foundation of the ASNR Symposium 2018

June 2 - 7, 2018 | Vancouver, B.C., CANADA



The Vancouver Convention Centre East  
© 2013 Vancouver Convention Centre

## Welcome and Greetings

Please join us in Vancouver, CANADA for the **56th Annual Meeting of the American Society of Neuroradiology** on June 2–7, 2018 at the Vancouver Convention Centre East. Surrounded by the coastal mountains and located on the waterfront, you can enjoy these spectacular views in the heart of downtown Vancouver. With its undeniable charm and friendly atmosphere, Vancouver is known around the world as both a popular tourist attraction and one of the best places to live.

ASNR enthusiastically presents **Neuroradiology: Adding Value and Improving Healthcare** at the Symposium of the Foundation of the ASNR, as well as the common thread throughout the Annual Meeting. Implementing a value-based strategy in imaging has grasped the attention of nearly every healthcare provider; in particular with Radiologists understanding that the future will demand their imaging practices deliver better value. Value in healthcare is typically defined as those imaging strategies that yield improved outcomes, lower costs, or both. As payment transitions from a fee-for-service to a value-based system, thus creating a fundamentally different marketplace dynamic, measuring good outcomes are at the center of this changeover. At this time of uncertainty what little remains clear is that without a well-defined knowledge of their outcomes, no medical specialty will be able to succeed in the future value-based system. The Symposium will feature how Neuroradiology, in its many subspecialty areas, adds value to clinical care pathways by directing healthcare practice towards better outcomes. The annual meeting programming will continue on this theme emphasizing imaging that improves health outcomes, while considering costs, thus adding value. Our discussions will incorporate many innovative approaches to how neuroimaging currently does and will continue to improve overall healthcare performance.

As the Program Chair for ASNR 2018, it is my pleasure and honor to welcome you to Vancouver, CANADA for our annual meeting! Vancouver is known for being a very walkable city with a compact downtown core hosting many places to enjoy. So pack your comfortable walking shoes and let's tour together with our colleagues and friends!

*Pina Sanelli*

Pina C. Sanelli, MD, MPH, FACR  
ASNR 2018 Program Chair/President-Elect



ASNR 2018 ■ VANCOUVER

ASFNR ASHNR ASPNR ASSR SNIS

THE FOUNDATION OF THE ASNR



**Pina C. Sanelli, MD, MPH, FACR**

**ASNR 2018 Program Chair/President-Elect**

*Programming developed in cooperation with the...*

**American Society of Functional Neuroradiology (ASFNR)**

Max Wintermark, MD

**American Society of Head and Neck Radiology (ASHNR)**

Deborah R. Shatzkes, MD

**American Society of Pediatric Neuroradiology (ASPNR)**

Ashok Panigrahy, MD

**American Society of Spine Radiology (ASSR)**

John D. Barr, MD, FACR, FSIR, FAHA

**Society of NeuroInterventional Surgery (SNIS)**

Mahesh V. Jayaraman, MD

**ASNR Health Policy (HPC) Committee**

William D. Donovan, MD, MPH, FACR,

Gregory N. Nicola, MD, FACR

**ASNR Computer Sciences & Informatics (CSI) Committee**

John L. Go, MD, FACR

**ASNR Research Scientist Programming Committee**

Dikoma C. Shungu, PhD, Timothy P.L. Roberts, PhD

**The International Hydrocephalus Imaging Working Group (IHIWG) / CSF Flow Group**

William G. Bradley, Jr., MD, PhD, FACR, Harold L. Rekate, MD  
and Bryn A. Martin, PhD

**Abstract Deadline: Friday, December 15, 2017**

Please visit [2018.asnr.org](http://2018.asnr.org) for more information



Fairmont Waterfront Hotel  
© Copyright 2017 FRHI



Pan Pacific Hotel  
© 2017 Pan Pacific Hotels and Resorts

**ASNR 56<sup>th</sup> Annual Meeting**

c/o American Society of Neuroradiology

800 Enterprise Drive, Suite 205

Oak Brook, Illinois 60523-4216

Phone: 630-574-0220 + Fax: 630 574-0661

[2018.asnr.org](http://2018.asnr.org)



# We're Inside Every Great Neuroradiologist!

## ASNR MEMBERS RECEIVE

### *American Journal of Neuroradiology (AJNR)*

The leading neuroradiology research journal, published monthly

### *Neurographics*

Bimonthly educational journal with CME for members

### *ASNR Annual Meeting*

Discounts for members on the field's premier conference

### *eCME*

Online collection of lectures and articles with SA-CME and Category 1 credit

### *Advocacy*

Coding/reimbursement, quality standards and practice guidelines; demonstrating neuroradiology's value!

### *Networking*

Access to 5,000 peers

... And More!

TR 4730.0  
TE 108.0  
TA 03:27  
BW 70.0  
M/ND  
A1  
HL1.2;HS1.2  
\*tseR2d1\_9 / 180  
SP F17.7  
SL 5.0  
FoV 194\*230  
190° 256s  
Tra>Cor(8.7)  
w 1469  
c 705  
MF 1.14  
D  
R  
5cm  
5cm

Join the leaders in neuroradiology today!

Learn more at [www.asnr.org/join](http://www.asnr.org/join)

# ASNR

## American Society of Neuroradiology

800 Enterprise Dr., Suite 205, Oak Brook, IL 60523 • (630)574-0220 • [membership@asnr.org](mailto:membership@asnr.org) • [www.asnr.org](http://www.asnr.org)



© Travel Portland



© Travel Portland



© Travel Portland



© Travel Portland



© 2010 Torsten Kjellstrand

**WE'VE MOVED TO FALL 2017!**



*11<sup>th</sup> Annual Meeting of the  
American Society of*

# **FUNCTIONAL NEURORADIOLOGY**

**October 9-11, 2017 • the Nines • Portland, Oregon**

**Optional Hands-on BOLD fMRI Workshop • October 8, 2017**



**PLEASE CONTACT EDUCATIONAL SYMPOSIA AT  
813-806-1000 or [ASFNR@edusymp.com](mailto:ASFNR@edusymp.com) or visit [www.ASFNR.org](http://www.ASFNR.org) for additional information.**



## Strengthen ASNR's representation at the national level.

Your membership in the American Medical Association strengthens ASNR's representation in the AMA House of Delegates—the policymaking body of the AMA that brings forth the views and interests of all physicians to establish national policy on health, medical, professional and governance matters.

Please activate your 2017 AMA membership, visit [ama-assn.org](http://ama-assn.org) or call AMA Member Relations at (800) 262-3211. If you are currently a member, thank you.

### AMA member benefits and resources include:

- Unlimited access to **The JAMA Network**<sup>®</sup> which brings together *JAMA* and all 11 specialty journals with CME.  
[jamanetwork.com](http://jamanetwork.com)
- **STEPS Forward**<sup>™</sup>, the AMA's new practice transformation series designed to help physicians achieve the Quadruple Aim: better patient experience, better population health and lower overall costs with improved professional satisfaction.  
[stepsforward.org](http://stepsforward.org)
- Free 18-month trial of **DynaMed Plus**<sup>®</sup>, an evidence-based, clinical support tool that features thousands of images and provides immediate answers to clinical questions.  
[offers.jamanetwork.com](http://offers.jamanetwork.com)



## Trevo® XP ProVue Retrievers

See package insert for complete indications, complications, warnings, and instructions for use.

### INDICATIONS FOR USE

1. The Trevo Retriever is indicated for use to restore blood flow in the neurovasculature by removing thrombus for the treatment of acute ischemic stroke to reduce disability in patients with a persistent, proximal anterior circulation, large vessel occlusion, and smaller core infarcts who have first received intravenous tissue plasminogen activator (IV t-PA). Endovascular therapy with the device should start within 6 hours of symptom onset.
2. The Trevo Retriever is indicated to restore blood flow in the neurovasculature by removing thrombus in patients experiencing ischemic stroke within 8 hours of symptom onset. Patients who are ineligible for intravenous tissue plasminogen activator (IV t-PA) or who fail IV t-PA therapy are candidates for treatment.

### COMPLICATIONS

Procedures requiring percutaneous catheter introduction should not be attempted by physicians unfamiliar with possible complications which may occur during or after the procedure. Possible complications include, but are not limited to, the following: air embolism; hematoma or hemorrhage at puncture site; infection; distal embolization; pain/headache; vessel spasm, thrombosis, dissection, or perforation; emboli; acute occlusion; ischemia; intracranial hemorrhage; false aneurysm formation; neurological deficits including stroke; and death.

### COMPATIBILITY

3x20mm retrievers are compatible with Trevo® Pro 14 Microcatheters (REF 90231) and Trevo® Pro 18 Microcatheters (REF 90238). 4x20mm retrievers are compatible with Trevo® Pro 18 Microcatheters (REF 90238). 4x30mm retrievers are compatible with Excelsior® XT-27® Microcatheters (150cm x 6cm straight REF 275081) and Trevo® Pro 18 Microcatheters (REF 90238). 6x25mm Retrievers are compatible with Excelsior® XT-27® Microcatheters (150cm x 6cm straight REF 275081). Compatibility of the Retriever with other microcatheters has not been established. Performance of the Retriever device may be impacted if a different microcatheter is used.

Balloon Guide Catheters (such as Merci® Balloon Guide Catheter and FlowGate® Balloon Guide Catheter) are recommended for use during thrombus removal procedures.

Retrievers are compatible with the Abbott Vascular DOC® Guide Wire Extension (REF 22260).

Retrievers are compatible with Boston Scientific RHV (Ref 421242).

### SPECIFIC WARNINGS FOR INDICATION 1

- The safety and effectiveness of the Trevo Retrievers in reducing disability has not been established in patients with large core infarcts (i.e., ASPECTS  $\leq 7$ ). There may be increased risks, such as intracerebral hemorrhage, in these patients.
- The safety and effectiveness of the Trevo Retrievers in reducing disability has not been established or evaluated in patients with occlusions in the posterior circulation (e.g., basilar or vertebral arteries) or for more distal occlusions in the anterior circulation.

### WARNINGS APPLIED TO BOTH INDICATIONS

- Administration of IV t-PA should be within the FDA-approved window (within 3 hours of stroke symptom onset).
- Contents supplied STERILE, using an ethylene oxide (EO) process. Nonpyrogenic.
- To reduce risk of vessel damage, adhere to the following recommendations:
  - Take care to appropriately size Retriever to vessel diameter at intended site of deployment.
  - Do not perform more than six (6) retrieval attempts in same vessel using Retriever devices.
  - Maintain Retriever position in vessel when removing or exchanging Microcatheter.
- To reduce risk of kinking/fracture, adhere to the following recommendations:
  - Immediately after unsheathing Retriever, position Microcatheter tip marker just proximal to shaped section. Maintain Microcatheter tip marker just proximal to shaped section of Retriever during manipulation and withdrawal.
  - Do not rotate or torque Retriever.
  - Use caution when passing Retriever through stented arteries.
- Do not resterilize and reuse. Structural integrity and/or function may be impaired by reuse or cleaning.
- The Retriever is a delicate instrument and should be handled carefully. Before use and when possible during procedure, inspect device carefully for damage. Do not use a device that shows signs of damage. Damage may prevent device from functioning and may cause complications.

- Do not advance or withdraw Retriever against resistance or significant vasospasm. Moving or torquing device against resistance or significant vasospasm may result in damage to vessel or device. Assess cause of resistance using fluoroscopy and if needed resheat the device to withdraw.
- If Retriever is difficult to withdraw from the vessel, do not torque Retriever. Advance Microcatheter distally, gently pull Retriever back into Microcatheter, and remove Retriever and Microcatheter as a unit. If undue resistance is met when withdrawing the Retriever into the Microcatheter, consider extending the Retriever using the Abbott Vascular DOC guidewire extension (REF 22260) so that the Microcatheter can be exchanged for a larger diameter catheter such as a DAC® catheter. Gently withdraw the Retriever into the larger diameter catheter.
- Administer anti-coagulation and anti-platelet medications per standard institutional guidelines.

### PRECAUTIONS

- Prescription only – device restricted to use by or on order of a physician.
- Store in cool, dry, dark place.
- Do not use open or damaged packages.
- Use by “Use By” date.
- Exposure to temperatures above 54°C (130°F) may damage device and accessories. Do not autoclave.
- Do not expose Retriever to solvents.
- Use Retriever in conjunction with fluoroscopic visualization and proper anti-coagulation agents.
- To prevent thrombus formation and contrast media crystal formation, maintain a constant infusion of appropriate flush solution between guide catheter and Microcatheter and between Microcatheter and Retriever or guidewire.
- Do not attach a torque device to the shaped proximal end of DOC® Compatible Retriever. Damage may occur, preventing ability to attach DOC® Guide Wire Extension.



**Concentric Medical**  
301 East Evelyn Avenue  
Mountain View, CA 94041

**Stryker Neurovascular**  
47900 Bayside Parkway  
Fremont, CA 94538

[strykerneurovascular.com](http://strykerneurovascular.com)

Date of Release: SEP/2016

EX\_EN\_US

Copyright © 2016 Stryker  
NV00018973.AB

## Target® Detachable Coil

See package insert for complete indications, contraindications, warnings and instructions for use.

### INTENDED USE / INDICATIONS FOR USE

Target Detachable Coils are intended to endovascularly obstruct or occlude blood flow in vascular abnormalities of the neurovascular and peripheral vessels.

Target Detachable Coils are indicated for endovascular embolization of:

- Intracranial aneurysms
- Other neurovascular abnormalities such as arteriovenous malformations and arteriovenous fistulae
- Arterial and venous embolizations in the peripheral vasculature

### CONTRAINDICATIONS

None known.

### POTENTIAL ADVERSE EVENTS

Potential complications include, but are not limited to: allergic reaction, aneurysm perforation and rupture, arrhythmia, death, edema, embolus, headache, hemorrhage, infection, ischemia, neurological/intracranial sequelae, post-embolization syndrome (fever, increased white blood cell count, discomfort), TIA/stroke, vasospasm, vessel occlusion or closure, vessel perforation, dissection, trauma or damage, vessel rupture, vessel thrombosis. Other procedural complications including but not limited to: anesthetic and contrast media risks, hypotension, hypertension, access site complications.

### WARNINGS

- Contents supplied STERILE using an ethylene oxide (EO) process. Do not use if sterile barrier is damaged. If damage is found, call your Stryker Neurovascular representative.
- For single use only. Do not reuse, reprocess or resterilize. Reuse, reprocessing or resterilization may compromise the structural integrity of the device and/or lead to device failure which, in turn, may result in patient injury, illness or death. Reuse, reprocessing or resterilization may also create a risk of contamination of the device and/or cause patient infection or cross-infection, including, but not limited to, the transmission of infectious disease(s) from one patient to another. Contamination of the device may lead to injury, illness or death of the patient.

- After use, dispose of product and packaging in accordance with hospital, administrative and/or local government policy.

**This device should only be used by physicians who have received appropriate training in interventional neuroradiology or interventional radiology and preclinical training on the use of this device as established by Stryker Neurovascular.**

- Patients with hypersensitivity to 316LVM stainless steel may suffer an allergic reaction to this implant.
- MR temperature testing was not conducted in peripheral vasculature, arteriovenous malformations or fistulae models.
- The safety and performance characteristics of the Target Detachable Coil System (Target Detachable Coils, InZone Detachment Systems, delivery systems and accessories) have not been demonstrated with other manufacturer's devices (whether coils, coil delivery devices, coil detachment systems, catheters, guidewires, and/or other accessories). Due to the potential incompatibility of non Stryker Neurovascular devices with the Target Detachable Coil System, the use of other manufacturer's device(s) with the Target Detachable Coil System is not recommended.
- To reduce risk of coil migration, the diameter of the first and second coil should never be less than the width of the ostium.
- In order to achieve optimal performance of the Target Detachable Coil System and to reduce the risk of thromboembolic complications, it is critical that a continuous infusion of appropriate flush solution be maintained between a) the femoral sheath and guiding catheter, b) the 2-tip microcatheter and guiding catheters, and c) the 2-tip microcatheter and Stryker Neurovascular guidewire and delivery wire. Continuous flush also reduces the potential for thrombus formation on, and crystallization of infusate around, the detachment zone of the Target Detachable Coil.
- Do not use the product after the “Use By” date specified on the package.
- Reuse of the flush port/dispenser coil or use with any coil other than the original coil may result in contamination of, or damage to, the coil.
- Utilization of damaged coils may affect coil delivery to, and stability inside, the vessel or aneurysm, possibly resulting in coil migration and/or stretching.
- The fluoro-saver marker is designed for use with a Rotating Hemostatic Valve (RHV). If used without an RHV, the distal end of the coil may be beyond the alignment marker when the fluoro-saver marker reaches the microcatheter hub.

- If the fluoro-saver marker is not visible, do not advance the coil without fluoroscopy.
- Do not rotate delivery wire during or after delivery of the coil. Rotating the Target Detachable Coil delivery wire may result in a stretched coil or premature detachment of the coil from the delivery wire, which could result in coil migration.
- Verify there is no coil loop protrusion into the parent vessel after coil placement and prior to coil detachment. Coil loop protrusion after coil placement may result in thromboembolic events if the coil is detached.
- Verify there is no movement of the coil after coil placement and prior to coil detachment. Movement of the coil after coil placement may indicate that the coil could migrate once it is detached.
- Failure to properly close the RHV compression fitting over the delivery wire before attaching the InZone® Detachment System could result in coil movement, aneurysm rupture or vessel perforation.
- Verify repeatedly that the distal shaft of the catheter is not under stress before detaching the Target Detachable Coil. Axial compression or tension forces could be stored in the 2-tip microcatheter causing the tip to move during coil delivery. Microcatheter tip movement could cause the aneurysm or vessel to rupture.
- Advancing the delivery wire beyond the microcatheter tip once the coil has been detached involves risk of aneurysm or vessel perforation.
- The long term effect of this product on extravascular tissues has not been established so care should be taken to retain this device in the intravascular space.

Damaged delivery wires may cause detachment failures, vessel injury or unpredictable distal tip response during coil deployment. If a delivery wire is damaged at any point during the procedure, do not attempt to straighten or otherwise repair it. Do not proceed with deployment or detachment. Remove the entire coil and replace with undamaged product.

- After use, dispose of product and packaging in accordance with hospital, administrative and/or local government policy.

### CAUTIONS / PRECAUTIONS

- Federal Law (USA) restricts this device to sale by or on the order of a physician.
- Besides the number of InZone Detachment System units needed to complete the case, there must be an extra InZone Detachment System unit as back up.

- Removing the delivery wire without grasping the introducer sheath and delivery wire together may result in the detachable coil sliding out of the introducer sheath.
- Failure to remove the introducer sheath after inserting the delivery wire into the RHV of the microcatheter will interrupt normal infusion of flush solution and allow back flow of blood into the microcatheter.
- Some low level overhead light near or adjacent to the patient is required to visualize the fluoro-saver marker; monitor light alone will not allow sufficient visualization of the fluoro-saver marker.
- Advance and retract the Target Detachable Coil carefully and smoothly without excessive force. If unusual friction is noticed, slowly withdraw the Target Detachable Coil and examine for damage. If damage is present, remove and use a new Target Detachable Coil. If friction or resistance is still noted, carefully remove the Target Detachable Coil and microcatheter and examine the microcatheter for damage.
- If it is necessary to reposition the Target Detachable Coil, verify under fluoroscopy that the coil moves with a one-to-one motion. If the coil does not move with a one-to-one motion or movement is difficult, the coil may have stretched and could possibly migrate or break. Gently remove both the coil and microcatheter and replace with new devices.
- Increased detachment times may occur when:
  - Other embolic agents are present.
  - Delivery wire and microcatheter markers are not properly aligned.
  - Thrombus is present on the coil detachment zone.
- Do not use detachment systems other than the InZone Detachment System.
- Increased detachment times may occur when delivery wire and microcatheter markers are not properly aligned.
- Do not use detachment systems other than the InZone Detachment System.



**Stryker Neurovascular**  
47900 Bayside Parkway  
Fremont, CA 94538

[strykerneurovascular.com](http://strykerneurovascular.com)

Date of Release: MAR/2016

EX\_EN\_US

Copyright © 2016 Stryker  
NV00018669.AB

**NEW**

# Indication for Trevo<sup>®</sup> Retrievers

A New Standard of Care in Stroke



**FIRST**

mechanical thrombectomy device  
indicated to reduce disability in stroke.\*

**FIRST**

new treatment indication for  
stroke in 20 years.

## Trevo XP

PROVUE RETRIEVER

Success accelerated.

\*The Trevo Retriever is indicated for use to restore blood flow in the neurovasculature by removing thrombus for the treatment of acute ischemic stroke to reduce disability in patients with a persistent, proximal anterior circulation, large vessel occlusion, and smaller core infarcts who have first received intravenous tissue plasminogen activator (IV t-PA). Endovascular therapy with the device should start within 6 hours of symptom onset.

# THE PROVEN LEADER

The STAR™ Tumor Ablation System is the proven leader in spine RF ablation with thousands of patients treated.



Dual thermocouples for active temperature monitoring on a single instrument



Steerable and navigational RF ablation instrument



SpineSTAR® delivers RF energy directly to the tumor



Tumor is debulked

#### STAR Clinical Studies Demonstrate<sup>1-4</sup>:

- Fast, durable pain relief
- Rapid improvement in mobility and quality of life
- Reduction or discontinuation of pain medication
- Site-specific ablation zones and real time temperature monitoring
- May be combined with radiation and/or chemotherapy



[Merit.com/star](http://Merit.com/star)

Indications for Use: The STAR™ Tumor Ablation System is indicated for palliative treatment in spinal procedures by ablation of metastatic malignant lesions in a vertebral body. As with most surgical procedures, there are risks associated with the STAR procedure, including serious complications. For complete information regarding risks, contraindications, warnings, precautions, and adverse events please review the System's Instructions for Use.

#### References

1 Pain Physician 2014 Jul-Aug; 17(4):317-27 2 Radiology 2014 Oct; 273 (1): 261-7 3 J. Vasc Interv Radiol 2015; 18: 573-581 4 Pain Physician 2015; 18: 573-581

### Official Journal:

American Society of Neuroradiology  
American Society of Functional Neuroradiology  
American Society of Head and Neck Radiology  
American Society of Pediatric Neuroradiology  
American Society of Spine Radiology

### EDITOR-IN-CHIEF

**Jeffrey S. Ross, MD**

Professor of Radiology, Department of Radiology,  
Mayo Clinic College of Medicine, Phoenix, AZ

### SENIOR EDITORS

**Harry J. Cloft, MD, PhD**

Professor of Radiology and Neurosurgery,  
Department of Radiology, Mayo Clinic College of  
Medicine, Rochester, MN

**Thierry A.G.M. Huisman, MD**

Professor of Radiology, Pediatrics, Neurology, and  
Neurosurgery, Chairman, Department of Imaging  
and Imaging Science, Johns Hopkins Bayview,  
Director, Pediatric Radiology and Pediatric  
Neuroradiology, Johns Hopkins Hospital,  
Baltimore, MD

**Yvonne W. Lui, MD**

Associate Professor of Radiology,  
Chief of Neuroradiology,  
New York University School of Medicine,  
New York, NY

**C.D. Phillips, MD, FACR**

Professor of Radiology, Weill Cornell Medical  
College, Director of Head and Neck Imaging,  
New York-Presbyterian Hospital, New York, NY

**Pamela W. Schaefer, MD**

Clinical Director of MRI and Associate Director of  
Neuroradiology, Massachusetts General Hospital,  
Boston, Massachusetts, Associate Professor,  
Radiology, Harvard Medical School, Cambridge, MA

**Charles M. Strother, MD**

Professor of Radiology, Emeritus, University of  
Wisconsin, Madison, WI

### STATISTICAL SENIOR EDITOR

**Bryan A. Comstock, MS**

Senior Biostatistician,  
Department of Biostatistics,  
University of Washington, Seattle, WA

### EDITORIAL BOARD

Ashley H. Aiken, *Atlanta, GA*  
Lea M. Alhilali, *Phoenix, AZ*  
John D. Barr, *Dallas, TX*  
Ari Blitz, *Baltimore, MD*  
Barton F. Branstetter IV, *Pittsburgh, PA*  
Jonathan L. Brisman, *Lake Success, NY*  
Julie Bykowski, *San Diego, CA*  
Keith Cauley, *Danville, PA*  
Asim F. Choudhri, *Memphis, TN*  
Alessandro Cianfoni, *Lugano, Switzerland*  
J. Matthew Debnam, *Houston, TX*  
Seena Dehkharghani, *New York, NY*  
Colin Derdeyn, *Iowa City, IA*  
Rahul S. Desikan, *San Francisco, CA*  
Yonghong Ding, *Rochester, MN*  
Clifford J. Eskey, *Hanover, NH*  
Saeed Fakhran, *Phoenix, AZ*  
Massimo Filippi, *Milan, Italy*  
Allan J. Fox, *Toronto, Ontario, Canada*  
Wende N. Gibbs, *Los Angeles, CA*  
Christine M. Glastonbury, *San Francisco, CA*  
John L. Go, *Los Angeles, CA*  
Allison Grayev, *Madison, WI*  
Brent Griffith, *Detroit, MI*  
Wan-Yuo Guo, *Taipei, Taiwan*  
Ajay Gupta, *New York, NY*  
Rakesh K. Gupta, *Lucknow, India*  
Lotfi Hacein-Bey, *Sacramento, CA*  
Christopher P. Hess, *San Francisco, CA*  
Andrei Holodny, *New York, NY*  
Benjamin Huang, *Chapel Hill, NC*  
George J. Hunter, *Boston, MA*  
Mahesh V. Jayaraman, *Providence, RI*  
Valerie Jewells, *Chapel Hill, NC*  
Christof Karmonik, *Houston, TX*  
Timothy J. Kaufmann, *Rochester, MN*  
Hillary R. Kelly, *Boston, MA*  
Toshibumi Kinoshita, *Akita, Japan*  
Kenneth F. Layton, *Dallas, TX*  
Michael M. Lell, *Nürnberg, Germany*  
Michael Lev, *Boston, MA*  
Karl-Olof Lovblad, *Geneva, Switzerland*  
Franklin A. Marden, *Chicago, IL*  
M. Gisele Matheus, *Charleston, SC*  
Joseph C. McGowan, *Merion Station, PA*  
Stephan Meckel, *Freiburg, Germany*  
Christopher J. Moran, *St. Louis, MO*  
Takahisa Mori, *Kamakura City, Japan*  
Suresh Mukherji, *Ann Arbor, MI*  
Amanda Murphy, *Toronto, Ontario, Canada*  
Alexander J. Nemeth, *Chicago, IL*  
Sasan Partovi, *Cleveland, OH*  
Laurent Pierot, *Reims, France*  
Jay J. Pillai, *Baltimore, MD*

Whitney B. Pope, *Los Angeles, CA*  
M. Judith Donovan Post, *Miami, FL*  
Tina Young Poussaint, *Boston, MA*  
Joana Ramalho, *Lisbon, Portugal*  
Otto Rapalino, *Boston, MA*  
Álex Rovira-Cañellas, *Barcelona, Spain*  
Paul M. Ruggieri, *Cleveland, OH*  
Zoran Rumboldt, *Rovinj-Rovigno, Croatia*  
Amit M. Saindane, *Atlanta, GA*  
Erin Simon Schwartz, *Philadelphia, PA*  
Lubdha M. Shah, *Salt Lake City, UT*  
Aseem Sharma, *St. Louis, MO*  
J. Keith Smith, *Chapel Hill, NC*  
Maria Vittoria Spampinato, *Charleston, SC*  
Gordon K. Sze, *New Haven, CT*  
Krishnamoorthy Thamburaj, *Hershey, PA*  
Cheng Hong Toh, *Taipei, Taiwan*  
Thomas A. Tomsick, *Cincinnati, OH*  
Aquila S. Turk, *Charleston, SC*  
Willem Jan van Rooij, *Tilburg, Netherlands*  
Arastoo Vossough, *Philadelphia, PA*  
Elysa Widjaja, *Toronto, Ontario, Canada*  
Max Wintermark, *Stanford, CA*  
Ronald L. Wolf, *Philadelphia, PA*  
Kei Yamada, *Kyoto, Japan*  
Carlos Zamora, *Chapel Hill, NC*

### EDITORIAL FELLOW

Vahe Zohrabian, *New Haven, CT*

### SPECIAL CONSULTANTS TO THE EDITOR

#### AJNR Blog Editor

Neil Lall, *Denver, CO*

#### Case of the Month Editor

Nicholas Stence, *Aurora, CO*

#### Case of the Week Editors

Juan Pablo Cruz, *Santiago, Chile*  
Sapna Rawal, *Toronto, Ontario, Canada*

#### Classic Case Editor

Sandy Cheng-Yu Chen, *Taipei, Taiwan*

#### Facebook Editor

Peter Yi Shen, *Sacramento, CA*

#### Health Care and Socioeconomics Editor

Pina C. Sanelli, *New York, NY*

#### Physics Editor

Greg Zaharchuk, *Stanford, CA*

#### Podcast Editor

Wende N. Gibbs, *Los Angeles, CA*

#### Twitter Editor

Jennifer McCarty, *Atlanta, Georgia*

### YOUNG PROFESSIONALS ADVISORY COMMITTEE

Asim K. Bag, *Birmingham, AL*  
Anna E. Nidecker, *Sacramento, CA*  
Peter Yi Shen, *Sacramento, CA*

Founding Editor  
Juan M. Taveras

Editors Emeriti  
Mauricio Castillo, Robert I. Grossman,  
Michael S. Huckman, Robert M. Quencer

Managing Editor  
Karen Halm

Assistant Managing Editor  
Laura Wilhelm

Digital Publications and Social Media Coordinator  
Kylie Mason

Executive Director, ASNR

Mary Beth Hepp

Director of Communications, ASNR

Angelo Artemakis

# AJNR

## AMERICAN JOURNAL OF NEURORADIOLOGY

AUGUST 2017  
VOLUME 38  
NUMBER 8  
WWW.AJNR.ORG

Publication Preview at [www.ajnr.org](http://www.ajnr.org) features articles released in advance of print. Visit [www.ajnrblog.org](http://www.ajnrblog.org) to comment on AJNR content and chat with colleagues and AJNR's News Digest at <http://ajnrdigest.org> to read the stories behind the latest research in neuroimaging.

1463 **PERSPECTIVES** *A. Kapadia*

### EDITORIAL

1464 **To tPA or Not to tPA, That Is the Question** *T.M. Leslie-Mazwi, et al.*

### REVIEW ARTICLE

  1467 **Dentate Update: Imaging Features of Entities That Affect the Dentate Nucleus** *K.M. Bond, et al.* **ADULT BRAIN**

### PRACTICE PERSPECTIVES

  1475 **MR Imaging in Sudden Sensorineural Hearing Loss. Time to Talk** *G. Conte, et al.* **HEAD & NECK**

 1480 **Introduction of a Dedicated Emergency Department MR Imaging Scanner at the Barrow Neurological Institute** *M. Buller, et al.*

### GENERAL CONTENTS

1486 **Cumulative Dose of Macrocyclic Gadolinium-Based Contrast Agent Improves Detection of Enhancing Lesions in Patients with Multiple Sclerosis** *A. Rovira, et al.* **ADULT BRAIN**

1494 **Diffusional Kurtosis Imaging of the Corticospinal Tract in Multiple Sclerosis: Association with Neurologic Disability** *M.V. Spampinato, et al.* **ADULT BRAIN**

   1501 **Volumetric Analysis from a Harmonized Multisite Brain MRI Study of a Single Subject with Multiple Sclerosis** *R.T. Shinohara, et al.* **ADULT BRAIN**

   1510 **Reliability of White Matter Microstructural Changes in HIV Infection: Meta-Analysis and Confirmation** *E.E. O'Connor, et al.* **ADULT BRAIN**

 1520 **Differentiation between Treatment-Induced Necrosis and Recurrent Tumors in Patients with Metastatic Brain Tumors: Comparison among <sup>11</sup>C-Methionine-PET, FDG-PET, MR Permeability Imaging, and MRI-ADC—Preliminary Results** *N. Tomura, et al.* **ADULT BRAIN**

  1528 **The Initial Area Under the Curve Derived from Dynamic Contrast-Enhanced MRI Improves Prognosis Prediction in Glioblastoma with Unmethylated *MGMT* Promoter** *Y.S. Choi, et al.* **ADULT BRAIN**

1536 **Retrospective Validation of a Computer-Assisted Quantification Model of Intracerebral Hemorrhage Volume on Accuracy, Precision, and Acquisition Time, Compared with Standard ABC/2 Manual Volume Calculation** *W. Xue, et al.* **ADULT BRAIN**

AJNR (Am J Neuroradiol ISSN 0195–6108) is a journal published monthly, owned and published by the American Society of Neuroradiology (ASNR), 800 Enterprise Drive, Suite 205, Oak Brook, IL 60523. Annual dues for the ASNR include \$170.00 for journal subscription. The journal is printed by Cadmus Journal Services, 5457 Twin Knolls Road, Suite 200, Columbia, MD 21045; Periodicals postage paid at Oak Brook, IL and additional mailing offices. Printed in the U.S.A. POSTMASTER: Please send address changes to American Journal of Neuroradiology, P.O. Box 3000, Denville, NJ 07834, U.S.A. Subscription rates: nonmember \$390 (\$460 foreign) print and online, \$310 online only; institutions \$450 (\$520 foreign) print and basic online, \$895 (\$960 foreign) print and extended online, \$370 online only (basic), extended online \$805; single copies are \$35 each (\$40 foreign). Indexed by PubMed/Medline, BIOSIS Previews, Current Contents (Clinical Medicine and Life Sciences), EMBASE, Google Scholar, HighWire Press, Q-Sensei, RefSeek, Science Citation Index, and SCI Expanded. Copyright © American Society of Neuroradiology.

-  1543 **Transcranial Duplex Sonography Predicts Outcome following an Intracerebral Hemorrhage** *P. Camps-Renom, et al.* **ADULT BRAIN**
- 1550 **Perfusion MR Imaging Using a 3D Pulsed Continuous Arterial Spin-Labeling Method for Acute Cerebral Infarction Classified as Branch Atheromatous Disease Involving the Lenticulostriate Artery Territory** *Y. Shinohara, et al.* **ADULT BRAIN**
-   1555 **Temporal and Spatial Variances in Arterial Spin-Labeling Are Inversely Related to Large-Artery Blood Velocity** *A.D. Robertson, et al.* **ADULT BRAIN**
- 1562 **Head-to-Head Visual Comparison between Brain Perfusion SPECT and Arterial Spin-Labeling MRI with Different Postlabeling Delays in Alzheimer Disease** *T. Kaneta, et al.* **ADULT BRAIN**
-  1569 **CT Angiography ASPECTS Predicts Outcome Much Better Than Noncontrast CT in Patients with Stroke Treated Endovascularly** *F. Sallustio, et al.* **ADULT BRAIN**  
**INTERVENTIONAL**
- 1574 **State of Practice: Endovascular Treatment of Acute Aneurysmal SAH in Germany** *H. Janssen, et al.* **INTERVENTIONAL**
-   1580 **The Impact of Conscious Sedation versus General Anesthesia for Stroke Thrombectomy on the Predictive Value of Collateral Status: A Post Hoc Analysis of the SIESTA Trial** *S. Schönenberger, et al.* **INTERVENTIONAL**
-   1586 **Effect of Retrievable Stent Size on Endovascular Treatment of Acute Ischemic Stroke: A Multicenter Study** *D. Yang, et al.* **INTERVENTIONAL**
-   1594 **e-ASPECTS Correlates with and Is Predictive of Outcome after Mechanical Thrombectomy** *J. Pfaff, et al.* **INTERVENTIONAL**
-  1600 **Acute Basilar Artery Occlusion: Differences in Characteristics and Outcomes after Endovascular Therapy between Patients with and without Underlying Severe Atherosclerotic Stenosis** *Y.Y. Lee, et al.* **INTERVENTIONAL**
- 1605 **Treatment of Tandem Internal Carotid Artery Aneurysms Using a Single Pipeline Embolization Device: Evaluation of Safety and Efficacy** *N. Adeeb, et al.* **INTERVENTIONAL**
-  1610 **Non-Contrast-Enhanced Silent Scan MR Angiography of Intracranial Anterior Circulation Aneurysms Treated with a Low-Profile Visualized Intraluminal Support Device** *N. Takano, et al.* **INTERVENTIONAL**
-  1617 **Jugular Anomalies in Multiple Sclerosis Are Associated with Increased Collateral Venous Flow** *S.K. Sethi, et al.* **EXTRACRANIAL VASCULAR**
-  1623 **Functional Connectivity in Virally Suppressed Patients with HIV-Associated Neurocognitive Disorder: A Resting-State Analysis** *J.R. Chaganti, et al.* **FUNCTIONAL**
- 1630 **Influence of Ultra-Low-Dose and Iterative Reconstructions on the Visualization of Orbital Soft Tissues on Maxillofacial CT** *G. Widmann, et al.* **HEAD & NECK**
-   1636 **Does 3T Fetal MRI Improve Image Resolution of Normal Brain Structures between 20 and 24 Weeks' Gestational Age?** *G. Priego, et al.* **PEDIATRICS**
-   1643 **MR Imaging Diagnosis of Diencephalic-Mesencephalic Junction Dysplasia in Fetuses with Developmental Ventriculomegaly** *M. Severino, et al.* **PEDIATRICS**
- 1647 **Temporal Evolution of Disc in Young Patients with Low Back Pain and Stress Reaction in Lumbar Vertebrae** *A. Sharma, et al.* **SPINE**
- 1653 **Percutaneous Spinal Ablation in a Sheep Model: Protective Capacity of an Intact Cortex, Correlation of Ablation Parameters with Ablation Zone Size, and Correlation of Postablation MRI and Pathologic Findings** *A.N. Wallace, et al.* **SPINE**
- 1660 **Commentary**  
**Is an Intact Posterior Vertebral Body Cortex Protective for Percutaneous Ablation?** *JJ. Gemmete*

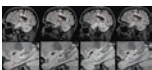
## ONLINE FEATURES

### LETTERS

- E51 **Regarding “Differences in Hemodynamics and Rupture Rate of Aneurysms at the Bifurcation of the Basilar and Internal Carotid Arteries”** *W. Li, et al.*
- E52 **Reply** *R. Doddasomayajula, et al.*
- E53 **Regarding “What Is the Ideal Core Number for Ultrasonography-Guided Thyroid Biopsy of Cytologically Inconclusive Nodules?”** *H.S. Park, et al.*
- E55 **Regarding “Measured Head CT/CTA Skin Dose and Intensive Care Unit Patient Cumulative Exposure”** *I. Ikuta, et al.*
- E56 **Reply** *R.D. Nawfel, et al.*
- E57 **ERRATUM**

### BOOK REVIEWS *R.M. Quencer, Section Editor*

Please visit [www.ajnrblog.org](http://www.ajnrblog.org) to read and comment on Book Reviews.



Comparison of manual segmentation of cerebral T2 hyperintense lesions from 3T MR imaging scans of a single subject with multiple sclerosis. Images shown are from sagittal FLAIR sequences (top) from 4 different North American Imaging in Multiple Sclerosis Cooperative sites and scanner models with magnified views at the bottom.



Indicates Editor's Choices selection



Indicates Fellows' Journal Club selection



Indicates open access to non-subscribers at [www.ajnr.org](http://www.ajnr.org)



Indicates article with supplemental on-line table



Indicates article with supplemental on-line photo



Indicates article with supplemental on-line video



Evidence-Based Medicine Level 1



Evidence-Based Medicine Level 2



Title: Echoes of (the) Sunset, 36" x 48" Oil on Canvas. This is an attempted abstraction of the beauty of the twilight hours, with dominance of oranges and reds. The colors melt into each other, a representation of the natural transition of time.

*Anish Kapadia, Radiology Resident, University of Toronto, Toronto, Ontario, Canada*

## To tPA or Not to tPA, That Is the Question

T.M. Leslie-Mazwi, R.V. Chandra, and J.A. Hirsch

For decades, the acute treatment of stroke has centered on delivery of intravenous recombinant tissue plasminogen activator. Endovascular stroke therapy was historically dogged by a dearth of high-level evidence supporting its application. Refinements in imaging selection, improved treatment logistics, and increased reperfusion rates came together in 2015 with the publication of multiple randomized trials that changed that, unequivocally identifying the benefit of endovascular therapy combined with medical management over medical management alone for patients with proximal large vessel occlusions (LVO).<sup>1-5</sup> With a number needed to treat of merely 2.6 to reduce disability (measured by the modified Rankin score), endovascular stroke therapy is now arguably one of the most effective treatments in medicine.<sup>6</sup>

Attention therefore turns to refinements and the remaining gaps in knowledge for this powerful therapy. This requires examination of every aspect of the care of patients with LVO. It is in this context that the role of IV tPA in patients with LVO undergoing endovascular therapy has come under scrutiny. Specifically, should IV tPA be administered at all?

### The State of the Science

In the original 5 published randomized controlled trials (RCTs) demonstrating the superiority of endovascular therapy over medical management alone, IV tPA had no impact on the endovascular therapy results.<sup>1-5</sup> Both the Multicenter Randomized Clinical trial of Endovascular treatment for Acute ischemic stroke in the Netherlands (MR CLEAN)<sup>1</sup> and Endovascular Revascularization With Solitaire Device Versus Best Medical Therapy in Anterior Circulation Stroke Within 8 Hours (REVASCAT)<sup>4</sup> required IV tPA failure before randomization for endovascular treatment, selecting patients likely to do poorly with isolated medical management. However, the remaining 3 trials (Endovascular Treatment for Small Core and Proximal Occlusion Ischemic Stroke [ESCAPE], Extending the Time for Thrombolysis in Emergency Neurological Deficits–Intra-Arterial [EXTEND-IA], and Solitaire With the Intention For Thrombectomy as PRIMARY Endovascular Treatment for Acute Ischemic Stroke [SWIFT PRIME])<sup>2,3,5</sup> were more selective and had no such requirement; 2 of these (EXTEND-IA and SWIFT PRIME) administered IV tPA to all participants. More recently the Trial and Cost Effectiveness Evaluation of Intra-Arterial Thrombectomy in Acute Ischemic Stroke [THRACE] trial, with wide inclusions, also reported similar findings: outcome was independent of IV tPA status.<sup>7</sup>

The HERMES meta-analysis aggregates these collective data at the individual patient level (excluding THRACE).<sup>6</sup> For the endovascular cohort, 526/634 (83%) received tPA, compared

with 87% of the control population. From the thrombectomy group, 108 patients were ineligible for IV tPA of 188 total. There was no treatment-effect heterogeneity across a range of prespecified variables; the administration of tPA caused neither benefit nor harm. The authors concluded that endovascular therapy should be pursued irrespective of tPA eligibility or status.

These are specific trial populations, and even in aggregate, there are reasons that generalizing to patients in everyday practice requires caution. However, several recent publications have explored this in typical clinical scenarios.

Weber et al<sup>8</sup> retrospectively analyzed patients treated with combination therapy with IV tPA and thrombectomy ( $n = 105$ ) compared to patients receiving thrombectomy alone ( $n = 145$ ) during a 14-month period at a tertiary neurovascular center. Administration of IV tPA added a 36-minute delay in picture-to-puncture times. This finding is striking in an efficient, high-volume center. No significant differences existed in 90-day outcomes (modified Rankin Scale score, 0–2; 35.2% versus 40%;  $P = .444$ ). Similarly, TICI 2b/3 (73.8% versus 73.1,  $P = .952$ ) and symptomatic hemorrhage rates (5.9% versus 3.5%,  $P = .387$ ) were equivalent.

A similar experience is reported during nearly 6 years in a high-volume stroke center.<sup>9</sup> Like the groups in Weber et al,<sup>8</sup> treatment decisions were individualized by the multidisciplinary treating team, excepting clear exclusions to IV tPA use. They reviewed 239 patients with anterior circulation stroke treated with mechanical thrombectomy alone and identified 40 IV tPA-eligible patients who were treated with thrombectomy alone. Multivariate matched-pairs analysis was used to compare these patients with controls treated with combination therapy. There were no significant differences in 90-day favorable outcome (mRS, 0–2; 42.5% versus 42.5%;  $P = 1.0$ ), successful reperfusion (TICI 2b/3, 87.5% versus 77.5;  $P = .39$ ), or symptomatic intracerebral hemorrhage (2.5% versus 2.5%  $P = 1.0$ ). The patients who went directly to thrombectomy had lower rates of asymptomatic intracranial hemorrhage (12.5% versus 35%,  $P = .023$ ) compared with those receiving bridging IV tPA.

Most recently, Coutinho et al<sup>10</sup> published an analysis of 2 large prospective clinical trials, Solitaire FR Thrombectomy for Acute Revascularization (STAR) and Solitaire With the Intention for Thrombectomy (SWIFT), further questioning the role of IV tPA for patients with LVO eligible for thrombectomy.<sup>10</sup> The authors analyzed 291 patients, 55% treated with combination therapy compared with thrombectomy alone. The groups were well-matched except that the baseline Alberta Stroke Program Early CT Score favored the combination therapy group (8 versus 9,  $P = .4$ ). Outcomes between the 2 groups were the same at 90 days, as was symptomatic hemorrhage. Technical considerations were identical between groups, with no difference in clot fragmentation (measured by emboli to new territory). The authors concluded that IV tPA and thrombectomy offered no obvious benefit over thrombectomy alone.<sup>10</sup>

### IV tPA in Patients with LVO

We have previously published on this topic, outlining the arguments both for and against IV tPA in this setting.<sup>11</sup> IV tPA has distinct positives: It may produce recanalization without the need for mechanical thrombectomy. It may enhance the success of thrombectomy, by both making clot extraction easier and lysing smaller fragments that may embolize distally during the procedure. It may prevent microvascular thrombosis, maintaining cerebral perfusion distal to the occlusion. Finally, it offers a chance (albeit small) at recanalization for those patients who, for technical or logistic reasons, are unable to undergo mechanical thrombectomy or in whom this is delayed.<sup>11</sup>

The arguments against the use of tPA are similarly varied. IV tPA has limited efficacy in the presence of large-volume clot, with an efficacy range of 8%–32%, depending on the occlusion level. Administration of tPA produces delays, both in the act of delivering the drug and tPA prioritization in the care delivery system. In comprehensive centers, thrombectomy may be accomplished before the tPA infusion has been completed. Moreover, the potential for hemorrhage in patients who receive IV tPA is difficult to ignore, despite the equivalent symptomatic hemorrhage rates in recent endovascular trials.<sup>11</sup> At this stage, there is no clear clinical benefit or harm incurred by administering IV tPA. However, the routine use of IV tPA for patients with LVO does erode the overall health care value.

Both resource-intensive and expensive, endovascular stroke treatment makes an attractive target for organizations aiming to control expenditure. Maximizing value through cost-effectiveness and cost-utility, therefore, becomes a priority.<sup>12</sup> One prominent question that remains to be answered in this new landscape of endovascular stroke therapy is about the most cost-effective method to deliver this care within our ever-more-constrained health care budget. Value is best viewed as the relationship between the cost of the treatment and outcome. In patients with LVO, this references overall expenditure (from onset to return to the community) weighted against the eventual patient outcome.

A recent cost-utility analysis using data with contemporary cost information found that combination therapy is approximately \$17,000 more expensive than IV tPA alone in initial hospital costs.<sup>13</sup> By 90 days, this difference had shrunk to \$12,000 because of an average of \$5000 saved in the combination therapy cohort through earlier hospital discharge and reduced rehabilitation costs. When lifetime projections were incorporated, however, mechanical thrombectomy was economically dominant, with substantial overall cost savings of more than \$23,000 and both life-expectancy and quality-adjusted life expectancy gains.<sup>13</sup> Effort to reduce the initial cost of thrombectomy treatment will further cement this economic dominance. The direct cost of IV tPA in the United States approximates \$7000/100-mg vial. This reflects only the actual price of the drug and not the additional ancillary expenses of delivering it. This expense represents an area of potential savings for patients treated with combination therapy. Indeed, the questions may well be more nuanced than “Does tPA provide any value?” It may be more appropriate to ask, “In select patients, does IV tPA provide \$7000 worth of value?”

A similar outcome at reduced cost improves value. Therefore, the concern that IV tPA adds little benefit to the patient with LVO should be evaluated in a randomized fashion. The RCT design would be pragmatic: direct to thrombectomy versus combination therapy in patients presenting early to centers with neuroendovascular capability. This would have important implications for future stroke treatment as episodic care, alternative payment, and physician-focused payment models grow increasingly important. Several trials have been proposed, and while published protocols are lacking, these trials are close to commencing.

The implications of a randomized trial proving that the addition of IV tPA carries no additional benefit for selected patients will be momentous. Resistance may be anticipated, but a well-designed trial would win over many in the stroke neurology community, overcoming the ethics of withholding a proved treatment. A particular concern will be to prevent undue interruption of current tPA delivery networks, which must be protected for the general stroke population. A randomized trial will raise these and more questions. The stroke community should embrace the opportunity.

Disclosures: Joshua A. Hirsch—UNRELATED: Consultancy: Medtronic, Codman Neurovascular, CareFusion, Globus, Comments: Medtronic, ongoing spine; Codman Neurovascular, ongoing Data and Safety Monitoring Board; CareFusion, taught spine-related procedures in a single educational event; Globus, single consulting event.

### REFERENCES

1. Berkhemer OA, Fransen PS, Beumer D, et al. **A randomized trial of intraarterial treatment for acute ischemic stroke.** *N Engl J Med* 2015; 372:11–20 CrossRef Medline
2. Campbell BC, Mitchell PJ, Kleinig TJ, et al; EXTEND-IA Investigators. **Endovascular therapy for ischemic stroke with perfusion-imaging selection.** *N Engl J Med* 2015;372:1009–18 CrossRef Medline
3. Goyal M, Demchuk AM, Menon BK, et al; ESCAPE Trial Investigators. **Randomized assessment of rapid endovascular treatment of ischemic stroke.** *N Engl J Med* 2015;372:1019–30 CrossRef Medline
4. Jovin TG, Chamorro A, Cobo E, et al; REVASCAT Trial Investigators. **Thrombectomy within 8 hours after symptom onset in ischemic stroke.** *N Engl J Med* 2015;372:2296–306 CrossRef Medline
5. Saver JL, Goyal M, Bonafe A, et al; SWIFT PRIME Investigators. **Stent-retriever thrombectomy after intravenous t-PA vs. t-PA alone in stroke.** *N Engl J Med* 2015;372:2285–95 CrossRef Medline
6. Goyal M, Menon BK, van Zwam WH, et al; HERMES collaborators. **Endovascular thrombectomy after large-vessel ischaemic stroke: a meta-analysis of individual patient data from five randomised trials.** *Lancet* 2016;387:1723–31 CrossRef Medline
7. Bracard S, Ducrocq X, Mas JL, et al; THRACE investigators. **Mechanical thrombectomy after intravenous alteplase versus alteplase alone after stroke (THRACE): a randomised controlled trial.** *Lancet Neurol* 2016;15:1138–47 CrossRef Medline
8. Weber R, Nordmeyer H, Hadisurya J, et al. **Comparison of outcome and interventional complication rate in patients with acute stroke treated with mechanical thrombectomy with and without bridging thrombolysis.** *J Neurointerv Surg* 2017;9: 229–33 CrossRef Medline
9. Broeg-Morvay A, Mordasini P, Bernasconi C, et al. **Direct mechanical intervention versus combined intravenous and mechanical intervention in large artery anterior circulation stroke: a matched-pairs analysis.** *Stroke* 2016;47:1037–44 CrossRef Medline
10. Coutinho JM, Liebeskind DS, Slater LA, et al. **Combined intravenous thrombolysis and thrombectomy vs thrombectomy alone for acute**

- ischemic stroke: a pooled analysis of the SWIFT and STAR studies. *JAMA Neurol* 2017;74:268–74 CrossRef Medline
11. Chandra RV, Leslie-Mazwi TM, Mehta BP, et al. **Does the use of IV tPA in the current era of rapid and predictable recanalization by mechanical embolectomy represent good value?** *J Neurointerv Surg* 2016;8:443–46 CrossRef Medline
  12. Hirsch JA, Harvey HB, Barr RM, et al. **Sustainable growth rate re-pealed, MACRA revealed: historical context and analysis of recent changes in Medicare physician payment methodologies.** *AJNR Am J Neuroradiol* 2016;37:210–14 CrossRef Medline
  13. Shireman TI, Wang K, Saver JL, et al; SWIFT-PRIME Investigators. **Cost-effectiveness of Solitaire stent retriever thrombectomy for acute ischemic stroke: results from the SWIFT-PRIME trial (Solitaire With the Intention for Thrombectomy as Primary Endovascular Treatment for Acute Ischemic Stroke).** *Stroke* 2017;48:379–87 CrossRef Medline

# Dentate Update: Imaging Features of Entities That Affect the Dentate Nucleus

 K.M. Bond,  W. Brinjikji,  L.J. Eckel,  D.F. Kallmes,  R.J. McDonald, and  C.M. Carr



## ABSTRACT

**SUMMARY:** The dentate nucleus is a cerebellar structure involved in voluntary motor function and cognition. There are relatively few entities that affect the dentate, and the clinical features of these conditions are often complex and nonspecific. Because these entities are rarely encountered, the formulation of a differential diagnosis can be difficult. Many of the conditions are reversible or treatable with early intervention. Therefore, it is important to recognize classic clinical presentations and their associated characteristic imaging findings. We provide a summary of entities that affect the dentate nucleus and a diagnostic workflow for approaching dentate nucleus imaging abnormalities.

**ABBREVIATION:** Gd<sup>3+</sup> = free gadolinium

The deep cerebellar nuclei are key structures of the cerebrocerebellar circuitry that relay output from the cerebellar cortex to supratentorial cortical and subcortical targets. The dentate nucleus is the largest of the deep cerebellar nuclei, and it is involved in planning, initiating, and modifying voluntary movements as well as cognition. Because it is buried deep within cerebellar white matter, the dentate is uncommonly lesioned as a result of trauma or surgical interventions. However, a few entities specifically involve the dentate nuclei. Many of the conditions that affect the dentate are medically manageable, and prognoses can be favorable with early intervention. Despite the fact that they are rare entities, knowing the characteristic imaging findings for these conditions will allow the formulation of an appropriate differential diagnosis of dentate nucleus abnormalities and will assist in making a timely diagnosis. In this article, we review the clinical presentations and imaging features of many of the most common entities that involve the dentate. We also provide a summary of major inherited conditions and their presentations (On-line Table) and a diagnostic approach for evaluating dentate nucleus abnormalities (Fig 1).

## Normal Anatomy and Function of the Dentate

The dentate nucleus is the largest and most lateral of the 4 deep cerebellar nuclei (Fig 2). The emboliform and globose nuclei, collectively referred to as the interposed nuclei, are positioned more medially, and the fastigial nucleus lies adjacent to the midline. The dentate nucleus is located within the cerebellar white matter and is directly adjacent to the vermis and the roof of the fourth ventricle bilaterally.<sup>1,2</sup> While the dentate is classically known to be involved in planning and executing voluntary movements, it has also been implicated in higher level cognition and sensory processing.<sup>3-5</sup> It contains anatomically separate domains that mediate these motor and nonmotor functions.<sup>6,7</sup>

The dentate receives ascending projections from the spinocerebellar tract via the inferior cerebellar peduncle, which convey proprioceptive information about the length and tension of muscle fibers. It also receives descending projections from the premotor and supplementary motor cortices, which are involved in planning and initiating voluntary movements.<sup>2</sup> By integrating these 2 inputs, the dentate is able to compare intended movement with muscle feedback to maintain equilibrium and balance. Its efferent projections travel through the superior cerebellar peduncle and red nucleus to the ventrolateral thalamus, where it is involved in timing and fine-tuning voluntary movements.<sup>8</sup>

It is 1 of 3 interconnected structures collectively referred to as the myoclonic triangle or the triangle of Guillain-Mollaret. This triangular circuit comprises the red nucleus, the inferior olivary nucleus, and the dentate nucleus.<sup>9,10</sup> Parvocellular red nucleus fibers project to the ipsilateral inferior olivary nucleus by way of the central tegmental tract. Efferents of the inferior olivary nu-

From Mayo Clinic School of Medicine (K.M.B.) and the Department of Radiology (W.B., L.J.E., D.F.K., R.J.M., C.M.C.), Mayo Clinic, Rochester, Minnesota.

Please address correspondence to Carrie M. Carr, MD, Department of Radiology, Mayo Clinic, 200 First St SW, Rochester MN 55905; e-mail: carr.carrie@mayo.edu

 Indicates open access to non-subscribers at [www.ajnr.org](http://www.ajnr.org)

 Indicates article with supplemental on-line table.

<http://dx.doi.org/10.3174/ajnr.A5138>

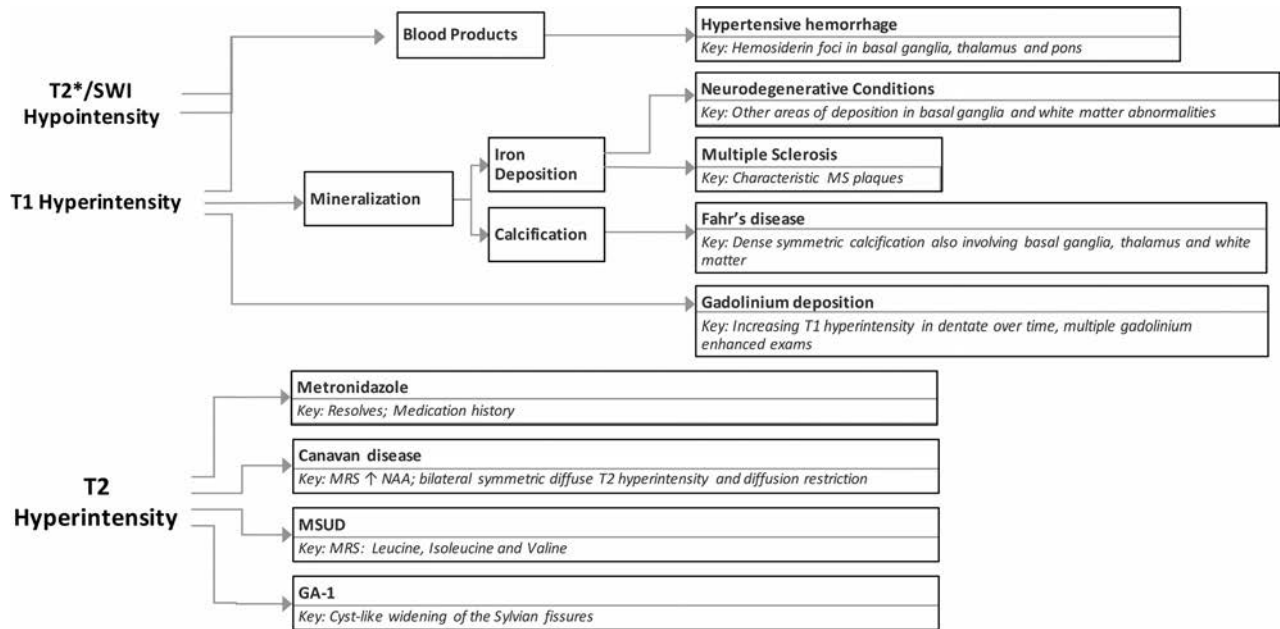


**FIG 1.** Diagnostic approach for dentate nucleus imaging abnormalities.

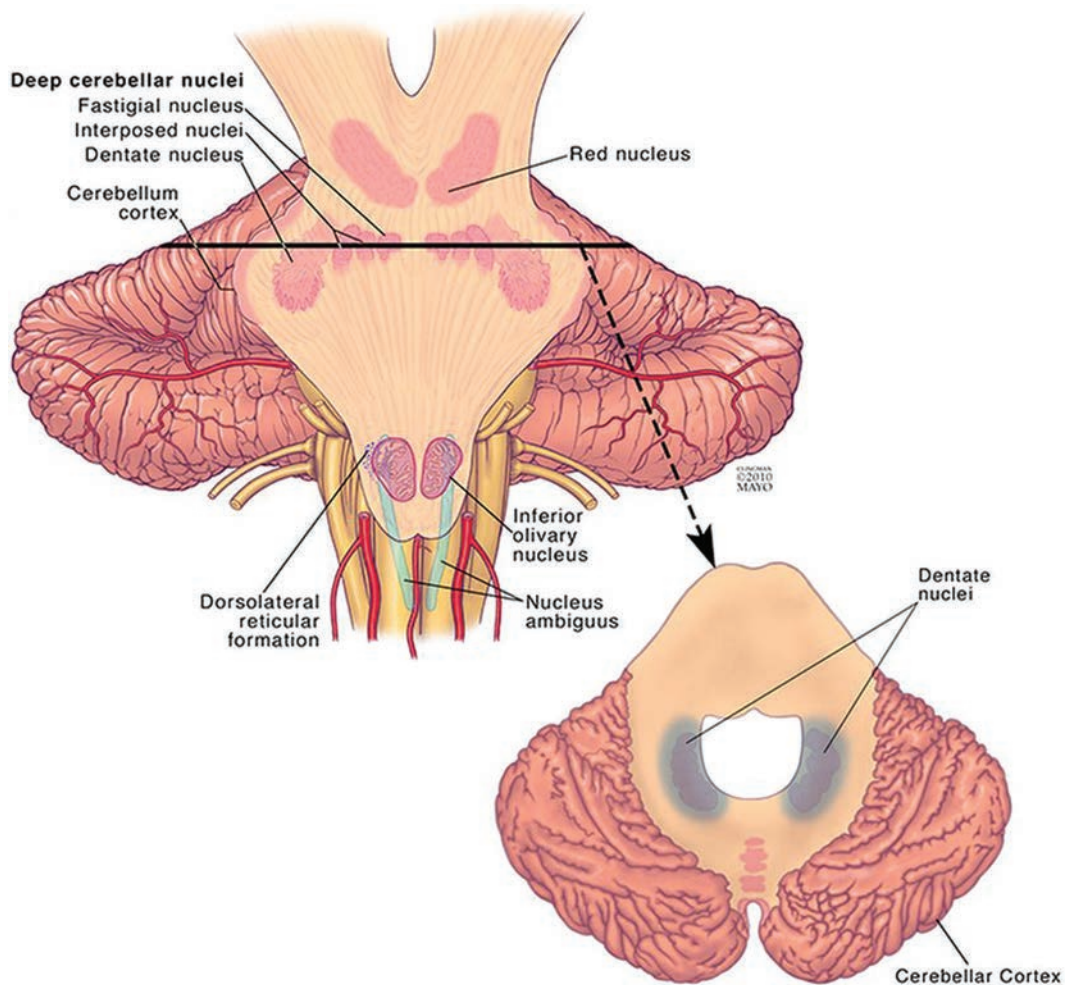


**FIG 2.** Illustration of the location of the dentate nucleus within the cerebellum. Used with permission of Mayo Foundation for Medical Education and Research, all rights reserved.

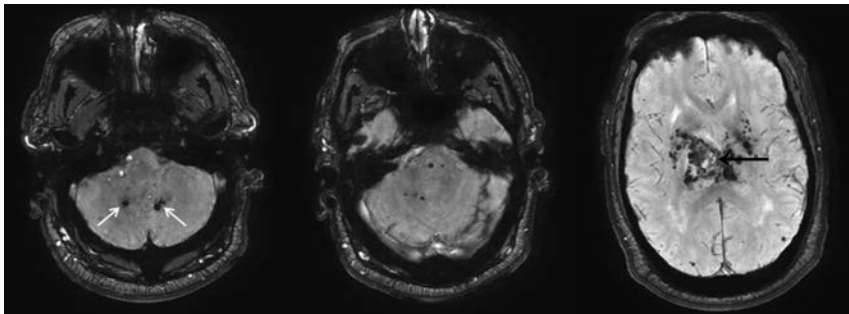


**FIG 3.** Hypertensive hemorrhage. A 55-year-old man who presented with a thalamic hemorrhage. Three selected images from 3D susceptibility-weighted imaging demonstrate microhemorrhages and hemosiderin deposition within the dentate nuclei (*white arrows*), brain stem, thalamus, and basal ganglia. The sentinel bleed is shown with *black arrows*. This distribution is characteristic of hypertensive microhemorrhages. The patient was being treated with multiple medications to control his hypertension, which remained elevated even during his hospitalization.

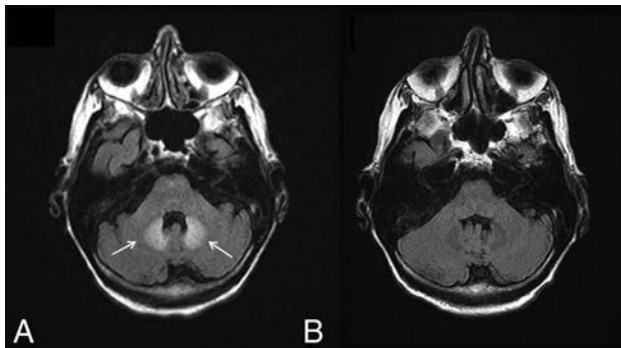


**FIG 4.** Metronidazole toxicity. A 74-year-old woman was treated for 6 weeks with metronidazole and developed dysarthria. T2 FLAIR images demonstrate T2 hyperintensity within the dentate nuclei (*A, arrows*), which resolved on MR imaging 1 month later (*B*).

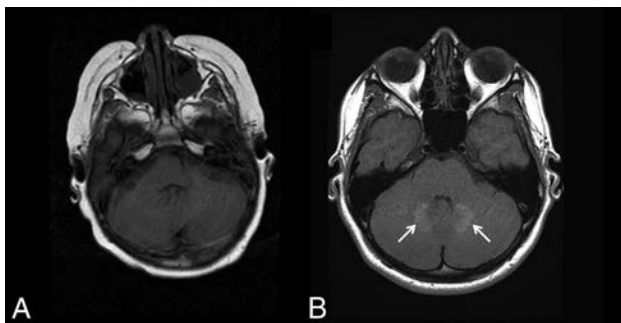


**FIG 5.** Gadolinium deposition. A 13-year-old boy was diagnosed with a pilocytic astrocytoma and treated with chemotherapy, but no radiation. *A*, the first available pre-gadolinium T1WI without any abnormality in the dentate. *B*, A follow-up examination performed 10 years later now demonstrates T1 hyperintensity on T1WI within the dentate nuclei (*arrows*). The patient had undergone 37 gadolinium-enhanced examinations at this time point.

cleus travel through the inferior cerebellar peduncle to the contralateral dentate nucleus. The dentate nucleus sends inhibitory GABAergic fibers through the superior cerebellar peduncle to the contralateral red nucleus, completing the triangular circuit.<sup>11</sup> Together, these structures control fine voluntary movement. Disruptions in the circuit that disinhibit the inferior olivary nucleus give rise to hypertrophic olivary degeneration, which can result in the clinical syndrome of palatal tremor.<sup>9</sup>

### Entities Involving the Dentate Nuclei

**Hypertensive Hemorrhages.** Long-standing hypertension is associated with the formation and rupture of Charcot-Bouchard microaneurysms in small penetrating blood vessels of the cerebral circulation.<sup>12</sup> Intracerebral hemorrhage is characterized by sudden onset of a focal neurologic deficit and may be associated with headache, altered consciousness, nausea, and vomiting. Cerebellar hypertensive hemorrhage is typically caused by rupture of the perforating arteries of the superior cerebellar artery. The most common symptoms of cerebellar hemorrhage are ataxia, vertigo, severe nausea, and vomiting.

Bleeding often begins in the dentate nucleus and spreads throughout the ipsilateral hemisphere to include the cerebellar peduncles and fourth ventricle.<sup>13</sup> There is a potential for the hemorrhage to extend through the vermis to the contralateral hemisphere.

As with all hemorrhages, CT can be used to quickly identify acute bleeding. On MR imaging, T2\* sequences are key to identifying areas of prior microhemorrhage and hemosiderin deposition. These T2\* hypointense microhemorrhages are characteristically concentrated in the dentate, basal ganglia, thalamus, and pons (Fig 3).<sup>14</sup>

**Transient Edema from Metronidazole.** Metronidazole is an antibiotic indicated in the treatment of a variety of bacterial and protozoan infections. While it is generally a safe medication, it crosses the blood-brain barrier and can cause serious neurologic side effects at high doses and with prolonged use. Symptoms of metronidazole toxicity include ataxia, encephalopathy, peripheral neuropathy, and seizures.<sup>15</sup> Symptoms often resolve completely following metronidazole discontinuation.

There have been reports of bilateral signal changes in the supratentorial white matter and the dentate nucleus (Fig 4) following the initiation of metronidazole therapy, both at doses within and above the recommended range.<sup>16-18</sup> These lesions are symmetric and hyperintense on T2WI and can demonstrate associated restricted diffusion. Like the symptoms associated with metronidazole toxicity, edema is reversible and imaging studies return to baseline within a few weeks of metronidazole discontinuation.<sup>18</sup>

**Gadolinium Deposition.** Gadolinium-based contrast agents are frequently used in imaging studies. Because free gadolinium ( $Gd^{3+}$ ) is a cytotoxic element, it must be bound to a chelator that is eliminated by renal excretion when given as a contrast agent. From a safety standpoint, it is imperative that the gadolinium-chelator bond remain stable to ensure that free gadolinium is not deposited in tissues. However,  $Gd^{3+}$  deposition has been found in the bones of patients and animals with normal renal function following gadolinium-based contrast exposure.<sup>19</sup>

The dentate nucleus and globus pallidus have also shown high signal intensity on unenhanced T1-weighted MR imaging following multiple contrast imaging studies.<sup>20-22</sup> The number of previous contrast administrations is positively correlated with abnormal signal intensity.<sup>20</sup> Recently, it has been confirmed that the high T1 signal in the dentate nucleus (Fig 5) and globus pallidus is

due to  $Gd^{3+}$  deposition.<sup>23</sup> The mechanism by which  $Gd^{3+}$  deposits preferentially in the dentate is not known, and to date, there have been no studies linking  $Gd^{3+}$  deposition to deficits in neurocognitive function or movement disorders.<sup>24</sup>

**Multiple Sclerosis.** Multiple sclerosis is an autoimmune disease of the central nervous system that affects 90 in every 100,000 individuals in the United States, with a higher prevalence in women.<sup>25</sup> It is characterized by a cell-mediated autoimmune response against oligodendrocyte components, leading to demyelination and axonal degeneration in the brain and spinal cord. Although MS is classically known to be a disease of white matter, substantial damage and volume loss of gray matter structures can be present.<sup>26-28</sup>

Prior studies have demonstrated high intrinsic T1 signal in the dentate nuclei of patients with MS. However, patients with MS tend to undergo multiple contrast-enhanced MRIs for both diag-

nosis and disease surveillance. Thus, the T1-weighted hyperintensity seen in the dentate nucleus in patients with MS may be a result of their large cumulative gadolinium load rather than a manifestation of their disease. Lesions demonstrating T1 hyperintensity and T2 hypointensity in deep gray matter structures, including the dentate nucleus, thalamus, striatum, and globus pallidus, can be present as well. Such lesions have been attributed to abnormal deposition of nonheme iron and evidence of MS progression.<sup>29-31</sup> It is possible that iron deposition is a by-product of neural degeneration rather than a true marker of MS progression. However, treatment with natalizumab decreases the rate of iron deposition in patients with MS, suggesting that MS-mediated inflammatory processes contribute to the phenomenon.<sup>32,33</sup> Future studies would be needed to determine whether gadolinium or iron deposition is responsible for signal changes in the dentate of these patients.

**Iron Deposition in Neurodegenerative Conditions.** There are 10 inherited neurodegenerative diseases that are characterized by iron accumulation in the basal ganglia, substantia nigra, and deep cerebellar nuclei. These rare diseases are collectively referred to as neurodegeneration with brain iron accumulation, and their combined incidence is estimated to be <1 in 1,000,000.<sup>34</sup> Their etiologies are heterogeneous and related to defects in iron metabolism and homeostasis, cell membrane integrity, and myelin synthesis.<sup>35</sup> The clinical symptoms of neurodegeneration with brain iron accumulation depend on which structures are involved, but many present with extrapyramidal abnormalities and cognitive dysfunction during young adulthood.<sup>34</sup> All neurodegeneration with brain iron accumulation subtypes are progressive, and treatment consists of symptom management because there are currently no cures for the underlying disorders.

The iron deposition is best visualized on 3D susceptibility-weighted imaging as symmetric hypointensity in the affected structures. Woodhouse-Sakati syndrome is a neurodegeneration with brain iron accumulation subtype characterized by iron deposition in the globus pallidus and dentate as well as white matter abnormalities (Fig 6).

**Fahr Disease.** Fahr disease is a rare, autosomal dominant disorder that affects <1 per 1,000,000 individuals.<sup>36</sup> It most often presents in the fourth or fifth decade of life, with progressive extrapyramidal and neuropsychiatric symptoms such as spasticity, athetosis, dysarthria, and dementia.<sup>36</sup> While the molecular underpinnings of Fahr disease are not well-elucidated, it has been associated with a number of endocrine disorders that affect circulating calcium levels. Treatment currently aims to alleviate symptoms and manage any co-existing hormone imbalances.

Fahr disease is characterized by idiopathic calcification of the basal ganglia and other brain regions involved in motor control, including the dentate nucleus (Fig 7) and thalamus.<sup>37-39</sup> This en-

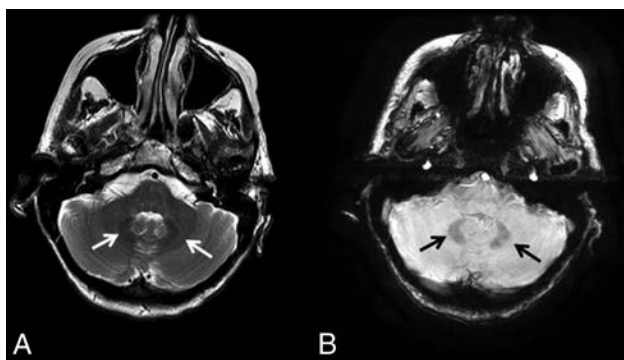


**FIG 6.** Neurodegeneration with brain iron accumulation. A 40-year-old woman with Woodhouse-Sakati syndrome found to have neurodegenerative iron accumulation. Marked hypointensity within the dentate on T2WI (A, white arrows) and 3D SWI (B, black arrows) is consistent with iron deposition.

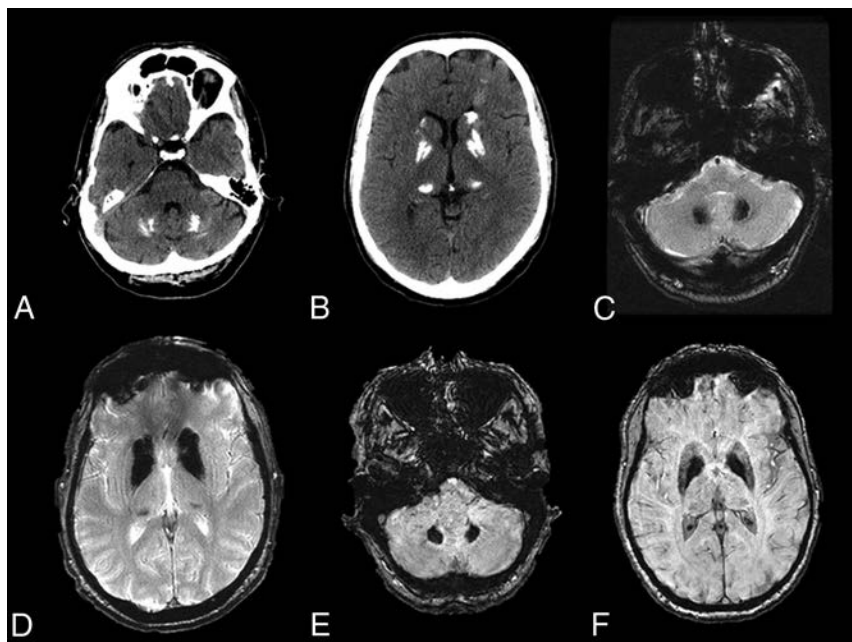


**FIG 7.** Fahr disease. A–D, CT and T2\* gradient recalled-echo images from a 49-year-old patient with Fahr disease demonstrate dense calcification of the dentate nuclei and basal ganglia. E and F, Dense calcification within the dentate nuclei and basal ganglia is also well-demonstrated on susceptibility-weighted imaging, in this case from a 68-year-old affected woman.

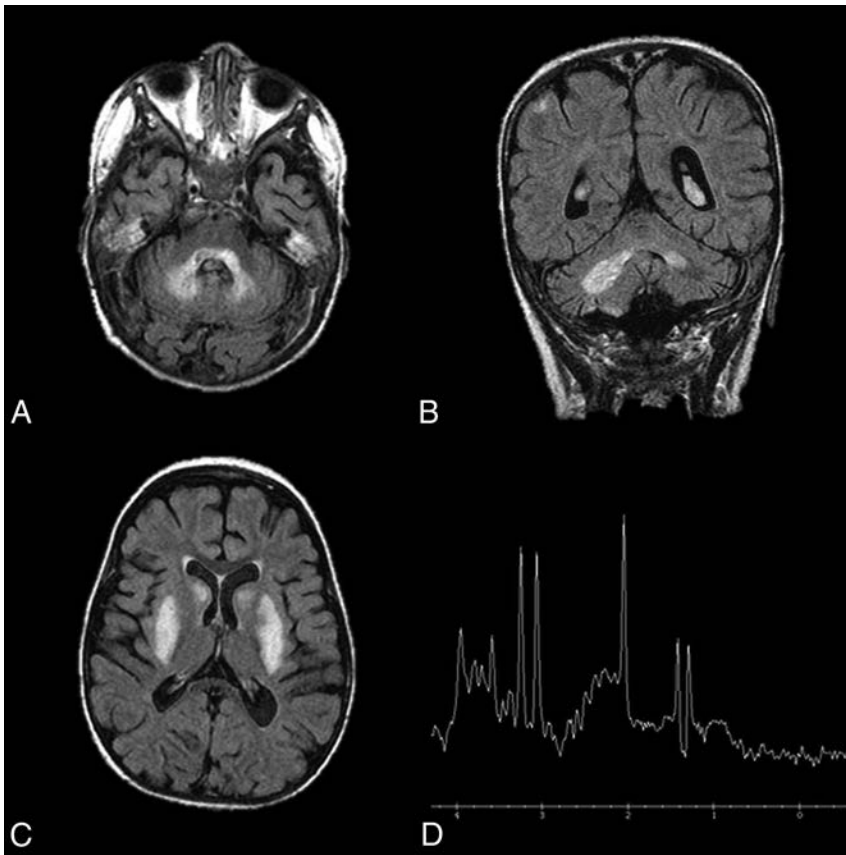


**FIG 8.** Leigh disease. An 11-year-old girl diagnosed at 2 years of age with Leigh disease. Marked T2 hyperintensity on FLAIR within the dentate nuclei (A and B) and basal ganglia (C). MR spectroscopy with voxel sampling of the basal ganglia (D) demonstrates a prominent lactate doublet (at 1.3 ppm) and elevated choline (at 3.2 ppm).

tity has a characteristic appearance on CT of dense, symmetric calcification most commonly in the basal ganglia, but also within the dentate nucleus, thalamus, and subcortical white matter.<sup>38</sup> The globus pallidus is typically the first structure to be affected.<sup>36</sup> There is no correlation between the degree of calcification and the severity of symptoms. On MR imaging, these areas of calcification can have variable T1 and T2 signal intensities that relate to the stage of disease, the degree of calcium deposition, and variance in calcium metabolism. In general, these areas will be markedly hypointense on T2\*-based imaging and hypointense on T2WI and have hyperintense regions on T1WI.<sup>40</sup> In addition, MR imaging can depict associated inflammatory changes that can later calcify and may be responsible for current symptoms.<sup>39</sup>

**Leigh Syndrome.** Leigh syndrome, or subacute necrotizing encephalomyelopathy, is a rare mitochondrial disease that affects 1 in 50,000 neonates.<sup>41</sup> It is most commonly associated with a mutation in *SURF1*, a gene necessary for cytochrome C oxidase assembly and a functional mitochondrial respiratory chain.<sup>42</sup> Early signs of the disease usually present within the first year of life, though it can have a late onset in adolescents and adults.<sup>43</sup> Infants typically present with developmental delay or regression.<sup>43,44</sup> Other signs may include seizures, dysphagia, ophthalmoparesis, nystagmus, dystonia, and ataxia. The prognosis is poor, and affected children are expected to live for only a few months after

diagnosis.<sup>43,44</sup> There is no cure for Leigh disease, and treatment is targeted at symptom management.

Leigh disease characteristically presents on imaging as symmetric T2 hyperintensity (Fig 8) and restricted diffusion of the dentate nuclei, basal ganglia, thalamus, periaqueductal gray, substantia nigra, pons, and medulla.<sup>43,45,46</sup> White matter is typically spared. The T2 hyperintensities and T1 hypointensities on MR imaging are reflective of vacuolation and spongiform changes.<sup>46</sup> MR spectroscopy may demonstrate high levels of choline and lactate. Evidence of global atrophy can be seen as the disease progresses.<sup>46</sup>

**Friedreich Ataxia.** Friedreich ataxia is an autosomal recessive disease that affects approximately 2 in every 100,000 people.<sup>47</sup> It is the most common type of inherited ataxia. Clinical presentation is variable because the disease has a variety of manifestations in the central and peripheral nervous system, heart, pancreas, and skeletal muscle. Friedreich ataxia typically presents during childhood and progresses with time, though there have been reports of onset as late as 75 years of age.<sup>47</sup> The most common presenting symptom is progressive gait ataxia. Care is targeted at managing symptoms and addressing cardiac or endocrine manifestations of the disease.

The most common primary sites of pathologic changes in patients with Friedreich ataxia are the spinal cord and peripheral nerves.<sup>48</sup> Thus, MR imaging consistently demonstrates atrophy of the cervical spine.<sup>49</sup> Friedreich ataxia is also associated with selective atrophy of large neurons of the dentate nucleus with sparing of small neurons.<sup>50-52</sup> It is unclear whether the high concentration of iron in the dentate nucleus makes it particularly susceptible to disease-mediated degeneration because other iron-rich structures, such as the substantia nigra, red nucleus, and globus pallidus, are spared.<sup>50</sup> Wallerian degeneration of the superior cerebellar peduncle is supportive of a diagnosis of Friedreich ataxia because the efferent fibers of the dentate are carried by this tract. However, involvement of these nuclei and tracts is typically not visible with conventional imaging sequences. Diffusion-weighted and diffusion tensor imaging have been used to detect these changes that are not readily apparent.<sup>53</sup>

**Canavan Disease.** Canavan disease, or spongiform leukodystrophy, is an autosomal recessive disorder. The incidence of Canavan disease is estimated to be <1:100,000 in the general population and between 1:6000 and 1:14,000 in the Ashkenazi Jewish population.<sup>54,55</sup> A mutation in the *ASPA* gene causes a deficiency of aspartoacylase, resulting in a buildup of NAA, which impedes the production of new myelin and causes progressive damage to existing myelin.<sup>56,57</sup> At postmortem examination, the white matter

of brains with Canavan disease is described as edematous, gelatinous, and vacuolated, and these changes can be seen with imaging.<sup>58</sup> Symptoms present within the first 3–6 months of life and prognosis is poor, with most affected children dying before 5 years of age.<sup>57</sup> Treatment consists of symptom management and supportive care.

Diffuse cerebral atrophy and extensive white matter changes are characteristic of Canavan disease. The peripheral white matter is affected preferentially in the early stages of the disease.<sup>59</sup> As the disease progresses, the globus pallidus is often atrophied, with sparing of the putamen.<sup>58,60</sup> MR spectroscopy can be helpful in detecting elevated NAA ratios.<sup>59,61</sup> There is variable involvement of the dentate, thalamus, brain stem, and dorsal pons. MR imaging is most helpful for evaluating the extensive white matter involvement characterized by bilaterally symmetric diffuse T2 hyperintensity and diffusion restriction.<sup>58,60</sup>

**Glutaric Aciduria Type 1.** Glutaric aciduria type 1 is a rare autosomal recessive disorder that is estimated to affect 1 in every 100,000 neonates.<sup>62</sup> In glutaric aciduria type 1, glutaric acid and 3-hydroxyglutaric acid accumulation causes neuronal hypoplasia. Glutaric aciduria type 1 usually has no signs or symptoms in the first few months of life except for microencephalic macrocephaly.<sup>63</sup> Acute decompensation and rapid neurologic deterioration often occur following a febrile illness between 6 and 18 months of age. Symptoms include hypotonia, spasticity, dysphagia, and an increased propensity for bleeding.<sup>64</sup> Chronic treatment involves a low lysine diet and carnitine supplementation. Many patients survive to adulthood with marked motor and coordination disability.

Even before the acute decompensation stage, patients with glutaric aciduria type 1 almost invariably have bilateral, cystlike widening of the Sylvian fissures and mesencephalic cistern, with atrophy of the frontotemporal cortices.<sup>63,65</sup> During and after an acute decompensation event, T2-weighted hyperintensity on MR imaging and diffusion restriction on DWI are seen in the dentate nucleus, basal ganglia, periventricular white matter, and pontine medial lemniscus.<sup>65</sup> These changes represent demyelination and edema following toxic metabolic by-product buildup. Subdural hemorrhage and hygroma can present following minor head trauma because these patients have a propensity for tearing bridging veins and arachnoid membrane fenestrations.<sup>66</sup>

**Maple Syrup Urine Disease.** Maple syrup urine disease is an autosomal recessive disorder that has been estimated to affect 1 in 185,000 neonates worldwide.<sup>67</sup> Mutations in the genes that encode for the branched-chain  $\alpha$ -keto acid dehydrogenase complex cause a defect in the catabolism of leucine, isoleucine, and valine. If left untreated, buildup of these branched-chain amino acids and their ketoacidotic by-products can lead to rapid neurologic decline, coma, and death. With the adoption of neonate screening for maple syrup urine disease, prognosis is good in the modern world.

Untreated patients with maple syrup urine disease show no abnormalities on CT or MR imaging during their asymptomatic first few days of life.<sup>68</sup> The 4 deep cerebellar nuclei, dorsal brain stem, cerebral peduncles, and posterior limb of the internal capsule become severely edematous about 1 week after birth at the

onset of symptoms.<sup>69</sup> Generalized edema of the brain is often superimposed on these severe, localized changes. DWI will demonstrate markedly restricted diffusion within the affected structures.<sup>69</sup> MR spectroscopy can demonstrate abnormal peaks corresponding to increased levels of leucine, isoleucine, and valine. Edema can persist for up to 7 weeks, even if treatment is initiated promptly after the onset of symptoms. If maple syrup urine disease is treated and edema subsides, MR imaging and DWI findings rarely return to normal. Residual abnormalities include diffuse atrophy, dysmyelination, and demarcated lesions in the dentate nuclei, hypothalamus, and cerebral white matter. MR spectroscopy may show decreased, but still abnormally high, peaks corresponding to the branched-chain amino acids.<sup>69</sup>

### **Clues from Commonalities and Avenues for Future Research**

The dentate nucleus is particularly susceptible to insults, whether demyelination, mineral deposition, or metabolic by-product buildup. The 3 other deep cerebellar nuclei and other deep gray matter structures are, for unclear reasons, often spared in these conditions. It may be that the dentate has innate biologic and metabolic characteristics that allow pathologic processes to preferentially affect it. The neurologic and pathologic effects of dentate involvement in the above-mentioned diseases have not been well-studied. Future studies examining disease-associated histopathologic changes, imaging characteristics, and natural history are needed to better characterize the pathophysiology and consequences of disease involvement of the dentate.

### **CONCLUSIONS**

Relatively few inheritable diseases and pathologic processes affect the dentate nucleus. A summary of these diseases, their classic clinical presentations, and their radiographic features are provided in the On-line Table. The symptoms associated with these conditions can be nonspecific and complex, but the use of imaging can aid in narrowing wide differential diagnoses. Because some of these conditions are reversible or medically manageable if the diagnosis is made early enough, it is important to have a diagnostic approach for evaluating imaging features of the dentate (Fig 1).

Disclosures: David F. Kallmes—UNRELATED: Grants/Grants Pending: GE Healthcare, Comments: preclinical research support.\* \*Money paid to the institution.

### **REFERENCES**

1. Rhoton AL Jr. **Cerebellum and fourth ventricle.** *Neurosurgery* 2000; 47:S7–27 CrossRef Medline
2. Akakin A, Peris-Celda M, Kilic T, et al. **The dentate nucleus and its projection system in the human cerebellum: the dentate nucleus microsurgical anatomical study.** *Neurosurgery* 2014;74:401–24; discussion 424–25 CrossRef Medline
3. O'Halloran CJ, Kinsella GJ, Storey E. **The cerebellum and neuropsychological functioning: a critical review.** *J Clin Exp Neuropsychol* 2012;34:35–56 CrossRef Medline
4. Schmahmann JD, Sherman JC. **The cerebellar cognitive affective syndrome.** *Brain* 1998;121(pt 4):561–79 CrossRef Medline
5. Timmann D, Dreyer J, Frings M, et al. **The human cerebellum contributes to motor, emotional and cognitive associative learning: a review.** *Cortex* 2010;46:845–57 CrossRef Medline
6. Salamon N, Sicotte N, Drain A, et al. **White matter fiber tractography**

- and color mapping of the normal human cerebellum with diffusion tensor imaging. *J Neuroradiol* 2007;34:115–28 CrossRef Medline
7. Suzuki L, Coulon P, Sabel-Goedknecht EH, et al. **Organization of cerebral projections to identified cerebellar zones in the posterior cerebellum of the rat.** *J Neurosci* 2012;32:10854–69 CrossRef Medline
  8. Hoover JE, Strick PL. **The organization of cerebellar and basal ganglia outputs to primary motor cortex as revealed by retrograde transneuronal transport of herpes simplex virus type I.** *J Neurosci* 1999;19:1446–63 Medline
  9. Guillan G, Mollaret P. **Two cases of synchronous and rhythmical velopharyngo-laryngo-oculo-diaphragmatic myoclonus: the anatomical and physiopathological problem of this syndrome.** *Rev Neurol* 1931;2:545–66
  10. Murdoch S, Shah P, Jampana R. **The Guillain-Mollaret triangle in action.** *Pract Neurol* 2016;16:243–46 CrossRef Medline
  11. Shaikh AG, Hong S, Liao K, et al. **Oculopalatal tremor explained by a model of inferior olivary hypertrophy and cerebellar plasticity.** *Brain* 2010;133:923–40 CrossRef Medline
  12. Wakai S, Nagai M. **Histological verification of microaneurysms as a cause of cerebral-hemorrhage in surgical specimens.** *J Neurol Neurosurg Psychiatry* 1989;52:595–99 CrossRef Medline
  13. Kanno T, Sano H, Shinomiya Y, et al. **Role of surgery in hypertensive intracerebral hematoma: a comparative study of 305 nonsurgical and 154 surgical cases.** *J Neurosurg* 1984;61:1091–99 CrossRef Medline
  14. Fazekas F, Kleinert R, Roob G, et al. **Histopathologic analysis of foci of signal loss on gradient-echo T2\*-weighted MR images in patients with spontaneous intracerebral hemorrhage: evidence of microangiopathy-related microbleeds.** *AJNR Am J Neuroradiol* 1999;20:637–42 Medline
  15. Frytak S, Moertel CH, Childs DS. **Neurologic toxicity associated with high-dose metronidazole therapy.** *Ann Intern Med* 1978;88:361–62 CrossRef Medline
  16. Ahmed A, Loes DJ, Bressler EL. **Reversible magnetic resonance imaging findings in metronidazole-induced encephalopathy.** *Neurology* 1995;45:588–89 CrossRef Medline
  17. Horlen CK, Seifert CF, Malouf CS. **Toxic metronidazole-induced MRI changes.** *Ann Pharmacother* 2000;34:1273–75 CrossRef Medline
  18. Woodruff BK, Wijidicks EF, Marshall WF. **Reversible metronidazole-induced lesions of the cerebellar dentate nuclei.** *N Engl J Med* 2002;346:68–69 CrossRef Medline
  19. White GW, Gibby WA, Tweedle MF. **Comparison of Gd(DTPA-BMA) (Omniscan) versus Gd(HP-DO3A) (ProHance) relative to gadolinium retention in human bone tissue by inductively coupled plasma mass spectroscopy.** *Invest Radiol* 2006;41:272–78 CrossRef Medline
  20. Kanda T, Ishii K, Kawaguchi H, et al. **High signal intensity in the dentate nucleus and globus pallidus on unenhanced T1-weighted MR images: relationship with increasing cumulative dose of a gadolinium-based contrast material.** *Radiology* 2014;270:834–41 CrossRef Medline
  21. Radbruch A, Weberling LD, Kieslich PJ, et al. **Gadolinium retention in the dentate nucleus and globus pallidus is dependent on the class of contrast agent.** *Radiology* 2015;275:783–91 CrossRef Medline
  22. Stojanov D, Aracki-Trenkic A, Benedeto-Stojanov D. **Gadolinium deposition within the dentate nucleus and globus pallidus after repeated administrations of gadolinium-based contrast agents-current status.** *Neuroradiology* 2016;58:433–41 CrossRef Medline
  23. McDonald RJ, McDonald JS, Kallmes DF, et al. **Intracranial gadolinium deposition after contrast-enhanced MR imaging.** *Radiology* 2015;275:772–82 CrossRef Medline
  24. Welk B, McArthur E, Morrow SA, et al. **Association between gadolinium contrast exposure and the risk of parkinsonism.** *JAMA* 2016;316:96–98 CrossRef Medline
  25. Noseworthy JH, Lucchinetti C, Rodriguez M, et al. **Multiple sclerosis.** *N Engl J Med* 2000;343:938–52 CrossRef Medline
  26. Anderson VM, Fisniku LK, Altmann DR, et al. **MRI measures show significant cerebellar gray matter volume loss in multiple sclerosis and are associated with cerebellar dysfunction.** *Mult Scler* 2009;15:811–17 CrossRef Medline
  27. Fisher E, Lee JC, Nakamura K, et al. **Gray matter atrophy in multiple sclerosis: a longitudinal study.** *Ann Neurol* 2008;64:255–65 CrossRef Medline
  28. Gilmore CP, Geurts JJ, Evangelou N, et al. **Spinal cord grey matter lesions in multiple sclerosis detected by post-mortem high field MR imaging.** *Mult Scler* 2009;15:180–88 Medline
  29. Du SL, Sah SK, Zeng C, et al. **Iron deposition in the gray matter in patients with relapse-remitting multiple sclerosis: a longitudinal study using three-dimensional (3D)-enhanced T2\*-weighted angiography (ESWAN).** *Eur J Radiol* 2015;84:1325–32 CrossRef Medline
  30. Roccatagliata L, Vuolo L, Bonzano L, et al. **Multiple sclerosis: hyperintense dentate nucleus on unenhanced T1-weighted MR images is associated with the secondary progressive subtype.** *Radiology* 2009;251:503–10 CrossRef Medline
  31. Tjoa CW, Benedict RH, Weinstock-Guttman B, et al. **MRI T2 hypointensity of the dentate nucleus is related to ambulatory impairment in multiple sclerosis.** *J Neurol Sci* 2005;234:17–24 CrossRef Medline
  32. Pawate S, Wang L, Song Y, et al. **Analysis of T2 intensity by magnetic resonance imaging of deep gray matter nuclei in multiple sclerosis patients: effect of immunomodulatory therapies.** *J Neuroimaging* 2012;22:137–44 CrossRef Medline
  33. Stankiewicz JM, Neema M, Ceccarelli A. **Iron and multiple sclerosis.** *Neurobiol Aging* 2014;35(suppl 2):S51–58 CrossRef Medline
  34. Hogarth P. **Neurodegeneration with brain iron accumulation: diagnosis and management.** *J Mov Disord* 2015;8:1–13 CrossRef Medline
  35. Salomão RP, Pedroso JL, Gama MT, et al. **A diagnostic approach for neurodegeneration with brain iron accumulation: clinical features, genetics and brain imaging.** *Arq Neuropsiquiatr* 2016;74:587–96 CrossRef Medline
  36. Saleem S, Aslam HM, Anwar M, et al. **Fahr's syndrome: literature review of current evidence.** *Orphanet J Rare Dis* 2013;8:156 CrossRef Medline
  37. Avrahami E, Cohn DF, Feibel M, et al. **MRI demonstration and CT correlation of the brain in patients with idiopathic intracerebral calcification.** *J Neurol* 1994;241:381–84 CrossRef Medline
  38. Elshimali Y. **The value of differential diagnosis of Fahr's disease by radiology.** *Internet J Radiol* 2004;4. <http://ispub.com/IJRA/4/1/9320>. Accessed April 3, 2017
  39. Govindarajan A. **Imaging in Fahr's disease: how CT and MRI differ?** *BMJ Case Rep* 2013;2013 CrossRef Medline
  40. Kobari M, Nogawa S, Sugimoto Y, et al. **Familial idiopathic brain calcification with autosomal dominant inheritance.** *Neurology* 1997;48:645–49 CrossRef Medline
  41. Castro-Gago M, Blanco-Barca MO, Campos-González Y, et al. **Epidemiology of pediatric mitochondrial respiratory chain disorders in north-west Spain.** *Pediatr Neurol* 2006;34:204–11 CrossRef Medline
  42. Zhu ZQ, Yao JB, Johns T, et al. **SURF1, encoding a factor involved in the biogenesis of cytochrome c oxidase, is mutated in Leigh syndrome.** *Nat Genet* 1998;20:337–43 CrossRef Medline
  43. Lee HF, Tsai CR, Chi CS, et al. **Leigh syndrome: clinical and neuroimaging follow-up.** *Pediatr Neurol* 2009;40:88–93 CrossRef Medline
  44. Finsterer J. **Leigh and Leigh-like syndrome in children and adults.** *Pediatr Neurol* 2008;39:223–35 CrossRef Medline
  45. Arii J, Tanabe Y. **Leigh syndrome: serial MR imaging and clinical follow-up.** *AJNR Am J Neuroradiol* 2000;21:1502–09 Medline
  46. Sonam K, Khan NA, Bindu PS, et al. **Clinical and magnetic resonance imaging findings in patients with Leigh syndrome and SURF1 mutations.** *Brain Dev* 2014;36:807–12 CrossRef Medline
  47. Pandolfo M. **Friedreich ataxia: the clinical picture.** *J Neurol* 2009;256(suppl 1):3–8 CrossRef
  48. Koeppen AH. **Friedreich's ataxia: pathology, pathogenesis, and molecular genetics.** *J Neurol Sci* 2011;303:1–12 CrossRef Medline
  49. Mascalchi M, Salvi F, Piacentini S, et al. **Friedreich's ataxia: MR findings involving the cervical portion of the spinal cord.** *AJR Am J Roentgenol* 1994;163:187–91 CrossRef Medline
  50. Koeppen AH, Michael SC, Knutson MD, et al. **The dentate nucleus in**

- Friedreich's ataxia: the role of iron-responsive proteins.** *Acta Neuropathol* 2007;114:163–73 CrossRef Medline
51. Koeppen AH, Ramirez RL, Yu D, et al. **Friedreich's ataxia causes redistribution of iron, copper, and zinc in the dentate nucleus.** *Cerebellum* 2012;11:845–60 CrossRef Medline
  52. Selvadurai LP, Harding IH, Corben LA, et al. **Cerebral and cerebellar grey matter atrophy in Friedreich ataxia: the IMAGE-FRDA study.** *J Neurol* 2016;263:2215–23 CrossRef Medline
  53. Rizzo G, Tonon C, Valentino ML, et al. **Brain diffusion-weighted imaging in Friedreich's ataxia.** *Mov Disord* 2011;26:705–12 CrossRef Medline
  54. Feigenbaum A, Moore R, Clarke J, et al. **Canavan disease: carrier-frequency determination in the Ashkenazi Jewish population and development of a novel molecular diagnostic assay.** *Am J Med Genet A* 2004;124A:142–47 CrossRef Medline
  55. Kronn D, Oddoux C, Phillips J, et al. **Prevalence of Canavan disease heterozygotes in the New York metropolitan Ashkenazi Jewish population.** *Am J Hum Genet* 1995;57:1250–52 Medline
  56. Matalon R, Michals K, Sebesta D, et al. **Aspartoacylase deficiency and N-acetylaspartic aciduria in patients with Canavan disease.** *Am J Med Genet* 1988;29:463–71 CrossRef Medline
  57. Namboodiri AM, Peethambaran A, Mathew R, et al. **Canavan disease and the role of N-acetylaspartate in myelin synthesis.** *Mol Cell Endocrinol* 2006;252:216–23 CrossRef Medline
  58. Brismar J, Brismar G, Gascon G, et al. **Canavan disease: CT and MR imaging of the brain.** *AJNR Am J Neuroradiol* 1990;11:805–10 Medline
  59. Sener RN. **Canavan disease: diffusion magnetic resonance imaging findings.** *J Comput Assist Tomogr* 2003;27:30–33 CrossRef Medline
  60. McAdams HP, Geyer CA, Done SL, et al. **CT and MR imaging of Canavan disease.** *AJNR Am J Neuroradiol* 1990;11:397–99 Medline
  61. Wittsack HJ, Kugel H, Roth B, et al. **Quantitative measurements with localized 1H MR spectroscopy in children with Canavan's disease.** *J Magn Reson Imaging* 1996;6:889–93 CrossRef Medline
  62. Lindner M, Kölker S, Schulze A, et al. **Neonatal screening for glutaryl-CoA dehydrogenase deficiency.** *J Inherit Metab Dis* 2004;27:851–59 CrossRef Medline
  63. Mohammad SA, Abdelkhalik HS, Ahmed KA, et al. **Glutaric aciduria type I: neuroimaging features with clinical correlation.** *Pediatr Radiol* 2015;45:1696–705 CrossRef Medline
  64. Wang Q, Li X, Ding Y, et al. **Clinical and mutational spectra of 23 Chinese patients with glutaric aciduria type 1.** *Brain Dev* 2014;36:813–22 CrossRef Medline
  65. Brismar J, Ozand PT. **CT and MR of the brain in glutaric acidemia type I: a review of 59 published cases and a report of 5 new patients.** *AJNR Am J Neuroradiol* 1995;16:675–83 Medline
  66. Vester ME, Visser G, Wijburg FA, et al. **Occurrence of subdural hematomas in Dutch glutaric aciduria type 1 patients.** *Eur J Pediatr* 2016;175:1001–06 CrossRef Medline
  67. Harper PA, Healy PJ, Dennis JA. *Maple Syrup Urine Disease (Branched-Chain Ketoaciduria)*. New York: McGraw-Hill; 2001:1971–2006
  68. Brismar J, Aqeel A, Brismar G, et al. **Maple syrup urine disease: findings on CT and MR scans of the brain in 10 infants.** *AJNR Am J Neuroradiol* 1990;11:1219–28 Medline
  69. Gupta AK, Chowdhury V, Khandelwal N. *Diagnostic Radiology Paediatric Imaging*. New Delhi: Jaypee Brothers Medical Publishers; 2011: 522

# MR Imaging in Sudden Sensorineural Hearing Loss. Time to Talk

 G. Conte,  F. Di Bernardino,  C. Sina,  D. Zanetti,  E. Scola,  C. Gavagna,  L. Gaini,  G. Palumbo,  P. Capaccio, and  F. Triulzi



## ABSTRACT

**SUMMARY:** Sudden sensorineural hearing loss is defined as acute hearing loss of the sensorineural type of at least 30 dB over 3 contiguous frequencies that occurs within a 72-hour period. Although many different causative factors have been proposed, sudden sensorineural hearing loss is still considered “idiopathic” in 71%–85% of cases, and treatments are empiric, not based on etiology. MR imaging implemented with a 3D FLAIR sequence has provided new insights into the etiology of sudden sensorineural hearing loss. Herein, we review the current management trends for patients with sudden sensorineural hearing loss, from the initial clinical diagnosis to therapeutic strategies and diagnostic work-up. We focused primarily on MR imaging assessment and discuss the relevance that MR imaging findings might have for patient management, pointing out different perspectives for future clinical research.

**ABBREVIATION:** SSHL = sudden sensorineural hearing loss

According to the guidelines of the Committee on Hearing and Equilibrium of the American Academy of Otolaryngology, sudden sensorineural hearing loss (SSHL) is defined as acute hearing loss of the sensorineural type of at least 30 dB over 3 contiguous frequencies occurring within a 72-hour period.<sup>1</sup> SSHL occurs most often in the fourth decade of life, with an annual incidence that varies between 5 and 20 cases among 100,000 people. The severity of hearing loss is variable and is usually unilateral, though bilateral involvement has been reported in up to 4% of patients.<sup>2</sup>

Although SSHL has been attributed to many different causative factors,<sup>3</sup> there are still no audiologic means of accurately assessing its etiology,<sup>4</sup> so it is still considered “idiopathic” in 71%–85% of cases.<sup>5</sup> Consequently, there is not a treatment that targets the etiology, which partly explains the inconsistent results of the various empiric drug protocols proposed, which include systemic steroids, antiviral medications, vasodilators, and carbogen or hy-

perbaric oxygen alone or in combination, none of which has been proved to be superior to the others.<sup>6–8</sup>

Over the past decade, MR imaging has provided new insights about SSHL etiology because of high-resolution sequences that are able to detect subtle changes in the inner ear.<sup>9–15</sup> However, for many reasons, the use of this imaging technique for SSHL is still not widespread. First, many radiologists are not yet aware of the possibilities offered by advanced MR imaging studies of the inner ear and/or of the possible MR imaging findings in SSHL. Second, it is still unclear and is not yet addressed in the literature how MR imaging could change therapeutic strategies.

In this paper, we review the current management trends of patients with SSHL, from the initial clinical diagnosis to the therapeutic strategies, through the diagnostic work-up. Our work focuses particularly on MR imaging assessment. We discussed how MR imaging should be performed and the relevance that the possible MR imaging findings in the inner ear might have. Finally, we addressed the perspectives of possible changes in the therapeutic management of SSHL based on MR imaging findings, which could impact the patient’s prognosis.

## Current Diagnostic Work-Up of SSHL

SSHL is suspected in patients with a sudden onset of generally unilateral decrease or loss of hearing, occurring instantaneously or rapidly developing over a period of hours or days.<sup>3</sup> In other instances, primary care or emergency department physicians refer patients to an audiologist.<sup>16,17</sup>

The evaluation usually begins with a careful history and physical examination to look for potential causes such as infections,

Received January 5, 2017; accepted after revision March 20.

From the Postgraduation School of Radiodiagnosics (G.C.); Audiology (F.D.B., D.Z.), Neuroradiology (C.S., E.S., C.G., F.T.), and Otolaryngology (L.G., P.C.) Units, Department of Clinical Sciences and Community Health, Fondazione IRCCS Ca’Granda Ospedale Maggiore Policlinico; School of Medicine (G.P.), and Department of Pathophysiology and Transplantation (F.T.), Università degli Studi di Milano, Milan, Italy.

Please address correspondence to Dr. Giorgio Conte, MD, Postgraduation School in Radiodiagnosics, Università degli Studi di Milano, Via Festa del Perdono 7, 20122 Milan, Italy; e-mail: giorgioconte.unimed@gmail.com

 Indicates article with supplemental on-line table.

 Indicates article with supplemental on-line photo.

<http://dx.doi.org/10.3174/ajnr.A5230>

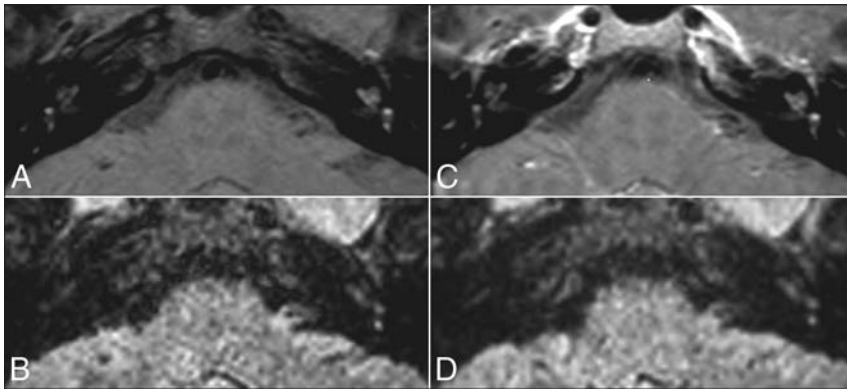


**FIG 1.** Vascular pattern in a 20-year-old woman with left SSSL. Precontrast T1-weighted (A) and precontrast 3D-FLAIR (B) sequences show a high signal in the middle and upper turns of the left cochlea without enhancement on postcontrast T1-weighted (C) and 3D-FLAIR images (D).

systemic diseases, and exposure to known ototoxic medications. Otomicroscopy is generally negative for external and middle ear pathologies. Pure-tone audiometry is the main diagnostic tool used to differentiate between conductive and sensorineural hearing loss, which have very different management strategies. The physician can differentiate SSSL (symptoms occur within 3 days) from progressive or fluctuating SSSL. The presence of bilateral sudden hearing loss, recurrent episodes of sudden hearing loss, or focal neurologic findings suggests systemic disorders, autoimmune or metabolic disorders, bilateral Menière disease, or primary neurologic disorders.

If SSSL is diagnosed, an empiric treatment is started while the diagnostic work-up continues. A complete audiovestibular evaluation, including speech audiometry, speech in noise test, tympanometry, acoustic reflexes, and otoacoustics emissions, is performed in an attempt to investigate whether the SSSL is cochlear or retrocochlear.<sup>8</sup>

Brain MR imaging with and without gadolinium is often used to exclude a vestibular schwannoma (reported in up to 10%–20% of patients with SSSL) as well as rarer causes of retrocochlear hearing loss such as other cerebellopontine tumors, brain stem infarctions, and demyelinating disease.<sup>3,8,18–21</sup> A number of studies have advocated the use of MR imaging without gadolinium as the more appropriate means of screening patients with asymmetric SSSL suspected to be retrocochlear.<sup>22</sup>

In cases of suspected cochlear SSSL, different studies have proposed a tailored temporal bone MR imaging with 3D-FLAIR sequence to exclude abnormalities in the inner ear structures.<sup>9–15</sup> MR imaging of the temporal bone can be negative, and the SSSL is therefore defined as idiopathic, or the MR imaging can show abnormalities in the inner ear structures, suggesting a specific etiopathogenesis (vascular or inflammatory).<sup>14</sup> In both cases, because no trial has yet investigated different medical protocols guided by MR imaging findings, physicians continue with empiric therapy, so temporal bone MR imaging with a 3D-FLAIR sequence has not had any effect on the therapeutic management of cochlear SSSL in clinical practice. Nevertheless, in our opinion, it is important that radiologists perform temporal bone MR imaging with a 3D-FLAIR sequence to clarify the cochlear origin of SSSL, suggesting the probable pathogenesis, and provide prognostic information to physicians.

### How We Perform MR Imaging in Patients with SSSL

MR imaging of the temporal bone is challenging because of the complexity and small dimensions of the anatomic structures. Thus, MR imaging should preferably be performed on a 3T scanner, which provides high-resolution images with a higher signal-to-noise ratio compared with a 1.5T scanner. The basic MR imaging protocol should include an axial precontrast 3D steady-state free precession sequence, a pre- and postcontrast T1-weighted FSE sequence, and a pre- and postcontrast 3D-FLAIR sequence.<sup>4–15</sup> The On-line Table summarizes the MR imaging scan parameters

used in our department. It is recommended to use both postcontrast 3D-FLAIR and postcontrast T1-weighted FSE sequences because the former are more sensitive than a T1-weighted sequence in detecting intralabyrinthine contrast enhancement,<sup>11,14,23</sup> and the latter can clarify the presence of a small schwannoma.

Postcontrast sequences should be acquired approximately 10 minutes after administration of the contrast agent.<sup>13,15</sup> To cover part of the 10 minutes needed before the acquisition of postcontrast sequences, it is advantageous to inject a contrast agent before the acquisition of the 3D steady-state free precession sequence. Although the contrast enhancement of some structures can be seen on the 3D steady-state free precession sequence,<sup>24</sup> the assessment of the inner ear anatomic structures and internal auditory canal on this sequence is usually not hindered by the presence of the contrast agent.

### What Can MR Imaging Detect?

Neuroradiologists should review MRIs and look for asymmetry of the signal between the affected and unaffected sides. In the literature, abnormalities on MR imaging are reported in 27%–53% of SSSL cases.<sup>10,14</sup>

Two patterns can be recognized based on the MR imaging signal of the inner ear on precontrast T1-weighted and 3D-FLAIR images:

1) The vascular pattern shows hyperintensity on precontrast T1-weighted and 3D-FLAIR images because of the presence of methemoglobin in the inner ear (Fig 1); and

2) The inflammatory pattern shows hyperintensity only on 3D-FLAIR images because of the presence of proteinaceous exudate in the inner ear (Fig 2).

Regarding the vascular pattern, radiologists should be aware that pseudohyperintensity of the intralabyrinthine fluid can normally be detected on fat-suppressed T1-weighted images, which could hamper the diagnosis. This pseudohyperintensity has previously been described as an artifact<sup>25</sup> and can be differentiated from methemoglobin because it is symmetrical and less evident on postcontrast fat-suppressed T1-weighted images (see Fig 3 for a detailed explanation).

Recent studies have investigated the relationship between precontrast 3D-FLAIR signals and clinical findings regardless of the hyperintensity on precontrast T1-weighted sequences.<sup>9–11,23</sup> The rate of abnormalities on precontrast 3D-FLAIR images correlated

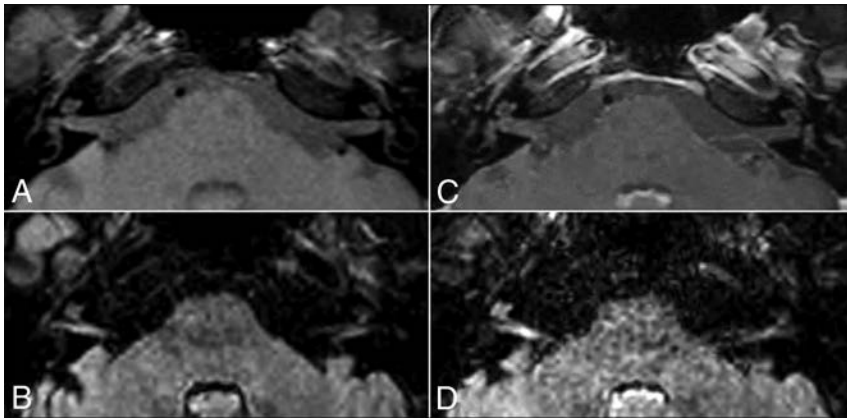


**FIG 2.** Inflammatory pattern in a 35-year-old man with right SSSL. The precontrast T1-weighted sequence (A) shows no signal abnormalities. The precontrast 3D-FLAIR sequence (B) shows a high signal in the right cranial nerves VII and VIII and in the middle and upper turns of the left cochlea. A postcontrast T1-weighted sequence (C) does not show enhancement, whereas a postcontrast 3D-FLAIR sequence (D) shows the cochlea and cranial nerves VII and VIII as markedly enhanced on the right side.

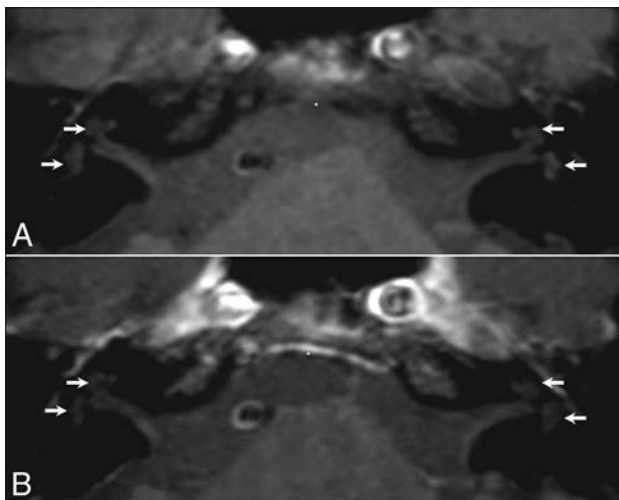


**FIG 3.** Normal MR imaging findings in a 59-year-old man with right SSSL. The precontrast T1-weighted sequence (A) shows spontaneous hyperintense intralabyrinthine fluid in both inner ear structures (arrows), which is symmetric and less evident on the same sequence after contrast injection (B). This hyperintensity is an artifact caused by the altered dynamic range when the fat signal is subtracted, but also reflects an alteration in the visual appearance of signal intensity as the ambient contrast is changed (checker-shadow illusion).<sup>24</sup>

with the level of hearing loss at onset, resulting in fewer abnormalities in patients with mild to moderate hearing loss compared with patients with profound hearing loss.<sup>10,14,15</sup> However, Yoshida et al<sup>11</sup> did not observe similar results. Inflammatory diseases can also affect the vestibule, the semicircular canals, or cranial nerve VIII, and precontrast 3D-FLAIR images can detect signal abnormalities in these structures (Fig 3).<sup>10-14,23</sup> Hyperintensity on precontrast 3D-FLAIR images of the vestibule or the semicircular canals has been associated with vertigo,<sup>11,14</sup> which is reported in approximately 30% of SSSL cases.<sup>9</sup>

The 2 MR imaging patterns are not always associated with inner ear enhancement on postcontrast 3D-FLAIR, which is consistent with blood-labyrinth barrier breakdown.<sup>14</sup> The advantage of postcontrast 3D-FLAIR images is that they identify patients with more

severe blood-labyrinth barrier breakdown when signal abnormalities are subtle on precontrast 3D-FLAIR images.<sup>23</sup> However, the significance of the inner ear enhancement is still unclear. Viral infection, immune-mediated inner ear disease, and perilymphatic fistulas have been suggested as possible causes of cochlear enhancement.<sup>26,27</sup>

Usually, the 3D T2-weighted steady-state free precession sequence does not show any pathologic findings<sup>23</sup>; nevertheless, it is essential to investigate the morphology of the inner ear structures, cranial nerve VIII, internal auditory canal, and cerebellopontine angle.

### Prognostic Value of MR Imaging

To the best of our knowledge, no published studies have investigated the difference in prognosis and outcome between the 2 MR imaging patterns mentioned above, though a vascular pattern has been associated with a poor prognosis.<sup>28</sup> On the contrary, the published studies have concentrated on the prognostic value of 3D-FLAIR abnormalities and reported conflicting results. Two studies showed that a high signal in the affected inner ear on precontrast 3D-FLAIR was associated with a poor prognosis.<sup>11,15</sup> In 2 other studies, the hearing outcome was worse in patients with multiple-location hyperintensities on precontrast 3D-FLAIR (cochlea plus vestibule) than in patients with a single-subsite hyperintensity (cochlea only).<sup>12,29</sup> A recent study by Liao et al<sup>23</sup> showed that the more asymmetric FLAIR signal between the affected ear and the normal one and presence of a high signal beyond the cochlea indicated a poorer prognosis. Lee et al<sup>10</sup> demonstrated that precontrast 3D-FLAIR abnormalities do not affect the prognosis when the initial hearing loss is mild to moderate, whereas such abnormalities represent a negative prognostic factor in patients with initial profound hearing loss. However, Berrettini et al<sup>14</sup> failed to find a correlation between the severity of precontrast 3D-FLAIR abnormalities and hearing improvement. Lee et al<sup>9</sup> reported that a high signal on precontrast 3D-FLAIR did not significantly affect the final hearing ability.

These inconsistent results are partially explained by methodologic differences, including the time span between SSSL onset and MR imaging, method of MR imaging assessment, pharmacologic protocols of drug administration during follow-up, length of follow-up, and assessment criteria used to determine hearing improvement.<sup>30</sup> A meta-analysis by Gao and Chi<sup>30</sup> that included studies of patients without primary treatment before temporal bone MR imaging concluded that precontrast 3D-FLAIR hyperintensity in the inner ear is associated with more severe initial hearing loss and a lower chance of recovery.

These inconsistent results are partially explained by methodologic differences, including the time span between SSSL onset and MR imaging, method of MR imaging assessment, pharmacologic protocols of drug administration during follow-up, length of follow-up, and assessment criteria used to determine hearing improvement.<sup>30</sup> A meta-analysis by Gao and Chi<sup>30</sup> that included studies of patients without primary treatment before temporal bone MR imaging concluded that precontrast 3D-FLAIR hyperintensity in the inner ear is associated with more severe initial hearing loss and a lower chance of recovery.

### Current Management of SSSL and Perspectives in MR Imaging Research

The results of SSSL treatment are still largely unpredictable; a very large variability in responses has been reported, ranging

from no response to total recovery.<sup>7,31</sup> Moreover, the high rate of spontaneous recovery, which varies from 45%–65%,<sup>21</sup> should be considered.

Although cochlear vascular microthrombosis has been hypothesized as the main pathogenic mechanism,<sup>32–34</sup> because there is no objective test that can detect the occlusion of microvessels, the pharmacologic treatment remains highly empirical, and its overall efficacy is controversial because of the absence of prospective double-blind studies.<sup>3</sup> Pharmacologic treatment includes many drugs that, without a certain etiology of SSHL, are often prescribed in combination: oral and/or intratympanic corticosteroids, hyperbaric oxygen therapy, antiviral drugs, vasodilators, and vasoactive substances.

For decades, the “gold standard” treatment for SSHL has been the oral administration of corticosteroids.<sup>35,36</sup> The exact mechanism by which steroids improve hearing is still unknown, though some of the major hypotheses are that they modulate cochlear function, decrease inflammation and edema, improve cochlear blood flow, and protect against cochlear ischemia. Although the evidence concerning the use of oral corticosteroids remains contradictory,<sup>37</sup> it seems reasonable to offer them because of the potentially devastating disability caused by SSHL and the relatively low morbidity of the treatment.<sup>3</sup> Intratympanic steroid treatment allows high steroid concentrations to be reached in the perilymph while avoiding the common side effects of systemic steroids. A recent meta-analysis has shown the benefits of intratympanic steroid treatment in combination with oral corticosteroids as the first-line therapy and salvage monotherapy in idiopathic SSHL.<sup>38</sup> Hyperbaric oxygen treatment is also used as primary, adjuvant, or salvage therapy because it is thought to protect hair cells from ischemic damage by increasing oxygenation.<sup>39,40</sup> However, cost/benefit issues, limited availability, and the absence of strong evidence because of the difficulties of organizing controlled randomized studies have halted its widespread application. Although there is no clear evidence supporting their use, antiviral drugs are often used in pharmacologic protocols for the treatment of SSHL because various viruses have been implicated in its etiology.<sup>41</sup> Vasodilators and vasoactive substances are sometimes used because obstructed vascular flow to the cochlea is a theoretic cause of SSHL, but there is currently insufficient evidence to support their routine use.<sup>3</sup>

Future research should investigate the role of MR imaging with a 3D-FLAIR sequence in the therapeutic management of SSHL (On-line Figure). Before future trials can investigate different medical protocols guided by MR imaging findings, longitudinal studies should investigate the effects of early steroid treatment and the time interval between disease onset and scanning on the sensitivity of MR imaging. In our opinion, its optimal timing would be upon admission to the emergency department or on the same day as a clinical assessment by an audiologist or otolaryngologist. We hypothesize that precontrast and contrast-enhanced MR imaging abnormalities are more easily detected before steroid treatment is started, so MR imaging should be performed as soon as possible, and preferably before the masking effect of steroids becomes apparent.<sup>28</sup> In line with this suggestion, Berrettini et al<sup>14</sup> have reported that the time interval between SSHL onset and MR imaging tended to be shorter in patients

with 3D-FLAIR abnormalities than in those without 3D-FLAIR abnormalities ( $P = .06$ ). However, this has not been confirmed by other authors.

## CONCLUSIONS

MR imaging with 3D-FLAIR sequences provides new insights into SSHL etiology and may change current clinical and therapeutic practices. Radiologists should therefore be trained to perform tailored temporal bone MR imaging in the case of SSHL and recognize the common findings and pitfalls of the technique to provide clinicians with information useful for patient management.

## REFERENCES

1. Rauch SD. **Clinical practice. Idiopathic sudden sensorineural hearing loss.** *N Eng J Med* 2008;359:833–40 CrossRef Medline
2. Byl FM Jr. **Sudden hearing loss: eight years' experience and suggested prognostic table.** *Laryngoscope* 1984;94:647–61 Medline
3. Lawrence R, Thevasagayam R. **Controversies in the management of sudden sensorineural hearing loss: an evidence-based review.** *Clin Otolaryngol* 2015;40:176–82 CrossRef Medline
4. Kuhn M, Heman-Ackah SE, Shaikh JA, et al. **Sudden sensorineural hearing loss: a review of diagnosis, treatment, and prognosis.** *Trends Amplif* 2011;15:91–105 CrossRef Medline
5. Chau JK, Lin JR, Atashband S, et al. **Systematic review of the evidence for the etiology of adult sudden sensorineural hearing loss.** *Laryngoscope* 2010;120:1011–21 CrossRef Medline
6. Schreiber BE, Agrup C, Haskard DO, et al. **Sudden sensorineural hearing loss.** *Lancet* 2010;375:1203–11 CrossRef Medline
7. Conlin AE, Parnes LS. **Treatment of sudden sensorineural hearing loss: I. A systematic review.** *Arch Otolaryngol Head Neck Surg* 2007; 133:573–81 CrossRef Medline
8. Stachler RJ, Chandrasekhar SS, Archer SM, et al. **Clinical practice guideline: sudden hearing loss.** *Otolaryngol Head Neck Surg* 2012; 146:S1–35 CrossRef Medline
9. Lee HY, Jung SY, Park MS, et al. **Feasibility of three-dimensional fluid-attenuated inversion recovery magnetic resonance imaging as a prognostic factor in patients with sudden hearing loss.** *Eur Arch Otorhinolaryngol* 2012;269:1885–91 CrossRef Medline
10. Lee JI, Yoon RG, Lee JH, et al. **Prognostic value of labyrinthine 3D-FLAIR abnormalities in idiopathic sudden sensorineural hearing loss.** *AJNR Am J Neuroradiol* 2016;37:2317–22 CrossRef Medline
11. Yoshida T, Sugiura M, Naganawa S, et al. **Three-dimensional fluid-attenuated inversion recovery magnetic resonance imaging findings and prognosis in sudden sensorineural hearing loss.** *Laryngoscope* 2008;118:1433–37 CrossRef Medline
12. Ryu IS, Yoon TH, Ahn JH, et al. **Three-dimensional fluid-attenuated inversion recovery magnetic resonance imaging in sudden sensorineural hearing loss: correlations with audiologic and vestibular testing.** *Otol Neurotol* 2011;32:1205–09 CrossRef Medline
13. Kim TY, Park DW, Lee YJ, et al. **Comparison of inner ear contrast enhancement among patients with unilateral inner ear symptoms in MR images obtained 10 minutes and 4 hours after gadolinium injection.** *AJNR Am J Neuroradiol* 2015;36:2367–72 CrossRef Medline
14. Berrettini S, Seccia V, Fortunato S, et al. **Analysis of the 3-dimensional fluid-attenuated inversion-recovery (3D-FLAIR) sequence in idiopathic sudden sensorineural hearing loss.** *JAMA Otolaryngol Head Neck Surg* 2013;139:456–64 CrossRef Medline
15. Zhu H, Ou Y, Fu J, et al. **A comparison of inner ear imaging features at different time points of sudden sensorineural hearing loss with three-dimensional fluid-attenuated inversion recovery magnetic resonance imaging.** *Eur Arch Otorhinolaryngol* 2015;272:2659–65 CrossRef Medline
16. Witsell DL, Khoury T, Schulz KA, et al. **Evaluation of compliance for**

- treatment of sudden hearing loss: a CHEER Network study.** *Otolaryngol Head Neck Surg* 2016;155:48–55 CrossRef Medline
17. Coelho DH, Thacker LR, Hsu DW. **Variability in the management of idiopathic sudden sensorineural hearing loss.** *Otolaryngol Head Neck Surg* 2011;145:813–17 CrossRef Medline
  18. Portmann M, Dauman R, Duriez F, et al. **Modern diagnostic strategy for acoustic neuromas.** *Arch Otorhinolaryngol* 1989;246:286–91 CrossRef Medline
  19. Biavati MJ, Gross JD, Wilson WR, et al. **Magnetic resonance imaging evidence of a focal pontine ischemia in sudden hearing loss and seventh nerve paralysis.** *Am J Otol* 1994;15:250–53 CrossRef Medline
  20. Franklin DJ, Coker NJ, Jenkins HA. **Sudden sensorineural hearing loss as a presentation of multiple sclerosis.** *Arch Otolaryngol Head Neck Surg* 1989;115:41–45 CrossRef Medline
  21. Hagiwara M, Roland JT Jr, Wu X, et al. **Identification of endolymphatic hydrops in Ménière's disease utilizing delayed postcontrast 3D FLAIR and fused 3D FLAIR and CISS color maps.** *Otol Neurotol* 2014;35:e337–42 CrossRef Medline
  22. Ryan M, Weissman JL, Kaylie D. **Is Gadolinium contrast enhancement necessary in screening MRI for asymmetric sensorineural hearing loss?** *Laryngoscope* 2015;125:783–84 CrossRef Medline
  23. Liao WH, Wu HM, Wu HY, et al. **Revisiting the relationship of three-dimensional fluid attenuation inversion recovery imaging and hearing outcomes in adults with idiopathic unilateral sudden sensorineural hearing loss.** *Eur J Radiol* 2016;85:2188–94 CrossRef Medline
  24. Yagi A, Sato N, Takahashi A, et al. **Added value of contrast-enhanced CISS imaging in relation to conventional MR images for the evaluation of intracavernous cranial nerve lesions.** *Neuroradiology* 2010; 52:1101–09 CrossRef Medline
  25. Huynh TN, Johnson T, Poder L, et al. **T1 pseudohyperintensity on fat-suppressed magnetic resonance imaging: a potential diagnostic pitfall.** *J Comput Assist Tomogr* 2011;35:459–61 CrossRef Medline
  26. Mark AS, Fitzgerald D. **Segmental enhancement of the cochlea on contrast-enhanced MR: correlation with the frequency of hearing loss and possible sign of perilymphatic fistula and autoimmune labyrinthitis.** *AJNR Am J Neuroradiol* 1993;14:991–96 Medline
  27. Fitzgerald DC, Mark AS. **Sudden hearing loss: frequency of abnormal findings on contrast-enhanced MR studies.** *AJNR Am J Neuroradiol* 1998;19:1433–36 Medline
  28. Lee JW, Park YA, Park SM, et al. **Clinical features and prognosis of sudden sensorineural hearing loss secondary to intralabyrinthine hemorrhage.** *J Audiol Otol* 2016;20:31–35 CrossRef Medline
  29. Ramos HV, Barros FA, Yamashita H, et al. **Magnetic resonance imaging in sudden deafness.** *Braz J Otorhinolaryngol* 2005;71:422–26 CrossRef Medline
  30. Gao Z, Chi FL. **The clinical value of three-dimensional fluid-attenuated inversion recovery magnetic resonance imaging in patients with idiopathic sudden sensorineural hearing loss: a meta-analysis.** *Otol Neurotol* 2014;35:1730–35 CrossRef Medline
  31. Conlin AE, Parnes LS. **Treatment of sudden sensorineural hearing loss: II. A meta-analysis.** *Arch Otolaryngol Head Neck Surg* 2007;133: 582–86 CrossRef Medline
  32. Passamonti SM, Di Bernardino F, Bucciarelli P, et al. **Risk factors for idiopathic sudden sensorineural hearing loss and their association with clinical outcome.** *Thromb Res* 2015;135:508–12 CrossRef Medline
  33. Capaccio P, Ottaviani F, Cuccarini V, et al. **Genetic and acquired prothrombotic risk factors and sudden hearing loss.** *Laryngoscope* 2007;117:547–51 CrossRef Medline
  34. Quaranta N, De Ceglie V, D'Elia A. **Endothelial dysfunction in idiopathic sudden sensorineural hearing loss: a review.** *Audiol Res* 2016; 6:151 CrossRef Medline
  35. Moskowitz D, Lee KJ, Smith HW. **Steroid use in idiopathic sudden sensorineural hearing loss.** *Laryngoscope* 1984;94:664–66 Medline
  36. Wilson WR, Byl FM, Laird N. **The efficacy of steroids in the treatment of idiopathic sudden hearing loss. A double-blind clinical study.** *Arch Otolaryngol* 1980;106:772–76 CrossRef Medline
  37. Crane RA, Camilon M, Nguyen S, et al. **Steroids for treatment of sudden sensorineural hearing loss: a meta-analysis of randomized controlled trials.** *Laryngoscope* 2015;125:209–17 CrossRef Medline
  38. Lavigne P, Lavigne F, Saliba I. **Intratympanic corticosteroids injections: a systematic review of literature.** *Eur Arch Otorhinolaryngol* 2016;273:2271–78 CrossRef Medline
  39. Fattori B, Berrettini S, Casani A, et al. **Sudden hypoacusis treated with hyperbaric oxygen therapy: a controlled study.** *Ear Nose Throat J* 2001;80:655–60 Medline
  40. Narozny W, Sicko Z, Przewozny T, et al. **Usefulness of high doses of glucocorticoids and hyperbaric oxygen therapy in sudden sensorineural hearing loss treatment.** *Otol Neurotol* 2004;25:916–23. CrossRef Medline
  41. Awad Z, Huins C, Pothier DD. **Antivirals for idiopathic sudden sensorineural hearing loss.** *Cochrane Database Syst Rev* 2012;8:CD006987 CrossRef Medline

# Introduction of a Dedicated Emergency Department MR Imaging Scanner at the Barrow Neurological Institute

M. Buller and J.P. Karis



## ABSTRACT

**SUMMARY:** Use of advanced imaging in the emergency department has been increasing in the United States during the past 2 decades. This trend has been most notable in CT, which has increased concern over the effects of increasing levels of medical ionizing radiation. MR imaging offers a safe, nonionizing alternative to CT and is diagnostically superior in many neurologic conditions encountered in the emergency department. Herein, we describe the process of developing and installing a dedicated MR imaging scanner in the Neuroscience Emergency Department at the Barrow Neurological Institute and its effects on neuroradiology and the emergency department in general.

**ABBREVIATION:** ED = emergency department

In the United States, use of advanced imaging in the emergency department (ED) has been steadily increasing during the past 2 decades.<sup>1,2</sup> This trend has outpaced the increasing number of ED visits, indicating that at least part of this rise is due to increasing demand for these imaging tests.<sup>3</sup> While this increasing use has been successfully reversed in some centers with education programs, clinical decision support systems, pay-for-performance incentive systems, and other methods,<sup>3,4</sup> national data continue to demonstrate growth, most notably in CT.<sup>1</sup> Neuroimaging makes up a substantial portion of this use, constituting a large proportion of total CT imaging<sup>3,5</sup> and most MR imaging ordered in the ED.<sup>2,5</sup> These trends have led to increasing concern regarding the rising health care costs and the radiation dose attributable to increasing CT use. MR imaging provides a nonionizing alternative to CT for many neuroimaging indications; however, factors such as availability, scan length, and cost can limit its utility as a practical substitute for CT.

The dedicated Neuroscience Emergency Department at the Barrow Neurological Institute sees >18,500 patients per year, with >2500 hospital admissions per year for neurologic concerns. This number of patient encounters generates a high volume of

neuroimaging. In an effort to increase access to MR imaging and create a viable alternative to CT in this patient population, the Barrow Neurological Institute installed a dedicated ED MR imaging scanner in 2015. Herein, we describe our experience with this process and the effects of a dedicated ED MR imaging scanner on neuroradiology and the emergency department.

## Impetus for Change

On the basis of CT usage data from the early 1990s and extrapolation to 2007, Brenner and Hall<sup>6</sup> estimated that 1.5%–2% of all cancers in the United States could be attributed to radiation from CT studies. Using BEIR VII data and CT head usage data from 2008, Smith-Bindman et al<sup>7</sup> estimated that the risk of developing cancer from a CT of the head at age 40 is 1 in 8100 for women and 1 in 11,080 for men. This risk was estimated to double if the age at scanning was halved. Berrington de González et al<sup>8</sup> suggested that CT head scans performed in the United States in 2007 caused approximately 4000 new cancers. These risks were qualified somewhat in a retrospective review by Sodickson et al<sup>9</sup> in 2009, which suggested that while there was only an incrementally increased risk of CT-induced cancer for patients undergoing a limited number of scans, there was significantly increased risk to those undergoing recurrent scanning. Their data demonstrated that 33% of their cohort of 31,462 patients had undergone  $\geq 5$  CT scans during the 22-year study period and that 15% had a cumulative dose of >100 mSv.<sup>9</sup>

Multiple techniques are available to reduce the radiation dose from CT scans, particularly to radiosensitive tissues such as the lens of the eye and the thyroid gland. These include iterative reconstruction and organ-based dose-reduction algorithms specifically targeting the lens and thyroid glands. There is evidence that

Received January 24, 2017; accepted after revision February 23.

From the Neuroradiology Department, Barrow Neurological Institute, Phoenix, Arizona.

Paper previously presented in part at: Annual Meeting of the Western Neuroradiological Society, October 14–16, 2016; Austin Texas.

Please address correspondence to John P. Karis, MD, Neuroradiology Department, Barrow Neurological Institute, 350 W Thomas Rd, Phoenix, AZ 85013; e-mail: jkaris@sniweb.net

Indicates open access to non-subscribers at [www.ajnr.org](http://www.ajnr.org)

<http://dx.doi.org/10.3174/ajnr.A5210>

these strategies can result in moderate dose reduction (up to 50%)<sup>10</sup> without compromising image quality.<sup>11,12</sup> MR imaging offers an imaging solution that uses nonionizing radiation, eliminating radiation dose concerns associated with medical imaging.

While most acute neurologic encounters in the ED can be assessed with CT, MR imaging offers a more detailed assessment, given its superior soft-tissue contrast, without using ionizing radiation. Apart from trauma and conductive hearing loss, the Appropriateness Criteria of the American College of Radiology list MR imaging as the preferred examination for most neurologic symptoms. These include ataxia, cranial neuropathies, dementia, altered mental status, focal neurologic deficits, headache (except thunderclap headaches), seizure, and vision loss.<sup>13</sup>

MR imaging and specifically diffusion-weighted imaging have been shown to be more sensitive in diagnosing acute stroke compared with CT.<sup>14</sup> Chalela et al<sup>15</sup> conducted a prospective, blinded comparison of MR imaging and CT for the assessment of acute stroke in the emergency department and concluded that MR imaging was superior to CT for the detection of acute ischemia and could detect acute and chronic hemorrhage, suggesting that MR imaging should be the preferred test for the accurate diagnosis of patients with suspected acute stroke. Other studies have confirmed that MR imaging is as accurate as CT for acute hemorrhage and more accurate for chronic hemorrhage.<sup>16,17</sup> Indeed, evidence suggests that the increased sensitivity of MR imaging for intracranial blood, and particularly microbleeds, may help identify those patients at higher risk for secondary intracerebral hemorrhage when considering intravenous thrombolytic therapy.<sup>18,19</sup>

Growing evidence suggests that the combination of fluid-attenuated inversion recovery pulse sequences and diffusion-weighted imaging is useful in determining which patients with strokes and unknown time of symptom onset or wake-up strokes are within the therapeutic window at presentation.<sup>20-23</sup> Triaging patients with stroke to MR imaging instead of CT results in a better safety profile and a higher chance of favorable outcome when treating beyond 3 hours of symptom onset.<sup>24</sup>

When evaluating patients for possible endovascular therapy, contrast-enhanced MR angiography has been shown to be accurate in detecting stenosis of the carotid<sup>25</sup> and vertebrobasilar circulations<sup>26</sup> and correlates well with digital subtraction angiography for carotid stenosis.<sup>27</sup> Contrast-enhanced MRA has also been shown to be equivalent or superior to time-of-flight angiography with much shorter scan times<sup>28,29</sup> and to improve detection of carotid terminus occlusion.<sup>30</sup>

Although MR imaging is not the primary technique for assessing trauma, mounting evidence demonstrates that MR imaging offers considerable value as an ancillary test in the acute phase. Fluid-attenuated inversion recovery sequences have been shown to be equivalent or better than CT for the detection of acute subarachnoid hemorrhage,<sup>31</sup> with increased sensitivity for acute and subacute hemorrhage with the addition of T2\* sequences.<sup>32,33</sup> MR imaging has also been shown to be superior to CT in detecting diffuse axonal injury.<sup>34-36</sup> In acute spinal trauma, Morais et al<sup>37</sup> demonstrated that MR imaging is superior to CT for the detection of bone swelling, posterior ligamentous complex injury, disc herniation, cord compression, and cord swelling.

## **Program Development**

For use of MR imaging in the ED to achieve maximal success, it was thought that the turnaround times for MR imaging needed to be as close to CT as possible. Multiple factors, from placement of the equipment through training of technologists, were optimized to maximize efficiency and patient throughput.

The location of the MR imaging scanner within the ED itself was an extremely important achievement in the development of a viable ED MR imaging program because it permitted simplification of workflow from the multitransfer inpatient workflow to a no-transfer workflow, which more closely resembles the ED CT process.

Before the installation of the MR imaging scanner within the ED, patients requiring MR imaging would be entered into the hospital transport queue and would be taken to the inpatient scanners, accompanied by the responsible ED nurse. Once arriving at the inpatient scanner, care would be transferred to the MR imaging nurse for the duration of the scan, with all the potential delays that are inherent in any transfer-of-care process. Following the patient's scan, this process was repeated in reverse, essentially doubling the potential for delays.

When the MR imaging scanner was placed in the ED, the use of the hospital transport queue was eliminated, with patients being moved by the dedicated ED transport system for more efficient transport. Both transfers of care were eliminated because the ED nurses are able to maintain care of their patients throughout the MR imaging process. Additionally, because the scanner was placed in the ED, only patients who would require nursing support for ED CT would require nursing support for ED MR imaging. These alterations essentially created an MR imaging workflow that was identical to the existing CT workflow, markedly reducing the previous temporal disadvantage of MR imaging. A comparison of the current and prior workflows can be seen in the *Figure*.

The next portion of the care process that required alteration was the scan itself. Barrow Neurological Institute inpatient MR imaging protocols last from 30 minutes to >1 hour; this timeframe is not conducive to high patient throughput. New ED scan protocols were created to limit scan time while providing adequate information to make emergent treatment and admit/discharge decisions. These protocols were designed to be completed in 10 minutes. A full listing of the sequences is detailed in the *Table*.

These new workflows and scan sequences necessitated education of referring physicians, nursing services, and technologists because they were substantially different from the inpatient protocols they were replacing. To this end, multiple meetings were held with the emergency physicians and the inpatient services (predominantly neurosurgery and neurology) before launch. Discussions were also held with the neurosurgery residents, nursing services, and technologists. The emergency physicians as a group were generally willing to transition from CT to MR imaging if the turnaround times would indeed be similar. There was some initial concern from the ED nurses that they would be forced to be away from their other patients for extended lengths of time. The nursing service was skeptical about the claim that the turnaround times for patients would be similar to those of CT. The inpatient services also expressed concern with the new processes, partic-

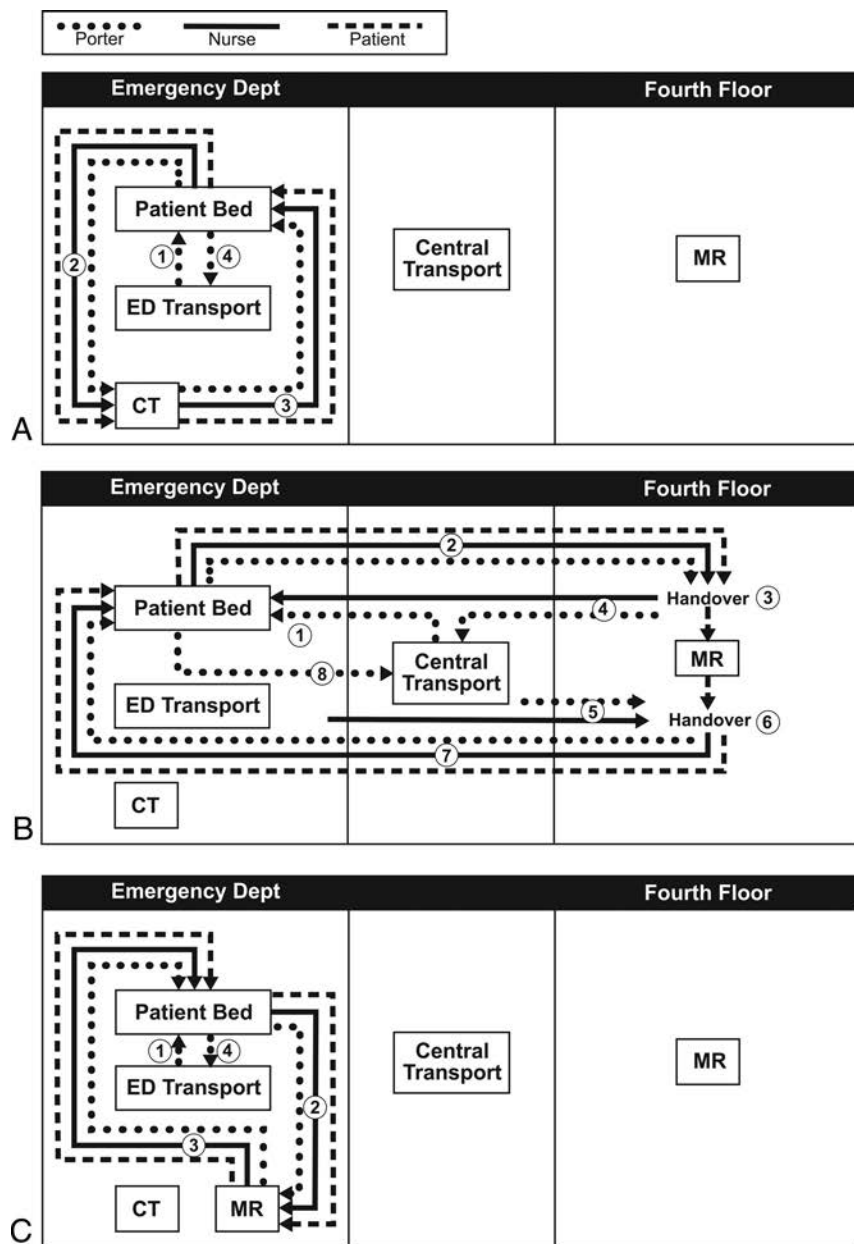


**FIGURE.** Workflow diagram. A, ED CT workflow: the ED porter collects the patient (1); porter, patient, and nurse go to CT (2); porter, patient, and nurse go to the patient's bed (3); porter goes to ED Transport (4). B, Prior MR workflow: central porter collects the patient (1); porter, patient, and nurse go to MR imaging (2); nursing handover with MR imaging nurses (3); nurse goes to ED, porter goes to Central Transport (4); ED nurse and central porter go to MR imaging (5); nursing handover with MR imaging nurses (6); porter, patient, and nurse go to patient's bed (7); porter goes to Central Transport (8). C, ED MR imaging workflow: ED porter collects the patient (1); porter, patient, and nurse go to ED MR imaging (2); porter, patient, and nurse go to patient's bed (3); porter goes to ED Transport (4).

ularly relating to the loss of information secondary to the limited protocols. It was emphasized that these scans were for emergent treatment and admit/discharge decisions and that any additional information required could be obtained with an inpatient scan should the patient in question require admission.

#### Program Deployment

The installation of the MR imaging scanner in the ED took approximately 2 years from the time it was initially approved. This

process was substantially expedited because the ED had preexisting space available to house the scanner, avoiding extensive renovations/additions to the existing structure of the ED. Overall, there were no lengthy or unexpected delays, and the scanner went live in May 2015.

The new scan protocols were deployed in 2 phases. In phase 1, ordering guidelines were created with MR imaging replacing CT of the head as the primary imaging technique for all non-trauma, nonstroke indications in the ED. This phase was initiated in May 2015. Phase 2 was initiated in July 2016, when MR imaging of the head and contrast-enhanced MRA of the head and neck replaced CT of the head and CT angiography of the head and neck as the primary imaging technique for acute stroke. Scan data were collected from August through November in 2015 and 2016 and were compared with baseline data collected from August through November in 2014. Statistical significance was calculated by using the  $\chi^2$  test. Results are reported as the percentage change between phases (number of CT scans/number of total scans, *P* value).

Before the installation of the ED MR imaging scanner, 86% (5538/6430) of the monthly scans performed in the emergency department were CT. Following initiation of phase 1, there was a statistically significant drop in the percentage of CT studies to 62% (4518/7288, *P* < .001). The distribution of these CT scans changed slightly with fewer CT angiography studies (22% to 15%) and an associated increase in the proportion of time-of-flight MRAs (5% to 13%). There was also a large increase in the percentage of unenhanced MR imaging of the brain (17% to 29%).

Following the initiation of phase 2, there was an additional statistically significant drop in the overall CT scan percentage to 48% (4161/8669, *P* < .001). The distribution of CT scans again changed slightly, with a continued decrease in the proportion of CTA studies (15% to 9%) and a marked increase in contrast-enhanced MRA, accounting for 11% of MR imaging studies. This change was associated with an increase in the proportion of enhanced MR imaging of the brain related to the new stroke protocol.

Throughput following phase 1 averaged between 25 and 26 scans per day during the 4-month period. This number increased

## New ED scan protocols at Barrow Neurological Institute

Scan	Sequences
Unenhanced brain	Sagittal T1, axial DWI, axial FLAIR, axial T2 GRE
Enhanced brain	Sagittal T1, axial DWI, axial FLAIR, 3D-T1 with and without contrast
Unenhanced C/T spine	Sagittal T1, sagittal mDixon T2, axial T2 GRE
Enhanced C/T spine	Sagittal T1, sagittal STIR, sagittal and axial mDixon T1 with contrast
Unenhanced L spine	Sagittal T1, sagittal mDixon T2, axial T2 TSE, coronal T1
Enhanced L spine	Sagittal T1, sagittal mDixon T2, axial T2 TSE, sagittal and axial mDixon T1 with contrast
Unenhanced MRA	Axial 2D TOF of the neck, 3D TOF of the head
Enhanced MRA	3D bolus dynamic contrast-enhanced

**Note:**—GRE indicates gradient-echo; mDixon, modified Dixon; C, cervical; T, thoracic; L, lumbar.

to between 39 and 40 scans per day in phase 2, a 65% increase in daily throughput. Because phase 1 occurred when the workflows and protocols were new, this increase was likely due to an increase in ordering and improving familiarity with the new workflows for both nurses and technologists.

The culture shift associated with these changes, with an emphasis on throughput as opposed to completeness, was challenging for the technologists. Before the addition of the ED MR imaging scanner, technologists had been working for years in a setting where attention to detail and completeness were routinely applauded. Adding extra sequences based on already completed series or additional patient history was helpful and reduced the need for separate, additional scans. However, in the new ED environment where efficiency was paramount, the addition of extra sequences or deviation from the established protocols had a profoundly negative effect on patient throughput and turnaround times. This transition was substantially more difficult than anticipated and required continued communication following the launch of the new protocols. In hindsight, increased effort on education of technologists, focusing on this culture shift, would likely have eased this transition and increased initial patient throughput.

Conversely, the concerns expressed before launch by the ED nursing staff regarding the amount of time the new workflow would require them to be away from their patients were alleviated very shortly following launch. Once the 10-minute scan time was established as a reality, the temporal difference between MR imaging and CT from a nursing perspective was minimal and the ED nursing staff adapted to the new routine within a few weeks.

The initiation of the new scanner and subsequent increase in MR imaging volume from the ED necessitated some reordering of scan allocations among the neuroradiology fellows to compensate for the changing distribution of scans. The average MR imaging turnaround time (time from when a scan is ordered to when the scan is started) for the ED changed from 3 hours 51 minutes before phase 1 to 1 hour 50 minutes following phase 1 and 2 hours 26 minutes following phase 2. We hypothesize that this increase in turnaround time seen between phases 1 and 2 was related to the overall increase in MR imaging volume in the ED seen in phase 2. When we specifically selected for patients imaged for acute stroke, MR imaging in phase 2 had an average turnaround time of 15 minutes 30 seconds, lower than the CT turnaround time for phase 1 of 19 minutes 9 seconds.

Reactions from the attending neuroradiologists were varied, with some lauding the efficiency and decreased read time of the new scans, while others expressed concern over the limitations of

the new sequences. A good example of these concerns is the decreased sensitivity of contrast-enhanced MRA for aneurysms. There were also concerns raised that the new, limited examinations would not meet the expectations of referring physicians and patients who expect a thorough and detailed examination from a specialized center like the Barrow Neurological Institute. In response to these concerns, statements detailing the purpose and limitations of the new ED protocols were included in reporting templates for these studies.

The effects on referring physicians were also varied. ED physicians have been satisfied with the turnaround and throughput and have expressed greater confidence with decisions to both admit and discharge patients. Concerns from inpatient services over missing diagnostic information have translated into persistent ordering of time-intensive scans despite the prelaunch education. These scans generally come in 2 variations: either large-area scans such as MR imaging of the brain and cervical, thoracic, and lumbar spine with and without contrast for investigation of multiple sclerosis, or small-FOV, thin-section imaging such as pituitary or orbit scans. Continued effort to emphasize the purpose of the ED scans is ongoing, including collaborative research projects to establish the value of certain scans in admit/discharge decisions. During our data collection, there were no instances of patients being recalled for additional images due to insufficient diagnostic information.

While the challenges with respect to the day-to-day ordering trends of the inpatient services were anticipated, the effects on the learners, particularly the neurosurgery residents, were not. Through hours of on-call work, the neurosurgery residents at Barrow Neurological Institute had become extremely proficient in extracting the information they needed to make decisions on call from inpatient MR imaging sequences with which they were familiar. The addition of ED MR imaging scan protocols optimized to reduce scan time replaced these familiar sequences with new sequences and severely undermined the residents' confidence in their on-call decision-making. The magnitude of this disruption was much greater than anticipated before launch and required additional education sessions with the neurosurgery residents to familiarize them with the new scan protocols and draw parallels between the sequences they knew and the corresponding new sequences. Provided with this foundation, the residents acclimated within 2–3 months to the new protocols and concerns regarding the ED scanner became infrequent.

### Future Directions

Continued evaluation and improvement of the ED MR imaging workflows and protocols are ongoing to ensure that patients in the ED receive the maximal benefit from their imaging study. An example of this improvement is the development of a new T2\*-weighted sequence to replace the currently used gradient-echo sequence in the MR imaging brain protocol, which will provide improved spatial resolution with approximately 60-second shorter scan times. Additional fine-tuning of the protocols will

continue as more experience is gained with a dedicated ED MR imaging scanner.

There are currently no plans to add additional MR imaging scanners to the emergency department. However, 2 new inpatient MR imaging scanners are scheduled to be installed adjacent to the ED, which will allow decompression of the ED scanner should ED scan volumes continue to rise and outstrip current capacity.

While we were able to significantly reduce the proportion of CT imaging studies ordered in the ED (86% to 48%, a 56% relative reduction), the overall volume of imaging rose continuously during the 2-year period, from 6430 per 4-month period in 2014, to 7288 in 2015, and 8669 in 2016. Based on this rise, the absolute reduction in CT scans performed was 1379 studies per 4-month period, a 25% reduction. Concern has been raised that the installation of an MR imaging scanner in the ED has simply replaced inappropriately ordered CT scans with inappropriately ordered MRIs and that the underlying problem of rising use remains unaddressed. This argument merits attention, and other interventions such as persistent physician education, clinical decision support, updated guidelines, and pay-for-performance systems have been shown to be effective in decreasing use in academic centers.<sup>3,4</sup> However, the issue of increased use is multifactorial, and a permanent solution would likely require systematic changes to payment structures and extensive alterations in the medicolegal landscape, both of which are extremely complex environments. Fast access to MR imaging from the ED has, at least in the interim, provided a safer and diagnostically superior replacement for CT.

## CONCLUSIONS

The installation of a dedicated ED MR imaging scanner significantly reduced the number of CT scans performed in the ED by providing a diagnostically superior and safer imaging alternative with a drastically improved turnaround time. This was achieved by altering the MR imaging workflow and existing scan protocols with an emphasis on efficiency and patient throughput. This change has resulted in increased confidence in clinical decision-making for the ED physicians and, with the exception of the unanticipated severity of the culture shift on the MR imaging technologists and neurosurgery residents, has been relatively well-received. Whether this change has resulted in improved patient outcomes was not addressed and further investigation is required.

## ACKNOWLEDGMENTS

We thank Kevin King and Jana Mahl for their tireless assistance with data collection for this project.

## REFERENCES

1. Levin DC, Rao VM, Parker L, et al. **Continued growth in emergency department imaging is bucking the overall trends.** *J Am Coll Radiol* 2014;11:1044–47 CrossRef Medline
2. Rankey D, Leach JL, Leach SD. **Emergency MRI utilization trends at a tertiary care academic medical center: baseline data.** *Acad Radiol* 2008;15:438–43 CrossRef Medline
3. Arasu VA, Abujudeh HH, Biddinger PD, et al. **Diagnostic emergency imaging utilization at an academic trauma center from 1996 to 2012.** *J Am Coll Radiol* 2015;12:467–74 CrossRef Medline
4. Raja AS, Ip IK, Sodickson AD, et al. **Radiology utilization in the emergency department: trends of the past 2 decades.** *AJR Am J Roentgenol* 2014;203:355–60 CrossRef Medline
5. Ahn S, Kim WY, Lim KS, et al. **Advanced radiology utilization for a tertiary care emergency department from 2001 to 2010.** *PLoS One* 2014;9:e112650 CrossRef Medline
6. Brenner DJ, Hall EJ. **Computed tomography: an increasing source of radiation exposure.** *N Engl J Med* 2007;357:2277–84 CrossRef Medline
7. Smith-Bindman R, Lipson J, Marcus R, et al. **Radiation dose associated with common computed tomographic examinations and the associated life-time attributable risk of cancer.** *Arch Intern Med* 2009;169:2078–86 CrossRef Medline
8. Berrington de González A, Mahesh M, Kim KP, et al. **Projected cancer risks from computed tomographic scans performed in the United States in 2007.** *Arch Intern Med* 2009;169:2071–77 CrossRef Medline
9. Sodickson A, Baeyens PF, Andriole KP, et al. **Recurrent CT, cumulative radiation exposure and associated radiation-induced cancer risks from CT of adults.** *Radiology* 2009;251:175–84 CrossRef Medline
10. Zhang WI, Li M, Zhang B, et al. **CT angiography of the head-and-neck vessels acquired with low tube voltage, low iodine, and iterative image reconstruction: clinical evaluation of radiation dose and image quality.** *PLoS One* 2013;8:e81486 CrossRef Medline
11. Reimann AJ, Davison C, Bjarnason T, et al. **Organ-based computed tomographic (CT) radiation dose reduction to the lenses: impact on image quality for CT of the head.** *J Comput Assist Tomogr* 2012;36:334–38 CrossRef Medline
12. Ketelsen D, Buchgeister M, Fenchel M, et al. **Automated computed tomography dose-saving algorithm to protect radiosensitive tissue: estimation of radiation exposure and image quality considerations.** *Invest Radiol* 2012;47:148–52 CrossRef Medline
13. American College of Radiology: Appropriateness Criteria. <https://acsearch.acr.org/list>. Accessed December 27, 2016
14. Fiebich JB, Schellinger PD, Jansen O, et al. **CT and diffusion-weighted MR imaging in randomized order: diffusion-weighted imaging results in higher accuracy and lower interrater variability in the diagnosis of hyperacute ischemic stroke.** *Stroke* 2002;33:2206–10 CrossRef Medline
15. Chalela JA, Kidwell CS, Nentwich LM, et al. **Magnetic resonance imaging and computed tomography in emergency assessment of patients with suspected acute stroke: a prospective comparison.** *Lancet* 2007;369:293–98 CrossRef Medline
16. Kidwell CS, Chalela JA, Saver JL, et al. **Comparison of MRI and CT for detection of acute intracerebral hemorrhage.** *JAMA* 2004;292:1823–30 CrossRef Medline
17. Fiebich JB, Schellinger PD, Gass A, et al. **Stroke magnetic resonance imaging is accurate in hyperacute intracerebral hemorrhage: a multicenter study on the validity of stroke imaging.** *Stroke* 2004;35:502–06 CrossRef Medline
18. Dannenberg S, Scheitz JF, Rozanski M, et al. **Number of cerebral microbleeds and risk of intracerebral hemorrhage after intravenous thrombolysis.** *Stroke* 2014;45:2900–05 CrossRef Medline
19. Kidwell CS, Saver JL, Villablanca JP, et al. **Magnetic resonance imaging detection of microbleeds before thrombolysis: an emerging application.** *Stroke* 2002;33:95–98 CrossRef Medline
20. Thomalla G, Cheng B, Ebinger M, et al. **STIR and VISTA Imaging Investigators. DWI-FLAIR mismatch for the identification of patients with acute ischaemic stroke within 4.5 h of symptom onset (PRE-FLAIR): a multicenter observational study.** *Lancet Neurol* 2011;10:978–86 CrossRef Medline
21. Thomalla G, Rossbach P, Rosenkranz M, et al. **Negative fluid-attenuated inversion recovery imaging identifies acute ischemic stroke at 3 hours or less.** *Ann Neurol* 2009;65:724–32 CrossRef Medline
22. Aoki J, Kimura K, Iguchi Y, et al. **FLAIR can estimate the onset time in acute ischemic stroke patients.** *J Neurol Sci* 2010;293:39–44 CrossRef Medline
23. Petkova M, Rodrigo S, Lamy C, et al. **MR imaging helps predict time from symptom onset in patients with acute stroke: implications for**

- patients with unknown onset time. *Radiology* 2010;257:782–92 CrossRef Medline
24. Schellinger PD, Thomalla G, Fiehler J, et al. **MRI-based and CT-based thrombolytic therapy in acute stroke within and beyond established time windows: an analysis of 1210 patients.** *Stroke* 2007;38:2640–45 CrossRef Medline
  25. Randoux B, Marro B, Koskas F, et al. **Carotid artery stenosis: prospective comparison of CT, three-dimensional gadolinium-enhanced MR, and conventional angiography.** *Radiology* 2001;220:179–85 CrossRef Medline
  26. Yang CW, Carr JC, Futterer SF, et al. **Contrast-enhanced MR angiography of the carotid and vertebrobasilar circulations.** *AJNR Am J Neuroradiol* 2005;26:2095–101 Medline
  27. U-King-Im JM, Trivedi RA, Cross JJ, et al. **Measuring carotid stenosis on contrast-enhanced magnetic resonance angiography: diagnostic performance and reproducibility of 3 different methods.** *Stroke* 2004;35:2083–88 CrossRef Medline
  28. Nael K, Meshksar A, Ellingson B, et al. **Combined low-dose contrast-enhanced MR angiography and perfusion for acute ischemic stroke at 3T: a more efficient stroke protocol.** *AJNR Am J Neuroradiol* 2014;35:1078–84 CrossRef Medline
  29. Alfke K, Jensen U, Pool C, et al. **Contrast-enhanced magnetic resonance angiography in stroke diagnostics: additional information compared with time-of-flight magnetic resonance angiography?** *Clin Neuroradiol* 2011;21:5–10 CrossRef Medline
  30. Saager C, Fitting T, Goebell E, et al. **Contrast-enhanced MR angiography improves detection of carotid T-occlusion by acute stroke MRI.** *Clin Neuroradiol* 2008;18:163–67 CrossRef
  31. da Rocha AJ, da Silva CJ, Gama HP, et al. **Comparison of magnetic resonance imaging sequences with computed tomography to detect low-grade subarachnoid hemorrhage: role of fluid-attenuated inversion recovery sequence.** *J Comput Assist Tomogr* 2006;30:295–303 CrossRef Medline
  32. Yuan MK, Lai PH, Chen JY, et al. **Detection of subarachnoid hemorrhage at acute and subacute/chronic stages: comparison of four magnetic resonance imaging pulse sequences and computed tomography.** *J Chin Med Assoc* 2005;68:131–37 CrossRef Medline
  33. Verma RK, Kottke R, Andereggen L, et al. **Detecting subarachnoid hemorrhage: comparison of combined FLAIR/SWI versus CT.** *Eur J Radiol* 2013;82:1539–45 CrossRef Medline
  34. Paterakis K, Karantanis AH, Komnos A, et al. **Outcome of patients with diffuse axonal injury: the significance and prognostic value of MRI in the acute phase.** *J Trauma* 2000;49:1071–75 CrossRef Medline
  35. Lee H, Wintermark M, Gean AD, et al. **Focal lesions in acute mild traumatic brain injury and neurocognitive outcome CT vs 3T MRI.** *J Neurotrauma* 2008;25:1049–56 CrossRef Medline
  36. Mittl RG, Grossman RI, Hiehle JF, et al. **Prevalence of MR evidence of diffuse axonal injury in patients with mild head injury and normal head CT findings.** *AJNR Am J Neuroradiol* 1994;15:1583–89 Medline
  37. Morais DF, de Melo Neto JS, Meguins LC, et al. **Clinical applicability of magnetic resonance imaging in acute spinal cord trauma.** *Eur Spine J* 2014;23:1457–63 CrossRef Medline

# Cumulative Dose of Macrocytic Gadolinium-Based Contrast Agent Improves Detection of Enhancing Lesions in Patients with Multiple Sclerosis

A. Rovira, C. Auger, E. Huerga, J.F. Corral, R. Mitjana, J. Sastre-Garriga, M. Tintoré, and X. Montalban

## ABSTRACT

**BACKGROUND AND PURPOSE:** Gadolinium-enhanced MR imaging is currently the reference standard for detecting active inflammatory lesions in patients with multiple sclerosis. The sensitivity of MR imaging for this purpose may vary according to the physicochemical characteristics of the contrast agent used and the acquisition strategy. The purpose of this study was to compare detection of gadolinium-enhancing lesions or active disease following a single or cumulative dose of a macrocytic gadolinium-based contrast agent with different image acquisition delays in patients with clinically isolated syndrome or relapsing multiple sclerosis.

**MATERIALS AND METHODS:** All patients received a first dose (0.1 mmol/kg) of gadobutrol and, 20 minutes later, a second dose (0.1 mmol/kg), with a cumulative dose of 0.2 mmol/kg. Two contrast-enhanced T1-weighted sequences were performed at 5 and 15 minutes after the first contrast administration, and 2 additional T1-weighted sequences at 5 and 15 minutes after the second contrast administration with a 3T magnet.

**RESULTS:** One hundred fifteen patients were considered evaluable. A significantly larger number of lesions were detected in scans obtained at 5 and 15 minutes after the second contrast injection compared with scans obtained at 5 and 15 minutes after the first injection ( $P < .001$ ). The number of patients with active lesions on MR imaging was significantly higher after the second dose administration (52.0%, first dose versus 59.2%, second dose;  $P < .001$ ).

**CONCLUSIONS:** Cumulative dosing of a macrocytic gadolinium-based contrast agent increases detection of enhancing lesions and patients with active lesions. These data could be considered in the design of MR imaging protocols aimed at detecting active multiple sclerosis lesions.

**ABBREVIATIONS:** CIS = clinically isolated syndrome; GBCA = gadolinium-based contrast agent; GRE = gradient recalled-echo

Gadolinium-enhanced MR imaging is currently the reference standard for detecting inflammatory demyelinating lesions associated with increased permeability of the blood-brain barrier in patients with multiple sclerosis, and is commonly used as a marker of acute focal inflammatory activity.<sup>1,2</sup> The sensitivity of the technique for this purpose may vary according to the physicochemical characteristics of the contrast agent used and the acquisition strategy (eg, delay between injection and image acquisition, contrast dose, field strength, and parameters of the postin-

jection T1-weighted sequence).<sup>3-12</sup> A large body of evidence has indicated that various approaches can increase the visibility of contrast-enhancing lesions and lead to a notable improvement in sensitivity.<sup>3,4,8,9,12-15</sup> One potential strategy that has not yet been explored is the combination of an increased contrast dose and a longer delay time at 3T MR imaging with a 2D gradient recalled-echo (GRE) T1-weighted sequence. To examine this option, we designed the present open-label, prospective study to assess the advantages of combining a high-field-strength MR imaging magnet (3T) and a cumulative gadolinium dose (0.1 mmol/kg + 0.1 mmol/kg) at different delay times compared with a single dose (0.1 mmol/kg) to detect active lesions in patients with clinically isolated syndrome (CIS) or relapsing MS. The hypothesis was that the combined advantages of a cumulative gadolinium dose and a longer delay time would significantly increase the detection rate of active lesions and the percentage of patients showing disease activity, measures that have a strong impact for the diagnosis of the disease, therapy optimization, and predicting disease course and treatment response.<sup>1,2,16</sup>

Received December 29, 2016; accepted after revision April 2, 2017.

From the Neuroradiology and Magnetic Resonance Units (A.R., C.A., E.H., J.F.C., R.M.), Department of Radiology, and Centre d'Esclerosi Múltiple de Catalunya (J.S.-G., M.T., X.M.), Department of Neurology/Neuroimmunology, Hospital Universitari Vall d'Hebron, Universitat Autònoma de Barcelona, Barcelona, Spain.

This work was funded by Bayer HealthCare Pharmaceuticals.

Please address correspondence to Àlex Rovira Cañellas, MD, Unitat de Resonància Magnètica, Servei de Radiologia, Hospital Universitari Vall d'Hebron, Pg. Vall d'Hebron 119-129, Barcelona 08035, Spain; e-mail: alex.rovira@idi.gencat.cat

<http://dx.doi.org/10.3174/ajnr.A5253>

## MATERIALS AND METHODS

### Patients

From January 2010 to December 2011, a prospective, single-center, open-label experimental phase IV study was performed at Vall d'Hebron University Hospital. The study compared a single dose and cumulative double dose of a macrocyclic gadolinium-based contrast agent (GBCA) (gadobutrol, Gadovist; Bayer Schering Pharma, Berlin, Germany) administration with different delay times at 3T to detect enhancing lesions in patients with CIS and relapsing MS using blinded, centralized MR imaging assessment.

Patients 18–50 years of age with CIS suggestive of central nervous system demyelination not attributable to other diseases and those with a diagnosis of relapsing MS based on the McDonald 2010 criteria<sup>17</sup> showing at least 2 brain T2 lesions of the type seen in MS were eligible for inclusion in the study.

The exclusion criteria were as follows: pregnant or nursing women, patients having a pacemaker or any other factor that would preclude proximity to a strong magnetic field, those with severe claustrophobia or a known allergy to GBCAs, previous participants in a clinical trial of an investigational drug within 30 days before MR imaging, those with any medical condition that might decrease the chance of obtaining reliable data, and patients with known impaired renal function (glomerular filtration rate, <60 mL/min/1.73 m<sup>2</sup>).

The study protocol and consent documents were approved by the Clinical Research Ethics Committee of Hospital Vall d'Hebron, and the procedures were in accordance with the ethical standards of the Declaration of Helsinki, as revised in 2000. The blinded read was conducted in compliance with the International Conference on Harmonization of Good Clinical Practice guidelines and all applicable regulatory requirements. Before participation, eligible patients were informed of all aspects of the study and provided written informed consent.

### Study Design and MR Imaging Protocol

Two visits took place before MR imaging acquisition. During the initial visit, consecutive patients with CIS (demonstrating on a previous MR imaging at least 2 focal brain lesions suggestive of MS) or relapsing MS were identified. All these patients were referred to the MR imaging unit as part of the diagnostic work-up in patients with CIS and of the monitoring process in patients with relapsing MS with suspected disease activity or progression.

A total of 122 patients were initially identified, though 7 (6%) were excluded because 5 did not have either CIS or relapsing MS and 2 had exclusion criteria. Ultimately, 115 patients were included in the study and analyzed; approximately one-quarter had CIS and three-quarters had relapsing MS.

During the second visit (visit 0), a pregnancy test was performed within 24 hours before MR imaging acquisition in women with childbearing potential, and demographic and clinical data were recorded. These included the patient's medical history, CIS or relapsing MS diagnosis, current medication, and neurologic examination results, including the Expanded Disability Status Scale score.

During visit 1, the MR imaging acquisition visit, all patients were examined on a 3T MR imaging scanner equipped with a 12-channel phased array head coil. The imaging protocol in-

cluded the following sequences: 1) transverse proton density and T2-weighted fast spin-echo (TR, 2500 ms; TE, 16–91 ms; NEX, 1); and 2) transverse fast T2-FLAIR (TR, 9000 ms; TE, 100 ms; TI, 2500 ms; NEX, 2; flip angle, 120°). Both sequences were acquired with an FOV of 250 mm, and contiguous, 3-mm sections covering the whole brain (voxel size, 0.78 × 0.78 × 3.0 mm).

In patients in whom the previous sequences confirmed the presence of at least 2 T2 lesions, an unenhanced 2D GRE T1-weighted sequence was performed before the first GBCA dose, which was manually administered as an intravenous bolus at a rate of 1 mL/s. This first 0.1-mmol/kg dose (equivalent to 0.1 mL/kg) was followed by a 20-mL saline flush, and a first contrast-enhanced 2D GRE T1-weighted sequence was performed 5 minutes after contrast administration (scan A), and a second contrast-enhanced 2D GRE T1-weighted sequence was performed 10 minutes after scan A (scan B). Twenty minutes after the start of the first contrast administration, a second dose of GBCA (0.1 mmol/kg) was administered, followed by another saline flush, resulting in a cumulative dose of 0.2 mmol/kg (0.2 mL/kg). A third contrast-enhanced 2D GRE T1-weighted sequence was performed 5 minutes later (scan C), and a fourth contrast-enhanced 2D GRE T1-weighted sequence, 10 minutes after scan C (scan D).

The following parameters were used in all the 2D GRE T1-weighted sequences: TR, 297 ms; TE, 2.46 ms; NEX, 3; flip angle, 70°; FOV, 250 mm, acquiring contiguous 3-mm sections covering the whole brain (voxel size, 0.78 × 0.78 × 3.0 mm<sup>3</sup>).

### Image Analysis

To determine the number of enhancing lesions, we independently evaluated each of the 4 sets of contrast-enhanced 2D GRE T1-weighted images in a random fashion. Three neuroradiologists with >10 years of experience (not affiliated with the center where the scans were obtained) read the images, blinded to the time point at which the enhanced T1-weighted sequences had been obtained and using proton density/T2, T2-FLAIR, and unenhanced T1-weighted sequences as references.

The 3 readers independently recorded the number and topography of enhancing lesions in each contrast-enhanced T1-weighted scan. The number of lesions per patient was restricted to a maximum of 20 lesions for each scan. Patients with MR imaging–active lesions were defined as those showing at least 1 enhancing lesion in any of the contrast-enhanced T1-weighted sequences. In addition, the readers graded the quality of the images in 3 groups, good, average, or poor, and expressed their level of confidence in the detection of each enhancing lesion in each scan as very confident, confident, or not confident.

### Efficacy Analysis: End Points

The end points of the study were the number of enhancing lesions and the number of patients with MR imaging–active lesions detected with a cumulative dose of a macrocyclic GBCA versus a single dose obtained at different time delays.

### Adverse Events

Adverse events were recorded and classified into mild, moderate, or severe. The observation period for recording adverse events ran

**Table 1: Baseline characteristics**

	Patients with CIS (n = 26)	Patients with MS (n = 89)	Total (n = 115)
Sex (No.) (%)			
Female	17 (65.4)	66 (74.2)	83 (72.2)
Male	9 (34.6)	23 (25.8)	32 (27.8)
Age (yr)			
Mean (SD)	32.9 (7.1)	36.0 (6.5)	35.3 (6.7)
Median	31.0	36.0	35.0
Min, max	(25.0, 47.0)	(23.0, 50.0)	(23.0, 50.0)
EDSS score			
Mean (SD)	1.6 (1.1)	3.0 (1.7)	2.7 (1.7)
Median	1.5	3	2.5
Min, max	(0.0, 4.0)	(0.0, 7.5)	(0.0, 7.5)

**Note:**—EDSS indicates Expanded Disability Status Scale; Min, minimum; max, maximum.

from the start of administration of the first gadolinium dose up to 24 hours after administration of the second dose.

### Sample Size Calculation

To assess differences in active lesion detection in the 2 types of patients following administration of a single or cumulative contrast dose, we would have to include a minimum of 115 patients in the study. The sample size was determined on the basis of an expected mean of 2.1 enhancing lesions detected with a single dose of gadolinium (1.5 lesions in CIS and 2.7 in relapsing MS)<sup>18,19</sup> and a 15% minimum increase in the number of lesions detected after the second dose,<sup>12,20</sup> considering that 15% of patients initially included in the study would be excluded from the final analysis.

### Statistical Analysis

Descriptive analyses (mean, median, SD, minimum, and maximum) were performed for the quantitative variables, and frequency counts by category were calculated for the qualitative variables. Confidence intervals, given when appropriate, were 2-sided in each case and provided 95% confidence.

The total number of enhancing lesions per patient between each time point was compared with Poisson regression based on generalized estimations. The number of patients with active lesions at each time point was compared using a  $\chi^2$  test. Statistical significance was set at a *P* value of  $<.05$ .  $\kappa$  coefficients were calculated to assess the agreement among the readers' assessments in pair-wise comparisons. Statistical analyses were performed with SAS, Version 9.3 (SAS Institute, Cary, North Carolina).

## RESULTS

Baseline demographic and clinical characteristics were homogeneous between the groups, with more women than men in both the CIS and relapsing MS groups (Table 1). Six (5.2%) patients had  $\leq 8$  T2 lesions, whereas 109 patients (94.8%) had  $> 8$  T2 lesions. Three (11.5%) patients with CIS and 47 (52.8%) with relapsing MS were under a disease-modifying treatment at the time of the study. There was 1 mild adverse event (nausea after the first contrast injection), which did not require any treatment other than observation.

**Table 2: Enhancing lesion count per scan and reader<sup>a</sup>**

Scan <sup>b</sup>	Lesion No.
Reader 1	
A	243
B	238
C	362
D	379
Reader 2	
A	260
B	308
C	373
D	402
Reader 3	
A	325
B	358
C	455
D	490
Total lesion No. (mean)	
A	828 (2.4)
B	904 (2.6)
C	1190 (3.5)
D	1271 (3.7)

<sup>a</sup> The number of enhancing lesions detected in each MRI scan did not significantly differ among the 3 readers (*P* = .4280).

<sup>b</sup> A, early single dose; B, delayed single dose; C, early cumulative dose; D, delayed cumulative dose.

### Contrast-Enhancing Lesions

All 115 evaluable patients received the first and second gadolinium injections. The mean time interval between the first and second injections was  $20.3 \pm 1.7$  minutes ( $19.8 \pm 1.0$  in CIS and  $20.4 \pm 1.8$  in relapsing MS). After the first gadolinium dose, the 2D GRE T1-weighted scans were obtained at a mean postinjection time of  $5.0 \pm 0.2$  minutes (scan A) and  $15.1 \pm 0.7$  minutes (scan B). After the second dose, the scans were obtained at a mean postinjection time of  $5.0 \pm 0.0$  minutes (scan C) and  $15.1 \pm 0.8$  minutes (scan D).

The number of enhancing lesions detected on each MR imaging scan did not significantly differ among the 3 readers (Table 2). The total number of enhancing lesions was similar in images obtained at 5 (scan A) and 15 minutes (scan B) after the first contrast injection (276 versus 301) and at 5 (scan C) and 15 (scan D) minutes after the second dose (397 versus 424) (Fig 1). However, a significantly larger number of lesions were detected in scans obtained at 5 (mean, 5.8) and 15 minutes (mean, 6.2) after the second contrast injection than at 5 (mean, 4.5) and 15 minutes after the first injection (mean, 4.9) (*P*  $<.001$ ). The increase in total lesion count between the single-dose scan obtained at 5 minutes and the cumulative scan at 15 minutes was 58% (Table 3). This increase was only 8.7% between the 5- and 15-minute single-dose scans, and 6.6% between the 5- and 15-minute cumulative-dose scans, but an increase of 27.3% was seen between the 15-minute single-dose scan and the 5-minute cumulative-dose scan. Examples of lesion detection on images obtained at different time points are shown in Figs 2–4.

The number of patients showing at least 1 gadolinium-enhancing lesion (MR imaging–active) increased from 52% in the single-dose scans to 58.9%–59.2% in the 2 cumulative-dose scans (*P*  $<.001$ ) (Fig 5).

As to reproducibility in the assessment of patients with active lesions, agreement between readers 1 and 2 was highest for scan D

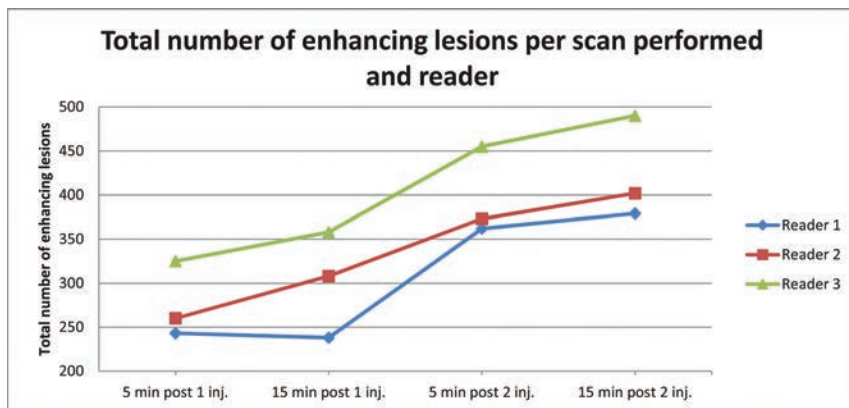


FIG 1. Total number of enhancing lesions per scan obtained and reader.

Table 3: Number of enhancing lesions in patients with active lesions by scan and reader<sup>a</sup>

Reader, Scan <sup>b</sup>	No. <sup>c</sup>	Total	Median (mean)	Minimum	Maximum <sup>d</sup>
1					
A	56	243	2.5 (4.3)	1.000	20.000
B	54	238	2.0 (4.4)	1.000	20.000
C	61	362	3.0 (5.9)	1.000	20.000
D	63	379	3.0 (6.0)	1.000	20.000
2					
A	58	260	2.0 (4.5)	1.000	20.000
B	61	308	3.0 (5.0)	1.000	20.000
C	68	373	3.0 (5.5)	1.000	20.000
D	64	402	3.0 (6.3)	1.000	20.000
3					
A	69	325	2.0 (4.7)	1.000	20.000
B	67	358	3.0 (5.3)	1.000	20.000
C	76	455	3.0 (6.0)	1.000	20.000
D	79	490	3.0 (6.2)	1.000	20.000

<sup>a</sup> A higher number of enhancing lesions was detected for cumulative-versus-single dose scans ( $P < .001$ ).

<sup>b</sup> A, early single dose; B, delayed single dose; C, early cumulative dose; D, delayed cumulative dose.

<sup>c</sup> No., number of patients with active lesions.

<sup>d</sup> The number of lesions was restricted to a maximum of 20 per patient.

(Table 4). Agreement between reader 3 and the other 2 readers did not show a high level of concordance for either the cumulative or delay scans.

### Postcontrast Image Quality

Image quality was rated as good for most images in all 4 scans obtained: reader 1, 93.97%; reader 2, 84.95%; and reader 3, 97.20% of the total. The readers showed no differences in their rating of image quality among the 4 scans. No scan was rated as poor; therefore, all images obtained were included in the analysis. Readers expressed a higher percentage of very confident assessments for scans performed after the second injection and 15 minutes' delay (reader 1,  $P = .022$ ; reader 2,  $P = .004$ ; and reader 3,  $P = .005$ ) (Table 3). Also across readers, significant differences were found between the image sets and the readers' assessment ( $P < .001$ ), but not for the interaction between image set and reader.

The mean percentages of enhancing lesions in the 4 sets of images for which the observers rated identification as very confident were 41%, 45%, 54%, and 54% (A, B, C, and D, respec-

tively), with higher values in the sets with longer delay times and higher doses ( $P < .001$ ).

### DISCUSSION

This study shows that a cumulative dose (0.2 mmol/kg) of a macrocyclic GBCA resulted in a significant increase in the sensitivity of contrast-enhanced 3T MR imaging for detecting active lesions in patients with CIS or relapsing MS, compared with a single contrast dose. Furthermore, this approach led to a higher percentage of patients with active lesions—that is, showing at least 1 gadolinium-enhancing lesion, which is an essential feature in the initial evaluation of patients suspected of having MS and a highly relevant prognostic marker, particularly in patients with MS under disease-modifying treatments.<sup>21,22</sup>

The readers found no differences in the quality of image sets obtained under different conditions of contrast dose and delay, whereas they conveyed higher confidence for detecting contrast-enhancing lesions with the cumulative-dose delayed scan. Moreover, a higher concordance in identifying patients with active lesions was observed between the first and second readers with the cumulative-dose delayed scan, but not between the third reader and the other 2, with a low level of concordance observed in all 4 scans. These discrepant results are because reader 3 detected a larger number of active lesions in each scan compared with readers 1 and 2, though this difference did not reach significance.

The results of our study are in line with those in previous studies, in which greater lesion detection was found with the use of higher gadolinium doses or time delays on 2D spin-echo sequences at 1.5T.<sup>3,6,7,12,14,20</sup> However, this study is the first to demonstrate this effect with 2D GRE sequences at 3T, a common scanning strategy used in clinical practice. In the present study, we selected a 2D GRE sequence because it reduces the flow artifacts seen with 2D spin-echo sequences, which are more problematic at 3T,<sup>23</sup> leading to a decrease in background noise and better lesion detection.

Gadolinium-enhanced brain MR imaging is the most sensitive tool for detecting focal inflammatory activity in MS and is essential for establishing an early MS diagnosis and for predicting the disease course.<sup>17</sup> Furthermore, the existence and degree of inflammatory activity are often used as an outcome measure in clinical trials, to select patients for initiation of disease-modifying treatment, to predict the risk of disability progression,<sup>24</sup> and to monitor and predict treatment effect.<sup>25–28</sup> In fact, several studies have attempted to define criteria and models for the early identification of incomplete response in individual patients via a combination of clinical and MR imaging measures during the first 6–12 months after treatment initiation, which are partially or completely based on the detection of disease activity.<sup>28–33</sup> All these data support the pivotal role of the presence and number of gadolinium-enhancing lesions to assess radiologic disease activity, which is used, in turn, for diagnosing and guiding therapeutic strategies and as a surrogate marker to evaluate treatment efficacy

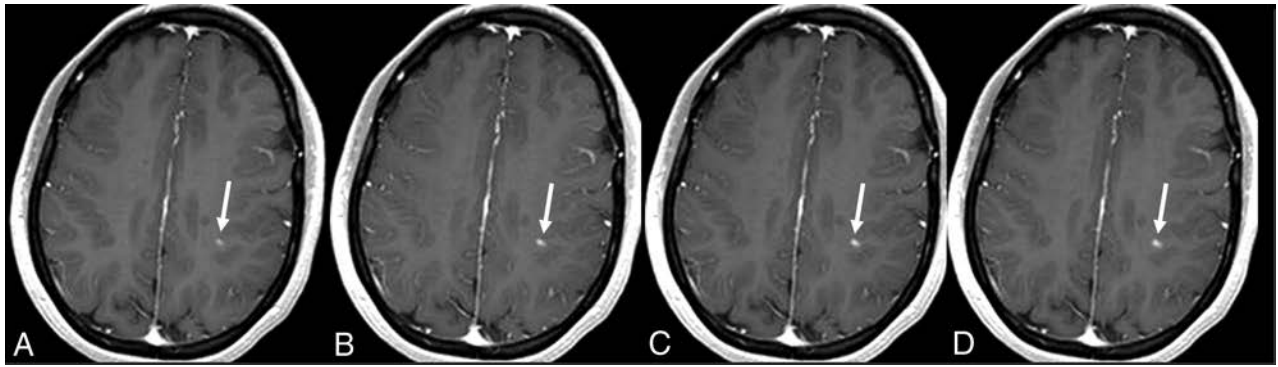


**FIG 2.** A 26-year-old woman with active relapsing-remitting multiple sclerosis. A small juxtacortical peri-Rolandic lesion located in the left brain hemisphere is identified on the 4 contrast-enhanced T1-weighted scans (arrows). Observe the increase in lesion size in the delayed single-dose scan (B) and cumulative-dose scans (C and D) compared with the early single-dose scan (A). Nonetheless, lesion detection is comparable in all 4 scan conditions.

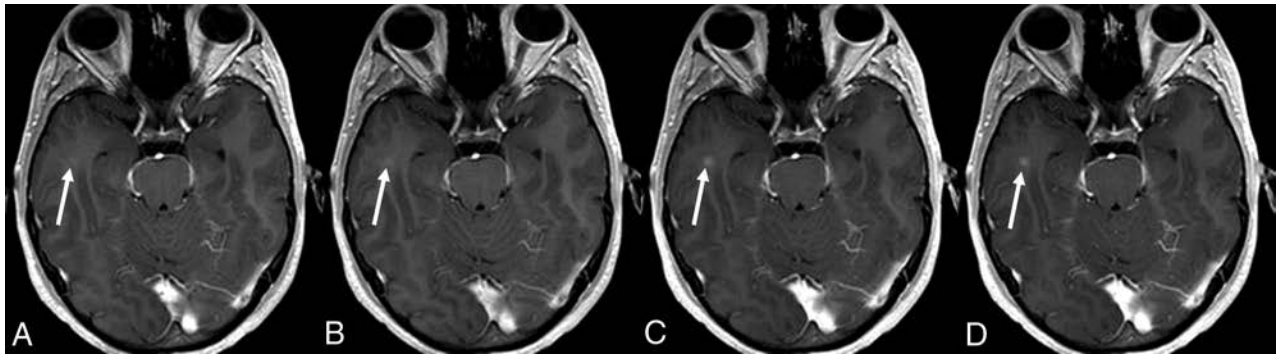


**FIG 3.** A 26-year-old man presenting with clinically isolated syndrome. A small enhancing lesion located in the right temporal subcortical white matter is seen on the 2 cumulative-dose contrast-enhanced T1-weighted scans (arrows in C and D) but is initially missed on the 2 single-dose scans. Mild enhancement is seen in the early and delayed single-dose scans (arrows in A and B) only in retrospect.

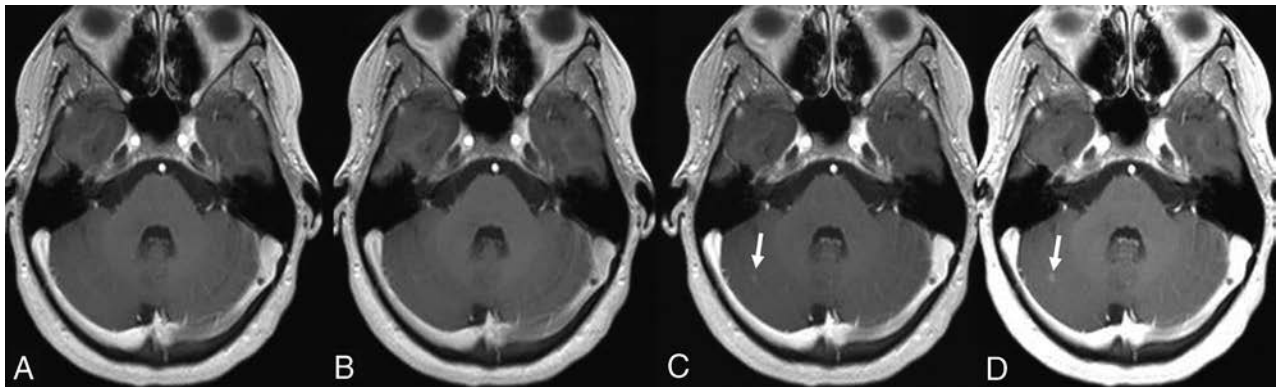


**FIG 4.** A 25-year-old woman presenting with clinically isolated syndrome. A nodular enhancing lesion located in the right cerebellar hemisphere is seen on the 2 cumulative-dose contrast-enhanced T1-weighted scans (arrows in C and D) but was not identified on the early and delayed single-dose scans (A and B). The intensity of lesion enhancement is higher on the delayed cumulative-dose scan (D).

in clinical trials. Thus, reliable detection of enhancing lesions is an important clinical and research goal in patients with CIS and MS, and considerable effort is required to optimize the parameters used in standard techniques to maximize the sensitivity of MR imaging for this purpose.

One strategy to increase the sensitivity of enhanced MR imaging for detecting active brain lesions in patients with MS is the use of high doses of contrast agent.<sup>3,6,8</sup> Our findings indicate that this factor is the main driver of the improved sensitivity found. In our patients with CIS and MS, the sensitivity increase was mainly due

to cumulative contrast dosing, whereas the influence of time was much weaker: Significant differences were detected between scans performed with single and cumulative doses, but not between the different delay times (5 and 15 minutes) used in each of the dosing regimens.

In a previous study, use of 1.0 mol/L (0.2 mmol/kg) of GBCA allowed detection of a larger number of enhancing lesions and patients with active disease than the use of 0.5 mol/L at the same dose, but the number of enhancing lesions did not differ significantly between images obtained 5 and 10 minutes after the injection.

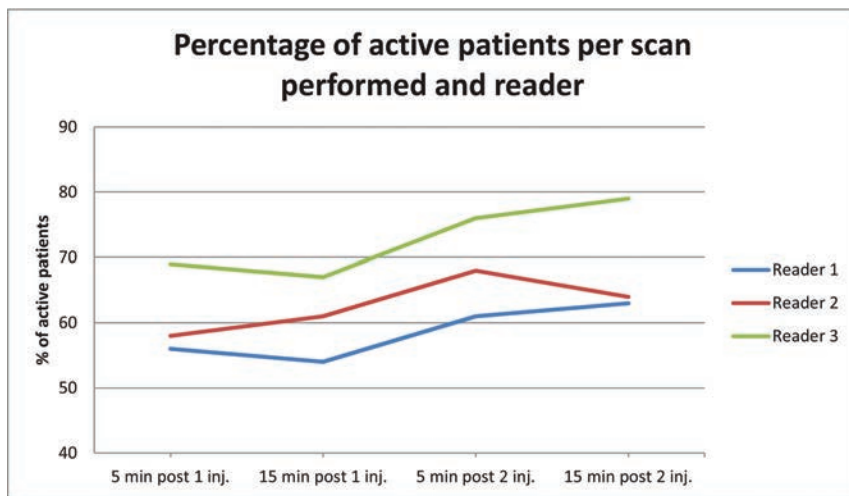


**FIG 5.** Percentage of patients with active lesions per scan performed and reader.

**Table 4:  $\kappa$  coefficients of the interreader agreement for the number of patients with active lesions**

Postgadolinium T1-Weighted Scan <sup>a</sup>	$\kappa$ (95% CI)		
	Reader 1 vs Reader 2	Reader 1 vs Reader 3	Reader 2 vs Reader 3
A	0.79 (0.68–0.90)	0.71 (0.58–0.83)	0.67 (0.54–0.80)
B	0.85 (0.75–0.94)	0.71 (0.59–0.83)	0.83 (0.72–0.93)
C	0.81 (0.70–0.92)	0.70 (0.58–0.83)	0.78 (0.67–0.90)
D	0.95 (0.89–1.00)	0.68 (0.55–0.81)	0.70 (0.57–0.82)

<sup>a</sup> A, early single dose; B, delayed single dose; C, early cumulative dose; D, delayed cumulative dose.

tion.<sup>8</sup> In contrast to that study, in which a single dose was followed by a double dose administered 24–48 hours later, we used 2 consecutive doses of GBCA, resulting in a cumulative dose of 0.2 mmol/kg. Our data support the results of other authors reporting that the combination of high contrast doses with other strategies, such as delayed acquisition, can increase the sensitivity of lesion detection compared with standard approaches.<sup>3,8</sup> In addition, the contrast administration schedule we used was not associated with severe adverse effects in the population studied.

The design used in this study would be very difficult to implement in clinical practice (2 consecutive injections of gadolinium to achieve the cumulative double dose). However, on the basis of the results of the present study that show a significant increase in the detection of active lesions and scans showing active lesions after the second injection of contrast, we may suggest the use of a single injection of a double dose of gadolinium and a minimum delay of 5 minutes before the acquisition of the T1-weighted sequence. This “dead” time can be used to perform the T2-FLAIR sequences, so that the total acquisition time is not lengthened.<sup>21</sup> This suggestion can facilitate the use of this strategy in clinical practice.

We also have to consider recent literature showing that with repeat contrast administration, gadolinium accumulates in the brain despite an intact blood-brain barrier and normal renal function, producing an increase in signal intensity in certain areas, such as the dentate nucleus and globus pallidus.<sup>34</sup> This effect, which has not been associated with histopathologic findings,<sup>35,36</sup> has mainly been detected with linear GBCAs.<sup>37–39</sup> Only 1 study has shown signal changes in the dentate nucleus and globus pal-

lidus after several administrations of a macrocyclic GBCA.<sup>40</sup> However, in this study, signal changes could not be detected visually (only quantitatively), and the design of the study could not control for or exclude the use of other GBCAs, including linear agents. Moreover, the results of this study contradict other clinical studies that could not find signal-intensity changes in patients receiving several doses of the same macrocyclic GBCA used in our study.<sup>41–46</sup> All these data have been recently analyzed in a systematic review article based on the analysis of 25 original publications,<sup>39</sup> showing that the signal changes in certain central nervous system structures identified with MR imaging correlated

positively with the exposure to linear agents but negatively with the stability of contrast agents, which is higher with macrocyclic agents. Nonclinical studies have indicated that all types of gadolinium can be deposited in different tissues, though the detected residual gadolinium concentration in the brain is approximately 1- to 15-fold higher for linear than for macrocyclic GBCAs.<sup>36,47</sup>

Although no symptoms or diseases linked to brain gadolinium deposition have been reported,<sup>35</sup> data on long-term effects are still limited.

This study has limitations. First, the design did not enable us to establish the relative influences of cumulative dose and delayed scanning on the increase in sensitivity, though the results obtained indicate that the differences were mainly driven by the cumulative gadolinium dose. Second, the high variability in the detection of active lesions by one of the readers limits the interpretation of the higher concordance observed in cumulative and delayed scans compared with single-dose early scans between the 2 other readers.

## CONCLUSIONS

The results of this study indicate that a cumulative dose (0.2 mmol/kg) of macrocyclic GBCA administered as an intravenous bolus in 2 injections of 0.1 + 0.1 mmol/kg is a safe procedure that significantly increases the detection rate of gadolinium-enhancing lesions in patients with CIS or relapsing MS. Furthermore, this approach enables identification of a larger number of patients with active lesions and provides higher confidence in lesion detection. On the basis of these results, the use of a single injection of a double dose of macrocyclic gadolinium-based contrast and a delay time of 5 minutes could be considered in brain MR imaging studies aimed at detecting active MS lesions whenever this purpose could have relevant therapeutic implications. However, on the basis of the limited data on the long-term effects of gadolinium deposition in the brain, which could also occur with macrocyclic GBCAs, the use of this strategy in all routine MR imaging examinations of patients with MS is not recommended.

Disclosures: Alex Rovira—RELATED: Grant: Bayer HealthCare, Comments: This research was funded by Bayer HealthCare Pharmaceuticals\*; UNRELATED: Board Membership: Biogen Idec, Novartis, Sanofi Genzyme, Olea Medical; Consultancy: Biogen Idec, Novartis, Sanofi Genzyme, Olea Medical; Payment for Lectures Including Service on Speakers Bureaus: Bayer HealthCare Pharmaceuticals, Sanofi Genzyme, Bracco, Merck Serono, Teva Pharmaceutical Industries Ltd, Novartis, Biogen Idec; Payment for Development of Educational Presentations: Bayer HealthCare Pharmaceuticals, Bracco, Teva Pharmaceutical Industries Ltd, Novartis, Biogen Idec. Cristina Auger—RELATED: Grant: Bayer HealthCare Pharmaceuticals\*; UNRELATED: Payment for Lectures Including Service on Speakers Bureaus: Novartis, Biogen Idec, Stendhal America SA. Elena Huerga—RELATED: Grant: Bayer HealthCare Pharmaceuticals.\* Juan Francisco Corral—RELATED: Grant: Bayer HealthCare Pharmaceuticals.\* Raquel Mitjana—RELATED: Grant: Bayer HealthCare Pharmaceuticals.\* Jaume Sastre-Garriga—RELATED: Grant: Bayer HealthCare Pharmaceuticals\*; Consultancy: Novartis, Biogen Idec, Celgene; Grants/Grants Pending: Sanofi Genzyme\*; Payment for Lectures Including Service on Speakers Bureaus: Teva Pharmaceutical Industries Ltd, Almirall, Novartis, Biogen Idec, Merck Serono, Sanofi Genzyme; Payment for Development of Educational Presentations: Novartis, Biogen Idec; Travel/Accommodations/Meeting Expenses Unrelated to Activities Listed: Novartis, Merck Serono.\* Mar Tintoré—UNRELATED: Board Membership: Biogen Idec, Sanofi Genzyme, Hoffmann-La Roche; Grants/Grants Pending: Biogen Idec, Novartis, Sanofi Genzyme, Merck Serono\*; Payment for Lectures Including Service on Speakers Bureaus: Amiral, Bayer HealthCare Pharmaceuticals, Biogen Idec, Sanofi Genzyme, Merck Serono, Novartis, Sanofi Aventis, Hoffmann-La Roche, Teva Pharmaceutical Industries Ltd; Payment for Development of Educational Presentations: Biogen Idec. Xavier Montalban—RELATED: Grant: Bayer HealthCare Pharmaceuticals\*; UNRELATED: Consultancy: Actelion, Bayer HealthCare Pharmaceuticals, Biogen Idec, Celgene, Sanofi Genzyme, Merck Serono, Novartis, Oryzon Genomics, Hoffmann-La Roche, Sanofi Genzyme, Teva Pharmaceutical Industries Ltd. \*Money paid to the institution.

## REFERENCES

- Filippi M, Rocca MA. MR imaging of multiple sclerosis. *Radiology* 2011;259:659–81 CrossRef Medline
- Zivadnov R, Stosic M, Cox JL, et al. The place of conventional MRI and newly emerging MRI techniques in monitoring different aspects of treatment outcome. *J Neurol* 2008;255(suppl 1):61–74 CrossRef Medline
- Wolansky LJ, Finden SG, Chang R, et al. Gadoteridol in multiple sclerosis patients: a comparison of single and triple dose with immediate vs. delayed imaging. *Clin Imaging* 1998;22:385–92 CrossRef Medline
- Filippi M, Rovaris M, Capra R, et al. A multi-centre longitudinal study comparing the sensitivity of monthly MRI after standard and triple dose gadolinium-DTPA for monitoring disease activity in multiple sclerosis: implications for phase II clinical trials. *Brain* 1998;121:2011–20 CrossRef Medline
- Rovaris M, Codella M, Moiola L, et al. Effect of glatiramer acetate on MS lesions enhancing at different gadolinium doses. *Neurology* 2002;59:1429–32 CrossRef Medline
- Sardanelli F, Iozzelli A, Losacco C, et al. Three subsequent single doses of gadolinium chelate for brain MR imaging in multiple sclerosis. *AJNR Am J Neuroradiol* 2003;24:658–62 Medline
- Stecco A, Migazzo E, Saponaro A, et al. Gadolinium dose optimization in patients with multiple sclerosis: intra- and inter-individual comparisons. *Eur J Radiol* 2006;57:37–42 CrossRef Medline
- Uysal E, Erturk SM, Yildirim H, et al. Sensitivity of immediate and delayed gadolinium-enhanced MRI after injection of 0.5 M and 1.0 M gadolinium chelates for detecting multiple sclerosis lesions. *AJR Am J Roentgenol* 2007;188:697–702 CrossRef Medline
- Sicotte NL, Voskuhl RR, Bouvier S, et al. Comparison of multiple sclerosis lesions at 1.5 and 3.0 Tesla. *Invest Radiol* 2003;38:423–27 Medline
- Hodel J, Outterlyck O, Ryo E, et al. Accuracy of postcontrast 3D turbo spin-echo MR sequence for the detection of enhanced inflammatory lesions in patients with multiple sclerosis. *AJNR Am J Neuroradiol* 2014;35:519–23 CrossRef Medline
- Cromb e A, Saranathan M, Ruet A, et al. MS lesions are better detected with 3D T1 gradient-echo than with 2D T1 spin-echo gadolinium-enhanced imaging at 3T. *AJNR Am J Neuroradiol* 2015;36:501–07 CrossRef Medline
- Silver NC, Good CD, Barker GJ, et al. Sensitivity of contrast enhanced MRI in multiple sclerosis: effects of gadolinium dose, magnetization transfer contrast and delayed imaging. *Brain* 1997;120:1149–61 CrossRef Medline
- Silver NC, Good CD, Sormani MP, et al. A modified protocol to improve the detection of enhancing brain and spinal cord lesions in multiple sclerosis. *J Neurol* 2001;248:215–24 CrossRef Medline
- Filippi M, Capra R, Campi A, et al. Triple dose of gadolinium-DTPA and delayed MRI in patients with benign multiple sclerosis. *J Neurol Neurosurg Psychiatry* 1996;60:526–30 CrossRef Medline
- van Waesberghe JH, Castelijns JA, Roser W, et al. Single-dose gadolinium with magnetization transfer versus triple-dose gadolinium in the MR detection of multiple sclerosis lesions. *AJNR Am J Neuroradiol* 1997;18:1279–85 Medline
- Tourdias T, Dousset V. Neuroinflammatory imaging biomarkers: relevance to multiple sclerosis and its therapy. *Neurotherapeutics* 2013;10:111–23 CrossRef Medline
- Polman CH, Reingold SC, Banwell B, et al. Diagnostic criteria for multiple sclerosis: 2010 revisions to the McDonald criteria. *Ann Neurol* 2011;69:292–302 CrossRef Medline
- Comi G, Martinelli V, Rodegher M, et al; PreCISe study group. Effect of glatiramer acetate on conversion to clinically definite multiple sclerosis in patients with clinically isolated syndrome (PreCISe study): a randomised, double-blind, placebo-controlled trial. *Lancet* 2009;374:1503–11 CrossRef Medline
- Fox RJ, Miller DH, Phillips JT, et al; CONFIRM Study Investigators. Placebo-controlled phase 3 study of oral BG-12 or glatiramer in multiple sclerosis. *N Engl J Med* 2012;367:1087–97 CrossRef Medline
- Filippi M, Yousry T, Rocca MA, et al. Sensitivity of delayed gadolinium-enhanced MRI in multiple sclerosis. *Acta Neurol Scand* 1997;95:331–34 CrossRef Medline
- Rovira  , Wattjes MP, Tintor e M, et al; MAGNIMS study group. Evidence-based guidelines: MAGNIMS consensus guidelines on the use of MRI in multiple sclerosis—clinical implementation in the diagnostic process. *Nat Rev Neurol* 2015;11:471–82 CrossRef Medline
- Wattjes MP, Rovira  , Miller D, et al; MAGNIMS study group. Evidence-based guidelines: MAGNIMS consensus guidelines on the use of MRI in multiple sclerosis—establishing disease prognosis and monitoring patients. *Nat Rev Neurol* 2015;11:597–606 CrossRef Medline
- Drangova M, Pelc NJ. Artifacts and signal loss due to flow in the presence of B(o) inhomogeneity. *Magn Reson Med* 1996;35:126–30 CrossRef Medline
- Bermel RA, You X, Foulds P, et al. Predictors of long-term outcome in multiple sclerosis patients treated with interferon  . *Ann Neurol* 2013;73:95–103 CrossRef Medline
- Kappos L, Moeri D, Radue EW, et al; Gadolinium MRI Meta-Analysis Group. Predictive value of gadolinium-enhanced magnetic resonance imaging for relapse rate and changes in disability or impairment in multiple sclerosis: a meta-analysis. *Lancet* 1999;353:964–69 CrossRef Medline
- Polman C, Kappos L, Freedman MS, et al; BENEFIT investigators. Subgroups of the BENEFIT study: risk of developing MS and treatment effect of interferon beta-1b. *J Neurol* 2008;255:480–87 CrossRef Medline
- Sormani MP, Bruzzi P. MRI lesions as a surrogate for relapses in multiple sclerosis: a meta-analysis of randomised trials. *Lancet Neurol* 2013;12:669–76 CrossRef Medline
- R o J, Castell o J, Rovira A, et al. Measures in the first year of therapy predict the response to interferon beta in MS. *Mult Scler* 2009;15:848–53 CrossRef Medline
- Sormani MP, R o J, Tintor e M, et al. Scoring treatment response in patients with relapsing multiple sclerosis. *Mult Scler* 2013;19:605–12 CrossRef Medline
- Prosperini L, Mancinelli CR, De Giglio L, et al. Interferon beta failure predicted by EMA criteria or isolated MRI activity in multiple sclerosis. *Mult Scler* 2014;20:566–76 CrossRef Medline

31. Freedman MS, Selchen D, Arnold DL, et al; Canadian Multiple Sclerosis Working Group. **Treatment optimization in MS: Canadian MS Working Group updated recommendations.** *Can J Neurol Sci* 2013; 40:307–23 CrossRef Medline
32. Stangel M, Penner IK, Kallmann BA, et al. **Towards the implementation of 'no evidence of disease activity' in multiple sclerosis treatment: the multiple sclerosis decision model.** *Ther Adv Neurol Disord* 2015;8:3–13 CrossRef Medline
33. Healy BC, Glanz BI, Stankiewicz J, et al. **A method for evaluating treatment switching criteria in multiple sclerosis.** *Mult Scler* 2010; 16:1483–89 CrossRef Medline
34. Kanda T, Ishii K, Kawaguchi H, et al. **High signal intensity in the dentate nucleus and globus pallidus on unenhanced T1-weighted MR images: relationship with increasing cumulative dose of a gadolinium-based contrast material.** *Radiology* 2014;270: 834–41 CrossRef Medline
35. McDonald RJ, McDonald JS, Kallmes DF, et al. **Intracranial gadolinium deposition after contrast-enhanced MR imaging.** *Radiology* 2015;275:772–82 CrossRef Medline
36. Lohrke J, Frisk AL, Frenzel T, et al. **Histology and gadolinium distribution in the rodent brain after the administration of cumulative high doses of linear and macrocyclic gadolinium-based contrast agents.** *Invest Radiol* 2017;52:324–33 CrossRef Medline
37. Ramalho J, Semelka RC, Ramalho M, et al. **Gadolinium-based contrast agent accumulation and toxicity: an update.** *AJNR Am J Neuroradiol* 2016;37:1192–98 CrossRef Medline
38. Runge VM. **Safety of the gadolinium-based contrast agents for magnetic resonance imaging, focusing in part on their accumulation in the brain and especially the dentate nucleus.** *Invest Radiol* 2016;51: 273–79 Medline
39. Olchoway C, Cebulski K, Lasecki M, et al. **The presence of the gadolinium-based contrast agent depositions in the brain and symptoms of gadolinium neurotoxicity: a systematic review.** *PLoS One* 2017;12:e0171704 CrossRef Medline
40. Stojanov DA, Aracki-Trenkic A, Vojinovic S, et al. **Increasing signal intensity within the dentate nucleus and globus pallidus on unenhanced T1W magnetic resonance images in patients with relapsing-remitting multiple sclerosis: correlation with cumulative dose of a macrocyclic gadolinium-based contrast agent, gadobutrol.** *Eur Radiol* 2016;26:807–15 CrossRef Medline
41. Cao Y, Huang DQ, Shih G, et al. **Signal change in the dentate nucleus on T1-weighted MR images after multiple administrations of gadopentetate dimeglumine versus gadobutrol.** *AJR Am J Roentgenol* 2016;206:414–19 CrossRef Medline
42. Radbruch A, Haase R, Kickingereder P, et al. **Pediatric brain: no increased signal intensity in the dentate nucleus on unenhanced T1-weighted MR images after consecutive exposure to a macrocyclic gadolinium-based contrast agent.** *Radiology* 2017;283:828–36 CrossRef Medline
43. Radbruch A, Haase R, Kieslich PJ, et al. **No signal intensity increase in the dentate nucleus on unenhanced T1-weighted MR images after more than 20 serial injections of macrocyclic gadolinium-based contrast agents.** *Radiology* 2017;282:699–707 CrossRef Medline
44. Radbruch A, Weberling LD, Kieslich PJ, et al. **Intraindividual analysis of signal intensity changes in the dentate nucleus after consecutive serial applications of linear and macrocyclic gadolinium-based contrast agents.** *Invest Radiol* 2016;51:683–90 CrossRef Medline
45. Schlemm L, Chien C, Bellmann-Strobl J, et al. **Gadopentetate but not gadobutrol accumulates in the dentate nucleus of multiple sclerosis patients.** *Mult Scler* 2017;23:963–72 CrossRef Medline
46. Langner S, Kromrey ML, Kuehn JP. **Repeated intravenous administration of gadobutrol does not lead to increased signal intensity on unenhanced T1-weighted images—a voxel-based whole brain analysis.** *Eur Radiol* 2017 Mar 13. [Epub ahead of print] CrossRef Medline
47. Robert P, Lehericy S, Grand S, et al. **T1-weighted hypersignal in the deep cerebellar nuclei after repeated administrations of gadolinium-based contrast agents in healthy rats: difference between linear and macrocyclic agents.** *Invest Radiol* 2015;50:473–80 CrossRef Medline

# Diffusional Kurtosis Imaging of the Corticospinal Tract in Multiple Sclerosis: Association with Neurologic Disability

M.V. Spampinato, M.R. Kocher, J.H. Jensen, J.A. Helpert, H.R. Collins, and N.U. Hatch

## ABSTRACT

**BACKGROUND AND PURPOSE:** Multiple sclerosis is an autoimmune disorder resulting in progressive neurologic disability. Our aim was to evaluate the associations between diffusional kurtosis imaging–derived metrics for the corticospinal tract and disability in multiple sclerosis.

**MATERIALS AND METHODS:** Forty patients with MS underwent brain MR imaging including diffusional kurtosis imaging. After we masked out T2 hyperintense lesions, the fractional anisotropy, mean diffusivity, radial diffusivity, axial diffusivity, mean kurtosis, radial kurtosis, and axial kurtosis were estimated for the corticospinal tract. Disability was quantified by using the Expanded Disability Status Scale at the time of MR imaging and 12 months post-MR imaging. The Pearson correlation coefficient and linear regression analyses were conducted to evaluate the associations between diffusion metrics and disability.

**RESULTS:** Significant correlations were found between the Expanded Disability Status Scale scores during the baseline visit and age ( $r = 0.47$ ), T2 lesion volume ( $r = 0.38$ ), corticospinal tract mean diffusivity ( $r = 0.41$ ), radial diffusivity ( $r = 0.41$ ), axial diffusivity ( $r = 0.34$ ), fractional anisotropy ( $r = -0.36$ ), and radial kurtosis ( $r = -0.42$ ). Significant correlations were also found between the Expanded Disability Status Scale scores at 12-month follow-up and age ( $r = 0.38$ ), mean diffusivity ( $r = 0.45$ ), radial diffusivity ( $r = 0.41$ ), axial diffusivity ( $r = 0.45$ ), mean kurtosis ( $r = -0.42$ ), radial kurtosis ( $r = -0.56$ ), and axial kurtosis ( $r = -0.36$ ). Linear regression analyses demonstrated significant associations among radial kurtosis, age, and Expanded Disability Status Scale score during the baseline visit, while radial kurtosis was the only variable associated with Expanded Disability Status Scale score for the 12-month follow-up.

**CONCLUSIONS:** Radial kurtosis of the corticospinal tract may have an association with neurologic disability in MS.

**ABBREVIATIONS:** CST = corticospinal tract; DKI = diffusional kurtosis imaging; EDSS = Expanded Disability Status Scale; EDSS<sub>12 m</sub> = EDSS score at 12-month follow-up; EDSS<sub>0</sub> = EDSS at baseline visit; FA = fractional anisotropy;  $K_{||}$  = axial kurtosis;  $K_{\perp}$  = radial kurtosis;  $\lambda_{||}$  = axial diffusivity;  $\lambda_{\perp}$  = radial diffusivity; MD = mean diffusivity; MK = mean kurtosis; NAWM = normal-appearing white matter; VIF = variance inflation factor

Multiple sclerosis is an autoimmune disorder of the central nervous system characterized by recurrent episodes of inflammation, demyelination, edema, and axonal loss, which can result in a progressive accumulation of neurologic disability.<sup>1</sup> MR

imaging is routinely performed to assess the burden of disease in patients with MS to guide therapeutic decisions.<sup>2</sup> Conventional MR imaging is widely used to evaluate macrostructural changes such as T2 hyperintense lesions, T1 black holes, gadolinium-enhancing lesions, and brain volume loss.<sup>3,4</sup> Although conventional MR imaging analysis has been used for years to assess the disease burden, it cannot fully explain the degree of neurologic dysfunction. The lack of correlation between neurologic disability and conventional MR imaging measures is commonly described as the “clinicoradiologic paradox.”<sup>4</sup>

DTI has been previously used to assess the integrity of brain tissue and to probe specific white matter tracts.<sup>5–12</sup> Prior studies have evaluated microstructural changes of the corticospinal tract (CST) in MS and the association between diffusivity of the CST and measures of neurologic disability.<sup>5,7,13–17</sup> However, a fundamental limitation of DTI is that the data analysis approximates the water diffusion dynamics within brain tissue as being a Gaussian

Received December 28, 2016; accepted after revision March 14, 2017.

From the Department of Radiology and Radiological Science (M.V.S., M.R.K., J.H.J., J.A.H., H.R.C., N.U.H.) and Center for Biomedical Imaging (M.V.S., J.H.J., J.A.H.), Medical University of South Carolina, Charleston, South Carolina.

Paper previously presented in part at: Annual Meeting of the International Society for Magnetic Resonance in Medicine and European Society for Magnetic Resonance in Medicine, May 10–16, 2014; Milan, Italy; Annual Meeting of the American Society of Neuroradiology and the Foundation of the ASNR Symposium, May 17–22, 2014; Montreal, Quebec, Canada; and Annual Meeting of the American Society of Neuroradiology and the Foundation of the ASNR Symposium, May 18–23, 2013; San Diego, California.

Please address correspondence to Maria Vittoria Spampinato, MD, Department of Radiology and Radiological Science, Medical University of South Carolina, 96 Jonathan Lucas, MSC 323, Charleston, SC 29425; e-mail: spampin@musc.edu; @mvspampinato

<http://dx.doi.org/10.3174/ajnr.A5225>

process, though considerable non-Gaussian diffusion effects are observed throughout the brain. Hence, DTI does not fully characterize water diffusion in the brain. Diffusional kurtosis imaging (DKI)<sup>18</sup> is a clinically feasible diffusion MR imaging method, which extends the DTI model to include non-Gaussian diffusion effects.<sup>18-20</sup> As a result, DKI has the potential to provide more sensitive biomarkers for probing microscopic structural changes occurring in the normal-appearing white matter (NAWM), which could lead to better predictive biomarkers for disease progression. Although DKI has been applied to MS in a few preliminary studies,<sup>18-22</sup> the potential of DKI to aid in the assessment of neurologic disability in MS is still not well-established.

The aim of this study was to examine the associations between DKI-derived diffusion metrics of the corticospinal tract and physical disability in patients affected by MS, as measured by the Extended Disability Status Scale (EDSS).<sup>23</sup> Our hypothesis was that DKI-derived metrics have stronger associations with neurologic dysfunction than DTI metrics.

## MATERIALS AND METHODS

### Participants

The study was approved by the institutional review board, who exempted the study from requiring individual patient consent. We retrospectively reviewed the PACS for all patients with multiple sclerosis who underwent brain MR imaging during an 18-month period. Inclusion criteria were the following: 1) age between 18 and 70 years; 2) diagnosis of multiple sclerosis according to established diagnostic criteria<sup>2</sup>; 3) brain MR imaging performed according to our standard multiple sclerosis protocol, including DKI; and 4) neurologic evaluation within 1 month of the MR imaging available in the electronic medical record (baseline visit). On the basis of the clinical phenotype, patients were categorized as having clinically isolated syndrome, relapsing-remitting MS, primary-progressive MS, secondary-progressive MS, or unknown type of MS.<sup>24</sup> We excluded patients with history of neurologic disorders other than multiple sclerosis. We also excluded all imaging datasets degraded by bulk head motion or other artifacts. The degree of neurologic impairment was assessed by using the Kurtzke EDSS during the baseline visit (EDSS<sub>0</sub>). If subsequent clinical neurologic encounters were documented in the electronic medical record, then we recorded the EDSS score for the neurologic visit 12 months after brain MR imaging (EDSS<sub>12 m</sub>).

### MR Imaging

Brain MRIs were performed on a 1.5T Avanto MR imaging scanner (Siemens, Erlangen, Germany). A sagittal T1-weighted MPRAGE (TR/TE/TI = 1900/2.91/1100 ms, flip angle = 15°, acquisition matrix = 225 × 199, FOV = 256 × 256 mm<sup>2</sup>, section thickness = 1 mm) and an axial FLAIR sequence (TR/TE/TI = 8000/88/2372 ms, flip angle = 180°, matrix = 424 × 512, FOV = 220 × 220 mm<sup>2</sup>, section thickness = 5 mm) were performed. Axial diffusion-weighted images were acquired with 3 b-values (0, 1000, and 2000 s/mm<sup>2</sup>) along 30 diffusion-encoding directions with a single-shot twice-refocused spin-echo EPI sequence with NEX = 1 (NEX = 10 for b=0). Imaging parameters of the diffusion sequence were the following: voxel size = 3 × 3 × 3 mm<sup>3</sup>, number of sections = 40, TR/TE = 5500/99 ms, FOV = 222 ×

222 mm<sup>2</sup>, acquisition matrix = 74 × 74, bandwidth/pixel = 1325 Hz, acceleration factor = 2, acquisition time ≈ 7 minutes.

### Data Processing

The Lesion Segmentation Tool toolbox (<http://www.applied-statistics.de/lst.html>), an open-source toolbox for SPM8 (<http://www.fil.ion.ucl.ac.uk/spm/software/spm12>), specifically the lesion-growth algorithm, was used to segment T2 hyperintense lesions from the MPRAGE and FLAIR images ( $\kappa$  value = 0.2).<sup>25</sup> Then, a neuroradiologist blinded to all clinical information inspected each lesion mask to ensure accurate lesion segmentation. With MRICron software (<http://www.nitrc.org/projects/mricron/>),<sup>26</sup> we calculated total white matter lesion volume for each patient.

With Diffusional Kurtosis Estimator software<sup>27</sup> (Version 2.6, <https://www.nitrc.org/projects/dke/>) implemented in Matlab (MathWorks, Natick, Massachusetts), we calculated the diffusion and kurtosis tensors on a voxel-by-voxel basis. Parametric maps for the following metrics were obtained from the DKI dataset: 1) diffusivity metrics: fractional anisotropy (FA), mean diffusivity (MD), axial diffusivity ( $\lambda_{\parallel}$ ), and radial diffusivity ( $\lambda_{\perp}$ ) diffusivity; 2) kurtosis metrics: mean kurtosis (MK), axial ( $K_{\parallel}$ ) and radial ( $K_{\perp}$ ) kurtosis. MK is the average kurtosis over all diffusion directions,  $K_{\parallel}$  is the kurtosis in the direction of the diffusion tensor eigenvector with the largest diffusion eigenvalue (typically along the direction of the axons), and  $K_{\perp}$  is the average kurtosis over all directions perpendicular to the diffusion eigenvector with the largest eigenvalue (typically all directions perpendicular to the axons).<sup>18</sup> FA maps were normalized to the Montreal Neurological Institute standard space FA template, a high-resolution average of 58 well-aligned good-quality FA images from healthy male and female subjects between 20 and 50 years of age, at 1 × 1 × 1 mm<sup>3</sup> resolution. The resulting normalization parameters were then applied to the remaining diffusion maps and to the lesion masks. The white matter skeleton was obtained by using Tract-Based Spatial Statistics (TBSS; <http://fsl.fmrib.ox.ac.uk/fsl/fslwiki/TBSS>) in FSL (FA threshold,  $\geq 0.4$ ).<sup>28</sup> The corticospinal tract volumes of interest were obtained from the WM skeleton with the Johns Hopkins University White Matter Tractography Atlas,<sup>29</sup> after masking out T2 hyperintense areas of individual patients (Fig 1). As a result, the CST VOI only included the NAWM of the CST. Then, average diffusion values of the CST VOIs were computed for all diffusion metrics and subjects by using Matlab.

Statistical analyses were conducted with SPSS (Version 22; IBM, Armonk, New York). Due to the small number of men in the study, sex differences in EDSS were examined with an independent-samples Mann-Whitney *U* test. Pearson correlations were examined between CST diffusion metrics and EDSS at baseline and at the 12-month follow-up to characterize basic relations among variables. Results of the Pearson correlations were considered statistically significant with  $P < .05$ , corrected for multiple comparisons with the false discovery rate method.<sup>30</sup> A linear regression equation with the stepwise method was calculated to evaluate the relationships among EDSS at baseline, the dependent variable, and the independent variables entered in the following order: age, white matter lesion volume, and CST diffusion param-

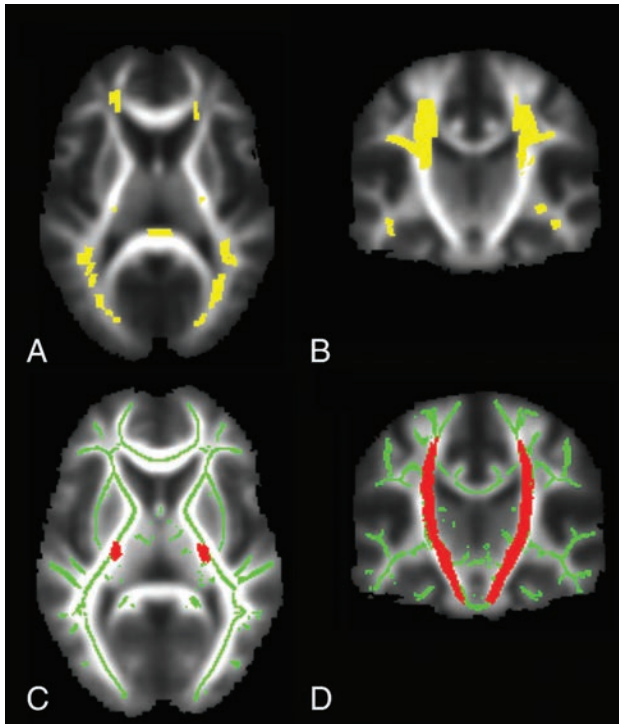


**FIG 1.** White matter lesion mask (yellow) of a representative patient with multiple sclerosis overlaid on axial (A) and coronal (B) mean fractional anisotropy images. The mean fractional anisotropy skeleton (green) and the Johns Hopkins University White Matter Tractography Atlas corticospinal tract (red) are overlaid onto the mean axial (C) and coronal (D) fractional anisotropy images. The white matter skeleton was obtained with FSL Tract-Based Spatial Statistics. The corticospinal tract VOIs were obtained from the white matter skeleton with the Johns Hopkins University White Matter Tractography Atlas, after masking out T2 hyperintense areas of individual patients. All images are in the Montreal Neurological Institute standard space.

eters. Additional linear regressions were also calculated to evaluate the associations between the same independent variables and EDSS at the 12-month follow-up and changes in the EDSS score between baseline and 12-month follow-up. Before the linear regression equation calculation, multicollinearity among independent variables was assessed with the variance inflation factor (VIF). Independent variables were excluded from the analysis when the VIF was  $>10$ .<sup>31</sup> The results of the linear regression analyses were considered statistically significant at  $P < .05$ .

## RESULTS

### Demographic and Clinical Characteristics

Forty patients with MS were included in this study. Table 1 shows demographic, clinical, and conventional MR imaging characteristics of the entire cohort and of the subgroup of 28 patients with 12-month follow-up. There was no significant difference in EDSS scores between men and women at baseline (women: median = 3, range = 1–8,  $n = 33$ ; men: median = 3, range = 1–3.5,  $n = 7$ ;  $U = 138.5$ ,  $P = .421$ ) and at the 12-month follow-up (women: median = 3, range = 0–9,  $n = 24$ ; men: median = 6, range = 1–6,  $n = 4$ ;  $U = 39.5$ ,  $P = .590$ ). Patients had a disease duration of at least 1 year since their first symptom before the brain MR imaging. The exact duration of disease was not documented in the chart for 3 patients. Of the 40 patients, 25 were receiving disease-modifying

**Table 1: Patient clinical characteristics and imaging metrics**

	Entire Cohort	Patients with 12-Month Follow-Up
No. of subjects	40	28
Sex (F/M)	33/7	24/4
Age (mean) (yr)	42.9 ± 12.5	42.1 ± 13.1
EDSS <sub>0</sub> (mean)	3.4 ± 1.9	3.6 ± 2
EDSS <sub>12m</sub> (mean)		4.2 ± 2.3
MS type (RR/SP/unknown/PP)	32/2/5/1	23/1/3/1
Disease duration (mean) (yr)	8.0 ± 6.4	6.9 ± 4.5
T2 lesion load (mean) (mL)	21.3 ± 22.8	23.3 ± 26.0
CST FA (mean)	0.44 ± 0.03	0.44 ± 0.03
CST MD (mean)	0.94 ± 0.06	0.93 ± 0.06
CST $\lambda_{\perp}$ (mean)	0.70 ± 0.06	0.70 ± 0.06
CST (mean)	1.41 ± 0.07	1.40 ± 0.07
CST MK (mean)	1.17 ± 0.06	1.17 ± 0.06
CST $K_{\perp}$ (mean)	1.60 ± 0.15	1.60 ± 0.14
CST $K_{\parallel}$ (mean)	0.96 ± 0.05	0.97 ± 0.05

**Note:**—RR indicates relapsing-remitting MS; SP, secondary-progressive MS; PP, primary-progressive MS.

**Table 2: Correlations between EDSS and age, T2 lesion volume, and diffusion metrics**

Diffusion Metrics	EDSS <sub>0</sub>		EDSS <sub>12m</sub>	
	<i>r</i>	<i>P</i> Value <sup>a</sup>	<i>r</i>	<i>P</i> Value <sup>a</sup>
Age	0.47	.009	0.38	.003
T2 lesion volume	0.38	.018	0.23	.117
MD	0.41	.018	0.45	.018
$\lambda_{\parallel}$	0.34	.023	0.45	.018
$\lambda_{\perp}$	0.41	.018	0.41	.023
FA	−0.36	.022	−0.30	.063
MK	−0.29	.046	−0.42	.023
$K_{\parallel}$	−0.25	.063	−0.36	.040
$K_{\perp}$	−0.42	.018	−0.56	.009

<sup>a</sup> *P* values were corrected for multiple comparisons with the false discovery rate method.

treatments, which included interferon  $\beta$  ( $n = 13$ ), glatiramer acetate ( $n = 8$ ), natalizumab ( $n = 3$ ), and fingolimod ( $n = 1$ ).

### Imaging Data

Table 2 demonstrates the correlations among age, T2 lesion volume, CST diffusion metrics, EDSS<sub>0</sub>, and EDSS<sub>12m</sub> (Fig 2). Analyses of the multicollinearity among independent variables resulted in inclusion in the regression model of the following independent variables with a VIF of  $<10$ : age (VIF = 1.30), T2 white matter lesion volume (VIF = 1.42), CST MK (VIF = 5.89), CST  $K_{\parallel}$  (VIF = 2.21), and CST  $K_{\perp}$  (VIF = 5.43). FA, MD,  $\lambda_{\perp}$ , and  $\lambda_{\parallel}$  were excluded from the analyses due to a VIF of  $>10$ . Then, a linear regression analysis was performed to evaluate the relationship between EDSS<sub>0</sub> and the following variables: age, T2 white matter lesion volume, MK,  $K_{\parallel}$ , and  $K_{\perp}$ . A significant regression equation was found ( $F [2,37] = 8.875$ ,  $P = .001$ ) with an  $R^2$  of 0.324.  $K_{\perp}$  ( $\beta = -0.329$ ,  $P = .023$ ) and age ( $\beta = 0.399$ ,  $P = .007$ ) were the only variables significantly associated with EDSS<sub>0</sub> (Table 3). A linear regression analysis was performed to evaluate the relationship between EDSS<sub>12m</sub> and the same variables (age, T2 lesion load, and CST diffusion metrics obtained at baseline). A significant regression equation was found ( $F [1,26] = 12.014$ ,  $P = .002$ ) with an  $R^2$  of 0.316.  $K_{\perp}$  ( $\beta = -0.562$ ,  $P = .002$ ) was the only variable to have a significant association with EDSS<sub>12m</sub> (Table 3). A linear re-

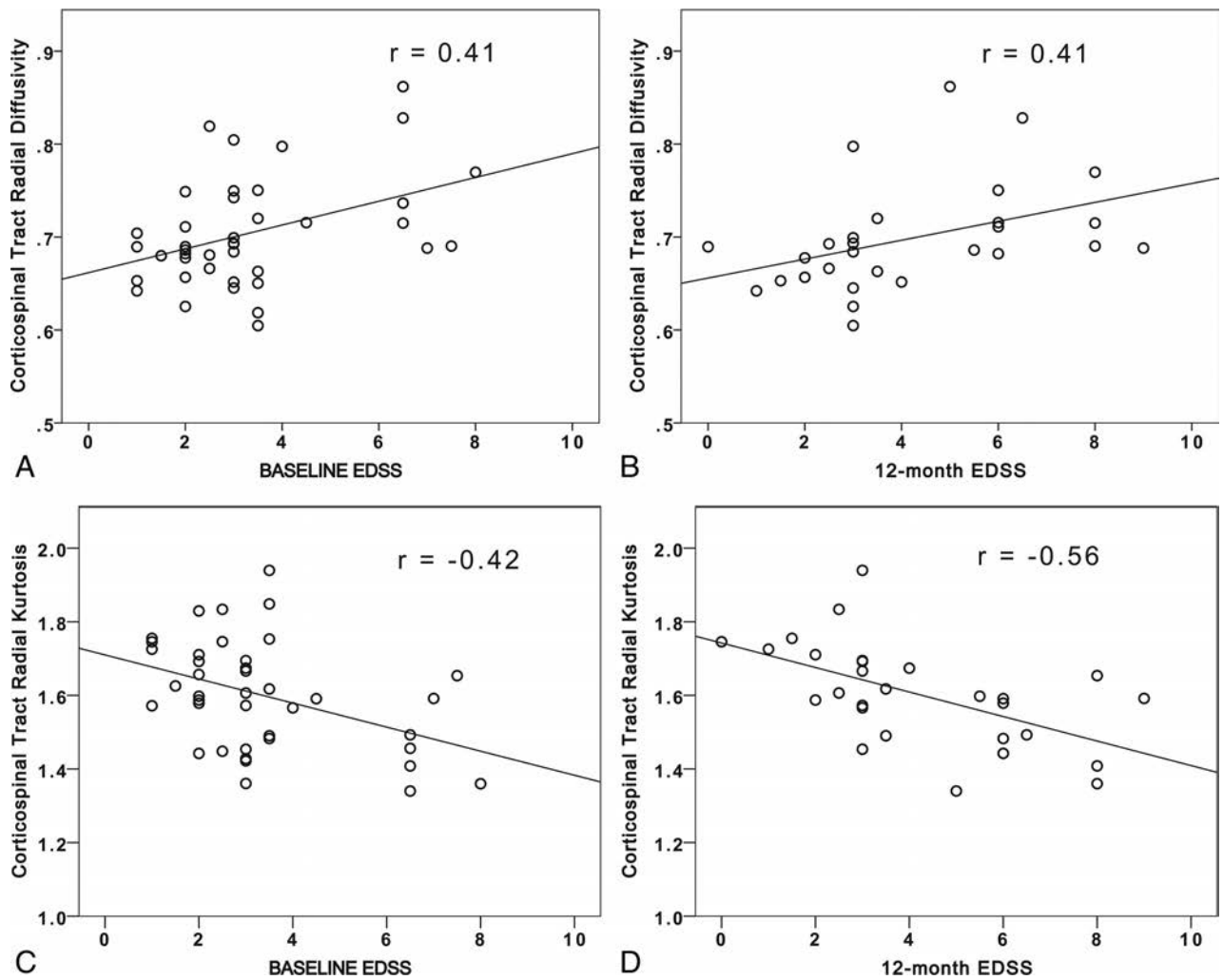


**FIG 2.** Scatterplots for the Expanded Disability Status Scale at the time of the brain MR imaging versus radial diffusivity (A) and radial kurtosis (C) of the corticospinal tracts, and EDSS at the follow-up visit 12 months after the brain MR imaging versus radial diffusivity (B) and radial kurtosis (D) of the corticospinal tracts in patients with MS.

**Table 3: Linear regression analyses: coefficients table**

	EDSS <sub>0</sub>		EDSS <sub>12_m</sub>	
	$\beta$	P Value	$\beta$	P Value
(Constant)		.022		<.001
Age	.399	.007	.172	.347
CST MK	.074	.811	.257	.432
CST K <sub>  </sub>	.055	.774	.006	.979
CST K <sub>⊥</sub>	-.329	.023	-.562	.002
T2 lesion volume	.153	.355	-.141	.491

gression analysis was also performed to evaluate the relationship between change in the EDSS score (baseline EDSS versus 12-month follow-up EDSS) and the same independent variables. None of the variables had significant associations with change in the EDSS score.

## DISCUSSION

We conducted a retrospective study designed to explore the hypothesis that DKI-derived metrics of the CST have stronger associations with physical disability than DTI-derived metrics in patients with MS. We have preliminarily found that K<sub>⊥</sub> of the CST has an association with physical disability. Associations were

found between DKI-derived metrics and neurologic disability at the time of brain MR imaging, as well as with the degree of disability at 12-month follow-up. Due to the retrospective nature of our study, however, our results will require validation with future prospective studies. If our preliminary observations are confirmed, DKI-derived metrics may play an important role in improving our understanding of physical disability and prognosis, as well as in guiding treatment considerations in multiple sclerosis.

The correlations between DTI-derived measures of CST integrity and functional disability in MS have been previously evaluated.<sup>7,9,10,13,16,32</sup> Lin et al<sup>13</sup> found greater MD and radial diffusivity in the normal-appearing CST in patients with MS than in healthy controls. Prior studies found significant associations between DTI-derived measures of CST integrity and functional disability. Bergsland et al<sup>32</sup> found significant correlations between the EDSS and diffusivity measures, including FA, MD,  $\lambda_{\perp}$ , and  $\lambda_{||}$  for the NAWM CST. Tovar-Moll et al<sup>5</sup> found an inverse association between CST FA and EDSS when correcting for lesion volume. Other authors found only trends for an inverse correlation between EDSS and CST FA in

MS<sup>14,15</sup> or found weak correlations between EDSS and DTI metrics of the CST (MD,  $\lambda_{\perp}$ , and  $\lambda_{\parallel}$ ).<sup>9</sup> Reich et al<sup>16</sup> did not find significant differences in FA, MD,  $\lambda_{\perp}$ , and  $\lambda_{\parallel}$  for the CST among patients with various degrees of ankle dorsiflexion impairment. Harrison et al<sup>33</sup> found that DTI indices of the CST were not able to predict EDSS scores. Overall, prior study results demonstrated that conventional DTI measures may have an association with physical disability, but this relationship has not been consistently demonstrated in the literature. Here, we report associations of conventional DTI metrics for the CST with EDSS, which confirm prior studies, and extend prior investigations by demonstrating significant correlations between kurtosis metrics, especially  $K_{\perp}$ , and EDSS.

The diffusional kurtosis metrics are complementary to the diffusion tensor metrics and provide microstructural information that more comprehensively characterizes brain tissue microstructure.<sup>18</sup> A few studies have previously evaluated the use of DKI-derived metrics in the characterization of demyelinating disease in animal models and in patients affected by MS. Using the cuprizone mouse model of CNS demyelination, Falangola et al<sup>34</sup> evaluated the associations between DKI-derived metrics in cuprizone-induced chronic demyelination of the corpus callosum and morphologic WM alterations associated with myelin pathology. DKI-derived metrics were found to have greater sensitivity than conventional DTI parameters in the detection of cuprizone-induced demyelination of the anterior corpus callosum. Guglielmetti et al<sup>35</sup> found that MK and  $K_{\perp}$ , but not DTI-derived parameters, were sensitive to cuprizone-induced cortical alterations. Yoshida et al<sup>19</sup> have conducted ROI-based quantitative analyses of MK for 24 cerebral NAWM regions in 11 patients with MS. The average MK for the NAWM was found to be lower in patients with MS than in healthy controls. Raz et al<sup>21</sup> evaluated the signal characteristics of the spinal cord by using DKI and found that MK was lower in patients with MS than in healthy controls. Abnormal DKI-derived metrics of the NAWM were found in patients with MS but not in individuals with neuromyelitis optica.<sup>22</sup> Bester et al<sup>20</sup> applied DKI to the evaluation of cortical gray matter microstructural changes and found that decreased cortical MK was associated with poor performance on the Delis-Kaplan Executive Function System test ( $r = 0.66$ ). De Kouchkovsky et al<sup>17</sup> assessed white matter integrity in MS by using DKI-derived white matter integrity metrics, specifically axonal water fraction, intra-axonal diffusivity, radial and axial extra-axonal diffusivity, and tortuosity of the extra-axonal space. The authors found a moderate association between axonal water fraction in the corpus callosum and the EDSS score ( $\rho = -0.39$ ). Our study design differs from the methodology used by de Kouchkovsky et al. In fact, our approach was to study the associations between physical disability and pure diffusion metrics of the CST, such as mean kurtosis and radial kurtosis, as opposed to model-dependent quantities such as axonal water fraction.

These prior studies have shown that kurtosis parameters provide more comprehensive information about brain tissue microstructure than that available with conventional DTI.<sup>18</sup> It is important to determine whether this enhanced sensitivity to microstructural changes provided by DKI translates into improved disability prediction. Our work demonstrates promising relations

between DKI-derived diffusion metrics for the CST and clinical disability. In this retrospective cohort, age and  $K_{\perp}$  were associated with neurologic disability and accounted for approximately 32% of the variability of EDSS scores at baseline. We also found that  $K_{\perp}$  was the only parameter significantly associated with disability at the 12-month follow-up examination and accounted for about 32% of the variability of EDSS scores. If the associations between  $K_{\perp}$  and disability are validated in future larger prospective studies, these metrics may ultimately prove to be powerful adjuncts to the clinical assessment of patients with MS.

Histopathology and MR imaging studies have shown that the NAWM is affected, to a lesser extent, by the same pathologic processes that are found in MS lesions, specifically inflammation, demyelination, microglial activation, axonal injury, Wallerian degeneration, and macrophage infiltration.<sup>36-39</sup> The pathologic basis of the stronger association between  $K_{\perp}$  and physical disability in MS requires further determination.  $K_{\perp}$  is the average kurtosis over all directions perpendicular to the diffusion eigenvector with the largest eigenvalue (typically all directions perpendicular to the axons). We hypothesized that the stronger association between physical disability and  $K_{\perp}$  than between other diffusion metrics may reflect a greater sensitivity of  $K_{\perp}$  to early pathologic changes of the NAWM, possibly myelin breakdown resulting in demyelination or hypomyelination or an increase of membrane barriers due to microgliosis.<sup>34,35</sup> Unfortunately, pathologic findings for the NAWM are not available for this patient cohort. Future studies on the correlations between DKI parameters and pathologic findings for the NAWM in MS will help clarify the histopathologic basis of our preliminary observations.

An alternative approach to DKI for quantifying diffusional non-Gaussianity is to fit the diffusion MR imaging signal to a stretched exponential model.<sup>40</sup> However, this model does not allow the estimation of kurtosis,<sup>18</sup> and it is less appropriate for white matter because incorporating the effects of diffusion anisotropy is challenging.<sup>41</sup> Biexponential fitting of the diffusion MR imaging signal is also feasible. This is fully consistent with DKI but requires the acquisition of more diffusion-weighted data than the truncated cumulant expansion signal model conventionally used with DKI (as in the present study).<sup>18</sup>

This study has limitations. First, it was a retrospective study that evaluated a relatively limited number of 40 patients, which precluded analysis of data in patients with relapsing-remitting, primary-progressive, and secondary-progressive MS separately. Twelve-month clinical follow-up information was available for only 28/40 patients (70%). We also did not evaluate the subsequent temporal evolution of the observed CST diffusion measures. Finally, while the EDSS is an effective tool widely used in clinical trials to assess the severity of MS, it is heavily weighted toward ambulation, and the multiple sclerosis functional composite may be a more sensitive method to evaluate disease progression.<sup>28</sup>

## CONCLUSIONS

We have found significant associations between the  $K_{\perp}$  of the CST and disability in MS. DKI metrics were found to have stronger

associations than DTI metrics with measures of disability in MS. It is important that this work be validated in future prospective studies with larger sample sizes.

## ACKNOWLEDGMENTS

The authors gratefully acknowledge Ali Tabesh for his contributions to study design, image postprocessing, and data analysis and Dr. Aljoeson Walker for performing the neurologic examinations.

Disclosures: Jens H. Jensen—*OTHER RELATIONSHIPS*: I am a coinventor on US Patent 8811706 that covers one of the imaging methods investigated in this article (DKI). The patent is owned by a former employer (New York University), but I could be entitled to a share of any royalties at some point. To date, I have not received royalties from this patent. Joseph A. Helpert—*UNRELATED*: Grant: The Litwin Foundation\*. Neal U. Hatch—*UNRELATED*: Support for Travel to Meetings for the Study or Other Purposes: partial reimbursement of travel expenses provided by the department. \*Money paid to the institution.

## REFERENCES

1. Compston A, Coles A. **Multiple sclerosis.** *Lancet* 2002;359:1221–31 CrossRef Medline
2. Polman CH, Reingold SC, Banwell B, et al. **Diagnostic criteria for multiple sclerosis: 2010 revisions to the McDonald criteria.** *Ann Neurol* 2011;69:292–302 CrossRef Medline
3. Filippi M, Rocca MA, Barkhof F, et al; Attendees of the Correlation between Pathological MRI findings in MS workshop. **Association between pathological and MRI findings in multiple sclerosis.** *Lancet Neurol* 2012;11:349–60 CrossRef Medline
4. Barkhof F. **MRI in multiple sclerosis: correlation with Expanded Disability Status Scale (EDSS).** *Mult Scler* 1999;5:283–86 Medline
5. Tovar-Moll F, Evangelou IE, Chiu AW, et al. **Diffuse and focal corticospinal tract disease and its impact on patient disability in multiple sclerosis.** *J Neuroimaging* 2015;25:200–06 CrossRef Medline
6. Sbardella E, Petsas N, Tona F, et al. **Assessing the correlation between grey and white matter damage with motor and cognitive impairment in multiple sclerosis patients.** *PLoS One* 2013;8:e63250 CrossRef Medline
7. Wilson M, Tench CR, Morgan PS, et al. **Pyramidal tract mapping by diffusion tensor magnetic resonance imaging in multiple sclerosis: improving correlations with disability.** *J Neurol Neurosurg Psychiatry* 2003;74:203–07 CrossRef Medline
8. Onu M, Roceanu A, Sbotto-Frankensteen U, et al. **Diffusion abnormality maps in demyelinating disease: correlations with clinical scores.** *Eur J Radiol* 2012;81:e386–391 CrossRef Medline
9. Daams M, Steenwijk MD, Wattjes MP, et al. **Unraveling the neuroimaging predictors for motor dysfunction in long-standing multiple sclerosis.** *Neurology* 2015;85:248–55 CrossRef Medline
10. Inglese M, Bester M. **Diffusion imaging in multiple sclerosis: research and clinical implications.** *NMR Biomed* 2010;23:865–72 CrossRef Medline
11. Koenig KA, Sakaie KE, Lowe MJ, et al. **The relationship between cognitive function and high-resolution diffusion tensor MRI of the cingulum bundle in multiple sclerosis.** *Mult Scler* 2015;21:1794–801 CrossRef Medline
12. Preziosa P, Rocca MA, Mesaros S, et al. **Relationship between damage to the cerebellar peduncles and clinical disability in multiple sclerosis.** *Radiology* 2014;271:822–30 CrossRef Medline
13. Lin F, Yu C, Jiang T, et al. **Diffusion tensor tractography-based group mapping of the pyramidal tract in relapsing-remitting multiple sclerosis patients.** *AJNR Am J Neuroradiol* 2007;28:278–82 Medline
14. Giorgio A, Palace J, Johansen-Berg H, et al. **Relationships of brain white matter microstructure with clinical and MR measures in relapsing-remitting multiple sclerosis.** *J Magn Reson Imaging* 2010;31:309–16 CrossRef Medline
15. Gorgoraptis N, Wheeler-Kingshott CA, Jenkins TM, et al. **Combining tractography and cortical measures to test system-specific hypotheses in multiple sclerosis.** *Mult Scler* 2010;16:555–65 CrossRef Medline
16. Reich DS, Zackowski KM, Gordon-Lipkin EM, et al. **Corticospinal tract abnormalities are associated with weakness in multiple sclerosis.** *AJNR Am J Neuroradiol* 2008;29:333–39 CrossRef Medline
17. de Kouchkovsky I, Fieremans E, Fleysher L, et al. **Quantification of normal-appearing white matter tract integrity in multiple sclerosis: a diffusion kurtosis imaging study.** *J Neurol* 2016;263:1146–55 CrossRef Medline
18. Jensen JH, Helpert JA. **MRI quantification of non-Gaussian water diffusion by kurtosis analysis.** *NMR Biomed* 2010;23:698–710 CrossRef Medline
19. Yoshida M, Hori M, Yokoyama K, et al. **Diffusional kurtosis imaging of normal-appearing white matter in multiple sclerosis: preliminary clinical experience.** *Jpn J Radiol* 2013;31:50–55 CrossRef Medline
20. Bester M, Jensen JH, Babb JS, et al. **Non-Gaussian diffusion MRI of gray matter is associated with cognitive impairment in multiple sclerosis.** *Mult Scler* 2015;21:935–44 CrossRef Medline
21. Raz E, Bester M, Sigmund EE, et al. **A better characterization of spinal cord damage in multiple sclerosis: a diffusional kurtosis imaging study.** *AJNR Am J Neuroradiol* 2013;34:1846–52 CrossRef Medline
22. Qian W, Chan KH, Hui ES, et al. **Application of diffusional kurtosis imaging to detect occult brain damage in multiple sclerosis and neuromyelitis optica.** *NMR Biomed* 2016;29:1536–45 CrossRef Medline
23. Kurtzke JF. **Rating neurologic impairment in multiple sclerosis: an expanded disability status scale (EDSS).** *Neurology* 1983;33:1444–52 CrossRef Medline
24. Lublin FD, Reingold SC, Cohen JA, et al. **Defining the clinical course of multiple sclerosis: the 2013 revisions.** *Neurology* 2014;83:278–86 CrossRef Medline
25. Schmidt P, Gaser C, Arsic M, et al. **An automated tool for detection of FLAIR-hyperintense white-matter lesions in multiple sclerosis.** *Neuroimage* 2012;59:3774–83 CrossRef Medline
26. Rorden C, Karnath HO, Bonilha L. **Improving lesion-symptom mapping.** *J Cogn Neurosci* 2007;19:1081–88 CrossRef Medline
27. Tabesh A, Jensen JH, Ardekani BA, et al. **Estimation of tensors and tensor-derived measures in diffusional kurtosis imaging.** *Magn Reson Med* 2011;65:823–36 CrossRef Medline
28. Smith SM, Jenkinson M, Woolrich MW, et al. **Advances in functional and structural MR image analysis and implementation as FSL.** *Neuroimage* 2004;23(suppl 1):S208–19 CrossRef Medline
29. Hua K, Zhang J, Wakana S, et al. **Tract probability maps in stereotaxic spaces: analyses of white matter anatomy and tract-specific quantification.** *Neuroimage* 2008;39:336–47 CrossRef Medline
30. Benjamini Y, Hochberg Y. **Controlling the false discovery rate: a practical and powerful approach to multiple testing.** *Journal of the Royal Statistical Society Series B (Methodological)* 1995;57:289–300
31. Neter J, Wasserman W, Kutner MH. *Applied Linear Regression Models.* Homewood: R.D. Irwin; 1983
32. Bergsland N, Laganà MM, Tavazzi E, et al. **Corticospinal tract integrity is related to primary motor cortex thinning in relapsing-remitting multiple sclerosis.** *Mult Scler* 2015;21:1771–80 CrossRef Medline
33. Harrison DM, Shiee N, Bazin PL, et al. **Tract-specific quantitative MRI better correlates with disability than conventional MRI in multiple sclerosis.** *J Neurol* 2013;260:397–406 CrossRef Medline
34. Falangola MF, Guilfoyle DN, Tabesh A, et al. **Histological correlation of diffusional kurtosis and white matter modeling metrics in cuprizone-induced corpus callosum demyelination.** *NMR Biomed* 2014;27:948–57 CrossRef Medline
35. Guglielmetti C, Veraart J, Roelant E, et al. **Diffusion kurtosis imaging probes cortical alterations and white matter pathology following cuprizone induced demyelination and spontaneous remyelination.** *Neuroimage* 2016;125:363–77 CrossRef Medline

36. Evangelou N, Konz D, Esiri MM, et al. **Regional axonal loss in the corpus callosum correlates with cerebral white matter lesion volume and distribution in multiple sclerosis.** *Brain* 2000;123(pt 9):1845–49 CrossRef Medline
37. Allen IV, McQuaid S, Mirakhur M, et al. **Pathological abnormalities in the normal-appearing white matter in multiple sclerosis.** *Neurol Sci* 2001;22:141–44 CrossRef Medline
38. Trapp BD, Peterson J, Ransohoff RM, et al. **Axonal transection in the lesions of multiple sclerosis.** *N Engl J Med* 1998;338:278–85 CrossRef Medline
39. Evangelou N, Esiri MM, Smith S, et al. **Quantitative pathological evidence for axonal loss in normal appearing white matter in multiple sclerosis.** *Ann Neurol* 2000;47:391–95 Medline
40. Bennett KM, Schmainda KM, Bennett RT, et al. **Characterization of continuously distributed cortical water diffusion rates with a stretched-exponential model.** *Magn Reson Med* 2003;50:727–34 CrossRef Medline
41. Meerschaert MM, Magin RL, Ye AQ. **Anisotropic fractional diffusion tensor imaging.** *J Vib Control* 2016;22:2211–21 CrossRef Medline

# Volumetric Analysis from a Harmonized Multisite Brain MRI Study of a Single Subject with Multiple Sclerosis

R.T. Shinohara, J. Oh, G. Nair, P.A. Calabresi, C. Davatzikos, J. Doshi, R.G. Henry, G. Kim, K.A. Linn, N. Papinutto, D. Pelletier, D.L. Pham, D.S. Reich, W. Rooney, S. Roy, W. Stern, S. Tummala, F. Yousuf, A. Zhu, N.L. Sicotte, R. Bakshi, and the NAIMS Cooperative



## ABSTRACT

**BACKGROUND AND PURPOSE:** MR imaging can be used to measure structural changes in the brains of individuals with multiple sclerosis and is essential for diagnosis, longitudinal monitoring, and therapy evaluation. The North American Imaging in Multiple Sclerosis Cooperative steering committee developed a uniform high-resolution 3T MR imaging protocol relevant to the quantification of cerebral lesions and atrophy and implemented it at 7 sites across the United States. To assess intersite variability in scan data, we imaged a volunteer with relapsing-remitting MS with a scan-rescan at each site.

**MATERIALS AND METHODS:** All imaging was acquired on Siemens scanners (4 Skyra, 2 Tim Trio, and 1 Verio). Expert segmentations were manually obtained for T1-hypointense and T2 (FLAIR) hyperintense lesions. Several automated lesion-detection and whole-brain, cortical, and deep gray matter volumetric pipelines were applied. Statistical analyses were conducted to assess variability across sites, as well as systematic biases in the volumetric measurements that were site-related.

**RESULTS:** Systematic biases due to site differences in expert-traced lesion measurements were significant ( $P < .01$  for both T1 and T2 lesion volumes), with site explaining  $>90\%$  of the variation (range, 13.0–16.4 mL in T1 and 15.9–20.1 mL in T2) in lesion volumes. Site also explained  $>80\%$  of the variation in most automated volumetric measurements. Output measures clustered according to scanner models, with similar results from the Skyra versus the other 2 units.

**CONCLUSIONS:** Even in multicenter studies with consistent scanner field strength and manufacturer after protocol harmonization, systematic differences can lead to severe biases in volumetric analyses.

**ABBREVIATIONS:** NAIMS = North American Imaging in Multiple Sclerosis Cooperative; T1LV = T1-hypointense lesion volume; T2LV = T2 lesion volume

Conventional MR imaging is an established tool for measuring CNS lesions and tissue compartment volumes in vivo in individuals with multiple sclerosis. In the brain and spinal cord,

inflammatory demyelinating lesions appear hyperintense on T2-weighted images. Total cerebral T2 lesion volume (T2LV) is a key metric for the longitudinal monitoring of disease severity, as well as a standard outcome in clinical trials of MS therapeutics.<sup>1–3</sup> Many T2 lesions exhibit pulse-sequence-dependent hypointensity on T1-weighted images, which has been shown to be associated with more severe (destructive) histopathology and worse clinical outcomes.<sup>4–8</sup> MR imaging is also used to measure cerebral

Received February 2, 2017; accepted after revision April 6.

From the Departments of Biostatistics and Epidemiology (R.T.S., K.A.L.) and Radiology (C.D., J.D.), Perelman School of Medicine, University of Pennsylvania, Philadelphia, Pennsylvania; Department of Neurology (J.O., P.A.C., D.S.R.), Johns Hopkins University School of Medicine, Baltimore, Maryland; St. Michael's Hospital (J.O.), University of Toronto, Toronto, Ontario, Canada; Translational Neuroradiology Section (G.N., D.S.R.), National Institute of Neurological Disorders and Stroke, National Institutes of Health, Bethesda, Maryland; Department of Neurology (R.G.H., N.P., W.S., A.Z.), University of California, San Francisco, San Francisco, California; Laboratory for Neuroimaging Research (G.K., S.T., F.Y., R.B.), Partners Multiple Sclerosis Center, and Departments of Neurology and Radiology (R.B.), Brigham and Women's Hospital, Harvard Medical School, Boston, Massachusetts; Department of Neurology (D.P.), Yale Medical School, New Haven, Connecticut; Henry M. Jackson Foundation for the Advancement of Military Medicine (D.L.P., S.R.), Bethesda, Maryland; Advanced Imaging Research Center, Oregon Health & Science University (W.R.), Portland, Oregon; Department of Neurology (N.L.S.), Cedars-Sinai Medical Center, Los Angeles, California; a complete list of the NAIMS participants is provided in the "Acknowledgments."

Major support for this study was provided by the Race to Erase MS. Additional support came from ROINS085211, R21NS093349, R01EB017255, and S10OD016356 from the National Institutes of Health and RG-1507-05243 from the National Multi-

ple Sclerosis Society. The study was also partially supported by the Intramural Research Program of the National Institute of Neurological Disorders and Stroke.

Paper previously presented in preliminary form at: Annual Meeting of the European Committee on Treatment and Research in Multiple Sclerosis, September 14–17, 2016; London, UK.

The content is solely the responsibility of the authors and does not necessarily represent the official views of the funding agencies.

Please address correspondence to Russell T. Shinohara, MD, Department of Biostatistics and Epidemiology, University of Pennsylvania Perelman School of Medicine, 217 Blockley Hall, 423 Guardian Dr. Philadelphia, PA 19104; e-mail: rshi@mail.med.upenn.edu; @Penn\_SIVE

 Indicates open access to non-subscribers at [www.ajnr.org](http://www.ajnr.org)

 Indicates article with supplemental on-line photos.

<http://dx.doi.org/10.3174/ajnr.A5254>

### 3T brain MRI anatomic acquisition protocols<sup>a</sup>

	3D T2 FLAIR			3D T1 MPRAGE		
	Siemens Skyra	Siemens Verio	Siemens Tim Trio	Siemens Skyra	Siemens Verio	Siemens Tim Trio
Operation system version	syngo MR D13	syngo MR B17	syngo MR B17	syngo MR D13	syngo MR B17	syngo MR B17
Coil	32 or 64 Channel <sup>b</sup>	32 Channel	32 Channel	32 or 64 Channel <sup>b</sup>	32 Channel	32 Channel
Acceleration factor for parallel imaging	2	2	2	2	2	2
Orientation	Sagittal	Sagittal	Sagittal	Sagittal	Sagittal	Sagittal
FOV (cm)	25.6 × 25.6	25.6 × 25.6	25.6 × 25.6	25.6 × 25.6	25.0 × 25.0	25.0 × 25.0
Matrix size	512 × 512	512 × 512	512 × 512	256 × 256	256 × 256	256 × 256
No. of sections	176	176	176	176	176	176
TR (ms)	4800	4800	4800	1900	1900	1900
TE (ms)	353	354	355	2.52	2.52	2.52
Flip angle	120°	120°	120°	9°	9°	9°
Voxel size (mm)	0.5 × 0.5 × 1.0	0.5 × 0.5 × 1.0	0.5 × 0.5 × 1.0	1.0 × 1.0 × 1.0	0.977 × 0.977 × 1.0	0.977 × 0.977 × 1.0
Scan time (min:s)	6:53	7:00	7:00	4:15	4:16	4:16
No. of signal averages	1	1	1	1	1	1

<sup>a</sup> Each of the 7 sites used 1 of 3 different Siemens scanner models (Skyra, Verio, and Tim Trio), necessitating 3 model-specific protocols for the 2 pulse sequences.

<sup>b</sup> University of California, San Francisco = 64-channel (the other Skyra sites = 32 channel).

atrophy, a commonly used supportive outcome measure of the neurodegenerative aspects of the disease in both relapsing-remitting and progressive forms of MS.<sup>9–18</sup> Together, lesion and atrophy measures provide complementary quantitative information about disease progression that are considered central to patient assessment.<sup>19</sup>

Unfortunately, differences in acquisition methods have the potential to bias MR imaging metrics. Factors such as equipment manufacturer, magnetic field strength, and acquisition protocol can affect image contrast and resultant volumetric data. Indeed, several groups have investigated the reliability of volumetric measurements across scanners,<sup>20–27</sup> but little is understood about the variability in volumetric measurements of lesions and atrophy in individuals with MS. Furthermore, many automated segmentation algorithms depend on statistical atlases or models that are built with healthy volunteers or that depend on registration, which can be compromised by the presence of MS pathology.<sup>28</sup>

The North American Imaging in Multiple Sclerosis Cooperative (NAIMS) was established to accelerate the pace of imaging research. As a consortium, our first aim was to facilitate multicenter imaging studies by creating harmonized MR imaging protocols across sites. In this article, we describe initial results from our pilot study, which tested the feasibility of multisite standardization of MR imaging acquisitions for the quantification of lesion and tissue volumes. We compare inter- to intrasite scan-rescan variability in various MR imaging output metrics with consistently acquired 3T acquisitions.

## MATERIALS AND METHODS

### Participant

A 45-year-old man with clinically stable relapsing-remitting MS and mild-to-moderate physical disability was imaged at 7 NAIMS sites across the United States (Table). He developed the first symptoms of the disease 13 years before study enrollment and had been relapse-free in the previous year after starting dimethyl fumarate. His last intravenous corticosteroid administration was 5 years previously. His timed 25-foot walk at study entry was 5.3 seconds. His Expanded Disability Status Scale score was 3.5, both at study entry and exit, without any intervening relapses on-study. The participant signed in-

formed consent for this study, which was approved by the institutional review board of each site.

### Scan Acquisition

Through consensus agreement in the Cooperative, NAIMS developed a standardized high-resolution 3T MR imaging brain scan protocol. All imaging was acquired with Siemens scanners, which, at the time of the study, were used by most NAIMS sites. Scan-rescan pairs were acquired on these scanners; the most relevant acquisition sequences are shown in the Table. At each site, the scan-rescan experiment was performed on the same day, with the participant removed and repositioned between scans. None of the participant's scans were coregistered to each other, to replicate a "real world" clinical trial setting. The volunteer was also imaged at the National Institutes of Health NAIMS site at the beginning and end of the study (5 months later) to assess disease stability. Raw MR imaging scans were distributed to 4 NAIMS sites for postprocessing.

### Expert Lesion Tracing

De-identified images underwent manual quantification to assess total cerebral T1-hypointense lesion volume (T1LV) and T2LV from the native 3D FLAIR and T1 images by the consensus of trained observers (G.K., F.Y.) under the supervision of an experienced observer (S.T.). For T2LV, this process involved manually identifying all lesions on the FLAIR images. For T1LV, lesions were required to show hypointensity on T1-weighted images and at least partial hyperintensity on FLAIR images. The lesions were then segmented by 1 observer (G.K.) with a semiautomated edge-finding tool in Jim (Version 7.0; <http://www.xinapse.com/home.php>) to determine lesion volumes. Images were presented to the same reading panel for all of the above steps in random order in 1 batch and mixed into a stack of 50 other MS images to reduce scan-to-scan memory effects and preserve blinding.

### Automated Analysis

Several fully automated pipelines were also used to estimate T2LV and the volumes of total brain, normal-appearing white matter, and both cortical and deep gray matter structures. To prevent overfitting, we used all pipelines with their default settings, according to published recommendations for each

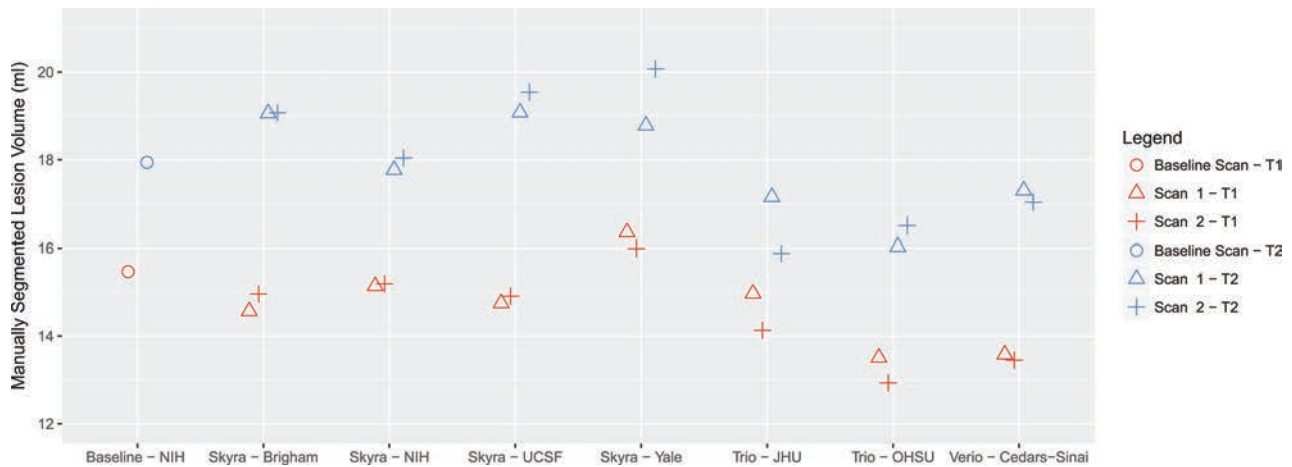


**FIG 1.** Manually measured T1 (red) and T2 (blue) lesion volumes for scan-rescan pairs at each of 7 NAIMS sites. Results from the baseline scan, acquired on the same Skyra scanner and subsequent imaging acquired at the National Institutes of Health, are shown with circles. Points have been slightly offset relative to one another for ease of visualization. UCSF indicates University of California, San Francisco; JHU, Johns Hopkins University; OHSU, Oregon Health & Science University.

method separately, in which appropriate images were inhomogeneity corrected, rigidly aligned across sequences from each scan session, processed for removal of extracerebral voxels for all processing pipelines, and intensity normalized. For lesion measurements, several algorithms were applied by the laboratories that developed or codeveloped the various methods: Lesion-TOADS (TOPOlogy-preserving Anatomical Segmentation; <https://www.nitrc.org/projects/toads-cruise/>),<sup>29</sup> a fuzzy C-means-based segmentation technique with topologic constraints; Automated Statistical Inference for Segmentation (OASIS),<sup>30</sup> a logistic-regression-based segmentation method leveraging statistical intensity normalization; Subject Specific Sparse Dictionary Learning (S3DL; <https://www.nitrc.org/projects/s3dl/>),<sup>31</sup> a patch-based dictionary learning multiclass method; and White Matter Lesion Segmentation (WMLS; <https://www.nitrc.org/projects/wmls/>),<sup>32</sup> a local support vector machine-based segmentation algorithm developed for vascular lesions that also uses corrective learning. To estimate the volume of gray matter structures, we used Lesion-TOADS; FMRIB Integrated Registration and Segmentation Tool (FSL-FIRST; <http://fsl.fmrib.ox.ac.uk/fsl/fslwiki/FIRST>)<sup>33</sup> (a Bayesian appearance method); Multi-atlas Segmentation with Brain Surface Estimation (MaCRUISE)<sup>34</sup> (a combined multiatlas segmentation and cortical reconstruction algorithm); and MUlti-atlas region Segmentation utilizing Ensembles of registration algorithms (MUSE)<sup>35</sup> (an ensemble multiatlas label-fusion method). The FSL-FIRST<sup>33</sup> analysis was applied directly to the raw T1 images according to common practice, and OASIS<sup>30</sup> was applied to the T1, FLAIR, and a 3D T2 high-resolution sequence after preprocessing; all other pipelines were applied to appropriately preprocessed T1 and FLAIR images. Not all algorithms measured volumes of the same set of structures. Lesion-filling was not performed. Lesion-TOADS, MaCRUISE, and MUSE also yielded estimates for total brain volume.

### Statistical Analysis

All statistical analyses were conducted in the R software environment (<http://www.r-project.org/>).<sup>36</sup> To compare estimated vol-

umes within and across sites, we computed mean volumes and SDs. *T* tests were also used for differences in within-site averages between scanner platforms. Correlations between these averages across segmentation algorithms were also explored. The proportion of variation explained by site was computed, and the association with site was assessed with permutation testing. The coefficients of variation were also estimated across sites. To assess associations between session-average measured total brain and lesional volumes and time of day (morning versus afternoon), we used Wald testing within a linear model framework, both marginally and adjusting for scanner platform.

### RESULTS

The participant was found to be stable regarding cerebral lesion load during the study. When we compared images acquired at the National Institutes of Health at study entry and exit, the manually measured T2LV in the participant was similar (17.9 mL in September 2015 versus 17.8 mL in February 2016). The T1LV was also stable (15.5 versus 15.1 mL). This imaging stability paralleled his clinical stability (see “Materials and Methods”).

The manually estimated T1LV and T2LV for each scan is shown in Fig 1. Site explained 95% of the variation observed in the estimated T2LV and 92% of the variation in the estimated T1LV, indicating marked scanner-to-scanner differences despite protocol harmonization, which clearly exceeded scan-rescan variability within sites. The range of T2LVs was 15.9 to 20.1 mL, indicating that differences of up to 25% of the lesion volume were observed across sites. The range of T1LVs was similarly wide, ranging from 13.0 to 16.4 mL. Further inspection of these volumes across platforms indicated that Skyra (Magnetom Skyra; Siemens, Erlangen, Germany) scanners showed larger lesion volumes compared with other Siemens platforms both on T1LV (Skyra: mean T1, 15.2 mL compared with non-Skyra: mean T1, 13.8 mL;  $P < .05$ ) and T2LV (Skyra: mean T2, 18.9 mL compared with non-Skyra: mean T2, 16.6 mL;  $P < .01$ ). An example of the segmented lesions across scanners is provided in Fig 2.

Results from the automated techniques for delineating and mea-

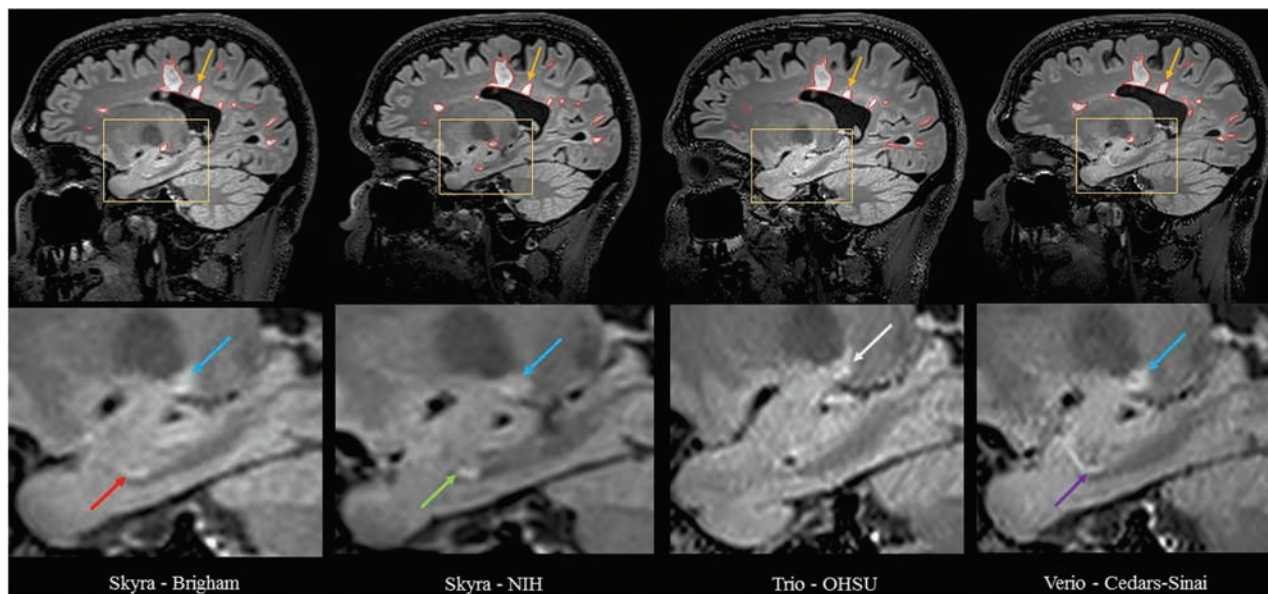


**FIG 2.** Comparison of manual segmentation of cerebral T2 hyperintense lesions at 4 NAIMS sites. 3T MR imaging scans on Siemens scanners from a single subject with multiple sclerosis showing T2 hyperintense lesions from sagittal fluid-attenuated inversion recovery sequences from 4 different North American Imaging in Multiple Sclerosis Cooperative sites and scanner models: Brigham and Women's Hospital, Skyra; National Institutes of Health, Skyra; Oregon Health & Science University (OHSU), Tim Trio; Cedars-Sinai, Verio. The upper panel shows the native images. The lower panel shows zoomed and cropped images to illustrate the key findings. The *green arrow* (lower panel) shows a possible lesion detected and traced on the National Institutes of Health scan; the *red arrow* shows the same lesion not detected by the expert procedure on the Brigham and Women's Hospital scan. The *purple arrow* shows a similar tubular area interpreted as a blood vessel on the Cedars-Sinai scan, which was not selected as a lesion by the expert tracing; no lesion was detected on the Oregon Health & Science University scan in this area on this section or any of the adjacent sections (not shown). The *blue arrow* shows a different lesion detected and traced on the Brigham and Women's Hospital, National Institutes of Health, and Cedars-Sinai scans but not detected by the expert review on the Oregon Health & Science University scan, appearing hazy/subtle (*white arrow*). The *yellow arrow* (upper panel) shows a lesion on all scans; however, when we added the tracing of all sections showing the lesion, the 3D volume of the lesion differed among sites: Brigham and Women's Hospital = 0.059 mL, National Institutes of Health = 0.053 mL, Oregon Health & Science University = 0.033 mL, Cedars-Sinai = 0.053 mL.

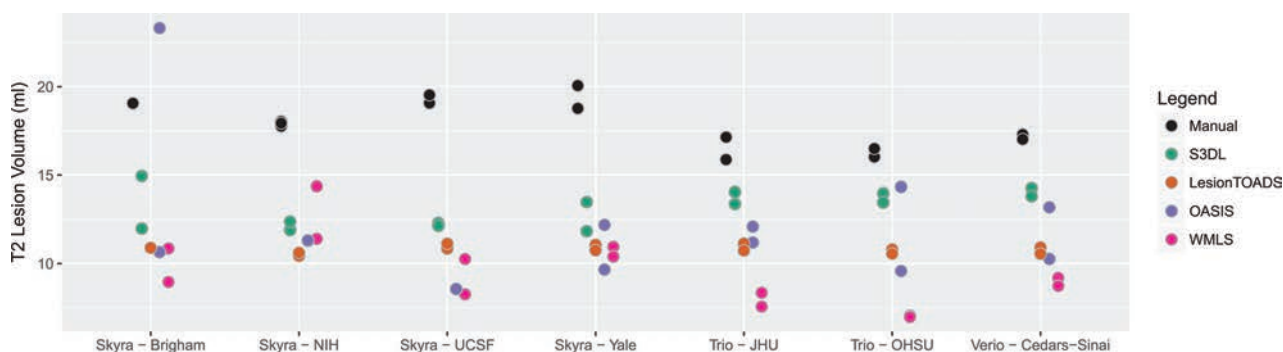


**FIG 3.** Comparison of manual and automated methods for measuring lesional volume. Scan-rescan imaging is shown by using *multiple dots* for each site and algorithm. UCSF indicates University of California, San Francisco; JHU, Johns Hopkins University; OHSU, Oregon Health & Science University.

asuring T2LV are shown in Fig 3. The automated lesion segmentations showed marked disagreement in the average lesional volume measurements compared with the manually assessed volumes, and all methods showed large site-to-site differences (in some cases up to 7.5 mL, or almost 50% of the manually measured lesion volume), except for Lesion-TOADS (range, 10.5–11.0 mL), which was more stable. For all methods, site explained >50% of the observed variation; 53% of the variation was explained by site (permutation  $P = .36$ ) for S3DL, 54% for Lesion-TOADS ( $P = .41$ ), 44% for OASIS ( $P = .57$ ), and 83% for WMLS ( $P = .002$ ), which clearly was most prone to site-related variation.

To measure brain structure volumes, we used several auto-

matized methods. As an example, results for the thalamus are shown in Figs 4 and 5. While Lesion-TOADS estimated smaller volumes, MUSE, FSL-FIRST, and MaCRUISE yielded similar average measurements. Nonetheless, site was strongly associated with measured thalamic volume, explaining 96% of the Lesion-TOADS volume variation ( $P < .01$ ), 89% of MUSE ( $P < .01$ ), 84% of FSL-FIRST ( $P = .04$ ), and 65% of MaCRUISE ( $P = .17$ ). Similar results for the putamen, caudate, cortical gray matter, normal-appearing white matter, and total brain volume were found, as provided in On-line Figs 1–5. Summaries of the coefficient of variation give an intuitive measure of the scale of the combined scan-rescan and across-site variation as shown in Fig 6.

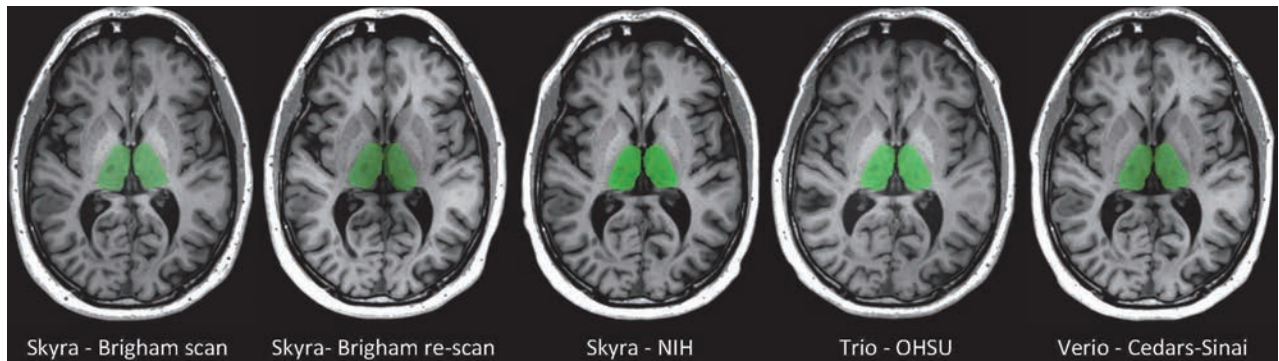


**FIG 4.** FSL-FIRST automated segmentation results: thalamus. Representative anatomic section showing segmentation of the thalamus (green) in the single subject. The segmentation maps are overlaid to the original raw 3D T1-weighted images after re-orientation to the axial plane. Segmentation was performed by the fully automated FSL-FIRST pipeline. The scan site and 3T Siemens model are shown for each image. The first 2 scans are from the scan/re-scan at Brigham and Women’s Hospital. OHSU indicates Oregon Health & Science University.



**FIG 5.** Comparison of automated methods for measuring thalamic volume. Scan-rescan imaging is shown by using *multiple dots* for each site and algorithm. UCSF indicates University of California, San Francisco; JHU, Johns Hopkins University; OHSU, Oregon Health & Science University.

Finally, the proportion of variation explained by site is shown in Fig 7. Note that in almost all cases, site explained >50% of the variation, with most measurement techniques showing >80% variation due to site for all structures assessed.

While all images were acquired on 3T Siemens scanners, the model type appeared to influence the results; there was evidence of systematic differences in many measurements between Skyra and non-Skyra scanners. Figure 8 shows the negative log *P* values for the comparison of volumes averaged across scan-rescan measurements, with larger values indicating more systematic differences between platforms. The largest platform-associated differences were observed in MaCRUISE measurements of normal-appearing white matter, cortical gray matter, and, consequently, total brain volume. Lesion-TOADS also showed large differences in total brain volume attributable to cortical gray matter, as did S3DL for T2LV measurements. MUSE showed major differences in thalamic volume across scanner models, and FSL-FIRST showed similar discrepancies in the thalamus and caudate. The correlation between site-averaged measurements varied dramatically, especially for lesional and total brain volume measurements (On-line Fig 6); this variation indicates that site differences resulted in contrasting effects on output from the different algorithms. While the other measurements showed less scanner model-related variation, most still showed prominent differences between Skyra and non-Skyra scanners.

The time of day of scan acquisition was not associated with

manually segmented T1 lesion volumes ( $t = 0.45$ ) or T2 lesion volumes ( $t = 0.38$ ) or total brain volume, as measured by any of the automated algorithms (On-line Figs 7 and 8).

## DISCUSSION

Clinical MS therapeutic trials have traditionally used 1.5T MR imaging platforms to provide metrics on cerebral lesions and atrophy as supportive outcome measures. However, there is growing interest in the use of high-resolution 3T imaging to assess disease activity and disease severity in MS. Such 3T imaging has the potential for increased sensitivity to lesions<sup>37,38</sup> and atrophy,<sup>39</sup> higher reliability,<sup>39,40</sup> and closer relationships to clinical status,<sup>38,39</sup> compared with scanning at 1.5T. The purpose of this study was to evaluate the consistency of metrics obtained from a single MS participant with a high-resolution 3T brain MR imaging protocol distributed to 7 sites. The results of our study indicate that even in multicenter acquisitions from the same scanner vendor after careful protocol harmonization, systematic differences in images led to severe biases in volumetric analyses. These biases were present in manually and automatically measured volumes of white matter lesions, as well as in automatically measured volumes of whole-brain and gray and white matter structures. These biases were also highly dependent on scanning equipment, which resulted from a higher sensitivity to lesions in newer scanners from the same manufacturer compared with earlier models, even at the same field strengths.

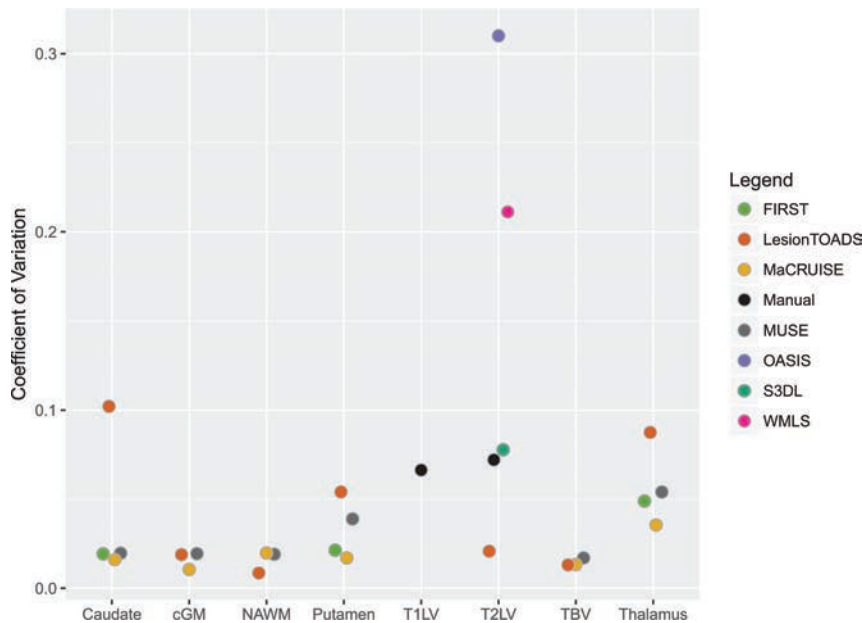


**FIG 6.** Estimated across-site coefficient of variation for each structure with various methods for volumetric measurement. cGM indicates cortical gray matter; NAWM, normal-appearing white matter; TBV, total brain volume.

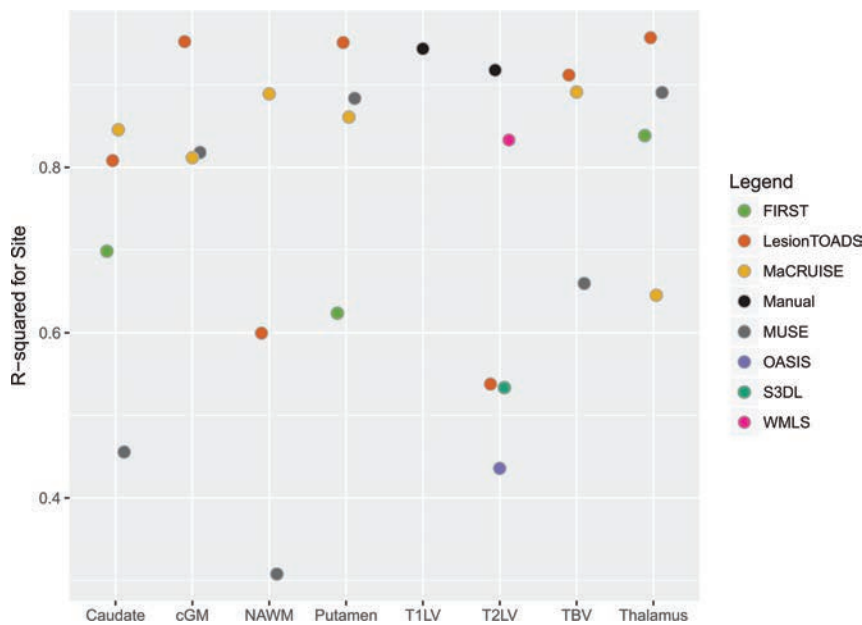


**FIG 7.** Estimated proportion of variation explained by site for using various segmentation methods for different structures in the brain. cGM indicates cortical gray matter; NAWM, normal-appearing white matter; TBV, total brain volume.

In comparison with past estimates of reliability of volumetric measurements of brain structures, our findings point to higher between-site variation than previously documented. In particular, Cannon et al<sup>27</sup> reported that between 3% and 26% of the observed variation in global and subcortical volumes were attributable to site; this was a study of 8 healthy participants imaged on 2 successive days across 8 sites with 3T Siemens and GE Healthcare scanners. However, the proportion of explained variation has a different interpretation from that reported here. The total variation in Cannon et al consisted of 4 contributors to variance: first, across-site differences; second, across-scan differences; third,

across-day differences; and fourth, across-subject differences. In our single-participant study, we isolated only the first 2 variance components, allowing us to compare variation because it is relevant for precision medicine (subject-specific) applications.

Previous work indicated that the observed variation attributable to scanning occasion was small<sup>25,27</sup>; indeed, Cannon et al<sup>27</sup> found this to constitute <1% of the variation. Thus, we did not scan our participant on subsequent days but rather simply repositioned the participant between scans during the same imaging session. A notable difference between our study and that of Cannon et al is that we did not use data from a standardized phantom concurrently acquired for correction of between-scanner variations in gradient nonlinearity and scaling. Cannon et al found that this correction improved between-site intraclass correlations and greatly reduced differences between scanner manufacturers. Similarly, Gunter et al<sup>41</sup> reported the usefulness of a phantom for scanner harmonization and quality control in the Alzheimer's Disease Neuroimaging Initiative (<http://www.adni-info.org/>). In future studies, we will focus on applying phantom calibrations across NAIMS sites to extend our current observations. Despite the growing literature on the importance of diurnal variation and hydration status for volumetric analyses,<sup>42-45</sup> we found no significant associations between time of day and measured volumes. This may indicate that in single-participant analyses, time of day and day-to-day variation may be of less concern than the much larger source of variation of scanner platform. Most interesting, Cannon et al also found that measurements acquired with scanners from the same manufacturer and similar

receive coils had higher reliability. In our study, we found that even scanner models (ie, Skyra versus non-Skyra) from the same manufacturer varied markedly in their estimates of lesion volume; this variation highlights the importance of between-scanner differences for assessing MS-related structural changes.

To assess differences across processing pipelines, we used a variety of techniques for automated segmentation of lesion and white and gray matter volumes. Different segmentation algorithms showed a range of variability in their estimates, as well as their sensitivity to differences between scanners. For example, Lesion-TOADS showed much less variable lesion measurements

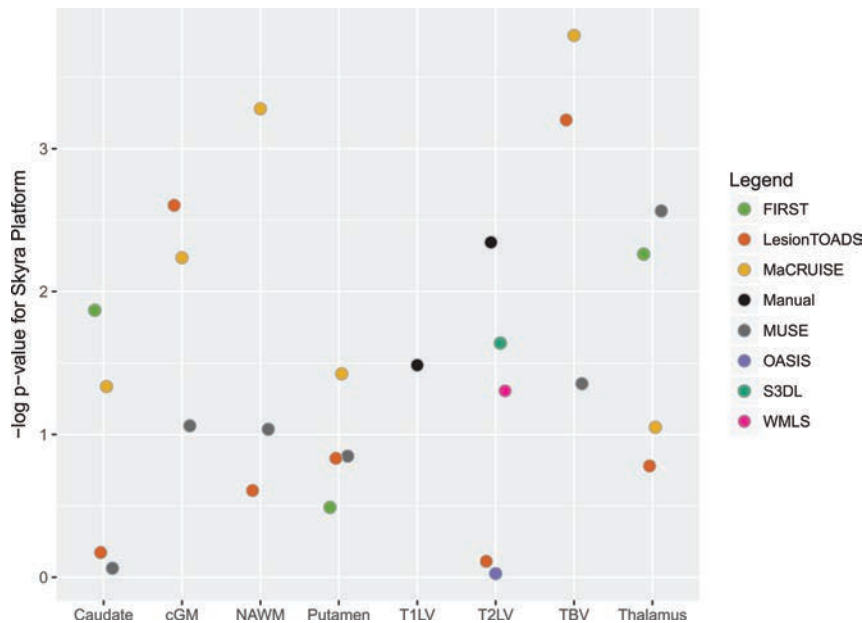


**FIG 8.** Negative logarithm (base 10)  $P$  value from  $t$  tests describing the difference in average volume between Skyra-versus-non-Skyra platforms explained by site with various segmentation methods for different structures in the brain. cGM indicates cortical gray matter; NAWM, normal-appearing white matter; TBV, total brain volume.

than any other technique and was not as sensitive to differences in scanner platform. Lesion-TOADS was the only unsupervised lesion-segmentation technique used. Contrast differences between the participant data and the training data of the other supervised methods could be associated with greater sensitivity to scanner differences, and this might be mitigated by specific (albeit potentially laborious) tuning to individual platforms. However, while sensitivity to biologic change is generally higher for methods yielding less noisy estimates, because only a single individual was studied here, our data cannot be taken to indicate that Lesion-TOADS is superior to other methods of estimating thalamic volume, for example. Additionally, both purely intensity-based segmentation algorithms, OASIS and WMLS, appeared to be more sensitive to site differences, which may indicate that methods that rely more on topology, shape, or spatial context may be more stable across scanners. This finding indicates that across-scanner differences may be driven by contrast differences rather than geometric distortions. Future investigation to extend these findings could involve quantitative contrast-to-noise and signal-to-noise comparisons across scanners. Allowing segmentation parameters to vary across sites could also help stability.

A limitation of this study is its single-subject and single time point design, which makes the generalizability of the findings dependent on further investigation. In particular, the degree to which across-site differences might vary by lesion burden and degree of atrophy, as well as demographic variables, requires additional study. Future larger studies of multiple participants across disease stages, including longitudinal measurements, are necessary for understanding the implications of the biases described in this pilot study. Indeed, such studies would also allow the assessment of the trade-off between stability in measures across sites, with sensitivity to biologic differences. Differences between scanning equipment and scanner software versions have

also been noted in past studies of reliability,<sup>23,25,27,46,47</sup> but their implications for the assessment of pathology remain unclear. In particular, repeat acquisitions on scanners with different receive coils could provide additional insight concerning reliability. In addition, our study was from a single time point across scanners, whereas clinical trials rely on the quantification of intra-subject longitudinal change.<sup>48</sup> Each participant is typically scanned on the same platform, which may limit the variability in on-study change between participants. Further studies are necessary to assess whether scan platform introduces the same level of acquisition-related variability when assessing longitudinal changes.

Given the intersite differences observed in lesional measurements, across-site-inference statistical adjustment for site is clearly necessary when analyzing volumetrics from multisite studies, even when images are acquired with a harmonized protocol on 3T scanners produced by the same manufacturer.

From a single participant, it is unclear what the role of differential sensitivity to lesions might be across individuals with heterogeneity in lesion location. For example, while lesion detection in the supratentorial white matter might be more straightforward and comparable across individuals, detection of lesions in the brain stem, cerebellum, and spinal cord may be more sensitive to differences in equipment. New statistical methods for measuring and correcting systematic biases are warranted, especially for studies in which patient populations may differ across sites. Indeed, intensity normalization and scan-effect removal techniques<sup>49-55</sup> (akin to batch-effect removal methods in genomic studies<sup>56</sup>) are an active area of methodologic research and promise to improve comparability of volumetric estimates from automated segmentation methods. After volumes are measured, statistical techniques for modeling estimated volumes from multicenter studies are also rapidly evolving.<sup>18,57</sup> These techniques bring the potential to mitigate site-to-site biases in group-level analyses, with better external validity at the cost of increased sample size.

## CONCLUSIONS

By imaging the same subject with stable relapsing-remitting MS during 5 months, we assessed scanner-related biases in volumetric measurements at 7 NAIMS centers. Despite careful protocol harmonization and the acquisition of all imaging at 3T on Siemens scanners, we found significant differences in lesion and structural volumes. These differences were especially pronounced when comparing Skyra scanners with other Siemens 3T platforms. The results from this study highlight the potential for interscanner and intersite differences that, unless properly accounted for, might

confound MR imaging volumetric data from multicenter studies of brain disorders.

Our findings raise a key issue of the interpretability of MR imaging measurements in the context of personalized medicine, even in carefully controlled studies with harmonized imaging protocols.

## ACKNOWLEDGMENTS

The following is a full list of individuals who contributed to this NAIMS study—Brigham and Women's Hospital, Harvard Medical School (Boston, Massachusetts): Rohit Bakshi, Renxin Chu, Gloria Kim, Shahamat Tauhid, Subhash Tummala, Fawad Yusuf; Cedars-Sinai Medical Center (Los Angeles, California): Nancy L. Sicotte; Henry M. Jackson Foundation for the Advancement of Military Medicine (Bethesda, Maryland): Dzung Pham, Snehashis Roy; National Institutes of Health (Bethesda, Maryland): Frances Andrada, Irene C.M. Cortese, Jenifer Dwyer, Rosalind Hayden, Haneefa Muhammad, Govind Nair, Joan Ohayon, Daniel S. Reich, Pascal Sati, Chevaz Thomas; Johns Hopkins University (Baltimore, Maryland): Peter A. Calabresi, Sandra Casard, Jiwon Oh; Oregon Health & Science University (Portland, Oregon): William Rooney, Daniel Schwartz, Ian Tagge; University of California (San Francisco, California): Roland G. Henry, Nico Papinutto, William Stern, Alyssa Zhu; University of Pennsylvania (Philadelphia, Pennsylvania): Christos Davatzikos, Jimit Doshi, Guray Erus, Kristin Linn, Russell Shinohara; University of Toronto (Toronto, Ontario, Canada): Jiwon Oh; Yale University (New Haven, Connecticut): R. Todd Constable, Daniel Pelletier.

Disclosures: Russell T. Shinohara—RELATED: Grant: National Institutes of Health\*; Support for Travel to Meetings for the Study or Other Purposes: Race to Erase MS, Comments: travel to consortium meetings; UNRELATED: Board Membership: Genentech, Comments: Scientific Advisory Board; Consultancy: Hoffmann-La Roche, Comments: expert legal consulting; Grants/Grants Pending: Gates Foundation\*; Travel/Accommodations/Meeting Expenses Unrelated to Activities Listed: Government of Canada—Banff Research Institute—European Committee for Treatment and Research in Multiple Sclerosis, Comments: conference travel.\* Jiwon Oh—UNRELATED: Consultancy: Consortium of Multiple Sclerosis Centers, EMD Serono, Novartis, Hoffmann-La Roche, Biogen Idec, Teva Pharmaceuticals; Grants/Grants Pending: MS Society of Canada, National MS Society, Biogen Idec, Genzyme\*; Support for Travel to Meetings for the Study or Other Purposes: Consortium of Multiple Sclerosis Centers. Peter Calabresi—RELATED: Grant: Race to Erase MS, Comments: foundation grant\*; Support for Travel to Meetings for the Study or Other Purposes: Race to Erase MS, Comments: The foundation pays for my travel to semi-annual meetings; UNRELATED: Consultancy: Biogen Idec, Vertex Pharmaceuticals; Grants/Grants Pending: Biogen Idec, Teva Pharmaceuticals, Annexon Biosciences, Novartis, Medimmune\*; Royalties: Cambridge Press, Comments: for editing a book on optical coherence tomography. Christos Davatzikos—RELATED: Grant: National Institutes of Health/National Institute on Aging computational neuroanatomy of aging and Alzheimer disease via pattern analysis, Comments: R01-AG014971.\* Roland G. Henry—RELATED: Grant: Race to Erase MS, Comments: nominal/standard cost for MRI scans\*; UNRELATED: Consultancy: Hoffmann-La Roche, AbbVie, Novartis, Genzyme, StemCells Inc\*; Grants/Grants Pending: Hoffmann-La Roche\*; Payment for Lectures Including Service on Speakers Bureaus: Genzyme.\* Daniel Pelletier—UNRELATED: Consultancy: Genzyme, Novartis, EMD-Serono, Genentech; Grants/Grants Pending: Biogen Idec, Comments: investigator-initiated research grant.\* Dzung L. Pham—RELATED: Grant: National MS Society, Comments: RG-1507-05243.\* Daniel S. Reich—RELATED: Support for Travel to Meetings for the Study or Other Purposes: Race to Erase MS.\* William Rooney—RELATED: Grant: Race to Erase MS, Comments: This organization provided pilot funds for the study\*; UNRELATED: Employment: Oregon Health & Science University, Comments: employs me as professor/director; Patents (Planned, Pending, or Issued): Oregon Health & Science University, Brookhaven National Laboratory; Royalties: Oregon Health & Science University. Rohit Bakshi—RELATED: Grant: Race to Erase MS.\* Nancy L. Sicotte—RELATED: Grant: Race to Erase MS.\* \*Money paid to the institution.

## REFERENCES

1. García-Lorenzo D, Francis S, Narayanan S, et al. Review of automatic segmentation methods of multiple sclerosis white matter lesions on conventional magnetic resonance imaging. *Med Image Anal* 2013; 17:1–18 CrossRef Medline
2. Lublin FD, Reingold SC, Cohen JA, et al. Defining the clinical course of multiple sclerosis: the 2013 revisions. *Neurology* 2014;83:278–86 CrossRef Medline
3. Simon JH, Jacobs LD, Campion M, et al. Magnetic resonance studies of intramuscular interferon beta-1a for relapsing multiple sclerosis: the Multiple Sclerosis Collaborative Research Group. *Ann Neurol* 1998;43:79–87 CrossRef Medline
4. Bagnato F, Jeffries N, Richert ND, et al. Evolution of T1 black holes in patients with multiple sclerosis imaged monthly for 4 years. *Brain* 2003;126(pt 8):1782–89 CrossRef Medline
5. Sahraian MA, Radue EW, Haller S, et al. Black holes in multiple sclerosis: definition, evolution, and clinical correlations. *Acta Neurol Scand* 2010;122:1–8 CrossRef Medline
6. Giorgio A, Stromillo ML, Bartolozzi ML, et al. Relevance of hypointense brain MRI lesions for long-term worsening of clinical disability in relapsing multiple sclerosis. *Mult Scler* 2014;20:214–19 CrossRef Medline
7. van Walderveen MA, Kamphorst W, Scheltens P, et al. Histopathologic correlate of hypointense lesions on T1-weighted spin-echo MRI in multiple sclerosis. *Neurology* 1998;50:1282–88 Medline
8. Truyen L, van Waesberghe JH, van Walderveen MA, et al. Accumulation of hypointense lesions (“black holes”) on T1 spin-echo MRI correlates with disease progression in multiple sclerosis. *Neurology* 1996;47:1469–76 Medline
9. Evangelou N, Esiri MM, Smith S, et al. Quantitative pathological evidence for axonal loss in normal appearing white matter in multiple sclerosis. *Ann Neurol* 2000;47:391–95 Medline
10. Evangelou N, Konz D, Esiri MM, et al. Regional axonal loss in the corpus callosum correlates with cerebral white matter lesion volume and distribution in multiple sclerosis. *Brain* 2000;123(pt 9): 1845–49 Medline
11. Sastre-Garriga J, Ingle GT, Chard DT, et al. Grey and white matter volume changes in early primary progressive multiple sclerosis: a longitudinal study. *Brain* 2005;128(pt 6):1454–60 CrossRef Medline
12. Sanfilippo MP, Benedict RH, Weinstock-Guttman B, et al. Gray and white matter brain atrophy and neuropsychological impairment in multiple sclerosis. *Neurology* 2006;66:685–92 CrossRef Medline
13. Ge Y, Grossman RI, Udupa JK, et al. Brain atrophy in relapsing-remitting multiple sclerosis: fractional volumetric analysis of gray matter and white matter. *Radiology* 2001;220:606–10 CrossRef Medline
14. Fisher E, Lee JC, Nakamura K, et al. Gray matter atrophy in multiple sclerosis: a longitudinal study. *Ann Neurol* 2008;64:255–65 CrossRef Medline
15. Fisniku LK, Chard DT, Jackson JS, et al. Gray matter atrophy is related to long-term disability in multiple sclerosis. *Ann Neurol* 2008; 64:247–54 CrossRef Medline
16. De Stefano N, Matthews PM, Filippi M, et al. Evidence of early cortical atrophy in MS: relevance to white matter changes and disability. *Neurology* 2003;60:1157–62 Medline
17. Losseff NA, Wang L, Lai HM, et al. Progressive cerebral atrophy in multiple sclerosis: a serial MRI study. *Brain* 1996;119(pt 6):2009–19 Medline
18. Keshavan A, Paul F, Beyer MK, et al. Power estimation for non-standardized multisite studies. *Neuroimage* 2016;134:281–94 CrossRef Medline
19. Bakshi R, Thompson AJ, Rocca MA, et al. MRI in multiple sclerosis: current status and future prospects. *Lancet Neurol* 2008;7:615–25 CrossRef Medline
20. Agartz I, Okuguwa G, Nordström M, et al. Reliability and reproducibility of brain tissue volumetry from segmented MR scans. *Eur Arch Psychiatry Clin Neurosci* 2001;251:255–61 CrossRef Medline
21. Bartzokis G, Mintz J, Marx P, et al. Reliability of in vivo volume

- measures of hippocampus and other brain structures using MRI. *Magn Reson Imaging* 1993;11:993–1006 CrossRef Medline
22. Maclaren J, Han Z, Vos SB, et al. **Reliability of brain volume measurements: a test-retest dataset.** *Sci Data* 2014;1:140037 CrossRef Medline
  23. Morey RA, Selgrade ES, Wagner HR 2nd, et al. **Scan-rescan reliability of subcortical brain volumes derived from automated segmentation.** *Hum Brain Mapp* 2010;31:1751–62 CrossRef Medline
  24. Schnack HG, van Haren NE, Hulshoff Pol HE, et al. **Reliability of brain volumes from multicenter MRI acquisition: a calibration study.** *Hum Brain Mapp* 2004;22:312–20 CrossRef Medline
  25. Jovicich J, Marizzoni M, Sala-Llonch R, et al; PharmaCog Consortium. **Brain morphometry reproducibility in multi-center 3T MRI studies: a comparison of cross-sectional and longitudinal segmentations.** *Neuroimage* 2013;83:472–84 CrossRef Medline
  26. Schnack HG, van Haren NE, Brouwer RM, et al. **Mapping reliability in multicenter MRI: voxel-based morphometry and cortical thickness.** *Hum Brain Mapp* 2010;31:1967–82 CrossRef Medline
  27. Cannon TD, Sun F, McEwen SJ, et al. **Reliability of neuroanatomical measurements in a multisite longitudinal study of youth at risk for psychosis.** *Hum Brain Mapp* 2014;35:2424–34 CrossRef Medline
  28. Eloyan A, Shou H, Shinohara R, et al. **Health effects of lesion localization in multiple sclerosis: spatial registration and confounding adjustment.** *PLoS One* 2014;9:e107263 CrossRef Medline
  29. Shiee N, Bazin PL, Ozturk A, et al. **A topology-preserving approach to the segmentation of brain images with multiple sclerosis lesions.** *Neuroimage* 2010;49:1524–35 CrossRef Medline
  30. Sweeney EM, Shinohara RT, Shiee N, et al. **OASIS is Automated Statistical Inference for Segmentation, with applications to multiple sclerosis lesion segmentation in MRI.** *Neuroimage Clin* 2013;2:402–13 CrossRef Medline
  31. Roy S, He Q, Sweeney E, et al. **Subject-Specific Sparse Dictionary Learning for atlas-based brain MRI segmentation.** *IEEE J Biomed Health Inform* 2015;19:1598–609 CrossRef Medline
  32. Lao Z, Shen D, Liu D, et al. **Computer-assisted segmentation of white matter lesions in 3D MR images using support vector machine.** *Acad Radiol* 2008;15:300–13 CrossRef Medline
  33. Patenaude B, Smith SM, Kennedy DN, et al. **A Bayesian model of shape and appearance for subcortical brain segmentation.** *Neuroimage* 2011;56:907–22 CrossRef Medline
  34. Huo Y, Carass A, Resnick SM, et al. **Combining multi-atlas segmentation with brain surface estimation.** *Proc SPIE Int Soc Opt Eng* 2016;9784. pii: 97840E CrossRef Medline
  35. Doshi J, Erus G, Ou Y, et al; Alzheimer's Neuroimaging Initiative. **MUSE: MULTI-atlas region Segmentation utilizing Ensembles of registration algorithms and parameters, and locally optimal atlas selection.** *Neuroimage* 2016;127:186–95 CrossRef Medline
  36. R Core Team. *R: A Language and Environment for Statistical Computing.* Vienna, Austria: R Foundation for Statistical Computing; 2016
  37. Sicotte NL, Voskuhl RR, Bouvier S, et al. **Comparison of multiple sclerosis lesions at 1.5 and 3.0 Tesla.** *Invest Radiol* 2003;38:423–27 CrossRef Medline
  38. Stankiewicz JM, Glanz BI, Healy BC, et al. **Brain MRI lesion load at 1.5T and 3T versus clinical status in multiple sclerosis.** *J Neuroimaging* 2011;21:e50–56 CrossRef Medline
  39. Chu R, Tauhid S, Glanz BI, et al. **Whole-brain volume measured from 1.5T versus 3T MRI in healthy subjects and patients with multiple sclerosis.** *J Neuroimaging* 2016;26:62–67 CrossRef Medline
  40. Chu R, Hurwitz S, Tauhid S, et al. **Deep gray matter segmentation from 1.5T vs. 3T MRI in normal controls and patients with multiple sclerosis.** *Neurology* 2016;86(16 suppl):P4.171
  41. Gunter JL, Bernstein MA, Borowski BJ, et al. **Measurement of MRI scanner performance with the ADNI phantom.** *Med Phys* 2009;36:2193–205 CrossRef Medline
  42. Duning T, Kloska S, Steinsträter O, et al. **Dehydration confounds the assessment of brain atrophy.** *Neurology* 2005;64:548–50 CrossRef Medline
  43. Sampat MP, Healy BC, Meier DS, et al. **Disease modeling in multiple sclerosis: assessment and quantification of sources of variability in brain parenchymal fraction measurements.** *Neuroimage* 2010;52:1367–73 CrossRef Medline
  44. Nakamura K, Brown RA, Araujo D, et al. **Correlation between brain volume change and T2 relaxation time induced by dehydration and rehydration: implications for monitoring atrophy in clinical studies.** *Neuroimage Clin* 2014;6:166–70 CrossRef Medline
  45. Nakamura K, Brown RA, Narayanan S, et al; Alzheimer's Disease Neuroimaging Initiative. **Diurnal fluctuations in brain volume: statistical analyses of MRI from large populations.** *Neuroimage* 2015;118:126–32 CrossRef Medline
  46. Jovicich J, Czanner S, Han X, et al. **MRI-derived measurements of human subcortical, ventricular and intracranial brain volumes: reliability effects of scan sessions, acquisition sequences, data analyses, scanner upgrade, scanner vendors and field strengths.** *Neuroimage* 2009;46:177–92 CrossRef Medline
  47. Kruggel F, Turner J, Muftuler LT; Alzheimer's Disease Neuroimaging Initiative. **Impact of scanner hardware and imaging protocol on image quality and compartment volume precision in the ADNI cohort.** *Neuroimage* 2010;49:2123–33 CrossRef Medline
  48. Filippi M, Wolinsky JS, Comi G. **Effects of oral glatiramer acetate on clinical and MRI-monitored disease activity in patients with relapsing multiple sclerosis: a multicentre, double-blind, randomised, placebo-controlled study.** *Lancet Neurol* 2006;5:213–20 CrossRef Medline
  49. Shinohara RT, Sweeney EM, Goldsmith J, et al. **Statistical normalization techniques for magnetic resonance imaging.** *Neuroimage Clin* 2014;6:9–19 CrossRef Medline
  50. Nyúl LG, Udupa JJ, Zhang X. **New variants of a method of MRI scale standardization.** *Med Imaging IEEE Trans* 2000;19:143–50 Medline
  51. Ghassemi R, Brown R, Narayanan S, et al. **Normalization of white matter intensity on T1-weighted images of patients with acquired central nervous system demyelination.** *J Neuroimaging* 2015;25:184–90 CrossRef Medline
  52. Fortin JP, Sweeney EM, Muschelli J, et al; Alzheimer's Disease Neuroimaging Initiative. **Removing inter-subject technical variability in magnetic resonance imaging studies.** *Neuroimage* 2016;132:198–212 CrossRef Medline
  53. Madabhushi A, Udupa JK. **New methods of MR image intensity standardization via generalized scale.** *Med Phys* 2006;33:3426–34 CrossRef Medline
  54. Nyúl LG, Udupa JK. **On standardizing the MR image intensity scale.** *Magn Reson Med* 1999;42:1072–81 Medline
  55. Chua AS, Egorova S, Anderson MC, et al. **Handling changes in MRI acquisition parameters in modeling whole brain lesion volume and atrophy data in multiple sclerosis subjects: comparison of linear mixed-effect models.** *Neuroimage Clin* 2015;8:606–10 CrossRef Medline
  56. Leek JT, Scharpf RB, Bravo HC, et al. **Tackling the widespread and critical impact of batch effects in high-throughput data.** *Nat Rev Genet* 2010;11:733–39 CrossRef Medline
  57. Fennema-Notestine C, Gamst AC, Quinn BT, et al. **Feasibility of multi-site clinical structural neuroimaging studies of aging using legacy data.** *Neuroinformatics* 2007;5:235–45 CrossRef Medline

# Reliability of White Matter Microstructural Changes in HIV Infection: Meta-Analysis and Confirmation

E.E. O'Connor, A. Jaillard, F. Renard, and T.A. Zeffiro



## ABSTRACT

**BACKGROUND:** Diffusion tensor imaging has been widely used to measure HIV effects on white matter microarchitecture. While many authors have reported reduced fractional anisotropy and increased mean diffusivity in HIV, quantitative inconsistencies across studies are numerous.

**PURPOSE:** Our aim was to evaluate the consistency across studies of HIV effects on DTI measures and then examine the DTI reliability in a longitudinal seropositive cohort.

**DATA SOURCES:** Published studies and investigators.

**STUDY SELECTION:** The meta-analysis included 16 cross-sectional studies reporting fractional anisotropy and 12 studies reporting mean diffusivity in the corpus callosum.

**DATA ANALYSIS:** Random-effects meta-analysis was used to estimate study standardized mean differences and heterogeneity. DTI longitudinal reliability was estimated in seropositive participants studied before and 3 and 6 months after beginning treatment.

**DATA SYNTHESIS:** Meta-analysis revealed lower fractional anisotropy (standardized mean difference,  $-0.43$ ;  $P < .001$ ) and higher mean diffusivity (standardized mean difference,  $0.44$ ;  $P < .003$ ) in seropositive participants. Nevertheless, between-study heterogeneity accounted for 58% and 66% of the observed variance ( $P < .01$ ). In contrast, the longitudinal cohort fractional anisotropy was higher and mean diffusivity was lower in seropositive participants (both,  $P < .001$ ), and fractional anisotropy and mean diffusivity measures were very stable during 6 months, with intraclass correlation coefficients all  $>0.96$ .

**LIMITATIONS:** Many studies pooled participants with varying treatments, ages, and disease durations.

**CONCLUSIONS:** HIV effects on WM microstructure had substantial variations that could result from acquisition, processing, or cohort-selection differences. When acquisition parameters and processing were carefully controlled, the resulting DTI measures did not show high temporal variation. HIV effects on WM microstructure may be age-dependent. The high longitudinal reliability of DTI WM microstructure measures makes them promising disease-activity markers.

**ABBREVIATIONS:** AD = axial diffusivity; cART = combination antiretroviral therapy; CPE = CNS penetration effectiveness; FA = fractional anisotropy; MD = mean diffusivity; RD = radial diffusivity; SMD = standardized mean difference

The advent of combination antiretroviral therapies (cART) for HIV has resulted in both increases in life expectancy and decreases in mortality.<sup>1</sup> While cART successfully controls HIV

viremia and reconstitutes immune function,<sup>2</sup> the effects of persisting HIV infection and its treatments on brain structure and function are less clear. The incidence of HIV-associated dementia declines following cART initiation,<sup>3</sup> and cART is sometimes asso-

Received September 15, 2016; accepted after revision March 18, 2017.

From the Department of Radiology and Nuclear Medicine (E.E.O.), University of Maryland Medical System, Baltimore, Maryland; Unité IRM 3T-Recherche-IRMaGe-Inserm US 17/CNRS UMS 3552 (A.J., F.R.) and Laboratoire MATICE-Pôle Recherche (A.J., F.R.), Centre Hospitalier Universitaire Grenoble Alpes, Grenoble, France; Neurometrika (T.A.Z.), Potomac, Maryland; and Department of Human Development (T.A.Z.), University of Maryland College Park, Maryland.

This work was partially supported by the Comprehensive NeuroAIDS Center (National Institutes of Health grant P30MH092177).

Please address correspondence to Erin E. O'Connor, MD, Department of Diagnostic Radiology and Nuclear Medicine, University of Maryland Medical System, 22 S Greene St, Baltimore, MD 21201; e-mail: erin.oconnor@umm.edu; @LanternLab

Indicates open access to non-subscribers at [www.ajnr.org](http://www.ajnr.org)

Indicates article with supplemental on-line appendix and tables.

Indicates article with supplemental on-line photos.

<http://dx.doi.org/10.3174/ajnr.A5229>

ciated with improved cognitive function.<sup>4</sup> Nevertheless, cognitive deficits can persist in treated HIV infection,<sup>3</sup> with some suggesting that the neuropsychological impairment pattern changes, rather than its prevalence.<sup>5</sup> Factors such as comorbidity burden, cognitive reserve, nadir T-helper (CD4) cell count, and age may also contribute to cognitive impairment.<sup>6-9</sup>

While CD4 cell count and viral load are generally used to diagnose infection and monitor treatment response, they do not necessarily reflect the direct and indirect brain effects of HIV infection. HIV enters the central nervous system soon after infection<sup>10</sup> and persists after treatment.<sup>11</sup> Before the cART era, CSF HIV RNA levels correlated with the severity of cognitive impairment<sup>12</sup> but cART reduced CSF levels of HIV-1 RNA.<sup>13</sup> Nevertheless, with cART there is no strong association between cognitive impairment and concurrent CSF or peripheral viral load,<sup>14</sup> and several studies have shown that cognitive impairment may develop during viral suppression.<sup>15-18</sup>

Neuropsychological testing is often used to estimate HIV CNS effects, even though assessment is time-intensive and possibly subject to practice effects.<sup>19</sup> Nevertheless, the HIV neuropsychological profile associated with cognitive impairment is debated,<sup>5,9,20</sup> suggesting that behavioral measures may not be optimal for measuring the ongoing CNS involvement.

The absence of measurable, consistent cognitive changes related to HIV disease activity motivates the search for objective biomarkers of the CNS effects of HIV infection. Histopathologic evidence of HIV infection effects ranges from inflammation associated with gliosis and increased perivascular macrophages to degenerative pathology manifested as diffuse myelin pallor and axonal damage.<sup>21,22</sup> This evidence of white matter involvement has led to cross-sectional studies with diffusion tensor imaging to study WM microarchitecture following HIV infection, with many finding decreased fractional anisotropy (FA)<sup>21,23-32</sup> and increased mean diffusivity (MD).<sup>21,26,29,30,32,33</sup> However, there have also been puzzling inconsistencies, with studies demonstrating results of opposite polarity, namely increased FA and decreased MD in the corpus callosum or other WM tracts.<sup>30,31,33-35</sup> It would be useful to have consistency estimates of any serostatus effects across studies and temporal reliability estimates of these effects in individuals to evaluate the utility of using WM microstructure measures for tracking the progression of HIV infection in the brain.

These issues prompted us to first do a meta-analysis of studies reporting callosal microstructure changes following HIV infection and then to examine the longitudinal stability of WM microstructural measures in seropositive participants before the initiation of cART and 3 and 6 months thereafter.

## **MATERIALS AND METHODS**

### **Meta-Analysis of HIV Effects in the Corpus Callosum**

To summarize the literature on WM microstructure changes associated with HIV infection, we performed a computerized literature PubMed search on April 25, 2016, by using the terms (“hiv”[MeSH Terms] OR “hiv”) AND (“brain”[MeSH Terms] OR “brain”[All Fields]) AND (“diffusion tensor imaging”[MeSH Terms] OR (“diffusion”[All Fields] AND “tensor”[All Fields]) AND “imaging”[All Fields]) OR “diffusion tensor imaging” [All

Fields]),” yielding 82 records. Of these, 28 studies were excluded for the following reasons: 1) Studied participants were not infected with HIV, 2) studies were performed in animal models, 3) they were review articles, 4) they were case reports, or 5) they examined participants with perinatal HIV exposure who were not infected. Given the variability in the ROIs from which FA and MD were measured, we chose to focus on the corpus callosum because it is the largest WM fiber tract in the brain and was the most frequent measurement target.

Of the 54 eligible full-text articles, 16 cross-sectional studies of patients with HIV infection and controls that were completed between 2001 and 2016 were included in the meta-analysis, with 12 studies reporting both FA and MD values and 4 studies reporting only FA values. Because 3 articles did not report complete FA and MD values, the results were obtained from the authors. The remaining studies were excluded for the following reasons: 1) Numeric values for FA and MD were not reported for either seropositive or seronegative participants (authors of these articles were contacted in an effort to obtain the missing values); 2) only whole-brain FA or MD was reported; 3) the studies examined the relationships of clinical variables, biomarkers, or treatment on DTI measures without including a seronegative control group; 4) FA and MD were not measured in the corpus callosum; 5) prior published DTI data were used for fMRI connectivity analysis ROI selection; 6) a single case-control pair was reported; 7) the study focused on imaging measures other than diffusion parameters; or 8) the article reported a new processing algorithm for DTI data (Fig 1). See the On-line Appendix for excluded study references. Mean FA and MD values and their SDs were taken from the article tables, or the corresponding author was contacted if results were presented in a different form.

We used the R meta-analysis library *meta*<sup>36</sup> to estimate the standardized mean difference (SMD) in FA or MD for each study and then calculated a weighted average of these estimates across studies. If multiple values for callosal subregions were reported in a study, we used their average in inverse-variance-weighted random-effects models, estimating the mean effect and incorporating estimates of between-study variation in the weighting of each study.  $I^2$  was used to estimate study heterogeneity.<sup>37,38</sup> Study bias was checked by examining plots of sample size versus effect size. Meta-regression was used to examine imaging protocol effects.

### **Meta-Analysis of Callosal Regional Variation in HIV Serostatus Effects**

Eight of the selected studies reported FA, MD, axial diffusivity (AD), and radial diffusivity (RD) for callosal subregions, including the genu, body, and splenium. Because qualitative examination of the values revealed anatomic variation in diffusion measures, we performed a separate repeated-measures, mixed-effects regression analysis, examining regional and serostatus effects on callosal diffusion measures. If the callosal microstructure exhibited regional variation, differential regional sampling across studies could result in high experimental error.

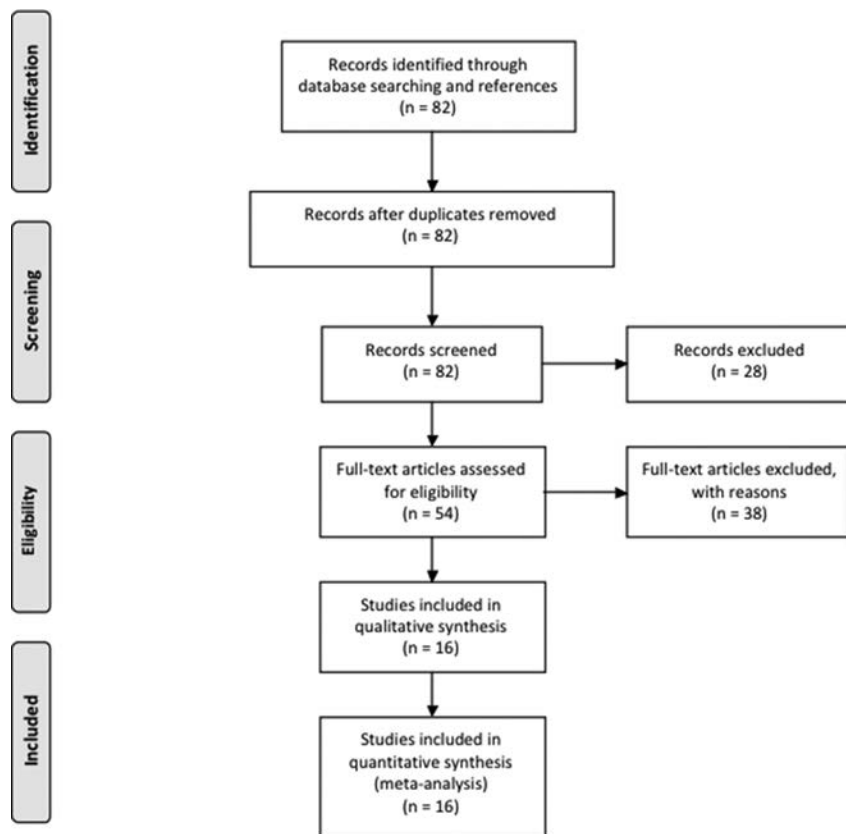


**FIG 1.** Flow diagram showing selection of articles examining WM microstructure changes in HIV infection for the meta-analysis.<sup>82</sup>

### Comparison Study

To compare the meta-analysis serostatus effects with a new sample and to characterize within-subject temporal variations in diffusion measures, we collected longitudinal DTI in seropositive participants before the initiation of cART and 3 and 6 months thereafter, comparing the results with those in a seronegative control group.

After we obtained Temple University institutional review board approval and consent, 10 seropositive participants, 22–50 years of age, cART-naive but ready to begin antiretroviral therapy, were studied. Nine were followed longitudinally for 6 months. We excluded participants who met the *Diagnostic and Statistical Manual of Mental Disorders-IV* criteria for substance dependence or abuse in the past 6 months and/or who had other major psychiatric disorders, neurologic illnesses unrelated to HIV, MR imaging contraindications, cancer, hepatic disease, renal disease, cardiac disease, or pulmonary disease.

The serologic status of HIV participants was confirmed by positive HIV enzyme-linked immunoassay and Western blot or detection of plasma HIV RNA by the polymerase chain reaction. Plasma viral load, CD4, and CD8 T-cell counts were collected before initiation of cART and from 0.5 to 6.0 months after beginning therapy. Urine toxicology was collected before each imaging visit, testing the presence of marijuana, cocaine, opiates, methamphetamines, barbiturates, benzodiazepines, and phencyclidine. Participants testing positive for any of these substances with the exception of marijuana were excluded.

For comparison, 12 seronegative participants 21–26 years of age were studied once. None of this group reported past or present symptoms of a major psychiatric or neurologic disorder or head injury with loss of consciousness or were taking psychoactive medications.

To assess posttreatment cognitive and motor performance, we gave participants a brief test battery for psychomotor function, dexterity, learning, and memory skills, including the International HIV Dementia Scale,<sup>39</sup> the Hopkins Verbal Learning Test,<sup>40</sup> the HIV-Dementia Motor Scale,<sup>41</sup> the Unified Parkinson's Disease Rating Scale motor examination,<sup>42</sup> and the Grooved Pegboard Test.<sup>43</sup>

Neuroimaging was performed with a 3T Verio MR imaging system (Siemens, Erlangen, Germany) equipped with a 12-channel matrix head coil. We performed the following scans: a high-resolution, 3D sagittal T1-weighted, magnetization-prepared rapid acquisition of gradient echo (TR/TE/flip angle = 1600 ms/2.5 ms/9°, 256 × 256 matrix, 1-mm<sup>3</sup> voxels); a 2D multisection oblique axial T2-weighted fast spin-echo (TR/TE = 3000 ms/85 ms, 320 × 320 matrix,

5-mm<sup>3</sup> voxels); and DTI for WM microstructure assessment (2.0 × 2.0 × 2.2 mm voxels, TR/TE/flip angle = 14,700 ms/95 ms/90°, and 30 diffusion gradient directions with b-values of 0 and 1000). Images were inspected at the time of scanning, and a repeat scan was performed if motion artifacts were observed.

DTI data were preprocessed with a script implementing gradient direction, head motion, and eddy current correction by using the FMRIB 5.0 Diffusion Toolbox (FDT; <http://fsl.fmrib.ox.ac.uk/fsl/fslwiki/FDT>).<sup>44</sup> Quality assurance involved visual inspection of the individual images and elimination of corrupted images. FA, MD, RD, and AD values were computed for all voxels after we fitted a tensor model to the corrected diffusion data with FDT.

The FA map for each subject was then aligned with an FA atlas FMRIB58\_FA ([www.fmrib.ox.ac.uk/fsl/data/FMRIB58\\_FA](http://www.fmrib.ox.ac.uk/fsl/data/FMRIB58_FA)) with the FMRIB Nonlinear Registration Tool (FNIRT; <http://fsl.fmrib.ox.ac.uk/fsl/fslwiki/FNIRT>).<sup>45</sup> Next, a mean FA image was created and thinned to create a mean FA skeleton representing the centers of all tracts common to the group. Then each subject's aligned FA data were projected onto the mean skeleton. The skeleton-creation steps are part of the Tract-Based Spatial Statistics (TBSS; <http://fsl.fmrib.ox.ac.uk/fsl/fslwiki/TBSS>) procedure.<sup>46</sup>

To increase the robustness of the measures and to facilitate the interpretation of the results, we averaged the different measures over the skeleton delimited by ROIs obtained from the ICBM-152 atlas,<sup>47</sup> previously aligned with the FNIRT procedure in the

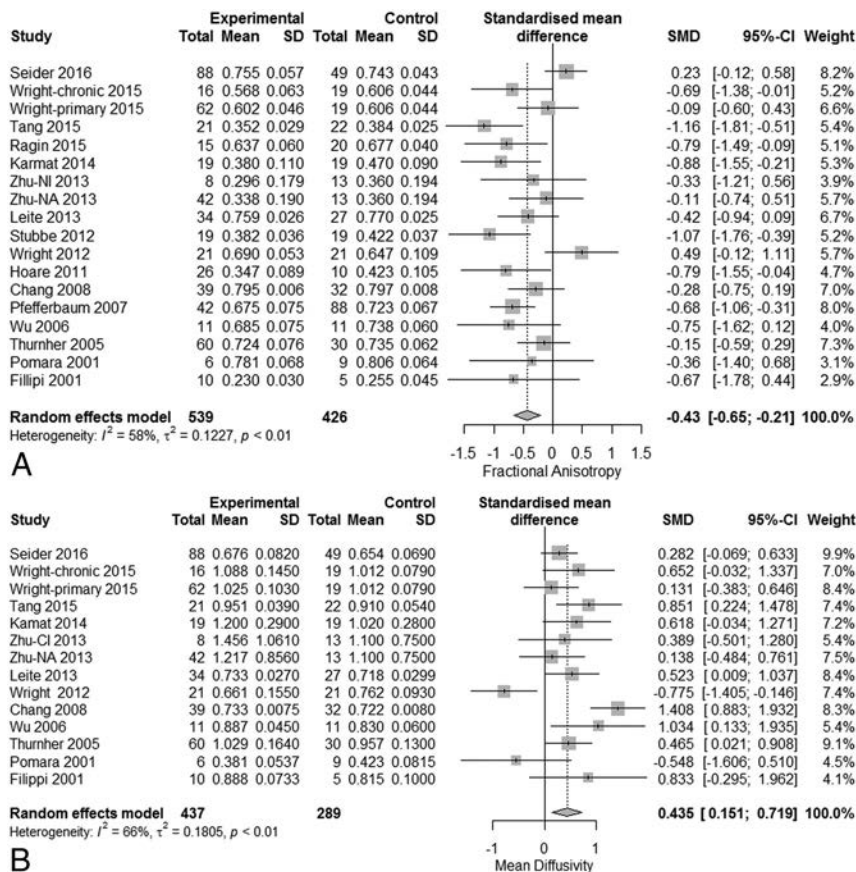


**FIG 2.** Meta-analysis results for HIV-positive versus HIV-negative comparisons of fractional anisotropy and mean diffusivity. A, FA differences (SMD =  $-0.43$ ; 95% CI,  $-0.65$  to  $-0.21$ ); test of SMD = 0:  $z = -3.82$ ;  $P < .001$ . B, MD differences (SMD =  $+0.44$ ; 95% CI,  $0.15$ – $0.72$ ; test of SMD = 0:  $z = 3.00$ ;  $P = .003$ ).

FMRI58\_FA common atlas, sampling the genu, body, and splenium callosal subregions (On-line Fig 1).

## RESULTS

### Meta-Analysis

Meta-analysis of serostatus effects on callosal microstructure revealed a small reduction in FA (SMD =  $-0.43$ ; 95% CI,  $-0.65$  to  $-0.21$ ) related to serostatus (test of SMD = 0:  $z = -3.82$ ,  $P < .001$ ), with high study heterogeneity ( $Q = 40.7$ ,  $df = 17$ ,  $P = .001$ , and  $I^2$  [variation in SMD attributable to heterogeneity] = 58%). The  $\tau^2$  of between-study variance was 0.12. Eleven of the 16 studies had confidence intervals that included zero (Fig 2A).

Meta-analysis of MD revealed a significant increase (SMD =  $+0.44$ ; 95% CI,  $0.15$ – $0.72$ ) related to serostatus (test of SMD = 0:  $z = 3.00$ ,  $P < .003$ ), with high study heterogeneity ( $Q = 38.4$ ,  $df = 13$ ,  $P = .0003$ , and  $I^2 = 66.0\%$ ). The estimate of between-study variance  $\tau^2$  was 0.18 (Fig 2B). Therefore, meta-analysis of both FA and MD revealed a small but statistically significant, change related to serostatus. Nevertheless, the observed high study heterogeneity suggests the existence of other unexplained experimental effects.

Because both FA and MD serostatus group differences were associated with high between-study heterogeneity, it was possible that the observed group differences in WM microstructure resulted from variations in image-acquisition parameters or bio-

logic variables. For image-acquisition parameters reported by the constituent publications, mixed-effects meta-regression revealed no significant effects on callosal FA and MD from variations in field strength (range, 1.5T–4T), voxel volume (range, 1.5–20 mm<sup>3</sup>), and diffusion direction number (range, 6–64). Mixed-effects meta-regression also revealed no significant effects of the biologic variables age (range, 27–53 years) and CD4 count (range, 211–678). In addition, there was no apparent trend in the DTI measures during the period spanned by the studies (2001–2016). Perhaps due to the relatively small sample of available studies, none of the variables examined appear to explain the high heterogeneity seen in the meta-analyses of FA or MD effects. Examination of funnel plots did not reveal asymmetries suggestive of bias.

To investigate the possibility that the high between-study heterogeneity arose from DTI processing variations, we coded studies according to whether the FSL/TBSS method was used, because it uses a unique step in which the FA maps are “skeletonized” to reduce potential partial volume effects. Meta-regression revealed a nonsignificant ( $P = .08$ ) trend for FSL/TBSS processing being associated with higher FA values. Details

of acquisition and processing for each study can be found in On-line Table 1.

Given some regional variation in measures, the observed between-study heterogeneity in callosal FA and MD group differences might also have resulted from sampling and combining diffusion measures from different callosal segments in different studies. To more closely examine callosal regional variations in FA and MD related to serostatus, we used repeated-measures multi-level models with region and serostatus as fixed effects and study as a random effect in the 8 studies providing all 4 diffusion measures for 3 callosal subregions. For both FA and MD, we found significant regional effects, with the splenium having higher FA and lower MD than the body and genu. Thus, the callosal region sampled appears to have a strong effect on group estimates of WM microstructure (On-line Appendix, On-line Tables 2 and 3, and On-line Figs 1 and 2).

### Comparison Study

For comparison with the meta-analysis, we collected DTI data from seropositive and seronegative participants for cross-sectional and longitudinal examination of WM microstructure changes.

Nine of 10 seropositive participants in our sample successfully completed 3 imaging visits, and 12 seronegative controls com-

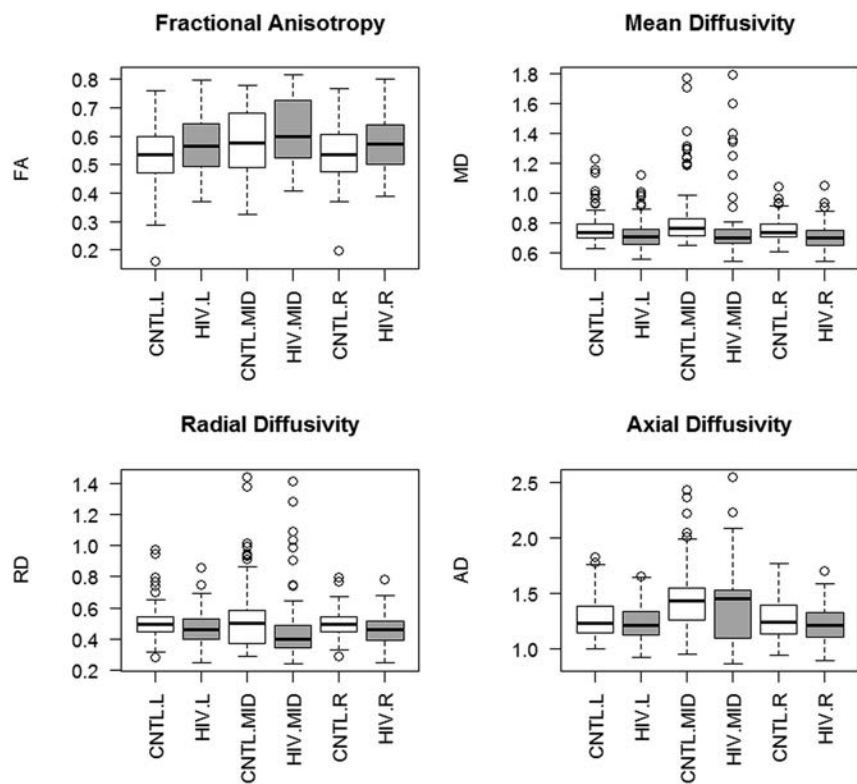


**FIG 3.** Differences in FA, MD, RD, and AD measures in the seronegative comparison group (CNTL) and seropositive (HIV) participants following HIV infection but before treatment was started. Seropositive participants had higher FA and lower MD, RD, and AD. Measurements from 28 white matter ROIs were aggregated into left hemisphere (L), midline (MID), and right hemisphere (R) regions.

pleted 1 visit. Although the mean age for our seropositive subjects ( $30.7 \pm 9.5$  years) was greater than that of controls ( $23.3 \pm 1.8$  years), age variations over this range are not known to result in variations in diffusion measures,<sup>48</sup> a finding consonant with the negative age meta-regression results reported above. While we would expect that the slightly older age of our seropositive cohort could potentially decrease the FA, this decrease was not observed. Seropositive participants had fewer years of education ( $11.9 \pm 2.0$  years) than controls ( $17.2 \pm 1.7$  years). On entry into the study, 6 of the 9 participants were seropositive during screening for sexually transmitted disease. The other 3 participants had signs and symptoms of clinical AIDS, with all 3 presenting with Pneumocystis pneumonia and 1 additionally having herpes zoster and esophageal candidiasis.

Seropositive participants began cART immediately after their first visit. All 9 seropositive participants were treated with at least 3 antiretroviral medications, including nucleoside reverse transcriptase inhibitor and a nucleoside analog, which were taken in combination with nonnucleoside reverse transcriptase inhibitors or an integrase inhibitor. The CNS penetration effectiveness (CPE) rank of each participant's cART regimen was calculated on the basis of a modified version of the CPE, which includes rilpivirine (personal communication, S. Letendre, January 14, 2015). Six participants were on regimens with a CPE rank of 6, and 3 participants had a CPE rank of 7, 1 of whom switched to a regimen with a rank of 6 after 4 months of therapy, and then to one with a rank of 8 after 5 months.

Laboratory testing included serial CD4 and CD8 T-cell counts and viral load, both assessed before initiation of cART and from 0.5 to 6.0 months after the initiation of cART (On-line Table 4). During 24 weeks of therapy, seropositive participants averaged CD4 cell count increases of 6.8 cells/week ( $P < .001$ ) and accompanying decreases in the log viral load ( $P < .001$ ), with no change in CD8 cell counts ( $P = .64$ ). These results are typical responses to cART.

Behavioral assessments revealed that while none of our subjects met the criteria for HIV dementia, a few exhibited mild-to-moderate degrees of impairment in verbal learning, with some subjects exhibiting mild degrees of impairment in motor function (On-line Table 5).

Although HIV infection can result in macroscopic changes in WM, visual inspection of the T1- and T2-weighted images revealed that our participants were generally free of these effects. One seropositive participant exhibited a mild degree of T2 prolongation in the periaxial WM bilaterally. T1- and T2-weighted images were otherwise unrevealing, with no parenchymal lesions, ventriculomegaly, or brain atrophy of the sort frequently reported before the widespread introduction of cART.<sup>49,50</sup>

requently reported before the widespread introduction of cART.<sup>49,50</sup>

To examine the regional pattern of diffusion changes following HIV infection but before treatment began, we compared the seropositive pretreatment ROI values with the seronegative control values, with repeated-measures multilevel models treating serostatus and hemisphere (left hemisphere, midline, and right hemisphere) as fixed effects and subject and ROI as random effects. With FA as the dependent measure, the seropositive group had higher FA values [ $F(2,21.06) = 14.31, P = .0011$ ]. FA values were also higher in the midline than the hemispheres [ $F(2,707.98) = 10.92, P < .001$ ] (Fig 3A). With MD as the dependent measure, the seropositive group had lower MD [ $F(1,76.23) = 18.45, P < .001$ ]. MD values were also higher in the midline compared with the hemispheres [ $F(2,81.52) = 31.31, P < .001$ ], with a significant serostatus by hemisphere interaction [ $F(2,81.52) = 3.31, P = .042$ ] (Fig 3B). For RD, we found an effect of serostatus, with the seropositive group showing lower values [ $F(1,17.40) = 15.16, P < .001$ ] and an effect of hemisphere [ $F(2,87.58) = 11.37, P < .001$ ], with the midline having a higher RD than the hemispheres. There was also a significant serostatus by hemisphere interaction [ $F(2,87.58) = 3.77, P = .027$ ] (Fig 3C). For AD, we found an effect of serostatus [ $F(1,92.12) = 7.03, P = .0095$ ], with the seropositive group exhibiting lower AD and an effect of hemisphere [ $F(2,98.73) = 0.30, P < .001$ ], with the midline showing higher values than the hemispheres (Fig 3D). Thus,

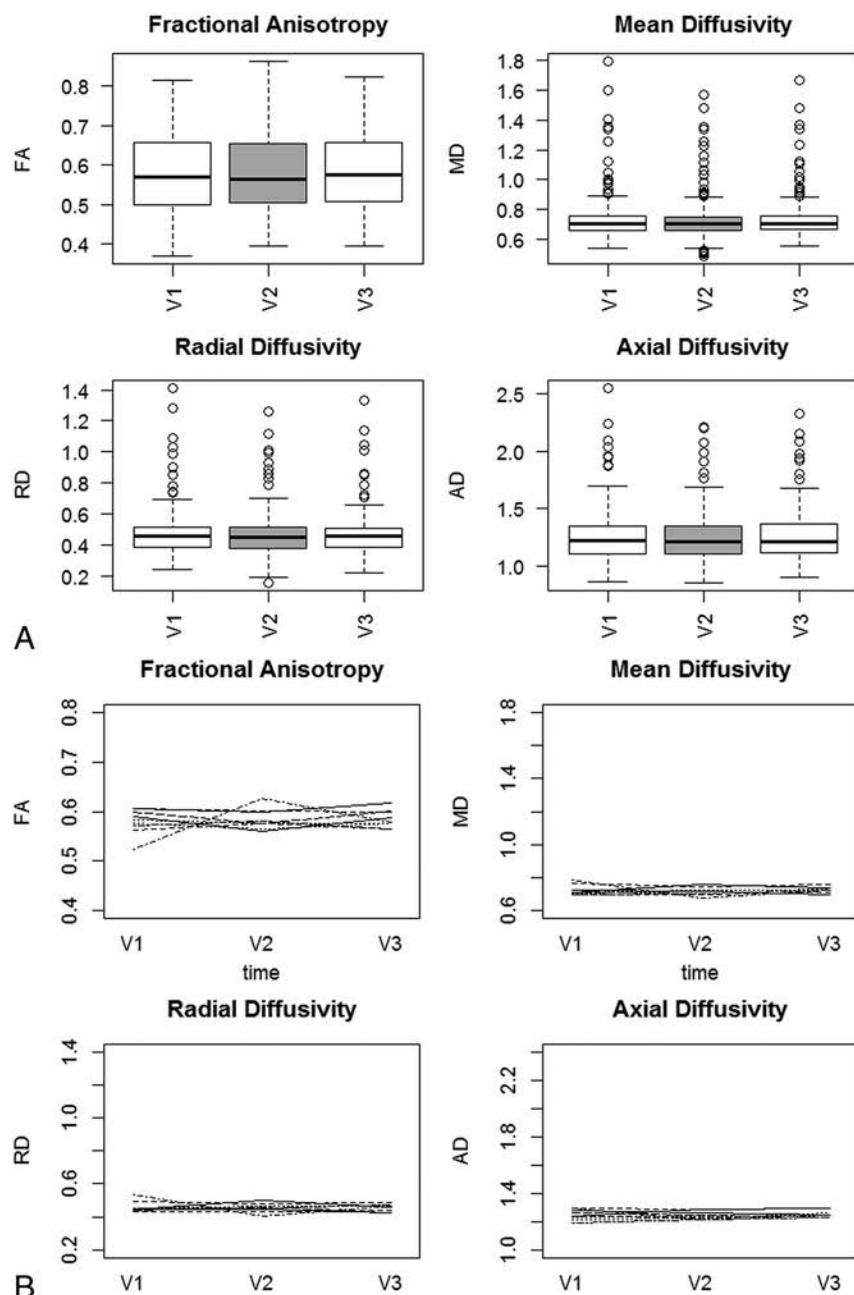


**FIG 4.** A, FA, MD, RD, and AD in seropositive participants following HIV infection but before treatment was started. Measurements are aggregated across 28 white matter ROIs.<sup>47</sup> Data were collected pretreatment (V1), 3 months later (V2), and 6 months later (V3). B, Individual time plots of FA, MD, RD, and AD in seropositive participants following HIV infection.

compared with seronegative controls, in the seropositive group, we observed higher FA and lower MD, RD, and AD.

To examine the within-subject reliability of FA, MD, RD, and AD measures, we examined temporal variations in the 4 diffusion measures during 6 months with a 2-way random-effects intraclass correlation coefficient model. Averaging across all 28 WM sampling regions, we observed excellent internal consistency, with Cronbach  $\alpha$  scores of FA = 0.91, MD = 0.96, AD = 0.98, and RD = 0.96. Cronbach  $\alpha$  indicates the degree to which items measure a single unidimensional latent variable. Intraclass correlation coefficient estimates were also high, with FA intraclass correlation coefficient = 0.97 (95% CI, 0.96–0.97), MD = 0.96 (95% CI,

0.96–.97), AD = 0.98 (95% CI, 0.98–.99), and RD = 0.96 (95% CI, 0.95–.97) (Fig 4A). In addition, examination of individual subject time plots of FA, MD, RD, and AD revealed that all subjects exhibited consistent mean WM architecture estimates across time (Fig 4B).

## DISCUSSION

### Summary of Results

Meta-analysis of HIV effects on WM microstructure revealed relatively small changes in FA and MD related to serostatus and high between-study heterogeneity. Variation in image-acquisition parameters across studies did not explain the high heterogeneity. More detailed examination of callosal WM microstructure measures revealed regional variations that could contribute to between-study differences if the same callosal regions were not sampled in each study. In our comparison study, HIV infection was associated with widespread changes in WM microstructure, with increases in FA and decreases in MD, RD, and AD. During a 6-month span, these measures showed excellent reliability, suggesting that within-subject experimental variation does not contribute substantially to high between-study heterogeneity.

### HIV Effects on White Matter Microstructure

HIV infection affects cerebral WM through a range of mechanisms. Histopathologic evidence includes inflammation associated with gliosis, an increased numbers of perivascular macrophages, and a type of degenerative pathology, manifested as myelin pallor,<sup>22</sup> which is thought to result from breakdown of the blood-brain barrier with resulting vasogenic edema.<sup>51</sup> WM metabolite alterations detected with MR spectroscopy paralleled those seen in subcortical gray matter, including elevated Cho/Cr, elevated mIns/Cr, and decreased NAA/Cr ratios,<sup>52</sup> with these metabolite differences increasing with disease progression.<sup>53</sup> Macrostructural evidence of HIV infection includes cerebral WM volume loss<sup>54</sup> and focal hyperintensities seen with T2-weighted imaging.<sup>55</sup>

DTI revealed changes associated with seropositivity, believed to reflect WM injury from both direct or indirect effects of infection.<sup>21,23–25,27–30,32,33,56,57</sup> While these studies have generally found elevated MD and reduced FA in the WM of seropositive participants relative to controls, results vary among the published accounts. These inconsistencies could arise from a number of sources, including pooling observations from both

treated and untreated participants,<sup>24-27,29-31,58,59</sup> diffusion imaging protocol variations, study sample variations in the duration of infection, age, premorbid and comorbid substance use, comorbid illness such as hepatitis, length and effectiveness of antiretroviral therapy treatment, CNS medication penetration, CD4 nadir, premorbid intelligence, and ethnicity.

### **Meta-Analysis of HIV Effects on White Matter Microstructure**

Meta-analysis of HIV DTI studies revealed wide variation in seropositivity effects on diffusion parameter estimates. If DTI is ever used as a diagnostic marker for HIV infection, high consistency in regional measurements will be required. In addition, there are growing concerns about the reproducibility and reliability of biomedical research,<sup>60,61</sup> prompting the National Institutes of Health to focus on initiatives to reduce the frequency and severity of irreproducibility.<sup>61</sup> There are many potential sources for the study heterogeneity effects we observed.

The specific choice of MR imaging acquisition parameters, with related SNR variation, might bias measurements of diffusion measures, particularly in higher magnetic fields.<sup>62,63</sup> Nevertheless, meta-regression of acquisition parameters across studies did not account for variation in diffusion measures, suggesting that the range of SNR values arising from variation in voxel volume, field strength, and diffusion direction number did not strongly influence FA and MD estimates. Keeping acquisition parameters constant in the comparison study, we observed high within-subject reproducibility across time.

While differences in DTI data-processing techniques may contribute to diffusion measure heterogeneity,<sup>63,64</sup> many of the studies included in the meta-analysis did not report data-processing details in sufficient detail to examine their specific effects by using meta-regression or subgroup analysis. Nevertheless, we were able to compare the effects using DTI processing methods that involved skeletonization of diffusion parameter maps with those that did not and observed a trend for FA values being higher when FSL/TBSS style processing was used. The skeletonization step that is a unique aspect of TBSS results in voxel selections that are more likely to contain pure WM, thereby having less contamination from partial volume effects, which might be expected to reduce the apparent directionality of diffusion. This preliminary finding will be explored in a subsequent subject-level meta-analysis of the effects of processing strategy on diffusion parameter estimates in HIV.

While HIV globally affects WM, regional variations in myelination, axon orientation, packing density, and membrane permeability may affect regional measurements.<sup>63</sup> Meta-analysis of callosal diffusion measures revealed regional variability, with FA consistently highest in the splenium. Therefore, between-study variation in the selection of subsequently aggregated sampling regions could result in higher between-study heterogeneity.

Differences in cohort characteristics, such as the duration of infection, age, premorbid and comorbid substance use, comorbid illness such as hepatitis, the length and effectiveness of treatment with antiretroviral therapy, CNS penetration effectiveness of the cART regimen, nadir CD4, premorbid intelligence, and ethnicity, may also contribute to a lack of reproducibility. Many studies in

our meta-analysis excluded subjects with current drug or alcohol use, but premorbid drug or alcohol use was often not addressed. Chronic alcoholism has been shown to reduce the corpus callosum FA.<sup>29,65,66</sup> Studies have also shown corpus callosum FA decreases following cocaine,<sup>67</sup> methamphetamine,<sup>68</sup> and opiate use.<sup>69</sup>

WM microstructure cross-sectional studies have shown that FA is lower and MD is higher in older compared with younger adults.<sup>70,71</sup> More recently, annual decreases in FA and annual increases in MD, AD, and RD have been shown in a longitudinal healthy cohort, with changes beginning in the fifth decade.<sup>48</sup> While we found no evidence for age effects in our meta-analysis, the maximum mean age in these studies was below the age when WM microstructural changes generally begin, highlighting the need to further explore age effects in older patients with HIV.

Higher general intelligence indices have been associated with higher FA and lower MD and RD, in typical middle-aged and older adults,<sup>72</sup> with these findings confirmed in studies involving younger adults.<sup>73</sup> Some studies used in our meta-analysis had control groups with more years of education than the seropositive participants.

Antiretroviral treatments may be injurious to brain cell elements. To our knowledge, there are no studies examining the effects of cART regimen CPE on WM microstructure. Nevertheless, in a study comparing simple motor task performance in seropositive participants on low- and high-CPE cART regimens, the fMRI response amplitude was significantly greater in the low-CPE group compared with the high-CPE or seronegative groups<sup>74</sup>; this finding suggests that treatment effects should be explored in future meta-analytic studies with subject-level data.

Two studies in the meta-analysis included HIV-infected participants with hepatitis,<sup>27,35</sup> and several studies did not list comorbidities such as chronic liver or renal disease as exclusionary criteria. Hepatitis C coinfection is found in 25%–30% of HIV-infected individuals<sup>75</sup> and has been associated with reduced FA and increased MD in the WM, including the corpus callosum.<sup>76</sup>

Finally, 10 of the 16 studies enrolled patients with longer infection duration than the subjects enrolled in our comparison study. Although the relationship between HIV infection duration and DTI measures is rarely addressed, infection duration can be negatively associated with callosal FA.<sup>77</sup>

The effects of many of the study characteristics discussed above are difficult to explore with meta-regression because aggregating individual subject variables can result in ecological bias in the resulting parameter estimates.<sup>78</sup> Although it was not possible to explore these biologic effects with the tools of study-level meta-analysis, it is very likely that many of these variables contributed strongly to the high observed between-study heterogeneity, motivating further exploration of potential modulating effects of biologic variables with datasets incorporating subject-level measures.

### **Comparison Study Results**

Our study found globally reduced MD and elevated FA in the WM of HIV-infected participants who were naive to antiretroviral therapy. Other studies have reported increased FA values and decreased MD, AD, and RD for multiple corpus callosum regions

and the centrum semiovale in cART-naive seropositive participants compared with seronegative controls.<sup>30,34</sup> Because cellular membranes hinder water diffusion,<sup>79</sup> activation of microglia, astrocytes, and perivascular macrophages associated with early CNS HIV infection may have caused reduced MD and increased FA in our seropositive cohort.<sup>80</sup> Because many of the studies in the meta-analysis included patients with longer infection duration than our subjects, the shorter infection duration in our sample might have resulted in different changes in diffusion parameters. Studies reporting higher FA in the seropositive group<sup>34,35</sup> included participants with shorter disease durations. The earlier phases of HIV infection might be associated with more robust neuroinflammatory changes, causing diffusion restriction effects resulting in higher FA and lower MD. On examining the details of the studies that agreed with our findings, we noted that the authors studied younger samples, many of whom were untreated at the time of imaging, as in our pilot longitudinal study. There is evidence of an age-by-HIV serostatus interaction, evidenced by higher FA and lower MD in younger individuals and lower FA and higher MD in older individuals in the posterior limbs of the internal capsules, cerebral peduncles, and anterior corona radiata.<sup>35</sup> Because most of the studies in the meta-analysis included samples with higher average ages, we believe that this age/serostatus interaction may explain the seeming contradictory results across studies. Unfortunately, we are unable to statistically confirm this explanation, given the study-level data sources used for this meta-analysis. Nevertheless, the biologic interactions among age, serostatus, and WM microstructure is a topic that might be profitably explored in subsequent meta-analyses based on subject-level data.

WM microstructure measures were examined in our seropositive participants at 3 and 6 months after the initiation of cART, demonstrating excellent reliability. We attribute these persistent alterations in WM microstructure, despite the initiation of cART, to the presence of continued activation of microglia and macrophages because this form of continuing inflammation during cART has been documented histologically.<sup>81</sup>

Global temporal stability of DTI measures was observable at the single-subject level, suggesting that the heterogeneity observed in the meta-analysis did not arise because of random temporal fluctuations in the measurement process. It is possible that use of more uniform imaging protocols and data-processing pipelines across studies will improve between-study reproducibility.

## CONCLUSIONS

Meta-analysis of DTI results from studies examining the effects of HIV serostatus on WM microstructure revealed high between-study heterogeneity and relatively small changes in measures. Regional variation in callosal WM architecture could contribute to between-study differences if the same callosal regions are not combined for total callosal estimates. In a longitudinal comparison sample, we observed widespread changes related to seropositivity in WM microstructure, with increases in FA and decreases in MD, RD, and AD. Effects of HIV infection on WM microstructure may be age-dependent, related to more prominent neuroinflammatory changes in younger patients. Examination of measures averaged over all brain WM structures during a 6-month

span revealed excellent reliability, suggesting that within-subject variation does not substantially contribute to the observed between-study variability. Further work will be required to isolate the sources of variation in WM microstructure estimates in HIV seropositive groups.

## ACKNOWLEDGMENTS

We gratefully acknowledge the assistance of Drs Schiffito, Wright, Seider, and Cohen for providing values not given in the original articles.

Disclosures: Erin E. O'Connor—RELATED: Grant: National Institute of Mental Health Grant P30 MH092177.\* \*Money paid to the institution.

## REFERENCES

1. Lima VD, Hogg RS, Harrigan PR, et al. **Continued improvement in survival among HIV-infected individuals with newer forms of highly active antiretroviral therapy.** *AIDS* 2007;21:685–92 CrossRef Medline
2. Hammer SM, Squires KE, Hughes MD, et al. **A controlled trial of two nucleoside analogues plus indinavir in persons with human immunodeficiency virus infection and CD4 cell counts of 200 per cubic millimeter or less: AIDS Clinical Trials Group 320 Study Team.** *N Engl J Med* 1997;337:725–33 CrossRef Medline
3. Simioni S, Cavassini M, Annoni JM, et al. **Cognitive dysfunction in HIV patients despite long-standing suppression of viremia.** *AIDS* 2010;24:1243–50 CrossRef Medline
4. Cohen RA, Boland R, Paul R, et al. **Neurocognitive performance enhanced by highly active antiretroviral therapy in HIV-infected women.** *AIDS* 2001;15:341–45 CrossRef Medline
5. Cysique LA, Maruff P, Brew BJ. **Prevalence and pattern of neuropsychological impairment in human immunodeficiency virus-infected/acquired immunodeficiency syndrome (HIV/AIDS) patients across pre-and post-highly active antiretroviral therapy eras: a combined study of two cohorts clinical report.** *J Neurovirol* 2004;10: 350–57 CrossRef Medline
6. Giancola ML, Lorenzini P, Balestra P, et al. **Neuroactive antiretroviral drugs do not influence neurocognitive performance in less advanced HIV-infected patients responding to highly active antiretroviral therapy.** *J Acquir Immune Defic Syndr* 2006;41:332–37 CrossRef Medline
7. Tozzi V, Balestra P, Bellagamba R, et al. **Persistence of neuropsychologic deficits despite long-term highly active antiretroviral therapy in patients with HIV-related neurocognitive impairment: prevalence and risk factors.** *J Acquir Immune Defic Syndr* 2007;45:174–82 CrossRef Medline
8. Maki PM, Rubin LH, Valcour V, et al. **Cognitive function in women with HIV: findings from the Women's Interagency HIV Study.** *Neurology* 2015;84:231–40 CrossRef Medline
9. Heaton RK, Franklin DR, Ellis RJ, et al. **HIV-associated neurocognitive disorders before and during the era of combination antiretroviral therapy: differences in rates, nature, and predictors.** *J Neurovirol* 2011;17:3–16 CrossRef Medline
10. Gray F, Scaravilli F, Everall I, et al. **Neuropathology of early HIV-1 infection.** *Brain Pathol* 1996;6:1–15 CrossRef Medline
11. Jellinger KA, Setinek U, Drlicek M, et al. **Neuropathology and general autopsy findings in AIDS during the last 15 years.** *Acta Neuropathol* 2000;100:213–20 CrossRef Medline
12. Chan P, Brew BJ. **HIV associated neurocognitive disorders in the modern antiviral treatment era: prevalence, characteristics, biomarkers, and effects of treatment.** *Curr HIV/AIDS Rep* 2014;11: 317–24 CrossRef Medline
13. Marra CM, Zhao Y, Clifford DB, et al; AIDS Clinical Trials Group 736 Study Team. **Impact of combination antiretroviral therapy on cerebrospinal fluid HIV RNA and neurocognitive performance.** *AIDS* 2009;23:1359–66 CrossRef Medline

14. Vitiello B, Goodkin K, Ashtana D, et al. **HIV-1 RNA concentration and cognitive performance in a cohort of HIV-positive people.** *AIDS* 2007;21:1415–22 CrossRef Medline
15. Robertson KR, Smurzynski M, Parsons TD, et al. **The prevalence and incidence of neurocognitive impairment in the HAART era.** *AIDS* 2007;21:1915–21 CrossRef Medline
16. Cysique LA, Brew BJ. **Prevalence of non-confounded HIV-associated neurocognitive impairment in the context of plasma HIV RNA suppression.** *J Neurovirol* 2011;17:176–83 CrossRef Medline
17. Cysique LA, Maruff P, Brew BJ. **Variable benefit in neuropsychological function in HIV-infected HAART-treated patients.** *Neurology* 2006;66:1447–50 CrossRef Medline
18. Sevigny J, Albert S, McDermott M, et al. **Evaluation of HIV RNA and markers of immune activation as predictors of HIV-associated dementia.** *Neurology* 2004;63:2084–90 CrossRef Medline
19. Grund B, Wright EJ, Brew BJ, et al; INSIGHT SMART Study Group. **Improved neurocognitive test performance in both arms of the SMART study: impact of practice effect.** *J Neurovirol* 2013;19:383–92 CrossRef Medline
20. Woods SP, Moore DJ, Weber E, et al. **Cognitive neuropsychology of HIV-associated neurocognitive disorders.** *Neuropsychol Rev* 2009;19:152–68 CrossRef Medline
21. Thurnher MM, Castillo M, Stadler A, et al. **Diffusion-tensor MR imaging of the brain in human immunodeficiency virus-positive patients.** *AJNR Am J Neuroradiol* 2005;26:2275–81 Medline
22. Budka H. **Human immunodeficiency virus (HIV)-induced disease of the central nervous system: pathology and implications for pathogenesis.** *Acta Neuropathol* 1989;77:225–36 CrossRef Medline
23. Leite SC, Corrêa DG, Doring TM, et al. **Diffusion tensor MRI evaluation of the corona radiata, cingulate gyri, and corpus callosum in HIV patients.** *J Magn Reson Imaging* 2013;38:1488–93 CrossRef Medline
24. Ragin AB, Wu Y, Gao Y, et al. **Brain alterations within the first 100 days of HIV infection.** *Ann Clin Transl Neurol* 2015;2:12–21 CrossRef Medline
25. Kamat R, Brown GG, Bolden K, et al. **Apathy is associated with white matter abnormalities in anterior, medial brain regions in persons with HIV infection.** *J Clin Exp Neuropsychol* 2014;36:854–66 CrossRef Medline
26. Zhu T, Zhong J, Hu R, et al. **Patterns of white matter injury in HIV infection after partial immune reconstitution: a DTI tract-based spatial statistics study.** *J Neurovirol* 2013;19:10–23 CrossRef Medline
27. Stubbe-Drger B, Deppe M, Mohammadi S, et al; German Competence Network HIV/AIDS. **Early microstructural white matter changes in patients with HIV: a diffusion tensor imaging study.** *BMC Neurol* 2012;12:23 CrossRef Medline
28. Hoare J, Fouche JP, Spottiswoode B, et al. **White-matter damage in Clade C HIV-positive subjects: a diffusion tensor imaging study.** *J Neuropsychiatry Clin Neurosci* 2011;23:308–15 CrossRef Medline
29. Pfefferbaum A, Rosenbloom MJ, Adalsteinsson E, et al. **Diffusion tensor imaging with quantitative fibre tracking in HIV infection and alcoholism comorbidity: synergistic white matter damage.** *Brain* 2007;130:48–64 Medline
30. Pomara N, Crandall DT, Choi SJ, et al. **White matter abnormalities in HIV-1 infection: a diffusion tensor imaging study.** *Psychiatry Res* 2001;106:15–24 CrossRef Medline
31. Filippi CG, Ulug AM, Ryan E, et al. **Diffusion tensor imaging of patients with HIV and normal-appearing white matter on MR images of the brain.** *AJNR Am J Neuroradiol* 2001;22:277–83 Medline
32. Wright PW, Vaida FF, Fernández RJ, et al. **Cerebral white matter integrity during primary HIV infection.** *AIDS* 2015;29:433–42 CrossRef Medline
33. Chang L, Wong V, Nakama H, et al. **Greater than age-related changes in brain diffusion of HIV patients after 1 year.** *J Neuroimmune Pharmacol* 2008;3:265–74 CrossRef Medline
34. Wright P, Heaps J, Shimony JS, et al. **The effects of HIV and combination antiretroviral therapy on white matter integrity.** *AIDS* 2012;26:1501–08 CrossRef Medline
35. Seider TR, Gongvatana A, Woods AJ, et al. **Age exacerbates HIV-associated white matter abnormalities.** *J Neurovirol* 2016;22:201–12 CrossRef Medline
36. Schwarzer G, Carpenter JR, Rücker G. *Meta-Analysis with R.* New York: Springer-Verlag; 2015
37. Higgins JP, Thompson SG, Deeks JJ, et al. **Measuring inconsistency in meta-analyses.** *BMJ* 2003;327:557–60 CrossRef Medline
38. Higgins JP, Thompson SG. **Controlling the risk of spurious findings from meta-regression.** *Stat Med* 2004;23:1663–82 CrossRef Medline
39. Sacktor NC, Wong M, Nakasujja N, et al. **The International HIV Dementia Scale: a new rapid screening test for HIV dementia.** *AIDS* 2005;19:1367–74 Medline
40. Brandt J. **The Hopkins Verbal Learning Test: development of a new memory test with six equivalent forms.** *Clinical Neuropsychologist* 1991;5:125–42 CrossRef
41. Robinson-Papp J, Byrd D, Mindt MR, et al; Manhattan HIV Brain Bank. **Motor function and human immunodeficiency virus-associated cognitive impairment in a highly active antiretroviral therapy-era cohort.** *Arch Neurol* 2008;65:1096–101 CrossRef Medline
42. Fahn S, Elton RL, UPDRS program members. **Unified Parkinsons Disease Rating Scale.** In: Fahn S, Marsden CD, Goldstein M, Calne DB, eds. *Recent Developments in Parkinsons Disease.* Vol 2. Florham Park, NJ: Macmillan Healthcare Information; 1987:153–63
43. Trites R. **Grooved Pegboard Test.** Lafayette: Lafayette Instrument; 1989
44. Smith SM, Jenkinson M, Woolrich MW, et al. **Advances in functional and structural MR image analysis and implementation as FSL.** *Neuroimage* 2004;23(suppl 1):S208–19 CrossRef Medline
45. Andersson JL, Jenkinson M, Smith S. **Non-linear registration, aka Spatial normalisation FMRIB technical report TR07JA2.** FMRIB Centre, Oxford, UK. June 28, 2007. <https://www.fmrib.ox.ac.uk/datasets/techrep/tr07ja2/tr07ja2.pdf>. Accessed May 2, 2017
46. Smith SM, Jenkinson M, Johansen-Berg H, et al. **Tract-based spatial statistics: voxelwise analysis of multi-subject diffusion data.** *Neuroimage* 2006;31:1487–505 CrossRef Medline
47. Oishi K, Faria AV, van Zijl PC, et al. *MRI Atlas of Human White Matter.* Amsterdam: Academic Press; 2010
48. Sexton CE, Walhovd KB, Storsve AB, et al. **Accelerated changes in white matter microstructure during aging: a longitudinal diffusion tensor imaging study.** *J Neurosci* 2014;34:15425–36 CrossRef Medline
49. Broderick DF, Wippold FJ 2nd, Clifford DB, et al. **White matter lesions and cerebral atrophy on MR images in patients with and without AIDS dementia complex.** *AJR Am J Roentgenol* 1993;161:177–81 CrossRef Medline
50. Jarvik JG, Hesselink JR, Kennedy C, et al. **Acquired immunodeficiency syndrome: magnetic resonance patterns of brain involvement with pathologic correlation.** *Arch Neurol* 1988;45:731–36 CrossRef Medline
51. Power C, Kong PA, Crawford TO, et al. **Cerebral white matter changes in acquired immunodeficiency syndrome dementia: alterations of the blood-brain barrier.** *Ann Neurol* 1993;34:339–50 CrossRef Medline
52. Chang L, Ernst T, Leonido-Yee M, et al. **Cerebral metabolite abnormalities correlate with clinical severity of HIV-1 cognitive motor complex.** *Neurology* 1999;52:100–08 CrossRef Medline
53. Mohamed MA, Barker PB, Skolasky RL, et al. **Brain metabolism and cognitive impairment in HIV infection: a 3-T magnetic resonance spectroscopy study.** *Magn Reson Imaging* 2010;28:1251–57 CrossRef Medline
54. Cardenas VA, Meyerhoff DJ, Studholme C, et al. **Evidence for ongoing brain injury in human immunodeficiency virus-positive patients treated with antiretroviral therapy.** *J Neurovirol* 2009;15:324–33 CrossRef Medline
55. McArthur JC, Kumar AJ, Johnson DW, et al. **Incidental white matter hyperintensities on magnetic resonance imaging in HIV-1 infection; multicenter AIDS Cohort Study.** *J Acquir Immune Defic Syndr* 1990;3:252–59 Medline
56. Ragin AB, Wu Y, Storey P, et al. **Diffusion tensor imaging of subcor-**

- tical brain injury in patients infected with human immunodeficiency virus. *J Neurovirol* 2005;11:292–98 CrossRef Medline
57. Ragin A, Storey P, Cohen B, et al. **Disease burden in HIV-associated cognitive impairment: a study of whole-brain imaging measures.** *Neurology* 2004;63:2293–97 CrossRef Medline
  58. Wang B, Liu Z, Liu J, et al. **Gray and white matter alterations in early HIV-infected patients: combined voxel-based morphometry and tract-based spatial statistics.** *J Magn Reson Imaging* 2016; 43:1474–83 CrossRef Medline
  59. Tang VM, Lang DJ, Giesbrecht CJ, et al. **White matter deficits assessed by diffusion tensor imaging and cognitive dysfunction in psychostimulant users with comorbid human immunodeficiency virus infection.** *BMC Res Notes* 2015;8:515 CrossRef Medline
  60. McNutt M. **Journals unite for reproducibility.** *Science* 2014;346:679 CrossRef Medline
  61. Collins FS, Tabak LA. **Policy: NIH plans to enhance reproducibility.** *Nature* 2014;505:612–13 CrossRef Medline
  62. Papinutto ND, Maule F, Jovicich J. **Reproducibility and biases in high field brain diffusion MRI: an evaluation of acquisition and analysis variables.** *Magn Reson Imaging* 2013;31:827–39 CrossRef Medline
  63. Jones DK, Knösche TR, Turner R. **White matter integrity, fiber count, and other fallacies: the do's and don'ts of diffusion MRI.** *Neuroimage*. 2013;73:239–54 CrossRef Medline
  64. Vollmar C, O'Muircheartaigh J, Barker GJ, et al. **Identical, but not the same: intra-site and inter-site reproducibility of fractional anisotropy measures on two 3.0T scanners.** *Neuroimage* 2010;51: 1384–94 CrossRef Medline
  65. Pfefferbaum A, Sullivan EV. **Microstructural but not macrostructural disruption of white matter in women with chronic alcoholism.** *Neuroimage* 2002;15:708–18 CrossRef Medline
  66. Pfefferbaum A, Sullivan EV, Hedehus M, et al. **In vivo detection and functional correlates of white matter microstructural disruption in chronic alcoholism.** *Alcohol Clin Exp Res* 2000;24:1214–21 CrossRef Medline
  67. Ma L, Hasan KM, Steinberg JL, et al. **Diffusion tensor imaging in cocaine dependence: regional effects of cocaine on corpus callosum and effect of cocaine administration route.** *Drug Alcohol Depend* 2009;104:262–67 CrossRef Medline
  68. Tobias MC, O'Neill J, Hudkins M, et al. **White-matter abnormalities in brain during early abstinence from methamphetamine abuse.** *Psychopharmacology* 2010;209:13–24 CrossRef Medline
  69. Bora E, Yücel M, Fornito A, et al. **White matter microstructure in opiate addiction.** *Addict Boil* 2012;17:141–48 CrossRef
  70. Pagani E, Agosta F, Rocca MA, et al. **Voxel-based analysis derived from fractional anisotropy images of white matter volume changes with aging.** *Neuroimage* 2008;41:657–67 CrossRef Medline
  71. Nusbaum AO, Tang CY, Buchsbaum MS, et al. **Regional and global changes in cerebral diffusion with normal aging.** *AJNR Am J Neuroradiol* 2001;22:136–42 Medline
  72. Haász J, Westlye ET, Fjær S, et al. **General fluid-type intelligence is related to indices of white matter structure in middle-aged and old adults.** *Neuroimage* 2013;83:372–83 CrossRef Medline
  73. Malpas CB, Genc S, Saling MM, et al. **MRI correlates of general intelligence in neurotypical adults.** *J Clin Neurosci* 2016;24:128–34 CrossRef Medline
  74. Ances BM, Roc AC, Korczykowski M, et al. **Combination antiretroviral therapy modulates the blood oxygen level-dependent amplitude in human immunodeficiency virus-seropositive patients.** *J Neurovirol* 2008;14:418–24 CrossRef Medline
  75. Alter MJ. **Epidemiology of viral hepatitis and HIV co-infection.** *J Hepatol* 2006;44(1 suppl):S6–9 Medline
  76. Bładowska J, Zimny A, Knysz B, et al. **Evaluation of early cerebral metabolic, perfusion and microstructural changes in HCV-positive patients: a pilot study.** *J Hepatol* 2013;59:651–57 CrossRef Medline
  77. Heaps-Woodruff JM, Wright PW, Ances BM, et al. **The impact of human immune deficiency virus and hepatitis C coinfection on white matter microstructural integrity.** *J Neurovirol* 2016;22:389–99 CrossRef Medline
  78. Berlin JA, Santanna J, Schmid CH, et al; Anti-Lymphocyte Antibody Induction Therapy Study Group. **Individual patient- versus group-level data meta-regressions for the investigation of treatment effect modifiers: ecological bias rears its ugly head.** *Stat Med* 2002;21: 371–87 CrossRef Medline
  79. Alexander AL, Lee JE, Lazar M, et al. **Diffusion tensor imaging of the brain.** *Neurotherapeutics* 2007;4:316–29 CrossRef Medline
  80. Hong S, Banks WA. **Role of the immune system in HIV-associated neuroinflammation and neurocognitive implications.** *Brain Behav Immun* 2015;45:1–12 CrossRef Medline
  81. Anthony IC, Ramage SN, Carnie FW, et al. **Influence of HAART on HIV-related CNS disease and neuroinflammation.** *J Neuropathol Exp Neurol* 2005;64:529–36 CrossRef Medline
  82. Moher D, Liberati A, Tetzlaff J, et al. **Preferred reporting items for systematic reviews and meta-analyses: the PRISMA statement.** *PLoS Med* 2009;6:e1000097 CrossRef Medline

# Differentiation between Treatment-Induced Necrosis and Recurrent Tumors in Patients with Metastatic Brain Tumors: Comparison among $^{11}\text{C}$ -Methionine-PET, FDG-PET, MR Permeability Imaging, and MRI-ADC—Preliminary Results

N. Tomura, M. Kokubun, T. Saginoya, Y. Mizuno, and Y. Kikuchi



## ABSTRACT

**BACKGROUND AND PURPOSE:** In patients with metastatic brain tumors after gamma knife radiosurgery, the superiority of PET using  $^{11}\text{C}$ -methionine for differentiating radiation necrosis and recurrent tumors has been accepted. To evaluate the feasibility of MR permeability imaging, it was compared with PET using  $^{11}\text{C}$ -methionine, FDG-PET, and DWI for differentiating radiation necrosis from recurrent tumors.

**MATERIALS AND METHODS:** The study analyzed 18 lesions from 15 patients with metastatic brain tumors who underwent gamma knife radiosurgery. Ten lesions were identified as recurrent tumors by an operation. In MR permeability imaging, the transfer constant between intra- and extravascular extracellular spaces (/minute), extravascular extracellular space, the transfer constant from the extravascular extracellular space to plasma (/minute), the initial area under the signal intensity–time curve, contrast-enhancement ratio, bolus arrival time (seconds), maximum slope of increase (millimole/second), and fractional plasma volume were calculated. ADC was also acquired. On both PET using  $^{11}\text{C}$ -methionine and FDG-PET, the ratio of the maximum standard uptake value of the lesion divided by the maximum standard uptake value of the symmetric site in the contralateral cerebral hemisphere was measured ( $^{11}\text{C}$ -methionine ratio and FDG ratio, respectively). The receiver operating characteristic curve was used for analysis.

**RESULTS:** The area under the receiver operating characteristic curve for differentiating radiation necrosis from recurrent tumors was the best for the  $^{11}\text{C}$ -methionine ratio (0.90) followed by the contrast-enhancement ratio (0.81), maximum slope of increase (millimole/second) (0.80), the initial area under the signal intensity–time curve (0.78), fractional plasma volume (0.76), bolus arrival time (seconds) (0.76), the transfer constant between intra- and extravascular extracellular spaces (/minute) (0.74), extravascular extracellular space (0.68), minimum ADC (0.60), the transfer constant from the extravascular extracellular space to plasma (/minute) (0.55), and the FDG-ratio (0.53). A significant difference in the  $^{11}\text{C}$ -methionine ratio ( $P < .01$ ), contrast-enhancement ratio ( $P < .01$ ), maximum slope of increase (millimole/second) ( $P < .05$ ), and the initial area under the signal intensity–time curve ( $P < .05$ ) was evident between radiation necrosis and recurrent tumor.

**CONCLUSIONS:** The present study suggests that PET using  $^{11}\text{C}$ -methionine may be superior to MR permeability imaging, ADC, and FDG-PET for differentiating radiation necrosis from recurrent tumors after gamma knife radiosurgery for metastatic brain tumors.

**ABBREVIATIONS:** BAT = bolus arrival time (seconds); CER = contrast-enhancement ratio; fPV = fractional plasma volume; GK = gamma knife radiosurgery; IAUGC = the initial area under the signal intensity–time curve;  $K_{ep}$  = the transfer constant from the extravascular extracellular space to plasma (/minute);  $K^{trans}$  = the transfer constant between intra- and extravascular extracellular spaces (/minute); MaxSlope = maximum slope of increase (millimole/second); MET =  $^{11}\text{C}$ -methionine;  $V_e$  = the extravascular extracellular space

Stereotactic radiosurgery such as gamma knife radiosurgery (GK) and CyberKnife (Accuray, Sunnyvale, California) is an effective method for treating intracranial neoplasms.<sup>1,2</sup> For met-

astatic tumors of the brain, stereotactic radiosurgery has generally been the main tool used in therapeutic regimens.<sup>3,4</sup> Although stereotactic radiosurgery is an effective treatment method, it has a risk of radiation necrosis. Radiation necrosis after stereotactic radiosurgery for metastatic tumors of the brain is more common than previously reported.<sup>5,6</sup> It generally occurs 3–12 months after therapy<sup>7</sup> and often resembles recurrent tumors on conventional imaging techniques, such as MR imaging,<sup>8–11</sup> CT,<sup>12</sup> and SPECT.<sup>13</sup> Differentiating radiation necrosis and recurrent tumor is extremely important because of the different treatment implications. Histologic examination from a biopsy or resection may aid

Received October 17, 2016; accepted after revision April 4, 2017.

From the Departments of Neuroradiology, Radiology, and Neurosurgery, Southern Tohoku Research Institute for Neuroscience, Southern Tohoku General Hospital, Koriyama City, Fukushima, Japan.

Please address correspondence to Noriaki Tomura, MD, 7-115, Yatsuyamada, Koriyama City, Fukushima, 963-8563, Japan; e-mail: tomura@bloom.ocn.ne.jp

<http://dx.doi.org/10.3174/ajnr.A5252>

**Table 1: Patient summary**

Case No.	Age (yr)	Sex	Disease	Location of Tumor	Duration (mo) from GK to MRP	Necrosis/Recurrence	Radiation Dose <sup>a</sup> by GK
1	45	F	Lung ca.	Rt. temporal	24	Necrosis	90%, 22 Gy
2	64	M	Lung ca.	Lt. cerebellum	18	Recurrence	54%, 22 Gy
3	70	F	Lung ca.	Rt. cerebellum	25	Necrosis	70%, 21 Gy
4	75	M	Lung ca.	Lt. occipital	25	Necrosis	60%, 22 Gy
5	78	M	Lung ca.	Lt. frontal	4	Necrosis	60%, 22 Gy
6	64	M	Lung ca.	Lt. occipital	14	Necrosis	55%, 20 Gy
7	56	F	Renal cell ca.	Lt. frontal	34	Necrosis	58%, 20 Gy
8	68	M	Breast ca.	Rt. cerebellum	18	Recurrence	55%, 20 Gy
9	76	M	Breast ca.	Midbrain	35	Necrosis	57%, 20 Gy
10	42	F	Lung ca.	Rt. parietal	52	Necrosis	55%, 21 Gy
11	75	F	Lung ca.	Lt. occipital	30	Recurrence	65%, 22 Gy
12	60	M	Breast ca.	Rt. frontal	52	Recurrence	80%, 20 Gy
13	63	M	Lung ca.	Rt. temporal	6	Recurrence	55%, 22 Gy
14	54	F	Lung ca.	Lt. frontal	14	Recurrence	52%, 20 Gy
15	59	M	Lung ca.	Lt. frontal	22	Recurrence	52%, 20 Gy
16	63	M	Lung ca.	Lt. frontal	14	Recurrence	53%, 20 Gy
17	54	F	Ovarian ca.	Rt. parietal	7	Recurrence	54%, 32 Gy
18	59	M	Lung ca.	Lt. frontal	16	Recurrence	50%, 18 Gy

**Note:**—Rt indicates right; Lt, left; ca., carcinoma; MRP, MR permeability imaging.

<sup>a</sup> A prescription dose of 18–32 Gy at 50%–90% isodose.

in differentiating these 2 events. However, a noninvasive method is needed for diagnosing whether a contrast-enhanced lesion with surrounding edema on conventional MR imaging is radiation necrosis or a recurrent tumor.

Advanced MR imaging techniques including MR spectroscopy,<sup>14</sup> DWI,<sup>15</sup> and DTI<sup>16</sup> have been used for differentiation of radiation necrosis and recurrent tumors. The CTP technique has also been reported as promising in this field.<sup>17</sup> CTP has the advantage of using widely available CT scanners, though x-ray exposure and administration of ionizing contrast material limit the clinical use. In radionuclide studies, SPECT with <sup>201</sup>Tl-chloride,<sup>18</sup> technetium Tc99m-sestamibi,<sup>19</sup> <sup>123</sup>I-alfa-methyl-L-tyrosine,<sup>20</sup> O-(2-[<sup>18</sup>F]-fluoroethyl)-L-tyrosine (FET-PET),<sup>21,22</sup> 6-[<sup>18</sup>F]-fluoro-L-dopa (FDOPA),<sup>23</sup> and FDG-PET<sup>24–26</sup> have been reported to differentiate between radiation necrosis and recurrent tumors. Compared with those studies, the superiority of PET with <sup>11</sup>C-methionine (MET) for differentiating radiation necrosis and recurrent tumors has been accepted because of the high sensitivity and specificity.<sup>27–31</sup> However, MET-PET is not widely available. Dynamic contrast-enhanced MR imaging with a contrast agent has been used to characterize brain tumors<sup>32,33</sup> and stroke.<sup>34</sup>

MR permeability imaging with dynamic contrast-enhanced–MR imaging based on the Tofts model<sup>35</sup> has recently been developed and used for evaluating cerebrovascular diseases,<sup>36</sup> brain tumors,<sup>37–39</sup> nasopharyngeal carcinomas,<sup>40,41</sup> rectal carcinomas,<sup>42</sup> and prostate carcinomas.<sup>43</sup> The endothelial permeability of vessels in brain tumors can be quantitatively acquired with MR permeability imaging. The vascular microenvironment in tumors can be measured by parameters such as influx transfer constant, reverse transfer constant, and the extravascular extracellular space.<sup>44</sup> These parameters may reflect tissue characteristics including vascular density, a damaged blood-brain barrier, vascularity, and neoangiogenesis.<sup>44</sup> If the feasibility of MR permeability imaging for differentiating radiation necrosis and recurrent tumors could be demonstrated, this technique may contribute to the management of patients after stereotactic radiosurgery and conventional radiation therapy because MR permeability imaging

is widely available. To evaluate the feasibility of MR permeability imaging in the present study, we compared it with MET-PET, FDG-PET, and DWI for differentiating radiation necrosis from recurrent tumor after GK in patients with metastatic brain tumors.

## MATERIALS AND METHODS

We analyzed 18 lesions from 15 patients (9 men, 6 women; mean age, 63.3 ± 10.9 years) with metastatic brain tumors who underwent GK (Table 1). Each patient provided written informed consent before PET/CT. This retrospective study was approved by the institutional review board at our hospital. Ten lesions were identified as recurrent tumors by an operation after both MR permeability imaging and MET-PET. In these 10 recurrent tumors, MR permeability imaging was performed 6–52 months (average, 19.7 months) after GK. Eight lesions were diagnosed as radiation necrosis because of a lack of change or a decrease in size >4 months after radiosurgery. In these 8 lesions, MR permeability imaging was performed 4–52 months (average, 26.6 months) after GK. MET-PET was performed immediately before FDG-PET on the same day. The protocol has been previously reported.<sup>45</sup> After CT, MET was injected, and MET-PET was performed 20 minutes later. FDG was injected 60 minutes after MET-PET. MR permeability imaging and DWI were performed within 1 week before or after PET. Dynamic contrast-enhanced MR imaging was acquired by using gadolinium contrast medium. A 3D fast-spoiled gradient-recalled acquisition in the steady-state was applied for dynamic contrast-enhanced MR imaging with a bolus injection of contrast material (total dose, 0.2 mL/kg body weight; dose rate, 3.0 mL/s). Parameters of dynamic contrast-enhanced MR imaging were as follows: TR/TE = minimum (5.7 ms)/minimum (1.3 ms), flip angle = 20°, FOV = 24 cm, matrix = 256 × 160, NEX = 1, number of sections = 16/phase, number of phases = 32, acquisition time = 3 minutes 59 seconds. Dynamic contrast-enhanced data were transferred to a workstation (Advantage Workstation, Version 4.6; GE Healthcare, Milwaukee, Wisconsin) and analyzed with commercially available software (GenIQ; GE Healthcare)

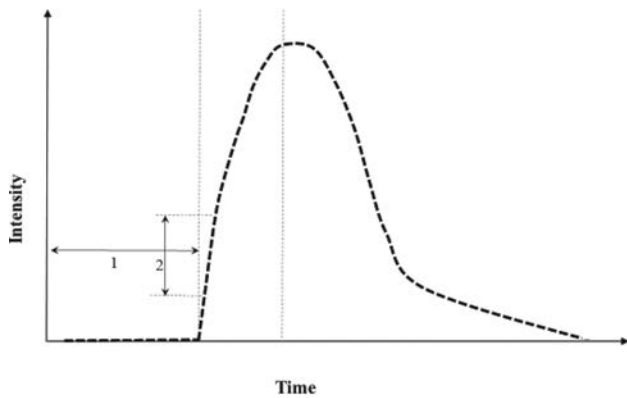


**FIG 1.** Schema of the time-intensity curve after administration of contrast material: 1) bolus arrival time, 2) maximum slope of increase.

with the general kinetic model based on a 2-compartment model and 3 parameters (vascular space, extravascular extracellular space, and fractional plasma volume).

The transfer constant between intra- and extravascular extracellular spaces ( $K^{\text{trans}}$ ) (/minute), the extravascular extracellular space ( $V_e$ ), the transfer constant from the extravascular extracellular space to plasma ( $K_{ep}$ ) (/minute), the initial area under the signal intensity–time curve (IAUGC), the contrast-enhancement ratio (CER), the bolus arrival time (BAT) (seconds), the maximum slope of increase (MaxSlope) (millimole/second), and fractional plasma volume (fPV) were calculated after setting an ROI on the solid portion of the lesion. CER was defined as [(maximum signal intensity [SI] – SI at Baseline) / SI at Baseline]. BAT and MaxSlope are shown in Fig 1. ADC ( $10^{-3}$  mm/s) was also acquired from DWI. On both MET-PET and FDG-PET, the ratio of the maximum standard uptake value of the lesion divided by the maximum standard uptake value of the symmetric site in the contralateral cerebral hemisphere was measured (MET-ratio and FDG-ratio, respectively). For measurement of each data point, ROIs were manually set on the fused images by using the Advantage Workstation. A single ROI was set in a lesion. On the workstation, when an ROI was set on a contrast-enhanced T1WI, its ROI could be set simultaneously in MR permeability images or PET images on the workstation. The ROI was set in the solid portion of the lesion by a neuroradiologist with >35 years of experience.

Receiver operating characteristic analysis was performed to evaluate the utility of those parameters for differentiating radiation necrosis from recurrent tumors. The area under the curve was evaluated for MET-PET, FDG-PET, DWI, and each parameter of MR permeability imaging. Each cutoff value was also acquired by receiver operating characteristic analysis. Each mean value was compared between radiation necrosis and recurrent tumors by using the *t* test. Statistical analysis was performed with Excel Statistics 2015, Version 1.02 (Social Survey Research Information, Tokyo, Japan).

## RESULTS

The minimum, average, and maximum values of each MR imaging parameter were obtained. After the minimum, average, and maximum values were evaluated by receiver operating characteristic analysis, the averages of  $K^{\text{trans}}$ ,  $V_e$ ,  $K_{ep}$ , IAUGC, CER, BAT, MaxSlope, and fPV were better than the minimum and maximum values for each. In ADC, the minimum value was better than the

average and maximum values. Figure 2 shows the receiver operating characteristic curve for each parameter. The area under the curve for differentiating radiation necrosis from recurrent tumors was best for the MET ratio (0.90) followed by CER (0.81), MaxSlope (0.80), IAUGC (0.78), fPV (0.76), BAT (0.76),  $K^{\text{trans}}$  (0.74),  $V_e$  (0.68), minimum ADC (0.60),  $K_{ep}$  (0.55), and the FDG ratio (0.53) (Table 2). For the MET ratio ( $P < .01$ ), CER ( $P < .01$ ), MaxSlope ( $P < .05$ ), and IAUGC ( $P < .05$ ), the area under the curve value was significantly better ( $\chi^2$  test) than the area under the curve of 0.5. The cutoff value for the best combination of sensitivity and specificity was 1.42 with the MET ratio, 0.61 with CER, 0.01 with MaxSlope, 0.2 with IAUGC, 0.02 with fPV, 44.0 with BAT, 0.05 with  $K^{\text{trans}}$ , 0.27 with  $V_e$ , 0.73 with the minimum ADC, 0.32 with  $K_{ep}$ , and 0.97 with the FDG ratio (Table 2). With the cutoff value, the sensitivity and specificity were 0.90 and 0.75 for the MET ratio, 0.80 and 0.88 for CER, 0.90 and 0.50 for MaxSlope, 0.60 and 1.0 for IAUGC, 0.50 and 0.88 for fPV, 0.70 and 0.75 for BAT, 0.70 and 0.67 for  $K^{\text{trans}}$ , 0.60 and 0.63 for  $V_e$ , 0.60 and 0.25 for minimum ADC, 0.80 and 0.05 for  $K_{ep}$ , and 0.40 and 0.50 for the FDG ratio, respectively (Table 2). We observed a significant difference for the MET ratio ( $P < .01$ ), CER ( $P < .01$ ), MaxSlope ( $P < .05$ ), and IAUGC ( $P < .05$ ) between radiation necrosis (Fig 3) and a recurrent tumor (Fig 4 and Table 3). The Welch *t* test was applied due to the unequal sample size and variances between the 2 groups.

## DISCUSSION

The present study showed that MET-PET was the most promising imaging technique for differentiating radiation necrosis and recurrent metastatic tumors after GK compared with MR permeability imaging, DWI, and FDG-PET. In our literature review, we did not find any previous reports comparing MR permeability imaging with nuclear medicine imaging. For distinguishing treatment-induced necrosis from a recurrent tumor in the brain, the superiority of MET-PET regarding the sensitivity and specificity is widely accepted.<sup>27-31</sup> In the present study, both MET-PET and FDG-PET were undertaken on a single day. This technique performing both PETs on a single day has previously been reported.<sup>45-50</sup> The interaction between the 2 tracers is considered minimal.

In tumors, MET preferably accumulates due to the high density and activity of amino acid transporters in tumors.<sup>27-31</sup> In recurrent tumors, MET can accumulate due to active transport and cell proliferation.<sup>27-31</sup> On the other hand, in radiation necrosis, accumulation is presumably due to passive diffusion via blood-brain barrier damage.<sup>27-31</sup> The different mechanisms of MET accumulation in the 2 pathologic processes could be a means of distinguishing recurrent tumors from radiation necrosis. MET-PET has preferable sensitivity and specificity for differentiation; however, this technique is not widely available for clinical use. Recently, the usefulness of FET-PET and FDOPA-PET has been reported for differentiating recurrent brain metastatic tumors and radiation injury.<sup>21-23</sup> Although high rates of sensitivity and specificity for these techniques have been demonstrated, use of these methods in patients with brain metastases is limited. Further studies regarding their contribution to the management of patients with brain metastases are required.

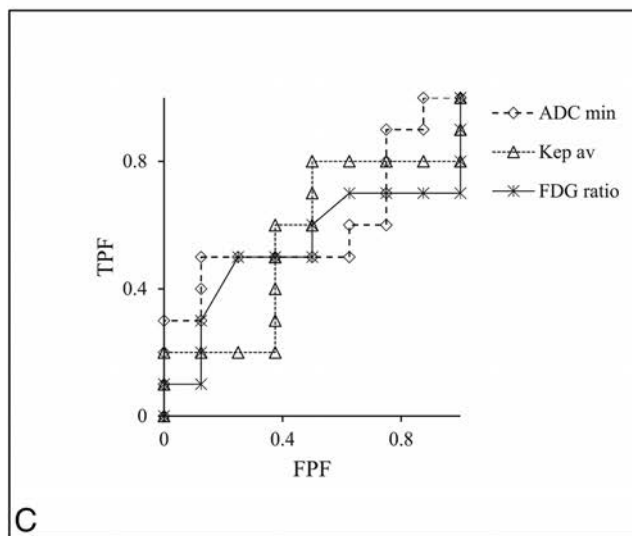
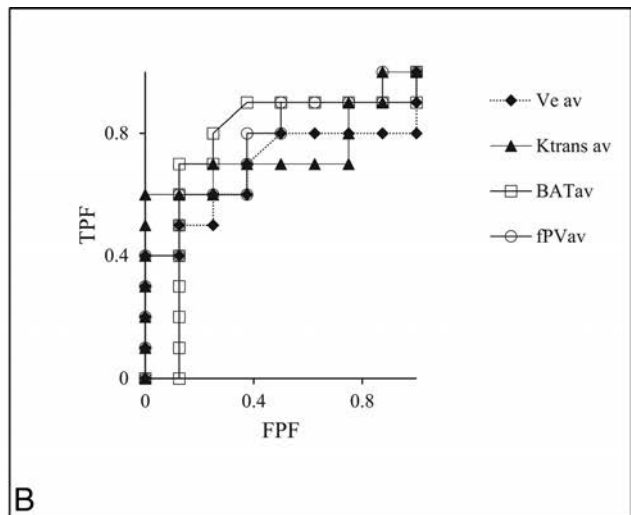
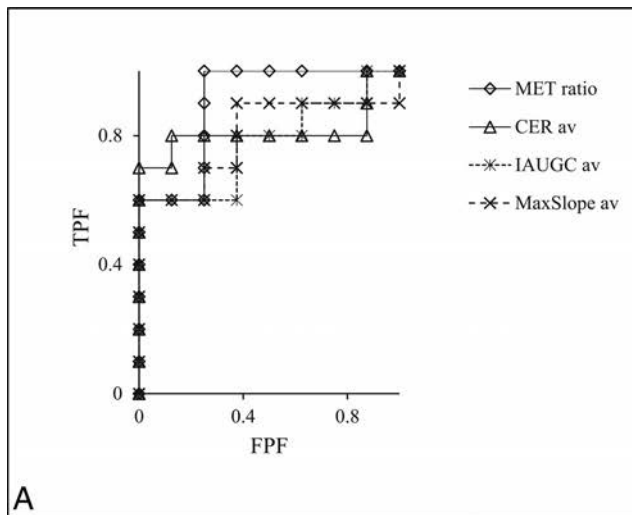


**FIG 2.** Receiver operating characteristic curve of each parameter. A, Receiver operating characteristic curve for the  $^{11}\text{C}$ -methionine ratio, contrast-enhanced ratio, the initial area under the curve of the MET ratio, CER, IAUGC, and MaxSlope. The area under the curve of the MET ratio, CER, IAUGC, and MaxSlope = 0.90, 0.81, 0.80, and 0.78, respectively; B, Receiver operating characteristic curve for the extravascular extracellular space, the transfer constant between intra- and extravascular extracellular spaces, BAT, and fractional plasma volume. The area under the curve of fPV, BAT,  $K^{\text{trans}}$ , and  $V_e$  = 0.76, 0.76, 0.74, and 0.68, respectively; C, The receiver operating characteristic curve for a minimum apparent diffusion coefficient, the transfer constant from the extravascular extracellular space to plasma, and FDG ratio. The area under the curve of minimum ADC, Kep, and FDG ratio = 0.60, 0.55, and 0.53, respectively.

**Table 2: Results of each parameter by ROC analysis**

	AUC ( $\chi^2$ test Compared with AUC = 0.5)	AUC, 95% CI	Cutoff Value	Sensitivity (95% CI)	Specificity (95% CI)
MET ratio	0.90 ( $P < .01$ )	0.75–1.05	1.42	0.90 ( $\pm 0.026$ )	0.75 ( $\pm 0.082$ )
CER av	0.81 ( $P < .01$ )	0.58–1.04	0.61	0.80 ( $\pm 0.035$ )	0.88 ( $\pm 0.023$ )
MaxSlope av	0.80 ( $P < .05$ )	0.58–1.02	0.01	0.90 ( $\pm 0.014$ )	0.50 ( $\pm 0.098$ )
IAUGC av	0.78 ( $P < .05$ )	0.55–1.00	0.2	0.60 ( $\pm 0.078$ )	1.0 (0)
fPV av	0.76	0.53–0.99	0.02	0.50 ( $\pm 0.082$ )	0.88 ( $\pm 0.017$ )
BAT av	0.76	0.48–1.03	44.0	0.70 ( $\pm 0.046$ )	0.75 ( $\pm 0.041$ )
$K^{\text{trans}}_{\text{av}}$	0.74	0.49–0.99	0.05	0.70 ( $\pm 0.046$ )	0.67 ( $\pm 0.041$ )
$V_e$ av	0.68	0.41–0.95	0.27	0.60 ( $\pm 0.052$ )	0.63 ( $\pm 0.051$ )
ADC min	0.60	0.32–0.88	0.73	0.60 ( $\pm 0.039$ )	0.25 ( $\pm 0.061$ )
Kep av	0.55	0.26–0.84	0.32	0.80 ( $\pm 0.026$ )	0.50 ( $\pm 0.082$ )
FDG ratio	0.53	0.23–0.82	0.97	0.40 ( $\pm 0.059$ )	0.50 ( $\pm 0.049$ )

**Note:**—AUC indicates area under the curve; av, average; min, minimum; ROC, receiver operating characteristic.

MR permeability imaging in the present study was performed with dynamic contrast-enhanced MR imaging. DSC MR imaging<sup>51</sup> has also been used for MR perfusion. However, DSC MR imaging has a limitation of susceptibility artifacts due to hemorrhage, calcification, and surgical clips. MR permeability imaging in the present study yielded many parameters, but interpretation of the results of those parameters remains somewhat difficult. Tissue enhancement following administration of a contrast agent

generally depends on various factors such as vessel density, vascular permeability, blood flow, and interstitial pressure.<sup>44,52,53</sup> Although qualitative visual evaluation of the images is possible, quantitative data could improve the results of analysis. The application package for MR permeability used in the present study is commercially available and was an easy tool to use for imaging and quantification of the data. In previous reports<sup>44,52,53</sup> with a technique similar to that in the present study,  $K^{\text{trans}}$ , Kep,  $V_e$ , and IAUGC were frequently evaluated. In the present study, other parameters including CER, MaxSlope, fPV, and BAT were also evaluated. CER, a relatively simple type of data, was the best for differentiating radiation necrosis and recurrent tumors. MaxSlope, which mainly reflects blood flow, followed CER. Increased vascularity and neovascularity could increase MaxSlope in recurrent tumors. IAUGC, which is nearly equal to blood volume, followed MaxSlope. BAT in recurrent tumors was shorter than in radiation necrosis. BAT can be short due to increased vascularity and/or

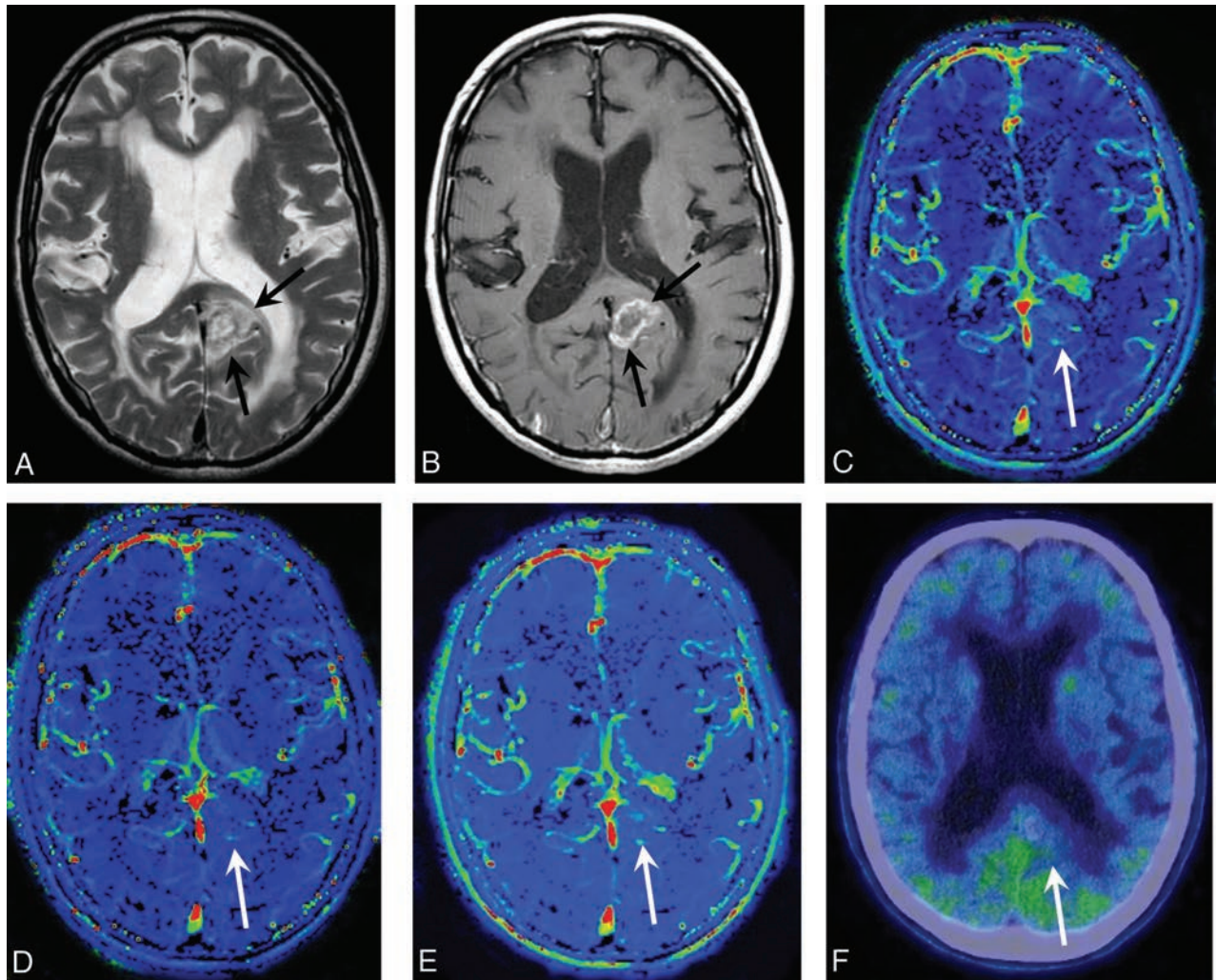


**FIG 3.** A 78-year-old man with lung cancer. He underwent GK for a metastatic tumor in the isthmus of the left cingulate gyrus. T2WI (A) reveals a hyperintense area (arrows) with mild swelling in the isthmus of the left cingulate gyrus, and contrast-enhanced T1WI (B) shows ringlike contrast enhancement of the lesion (arrows) 12 months after GK. MR permeability images (C, CER; D, MaxSlope; E, IAUGC) do not show the increased value of each parameter in the lesion (white arrows). MET-PET/CT (F) also does not show any increased activity of MET in the lesion (white arrow). It was presumably diagnosed as radiation necrosis.

arteriovenous shunting in the recurrent tumor. When MET-PET is not available, MR permeability imaging including these parameters could possibly replace MET-PET.

As previously reported,<sup>44,52</sup> IAUGC in recurrent tumors was higher than in radiation necrosis. Although vascular dilation may occur in radiation necrosis, increased neovascularity with dilated vessels can cause increased IAUGC in recurrent tumors.  $K^{trans}$  has been reported as a feasible parameter for grading gliomas<sup>38,39</sup> and detecting tumors in the prostate.<sup>43</sup> The present study showed that CER, MaxSlope, and IAUGC were superior to  $K^{trans}$  for differentiating radiation necrosis and recurrent tumors. This finding may be due to increased vascular permeability in recurrent tumors and in radiation necrosis. In recurrent tumors, newly proliferative tumor vessels in tissue with a damaged blood-brain barrier could play a role in increasing those parameters. Although we found no statistical differences, the mean value of  $K^{trans}$ , Kep, and Ve in recurrent tumors was higher than that in radiation necrosis. This finding also indicated increased permeability in recurrent tumors.

ADC is lower in malignant tumors than in benign tumors in

the brain and in other areas. Increased cellularity in malignant tumors causes a decrease in ADC.<sup>54</sup> In the present study, ADC was inferior to most MR permeability imaging parameters. The mean value of minimum ADC in recurrent tumors was not lower than that in radiation necrosis. Some blood components may influence the ADC value in radiation necrosis. Although cellularity was not histologically evaluated, cellularity in recurrent tumors is not necessarily high. Wang et al.<sup>16</sup> also reported that radiation necrosis has significantly lower ADC than malignant gliomas in rats with DTI MR imaging. In their report, the necrotic central zone in radiation necrosis had significantly lower ADC, parallel diffusivity, and perpendicular diffusivity than in the peripheral zone.

The feasibility of FDG-PET for detecting neoplasms and evaluating the treatment response in various organs is well-known,<sup>55,56</sup> and FDG is the most widely available tracer. The usefulness of FDG-PET for diagnosing radiation necrosis in the brain has been previously reported in the literature.<sup>24-26</sup> However, the inferiority of FDG-PET was evident compared with each parameter of MR permeability imaging used in the present study. The

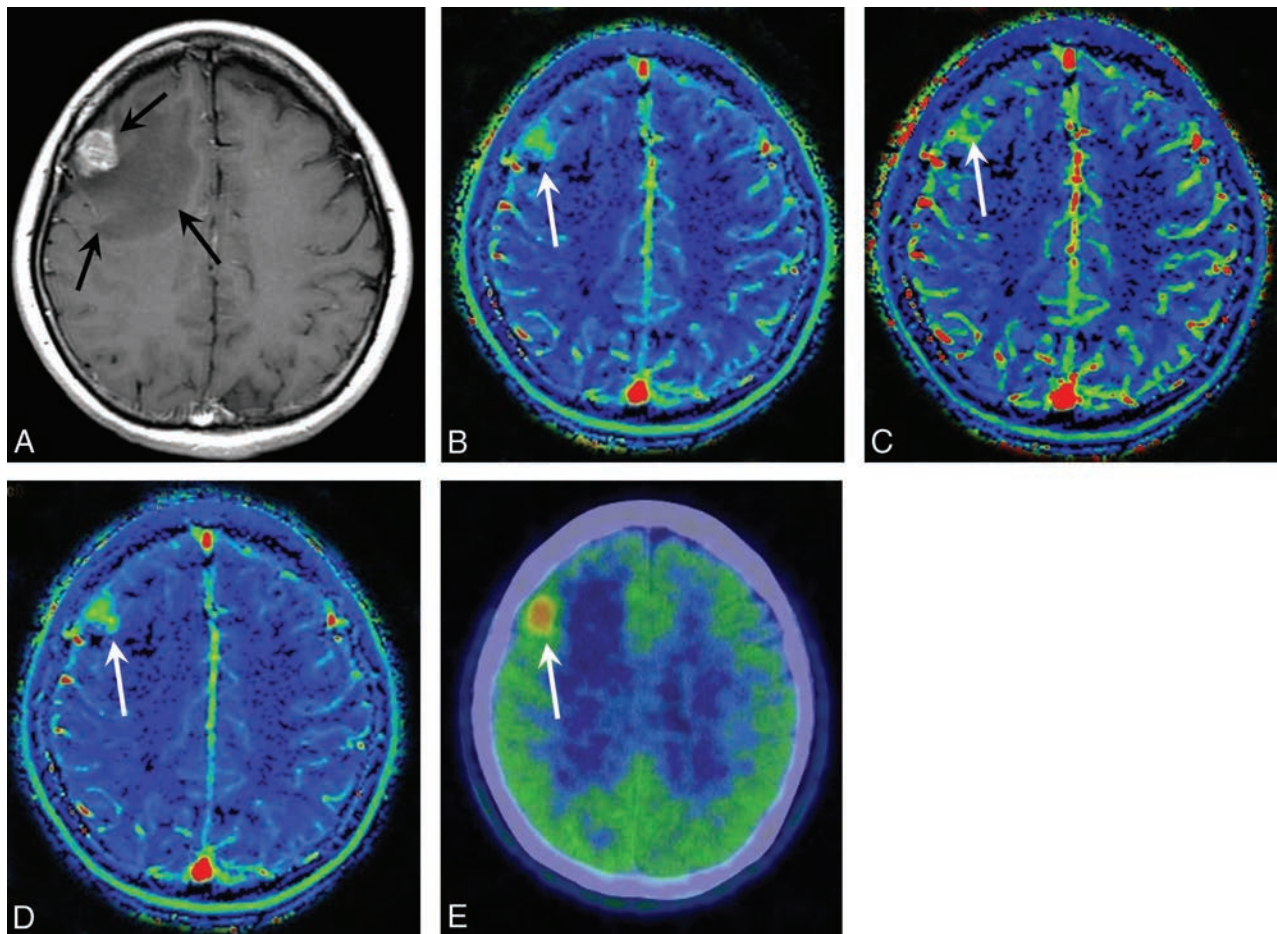


**FIG 4.** A 42-year-old woman with breast cancer. She underwent GK for a metastatic tumor in the right frontal lobe. Contrast-enhanced T1WI (A) reveals a contrast-enhanced lesion with surrounding edema in the right frontal lobe 59 months after GK (arrows). MR permeability images (B, CER; C, MaxSlope; D, IAUGC) show increased value of each parameter of the lesion (white arrows). MET-PET/CT (E) also shows an increased activity of MET in the lesion (white arrow). A recurrent tumor was demonstrated by an operation.

**Table 3: Mean value of each parameter in radiation necrosis and recurrence**

	Radiation Necrosis (mean ± SD)	Recurrence (mean ± SD)
MET ratio	1.23 ± 0.21	2.22 ± 0.91 <sup>a</sup>
CER av	0.49 ± 0.11	1.09 ± 0.56 <sup>a</sup>
MaxSlope av	0.01 ± 0.002	0.03 ± 0.018 <sup>b</sup>
IAUGC av	0.07 ± 0.04	0.40 ± 0.52 <sup>b</sup>
fPV av	0.01 ± 0.01	0.10 ± 0.17
BAT av	45.32 ± 5.05	41.30 ± 5.23
$K^{trans}$ av	0.05 ± 0.02	0.28 ± 0.38
Ve av	0.23 ± 0.11	0.43 ± 0.30
ADC min	0.59 ± 0.20	0.71 ± 0.31
Kep av	0.48 ± 0.25	0.54 ± 0.38
FDG ratio	0.91 ± 0.17	0.97 ± 0.20

<sup>a</sup> Statistical difference,  $P < .01$ .

<sup>b</sup> Statistical difference,  $P < .05$ .

present study indicated that the usefulness of FDG-PET was clearly questionable for differentiating recurrent metastatic tumors of the brain and radiation necrosis. MET is not as readily available as FDG. In Japan, FDG can be used in hospitals without a cyclotron because FDG can be commercially delivered from a medical company. The insurance system covers patients who undergo FDG-PET. The short half-life of  $^{11}\text{C}$  is problematic for MET availability because MET use requires a cyclotron in the hospital.

After these difficulties regarding the use of MET are resolved, MET-PET may become more widely available to more patients in the near future.

The present study has several major limitations. The number of subjects was small. Although recurrent tumors were proved by histopathology, radiation necrosis was presumably diagnosed only by our criteria. In a clinical study such as ours, obtaining histologic confirmation is often difficult. The term “stable disease” may be more suitable<sup>51</sup> than “radiation necrosis.” Clinically, radiation necrosis that is increasing in size, which was not observed in the present study, is sometimes experienced. The duration between MR permeability imaging and GK was variable (4–52 months) in each case. This wide range of duration was due to the interval of follow-up MR imaging studies after GK. The follow-up intervals were determined by neurosurgeons who performed GK and managed patients. The intervals of follow-up MR imaging were shorter in patients with recurrent tumors than in those with radiation necrosis. Neurosurgeons requested shorter intervals for follow-up MR imaging in patients with suspected recurrent tumors. ROIs were manually set to measure each parameter. Partial volume averaging within ROIs may influence the value of each parameter. Especially in the region near large vessels, CER and IAUGC may be affected by the partial volume effect.

Manual setting results in interobserver and intraobserver differences because ROI setting depends on each researcher. MR permeability imaging including many parameters depends on the applied application. The results may be a little different with other applications.

## CONCLUSIONS

The present study suggests that MET-PET may be superior to MR permeability imaging, ADC, and FDG-PET for differentiating radiation necrosis and recurrent tumors after GK for metastatic brain tumors. FDG-PET is questionable for differentiating them. Although MR permeability imaging is not a feasible alternative to MET-PET, MR permeability imaging, especially including CER, MaxSlope, and IAUGC, is feasible for differentiating radiation necrosis and recurrent tumors.

## REFERENCES

1. Tsao MN, Mehta MP, Whelan TJ, et al. **The American Society for Therapeutic Radiology and Oncology (ASTRO) evidence-based review of the role radiosurgery for malignant glioma.** *Int J Radiol Oncol Biol Phys* 2005;63:47–55 CrossRef Medline
2. Wowra B, Muacevic A, Tonn JC. **Cyber knife radiosurgery for brain metastasis.** *Prog Neurol Surg* 2012;25:201–09 CrossRef Medline
3. Mehta MP, Tsao MN, Whelan TJ, et al. **The American Society for Therapeutic Radiology and Oncology (ASTRO) evidence-based review of the role of radiosurgery for brain metastases.** *Int J Radiol Oncol Biol Phys* 2005;63:37–46 CrossRef Medline
4. Mohammadi AM, Schroeder JL, Angelov L, et al. **Impact of the radiosurgery prescription dose on the local control of the small (2 cm or smaller) brain metastases.** *J Neurosurg* 2017;126:735–743 CrossRef Medline
5. Leeman JE, Clump DA, Flickinger JC, et al. **Extent of perilesional edema differentiates radionecrosis from tumor recurrence following stereotactic radiosurgery for brain metastases.** *Neuro Oncol* 2013;15:1732–38 CrossRef Medline
6. Fabiano AJ, Qiu J. **Post-stereotactic radiosurgery brain metastases: a review.** *J Neurosurg Sci* 2015;59:157–67 Medline
7. Chang SD, Lee E, Sakamoto GT, et al. **Stereotactic radiosurgery in patients with multiple brain metastases.** *Neurosurg Focus* 2000;9:e3 Medline
8. Shah R, Vattoth S, Jacob R, et al. **Radiation necrosis in the brain: imaging features and differentiation from tumor recurrence.** *Radiographics* 2012;32:1343–59 CrossRef Medline
9. Verma N, Cowperthwaite MC, Burnett MG, et al. **Differentiating tumor recurrence from treatment necrosis: a review of neuro-oncologic imaging strategies.** *Neuro Oncol* 2013;15:515–34 CrossRef Medline
10. Stockham AL, Tievsky AL, Koyfman SA, et al. **Conventional MRI does not reliably distinguish radiation necrosis from tumor recurrence after stereotactic radiosurgery.** *J Neurooncol* 2012;109:149–58 CrossRef Medline
11. Ou SH, Klempner SJ, Azada MC, et al. **Radiation necrosis presenting as pseudoprogression (PsP) during alectinib treatment of previously radiated brain metastases in ALK-positive NSCLC: implications for disease assessment and management.** *Lung Cancer* 2015;88:355–59 CrossRef Medline
12. Valk PE, Dillon WP. **Radiation injury of the brain.** *AJNR Am J Neuroradiol* 1991;12:45–62 Medline
13. Chemov MF, Ono Y, Abe K, et al. **Differentiation of tumor progression and radiation-induced effects after intracranial radiosurgery.** *Acta Neurochir Suppl* 2013;116:193–210 CrossRef Medline
14. Chemov MF, Hayashi M, Izawa M, et al. **Multivoxel proton differentiation of radiation-induced necrosis and tumor recurrence after gamma knife radiosurgery for brain metastases.** *Brain Tumor Pathol* 2006;23:19–27 CrossRef Medline
15. Asao C, Korogi Y, Kitajima M, et al. **Diffusion-weighted imaging of radiation-induced brain injury for differentiation from tumor recurrence.** *AJNR Am J Neuroradiol* 2005;26:1455–60 Medline
16. Wang S, Chen Y, Lal B, et al. **Evaluation of radiation necrosis and malignant glioma in rat models using diffusion tensor imaging.** *J Neurooncol* 2012;107:51–60 CrossRef Medline
17. Jain R, Narang J, Schultz L, et al. **Permeability estimates in histopathology-proved treatment-induced necrosis using perfusion CT: can these add to other perfusion parameters in differentiating from recurrent/progressive tumors?** *AJNR Am J Neuroradiol* 2011;32:658–63 CrossRef Medline
18. Gómez-Río M, Martínez Del Valle Torres D, Rodríguez-Fernández A, et al. **(201)TI-SPECT in low-grade gliomas: diagnostic accuracy in differential diagnosis between tumour recurrence and radionecrosis.** *Eur J Nucl Med Mol Imaging* 2004;31:1237–43 Medline
19. Le Jeune FP, Dubois F, Blonde S, et al. **Sestamibi technetium-99m brain single-photon emission computed tomography to identify recurrent glioma in adults: 201 studies.** *J Neurooncol* 2006;77:177–83 CrossRef Medline
20. Samnick S1, Bader JB, Hellwig D, et al. **Clinical value of iodine-123-alpha-methyl-L-tyrosine single-photon emission tomography in the differential diagnosis of recurrent brain tumor in patients pretreated for glioma at follow-up.** *J Clin Oncol* 2002;20:396–404 Medline
21. Galldiks N, Stoffels G, Filss C, et al. **Role of O-(2-(18)F-fluoroethyl)-L-tyrosine PET for differentiation of local recurrent brain metastasis from radiation necrosis.** *J Nucl Med* 2012;53:1367–74 CrossRef Medline
22. Ceccon G, Lohmann P, Stoffels G, et al. **Dynamic O-(2-18F-fluoroethyl)-L-tyrosine positron emission tomography differentiates brain metastasis recurrence from radiation injury after radiotherapy.** *Neuro Oncol* 2017;19:281–288 CrossRef Medline
23. Lizarraga KJ, Allen-Auerbach M, Czernin J, et al. **(18)F-FDOPA PET for differentiating recurrent or progressive brain metastatic tumors from late or delayed radiation injury after treatment.** *J Nucl Med* 2014;55:30–36 CrossRef Medline
24. Kim EE, Chung SK, Haynie TP, et al. **Differentiation of residual or recurrent tumors from post-treatment changes with F-18 FDG PET.** *Radiographics* 1992;12:269–79 CrossRef Medline
25. Di Chiro G, Oldfield E, Wright DC, et al. **Cerebral necrosis after radiotherapy and/or intraarterial chemotherapy for brain tumors: PET and neuropathologic studies.** *AJR Am J Roentgenol* 1988;150:189–97 CrossRef Medline
26. Mogard J, Kihlström L, Ericson K, et al. **Recurrent tumor vs radiation effects after gamma knife radiosurgery of intracerebral metastases: diagnosis with PET-FDG.** *J Comput Assist Tomogr* 1994;18:177–81 CrossRef Medline
27. Sonoda Y, Kumabe T, Takahashi T, et al. **Clinical usefulness of 11C-MET PET and 201TI-SPECT for differentiation of recurrent glioma from radiation necrosis.** *Neuro Med Chir (Tokyo)* 1998;38:342–47 CrossRef Medline
28. Tsuyuguchi N, Sunada I, Iwai Y, et al. **Methionine positron emission tomography of recurrent metastatic brain tumor and radiation necrosis after stereotactic radiosurgery: is a differential diagnosis possible?** *J Neurosurg* 2003;98:1056–64 CrossRef Medline
29. Tsuyuguchi N, Takami T, Sunada I, et al. **Methionine positron emission tomography for differentiation of recurrent brain tumor and radiation necrosis after stereotactic radiosurgery: in malignant glioma.** *Ann Nucl Med* 2004;18:291–96 CrossRef Medline
30. Takenaka S, Asano Y, Shinoda J, et al. **Comparison of (11)C-methionine, (11)C-choline, and (18)F-fluorodeoxyglucose-PET for distinguishing glioma recurrence from radiation necrosis.** *Neurol Med Chir (Tokyo)* 2014;54:280–89 CrossRef Medline
31. Terakawa Y, Tsuyuguchi N, Iwai Y, et al. **Diagnostic accuracy of 11C-methionine PET for differentiation of recurrent brain tumors from radiation necrosis after radiotherapy.** *J Nucl Med* 2008;49:694–99 CrossRef Medline

32. Barrett T, Brechbiel M, Bernardo M, et al. **MRI of tumor angiogenesis.** *J Magn Reson Imaging* 2007;26:235–49 CrossRef Medline
33. Pauliah M, Saxena V, Haris M, et al. **Improved T(1)-weighted dynamic contrast-enhanced MRI to probe microvascularity and heterogeneity of human glioma.** *Magn Reson Imaging* 2007;25:1292–99 CrossRef Medline
34. Wu S, Thornhill RE, Chen S, et al. **Relative recirculation: a fast, model-free surrogate for the measurement of blood-brain barrier permeability and the prediction of hemorrhagic transformation in acute ischemic stroke.** *Invest Radiol* 2009;44:662–68 CrossRef Medline
35. Tofts PS, Brix G, Buckley DL, et al. **Estimating kinetic parameters from dynamic contrast-enhanced T(1)-weighted MRI of a diffusible tracer: standardized quantities and symbols.** *J Magn Reson Imaging* 1999;10:223–32 Medline
36. Vidarsson L, Thornhill RE, Liu F, et al. **Quantitative permeability magnetic resonance imaging in acute ischemic stroke: how long do we need to scan?** *Magn Reson Imaging* 2009;27:1216–22 CrossRef Medline
37. Yang S, Law M, Zagzag D, et al. **Dynamic contrast-enhanced perfusion MR imaging measurements of endothelial permeability: differentiation between atypical and typical meningiomas.** *AJNR Am J Neuroradiol* 2003;24:1554–59 Medline
38. Cha S, Yang L, Johnson G, et al. **Comparison of microvascular permeability measurements, K(trans), determined with conventional steady-state T1-weighted and first-pass T2\*-weighted MR imaging methods in gliomas and meningiomas.** *AJNR Am J Neuroradiol* 2006;27:409–17 Medline
39. Lee SK, Kim E, Choi H. **Glioma grading: comparison of parameters from dynamic contrast-enhanced (DCE) MRI, apparent diffusion coefficient (ADC), and fractional anisotropy (FA).** *Proc Intl Soc Mag Reson Med* 2011;19:4266
40. Zheng D, Chen Y, Chen Y, et al. **Dynamic contrast-enhanced MRI of nasopharyngeal carcinoma: a preliminary study of the correlations between quantitative parameters and clinical stage.** *J Magn Reson Imaging* 2014;39:940–48 CrossRef Medline
41. Huang B, Wong CS, Whitcher B, et al. **Dynamic contrast-enhanced resonance imaging for characterising nasopharyngeal carcinoma: comparison of semiquantitative and quantitative parameters and correlation with tumour stage.** *Eur Radiol* 2013;23:1495–502 CrossRef Medline
42. Kim YE, Lim JS, Choi J, et al. **Perfusion parameters of dynamic contrast-enhanced magnetic resonance imaging in patients with rectal cancer: correlation with microvascular density and vascular endothelial growth factor expression.** *Korean J Radiol* 2013;14: 878–85 CrossRef Medline
43. Verma S, Turkbey B, Muradyan N, et al. **Overview of dynamic contrast-enhanced MRI in prostate cancer diagnosis and management.** *AJR Am J Roentgenol* 2012;198:1277–88 CrossRef Medline
44. Narang J, Jain R, Arbab AS, et al. **Differentiating treatment-induced necrosis from recurrent/progressive brain tumor using nonmodel-based semiquantitative indices derived from dynamic contrast-enhanced T1-weighted MR perfusion.** *Neuro Oncol* 2011;13:1037–46 CrossRef Medline
45. Tomura N, Ito Y, Matsuoka H, et al. **PET findings of intramedullary tumors of the spinal cord using [18F]FDG and [11C]methionine.** *AJNR Am J Neuroradiol* 2013;34:1278–83 CrossRef Medline
46. Nuñez R, Macapinlac HA, Yeung HWD, et al. **Combined <sup>18</sup>F-FDG and <sup>11</sup>C-methionine PET scans in patients with newly progressive metastatic prostate cancer.** *J Nucl Med* 2002;43:46–55 Medline
47. Pirotte B, Goldman S, Massager N, et al. **Combined use of <sup>18</sup>F-fluorodeoxyglucose and <sup>11</sup>C-methionine in 45 positron emission tomography-guided stereotactic brain biopsies.** *J Neurosurg* 2004;101: 476–83 CrossRef Medline
48. Levivier M, Massager N, Wikler D, et al. **Use of stereotactic PET images in dosimetry planning of radiosurgery for brain tumors: clinical experience and proposed classification.** *J Nucl Med* 2004;45: 1146–54 Medline
49. Pirotte B, Goldman S, Massager N, et al. **Comparison of <sup>18</sup>F-FDG and <sup>11</sup>C-methionine for PET-guided stereotactic brain biopsy of gliomas.** *J Nucl Med* 2004;45:1293–98 Medline
50. Mitumoto T, Kubota K, Sato T, et al. **Validation for performing <sup>11</sup>C-methionine and <sup>18</sup>F-FDG-PET studies on the same day.** *Nucl Med Commun* 2012;33:297–304 CrossRef Medline
51. Barajas RF Jr, Chang JS, Segal MR, et al. **Differentiation of recurrent glioblastoma multiforme from radiation necrosis after external beam radiation therapy with dynamic susceptibility-weighted contrast-enhanced perfusion MR imaging.** *Radiology* 2009;253:486–96 CrossRef Medline
52. Bisdas S, Naegele T, Ritz R, et al. **Distinguishing recurrent high-grade gliomas from radiation injury: a pilot study using dynamic contrast-enhanced MR imaging.** *Acta Radiol* 2011;18:575–83 CrossRef Medline
53. Fatterpekar GM, Galheigo D, Narayana A, et al. **Treatment-related change versus tumor recurrence in high-grade gliomas: a diagnostic conundrum—use of dynamic susceptibility contrast-enhanced (DSC) perfusion MRI.** *AJR Am J Roentgenol* 2012;198:19–26 CrossRef Medline
54. Guo AC, Cummings TJ, Dash RC, et al. **Lymphomas and high-grade astrocytomas: comparison of water diffusibility and histologic characteristics.** *Radiology* 2002;224:177–83 CrossRef Medline
55. Conti PS, Lilien DL, Hawley K, et al. **PET and [<sup>18</sup>F]-FDG in oncology: a clinical update.** *Nucl Med Biol* 1996;23:717–35 CrossRef Medline
56. Hoh CK, Schiepers C, Seltzer MA, et al. **PET in oncology: will it replace the other modalities?** *Semin Nucl Med* 1997;27:94–106 CrossRef Medline

# The Initial Area Under the Curve Derived from Dynamic Contrast-Enhanced MRI Improves Prognosis Prediction in Glioblastoma with Unmethylated *MGMT* Promoter

Y.S. Choi, S.S. Ahn, H.-J. Lee, J.H. Chang, S.-G. Kang, E.H. Kim, S.H. Kim, and S.-K. Lee



## ABSTRACT

**BACKGROUND AND PURPOSE:** Although perfusion and permeability MR parameters have known to have prognostic value, they have reproducibility issues. Our aim was to evaluate whether the initial area under the time-to-signal intensity curve (IAUC) derived from dynamic contrast-enhanced MR imaging can improve prognosis prediction in patients with glioblastoma with known *MGMT* status.

**MATERIALS AND METHODS:** We retrospectively examined 88 patients with glioblastoma who underwent preoperative dynamic contrast-enhanced MR imaging. The means of IAUC values at 30 and 60 seconds (IAUC<sub>30,mean</sub> and IAUC<sub>60,mean</sub>) were extracted from enhancing tumors. The prognostic values of IAUC parameters for overall survival and progression-free survival were assessed with log-rank tests, according to the *MGMT* status. Multivariate overall survival and progression-free survival models before and after adding the IAUC parameters as covariates were explored by net reclassification improvement after receiver operating characteristic analysis for 1.5-year overall survival and 1-year progression-free survival and by random survival forest.

**RESULTS:** High IAUC parameters were associated with worse overall survival and progression-free survival in the unmethylated *MGMT* group, but not in the methylated group. In the unmethylated *MGMT* group, 1.5-year overall survival and 1-year progression-free survival prediction improved significantly after adding IAUC parameters (overall survival area under the receiver operating characteristic curve, 0.86; progression-free survival area under the receiver operating characteristic curve, 0.74–0.76) to the model with other prognostic factors (overall survival area under the receiver operating characteristic curve, 0.81; progression-free survival area under the receiver operating characteristic curve, 0.69;  $P < .05$  for all) except in the case of IAUC<sub>60,mean</sub> for 1-year progression-free survival prediction ( $P = .059$ ). Random survival forest models indicated that the IAUC parameters were the second or most important predictors in the unmethylated *MGMT* group, except in the case of the IAUC<sub>60,mean</sub> for progression-free survival.

**CONCLUSIONS:** IAUC can be a useful prognostic imaging biomarker in patients with glioblastoma with known *MGMT* status, improving prediction of glioblastoma prognosis with the unmethylated *MGMT* promoter status.

**ABBREVIATIONS:** AUC = area under the receiver operating characteristic curve; DCE = dynamic contrast-enhanced; *EGFR* = epidermal growth factor receptor; GBM = glioblastoma; IAUC = initial area under the time-to-signal intensity curve; *IDH1* = isocitrate dehydrogenase 1;  $K^{trans}$  = volume transfer constant; *MGMT* = *O*<sup>6</sup>-methylguanine-DNA methyltransferase; nCET = non-contrast-enhanced tumor; OS = overall survival; PFS = progression-free survival; rCBV = relative cerebral blood volume; ROC = receiver operating characteristic

**G**lioblastoma (GBM) is the most common primary malignant tumor in the adult brain. Although its prognosis remains poor (median survival, ~14.7 months),<sup>1</sup> some patients with GBM

show a distinct prognosis and response to chemoradiation. Previous studies have investigated the prognostic factors of GBM, including MR imaging<sup>2–4</sup> and molecular biomarkers (*O*<sup>6</sup>-methylguanine-DNA methyltransferase [*MGMT*] promoter methylation).<sup>5</sup>

Previous studies have shown that high relative cerebral blood volume (rCBV; derived via dynamic susceptibility contrast-enhanced MR imaging) and high volume transfer constant ( $K^{trans}$ ; derived via dynamic contrast-enhanced [DCE] MR imaging) are associated with poor survival outcomes.<sup>6–8</sup> However, rCBV and  $K^{trans}$  measurements have reproducibility issues related to post-processing techniques, including normalization, model-based calculation, arterial input function, and software.<sup>9–13</sup> In contrast, the initial area under the time-to-signal intensity curve (IAUC),

Received November 8, 2016; accepted after revision March 20, 2017.

From the Department of Radiology and Research Institute of Radiological Science (Y.S.C., S.S.A., H.-J.L., S.-K.L.) and Departments of Pathology (S.H.K.) and Neurosurgery (J.H.C., S.-G.K., E.H.K.), Yonsei University College of Medicine, Seoul, Korea.

Please address correspondence to Seung-Koo Lee, MD, PhD, Department of Radiology, College of Medicine, Yonsei University, 50 Yonsei-ro, Seodaemun-gu, Seoul 120-752, Korea; e-mail: SLEE@yuhs.ac

 Indicates article with supplemental on-line appendix and tables.

 Indicates article with supplemental on-line photos.

<http://dx.doi.org/10.3174/ajnr.A5265>

derived via DCE MR imaging, is a model-free parameter that does not require an arterial input function or a complicated model-based calculation and is highly reproducible.<sup>10,14</sup> Because IAUC reflects both tumor perfusion and permeability,<sup>9,10,15</sup> we hypothesized that IAUC might be useful for predicting the survival outcome in GBM. In this study, we used automatically calculated IAUC parameters to maximize reproducibility.

*MGMT* removes alkyl groups from the alkylation site of temozolomide. Methylation of the *MGMT* promoter inhibits *MGMT* activity and yields a better response to temozolomide and improved prognosis.<sup>5</sup> Because the *MGMT* status is available after surgery in most patients with GBM, the predictive ability of IAUC for prognosis in patients with GBM with known *MGMT* status is clinically relevant. Here, we aimed to assess whether IAUC can improve prognosis prediction in patients with GBM with known *MGMT* status.

## MATERIALS AND METHODS

Our institutional review board approved this retrospective study and waived the requirement for informed consent.

### Study Population

We reviewed the records of 101 consecutive patients who underwent preoperative DCE MR imaging for newly diagnosed GBM from October 2010 to July 2014. The enrollment process is shown in On-line Fig 1. The inclusion criteria were pathologically confirmed GBM, no prior biopsy or treatment, and available *MGMT* promoter methylation status. The exclusion criteria were previous brain biopsy or treatments ( $n = 6$ ), unavailable *MGMT* status ( $n = 3$ ), and inadequate DCE image quality, leading to processing errors ( $n = 4$ ). Thus, 88 patients were enrolled.

### Imaging

A 3T MR imaging unit (Achieva; Philips Healthcare, Best, the Netherlands) and an 8-channel sensitivity encoding head coil were used for preoperative MR imaging. The protocol included T1-weighted turbo spin-echo images with inversion recovery (TR, 2000 ms; TE, 10 ms; TI, 1000 ms; FOV, 240 mm; section thickness, 5 mm; matrix, 256 × 256), T2-weighted turbo spin-echo (TR, 3000 ms; TE, 80 ms; FOV, 240 mm; section thickness, 5 mm; matrix, 256 × 256), and T2-weighted fluid-attenuated inversion recovery (TR, 10,000 ms; TE, 125 ms; TI, 2500 ms; FOV, 240 mm; section thickness, 5 mm; matrix, 256 × 256) images. 3D T1-weighted turbo field echo images (TR, 9.8 ms; TE, 4.6 ms; FOV, 240 mm; section thickness, 1 mm; matrix, 224 × 224) were acquired after the injection of gadolinium-based contrast (0.1 mL/kg of gadobutrol, Gadovist; Bayer Schering Pharma, Berlin, Germany). For DCE-MR imaging, 60 dynamic phases of DCE T1-weighted images were acquired with the following parameters: TR, 6.3 ms; TE, 3.1 ms; FOV, 240 mm; matrix, 192 × 192; section thickness, 3 mm; flip angle, 15°. After we acquired the fifth phase, gadolinium-based contrast (0.1 mL/kg of gadobutrol) was injected (rate, 3 mL/s). The total acquisition time for DCE-MR imaging was 6 minutes 18 seconds and the temporal resolution was approximately 6 seconds.

### Image Postprocessing and Analysis

The ROIs were drawn by the consensus of 2 neuroradiologists (Y.S.C. and S.-K.L., with 4 and 20 years of experience in neuroradiology, respectively) who were blinded to the *MGMT* status and other clinical information, using a semiautomatic signal-intensity-threshold method to include the entire enhanced portion of the tumors on postcontrast T1-weighted images, while avoiding necrotic or cystic portions.

IAUC values were acquired by integrating the area under the time-to-signal-intensity curve, from 0 to 30 seconds (IAUC30) and 0 to 60 seconds (IAUC60) after contrast agent arrival on the basis of previous studies.<sup>10</sup> IAUC values were automatically calculated without any user-dependent input, to maximize interrater reliability, through automatic determination of the time of contrast agent arrival for each pixel; the time of contrast agent arrival was defined as the initial time at which a signal increase of >5% of the maximum signal increase was observed during >2 serial phases. The combination of this automatic calculation of IAUC and semiautomatic ROI segmentation of enhancing tumor yields almost perfect reproducibility.<sup>16</sup> The IAUC values were normalized to the maximum signal increase. A detailed description of the image processing is provided in the On-line Appendix. The mean values of IAUC30 (IAUC30<sub>mean</sub>) and IAUC60 (IAUC60<sub>mean</sub>) were extracted from the enhanced tumors. Images were analyzed with Medical Image Processing, Analysis, and Visualization (Version 7.0; National Institutes of Health, Bethesda, Maryland) and R software, Version 3.0.2 (R Foundation, <http://www.r-project.org/>).

### MGMT and Other Prognostic Parameters

*MGMT* promoter methylation status was evaluated with a methylation-specific polymerase chain reaction, which was retrospectively recorded from pathologic reports. Because IAUC may be related to other genetic profiles, including *isocitrate dehydrogenase 1 (IDH1)* mutation status, epidermal growth factor receptor (EGFR) expression, and the presence of 1p/19q codeletion, the data regarding these profiles were also recorded as described in the On-line Appendix. The presence of oligodendroglial components was also recorded because the presence of these components is related to better prognosis.<sup>17</sup> Furthermore, we recorded the following clinical factors: age, sex, Karnofsky performance status, extent of resection, and postoperative treatment, along with conventional MR imaging findings. The extent of resection was categorized as total, subtotal (<100% but ≥75% of gross tumor removal), or partial (<75% of gross tumor removal) resection/biopsy based on the intraoperative impressions of the surgeons (J.H.C., S.-G.K., and E.H.K., with 20, 16, and 10 years of experience in neurosurgery, respectively) and postoperative MR imaging. Postoperative treatment was categorized as concurrent chemoradiation with temozolomide, radiation therapy only, temozolomide-based chemotherapy only, and no postoperative treatment.

Conventional MR imaging findings included volume of enhanced tumor, degree of edema, presence of non-contrast-enhanced tumor (nCET), presence of deep white-matter invasion, and eloquent brain involvement, which are associated with prognosis.<sup>2,3</sup> Conventional MR imaging findings were de-

terminated on the basis of the consensus of 2 neuroradiologists (Y.S.C. and S.-K.L.), except for the enhanced tumor volume, which was automatically calculated from the ROIs on postcontrast T1-weighted images. Edema and nCET were assessed with axial T2-weighted or fluid-attenuated inversion recovery images, as described elsewhere.<sup>3,8</sup> Edema was scored as 0 (not apparent,  $\leq 1$  cm), 1 (mild-to-moderate,  $> 1$  cm and  $\leq 2$  cm), and 2 (severe,  $> 2$  cm) on the basis of the maximum length of the edema; and nCET was classified as positive if the volume was  $> 25\%$  of the enhanced tumor. The presence of eloquent brain involvement and deep white-matter invasion was determined with the Visually Accessible Repository for Molecular Brain Neoplasia Data Images lexicon.<sup>2,18</sup>

### Statistical Analysis

Overall survival (OS) duration was defined as the time from MR imaging–based diagnosis to death or the final follow-up in living cases. Progression-free survival (PFS) duration was defined as the time from MR imaging–based diagnosis to tumor progression, recurrence, death, or the final follow-up in cases in which no tumor progression or death was noted, according to the Response Assessment in Neuro-Oncology<sup>19</sup> as described elsewhere.<sup>4,8</sup>

Univariate survival analyses for OS and PFS of the entire cohort were performed with Kaplan-Meier estimates and the log-rank test; the analyses included IAUC30<sub>mean</sub>, IAUC60<sub>mean</sub>, MGMT status, the presence of an oligodendroglial component, clinical factors (age, sex, Karnofsky performance status, extent of tumor resection, and postoperative treatment), and conventional MR imaging findings (enhanced tumor volume, edema, nCET, eloquent brain involvement, and deep white matter invasion). Subgroup survival analyses of the methylated and unmethylated MGMT groups were performed with the IAUC parameters. If the variables were continuous or had  $> 3$  categories, they were dichotomized by the optimal cutoff values for OS and PFS that were calculated by using the “cutp” function of the “survMisc” R package, as defined by Contal and O’Quigley.<sup>20</sup> This method determines the optimal cutoff value yielding the most significant prognostic differences between the 2 groups based on test scores from the Cox regression model.<sup>20</sup>

The multivariate models were established with the significant factors of univariate analyses for OS and PFS in the unmethylated MGMT promoter group because the IAUC parameters were prognostic for the unmethylated MGMT group only, as shown later. In the multivariate models, all the variables that were continuous or had  $> 3$  categories were dichotomized, as in the univariate analyses. The multivariate models for OS and PFS were established from other prognostic factors only (model 0), and IAUC30<sub>mean</sub> and IAUC60<sub>mean</sub> were subsequently added as covariate parameters (IAUC30<sub>mean</sub> in model 1 and IAUC60<sub>mean</sub> in model 2). These multivariate models before (OS and PFS model 0) and after (OS and PFS models 1 and 2) adding IAUC parameters were explored and compared using 2 methods: 1) The diagnostic accuracies for 1.5-year OS and 1-year PFS prediction were assessed by receiver operative characteristic (ROC) analysis. Then, the reclassification improvement on adding the IAUC parameters was assessed using net reclassification improvement, as

described by Pencina et al.<sup>21</sup> 2) The random survival forest method was used to determine the variable importance of the IAUC parameters in prognosis prediction. The forests consisted of 50,000 trees, having a minimum of 3 samples in a terminal node. The IAUC parameters and other prognostic factors were ranked by the relative importance scores, and the C-indices of the random survival forest models were calculated. Representative trees were constructed with the variables that showed the highest importance scores.<sup>22,23</sup>

We compared the IAUC parameters according to MGMT status and the other genetic profiles using the Student *t* test, on the basis of the results of the Shapiro-Wilk test for normality. Statistical analyses were performed with Stata (Version 12.1; StataCorp, College Station, Texas) and R for Windows, Version 3.0.2. A *P* value  $< .05$  was considered significant.

## RESULTS

The clinical characteristics of the patients according to the MGMT status are summarized in On-line Table 1. None of the clinical characteristics, except for median OS and PFS, showed a significant difference between the methylated and unmethylated MGMT groups. The median OS and PFS were 442 days and 272 days, respectively, in the unmethylated MGMT group, whereas they were 790 days and 657 days, respectively, in the methylated MGMT group (log-rank test, *P* = .014 and .003 for OS and PFS, respectively). The other genetic characteristics of patients are summarized in On-line Table 2.

### Univariate Survival Analyses

The results of the univariate analyses for OS and PFS in the entire cohort are summarized in On-line Table 3. The IAUC parameters were not significant predictors of OS and PFS in the entire cohort, though high IAUC parameters tended to be associated with poor OS (*P* = .090 for IAUC30<sub>mean</sub>, *P* = .072 for IAUC60<sub>mean</sub>). Unmethylated MGMT, 66 years of age or older, less than total resection, postoperative treatment other than concurrent chemoradiation with temozolomide, and enhanced tumor volume of  $\geq 30.2$  cm<sup>3</sup> were associated with poor OS (*P*  $< .05$  for all). Similarly, unmethylated MGMT, 70 years of age or older, less than total resection, postoperative treatment other than concurrent chemoradiation with temozolomide, and enhanced tumor volume of  $\geq 30.2$  cm<sup>3</sup> were associated with poor PFS (*P*  $< .05$  for all). Eloquent brain involvement was associated with poor OS (*P* = .033), but not with PFS. Sex, Karnofsky performance status, edema, nCET, and deep white-matter invasion were not associated with OS or PFS.

The results of the subgroup univariate analyses of the IAUC parameters in the methylated and unmethylated MGMT groups are summarized in Table 1 and Fig 1. High IAUC parameters were significant predictors of poor OS (*P* = .008 for IAUC30<sub>mean</sub>, *P* = .015 for IAUC60<sub>mean</sub>) and poor PFS (*P* = .010 for IAUC30<sub>mean</sub>, *P* = .015 for IAUC60<sub>mean</sub>) in the unmethylated MGMT group, but not in the methylated MGMT group. Therefore, we established multivariate models for the unmethylated MGMT group alone. Representative cases of GBMs with unmethylated MGMT promoter status are shown in Figs 2 and 3.

**Table 1: Univariate analysis of IAUC histogram parameters as predictors of OS and PFS in the unmethylated and methylated MGMT subgroups.**

Survival/Parameters	Unmethylated MGMT (n = 51)			Methylated MGMT (n = 37)		
	Cutoff Value	HR (95% CI)	P Value <sup>a</sup>	Cutoff Value	HR (95% CI)	P Value <sup>a</sup>
OS						
IAUC30 <sub>mean</sub>	≥10.9	3.04 (1.28–7.21)	.008	≥15.1	0.60 (0.17–2.14)	.429
IAUC60 <sub>mean</sub>	≥28.4	3.48 (1.20–10.14)	.015	≥32.0	0.42 (0.16–1.14)	.079
PFS						
IAUC30 <sub>mean</sub>	≥10.9	2.60 (1.23–5.50)	.010	≥15.1	0.52 (0.18–1.56)	.238
IAUC60 <sub>mean</sub>	≥32.6	2.15 (1.14–4.05)	.015	≥32.8	0.24 (0.22–1.28)	.155

Note:—HR indicates hazard ratio.

<sup>a</sup>Calculated from the log-rank test.

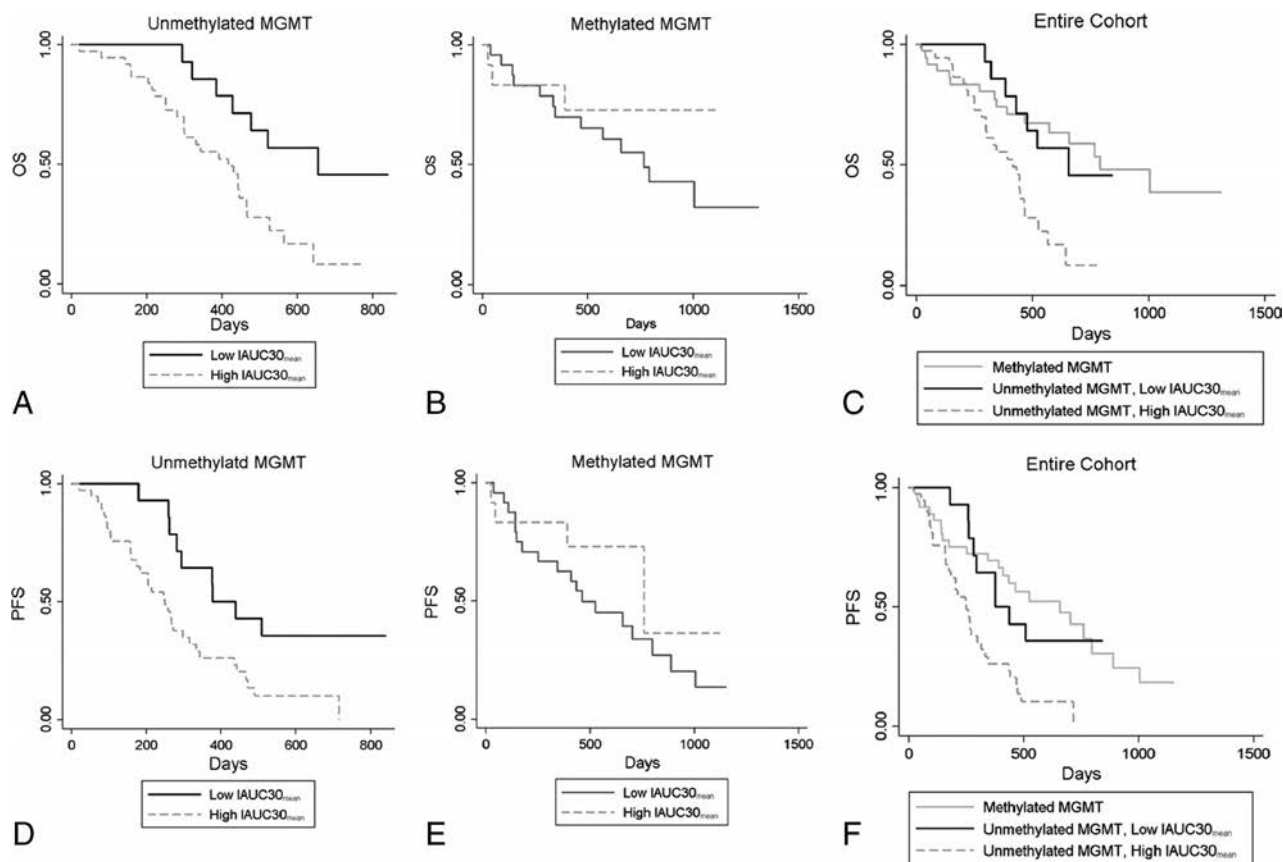


**FIG 1.** Kaplan-Meier curves of overall survival (A–C) and progression-free survival (D–F) with IAUC30<sub>mean</sub> in the unmethylated MGMT (A and D, n = 51) and methylated MGMT groups (B and E, n = 31) and the entire cohort (C and F, n = 88). IAUC30<sub>mean</sub> stratified OS (log-rank test,  $P = .008$ ) and PFS (log-rank test,  $P = .010$ ) only in the unmethylated MGMT group, but not in the methylated MGMT group (log-rank test,  $P = .429$  for OS,  $P = .238$  for PFS).

### ROC Analyses and Net Reclassification Improvement for Predicting 1.5-Year OS and 1-Year PFS

The results of the ROC analyses with the multivariate models for 1.5-year OS and 1-year PFS in the unmethylated MGMT group are summarized in Table 2. Among the 51 patients in the unmethylated MGMT group, 8 were excluded from the 1.5-year OS analysis and 1 was excluded from the 1-year PFS analysis because the follow-up duration was insufficient. Both OS and PFS model 0 included age, extent of resection, postoperative treatment, and enhanced tumor volume as covariates; eloquent brain involvement was included as a covariate in the OS model 0 only, according to the results of the univariate analyses. When the IAUC30<sub>mean</sub> or IAUC60<sub>mean</sub> were added in the OS model 0 and PFS model 0 as covariates, the diagnostic accuracies improved for

1.5-year OS prediction (OS models 1 and 2 area under the receiver operating characteristic curve [AUC], 0.86) and 1-year PFS prediction (PFS model 1 AUC, 0.76; PFS model 2 AUC, 0.74), compared with model 0 (OS model 0 AUC, 0.81; PFS model 0 AUC, 0.69). Reclassification improvement by adding IAUC parameters was statistically significant, as assessed by net reclassification improvement ( $P = .005$  and  $.018$  for OS models 1 and 2;  $P = .020$  with PFS model 1), except in the case of PFS model 2 with IAUC60<sub>mean</sub>, which showed borderline significance ( $P = .059$ ).

### Contribution of IAUC Parameters in the Multivariate Model of Random Survival Forest

Random survival forests for OS showed that IAUC parameters were the second most important variable, following the volume of

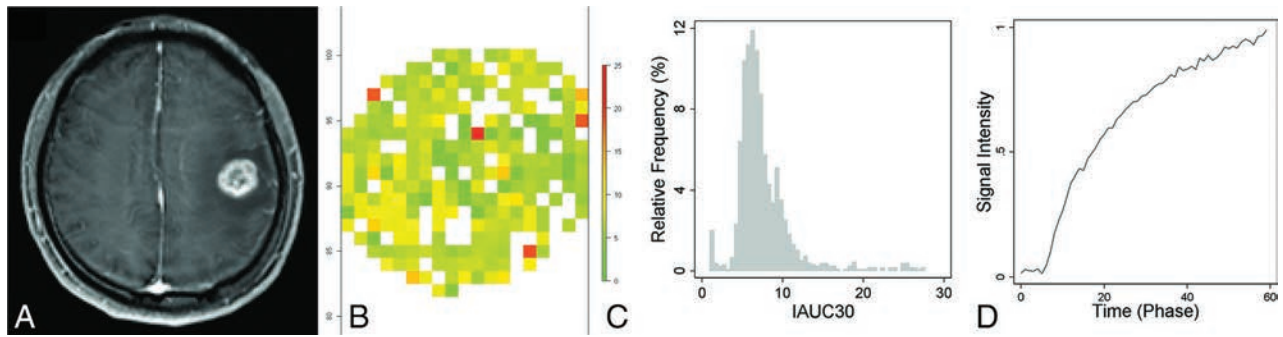


**FIG 2.** A 52-year-old male patient with glioblastoma with unmethylated *MGMT* promoter status, whose overall survival time was 477 days. T1 weighted images (A), IAUC30 parameter map of the enhancing tumor (B), the relative frequency histogram of IAUC30 (C), and the time to the mean signal-intensity curve of the enhancing tumor (D). The volume of enhancing tumor was 8.4 cm<sup>3</sup>, and the IAUC30<sub>mean</sub> was 5.4.

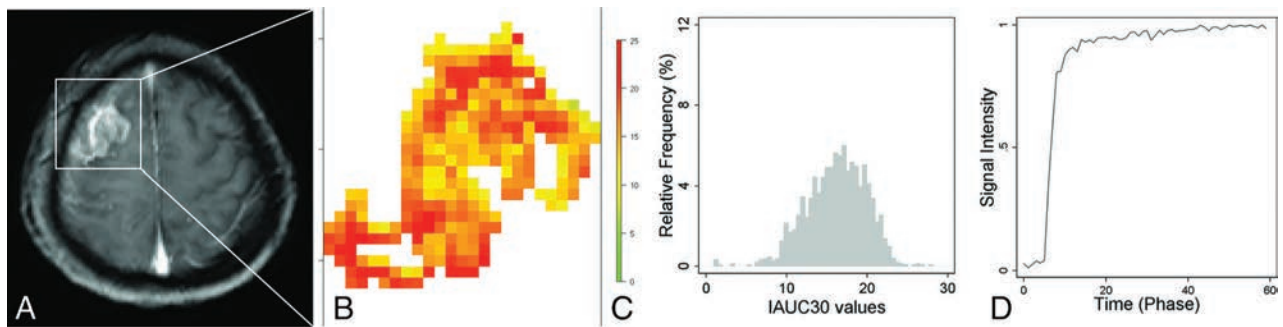


**FIG 3.** A 59-year-old female patient with glioblastoma with unmethylated *MGMT* promoter status, whose overall survival time was 250 days. T1-weighted image (A), IAUC30 parameter map of the enhancing tumor (B), the relative frequency histogram of IAUC30 (C), and the time to the mean signal-intensity curve of the enhancing tumor (D). The volume of the enhancing tumor was 7.4 cm<sup>3</sup>, and the IAUC30<sub>mean</sub> was 16.1.

**Table 2: Reclassification improvement by adding IAUC parameters for predicting 1.5-year OS (n = 43) and 1-year PFS (n = 50) in the unmethylated *MGMT* group**

Survival Time/Models		AUC (95% CI)	NRI (95% CI)	P Value <sup>a</sup>
1.5-year OS (n = 43)				
Model 0 (ref)	Age, extent of resection, postoperative treatment, volume of enhancing tumors, eloquent brain involvement	0.81 (0.65–0.96)	–	–
Model 1	IAUC30 <sub>mean</sub>	0.86 (0.74–0.98)	0.95 (0.61–1.29)	.005
Model 2	IAUC60 <sub>mean</sub>	0.86 (0.72–0.99)	0.81 (0.47–1.15)	.018
1-year PFS (n = 50)				
Model 0 (ref)	Age, extent of resection, postoperative treatment, volume of enhancing tumors	0.69 (0.54–0.84)	–	–
Model 1	IAUC30 <sub>mean</sub>	0.76 (0.62–0.90)	0.69 (0.39–0.98)	.020
Model 2	IAUC60 <sub>mean</sub>	0.74 (0.58–0.89)	0.56 (0.26–0.85)	.059

**Note:**—NRI indicates net reclassification improvement; ref, reference.

<sup>a</sup> Calculated from category-less NRI.

enhancing tumor as the top variable and followed by postoperative treatment as the third most important variable. The variable importance of random survival forests is shown in On-line Figs 2 and 3. The relative importance was 41% for IAUC30<sub>mean</sub> in OS model 1 and 57% for IAUC60<sub>mean</sub> in OS model 2, assuming that the relative importance of volume of enhancing tumor was 100%. Generation of a signal tree from this forest using the top 2 predictors (ie, volume of enhancing tumor and IAUC parameters) resulted in volume of enhancing tumor as the primary split and IAUC parameters as the secondary split for a group with a low volume of enhancing tumor (Fig 4). This splitting caused a significant difference in survival between the groups ( $P < .001$  for trees with IAUC30<sub>mean</sub> and IAUC60<sub>mean</sub>, log-rank test), with a difference in mean survival of 354 days and 388 days between the high

volume of enhancing tumors versus low volume of enhancing tumors with low IAUC30<sub>mean</sub> and IAUC60<sub>mean</sub>, respectively. The C-indices were higher after the IAUC parameters were added in OS models 1 and 2 (C-index = 0.67), compared with OS model 0 (C-index = 0.61).

Random survival forests for PFS showed that IAUC30<sub>mean</sub> in PFS model 1 was the most important variable, followed by extent of resection and volume of enhancing tumor as the second and third most important variables, respectively, whereas in PFS model 2, IAUC60<sub>mean</sub> was the third most important variable, following the extent of resection and volume of enhancing tumor as the first and second most important variables, respectively. The relative importance was 100% for IAUC30<sub>mean</sub> and 94% for extent of resection in PFS model 1. Generation of a single tree with

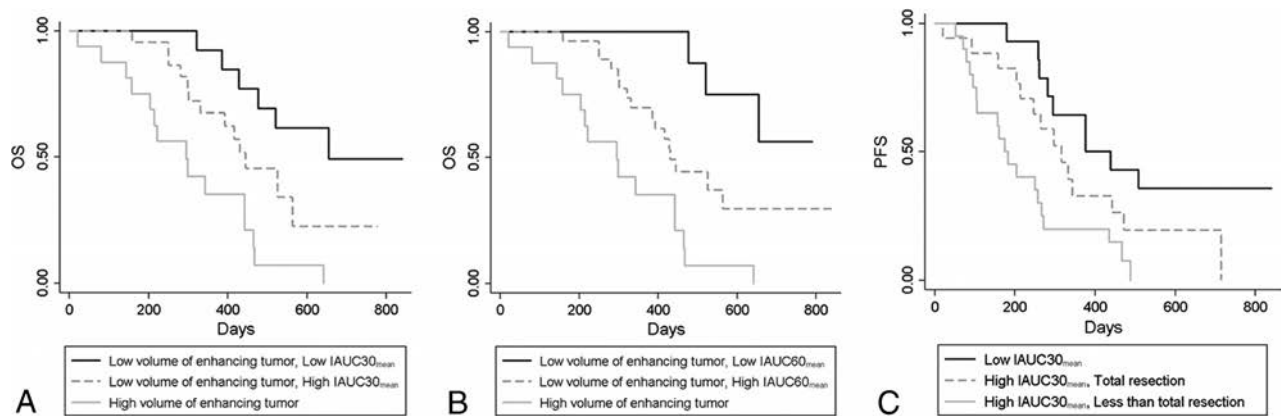


**FIG 4.** Kaplan-Meier curves depicting survival classification after random survival forest ranking of prognostic factors in glioblastomas with unmethylated *MGMT* promoter status ( $n = 51$ ). Representative trees with  $IAUC30_{mean}$  (A) and  $IAUC60_{mean}$  (B) for OS caused the volume of enhancing tumor to be the primary split and then the  $IAUC30_{mean}$  to split the subgroup with a low volume of enhancing tumor subsequently (log-rank test,  $P < .001$ ). C, A representative tree with  $IAUC30_{mean}$  for PFS caused the  $IAUC30_{mean}$  to be the primary split and then the extent of resection to split the subgroup with high  $IAUC30_{mean}$  subsequently (log-rank test,  $P < .002$ ).

the top 3 predictors of PFS model 1 resulted in  $IAUC30_{mean}$  as the primary split, and the low  $IAUC30_{mean}$  group was subsequently split by the extent of resection; this split caused significantly different survival among the groups (Fig 4,  $P = .002$ , log-rank test). The difference in mean survival was 293 days in tumors with high  $IAUC30_{mean}$  versus those with low  $IAUC30_{mean}$  and less than total resection. The C-indices were higher after adding the IAUC parameters in PFS models 1 and 2 (C-indices = 0.55 and 0.54, respectively), compared with that of PFS model 0 without IAUC parameters (C-index = 0.51).

#### Differences in IAUC Parameters between the Unmethylated and Methylated *MGMT* Promoter Groups

The differences in the IAUC parameters according to *MGMT* status are illustrated in On-line Fig 4. The IAUC parameters were significantly higher in the methylated *MGMT* group than in the unmethylated group ( $13.5 \pm 2.2$  versus  $12.2 \pm 2.1$ ,  $P = .007$  for  $IAUC30_{mean}$ ;  $33.7 \pm 4.6$  versus  $31.5 \pm 4.3$ ,  $P = .025$  for  $IAUC60_{mean}$ ). The differences in the IAUC parameters according to the other genetic profiles are described in the On-line Appendix.

## DISCUSSION

In this study, we found that higher IAUC values were predictors of poor OS and PFS in the unmethylated *MGMT* group and that IAUC parameters improved prognosis prediction of the unmethylated *MGMT* group, when added to other prognostic factors. Furthermore, IAUC values were paradoxically higher in the methylated *MGMT* group than in the unmethylated group.

rCBV and  $K^{trans}$  values are indicators of tumor perfusion and permeability, respectively, and high values are predictors of worse prognosis.<sup>6-8,22</sup> However, the variability of rCBV ranges from 24% to 67%, depending on the normalization method or software used for postprocessing.<sup>12</sup> Similarly,  $K^{trans}$  can vary according to the model selection, arterial input function, software, and pre-bolus T1 measurement.<sup>9-11</sup> In contrast, IAUC is a model-free parameter that does not depend on model selection and arterial input function and is highly reproducible.<sup>10,14</sup> Whether model-free parameters show high reproducibility and performance, compared with model-based parameters, was debated re-

cently.<sup>11,14,24</sup> While 1 study<sup>11</sup> reported that mean  $K^{trans}$  showed wider interobserver variability than model-free parameters, another study<sup>24</sup> reported that the reproducibility between the model-free parameter and  $K^{trans}$  did not differ significantly. In the latter study, the time of contrast agent arrival was manually defined to calculate the model-free parameters. In our study, the time of contrast agent arrival was automatically determined for each pixel; With this automatic determination of the time of contrast agent arrival, the IAUC has been reported to achieve almost perfect reproducibility.<sup>16</sup>

Despite the limitation of IAUC regarding the lack of a clear biologic association, IAUC values are correlated with  $K^{trans}$  and rCBV.<sup>9,15</sup> Hence, we hypothesized that IAUC would be useful for prognosis prediction because it reflects both perfusion and permeability, which are complementarily associated with prognosis. Although previous studies have reported that model-free parameters may be useful for differentiation of radiation necrosis and tumor,<sup>10,14</sup> the prognostic value of IAUC in GBM remains unclear. Moreover, to establish the practical role of an imaging biomarker, one must elucidate whether that imaging biomarker has prognostic value after other prognostic factors are considered in the usual clinical settings. We found that IAUC parameters have prognostic value even after clinical factors and conventional MR imaging findings are considered in the unmethylated *MGMT* group. Therefore, IAUC represents a useful imaging biomarker that has practicality and high reproducibility. Nevertheless, considering that  $IAUC60_{mean}$  did not achieve the same improvement in PFS prediction as  $IAUC30_{mean}$ , the optimal time point of IAUC needs to be determined in future investigations.

The association between high IAUC values and poor prognosis in the unmethylated group is consistent with findings in previous studies, which have reported the association between high rCBV and  $K^{trans}$  values and poor prognosis.<sup>6-8,22</sup> However, in our study, the IAUC values were not prognostic when applied to the methylated *MGMT* group or the entire GBM cohort, and IAUC values were paradoxically higher in the methylated *MGMT* group than in the unmethylated group. Some studies have reported the correlation between *MGMT* status and rCBV and  $K^{trans}$  values, with conflicting results; one study reported that rCBV values were

higher in GBM cases with unmethylated *MGMT* than in those with methylated *MGMT*.<sup>25</sup> In contrast, another study reported that  $K^{trans}$  values were higher in GBMs with methylated *MGMT*, a finding discordant with the previously reported association between high  $K^{trans}$  values and poor prognosis, and the authors hypothesized that high permeability of the methylated *MGMT* group allowed better penetration of temozolomide, yielding better response and prognosis.<sup>26</sup>

Although the underlying mechanism is unclear, our results may reflect IAUC values being more affected by permeability difference than perfusion difference between the methylated and unmethylated *MGMT* groups. Subsequently, a combination of these paradoxically high IAUC values of the methylated *MGMT* group and the effect of methylated *MGMT* as a good prognostic factor might have countervailed the association between high IAUC values and poor prognosis. This possibility is 1 explanation for our result that the IAUC values were not prognostic in the methylated *MGMT* group or the entire cohort. Similarly, a previous study<sup>27</sup> reported that low  $K^{trans}$  values were associated with poor prognosis in GBM, which is contradictory to the results of other studies on the association between high  $K^{trans}$  values and poor prognosis.<sup>7,8</sup> These conflicting results might be attributable to the complicated relationship among tumor permeability, *MGMT* status, and prognosis, as observed in our study. Future investigation with a larger cohort is necessary to analyze the relationship among tumor permeability, *MGMT* status, and prognosis. Given that the IAUC values have prognostic value only in the unmethylated *MGMT* group, the *MGMT* status should be known before IAUC may be considered a useful imaging biomarker. However, because the *MGMT* status is clinically available in most patients with GBM, in our opinion, this requirement does not mitigate the practicality of IAUC.

This study has several limitations, apart from its retrospective design. First, the IAUC parameters were not directly compared with rCBV and  $K^{trans}$ . Thus, the superiority of IAUC regarding its prognostic value, reflecting both rCBV and  $K^{trans}$ , was not directly proved in this study. Second, because IAUC values were prognostic in the unmethylated *MGMT* group only, the sample size was too small to be strictly validated to confirm the improvement in prognosis prediction by the addition of IAUC values. Third, although the IAUC is highly reproducible within the same scans from the same institutions, there may be variations among scans performed at separate times or at different institutions. Thus, this model-free parameter may have limited reproducibility.<sup>28</sup>

## CONCLUSIONS

Our study demonstrated that IAUC could be a useful prognostic imaging biomarker in patients with GBM with known *MGMT* status, improving the prognosis prediction of GBM with unmethylated *MGMT* promoter status. We propose that this complementary role of IAUC and *MGMT* status should be considered in future investigations.

## REFERENCES

- Stupp R, Mason WP, van den Bent MJ, et al; European Organisation for Research and Treatment of Cancer Brain Tumor and Radiotherapy Groups, National Cancer Institute of Canada Clinical Trials Group. **Radiation therapy plus concomitant and adjuvant temozolomide for glioblastoma.** *N Engl J Med* 2005;352:987–96 CrossRef Medline
- Wangaryattawanich P, Hatami M, Wang J, et al. **Multicenter imaging outcomes study of The Cancer Genome Atlas glioblastoma patient cohort: imaging predictors of overall and progression-free survival.** *Neuro Oncol* 2015;17:1525–37 CrossRef Medline
- Pope WB, Sayre J, Perlina A, et al. **MR imaging correlates of survival in patients with high-grade gliomas.** *AJNR Am J Neuroradiol* 2005;26:2466–74 Medline
- Choi YS, Ahn SS, Kim DW, et al. **Incremental prognostic value of ADC histogram analysis over *MGMT* promoter methylation status in patients with glioblastoma.** *Radiology* 2016;281:175–84
- Hegi ME, Diserens AC, Godard S, et al. **Clinical trial substantiates the predictive value of O-6-methylguanine-DNA methyltransferase promoter methylation in glioblastoma patients treated with temozolomide.** *Clin Cancer Res* 2004;10:1871–74 CrossRef Medline
- Law M, Young RJ, Babb JS, et al. **Gliomas: predicting time to progression or survival with cerebral blood volume measurements at dynamic susceptibility-weighted contrast-enhanced perfusion MR imaging.** *Radiology* 2008;247:490–98 CrossRef Medline
- Nguyen TB, Cron GO, Mercier JF, et al. **Preoperative prognostic value of dynamic contrast-enhanced MRI-derived contrast transfer coefficient and plasma volume in patients with cerebral gliomas.** *AJNR Am J Neuroradiol* 2015;36:63–69 CrossRef Medline
- Choi YS, Kim DW, Lee SK, et al. **The added prognostic value of preoperative dynamic contrast-enhanced MRI histogram analysis in patients with glioblastoma: analysis of overall and progression-free survival.** *AJNR Am J Neuroradiol* 2015;36:2235–41 CrossRef Medline
- Cheng HL. **Improved correlation to quantitative DCE-MRI pharmacokinetic parameters using a modified initial area under the uptake curve (mIAUC) approach.** *J Magn Reson Imaging* 2009;30:864–72 CrossRef Medline
- Chung WJ, Kim HS, Kim N, et al. **Recurrent glioblastoma: optimum area under the curve method derived from dynamic contrast-enhanced T1-weighted perfusion MR imaging.** *Radiology* 2013;269:561–68 CrossRef Medline
- Hamilton JD, Lin J, Ison C, et al. **Dynamic contrast-enhanced perfusion processing for neuroradiologists: model-dependent analysis may not be necessary for determining recurrent high-grade glioma versus treatment effect.** *AJNR Am J Neuroradiol* 2015;36:686–93 CrossRef Medline
- Prah MA, Stufflebeam SM, Paulson ES, et al. **Repeatability of standardized and normalized relative CBV in patients with newly diagnosed glioblastoma.** *AJNR Am J Neuroradiol* 2015;36:1654–61 CrossRef Medline
- Paulson ES, Schmainda KM. **Comparison of dynamic susceptibility-weighted contrast-enhanced MR methods: recommendations for measuring relative cerebral blood volume in brain tumors.** *Radiology* 2008;249:601–13 CrossRef Medline
- Narang J, Jain R, Arbab AS, et al. **Differentiating treatment-induced necrosis from recurrent/progressive brain tumor using nonmodel-based semiquantitative indices derived from dynamic contrast-enhanced T1-weighted MR perfusion.** *Neuro Oncol* 2011;13:1037–46 CrossRef Medline
- Walker-Samuel S, Leach MO, Collins DJ. **Evaluation of response to treatment using DCE-MRI: the relationship between initial area under the gadolinium curve (IAUGC) and quantitative pharmacokinetic analysis.** *Phys Med Biol* 2006;51:3593–602 CrossRef Medline
- Choi YS, Lee HJ, Ahn SS, et al. **Primary central nervous system lymphoma and atypical glioblastoma: differentiation using the initial area under the curve derived from dynamic contrast-enhanced MR and the apparent diffusion coefficient.** *Eur Radiol* 2017;27:1344–51 CrossRef Medline
- Appin CL, Gao J, Chisolm C, et al. **Glioblastoma with oligodendroglioma component (GBM-O): molecular genetic and clinical characteristics.** *Brain Pathol* 2013;23:454–61 CrossRef Medline
- Vasari MRI Visual Feature Guide.** The Cancer Imaging Archive (TCIA) Web site. <https://wiki.cancerimagingarchive.net/display/>

- Public/VASARI+Research+Project. Published March 25, 2015. Accessed December 12, 2015
19. Wen PY, Macdonald DR, Reardon DA, et al. **Updated response assessment criteria for high-grade gliomas: Response Assessment in Neuro-Oncology working group.** *J Clin Oncol* 2010;28:1963–72 CrossRef Medline
  20. Contal C, O'Quigley J. **An application of changepoint methods in studying the effect of age on survival in breast cancer.** *Computational Statistics & Data Analysis* 1999;30:253–70
  21. Pencina MJ, D'Agostino RB, D'Agostino RB, et al. **Evaluating the added predictive ability of a new marker: from area under the ROC curve to reclassification and beyond.** *Stat Med* 2008;27:157–72
  22. Jain R, Poisson LM, Gutman D, et al. **Outcome prediction in patients with glioblastoma by using imaging, clinical, and genomic biomarkers: focus on the nonenhancing component of the tumor.** *Radiology* 2014;272:484–93 CrossRef Medline
  23. Ishwaran H, Kogalur UB, Blackstone EH, et al. **Random survival forests.** *The Annals of Applied Statistics* 2008;2:841–60 CrossRef
  24. Roberts C, Issa B, Stone A, et al. **Comparative study into the robustness of compartmental modeling and model-free analysis in DCE-MRI studies.** *J Magn Reson Imaging* 2006;23:554–63 CrossRef Medline
  25. Ryoo I, Choi SH, Kim JH, et al. **Cerebral blood volume calculated by dynamic susceptibility contrast-enhanced perfusion MR imaging: preliminary correlation study with glioblastoma genetic profiles.** *PLoS One* 2013;8:e71704 CrossRef Medline
  26. Ahn SS, Shin NY, Chang JH, et al. **Prediction of methylguanine methyltransferase promoter methylation in glioblastoma using dynamic contrast-enhanced magnetic resonance and diffusion tensor imaging.** *J Neurosurg* 2014;121:367–73 CrossRef Medline
  27. Mills SJ, Patankar TA, Haroon HA, et al. **Do cerebral blood volume and contrast transfer coefficient predict prognosis in human glioma?** *AJNR Am J Neuroradiol* 2006;27:853–58 Medline
  28. Bammer R. *MR and CT Perfusion and Pharmacokinetic Imaging: Clinical Applications and Theoretical Principles.* Lippincott Williams and Wilkins; 2016

# Retrospective Validation of a Computer-Assisted Quantification Model of Intracerebral Hemorrhage Volume on Accuracy, Precision, and Acquisition Time, Compared with Standard ABC/2 Manual Volume Calculation

W. Xue, S. Vegunta, C.M. Zwart, M.I. Aguilar, A.C. Patel, J.M. Hoxworth, B.M. Demaerschalk, and J.R. Mitchell

## ABSTRACT

**BACKGROUND AND PURPOSE:** Intracerebral hemorrhage accounts for 6.5%–19.6% of all acute strokes. Initial intracerebral hemorrhage volume and expansion are both independent predictors of clinical outcomes and mortality. Therefore, a rapid, unbiased, and precise measurement of intracerebral hemorrhage volume is a key component of clinical management. The most commonly used method, ABC/2, results in overestimation. We developed an interactive segmentation program, SegTool, using a novel graphic processing unit, level set algorithm. Until now, the speed, bias, and precision of SegTool had not been validated.

**MATERIALS AND METHODS:** In a single stroke academic center, 2 vascular neurologists and 2 neuroradiologists independently performed a test-retest experiment that involved repeat measurements of static, unchanging intracerebral hemorrhage volumes on CT from 76 intracerebral hemorrhage cases. Measurements were made with SegTool and ABC/2. True intracerebral hemorrhage volumes were estimated from a consensus of repeat manual tracings by 2 operators. These data allowed us to estimate measurement bias, precision, and speed.

**RESULTS:** The measurements with SegTool were not significantly different from the true intracerebral hemorrhage volumes, while ABC/2 overestimated volume by 45%. The interrater measurement variability with SegTool was 50% less than that with ABC/2. The average measurement times for ABC/2 and SegTool were 35.7 and 44.6 seconds, respectively.

**CONCLUSIONS:** SegTool appears to have attributes superior to ABC/2 in terms of accuracy and interrater reliability with a 9-second delay in measurement time (on average); hence, it could be useful in clinical trials and practice.

**ABBREVIATIONS:** ICH = intracerebral hemorrhage; LS = level set; MDC = 95% minimum detectable change

Mortality from intracerebral hemorrhage (ICH) is between 31% and 34% at 7 days and 53% and 59% at 1 year.<sup>1</sup> Initial ICH volume and rate of growth are independent predictors of clinical outcome and mortality.<sup>2</sup> Attenuation of growth is an important treatment strategy.<sup>2</sup> Consequently, a rapid, unbiased, and precise measurement of ICH volume is an important component of clinical management.

CT is sensitive for identifying ICH and is commonly used for

clinical management.<sup>3</sup> The most common method to measure ICH volume is the simplified ellipsoid formula (ABC/2),<sup>4</sup> “where A is the greatest hemorrhage diameter by CT, B is the diameter 90° to A, and C is the approximate number of CT sections with hemorrhage multiplied by the section thickness.”<sup>5</sup> Use of this formula often results in large volume-estimation errors, particularly for large or irregularly shaped objects.<sup>4,6</sup>

There is particular interest in semiautomatic computer models that can offer fast, low-bias, and precise lesion volume measurements.<sup>7</sup> Among computer-based models, level set (LS) algorithms<sup>8</sup> have become widely used to determine lesion, organ, and bone volumes in recent years.<sup>9–11</sup> LS algorithms grow a “seed” placed within the ROI. Several parameters, including the rate of growth and curvature of the segmented surface, are controlled by local image properties and can also be adjusted by the reader.<sup>12</sup> LS algorithms are robust and flexible and prevent growth of the seed across weak, incidental connections into areas outside the lesion.<sup>13</sup>

For example, Cates et al<sup>14</sup> demonstrated, in a study of 9 me-

Received September 6, 2016; accepted after revision April 9, 2017.

From the Department of Biomedical Informatics (W.X., J.R.M.), Arizona State University, Scottsdale, Arizona; Moran Eye Center (S.V.), University of Utah, Salt Lake City, Utah; and Departments of Radiology (C.M.Z., A.C.P., J.M.H.), Neurology (M.I.A., B.M.D.), and Research (J.R.M.), Mayo Clinic, Scottsdale, Arizona.

The first authors, W. Xue and S. Vegunta, contributed equally to this work.

The senior authors, B.M. Demaerschalk and J.R. Mitchell, contributed equally to this work.

Please address correspondence to Bart M. Demaerschalk, MD, Mayo Clinic Hospital, 5777 E Mayo Blvd, Phoenix, AZ 85054; e-mail: demaerschalk.bart@mayo.edu; @demaerschalk

<http://dx.doi.org/10.3174/ajnr.A5256>

meningioma or low-grade glioma MR images, that LS volume measurements produce results that are similar to those from hand tracings. Colliot et al<sup>15</sup> found that measurement bias was low when they used LSs to measure cortical dysplasia lesions on MR imaging in 18 patients. Similarly, Saba et al<sup>16</sup> obtained a low bias with LSs to measure carotid artery wall thickness on MR images of 10 patients; the LS volumes were compared with volumes calculated with manual tracings in both studies.

However, LS algorithms require an enormous number of computations and long execution times on central processing units. To address this issue, we previously developed a novel LS algorithm that leverages the massive parallelism of commodity graphic processing units.<sup>13</sup> This algorithm is 14 times faster than the fastest previously reported parallel algorithm and hundreds of times faster than serial algorithms on current central processing units. The algorithm had low bias and variability when segmenting tissues in a realistic brain phantom, an anatomically accurate 3D simulation of the human brain.<sup>13</sup> Dang et al<sup>17</sup> reported that its speed, bias, and precision in measuring meningioma volume were superior to the modified McDonald criteria and manual outlining on 25 contrast-enhanced MR imaging examinations. To our knowledge, the speed, bias, and precision of LS algorithms have not been previously tested with a large sample size of ICH and multiple clinician readers, the objective of this study.

In summary, growth in ICH volume is often used to inform treatment decisions in clinical practice. For example, Dowlatshahi et al<sup>18</sup> reported that hematoma expansion of 33% or 12.5 mL was highly predictive of poor outcome. As described above, the ABC/2 method can be used to estimate hematoma volume. However, it has poor accuracy, which limits its clinical utility. Manual outlining by an expert can provide accurate volume measurements. However, the associated time penalty limits its clinical utility. Thus, there is an unmet clinical need for simple, rapid, and accurate measurement of ICH volume. Characterizing, validating, and integrating such a tool into clinical workflows would allow clinicians to provide more precise and personalized care.

## MATERIALS AND METHODS

After institutional review board approval, images for this study were obtained from an existing data base of hemorrhagic stroke cases presenting to Mayo Clinic Hospital in Arizona between January 2007 and January 2013. Seventy-six consecutive cases with CT imaging available showing intraparenchymal hematomas were selected. Exclusion criteria included extracerebral hemorrhage and/or intraventricular hematoma. Six cases were randomly withheld from the experimental dataset and used for training purposes.

Four operators, 2 neuroradiologists and 2 vascular neurologists, collected measurements in this study. ABC/2 measurements were acquired with OsiriX Imaging Software (<http://www.osirix-viewer.com>). LS measurements were acquired with SegTool, a custom-developed in-house program that runs on Windows 7 (Microsoft, Redmond, Washington) computers equipped with graphic processing units (CUDA; Nvidia, San Jose, California). During the measurements, SegTool ran on a stand-alone computer and was not integrated into the PACS workflow. All the operators had experience with the ABC/2 method but no prior knowledge of SegTool. The 70 evaluation cases were each mea-

sured twice by 4 operators using both methods, for a total of 1120 measurements (70 cases × 4 operators × 2 methods × 2 repeats). One of the neurologists and one of the neuroradiologists also manually outlined lesions with OsiriX (70 cases × 2 operators × 2 repeats) to estimate true lesion volumes (described below).

Repeat measurements of all cases in random order occurred after a minimum 2-week delay to limit learning effects. To minimize the bias from the results of SegTool, we conducted the measurements in the following order: Manual tracings were performed first, followed by ABC/2, and finally SegTool. An additional SegTool correction process was introduced after initial data analysis. Figure 1A reviews the workflow for both the ABC/2 and SegTool measurement processes.

### ABC/2 Method

The operator identified the axial sections with the largest lesion extent and then measured the 2 longest orthogonal diameters of the lesion with the OsiriX ROI Length Tool (Fig 1B). The lesion volume was estimated as

$$\text{Lesion Volume} = A \times B \times C/2,$$

where *A* and *B* are the length of the 2 diameters and *C* is section thickness multiplied by the number of sections where the lesion was visible.

### Level Set Method

The operator drew ≥1 green stroke in the ICH and ≥1 red stroke in the surrounding tissue that they did not want to include (surrounding brain parenchyma in our experiments). Strokes were placed on 2D axial sections (Figs 1C and 2A). The operator then clicked a “Play” button to initiate object growth. Growth occurred in real-time and could be visualized in 2 or 3 dimensions interactively (Fig 2B, -D). The algorithm naturally handles the simultaneous growth, merging, and separation of multiple distinctly seeded regions.

The surface propagation was guided by a K-nearest neighbor statistical model of the intensity values provided by the seed points and a curvature parameter between 0 and 1 that determined the surface stiffness. In all cases, the curvature parameter was initialized to 0.25. During or following region growth, the operator could adjust a slider to manipulate the curvature parameter. Higher values encouraged smoother, smaller volumes. Lower values encouraged larger, more irregular volumes. The effects of changes in the curvature parameter on the segmented volume occurred and were displayed in real-time.

The user had the ability to then review the segmentation in 2D or 3D by rotating the CT scan volume (Fig 2D). After the user accepted the results, SegTool calculated and recorded the ICH volume, measurement time, and binary mask (segmentation) of the ICH.

A common issue in LS segmentation is “leakage.” Artificial connections between blood and bone (both bright on CT) can be caused by partial volume effects between hemorrhage and skull (due, in part, to the large section thickness of clinical image examinations). These can be corrected by either increasing the LS surface stiffness (causing the leak to retract back into the segmented region) or removing the leaked regions with editing tools.

An informal review of the SegTool volume measurements was

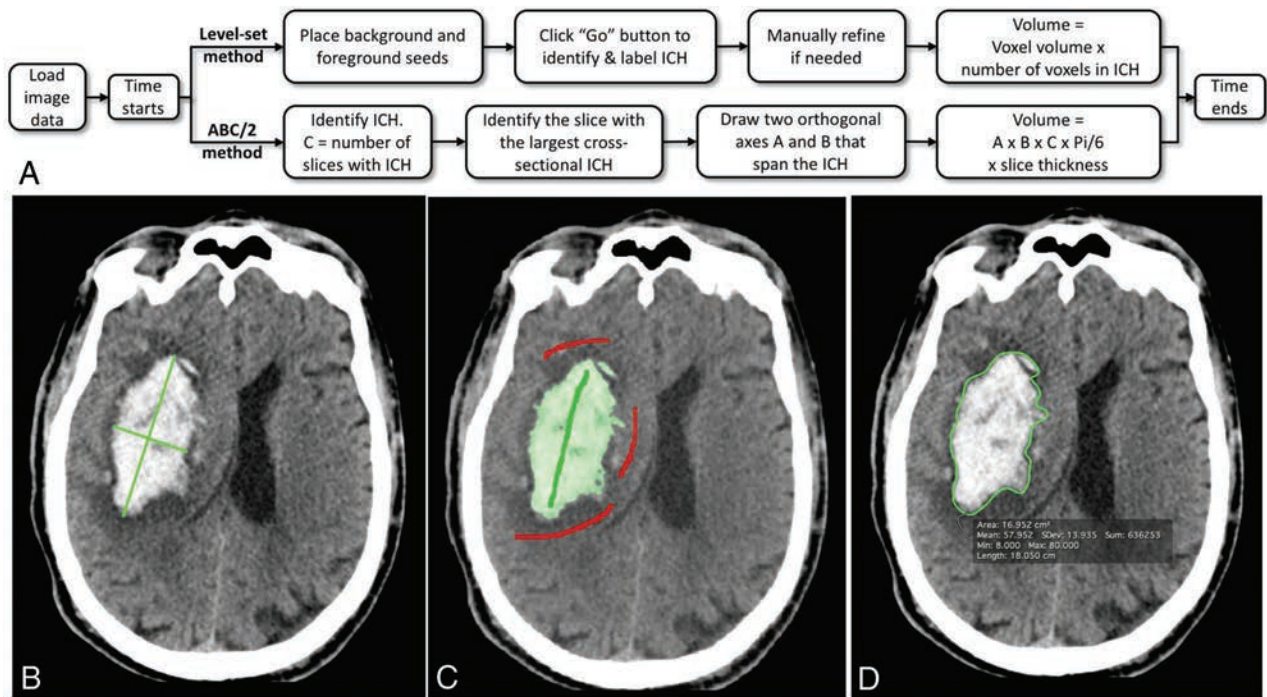


**FIG 1.** Hemorrhage measurement methods. *A*, A flowchart describes steps in the ABC/2 and level set measurement processes. *B*, Results from the ABC/2 method. *C*, Results from the level set method. *Green and red strokes* were placed by the user. Green indicates desired tissue (foreground), and red indicates undesired tissue (background). The level set region grows in 3D after the user clicks “Go” (Fig 2). *D*, Manual outlining of the boundary in a single axial section. This process was replicated in each axial section with visible ICH. Each true volume was determined from 4 manual tracings. Two operators each performed 2 repeat manual tracings. A minimum interval of 2 weeks between repeat tracings was required. Any voxel selected in at least 3 of the 4 manual tracings was labeled a “true” lesion voxel and was used to estimate the true lesion volume.

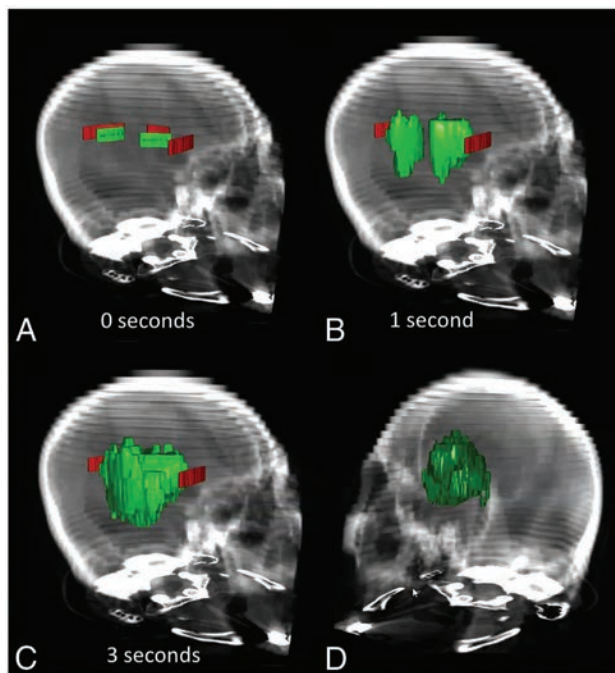


**FIG 2.** The SegTool ICH segmentation process in a CT scan with a  $512 \times 512 \times 36$  array. *A*, The user placed foreground (green) and background (red) seeds in an axial section (Fig 1C). Here the seeds are viewed in 3D. After the user clicks the “Play” button (not shown), the level set evolves to cover the ICH. In this example, a 41-mL ICH is segmented in 3 seconds (*B* and *C*). The final segmented region can be viewed in 2D or 3D by rotating the CT scan volume (*D*).

performed by several of the authors (S.V., W.X., C.M.Z., J.R.M.) to check for possible leaks. Results from this review were not shared with the operators. The review proceeded, step by step, through all ICHs. At each step, all measurements for a specific ICH were compared. Several of the ICHs had a single volume measurement that was more than double the median volume. Closer inspection of these saved segmented regions revealed that large leaks had occurred (Fig 3).

It was then discovered that the default transparency level of the segmented region was such that operators found it difficult to detect leaks into bone (Fig 3A). Consequently, all operators performed a review of their SegTool 3D measurements with the suggested workflow that reduced the transparency of the green region until it was opaque (Fig 3B). Readers were permitted to correct any segmentation by either editing or starting over. Readers recorded and compared both the initial and “after review” SegTool measurements using ABC/2.

### True ICH Volume Estimation

The true ICH volume was estimated from manual tracings. One neurologist and 1 neuroradiologist operator each independently manually traced the lesion on each axial section in which it was apparent with the ROI Pencil Tool of OsiriX (Fig 1D). OsiriX was used to calculate the area in each section, and the lesion volume was calculated as

$$\text{Lesion Volume} = \text{Section Thickness}$$

$$\times \text{Summation of Lesion Areas of All Sections.}$$

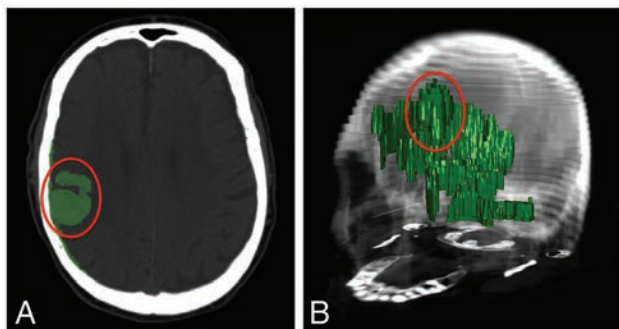


**FIG 3.** The level set algorithm may leak. An axial (A) and 3D view (B) of 1 segmented ICH lesion (enclosed in a red ellipse) along with level set leakage outside the lesion. Leakage was caused by partial volume effects between hemorrhage and skull (due, in part, to the large section thickness of the clinical imaging examinations). This can be corrected by either increasing the level set surface stiffness or removing the leaked regions with editing tools. However, when the transparency of the segmented (green) region was high (as it was by default), operators found it difficult to detect leaks. Consequently, we asked all operators to perform a blinded review of their level set segmentations. They performed this by interactively reducing the transparency of the green region until it was opaque and then viewing their segmentation in 3D (B). If, for any reason, they were not satisfied with the labeled region, they were asked to re-segment the lesion. In the text, we describe several enhancements to the tool that could be made to help operators detect leaks before saving the final segmented region.

Each true volume was estimated from 4 manual tracings by the 2 operators. Any voxel selected in at least 3 of the 4 manual tracings was labeled a “true” lesion voxel and was used to estimate the true lesion volume.

### Statistical Analysis

We used methodology recommended by the Quantitative Imaging Biomarker Alliance<sup>19</sup> to assess the uncertainty in volume measurement. In particular, we used a disaggregate approach to express uncertainty in terms of bias and precision. They defined “bias” as “the difference between the average (expected value) of measurements made on the same object and its true value.” They defined “precision” as “the closeness of agreement between measured quantity values obtained by replicate measurements on the same or similar experimental units under specified conditions.”

Precision is related to the variability in volume measurement. There are several ways it can be described numerically. Here, we chose to express precision as a clinically relevant threshold: the 95% minimum detectable change (MDC).<sup>19</sup> Magnitude changes in volume  $\leq$  MDC can be explained by variability in the measurement process alone with 95% confidence. Therefore, magnitude changes in volume  $>$  MDC can be ascribed to lesion growth (or shrinkage) with a type II error rate of 5%.

We used a 2-way random-effects analysis of variance as previously described<sup>20,21</sup> to estimate between- and within-operator variability for both measurement methods. These values were then used to calculate the between- and within-operator MDC for each method. The measurement bias of each method was determined by comparing the mean measured ICH volume with the estimated true ICH volume. The measurement time of ABC/2 was determined by timing the readers as they measured the volumes. The measurement time of SegTool in seconds was recorded directly by the program.

### Summary statistics for our experiments<sup>a</sup>

	ABC/2	SegTool (Initial)	SegTool (after Review)	SegTool (Revisions)
No.	560	560	560	140
Mean (SD)	35.28 (56.24)	26.02 (40.35)	25.32 (39.76)	-2.2 (12.7)
1st Quartile	7.00	4.77	4.84	-1.43
Median	18.48	13.19	13.09	-0.01
3rd Quartile	36.82	28.87	27.47	0.40

<sup>a</sup> All values are in milliliters, except No. that is dimensionless. The values in the SegTool (revisions) column indicate the change after operators reviewed their initial measurements. Negative values mean that the after-review value was smaller than the initial value.

### RESULTS

Summary statistics for our experiments are presented in the Table. ABC/2 produced larger volume estimates than SegTool. SegTool measurements, after review, were smaller, on average, than the initial SegTool measurements. Operators modified 140 (of 560) SegTool measurements during the review process.

Figure 4 shows the measurement bias (Fig 4A), precision (Fig 4B), and time (Fig 4C) for the ABC/2 and SegTool (after review) methods. On average, ABC/2 and SegTool produced measurements that were 45% and 3% larger than truth, respectively. (The slope of the line of best fit for ABC/2 and SegTool was 1.45 and 1.03, respectively.) The slope of the line of best fit for SegTool was not statistically different from 1.0, the line of perfect agreement between measured and true volumes ( $P > .05$ ).

Between-operator MDC for ABC/2 was 13.94 mL. This was significantly higher (worse) than the SegTool MDC before (11.93 mL,  $P < .02$ ) and after (9.51 mL,  $P < .02$ ) the operators reviewed for LS leakage.

Within-operator MDC for ABC/2 was 7.47 mL. This was significantly lower than the MDC for the initial group of SegTool measurements (9.93 mL,  $P < .001$ ). However, after the operators reviewed and revised their SegTool measurements to eliminate leaks, SegTool MDC improved to 7.37 mL. This value was not statistically significantly different from the ABC/2 MDC ( $P = .8$ ).

Measurement time is the total time required to complete the steps listed in Fig 1A, after the data were loaded. The average measurement times for ABC/2 and SegTool (initial) were 35.7 and 44.6 seconds, respectively. The average measurement time for repeating the SegTool measurements (after review) was not statistically significantly different from the average initial measurement time (data not shown). SegTool required an extra 8.9 seconds to complete measurements, on average. This difference was significantly different from zero ( $P < .001$ ).

### DISCUSSION

True lesion volumes are required to determine bias. These are often unknown in clinical experiments. A compromise is to estimate the true volume of each lesion with a consensus of expert segmentations in medical images. In our experiments, we assumed that true ICH voxels were those that were selected in at least 3 out of 4 manual outlineings by experts (2 experts  $\times$  2 repeated measurements each). Other schemes are also possible.<sup>19</sup> Several studies have reported that baseline ICH volume is highly predictive of 30-day morbidity and mortality.<sup>22,23</sup> It is also well-acknowledged that ABC/2 tends to overestimate lesion volumes.<sup>24,25</sup> In our study, ABC/2 overestimated ICH volume by 45%, on average. While the mean SegTool measurements were

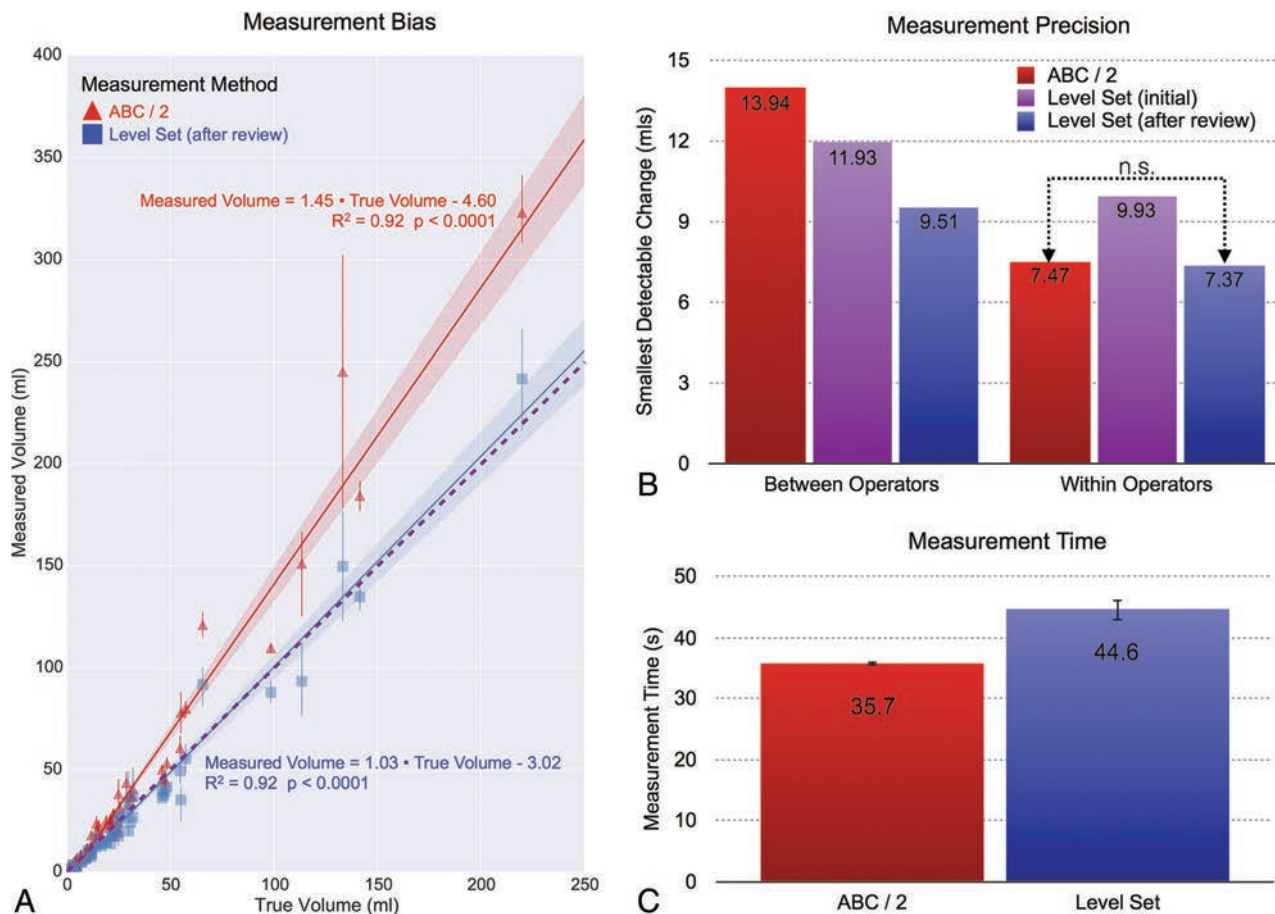


**FIG 4.** The bias (A), precision (B), and time (C) for ICH volume measurement. Measurements made using the ABC/2 method are shown in red. Those made using SegTool are shown purple (initial) or blue (after review). A, Bias: the dashed (purple) line indicates perfect agreement between measured and true volumes. Each true volume was determined from 4 manual tracings placed by experts (details in the text). The solid markers indicate the mean measured volume determined from 8 measurements (4 operators × 2 measurements/operator). The error bars indicate the 95% confidence interval for the mean measured volume. The solid lines show a linear regression fit through all measurements for each method. The shaded zone around each solid line indicates the 95% confidence interval for the slope of the line. Each line is labeled with its equation, the *P* value from the linear regression, and the coefficient of determination describing goodness of fit (1.0 equals a perfect fit). B, Precision: lower values are better. Changes in ICH volume less than the indicated value can be explained by measurement variability alone, with 95% confidence. The values in the “Between Operator” group are all statistically significantly different ( $P < .02$ ). The “SegTool (initial)” value in the “Within Operators” group is significantly different than the other values ( $P < .001$ ), which are not significantly different from each other ( $P = .8$ ). C, Time: each bar indicates the mean value from 560 measurements (70 ICH lesions × 4 operators × 2 repeated measurements). The SegTool time is based on the initial measurements. The error bars indicate the standard error of the mean. On average, SegTool required an extra 8.9 seconds to measure ICH volume. This difference is statistically significantly different from 0 ( $P < .0001$ ).

not significantly different from the estimated true ICH volumes, the low measurement bias of SegTool could be important for future clinical trials that rely on baseline ICH volume for patient stratification.

There was no significant difference in the within-operator MDC between ABC/2 and SegTool (after review to check for leaks). However, SegTool had between-operator MDC that was approximately 50% lower (better) than ABC/2. This is important because in many clinical scenarios, it is difficult to ensure that a single individual performs all volume measurements.

A recent study by Dowlatshahi et al<sup>18</sup> reported that hematoma expansion of 33% or 12.5 mL was highly predictive of poor outcome. The between-operator MDC of ABC/2 in our study was 13.94 mL. Consequently, an expansion of 12.5 mL measured this way can be explained by measurement variability alone (with 95% confidence) and may not correspond to true hematoma growth. SegTool, on the other hand, had a between-operator MDC of 9.51

mL. An expansion of 12.5 mL measured this way is too large to be explained by measurement variability alone. Consequently, it may be ascribed to ICH growth.

A number of previous studies have compared ABC/2 with ≥1 computer-assisted method for measuring ICH volume. For example, Divani et al<sup>4</sup> compared ABC/2 with planimetric measurements made with Medical Image Processing, Analysis, and Visualization (National Institutes of Health, Bethesda, Maryland) and with computer-assisted segmentation with Analyze software (AnalyzeDirect, Overland Park, Kansas) and Voxar 3D (Barco NV, Kortrijk, Belgium). Their study focused on determining measurement bias. Measurements were made from a silicone phantom and from simulated lesions implanted in cadaver brains. A variety of CT protocols were used. They found that ABC/2 produced large overestimations of lesion volume. They did not report measurement precision or time.

Freeman et al<sup>26</sup> compared ABC/2 with Analyze in a series of 8

patients with ICH treated with warfarin. They used the Analyze measurements to estimate true lesion volumes. These were then used to estimate the measurement bias of ABC/2. They concluded that ABC/2 has a small measurement bias for small lesions but can produce large errors (both over- and underestimation of true volume) for large or complex lesions. They did not exhaustively examine measurement time but reported that the most accurate method of measuring lesion volume with Analyze required 20–30 minutes per study, after a steep learning curve. They did not report measurement precision.

Xu et al<sup>24</sup> compared ABC/2 with computer-assisted measurements made with an intensity-threshold algorithm in 3D Slicer (<http://www.slicer.org>) in 294 CT examinations. Two physicians each made a single measurement of each lesion with each method. They used the Slicer measurements to estimate true lesion volumes. These were then used to estimate the measurement bias of ABC/2. They also divided the lesions into groups based on size and shape and compared the 2 measurement methods between groups. They concluded that ABC/2 overestimated lesion volumes and that these errors increased with lesion volume and more complex shape. They reported that the average time required to measure lesion volume with 3D Slicer was 96 seconds. They did not report measurement precision or ABC/2 measurement times.

Kosior et al<sup>7</sup> compared ABC/2 with computer-assisted measurements made using custom-developed software (Quantomo) that used an intensity-threshold algorithm available as part of the Insight Segmentation and Registration Toolkit (National Institutes of Health, Bethesda, Maryland). The study of Kosior et al was focused on evaluating measurement precision. As in our study, they used a test-retest experiment and a 2-way random-effects ANOVA to determine the MDC for each method. They also had 4 operators each perform 2 repeat measures using each measurement method. They reported the within-operator MDCs for ABC/2 and Quantomo as 15.7 and 5.3 mL, respectively (versus our values of 7.47 and 7.37 mL for ABC/2 and SegTool [after review], respectively). Their reported between-operator MDCs for ABC/2 and Quantomo were 37.0 and 8.1 mL, respectively (versus our results of 13.94 and 9.51 mL, respectively). There were several differences between their methods and ours. These include the following: 5 days between repeated measures (versus 2 weeks in our study) and measurement of 30 CT scans (versus 70 in our study). It is also likely that their CT protocol was more consistent among patients than ours because their patients were recruited from a clinical trial, whereas ours were recruited from our general patient population during several years. Finally, they did not report measurement bias or times.

One of the weaknesses of our study was the need to have operators review their initial SegTool measurements. This review was performed in a blinded fashion—operators were not provided with any information on which studies may have had leaks. They were free to redo or edit any, all, or none of their prior measurements. In total, 140 of the initial 560 segmentations were revised. The median result was to reduce the lesion volume by 0.01 mL. The mean effect was to reduce lesion volume by 2.2 mL. The impact on measurement precision was to reduce between-operator MDC from 11.93 to 9.51 mL and to reduce the within-operator MDC from 9.93 to 7.37 mL.

We could make several modifications to SegTool to increase the visibility of LS leaks and/or reduce their likelihood. By default, the segmented region was highly translucent. This made LS growth into brightly saturated bone very difficult to see. Simply increasing the default opacity of the segmented region would address this limitation. We could also preprocess the image volumes to strip skulls. Several open-source algorithms are available to perform this task; however, this would cause delays in interpretation.

## CONCLUSIONS

SegTool measurements took 9 seconds longer to complete on average. However, the SegTool measurements were not significantly different from the true ICH volumes, while ABC/2 overestimated ICH volume by 45%. The between-operator measurement variability with SegTool was 50% less than that with ABC/2. SegTool was capable of detecting clinically important differences in ICH volume, whereas the ABC/2 was not. Consequently, SegTool could be useful in clinical trials and clinical practice when intervention and prognostication rely on accurate baseline ICH volume or detecting changes in serial ICH volumetric measurements.

Disclosures: Bart M. Demaerschalk—UNRELATED; Other: Co-Editor-in-Chief of *Neurologist*.

## REFERENCES

1. Flaherty ML, Haverbusch M, Sekar P, et al. **Long-term mortality after intracerebral hemorrhage.** *Neurology* 2006;66:1182–86 CrossRef Medline
2. Davis SM, Broderick J, Hennerici M, et al; Recombinant Activated Factor VII Intracerebral Hemorrhage Trial Investigators. **Hematoma growth is a determinant of mortality and poor outcome after intracerebral hemorrhage.** *Neurology* 2006;66:1175–81 CrossRef Medline
3. Morgenstern LB, Hemphill JC 3rd, Anderson C, et al; American Heart Association Stroke Council and Council on Cardiovascular Nursing. **Guidelines for the management of spontaneous intracerebral hemorrhage: a guideline for healthcare professionals from the American Heart Association/American Stroke Association.** *Stroke* 2010;41:2108–29 CrossRef Medline
4. Divani AA, Majidi S, Luo X, et al. **The ABCs of accurate volumetric measurement of cerebral hematoma.** *Stroke* 2011;42:1569–74 CrossRef Medline
5. Kothari RU, Brott T, Broderick JP, et al. **The ABCs of measuring intracerebral hemorrhage volumes.** *Stroke* 1996;27:1304–05 CrossRef Medline
6. Wang CW, Juan CJ, Liu YJ, et al. **Volume-dependent overestimation of spontaneous intracerebral hematoma volume by the ABC/2 formula.** *Acta Radiol* 2009;50:306–11 CrossRef Medline
7. Kosior JC, Idris S, Dowlathshahi D, et al; PREDICT/Sunnybrook CTA ICH study investigators. **Quantomo: validation of a computer-assisted methodology for the volumetric analysis of intracerebral haemorrhage.** *Int J Stroke* 2011;6:302–05 CrossRef Medline
8. Osher S, Sethian JA. **Fronts propagating with curvature-dependent speed: algorithms based on Hamilton-Jacobi formulations.** *J Comput Phys* 1988;79:12–49 CrossRef
9. Anandh KR, Sujatha CM, Ramakrishnan S. **Segmentation of ventricles in Alzheimer MR images using anisotropic diffusion filtering and level set method.** *Biomed Sci Instrum* 2014;50:307–13 Medline
10. Göçeri E. **Fully automated liver segmentation using Sobolev gradient-based level set evolution.** *Int J Numer Method Biomed Eng* 2016; 32:e02765 CrossRef Medline
11. Ivanovska T, Laqua R, Wang L, et al. **An efficient level set method for**

- simultaneous intensity inhomogeneity correction and segmentation of MR images.** *Comput Med Imaging Graph* 2016;48:9–20 CrossRef Medline
12. Whitaker R. **Volumetric deformable models: active blobs.** *Proc SPIE Int Soc Opt Eng* 1994;2359:122–134
  13. Roberts M, Packer J, Sousa M, et al. **A work-efficient GPU algorithm for level set segmentation.** In: *Proceedings of the Conference on High Performance Graphics*. Saarbrücken, Germany: Eurographics Association. June 25–27, 2010
  14. Cates JE, Lefohn AE, Whitaker RT. **GIST: an interactive, GPU-based level set segmentation tool for 3D medical images.** *Med Image Anal* 2004;8:217–31 CrossRef Medline
  15. Colliot O, Mansi T, Bernasconi N, et al. **Segmentation of focal cortical dysplasia lesions using a feature-based level set.** *Med Image Comput Assist Interv* 2005;8:375–82 Medline
  16. Saba L, Gao H, Raz E, et al. **Semiautomated analysis of carotid artery wall thickness in MRI.** *J Magn Reson Imaging* 2014;39:1457–67 CrossRef Medline
  17. Dang M, Modi J, Roberts M, et al. **Validation study of a fast, accurate, and precise brain tumor volume measurement.** *Comput Methods Programs Biomed* 2013;111:480–87 CrossRef Medline
  18. Dowlatshahi D, Demchuk AM, Flaherty ML, et al; VISTA Collaboration. **Defining hematoma expansion in intracerebral hemorrhage: relationship with patient outcomes.** *Neurology* 2011;76:1238–44 CrossRef Medline
  19. Kessler LG, Barnhart HX, Buckler AJ, et al; QIBA Terminology Working Group. **The emerging science of quantitative imaging biomarkers terminology and definitions for scientific studies and regulatory submissions.** *Stat Methods Med Res* 2015;24:9–26 CrossRef Medline
  20. Eliasziw M, Young SL, Woodbury MG, et al. **Statistical methodology for the concurrent assessment of interrater and intrarater reliability: using goniometric measurements as an example.** *Phys Ther* 1994;74:777–88 CrossRef Medline
  21. Mitchell J, Karlik S, Lee D, et al. **The variability of manual and computer assisted quantification of multiple sclerosis lesion volumes.** *Med Phys* 1996;23:85–97 CrossRef Medline
  22. Broderick JP, Brott TG, Duldner JE, et al. **Volume of intracerebral hemorrhage: a powerful and easy-to-use predictor of 30-day mortality.** *Stroke* 1993;24:987–93 CrossRef Medline
  23. Hemphill JC 3rd, Bonovich DC, Besmertis L, et al. **The ICH score: a simple, reliable grading scale for intracerebral hemorrhage.** *Stroke* 2001;32:891–97 CrossRef Medline
  24. Xu X, Chen X, Zhang J, et al. **Comparison of the Tada formula with software slicer: precise and low-cost method for volume assessment of intracerebral hematoma.** *Stroke* 2014;45:3433–35 CrossRef Medline
  25. Webb AJ, Ullman NL, Morgan TC, et al; MISTIE and CLEAR Investigators. **Accuracy of the ABC/2 score for intracerebral hemorrhage: systematic review and analysis of MISTIE, CLEAR-IVH, and CLEAR III.** *Stroke* 2015;46:2470–76 CrossRef Medline
  26. Freeman WD, Barrett KM, Bestic JM, et al. **Computer-assisted volumetric analysis compared with ABC/2 method for assessing warfarin-related intracranial hemorrhage volumes.** *Neurocrit Care* 2008; 9:307–12 CrossRef Medline

# Transcranial Duplex Sonography Predicts Outcome following an Intracerebral Hemorrhage

 P. Camps-Renom,  J. Méndez,  E. Granell,  F. Casoni,  L. Prats-Sánchez,  A. Martínez-Domeño,  D. Guisado-Alonso,  J. Martí-Fàbregas, and  R. Delgado-Mederos



## ABSTRACT

**BACKGROUND AND PURPOSE:** Several radiologic features such as hematoma volume are related to poor outcome following an intracerebral hemorrhage and can be measured with transcranial duplex sonography. We sought to determine the prognostic value of transcranial duplex sonography in patients with intracerebral hemorrhage.

**MATERIALS AND METHODS:** We conducted a prospective study of patients diagnosed with spontaneous intracerebral hemorrhage. Transcranial duplex sonography examinations were performed within 2 hours of baseline CT, and we recorded the following variables: hematoma volume, midline shift, third ventricle and lateral ventricle diameters, and the pulsatility index in both MCAs. We correlated these data with the CT scans and assessed the prognostic value of the transcranial duplex sonography measurements. We assessed early neurologic deterioration during hospitalization and mortality at 1-month follow-up.

**RESULTS:** We included 35 patients with a mean age of  $72.2 \pm 12.8$  years. Median baseline hematoma volume was 9.85 mL (interquartile range, 2.74–68.29 mL). We found good agreement and excellent correlation between transcranial duplex sonography and CT when measuring hematoma volume ( $r = 0.791$ ;  $P < .001$ ) and midline shift ( $r = 0.827$ ;  $P < .001$ ). The logistic regression analysis with transcranial duplex sonography measurements showed that hematoma volume was an independent predictor of early neurologic deterioration (OR, 1.078; 95% CI, 1.023–1.135) and mortality (OR, 1.089; 95% CI, 1.020–1.160). A second regression analysis with CT variables also demonstrated that hematoma volume was associated with early neurologic deterioration and mortality. When we compared the rating operation curves of both models, their predictive power was similar.

**CONCLUSIONS:** Transcranial duplex sonography showed an excellent correlation with CT in assessing hematoma volume and midline shift in patients with intracerebral hemorrhage. Hematoma volume measured with transcranial duplex sonography was an independent predictor of poor outcome.

**ABBREVIATIONS:** END = early neurologic deterioration; HV = hematoma volume; ICH = intracerebral hemorrhage; IQR = interquartile range; LV = lateral ventricle; MLS = midline shift; IIIV = third ventricle; TDS = transcranial duplex sonography

Spontaneous intracerebral hemorrhage (ICH) is a major cause of morbidity and mortality,<sup>1</sup> with half of the events related to case fatality occurring within the first 48 hours.<sup>2</sup> Thus, identifying variables that contribute to early neurologic deterioration (END) and mortality is of enormous importance. An early estimation of

the prognosis is crucial for deciding on a treatment plan. Several neuroimaging prognostic factors include hematoma volume (HV), hematoma enlargement, midline shift (MLS), and intraventricular hemorrhage,<sup>3–9</sup> and CT is the technique most frequently used to assess them. However, in the early stages, it can be difficult to monitor these radiologic features with repeat CT due to the clinical and/or hemodynamic state of the patient and the risk of radiation overexposure.

Transcranial duplex sonography (TDS) is a noninvasive technique that provides simultaneous 2D imaging of brain parenchyma and hemodynamic information from the main cerebral arteries. The role of TDS is well-established in the assessment of ischemic stroke, but its usefulness in acute ICH has been reported in only a few studies.<sup>10–15</sup>

Visualization of acute ICH with TDS is feasible: The ICH can be identified as a hyperechoic mass.<sup>10–12</sup> Additionally, TDS allows

Received December 24, 2016; accepted after revision March 27, 2017.

From the Departments of Neurology (P.C.-R., F.C., L.P.-S., A.M.-D., D.G.-A., J.M.-F., R.D.-M.) and Radiology (J.M., E.G.), Biomedical Research Institute Sant Pau, Hospital de la Santa Creu i Sant Pau, Barcelona, Spain.

Paper previously presented at: European Stroke Organization Conference, April 17–19, 2015; Glasgow, UK.

Please address correspondence to Pol Camps-Renom, MD, Department of Neurology, Hospital de la Santa Creu i Sant Pau, Avda Sant Antoni Maria Claret, 167. 08025 Barcelona, Spain; e-mail: pcamps@santpau.cat

 Indicates article with supplemental on-line photos.

<http://dx.doi.org/10.3174/ajnr.A5248>

the assessment of the third ventricle (IIIIV), the lateral ventricles (LVs), MLS, and the presence of intraventricular hemorrhage.<sup>13-16</sup> TDS may have some potential advantages over CT, including the feasibility of performance at the bedside as many times as necessary and regardless of the hemodynamic situation of the patient. Despite a good correlation between TDS and CT having been previously reported,<sup>10-15</sup> the prognostic value of this technique in ICH is yet to be established.

The question of whether TDS may reliably measure ICH characteristics and predict END and mortality following ICH has important implications for clinical practice and research. In the current study, we sought to determine the prognostic value of TDS in patients with acute ICH.

## MATERIALS AND METHODS

We conducted a prospective observational study of consecutive adult patients admitted to our center with the diagnosis of spontaneous ICH during a 1-year period (2012–2013). Patients were included when the time from the onset of symptoms to admission CT was <24 hours and the TDS examination was performed within 2 hours of baseline CT. We excluded patients with primary intraventricular hemorrhage, infratentorial ICH, and secondary ICH related to fibrinolysis, trauma, central venous thrombosis, arteriovenous malformations, or aneurysms. During hospitalization, patients received treatment in accordance with the guidelines of the Spanish Society of Neurology.<sup>16</sup> All patients or their representatives gave written consent to participate in the study.

The following clinical data were collected from all patients at admission: 1) demographics (age and sex); 2) relevant medical history, including hypertension, diabetes, hypercholesterolemia, stroke, coronary artery disease, liver disease, and alcohol abuse; 3) previous treatments; 4) time from the onset of symptoms to admission; 5) admission blood pressure and blood glucose level; 6) NIHSS score and Glasgow Coma Scale score; and 7) results of blood tests including hematocrit level, hemoglobin level, white cell count, platelet count, electrolytes, glomerular filtration rate, liver function, and a basic hemostatic study (international normalized ratio and activated partial thromboplastin time).

### Neurosonographic Methods

A single experienced examiner (P.C.-R.) was trained in a Neurosonology Laboratory by R.D.-M. and J.M.-F. for 6 months before study initiation and was certified in Neurosonology by the Spanish Society of Neurology. The TDS examinations were performed with a CX50 Ultrasound (Philips Healthcare, Best, the Netherlands) with a sectorial probe with a 2- to 5-MHz range. For the explorations, the probe was set up at 5 MHz and placed on the contralateral temporal bone window with a penetration depth of 14–16 cm. The transducer was skewed approximately 10° upward to visualize the contralateral skull bone, and from there, insonation planes were adapted according to the hematoma location. Image brightness, contrast, and time-gain compensation were adjusted to get the best image. ICH was identified as a hyperechoic mass. The examiner was blinded to the CT findings, and he or she was informed only of the side of the ICH (left or right).

We recorded the following neurosonologic variables: 1) the longitudinal (*A*), axial (*B*), and coronal (*C*) diameters of the ICH as previously reported<sup>11</sup>; 2) HV, calculated with the formula  $A \times B \times C/2^{17}$ ; 3) IIIIV diameter, visualized at a depth of 6–8 cm and identified by its parallel hyperechoic margins and the surrounding hypoechoic thalami<sup>13</sup>; 4) MLS, calculated with the following formula:  $(A - B)/2$  (*A* and *B* being the distances between the transducer and the IIIIV, on each side of the skull); 5) LV axial diameter, visualized as 2 anterior and lateral hyperechoic margins corresponding to the frontal horns, which can be observed skewing the transducer upward from the IIIIV plane<sup>14</sup>; and 6) the pulsatility index in both proximal MCAs, calculated with the following formula:  $(\text{Peak Systolic Velocity} - \text{End Diastolic Velocity})/\text{Mean Velocity}$  at a depth of 4.5–5.5 cm. Figure 1 shows an example of 2 ICHs assessed with TDS. Examples showing the MLS, the IIIIV, and LV diameters and the pulsatility index measurements are provided in On-line Fig 1.

### CT

All CT scans were obtained with a 16-section CT scanner. The following variables were assessed by 2 experienced radiologists (J. M. and E.G.): 1) HV, also calculated by  $A \times B \times C/2^{17}$ ; 2) IIIIV diameter; 3) MLS; and 4) LV diameter.

### Follow-Up Variables

We collected the following data: 1) END, defined as a decrease of >1 point in the Glasgow Coma Scale score and/or an increase of  $\geq 4$  points in the NIHSS score within the first 72 hours; and 2) mortality at the 1-month follow-up.

### Statistical Analysis

Data are reported with mean and SD for quantitative variables, median and interquartile range for quantitative ordinal variables, and percentages for categoric variables. A logarithmic transformation of the variable HV was used to approximate the normal distribution. Correlations between measurements were assessed by the Pearson correlation coefficient, and Bland-Altman plots were performed to evaluate the agreement between CT and TDS. Comparison of variables was performed with contingency tables with the  $\chi^2$  test for categoric variables, the Student *t* test for quantitative variables with a normal distribution, and the Mann-Whitney *U* test when a nonparametric test was required. Only variables showing a significant trend ( $P < .1$ ) in the bivariate analyses were entered in the multivariable logistic regression model and were backward eliminated to a significance level of .05. Collinear factors (as measured through the variance inflation factor) were removed when appropriate. We conducted 2 different logistic regression analyses to construct a predictive model of END and mortality: one with the radiologic variables measured with CT and the other with the same variables calculated with TDS. This approach was used to avoid autocorrelation between variables measuring the same parameters.  $P < .05$  was considered statistically significant.

## RESULTS

During the study period, we screened 59 patients: Five were excluded due to the absence of a temporal bone window, 2 died

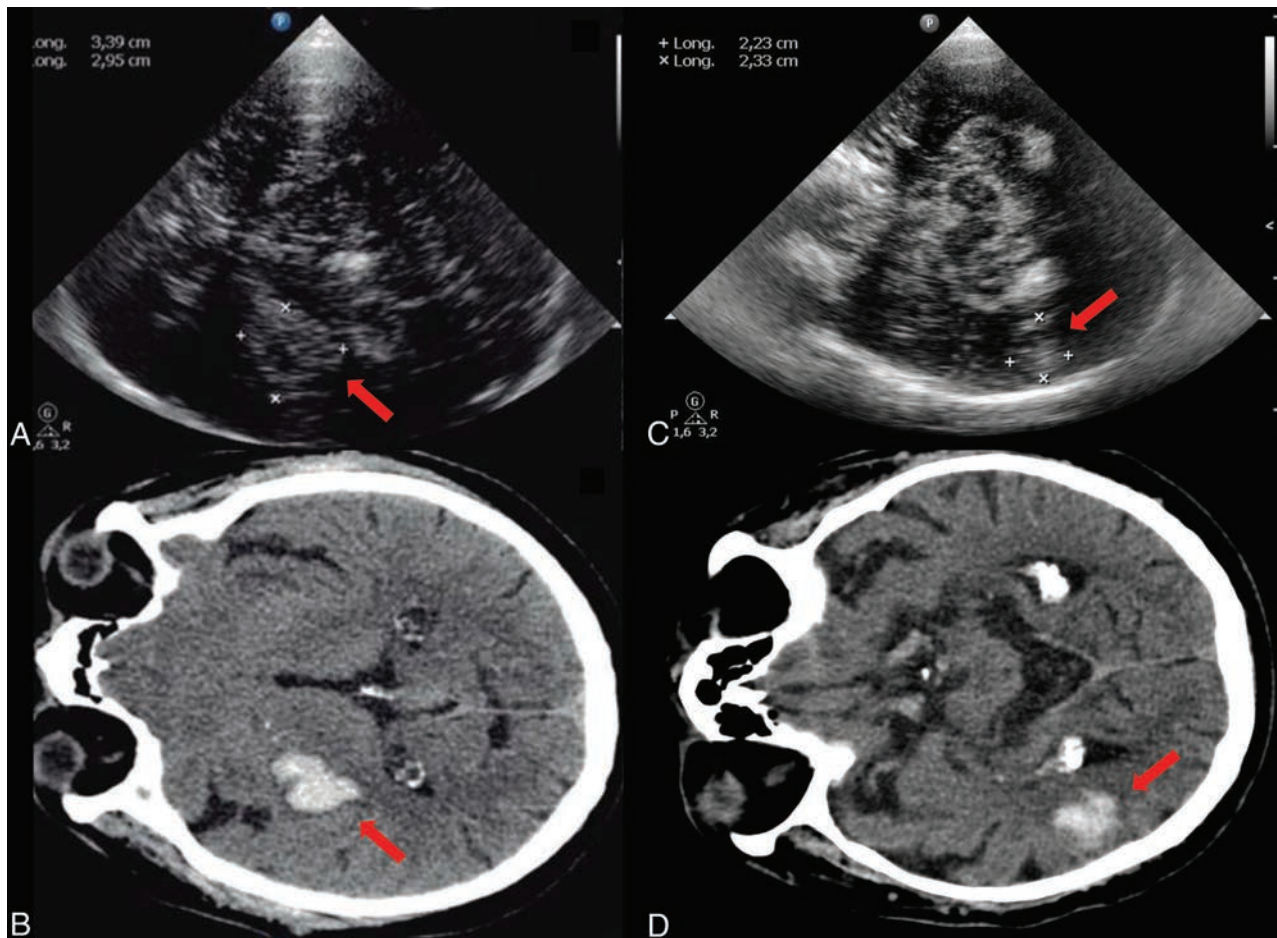


**FIG 1.** A and B, A right basal ganglia hemorrhage, assessed by TDS and CT, respectively. The red arrows correspond to the axial and longitudinal diameters. C and D, A right temporal lobar ICH in another patient, assessed by TDS and CT, respectively.

**Table 1: Clinical and radiologic characteristics of the patients**

Characteristics	
Men (No.) (%)	23 (65.7)
Age (mean) (SD) (yr)	72.2 (12.8)
Hypertension (No.) (%)	17 (48.6)
Diabetes mellitus (No.) (%)	5 (14.3)
Dyslipidemia (No.) (%)	10 (28.6)
Previous ischemic stroke (No.) (%)	4 (11.4)
Previous ICH (No.) (%)	2 (5.7)
Coronary artery disease (No.) (%)	3 (8.6)
Atrial fibrillation (No.) (%)	4 (11.4)
Glomerular filtration rate <30 mL/min (No.) (%)	2 (5.7)
Alcohol abuse (>80 g/day) (No.) (%)	1 (2.9)
Smoking (No.) (%)	7 (20)
Liver disease (No.) (%)	1 (2.9)
Prior antiplatelet therapy (No.) (%)	6 (17.1)
Previous use of oral anticoagulants (No.) (%)	4 (11.4)
Previous use of atorvastatin (No.) (%)	3 (8.6)
NIHSS score at admission (median) (IQR)	11 (3.5–19)
GCS at admission (median) (IQR)	15 (13–15)
Systolic blood pressure (mean) (SD) (mm Hg)	168.1 (32.8)
Blood glucose level (mean) (SD) (mg/dL)	137.8 (47.5)
Platelet count/mm <sup>3</sup> (mean) (SD)	220,469 (75,971)
Lobar ICH (No.) (%)	16 (45.7)
IVH (No.) (%)	10 (28.6)
HV (mL) (median) (IQR)	9.85 (2.74–68.29)

**Note:**—GCS indicates Glasgow Coma Scale; IVH, intraventricular hemorrhage.

before the TDS examination could be performed, 15 were excluded because the TDS examination was not available within 2 hours of the baseline CT or the patient underwent surgical evac-

uation before TDS could be performed, and eventually 2 patients were excluded because the ICH was not identified despite presentation of a reasonable temporal bone window. We finally included 35 patients with a mean age of  $72.2 \pm 12.8$  years; 23 (65.7%) were men. In 25 (71.4%) patients, the time from the onset of symptoms to baseline CT was <6 hours. Clinical and radiologic characteristics of the patients are detailed in Table 1. The median baseline NIHSS score was 11 (interquartile range [IQR], 3.5–19), and prior antithrombotic therapy was observed in 10 (28.6%) patients: Six (17.1%) were receiving aspirin and 4 (11.4%) were taking warfarin before admission.

There were 16 (45.7%) lobar (6 frontal, 6 parietal, 2 temporal, and 2 occipital) and 19 (54.3%) deep ICHs. The median HV was 9.85 mL (IQR, 2.74–68.29 mL) assessed with CT and 14.46 mL (IQR, 4.96–39.42 mL) as determined by TDS. As described in the “Materials and Methods,” all patients underwent a TDS examination within 2 hours of the baseline CT. We found an excellent correlation between the baseline TDS examination and the CT when measuring the HV ( $r = 0.791, P < .001$ ) and, separately, the longitudinal ( $r = 0.711, P < .001$ ), axial ( $r = 0.768, P < .001$ ), and coronal diameters ( $r = 0.754, P < .001$ ) (Fig 2). We repeated the same analysis dividing the population by ICH location, and the correlation remained excellent in both groups ( $r = 0.792, P < .001$  for the lobar ICH and  $r = 0.805, P < .001$  for the deep ICH).

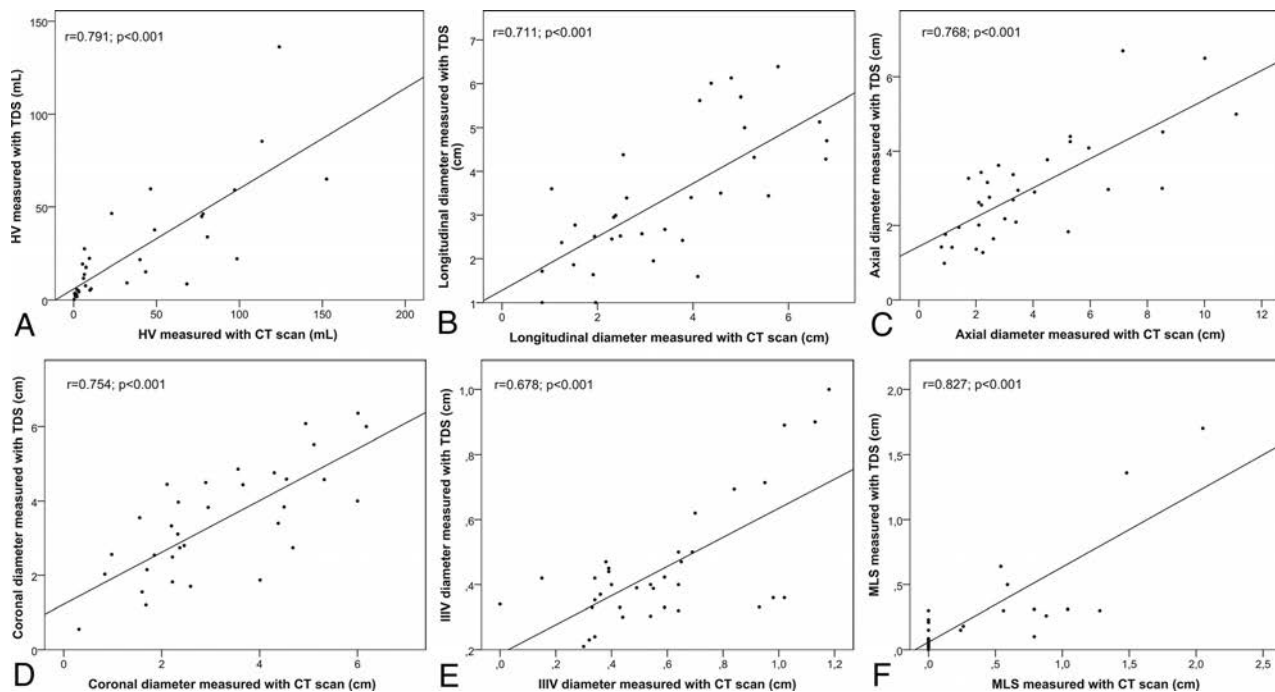


**FIG 2.** Correlation of measurements between CT and TDS.

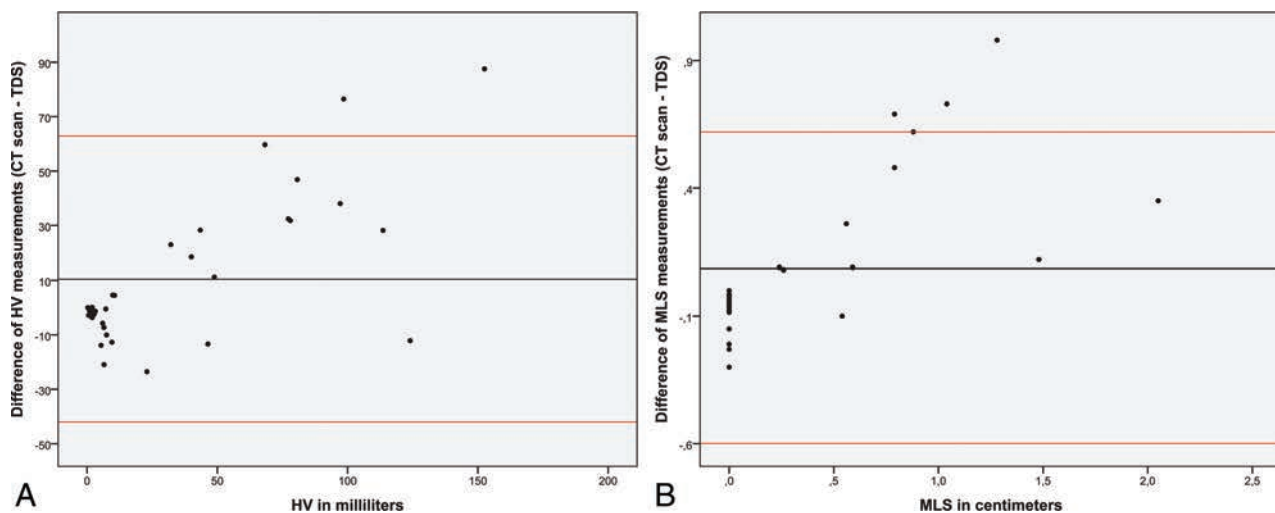


**FIG 3.** Bland-Altman plots comparing the difference between the measurements obtained by CT and TDS when assessing HV (A) and MLS (B). The horizontal black lines demonstrate the mean difference, and the red lines show the 95% confidence interval.

We also observed an excellent correlation when analyzing the IIIV diameter ( $r = 0.678, P < .001$ ) and the MLS ( $r = 0.827, P < .001$ ). Conversely, CT and TDS showed no correlation when measuring the LV diameter ( $r = 0.196, P = .327$ ).

For further comparison between techniques, we conducted a 1-sample  $t$  test contrast of the difference between the measurements obtained by CT and TDS. There were no significant differences when contrasting HV measurements (mean difference =  $-0.077; P = .624$ ) and MLS (mean difference =  $0.086; P = .134$ ). Conversely, despite showing a good correlation, the 2 techniques presented significant differences when measuring IIIV diameter (mean difference =  $0.132; P = .001$ ). We also constructed Bland-Altman plots with the HV and the MLS measurements (Fig 3). Most interesting, despite finding good agreement between tech-

niques, we detected a systematic bias between both techniques when measuring HV: TDS tended to overestimate the volumes of smaller ICH and, contrariwise, to underestimate volumes in larger ICHs.

During hospitalization, 9 (25.7%) patients presented with END during the first 3 days. Table 2 provides details of the patients presenting with and without END. Remarkably, prior antiplatelet therapy ( $P = .017$ ) was more frequently reported in patients presenting with END. Additionally, baseline HV measured with CT ( $P = .002$ ), baseline HV measured with TDS ( $P = .001$ ), baseline MLS assessed with CT ( $P = .018$ ), and baseline MLS calculated with TDS ( $P = .007$ ) showed an association with the probability of END. In the first logistic regression analysis with CT variables, only baseline HV showed an independent associa-

**Table 2: Differences between patients presenting with and without END**

	END (n = 9)	No END (n = 26)	P
Men (No.) (%)	6 (66.7)	17 (65.4)	.944
Age (mean) (SD) (yr)	72.56 (13.78)	72.12 (12.74)	.931
Prior antiplatelet therapy (No.) (%)	4 (44.4)	2 (8.3)	.017
Prior anticoagulant therapy (No.) (%)	1 (11.1)	3 (12.5)	.913
Systolic BP at admission (mean) (SD) (mm Hg)	166.63 (37.82)	168.64 (31.77)	.885
Blood glucose level at admission (mean) (SD) (mg/dL)	152.13 (23.09)	133.06 (52.78)	.334
Platelet count/mm <sup>3</sup> at admission (mean) (SD)	240,000 (87.311)	213,958 (72.678)	.41
Baseline HV measured with CT (median) (IQR) (mL)	97.14 (35.9–118.8)	6.85 (1.96–34.13)	.002
Baseline MLS measured with CT (median) (IQR) (cm)	0.59 (0–1.38)	0 (0–0.24)	.018
Significant HG assessed with CT (No.) (%) <sup>a</sup>	1 (33.3)	1 (6.3)	.298
Baseline HV measured with TDS (median) (IQR) (mL)	46.48 (29.83–75.21)	8.62 (4.08–20.38)	.001
Baseline MLS measured with TDS (median) (IQR) (cm)	0.31 (0.3–1.36)	0.09 (0.05–0.2)	.007
Pulsatility index from the ipsilateral MCA (mean) (SD) (cm/s)	1.47 (0.5)	1.19 (0.31)	.162
Pulsatility index from the contralateral MCA (mean) (SD) (cm/s)	1.33 (0.34)	1.12 (0.28)	.073
Lobar localization (No.) (%)	6 (66.7)	10 (38.5)	.245
IVH (No.) (%)	4 (44.4)	6 (23.1)	.393

**Note:**—BP indicates blood pressure; HG, hematoma growth.

<sup>a</sup> Analysis was restricted to 21 patients for whom a follow-up CT was available.

**Table 3: Variables associated with mortality at 1-month follow-up**

	Mortality (n = 7)	Survival (n = 28)	P
Men (No.) (%)	4 (57.1)	19 (67.9)	.593
Age (mean) (SD) (yr)	77.43 (10.85)	70.93 (13.1)	.235
Prior antiplatelet therapy (No.) (%)	2 (28.6)	4 (15.4)	.422
Prior anticoagulant therapy (No.) (%)	1 (14.3)	3 (11.5)	.843
Previous use of statins (No.) (%)	1 (14.3)	2 (7.7)	.590
Baseline NIHSS (median) (IQR)	23 (16–24)	7 (3–14)	<.001
Baseline GCS (median) (IQR)	10 (4–15)	15 (15–15)	.007
Systolic BP at admission (mean) (SD) (mm Hg)	164.86 (37.9)	169.09 (31.99)	.771
Blood glucose level at admission (mean) (SD) (mg/dL)	152 (20.14)	133.86 (52.34)	.381
Platelet count/mm <sup>3</sup> at admission (mean) (SD)	222,714 (89,582)	219,840 (73,803)	.931
Baseline HV measured with CT (median) (IQR) (mL)	98.51 (80.68–124.01)	6.85 (1.95–38.06)	<.001
Baseline MLS measured with CT (median) (IQR) (cm)	0.88 (0.56–1.48)	0 (0–0.18)	.001
Significant HG assessed with CT (No.) (%) (mL) <sup>a</sup>	1 (100)	1 (5.6)	.105
Baseline HV measured with TDS (median) (IQR)	59.13 (33.82–85.42)	8.62 (3.69–21.56)	<.001
Baseline MLS measured with TDS (median) (IQR) (cm)	0.4 (0.29–1.45)	0.09 (0.04–0.16)	.001
Pulsatility index from the ipsilateral MCA (mean) (SD) (cm/s)	1.54 (0.45)	1.2 (0.34)	.033
Pulsatility index from the contralateral MCA (mean) (SD) (cm/s)	1.37 (0.36)	1.12 (0.27)	.058
Lobar localization (No.) (%)	6 (85.7)	10 (35.7)	.018
IVH (No.) (%)	4 (44.4)	6 (23.1)	.393

**Note:**—GCS indicates Glasgow Coma Scale; IVH, intraventricular hemorrhage; BP, blood pressure; HG, hematoma growth.

<sup>a</sup> Analysis was restricted to 21 patients for whom a follow-up CT scan was available.

tion with END (OR, 1.043; 95% CI, 1.015–1.071). Most interesting, in the logistic regression analysis with the TDS variables, we also found that baseline HV (OR, 1.078; 95% CI, 1.023–1.135) was the only variable included in the final model. In both models, HV remained independently associated with END after adjusting for age and the baseline Glasgow Coma Scale. The receiver operating characteristic curve showed that the best threshold to predict END was an HV of 47.62 mL as assessed with CT (77.8% sensitivity and 88.5% specificity) and an HV of 21.80 mL as measured with TDS (88.9% sensitivity and 80% specificity). When we compared the receiver operating characteristic curves of both models, the predictive power was similar between them, and no significant differences were observed when contrasting the 2 areas under the curve (On-line Fig 2).

At the 1-month follow-up, 7 (20%) patients had died. Variables associated with mortality are shown in Table 3. Remarkably, baseline HV measured with CT ( $P < .001$ ), baseline HV measured with TDS ( $P < .001$ ), baseline MLS assessed with CT ( $P = .001$ ), and baseline MLS calculated with TDS ( $P = .001$ ) showed an

association with the risk of mortality. In addition, the pulsatility index from the ipsilateral MCA also showed an association with mortality risk ( $P = .033$ ). Finally, lobar localization ( $P = .018$ ), baseline NIHSS scores ( $P < .001$ ), and Glasgow Coma Scale scores ( $P = .007$ ) were variables also found to be related to the risk of mortality. In the first logistic regression model with CT variables, only baseline HV showed an independent association with mortality (OR, 1.064; 95% CI, 1.017–1.112). Most interesting, in the logistic regression model with the TDS variables, we once again found that baseline HV (OR, 1.089; 95% CI, 1.020–1.160) was the only variable included in the final model. The receiver operating characteristic curves of both models showed that the best threshold to predict mortality at 1-month follow-up was an HV of 47.62 mL as assessed with CT (85.7% sensitivity and 85.7% specificity) and an HV of 30.63 mL as measured with TDS (85.7% sensitivity and 82.2% specificity). Again, as shown in On-line Fig 2, the predictive power of both models was similar, and no significant differences were observed when contrasting both areas under the curve.

## DISCUSSION

We aimed to determine the prognostic value of TDS in a prospective cohort of patients presenting with spontaneous ICH. Our study confirms previously reported data concerning the strong correlation between TDS and CT and adds new information regarding the prognostic value of this technique in patients with ICH.

ICH is a devastating condition, and several radiologic features may predict poor outcome. Currently, the widespread availability of CT allows a rapid and reliable assessment of these variables. However, ICH is a dynamic process, and it can be difficult to monitor complications with repeat CT scans due to the clinical status of the patient. This issue led to interest in TDS, which may represent a viable, noninvasive alternative to CT and can be easily performed at the bedside.

Some previous studies have reported a good correlation between TDS and CT in measuring HV and other intracranial structures.<sup>11-13</sup> In accordance with these studies, we found an excellent correlation between CT and TDS when measuring HV and its longitudinal, axial, and coronal diameters, as well as MLS and the IIIV diameter. Conversely, we were unable to demonstrate a good correlation when measuring the LV diameter. Our results disagree with findings in previous studies that reported a good correlation.<sup>14,15</sup> A possible explanation for this discrepancy may be the difficulty in visualizing the real margins of the LV when skewing the transducer upward from the IIIV, which results in considerable variability in the measures.

In addition to the correlation analysis, our study presents new information regarding the agreement between both techniques. We found good agreement when measuring HV and MLS, but the IIIV measurements presented a significant difference between CT and TDS. In addition, we observed a systematic bias when assessing HV: TDS tended to overestimate the volumes of smaller ICHs and, contrariwise, to underestimate volumes in larger ICHs. Thus, TDS may be a useful complementary diagnostic tool but may not substitute for CT as the criterion standard technique to assess ICH characteristics.

In addition to the morphologic information, TDS allows assessment of some hemodynamic parameters, such as the pulsatility index, which has been related to increased intracranial pressure. Remarkably, in the univariate analysis, we found that the pulsatility index from the ipsilateral MCA was associated with the risk of mortality. Our results are in accordance with a previous study that assessed the prognostic value of the pulsatility index in an ICH,<sup>18</sup> though that study used transcranial Doppler and found a significant association between mortality and the pulsatility index from the contralateral MCA.

Baseline HV has been recognized as a major determinant of outcome in patients with acute ICH.<sup>4</sup> Remarkably, we found that HV measured with TDS was an independent predictor of END and mortality. The predictive power of the logistic regression model with TDS variables was similar to that of the same model with CT measurements. Therefore, it is prudent to conclude that TDS may be regarded as a potential tool for the noninvasive monitoring of these patients.

We must be aware of the limitations of TDS, including examiner dependency, susceptibility to an insufficient temporal bone

window, low spatial resolution, and possible imaging artifacts. Additionally, some specific limitations occur when assessing ICH, including the loss of echogenicity of the blood with time and the difficulty in evaluating the hematoma in some locations, for example in the infratentorial structures. These drawbacks designate TDS as a complementary diagnostic tool; CT remains the most reliable examination in acute ICH. Nevertheless, a TDS examination following the baseline CT may allow neurologists to monitor the HV at the bedside, regardless of the clinical status of the patient, and to avoid constant transfers to the CT room.

Our study has several limitations, including the small sample size, the limited follow-up of the patients, and the absence of a follow-up TDS examination, which prevented us from assessing hematoma expansion. In addition, a single examiner performed the TDS examinations; thus, we were not able to assess interrater reliability. Finally, we excluded patients who died before a TDS could be performed or who underwent surgical evacuation, which may represent a selection bias.

## CONCLUSIONS

TDS showed an excellent correlation with CT in assessing HV, MLS, and IIIV diameters in an acute ICH. HV measured with TDS was an independent predictor of poor outcome with a predictive power similar to that of CT. Further studies are warranted to continue testing TDS as a complementary technique for monitoring ICH and to establish whether this monitoring may improve clinical outcomes.

## ACKNOWLEDGMENT

We acknowledge Carly Calvert for English grammar revision.

Disclosures: Joan Martí-Fàbregas—UNRELATED: Consultancy: Boehringer Ingelheim, Bayer Pharma AG, Daichii Sankyo, Pfizer; Employment: Hospital Santa Creu i Sant Pau; Expert Testimony: Boehringer Ingelheim, Bayer Pharma AG, Daichii Sankyo, Pfizer; Grants/Grants Pending: Instituto de Salud Carlos III (RETICS INVICTUS PLUS RD16/0019/0010).

## REFERENCES

1. van Asch CJ, Luitse MJ, Rinkel GJ, et al. **Incidence, case fatality, and functional outcome of intracerebral haemorrhage over time, according to age, sex, and ethnic origin: a systematic review and meta-analysis.** *Lancet Neurol* 2010;9:167–76 CrossRef Medline
2. Balami JS, Buchan AM. **Complications of intracerebral haemorrhage.** *Lancet Neurol* 2012;11:101–18 CrossRef Medline
3. Leira R, Dávalos A, Silva Y, et al; Stroke Project, Cerebrovascular Diseases Group of the Spanish Neurological Society. **Early neurologic deterioration in intracerebral hemorrhage: predictors and associated factors.** *Neurology* 2004;63:461–67 CrossRef Medline
4. Mayer SA, Sacco RL, Shi T, et al. **Neurologic deterioration in non-comatose patients with supratentorial intracerebral hemorrhage.** *Neurology* 1994;44:1379–84 CrossRef Medline
5. Hemphill JC 3rd, Bonovich DC, Besmertis L, et al. **The ICH score: a simple, reliable grading scale for intracerebral hemorrhage.** *Stroke* 2001;32:891–97 CrossRef Medline
6. Rost NS, Smith EE, Chang Y, et al. **Prediction of functional outcome in patients with primary intracerebral hemorrhage: the FUNC score.** *Stroke* 2008;39:2304–09 CrossRef Medline
7. Davis SM, Broderick J, Hennerici M, et al; Recombinant Activated Factor VII Intracerebral Hemorrhage Trial Investigators. **Hematoma growth is a determinant of mortality and poor outcome after intracerebral hemorrhage.** *Neurology* 2006;66:1175–81 CrossRef Medline
8. Tuhirim S, Horowitz DR, Sacher M, et al. **Volume of ventricular blood is**

- an important determinant of outcome in supratentorial intracerebral hemorrhage.** *Crit Care Med* 1999;27:617–21 [CrossRef Medline](#)
9. Brott T, Broderick J, Kothari R, et al. **Early hemorrhage growth in patients with intracerebral hemorrhage.** *Stroke* 1997;28:1–5 [CrossRef Medline](#)
  10. Becker G, Winkler J, Hofmann E, et al. **Differentiation between ischemic and hemorrhagic stroke by transcranial color-coded real-time sonography.** *J Neuroimaging* 1993;3:41–47 [CrossRef Medline](#)
  11. Pérez ES, Delgado-Mederos R, Rubiera M, et al. **Transcranial duplex sonography for monitoring hyperacute intracerebral hemorrhage.** *Stroke* 2009;40:987–90 [CrossRef Medline](#)
  12. Kiphuth IC, Huttner HB, Breuer L, et al. **Sonographic monitoring of midline shift predicts outcome after intracerebral hemorrhage.** *Cerebrovasc Dis* 2012;34:297–304 [CrossRef Medline](#)
  13. Seidel G, Kaps M, Gerriets T, et al. **Evaluation of the ventricular system in adults by transcranial duplex sonography.** *J Neuroimaging* 1995;5:105–08 [CrossRef Medline](#)
  14. Kiphuth IC, Huttner HB, Struffert T, et al. **Sonographic monitoring of ventricular enlargement in posthemorrhagic hydrocephalus.** *Neurology* 2011;76:858–62 [CrossRef Medline](#)
  15. Becker G, Bogdahn U, Strassburg HM, et al. **Identification of ventricular enlargement and estimation of intracranial pressure by transcranial color-coded real-time sonography.** *J Neuroimaging* 1994;4:17–22 [CrossRef Medline](#)
  16. Rodríguez-Yañez M, Castellanos M, Freijo MM, et al. **Clinical practice guidelines in intracerebral haemorrhage** [in English, Spanish]. *Neurologia* 2013;28:236–49 [CrossRef Medline](#)
  17. Kothari RU, Brott T, Broderick JP, et al. **The ABCs of measuring intracerebral hemorrhage volumes.** *Stroke* 1996;27:1304–05 [CrossRef Medline](#)
  18. Martí-Fàbregas J, Belvis R, Guardia E, et al. **Prognostic value of pulsatility index in acute intracerebral hemorrhage.** *Neurology* 2003;61:1051–56 [CrossRef Medline](#)

# Perfusion MR Imaging Using a 3D Pulsed Continuous Arterial Spin-Labeling Method for Acute Cerebral Infarction Classified as Branch Atheromatous Disease Involving the Lenticulostriate Artery Territory

Y. Shinohara, A. Kato, K. Kuya, K. Okuda, M. Sakamoto, H. Kowa, and T. Ogawa

## ABSTRACT

**BACKGROUND AND PURPOSE:** Branch atheromatous disease is a stroke subtype considered a risk factor for early neurologic deterioration. Meanwhile, crossed cerebellar diaschisis is thought to be influenced by the degree and location of supratentorial perfusion abnormalities and is associated with the clinical outcome in the case of an ischemic stroke. In this article, our aim was to clarify the utility of using a whole-brain 3D pulsed continuous arterial spin-labeling method as an imaging biomarker for predicting neurologic severity in branch atheromatous disease.

**MATERIALS AND METHODS:** Twenty-three patients with branch atheromatous disease in the lenticulostriate artery territory were enrolled. All patients underwent MR imaging, including DWI, 3D-TOF-MRA, and 3D-arterial spin-labeling. We measured the asymmetry index of CBF in the affected area (branch atheromatous disease), the asymmetry index of the contralateral cerebellar hemisphere (crossed cerebellar diaschisis), and the DWI infarct volume in the lenticulostriate artery territory. We also compared each parameter with the initial NIHSS score with the Pearson correlation coefficient.

**RESULTS:** Among the 23 patients, we found no correlation between NIHSS score and the asymmetry index of CBF in the affected area (branch atheromatous disease) ( $r = -0.027, P = .724$ ), whereas the asymmetry index of the contralateral cerebellar hemisphere (crossed cerebellar diaschisis) and DWI infarct volumes were significantly correlated with NIHSS score ( $r = 0.515, P = .012$ ;  $r = 0.664, P = .001$ , respectively).

**CONCLUSIONS:** In patients with branch atheromatous disease, 3D-arterial spin-labeling can detect crossed cerebellar diaschisis, which is correlated with the degree of neurologic severity.

**ABBREVIATIONS:**  $AI_{BAD}$  = asymmetry index of the affected area (branch atheromatous disease);  $AI_{CCD}$  = asymmetry index of the contralateral cerebellar hemisphere (crossed cerebellar diaschisis); ASL = arterial spin-labeling; BAD = branch atheromatous disease; CCD = crossed cerebellar diaschisis; END = early neurologic deterioration; LSA = lenticulostriate artery; ref = reference

Intracranial branch atheromatous disease (BAD) is a stroke subtype that was first described in 1989.<sup>1</sup> BAD was originally determined on the basis of pathologic findings of occlusion or stenosis at the origin of a deep penetrating artery due to the presence of a microatheroma or a junctional plaque.<sup>2,3</sup> Representative vascular territories of BAD include the lenticulostriate artery (LSA), the pontine paramedian artery, and sometimes the anterior choroidal

artery.<sup>4,5</sup> Previous studies have mentioned that BAD is strongly associated with early neurologic deterioration (END), and some patients with BAD may experience a worsening of neurologic deficits despite intensive medical treatment, resulting in a worse functional outcome.<sup>6-10</sup> Although few pathologic studies for BAD have been reported, some articles have investigated its neuroradiologic characteristics, with MR imaging in particular.<sup>7-10</sup>

Arterial spin-labeling (ASL) is a noninvasive MR perfusion imaging technique that uses magnetically labeled blood as an intrinsic tracer.<sup>11-13</sup> ASL permits a quantitative measurement of cerebral perfusion and repetitive acquisitions with independent labeling because it requires neither an injection of a contrast medium nor radiation exposure.<sup>11-13</sup> 3D-ASL is considered an advanced method for ASL and uses pulsed continuous arterial spin-labeling with a volumetric spiral fast spin-echo readout, which enables the acquisition of high signal-to-noise ratio and quantitative whole-brain perfusion images.<sup>13,14</sup>

Received November 19, 2016; accepted after revision March 27, 2017.

From the Division of Radiology (Y.S., A.K., K.K., T.O.), Department of Pathophysiological and Therapeutic Science, Faculty of Medicine; Division of Clinical Radiology (K.O.); Division of Neurosurgery (M.S.), Department of Brain and Neurosciences, Faculty of Medicine; and Division of Neurology (H.K.), Department of Brain and Neurosciences, Faculty of Medicine, Tottori University, Yonago, Japan.

Please address correspondence to Yuki Shinohara, MD, Division of Radiology, Department of Pathophysiological and Therapeutic Science, Faculty of Medicine, Tottori University, 36-1 Nishi-cho, Yonago 683-8504, Japan; e-mail: shino-y@olive.plala.or.jp

<http://dx.doi.org/10.3174/ajnr.A5247>

Previous articles have suggested that 3D-ASL is useful for evaluating cerebral ischemia.<sup>12,15</sup> To the best of our knowledge, no report has used ASL imaging findings to assess BAD, and a few articles have examined the neuroradiologic features of BAD that are related to END.<sup>6-8</sup> In addition, some studies using <sup>15</sup>O-positron-emission tomography and perfusion CT imaging have indicated that crossed cerebellar diaschisis (CCD) occurrence is influenced by the degree and location of the supratentorial perfusion abnormalities and is associated with the clinical outcome.<sup>16,17</sup> Therefore, we hypothesized that perfusion abnormalities detected with 3D-ASL, including CCD, might be correlated with the degree of neurologic deterioration despite the small lesions found with BAD. The aim of our study is to clarify the utility of whole-brain 3D-ASL as an imaging biomarker for predicting the neurologic severity in BAD.

## MATERIALS AND METHODS

### Patients

This retrospective study analyzed data obtained from patients with acute cerebral infarctions who were admitted to our institution between October 2012 and November 2016. Patients were eligible if they met the following criteria: The NIHSS score on admission was obtained by stroke physicians; MR imaging, including 3D-ASL, DWI, and 3D-TOF-MRA, was performed; subtypes of intracranial BAD in the LSA region defined as a lesion of  $\geq 15$  mm in diameter and visible on  $>3$  sections were observed on DWI<sup>9</sup>; there was no occlusion or severe stenosis ( $\geq 50\%$ ) in the horizontal segment of the MCA on the MRA; and cardioembolism and large-artery atherosclerosis based on clinical features and other examinations, such as the pattern of symptom onset, resting electrocardiography, continuous electrocardiographic monitoring, transthoracic echocardiography, transesophageal echocardiography, and carotid ultrasonography, were excluded.<sup>18</sup> Our institutional review board approved this study and waived the need for written informed consent because of its retrospective design.

### Imaging Examinations

All MR imaging examinations were performed with a 3T MR imaging system (Discovery MR750w; GE Healthcare, Milwaukee, Wisconsin). For 3D-ASL, DWI, and MRA, the scanning parameters were the following: 3D-ASL: TR, 4554 ms; TE, 10.7 ms; FOV, 24 cm; matrix,  $512 \times 512$ ; section thickness, 4.0 mm; postlabel delay, 1525 ms; acquisition time, 1 minute 31 seconds; DWI: TR, 7000 ms; TE, 10.7 ms; FOV, 21 cm; matrix,  $128 \times 128$ ; section thickness, 5.0 mm; maximum b factor,  $1000 \text{ mm}^2/\text{s}$ ; acquisition time, 56 seconds; MRA: TR, 20 ms; TE, 3.4 ms; FOV, 20 cm; matrix,  $384 \times 224$ ; section thickness, 1.0 mm; acquisition time, 4 minutes 36 seconds.

### Image Analysis

3D-ASL maps were registered to DWIs by linear transformations (translation and rotation) by using SPM8 (<http://www.fil.ion.ucl.ac.uk/spm/software/spm8>). BAD lesions in the section of the largest infarcted area of the LSA territory were outlined semiautomatically to measure the regional CBF (milliliter/100 mL/min) on 3D-ASL (ASL-BAD) according to the consensus of 2 neuroradiologists (Y.S. and A.K., with 13 and 5 years of experience in

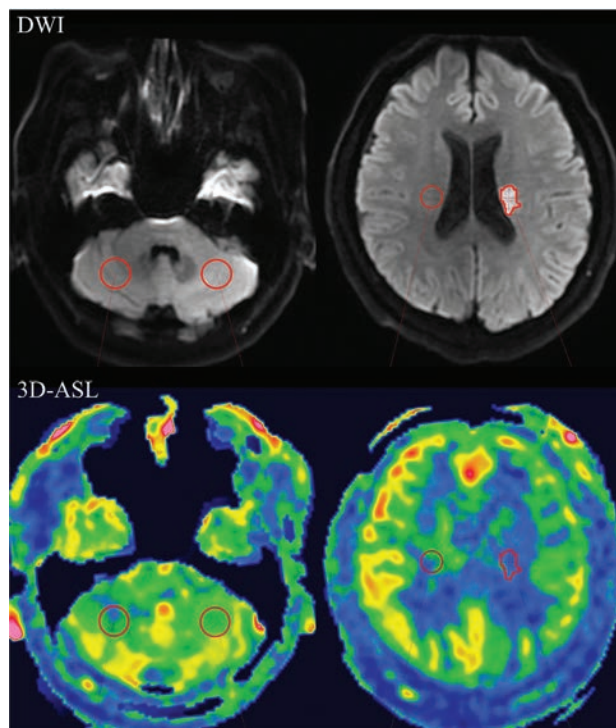


**FIG 1.** Representative sections of 3D-ASL images registered to the DWIs are shown with the locations of ROIs outlined with red circles. On the section of the middle cerebellar peduncles and pons, elliptic ROIs are marked on the bilateral cerebellum. On the section of the largest infarcted area, semiautomated ROI segmentation was performed in the affected area and an elliptic ROI was placed in the contralateral corona radiata.

diagnostic neuroradiology, respectively). ROIs with an elliptic shape were also marked on the contralateral corona radiata from the BAD lesions (ASL-BAD<sub>reference[ref]</sub>) and in the bilateral cerebellar hemispheres in the section of the middle cerebellar peduncles and pons (ASL-CCD and ASL-CCD<sub>ref</sub>) (Fig 1). The asymmetry index of the 3D-ASL based on the affected lesion was obtained as follows: asymmetry index of the affected area (branch atheromatous disease, AI<sub>BAD</sub>) or asymmetry index of the contralateral cerebellar hemisphere (crossed cerebellar diaschisis, AI<sub>CCD</sub>) = (ASL-BAD<sub>ref</sub> or -CCD<sub>ref</sub> - ASL-BAD or -CCD)/(ASL-BAD<sub>ref</sub> or -CCD<sub>ref</sub> + ASL-BAD or -CCD)  $\times 100$  (%). DWI infarct volume measurements of BAD were performed with a semiautomated commercially available image-analysis program (AnalyzePro; AnalyzeDirect, Overland Park, Kansas).

### Statistical Analysis

Linear regression analyses and Pearson correlation coefficients were used to compare the admission NIHSS score with each asymmetry index and DWI infarct volume. Each correlation was analyzed by using SPSS software (Version 23.0; IBM, Armonk, New York).  $P < .05$  was statistically significant.

## RESULTS

Twenty-three patients met our study criteria. Seventeen (73.9%) patients were men, and 10 (43.5%) lesions involved the left hemisphere. The mean patient age was  $69.3 \pm 13.3$  years. The mean interval between symptom onset and MR imaging examination

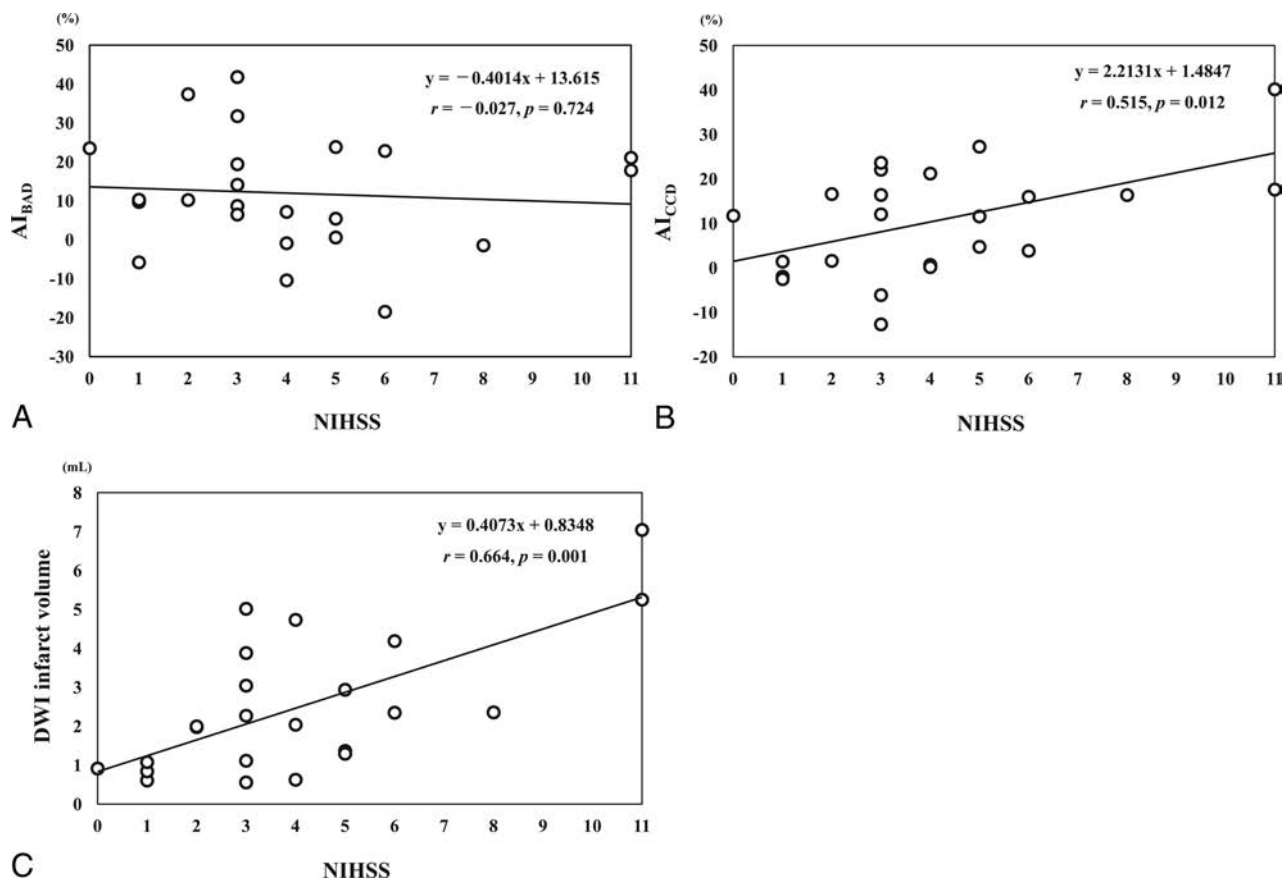


**FIG 2.** The relationships between admission NIHSS and the asymmetry index of the affected area (branch atheromatous disease,  $AI_{BAD}$ ) and contralateral cerebellar hemisphere (crossed cerebellar diaschisis,  $AI_{CCD}$ ) on 3D-ASL and DWI infarct volumes are shown. There was no significant correlation between admission NIHSS and  $AI_{BAD}$  (A,  $r = -0.027$ ,  $P = .724$ ). Significant correlation was found between admission NIHSS and  $AI_{CCD}$  (B,  $r = 0.515$ ;  $P = .012$ ) and DWI volume (C,  $r = 0.664$ ;  $P = .001$ ).

was  $40.6 \pm 37.6$  hours. The median admission NIHSS score was 3 (interquartile range, 2.5–5). The mean  $AI_{BAD}$  and  $AI_{CCD}$  were  $12.0\% \pm 14.5\%$  and  $10.5\% \pm 12.1\%$ , respectively, and the mean DWI infarct volume was  $2.50 \pm 1.72$  mL.

No significant correlation was found between NIHSS and  $AI_{BAD}$  ( $r = -0.027$ ,  $P = .724$ , Fig 2A). In contrast, we found a significant correlation between NIHSS and both  $AI_{CCD}$  ( $r = 0.515$ ,  $P = .012$ , Fig 2B) and DWI infarct volume ( $r = 0.664$ ,  $P = .001$ , Fig 2C). A demonstrable case is shown in Fig 3.

## DISCUSSION

Our results showed that the CCD on 3D-ASL and DWI infarct volume are strongly correlated with the degree of neurologic severity in patients with BAD-related infarcts. END can often occur in patients with BAD, and early management based on an accurate diagnosis is therefore needed in a clinical setting. These findings on 3D-ASL and DWI may represent important imaging biomarkers for predicting neurologic severity in the early stages of BAD.

Intracranial BAD was first described in 1989 as a new entity of atheromatous infarctions.<sup>1</sup> The pathogenesis of BAD is considered an occlusion or stenosis at the origin of a deep penetrating artery due to the presence of a microatheroma or large parent artery plaque.<sup>2,10</sup> Although the term BAD was originally presented on the basis of pathologic findings, few pathologic studies have been performed so far.<sup>3</sup> In contrast, many neuroimaging

studies of BAD have been performed, particularly with MR imaging.<sup>7–10</sup> DWI shows comma-shaped restricted diffusion that extends to the basal surface of the parent artery in patients with BAD, and noninvasive vessel imaging methods such as CTA or MRA usually reveal no or mild stenosis of the parent artery.<sup>19,20</sup>

Furthermore, BAD-related infarcts are considered predictive factors for END or progressive motor deficits.<sup>8</sup> Yamamoto et al<sup>21</sup> proposed that the severity of the neurologic status on admission (eg, initial NIHSS score) and preceding transient ischemic attacks could be predictors of END for LSA-type BAD. Meanwhile, a few reports have described the association between END and imaging findings of BAD.<sup>6–8</sup> A previous study on BAD suggested that DWI findings associated with poor outcomes include a larger lesion size in a direction perpendicular to the axial section.<sup>22</sup> This suggestion is compatible with our results in which the DWI infarct volume of BAD showed a favorable correlation with the initial NIHSS. Thus, an initial DWI may play an important role in estimating the neurologic severity of BAD-related infarcts.

3D-ASL is widely used as a noninvasive and repeatable whole-brain perfusion imaging method in clinical settings.<sup>11–15</sup> 3D-ASL enables acquisition of both the relative CBF near the affected lesions, including those associated with ischemia, tumors, or trauma, and the perfusion changes due to remote effects such as CCD.<sup>23–25</sup> CCD is a matched depression of blood flow and me-

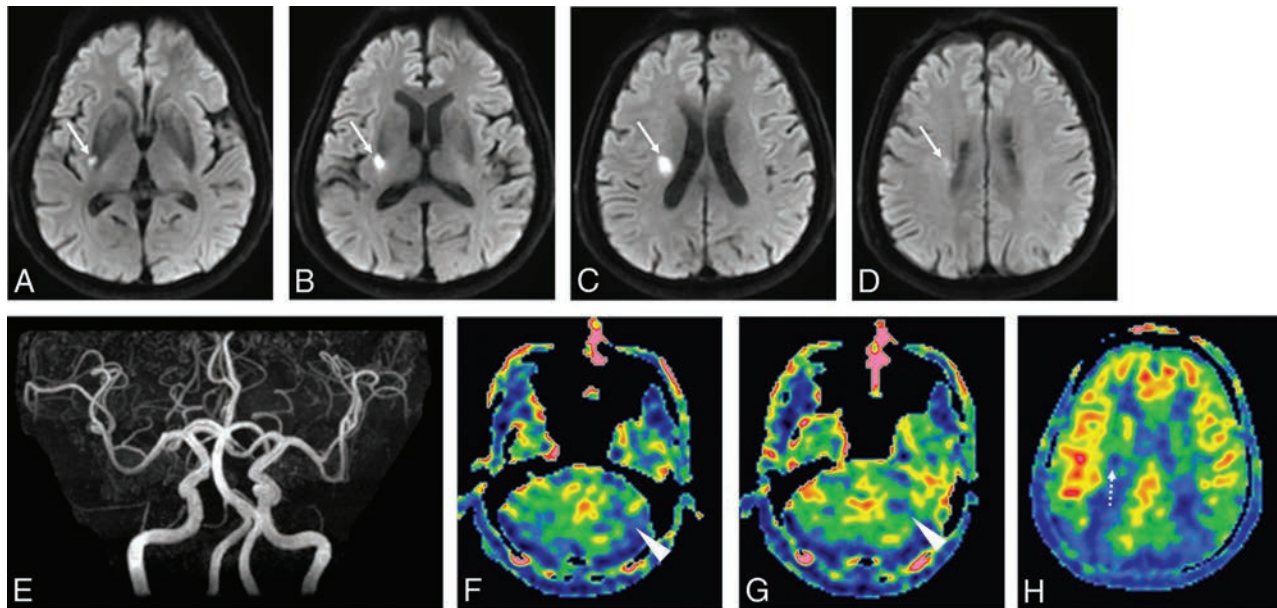


**FIG 3.** A 72-year-old man with a right BAD-related infarction. The admission NIHSS score was 5, and MR imaging was performed 24 hours after onset. A–D, DWIs show high signal intensity from the posterior putamen to the corona radiata (white arrows). E, MRA reveals no stenosis or occlusion in the right MCA. F, The 3D-ASL shows hypoperfusion signal intensity in the right corona radiata, corresponding to the infarcted area (white arrowhead). G and H, Hypoperfusion intensity in the left cerebellum (white arrowheads) can be observed, which indicates crossed cerebellar diaschisis due to the remote effect of the BAD-related infarction.

tabolism in the cerebellar hemisphere contralateral to a focal, supratentorial lesion and is a well-recognized phenomenon following cerebral infarctions.<sup>26</sup> Previous articles have also indicated that asymmetry indices for CCD in 3D-ASL were well-correlated with those of SPECT.<sup>25</sup> To the best of our knowledge, no reports have shown a relationship between 3D-ASL findings for BAD and neurologic status. In the present study, the CCD for BAD in 3D-ASL was much better correlated with the initial NIHSS score than the regional CBF of the 3D-ASL in the affected LSA region. Because the severity of neurologic status on admission is considered to be closely associated with the END in patients with BAD,<sup>21</sup> the degree of initial CCD on 3D-ASL, as well as initial DWI infarct volume, may be predictors of END for LSA-type BAD.

CCDs may demonstrate good correlations with the initial NIHSS score due to the localization of LSA-type BAD, which usually affects the pyramidal tract of the corona radiata or the internal capsule so that secondary degenerative changes along the corticospinal tract may easily occur. According to a previous report with MR tractography, the degree of pyramidal tract involvement within the LSA territory infarction is strongly related to the severity of the stroke and functional recovery.<sup>27</sup> Further studies with larger sample sizes are warranted to validate the relationship between CCD detected by 3D-ASL and the neurologic outcome, including follow-up by NIHSS.

Our study has several limitations. First, we examined the luminal patency with MRA and did not directly evaluate the parent artery wall. As previously mentioned, the pathogenesis of BAD is associated with proximal stenosis or occlusion of a penetrating artery due to a microatheroma or large parent artery plaque; and routine imaging techniques, such as MRA, are unable to visualize small vessel changes. However, recent studies showed that black-blood high-resolution MR imaging enables an evaluation of the intracranial artery vessel morphology, including the presence of

plaques involving parent arteries.<sup>28</sup> This capability could allow direct exploration of atheromatous small vessels and parent vessel lesions that cause BAD. Second, the interval from symptom onset to initial MR imaging examination varied widely among patients in this retrospective study. Finally, we only enrolled patients with LSA-type BAD. Patients with BAD involving other vascular territories, including the paramedian pontine artery, were not included because of the small sample size. A further prospective study that includes all types of BAD should be performed.

## CONCLUSIONS

In patients with LSA-type BAD, the CCD detected by 3D-ASL and DWI infarct volume was correlated with the severity of the neurologic status. Because the initial NIHSS score of BAD is considered a predictor of END and both 3D-ASL and DWI are noninvasive, repeatable, feasible sequences, they could be useful as radiologic imaging biomarkers for predicting the neurologic outcome in patients with BAD.

## REFERENCES

1. Caplan LR. **Intracranial branch atheromatous disease: a neglected, understudied, and underused concept.** *Neurology* 1989;39:1246–50 CrossRef Medline
2. Fisher CM, Caplan LR. **Basilar artery branch occlusion: a cause of pontine infarction.** *Neurology* 1971;21:900–05 CrossRef Medline
3. Tatsumi S, Yamamoto T. **An autopsied case of an apparent pontine branch atheromatous disease.** *Eur Neurol* 2010;63:184–85 CrossRef Medline
4. Kwan MW, Mak W, Cheung RT, et al. **Ischemic stroke related to intracranial branch atheromatous disease and comparison with large and small artery diseases.** *J Neurol Sci* 2011;303:80–84 CrossRef Medline
5. Arboix A, Blanco-Rojas L, Martí-Vilalta JL. **Advancements in understanding the mechanisms of symptomatic lacunar ischemic stroke:**

- translation of knowledge to prevention strategies. *Expert Rev Neurother* 2014;14:261–76 CrossRef Medline
6. Saia V, Pantoni L. **Progressive stroke in pontine infarction.** *Acta Neurol Scand* 2009;120:213–15 Medline
  7. Nakase T, Yamamoto Y, Takagi M; Japan Branch Atheromatous Disease Registry Collaborators. **The impact of diagnosing branch atheromatous disease for predicting prognosis.** *J Stroke Cerebrovasc Dis* 2015;24:2423–28 CrossRef Medline
  8. Yamamoto Y, Ohara T, Hamanaka M, et al. **Characteristics of intracranial branch atheromatous disease and its association with progressive motor deficits.** *J Neurol Sci* 2011;304:78–82 CrossRef Medline
  9. Nakase T, Yoshioka S, Sasaki M, et al. **Clinical evaluation of lacunar infarction and branch atheromatous disease.** *J Stroke Cerebrovasc Dis* 2013;22:406–12 CrossRef Medline
  10. Petrone L, Nannoni S, Del Bene A, et al. **Branch atheromatous disease: a clinically meaningful, yet unproven concept.** *Cerebrovasc Dis* 2016;41:87–95 CrossRef Medline
  11. Deibler AR, Pollock JM, Kraft RA, et al. **Arterial spin-labeling in routine clinical practice, part 1: technique and artifacts.** *AJNR Am J Neuroradiol* 2008;29:1228–34 CrossRef Medline
  12. Wolf RL, Detre JA. **Clinical neuroimaging using arterial spin-labeled perfusion magnetic resonance imaging.** *Neurotherapeutics* 2007;4:346–59 CrossRef Medline
  13. Alsop DC, Detre JA. **Multisection cerebral blood flow MR imaging with continuous arterial spin labeling.** *Radiology* 1998;208:410–16 CrossRef Medline
  14. Kimura H, Kabasawa H, Yonekura Y, et al. **Cerebral perfusion measurements using continuous arterial spin labeling: accuracy and limits of a quantitative approach.** *International Congress Series* 2004; 1265:238–47 CrossRef
  15. Kimura H, Kado H, Koshimoto Y, et al. **Multislice continuous arterial spin-labeled perfusion MRI in patients with chronic occlusive cerebrovascular disease: a correlative study with CO<sub>2</sub> PET validation.** *J Magn Reson Imaging* 2005;22:189–98 CrossRef Medline
  16. Sobesky J, Thiel A, Ghaemi M, et al. **Crossed cerebellar diaschisis in acute human stroke: a PET study of serial changes and response to supratentorial reperfusion.** *J Cereb Blood Flow Metab* 2005;25: 1685–91 CrossRef Medline
  17. Sommer WH, Bollwein C, Thierfelder KM, et al. **Crossed cerebellar diaschisis in patients with acute middle cerebral artery infarction: occurrence and perfusion characteristics.** *J Cereb Blood Flow Metab* 2016;36:743–54 CrossRef Medline
  18. Adams HP Jr, Bendixen BH, Kappelle LJ, et al. **Classification of subtype of acute ischemic stroke: definitions for use in a multicenter trial—TOAST.** *Trial of Org 10172 in Acute Stroke Treatment.* *Stroke* 1993;24:35–41 CrossRef Medline
  19. Bang OY. **Intracranial atherosclerosis: current understanding and perspectives.** *J Stroke* 2014;16:27–35 CrossRef Medline
  20. Tamura A, Yamamoto Y, Nagakane Y, et al. **The relationship between neurological worsening and lesion patterns in patients with acute middle cerebral artery stenosis.** *Cerebrovasc Dis* 2013;35: 268–75 CrossRef Medline
  21. Yamamoto Y, Ohara T, Hamanaka M, et al. **Predictive factors for progressive motor deficits in penetrating artery infarctions in two different arterial territories.** *J Neurol Sci* 2010;288:170–74 CrossRef Medline
  22. Moriya S, Adachi T, Goto J, et al. **Relationship between MRI findings and outcome in supratentorial branch atheromatous disease (BAD).** *Nosotchu* 2006;28:504–09 CrossRef
  23. Chen S, Guan M, Lian HJ, et al. **Crossed cerebellar diaschisis detected by arterial spin-labeled perfusion magnetic resonance imaging in subacute ischemic stroke.** *J Stroke Cerebrovasc Dis* 2014;23: 2378–83 CrossRef Medline
  24. Strother MK, Buckingham C, Faraco CC, et al. **Crossed cerebellar diaschisis after stroke identified noninvasively with cerebral blood flow-weighted arterial spin labeling MRI.** *Eur J Radiol* 2016;85: 136–42 CrossRef Medline
  25. Kang KM, Sohn CH, Kim BS, et al. **Correlation of asymmetry indices measured by arterial spin-labeling MR imaging and SPECT in patients with crossed cerebellar diaschisis.** *AJNR Am J Neuroradiol* 2015;36:1662–68 CrossRef Medline
  26. Baron JC, Bousser MG, Comar D, et al. **“Crossed cerebellar diaschisis” in human supratentorial brain infarction.** *Trans Am Neurol Assoc* 1981;105:459–61 Medline
  27. Konishi J, Yamada K, Kizu O, et al. **MR tractography for the evaluation of functional recovery from lenticulostriate infarcts.** *Neurology* 2005;64:108–13 CrossRef Medline
  28. Chung JW, Kim BJ, Sohn CH, et al. **Branch atheromatous plaque: a major cause of lacunar infarction (high-resolution MRI study).** *Cerebrovasc Dis Extra* 2012;2:36–44 CrossRef Medline

# Temporal and Spatial Variances in Arterial Spin-Labeling Are Inversely Related to Large-Artery Blood Velocity

A.D. Robertson, G. Matta, V.S. Basile, S.E. Black, C.K. Macgowan, J.A. Detre, and B.J. MacIntosh



## ABSTRACT

**BACKGROUND AND PURPOSE:** The relationship between extracranial large-artery characteristics and arterial spin-labeling MR imaging may influence the quality of arterial spin-labeling–CBF images for older adults with and without vascular pathology. We hypothesized that extracranial arterial blood velocity can explain between-person differences in arterial spin-labeling data systematically across clinical populations.

**MATERIALS AND METHODS:** We performed consecutive pseudocontinuous arterial spin-labeling and phase-contrast MR imaging on 82 individuals (20–88 years of age, 50% women), including healthy young adults, healthy older adults, and older adults with cerebral small vessel disease or chronic stroke infarcts. We examined associations between extracranial phase-contrast hemodynamics and intracranial arterial spin-labeling characteristics, which were defined by labeling efficiency, temporal signal-to-noise ratio, and spatial coefficient of variation.

**RESULTS:** Large-artery blood velocity was inversely associated with labeling efficiency ( $P = .007$ ), temporal SNR ( $P < .001$ ), and spatial coefficient of variation ( $P = .05$ ) of arterial spin-labeling, after accounting for age, sex, and group. Correction for labeling efficiency on an individual basis led to additional group differences in GM-CBF compared to correction using a constant labeling efficiency.

**CONCLUSIONS:** Between-subject arterial spin-labeling variance was partially explained by extracranial velocity but not cross-sectional area. Choosing arterial spin-labeling timing parameters with on-line knowledge of blood velocity may improve CBF quantification.

**ABBREVIATIONS:** ASL = arterial spin-labeling; CoV = coefficient of variation; PC = phase contrast; WMH = white matter hyperintensities

Quantitative CBF is a valuable measure to track pathophysiologic changes in cerebrovascular function and brain metabolism.<sup>1</sup> Two noninvasive MR imaging–based techniques, which capture distinct hemodynamic features, are arterial spin-labeling (ASL) and phase-contrast (PC) imaging. ASL measures regional CBF with tissue-level precision, using magnetized arterial blood water as an endogenous tracer.<sup>2,3</sup> PC imaging, by comparison, quantifies whole-brain CBF with a bipolar gradient to induce phase shifts proportional to blood velocity within the ca-

rotid and vertebral arteries.<sup>4</sup> Among the factors that influence ASL, CBF quantification is most sensitive to labeling efficiency and the equilibrium magnetization of arterial blood.<sup>5</sup> In practice, labeling efficiency is assumed constant (eg, 0.85).<sup>3</sup> Field inhomogeneity<sup>6</sup> and nonlinear effects of blood velocity,<sup>7–9</sup> however, contribute individual variability. Studies that have empirically estimated labeling efficiency by normalizing pseudocontinuous ASL-based whole-brain CBF to that measured with PC imaging report individual labeling efficiencies ranging from 0.7 to 1.1.<sup>8,10</sup> Recent work in a large middle-aged cohort, however, has questioned the validity of this normalization method due to substan-

Received October 28, 2016; accepted after revision April 10, 2017.

From the Heart and Stroke Foundation Canadian Partnership for Stroke Recovery (A.D.R., G.M., S.E.B., B.J.M.) and Hurvitz Brain Sciences (A.D.R., S.E.B., B.J.M.), Sunnybrook Research Institute, University of Toronto, Toronto, Ontario, Canada; Division of Neurology, Department of Medicine (V.S.B., S.E.B.), University of Toronto, Toronto, Ontario, Canada; Mackenzie Health (V.S.B.), Richmond Hill, Ontario, Canada; L.C. Campbell Cognitive Neurology Research Unit (S.E.B.), Sunnybrook Health Sciences Centre, Toronto, Ontario, Canada; Hospital for Sick Children (C.K.M.), Toronto, Ontario, Canada; Department of Medical Biophysics (C.K.M., B.J.M.), University of Toronto, Toronto, Ontario, Canada; and Department of Neurology (J.A.D.), University of Pennsylvania, Philadelphia, Pennsylvania.

This work was supported by a research grant from the Canadian Institutes of Health Research (MOP133568) and catalyst grants from the Heart and Stroke Foundation Canadian Partnership for Stroke Recovery.

Paper previously presented, in part, as a poster at: Annual Meeting and Exhibition of the International Society for Magnetic Resonance in Medicine, May 30 to June 5, 2015; Toronto, Ontario, Canada. G. Matta, A.D. Robertson, S.E. Black, and B.J. MacIntosh. "Quantifying Cerebral Blood Flow: A Comparison of Two Noninvasive Perfusion Imaging Techniques."

Please address correspondence to Andrew Robertson, PhD, Heart and Stroke Foundation Canadian Partnership for Stroke Recovery, Sunnybrook Research Institute, Rm M6–168, 2075 Bayview Ave, Toronto, ON, Canada, M4N 3M5; e-mail: adrobert@sri.utoronto.ca; @arob888

Indicates open access to non-subscribers at [www.ajnr.org](http://www.ajnr.org)

<http://dx.doi.org/10.3174/ajnr.A5257>

tial variability within individual measurements.<sup>11</sup> Rather than incorporating PC-based CBF as a normalization factor, corresponding knowledge of PC-based metrics, such as blood velocity, may be beneficial for planning ASL protocols because many labeling and acquisition parameters are timing-based.

Simulated and empiric ASL data suggest that labeling efficiency is highest for blood velocities of  $\sim 10$  cm/s.<sup>8</sup> These studies reflect hemodynamics in healthy adults, leaving questions regarding the reliability of ASL in patients with vascular pathology. Aging, cerebrovascular risk factors, and stroke status are associated with larger cross-sectional areas and slower, more pulsatile blood velocity within the large arteries.<sup>12,13</sup> Such changes occurring in proximity to the ASL labeling plane may confound CBF quantification in these clinical cohorts. For instance, age is associated with a decreased signal-to-noise ratio, due, in part, to increased variance between individual control-tag difference images.<sup>14</sup> Arterial transit time is another velocity-sensitive hemodynamic characteristic associated with aging<sup>15</sup> and the presence of white matter hyperintensities (WMH).<sup>16</sup> Prolonged transit time is visualized by localized regions of hyperintense ASL signal, contributing to greater spatial variance in whole-brain CBF.<sup>17</sup> To expand our understanding of the relationship between large-artery characteristics and CBF estimates, we compared ASL and PC in individuals across a range of age and vascular pathology. We hypothesized that large-artery blood velocity would be inversely related to labeling efficiency, temporal SNR, and spatial variance in ASL.

## MATERIALS AND METHODS

### Participants and Protocol

Participants were recruited into 4 groups: 1) healthy young adults (younger than 40 years); 2) healthy older adults (50 years or older); 3) older adults with WMH of presumed vascular origin; and 4) older adults with chronic stroke infarcts ( $\geq 3$  months post-stroke). Exclusion criteria included the presence of dementia, a genetic predisposition to WMH, and extracranial arterial occlusion. Participants underwent a single MR imaging scan. The Sunnysbrook Research Institute's research ethics board approved this study, and all participants provided written informed consent.

### MR Imaging Acquisition

We completed neuroimaging with a 3T MR imaging system (Achieva; Philips Healthcare, Best, the Netherlands) with a body coil transmitter and an 8-channel head coil receiver. Structural imaging included high-resolution T1 (TR/TE = 9.5/2.3 ms, flip angle = 8°, voxel dimensions =  $0.9 \times 0.7 \times 1.2$  mm<sup>3</sup>, FOV =  $240 \times 191 \times 168$  mm<sup>3</sup>) and FLAIR (TR/TE/TI = 9000/125/2800 ms, flip angle = 90°, voxel dimensions =  $0.4 \times 0.4 \times 3$  mm<sup>3</sup>, FOV =  $240 \times 240 \times 156$  mm<sup>3</sup>) acquisitions. Two 2D acquisitions independently quantified CBF: PC to measure large-artery blood flow and ASL to measure tissue-level CBF. The PC acquisition captured a single 5-mm section perpendicular to the extracranial internal carotid artery, with cardiac synchronization (finger pulse gating, single cardiac phase [acquisition delay = 250 ms, acquisition window = 500 ms], TR/TE = 20/9.1 ms, flip angle = 15°, maximum velocity encoding = 100 cm/s, voxel dimensions =  $0.5 \times 0.5$  mm<sup>2</sup>, FOV =  $150 \times 150$  mm<sup>2</sup>). Pseudocontinuous labeling for the ASL scan used a train of radiofrequency pulses

(duration = 0.5 ms, flip angle = 18°, interpulse pause = 0.5 ms) with a balanced gradient scheme for 1650 ms and occurred at a position identical to that of the PC acquisition. Thirty control and tag ASL volume pairs were acquired by single-shot echo-planar imaging (TR/TE = 4000/9.6 ms, flip angle = 90°, in-plane resolution =  $3 \times 3$  mm<sup>2</sup>, FOV =  $192 \times 192$  mm<sup>2</sup>, section thickness = 5 mm, number of sections = 18 [no gap], postlabel delay = 1600 ms at the first section and ascending for subsequent sections).

We did not select background suppression to maximize the detectability of deleterious individual-difference images that were spurious due to head motion. A proton density-weighted reference volume was acquired to estimate the equilibrium magnetization and extract a receiver coil sensitivity profile (TR = 10 seconds, but otherwise identical to ASL parameters). We prioritized the frontal cortices and subcortical tissue when setting the ASL FOV, leaving inconsistent coverage of the cerebellum and the most superior cerebrum. PC and ASL scan durations were 1.5 and 4.5 minutes, respectively. The 2 acquisitions were run sequentially, and the order was varied between participants.

### MR Imaging Processing

Images were processed with the FMRIB Software Library (FSL; www.fmrib.ox.ac.uk/fsl). Brain extraction<sup>18</sup> and segmentation<sup>19</sup> tools isolated GM and WM from the T1WI. Brain mass was estimated on the basis of tissue densities of 1.03 g/mL for GM and 1.04 g/mL for WM.<sup>20</sup> In-house software,<sup>21</sup> combined with manual editing, segmented WMH from the FLAIR image. Stroke lesions were identified by CSF segmentation from the T1WI, manual editing, and confirmation against the FLAIR image. WMH and infarct volumes were normalized to an intracranial capacity of 1300 mL. Older adults with a normalized hyperintensity burden of  $\geq 10$  mL across periventricular and deep brain regions were assigned to the WMH group.

Internal carotid and vertebral artery masks were isolated from the PC magnitude image by using FSL segmentation software and manual editing. Interrater reliability of this method was excellent (Cronbach  $\alpha > 0.99$  for the internal carotid artery and  $> 0.95$  for the vertebral artery between 1 experienced and 2 novice raters). These masks represent the cross-sectional area of each artery, and they were overlaid onto the PC phase image to compute mean blood velocity. Arterial blood flow is the product of area and mean velocity, and PC-CBF was calculated as the sum of flow through all 4 arteries, normalized to brain mass. Peak blood velocity was taken as the highest velocity signal from a voxel in the center of the vessel lumen.

ASL-CBF was calculated from the mean of the control-tag difference images. To maximize image quality, we systematically removed individual-difference images with high relative head motion before CBF calculation, as previously described.<sup>14</sup> The remaining difference images underwent in-plane spatial smoothing by using a Gaussian kernel of 5-mm full width at half maximum, section-by-section adjustment for incremental postlabel delay, and calibration to absolute CBF units with a proton density-weighted image.<sup>3</sup> The T1 relaxation time for arterial blood was set at 1.65 seconds for all participants. Calibration to absolute CBF units at this stage did not correct for labeling efficiency. Images with intravascular artifacts were retained. Although intravas-

**Table 1: Participant characteristics<sup>a</sup>**

	Young	Old	WMH	Stroke	P Value
No.	15	22	15	30	
Age (range) (yr)	25.7 ± 4.6 (20–36)	69.1 ± 7.0 <sup>b</sup> (55–81)	72.0 ± 8.2 <sup>b</sup> (51–83)	67.9 ± 10.4 <sup>b</sup> (51–88)	<.001
Sex, female (%)	7 (47)	17 (77)	8 (53)	9 (30)	.009
Hemodynamics					
ICA mean velocity (cm/s)	18.2 ± 4.5	11.9 ± 2.9 <sup>b</sup>	10.3 ± 3.3 <sup>b</sup>	9.7 ± 3.1 <sup>b</sup>	<.001
ICA area (cm <sup>2</sup> )	0.21 ± 0.04	0.24 ± 0.06	0.26 ± 0.06	0.26 ± 0.09	.102
VA mean velocity (cm/s)	10.0 ± 2.5	6.7 ± 1.6 <sup>b</sup>	6.5 ± 1.7 <sup>b</sup>	5.6 ± 2.1 <sup>b</sup>	<.001
VA area (cm <sup>2</sup> )	0.13 ± 0.03	0.13 ± 0.03	0.14 ± 0.04	0.12 ± 0.03	.190
PC-CBF (mL/100 g/min)	49.0 ± 8.5	41.4 ± 8.1	40.6 ± 12.9	33.8 ± 6.3 <sup>b,c</sup>	<.001
ASL-CBF (mL/100 g/min)	44.1 ± 10.2	40.8 ± 8.8	31.4 ± 9.6 <sup>b,c</sup>	34.3 ± 10.5 <sup>b</sup>	<.001

**Note:**—VA indicates vertebral artery.

<sup>a</sup>Data are mean ± SD or count (proportion). Area and velocity are reported as the mean of bilateral vessels. ASL-CBF is uncorrected for labeling efficiency.

<sup>b</sup>Group differences compared with the young group at  $P_{\text{Bonferroni}} < .05$ .

<sup>c</sup>Group differences compared with the old group at  $P_{\text{Bonferroni}} < .05$ .

cular artifacts are suggestive of prolonged arterial transit time, CBF calculations over the whole brain should remain valid in the absence of crushing gradients.<sup>3</sup>

We calculated 4 ASL variables to compare against extracranial hemodynamics: 1) GM-CBF, 2) individual labeling efficiency equal to the ratio between ASL-based and PC-based whole-brain CBF, 3) temporal SNR equal to the ratio between the mean and the SD of the individual-difference images, and 4) spatial coefficient of variation (CoV) equal to the ratio between the SD and mean of the GM-CBF image. A GM mask without any overlapping stroke lesion was created for the calculation of GM-CBF, temporal SNR, and spatial CoV. GM-CBF was subsequently corrected for labeling efficiency in 2 ways: 1) with a constant of 0.85, and 2) with the calculated labeling efficiency.

### Statistical Analysis

CBF, mean blood velocity, and cross-sectional area were compared between groups by ANOVA. We assessed the associations of mean blood velocity and cross-sectional area with GM-CBF, individual labeling efficiency, temporal SNR, and spatial CoV by linear regressions, adjusting for age, sex, and group. To account for between-vessel differences in area and velocity, we calculated flow-weighted measures in which the influence of each artery on the pooled variables was proportional to the contribution of that vessel to whole-brain CBF. Differences between whole-brain ASL-CBF and PC-CBF were characterized in a paired analysis by ratio and mean difference. Finally, we compared GM-CBF with the 2 distinct labeling efficiencies. Unpaired *t* tests with Bonferroni correction ( $P_{\text{Bonferroni}}$ ) were used for post hoc group comparisons. All statistical analyses were performed with R statistical and computing software (Version 3.3.1; <http://www.r-project.org/>), with  $P < .05$  being significant.

### RESULTS

Large-artery characteristics and whole-brain hemodynamics from 82 participants ( $n = 15$  young, 22 healthy older, 15 with WMH, and 30 with stroke) are reported in Table 1. In WMH, the normalized hyperintensity volume ranged from 10.9 to 52.2 mL. Stroke participants were 3–65 months postevent with cortical, subcortical, and subtentorial infarcts. The normalized infarct volume ranged from 0.03 to 98.2 mL. Group differences in velocity, but not cross-sectional area, were observed (Fig 1). Although the fraction of whole-brain CBF contributed by each extracranial ar-

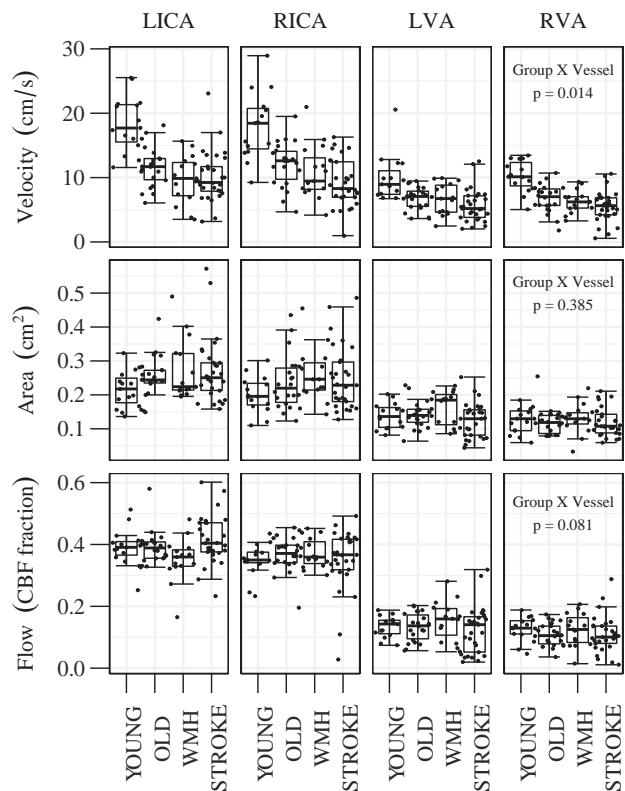


**FIG 1.** Vascular characteristics of the bilateral (left and right) internal carotid (LICA and RICA) and vertebral arteries (LVA and RVA) for each group. Panel 3 shows the relative contribution to total CBF by each vessel.

tery was similar across groups, greater within-group variability was observed in older adults with vascular pathology (Fig 1, lower panel).

### Labeling Efficiency

PC-CBF accounted for a significant proportion of the between-person variance in ASL-CBF ( $r^2 = 0.40$ ,  $P < .001$ ), though technique differences were evident. Intermodality analyses suggested that ASL-CBF was systematically lower than PC-CBF ( $t = -2.6$ ,  $P = .01$ ), and this difference was greater in WMH than in stroke or healthy older adults groups (Table 2). The ASL-CBF to PC-CBF ratio (ie, individual labeling efficiency) ranged from 0.48 to 1.60 across our entire sample. A group effect was observed ( $F = 4.3$ ,  $P = .008$ ), with the ratio being lower in WMH than in stroke and

**Table 2: Comparison of MRI methods for whole-brain CBF estimation<sup>a</sup>**

	No.	ASL:PC (ratio)	ASL-PC Difference (mL/100 g/min)
Young	15	0.91 ± 0.20	-4.9 ± 9.8
Old	22	1.00 ± 0.18 <sup>b</sup>	-0.6 ± 7.0 <sup>b</sup>
WMH	15	0.80 ± 0.20	-9.2 ± 9.4
Stroke	30	1.01 ± 0.23 <sup>b</sup>	0.5 ± 7.9 <sup>b</sup>
All	82	0.95 ± 0.22	-2.6 ± 9.0

<sup>a</sup>Data are mean ± SD.

<sup>b</sup>Group differences compared with WMH at  $P_{\text{Bonferroni}} < .05$ .

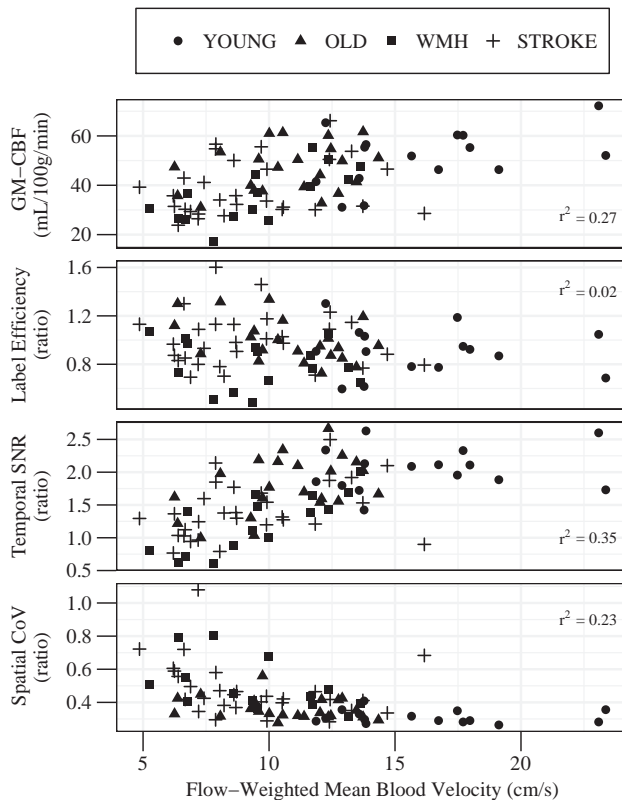


**FIG 2.** The association of mean blood velocity with GM-CBF (panel 1), ASL-to-PC ratio for whole-brain CBF (panel 2), ASL temporal SNR (panel 3), and CBF spatial CoV (panel 4). Velocity is shown as a weighted mean of all 4 extracranial vessels relative to their contribution to total CBF. GM-CBF is uncorrected for labeling efficiency. Age, sex, and group-adjusted linear models are reported in Table 3.

healthy older adults groups. Labeling efficiency was unrelated to mean blood velocity in bivariate linear regression (Fig 2), though labeling efficiency and peak blood velocity showed a modest correlation ( $r^2 = 0.05$ ,  $P = .043$ ). Furthermore, an inverse association between labeling efficiency and mean velocity was observed in a regression model that adjusted for age, sex, group status, and cross-sectional area (Table 3). This multivariate model was unaltered when peak velocity replaced mean velocity.

### Temporal and Spatial Variance

Group differences in the temporal SNR within gray matter were observed (young:  $2.05 \pm 0.33$  versus old:  $1.79 \pm 0.43$  versus WMH:  $1.23 \pm 0.44$  versus stroke:  $1.42 \pm 0.42$ ;  $F = 13.4$ ,  $P < .001$ ). No difference between young and healthy older adults was noted, but both groups had greater SNR than WMH and stroke groups ( $P_{\text{Bonferroni}} \leq 0.010$ ). Group differences in spatial CoV within

gray matter were also observed (young:  $0.31 \pm 0.04$  versus old:  $0.36 \pm 0.07$  versus WMH:  $0.49 \pm 0.15$  versus stroke:  $0.48 \pm 0.16$ ;  $F = 8.80$ ,  $P < .001$ ). Again, no difference between young and healthy older adults was noted, but both groups exhibited less spatial CoV than WMH and stroke groups ( $P_{\text{Bonferroni}} < .05$ ). Both temporal SNR and spatial CoV were associated with mean blood velocity in bivariate analysis (Fig 2) and remained significant after adjusting for age, sex, and group (Table 3). The spread of spatial CoV increased with decreasing velocity, particularly below 10 cm/s. Calculated label efficiency was directly related to temporal SNR ( $r^2 = 0.07$ ,  $P = .017$ ), but not spatial CoV ( $r^2 = 0.02$ ,  $P = .16$ ).

### GM-CBF

GM-CBF was directly correlated with mean blood velocity (Fig 2 and Table 3). A group-by-method interaction ( $F = 4.6$ ,  $P = .005$ ) indicated that additional group differences in GM-CBF were observed when using a PC-based correction for labeling efficiency compared with the constant 0.85 correction (Fig 3). When we used the constant correction across all participants, GM-CBF was lower in the WMH and stroke groups than in young adults and lower in the WMH group than in healthy older adults. Correction for PC-based labeling efficiency identified additional differences between the healthy young and old groups and between the healthy old and stroke groups.

### DISCUSSION

The accuracy of regional CBF maps—an important consideration for the clinical uptake of ASL imaging—depends on multiple parameters in the scanning protocol. In this study, we compared PC and ASL MR imaging in adults with and without vascular-related pathology to assess how large-artery characteristics relate to ASL signal. The regression results demonstrated an inverse relationship between labeling efficiency and arterial blood velocity, which is consistent with previous work.<sup>8</sup> However, label efficiency variance was high for low velocities; thus, we are unable to provide empiric support for the theorized inverted U-shaped profile.<sup>7-9</sup> Notably, features of ASL variance, namely temporal SNR and spatial CoV, were independently associated with mean blood velocity but not cross-sectional area in regression analyses. Reduced temporal SNR at a low velocity contributed to the increased variance of labeling efficiency within this range. These results reaffirm that hemodynamics at the labeling plane are an important consideration for CBF quantification in ASL, especially in older adults with cerebrovascular disease.

Previous work estimated ASL labeling efficiency based on PC,<sup>7-9</sup> though the validity of this method has recently come under scrutiny.<sup>11</sup> Our current findings contrast with ASL simulations that posited a direct association between velocity and labeling efficiency below peak velocities of 20 cm/s.<sup>7-9</sup> Whereas the previous findings were under the assumption of constant flow profiles, our PC implementation averaged velocities over the cardiac cycle; consequently, the velocity estimates more closely reflect data from Aslan et al,<sup>8</sup> who found an inverse association between velocity and labeling efficiency above 10 cm/s. ASL signal intensity and transit delays have been shown to vary as a function of the cardiac cycle,<sup>22</sup> so dissimilar relationships between mean and peak veloc-

**Table 3: Linear regression parameters for the association of extracranial mean blood velocity and cross-sectional area with ASL characteristics<sup>a</sup>**

Model	Independent Variables	$\beta$	95% CI	T-Statistic	P Value
GM-CBF	Area (cm <sup>2</sup> )	46.5	(8.2–84.7)	2.03	.046
	Velocity (cm/s)	1.5	(0.8–2.3)	3.42	.001
ASL-CBF:PC-CBF	Area (cm <sup>2</sup> )	−0.79	(−1.58–0.01)	−1.65	.103
	Velocity (cm/s)	−0.02	(−0.04–0.01)	−2.78	.007
GM-temporal SNR	Area (cm <sup>2</sup> )	1.78	(0.24–3.32)	1.93	.058
	Velocity (cm/s)	0.07	(0.04–0.10)	3.99	<.001
GM-spatial CoV	Area (cm <sup>2</sup> )	−0.11	(−0.61–0.39)	−0.36	.720
	Velocity (cm/s)	−0.01	(−0.02–0.00)	−2.01	.048

<sup>a</sup>All models were adjusted for age, sex, and group. GM-CBF is uncorrected for labeling efficiency.

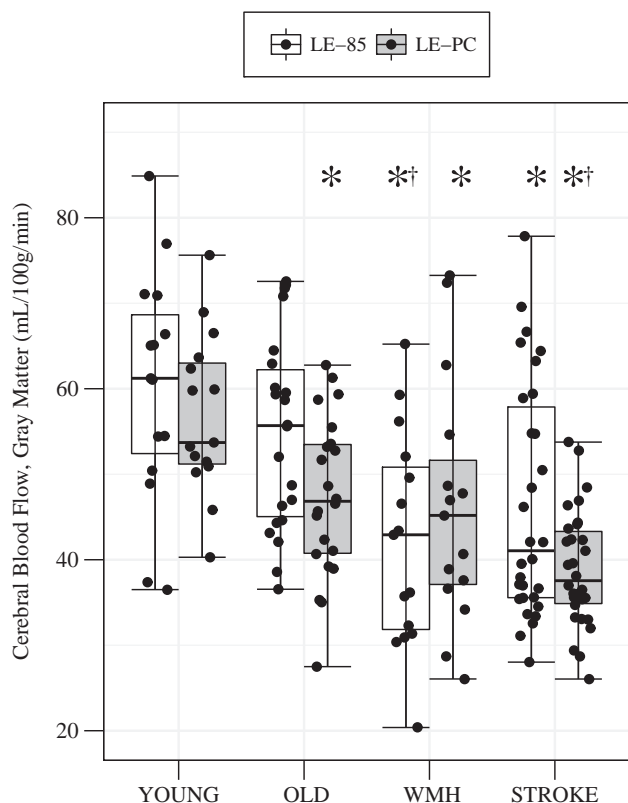


**FIG 3.** GM-CBF between groups calculated with 2 labeling efficiency estimates. *White bars* incorporate a constant labeling efficiency (ie, 0.85), and *gray bars* incorporate individual labeling efficiency based on the ASL-to-PC ratio for whole-brain CBF. Post hoc group comparisons are indicated at  $P_{\text{Bonferroni}} < .05$  for differences from the young group (*asterisk*) and differences from old group (*dagger*) within the same calibration technique.

ity may reflect temporal fluctuations in effective labeling efficiency. Of note, we found labeling efficiency to be more sensitive to peak velocity than mean velocity in unadjusted models.

In addition to labeling efficiency, the temporal and spatial variability of ASL signal were inversely related to mean blood velocity. At labeling, the volume of labeled blood is a function of blood velocity and label duration, the latter of which was held constant at 1650 ms. Intuitively, lower velocities will degrade ASL because the label volume directly translates to signal-to-noise ratio.<sup>3</sup> At acquisition, ASL signal is dependent on the arterial transit time and the T1 relaxation of arterial blood.<sup>23</sup> Arterial transit time increases with cerebrovascular disease.<sup>24,25</sup> Thus, labeled blood is more likely to remain in the macrovascular compartment and be

captured as hyperintense signal, contributing to greater heterogeneity within the perfusion-weighted image.<sup>26</sup> Indeed, a recent ASL study in hypertensive older adults demonstrated a direct relationship between single postlabel delay spatial CoV and arterial transit time.<sup>17</sup> To combat this, longer postlabel delays are recommended for imaging older adults to allow signal to reach the tissue before acquisition, albeit at a cost of lower signal intensity.<sup>3</sup> We observed

that slower velocity was related to greater spatial CoV of the perfusion-weighted image, which is consistent with greater macrovascular signal at the time of acquisition. Real-time monitoring of blood velocity before ASL planning may help mitigate these indices of ASL variance in 2 ways: First, acquiring additional tag and control volumes in individuals with low velocity would improve signal-to-noise ratio. Second, prescribing postlabel delay based on arterial blood velocity may help to distinguish aspects of arterial transit time that separate slower flow velocity from collateral or tortuous pathways.

The GM-CBF values observed here are consistent with those in other studies involving younger adults,<sup>27</sup> healthy older adults,<sup>28</sup> and individuals with chronic stroke.<sup>29</sup> Older adults with WMH, however, exhibited lower GM-CBF than previously reported.<sup>30</sup> Calibration of the GM-CBF to individual labeling efficiency on the basis of PC altered the sensitivity to distinguish clinical groups. With PC-based calibration, we noted GM-CBF differences between healthy young and older adults and between healthy older adults and those with stroke, which were not apparent with a constant labeling efficiency for all participants. Longitudinal relaxation time was held constant across all groups in our estimation of CBF with ASL. Age- and sex-dependent variability in blood T1 may have partially contributed to group differences in global ASL signal.<sup>31</sup> The change in group differences following calibration to PC-CBF, which is independent of blood T1 effects, may be partially due to correction for group differences in longitudinal relaxation. Nevertheless, these results raise important questions about the consideration of labeling efficiency and the design of ASL protocols for CBF quantification in clinical cohorts with altered large-artery velocity profiles.

Despite these proposed links between blood velocity and ASL, a large proportion of the variance remains unexplained in this study. In several cases, the calculated labeling efficiency exceeded 1.0, which is an implausible finding. We implemented gated cardiac PC-MRI to capture velocity data at a single phase in the cardiac cycle on the basis of a 500-ms acquisition window that was optimized for a range of R-R intervals centered at 1000 ms. Heart rate variability could shift this acquisition window to favor the diastolic phase of the cardiac cycle, which would influence the PC-CBF calculation and contribute to a higher ratio between ASL-CBF and PC-CBF. Vessel segmentation and partial volume errors related to vertebral artery tortuosity<sup>32</sup> and smaller arterial caliber may have reduced PC-CBF accuracy.<sup>33</sup> Another consideration is the ASL volume coverage. Whereas PC-CBF reflects whole-brain flow, the ASL FOV did not encapsulate the entire

brain for all participants. Anatomic variability in the circle of Willis (ie, distal to PC imaging) may also contribute to a mismatch between upstream and downstream flow measurements.<sup>34</sup>

These discrepancies may have contributed to a portion of the unexplained variance between ASL-CBF and PC-CBF and emphasize the need for caution when comparing ASL-CBF directly with PC-CBF.<sup>11</sup> Of note, our ASL protocol did not incorporate background suppression or involve 3D acquisition, which are now consensus guidelines for clinical ASL.<sup>3</sup> Two main reasons for these preferences were the following: 1) Study development predated the consensus article, and 2) a parallel objective of the data acquisition was to address deleterious head motion, which is more easily approached with multiple 2D sections as opposed to 3D readouts. Recently, a sequence that measures artery-specific label efficiency, thereby improving ASL-CBF accuracy, has been proposed and validated.<sup>35</sup> Comparison of PC-CBF with ASL-CBF using this calibration method may facilitate investigation into the impact of age- and disease-related increases in hemodynamic pulsatility on ASL after controlling for effects on label efficiency.

## CONCLUSIONS

The current study compared characteristics from ASL- and PC-based cerebral perfusion imaging in adults with and without vascular disease. Mean blood velocity through the ASL labeling plane was inversely related to labeling efficiency, as well as ASL temporal and spatial variance. These associations suggest that velocity impacts ASL at both the labeling and acquisition stages. ASL planning based on real-time velocity monitoring (eg, number of control/tag pairs, postlabel delay) may help optimize the signal-to-noise ratio and minimize the effect of arterial transit time on CBF maps.

## ACKNOWLEDGMENTS

The authors thank Dr Henk-Jan Mutsaerts for valuable discussions regarding this work and MR imaging technologists, Ms. Ruby Endre and Mr Garry Detzler, for their assistance with data collection.

Disclosures: Sandra E. Black—UNRELATED: Consultancy: Novartis, Merck, Pfizer, Eli Lilly, Comments: ad hoc consulting; Grants/Grants Pending: Hoffmann-La Roche, Eli Lilly, Pfizer, Lundbeck, Transition Therapeutics, GE Healthcare, Axovant Sciences, Cognoptix, Biogen, Canadian Institutes of Health Research, National Institutes of Health, Heart and Stroke Foundation of Canada, Alzheimer's Drug Discovery Foundation, Brain Canada, Ontario Brain Institute, Fondation Leducq, Weston Foundation, Canadian Partnership for Stroke Recovery, Comments: contract grants and grants from government agencies paid to the institution\*; Payment for Lectures Including Service on Speakers Bureaus: Medscape, Biogen, Comments: lecture presented at the Alzheimer's Association International Conference, 2016, Toronto. John A. Detre—UNRELATED: Board Membership: International Society for Magnetic Resonance in Medicine, Comments: board member, 2011–2014; Consultancy: Child Health and Development Institute, Ironwood Pharmaceuticals, National Institutes of Health, Wellcome Trust, Comments: I have been a paid consultant on neuroimaging for the Child Health and Development Institute (nonprofit Huntington disease research entity, Ironwood Pharmaceuticals company); I review grants for National Institutes of Health and the Wellcome Trust (UK) and have received honoraria for that work; Employment: University of Pennsylvania; Grants/Grants Pending: National Institutes of Health, Comments: I am a co-investigator on numerous National Institutes of Health grants that are funded or pending\*; Payment for Lectures Including Service on Speakers Bureaus: Stanford University, Moss Rehabilitation Research Institute, Korean Society for Magnetic Resonance in Medicine; Stock/Stock Options: Blackfynn, Comments: I am eligible for stock in Blackfynn, a Pennsylvania startup company in exchange for consulting, but I have not exercised this option. \*Money paid to the institution.

## REFERENCES

1. Detre JA, Wang J, Wang Z, et al. Arterial spin-labeled perfusion MRI in basic and clinical neuroscience. *Curr Opin Neurol* 2009;22:348–55 CrossRef Medline
2. Williams DS, Detre JA, Leigh JS, et al. Magnetic resonance imaging of perfusion using spin inversion of arterial water. *Proc Natl Acad Sci U S A* 1992;89:212–16 CrossRef Medline
3. Alsop DC, Detre JA, Golay X, et al. Recommended implementation of arterial spin-labeled perfusion MRI for clinical applications: a consensus of the ISMRM perfusion study group and the European consortium for ASL in dementia. *Magn Reson Med* 2015;73:102–16 CrossRef Medline
4. Bakker CJ, Hoogeveen RM, Viergever MA. Construction of a protocol for measuring blood flow by two-dimensional phase-contrast MRA. *J Magn Reson Imaging* 1999;9:119–27 Medline
5. Wu WC, St. Lawrence KS, Licht DJ, et al. Quantification issues in arterial spin labeling perfusion magnetic resonance imaging. *Top Magn Reson Imaging* 2010;21:65–73 CrossRef Medline
6. Jahanian H, Noll DC, Hernandez-Garcia L. B0 field inhomogeneity considerations in pseudo-continuous arterial spin labeling (pCASL): effects on tagging efficiency and correction strategy. *NMR Biomed* 2011;24:1202–09 CrossRef Medline
7. Dai W, Garcia De Bazelaire C, et al. Continuous flow-driven inversion for arterial spin labeling using pulsed radio frequency and gradient fields. *Magn Reson Med* 2008;60:1488–97 CrossRef Medline
8. Aslan S, Xu F, Wang PL, et al. Estimation of labeling efficiency in pseudocontinuous arterial spin labeling. *Magn Reson Med* 2010;63:765–71 CrossRef Medline
9. O'Gorman RL, Summers PE, Zelaya FO, et al. In vivo estimation of the flow-driven adiabatic inversion efficiency for continuous arterial spin labeling: a method using phase contrast magnetic resonance angiography. *Magn Reson Med* 2006;55:1291–97 CrossRef Medline
10. Vidorreta M, Wang Z, Rodriguez I, et al. Comparison of 2D and 3D single-shot ASL perfusion fMRI sequences. *Neuroimage* 2013;66:662–71 CrossRef Medline
11. Dolui S, Wang Z, Wang DJ, et al. Comparison of noninvasive MRI measurements of cerebral blood flow in a large multisite cohort. *J Cereb Blood Flow Metab* 2016;36:1244–56 CrossRef Medline
12. Bai CH, Chen JR, Chiu HC, et al. Lower blood flow velocity, higher resistance index, and larger diameter of extracranial carotid arteries are associated with ischemic stroke independently of carotid atherosclerosis and cardiovascular risk factors. *J Clin Ultrasound* 2007;35:322–30 CrossRef Medline
13. Homma S, Sloop GD, Zieske AW. The effect of age and other atherosclerotic risk factors on carotid artery blood velocity in individuals ranging from young adults to centenarians. *Angiology* 2009;60:637–43 CrossRef Medline
14. Shirzadi Z, Crane DE, Robertson AD, et al. Automated removal of spurious intermediate cerebral blood flow volumes improves image quality among older patients: a clinical arterial spin labeling investigation. *J Magn Reson Imaging* 2015;42:1377–85 CrossRef Medline
15. Liu Y, Zhu X, Feinberg D, et al. Arterial spin labeling MRI study of age and gender effects on brain perfusion hemodynamics. *Magn Reson Med* 2012;68:912–22 CrossRef Medline
16. Nasel C, Boubela R, Kalcher K, et al. Normalised time-to-peak-distribution curves correlate with cerebral white matter hyperintensities: could this improve early diagnosis? *J Cereb Blood Flow Metab* 2017;37:444–55 CrossRef Medline
17. Mutsaerts HJ, Petr J, Václavů L, et al. The spatial coefficient of variation in arterial spin labeling cerebral blood flow images. *J Cereb Blood Flow Metab* 2017 Jan 1. [Epub ahead of print] CrossRef Medline
18. Smith SM. Fast robust automated brain extraction. *Hum Brain Mapp* 2002;17:143–55 CrossRef Medline
19. Zhang Y, Brady M, Smith S. Segmentation of brain MR images through a hidden Markov random field model and the expectation-

- maximization algorithm. *IEEE Trans Med Imaging* 2001;20:45–57 CrossRef Medline
20. Harper CG, Kril JJ, Daly JM. **The specific gravity of the brains of alcoholic and control patients: a pathological study.** *Br J Addict* 1987;82:1349–54 CrossRef Medline
  21. Gibson E, Gao F, Black SE, et al. **Automatic segmentation of white matter hyperintensities in the elderly using FLAIR images at 3T.** *J Magn Reson* 2010;31:1311–22 CrossRef Medline
  22. Wu WC, Mazaheri Y, Wong EC. **The effects of flow dispersion and cardiac pulsation in arterial spin labeling.** *IEEE Trans Med Imaging* 2007;26:84–92 CrossRef Medline
  23. Buxton RB, Frank LR, Wong EC, et al. **A general kinetic model for quantitative perfusion imaging with arterial spin labeling.** *Magn Reson Med* 1998;40:383–96 CrossRef Medline
  24. Bokkers RP, van der Worp HB, Mali WP, et al. **Noninvasive MR imaging of cerebral perfusion in patients with a carotid artery stenosis.** *Neurology* 2009;73:869–75 CrossRef Medline
  25. MacIntosh BJ, Marquardt L, Schulz UG, et al. **Hemodynamic alterations in vertebrobasilar large artery disease assessed by arterial spin-labeling MR imaging.** *AJNR Am J Neuroradiol* 2012;33:1939–44 CrossRef Medline
  26. Mutsaerts HJ, van Dalen JW, Heijtel DF, et al. **Cerebral perfusion measurements in elderly with hypertension using arterial spin labeling.** *PLoS One* 2015;10:e0133717 CrossRef Medline
  27. Wu WC, Jiang SF, Yang SC, et al. **Pseudocontinuous arterial spin labeling perfusion magnetic resonance imaging: a normative study of reproducibility in the human brain.** *Neuroimage* 2011;56:1244–50 CrossRef Medline
  28. Guo L, Zhang Q, Ding L, et al. **Pseudo-continuous arterial spin labeling quantifies cerebral blood flow in patients with acute ischemic stroke and chronic lacunar stroke.** *Clin Neurol Neurosurg* 2014;125:229–36 CrossRef Medline
  29. Firbank MJ, He J, Blamire AM, et al. **Cerebral blood flow by arterial spin labeling in poststroke dementia.** *Neurology* 2011;76:1478–84 CrossRef Medline
  30. van Es AC, van der Grond J, ten Dam VH, et al; PROSPER Study Group. **Associations between total cerebral blood flow and age related changes of the brain.** *PLoS One* 2010;5:e9825 CrossRef Medline
  31. Lu H, Clingman C, Golay X, et al. **Determining the longitudinal relaxation time (T1) of blood at 3.0 Tesla.** *Magn Reson Med* 2004;52:679–82 CrossRef Medline
  32. Lotz J, Meier C, Leppert A, et al. **Cardiovascular flow measurement with phase-contrast MR imaging: basic facts and implementation.** *Radiographics* 2002;22:651–71 CrossRef Medline
  33. Tang C, Blatter DD, Parker DL. **Correction of partial-volume effects in phase-contrast flow measurements.** *J Magn Reson Imaging* 1995;5:175–80 CrossRef Medline
  34. Wu B, Wang X, Guo J, et al. **Collateral circulation imaging: MR perfusion territory arterial spin-labeling at 3T.** *AJNR Am J Neuroradiol* 2008;29:1855–60 CrossRef Medline
  35. Chen Z, Zhang X, Yuan C, et al. **Measuring the labeling efficiency of pseudocontinuous arterial spin labeling.** *Magn Reson Med* 2017;77:1841–52 CrossRef Medline

# Head-to-Head Visual Comparison between Brain Perfusion SPECT and Arterial Spin-Labeling MRI with Different Postlabeling Delays in Alzheimer Disease

T. Kaneta, O. Katsuse, T. Hirano, M. Ogawa, K. Yoshida, T. Odawara, Y. Hirayasu, and T. Inoue

## ABSTRACT

**BACKGROUND AND PURPOSE:** Arterial spin-labeling MR imaging has been recently developed as a noninvasive technique with magnetically labeled arterial blood water as an endogenous contrast medium for the evaluation of CBF. Our aim was to compare arterial spin-labeling MR imaging and SPECT in the visual assessment of CBF in patients with Alzheimer disease.

**MATERIALS AND METHODS:** In 33 patients with Alzheimer disease or mild cognitive impairment due to Alzheimer disease, CBF images were obtained by using both arterial spin-labeling–MR imaging with a postlabeling delay of 1.5 seconds and 2.5 seconds (PLD<sub>1.5</sub> and PLD<sub>2.5</sub>, respectively) and brain perfusion SPECT. Twenty-two brain regions were visually assessed, and the diagnostic confidence of Alzheimer disease was recorded.

**RESULTS:** Among all arterial spin-labeling images, 84.9% of PLD<sub>1.5</sub> and 9% of PLD<sub>2.5</sub> images showed the typical pattern of advanced Alzheimer disease (ie, decreased CBF in the bilateral parietal, temporal, and frontal lobes). PLD<sub>1.5</sub>, PLD<sub>2.5</sub>, and SPECT imaging resulted in obviously different visual assessments. PLD<sub>1.5</sub> showed a broad decrease in CBF, which could have been due to an early perfusion. In contrast, PLD<sub>2.5</sub> did not appear to be influenced by an early perfusion but showed fewer pathologic findings than SPECT.

**CONCLUSIONS:** The distinctions observed by us should be carefully considered in the visual assessments of Alzheimer disease. Further studies are required to define the patterns of change in arterial spin-labeling–MR imaging associated with Alzheimer disease.

**ABBREVIATIONS:** AD = Alzheimer disease; ASL = arterial spin-labeling; MCI = mild cognitive impairment; MMSE = Mini-Mental State Examination; PLD = postlabeling delay; PLD<sub>1.5</sub> = postlabeling delay of 1.5 seconds; PLD<sub>2.5</sub> = postlabeling delay of 2.5 seconds

For the imaging diagnosis of Alzheimer disease (AD), CBF is typically evaluated with brain perfusion SPECT.<sup>1,2</sup> MR imaging is also commonly performed, chiefly for the evaluation of atrophy and ischemic changes in the brain. Obtaining these images simultaneously would be significantly beneficial to both patients and caregivers. Arterial spin-labeling (ASL) MR imaging has been recently developed as a noninvasive technique with magnetically labeled arterial blood water as an endogenous contrast medium for the evaluation of CBF.<sup>3–6</sup> Several studies have reported interesting perfusion comparisons between patients with

various forms of dementia and demographically matched healthy controls. Both AD and mild cognitive impairment (MCI) have been associated with hypoperfusion in the middle occipital areas, medial temporal lobe, and especially the parietal lobe.<sup>7</sup> Similar hypoperfusion has been reported in the posterior cingulate and precuneus, in addition to frontal and parietal regions.<sup>8,9</sup> ASL-MR imaging is a potentially useful tool for the differential diagnosis of dementia.<sup>10,11</sup> However, most studies have performed voxelwise or ROI analyses to detect abnormal findings in patients with AD compared with healthy patients or those with other forms of dementia. To date, only a few studies of AD have focused on visual assessment with ASL-MR imaging, mainly because of the lack of established criteria for using ASL-MR imaging to diagnose AD.

Pseudocontinuous ASL, the most common form of ASL, is a distinct form of pulsed and continuous labeling and is recommended for clinical imaging by the International Society for Magnetic Resonance in Medicine Workshop on Perfusion Imaging.<sup>12</sup> For ASL imaging, arterial water in the neck is labeled with a radiofrequency pulse and the brain is imaged after a fixed time interval, which is termed the postlabeling delay (PLD) and is the key parameter of ASL imaging. However, the optimal PLD for the

Received September 15, 2016; accepted after revision March 24, 2017.

From the Departments of Radiology (T.K., T.H., M.O., K.Y., T.I.) and Psychiatry (O.K., T.O., Y.H.), Yokohama City University, Yokohama, Japan.

We declare that all human and animal studies have been approved by the institutional review board of Yokohama City University School of Medicine and have therefore been performed in accordance with the ethical standards laid down in the 1964 Declaration of Helsinki and its later amendments. We declare that all patients gave informed consent prior to inclusion in this study.

Please address correspondence to Tomohiro Kaneta, MD, PhD, Department of Radiology, Yokohama City University, 3-9 Fukuura, Kanazawa-ku, Yokohama, 236-0004 Japan; e-mail kaneta@yokohama-cu.ac.jp

<http://dx.doi.org/10.3174/ajnr.A5238>

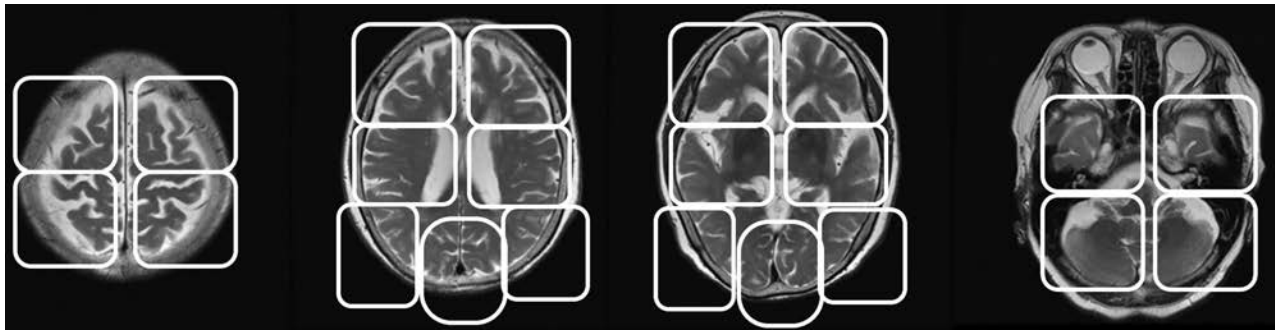


**FIG 1.** The regions used for scoring brain images. We evaluated 22 regions located at the levels of the vertex, lateral ventricle, basal ganglia, and cerebellum. The raters scored each region with a 4-point scale, where 0 is a normal CBF, 1 is a mild decrease, 2 is a moderate decrease, and 3 is a severe decrease.

evaluation of patients with dementia is unknown. Many previous studies of AD have used a PLD of 1.5 seconds (PLD<sub>1.5</sub>),<sup>13,14</sup> while others have used 2.0 seconds.<sup>15</sup> The International Society for Magnetic Resonance in Medicine Workshop recommends 2.0 seconds for adult clinical patients,<sup>12</sup> but a longer PLD might be appropriate for elderly patients due to their relatively slow blood flow. In the present study, we performed a clinical visual assessment to compare the CBF images obtained by using ASL-MR imaging or brain perfusion SPECT in patients with AD. PLDs of 1.5 and 2.5 seconds (PLD<sub>2.5</sub>) were used for ASL-MR imaging.

## MATERIALS AND METHODS

We recruited 33 patients who underwent brain MR imaging and SPECT for the diagnosis of AD or MCI due to AD between September 2015 and June 2016. Patients with AD met the criteria of the National Institute of Neurological and Communicative Disorders and Stroke–Alzheimer Disease and Related Disorders Association for probable AD.<sup>16</sup> Patients were excluded from the study if they had a significant history of psychiatric or neurologic disorders other than AD, including stroke, head injury, epilepsy, psychiatric disorders, alcohol abuse, and other serious medical conditions. All patients underwent MR imaging, SPECT, and standard dementia screening, which included a medical history and Mini-Mental State Examination (MMSE) and neuropsychological testing. SPECT and MR imaging were performed  $\leq 1$  month apart. The local institutional review board approved the study, and all subjects provided written informed consent.

### MR Imaging

MR imaging was performed with a 3T MR imaging system (Discovery 750w; GE Healthcare, Milwaukee, Wisconsin) and a 12-channel head coil. Structural imaging for anatomic information was performed with a sagittal 3D T1-weighted sequence (TR = 6.6 ms, TE = 2 ms, flip angle = 14°, matrix = 256 × 256, 170 sections, voxel size = 1.0 × 0.9 × 0.9 mm<sup>3</sup>, FOV = 23 × 23 cm) with an acquisition time of 6 minutes.

A whole-brain pseudocontinuous ASL 3D perfusion sequence was acquired (3D fast spin-echo acquisition with background suppression). The imaging protocol with PLD<sub>1.5</sub> was TR = 4641 ms, TE = 10.7 ms, locations = 36, FOV = 23 × 23 cm, voxel size = 2 × 2 × 4 mm<sup>3</sup>, labeling duration = 1.5 seconds, NEX = 1, and an acquisition time of 1 minute 33 seconds. The imaging protocol with PLD<sub>2.5</sub> was TR = 5336 ms, TE = 10.7 ms, and

**Table 1: Demographic and neuropsychological summary of the participants<sup>a</sup>**

	AD	MCI due to AD
Age (yr)	77.1 (7.7)	78.2 (5.6)
No. of patients	14	19
Sex (M/F)	3:11	8:11
MMSE score	16.9 (3.0) <sup>b</sup>	25.2 (2.6) <sup>b</sup>

<sup>a</sup>Data are presented as mean ( $\pm$ SD).

<sup>b</sup>There was a significant difference in the MMSE score ( $P < .01$ ) between AD and patients with AD-induced MCI.

NEX = 2. All other parameters were the same, and the acquisition time was 2 minutes 51 seconds.

### Brain Perfusion SPECT

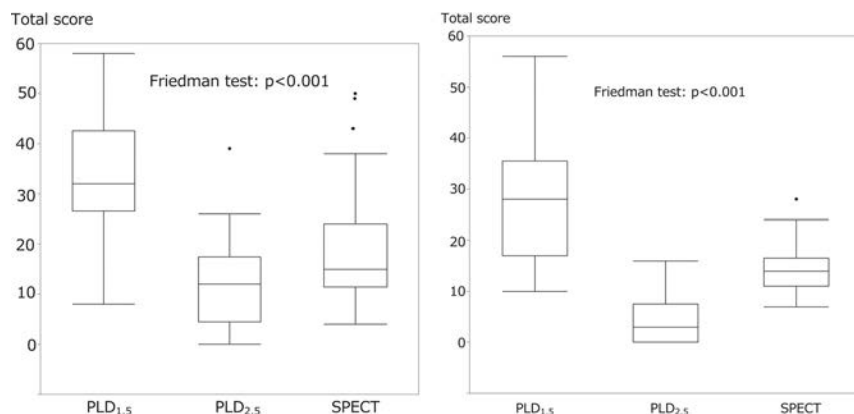
The SPECT scans began 15 minutes after the intravenous injection of 148 MBq of iodine 123 *N*-isopropyl-*p*-iodoamphetamine (<sup>123</sup>I-IMP) (Nihon Medipysics, Hyogo, Japan) and were performed for 30 minutes by using a SPECT/CT scanner (Symbia T16; Siemens, Erlangen, Germany). The SPECT scans were acquired by using low-medium-energy general purpose collimation, a 128 × 128 matrix of 3.3-mm pixel size, and 300 s/rotation in a continuous-rotation mode. SPECT reconstruction was performed with a Butterworth filter for filtered back-projection with a cutoff = 0.35/cm and an order of 8. A uniform attenuation correction was performed by using the Chang method, with  $\mu = 0.11$ .

### Visual Assessment

Two board-certified radiologists who are also nuclear medicine physicians with >10 years of experience in reading MR imaging and SPECT brain images and 2 years of experience reading ASL-MR imaging independently reviewed the images obtained in the present investigation without the clinical information of the patient. SPECT and ASL-MR imaging were shown with a section thickness of 6.6 and 6.4 mm, respectively. We used the scoring sheet shown in Fig 1 to assess 22 brain regions. The regions were located at the levels of the vertex, lateral ventricle, basal ganglia, and cerebellum. The raters scored each region by using a 4-point scale, in which zero indicated normal CBF; 1, a mild decrease; 2, a moderate decrease; and 3, a severe decrease. The diagnostic confidence of AD was also scored between 0 and 4, in which 0 indicated definitely not AD; 1, probably not AD; 2, undetermined; 3, probably AD; and 4, definitely AD. ASL-MR images were displayed in

**Table 2: The results of visual assessments for the diagnosis of AD**

	Overall Positive Rate (%)			Positive Rate in AD (%)			Positive Rate in MCI (%)		
	PLD <sub>1.5</sub>	PLD <sub>2.5</sub>	SPECT	PLD <sub>1.5</sub>	PLD <sub>2.5</sub>	SPECT	PLD <sub>1.5</sub>	PLD <sub>2.5</sub>	SPECT
Rater 1	87.9	9.1	69.7	92.9	14.3	92.9	84.2	28.6	52.6
Rater 2	97.0	12.1	90.1	100	28.6	92.9	94.7	0	89.5
Agreement	84.8	3.0	66.7	92.9	7.1	85.7	84.2	0	52.6

**FIG 2.** The comparisons of the total scores of the 2 raters for PLD<sub>1.5</sub>, PLD<sub>2.5</sub>, and SPECT images. The Friedman analysis of variance showed a significant difference among all 3 groups ( $P < .01$ ), and the Wilcoxon test showed a significant difference between the 2 raters for the PLD<sub>1.5</sub>, PLD<sub>2.5</sub>, and SPECT total scores ( $P < .01$ ).**Table 3: Interrater agreement**

	$\kappa$ Statistic	
	5-Point Scoring	Positive or Negative for AD Diagnosis
PLD <sub>1.5</sub>	0.033	0.3694
PLD <sub>2.5</sub>	0.141	0.203
SPECT	0.010	0.195

gray-scale and in color-scale fused with T1-weighted images. SPECT images were displayed in color.

### Statistical Analysis

The interrater variability was assessed for the diagnostic confidence of AD by using the  $\kappa$  statistic. The diagnostic confidence was evaluated with not only the 2-point scale but also positive (3 and 4) or negative (0–2) scores for AD diagnosis. The total scores for SPECT, PLD<sub>1.5</sub>, and PLD<sub>2.5</sub> from each rater were analyzed by using a Friedman test. Data were analyzed in Excel (Microsoft, Redmond, Washington) and JMP12 (SAS, Cary, North Carolina). A  $P < .01$  was statistically significant.

## RESULTS

### Demographic Findings

Patient demographics are shown in Table 1, including age, the male-to-female ratio, and MMSE scores. There was no difference in age, but a significant difference in MMSE ( $P < .01$ ) was observed between patients with AD and those with AD-induced MCI.

### Visual Assessment

Table 2 shows the results of the visual assessment as the percentage of patients diagnosed with AD (score of 3 or 4) for each rater. The agreement concerning the percentage of patients with an AD

diagnosis between the 2 raters is also shown. These results are presented for 3 groups: namely, the total population, the AD group (MMSE  $\leq 21$ ), and the AD-induced MCI group (MMSE  $> 21$ ). Both raters observed that for the total population, the AD group, and the AD-induced MCI group, PLD<sub>1.5</sub> imaging had the highest positive rate for AD diagnosis, while PLD<sub>2.5</sub> imaging had the lowest. Moreover, the positive rate for AD diagnosis was higher for the AD group than for the MCI group (Table 2). The Friedman analysis of variance test revealed a significant difference in total scores among all 3 imaging modalities ( $P < .01$ ), and the Wilcoxon test revealed a significant difference between

the 2 groups in the assessment of PLD<sub>1.5</sub>, PLD<sub>2.5</sub>, and SPECT images ( $P < .01$ ) (Fig 2). There were no significant differences between the AD and AD-induced MCI groups in the total score for 3 imaging modalities. The interrater agreements were low for both the 5-point or 2-alternative scoring of AD (Table 3).

### Case Presentations

Case 1 was an 86-year-old woman with AD. Her MMSE score was 14. The ASL-MR imaging and SPECT images for this patient are shown in Fig 3. Case 2 was an 83-year-old woman with AD. Her MMSE score was 19. The images for this patient are shown in Fig 4. Case 3 was a 73-year-old woman with MCI due to AD. Her MMSE score was 23. The images for this patient are shown in Fig 5.

## DISCUSSION

We clearly observed differences in the visual assessments of PLD<sub>1.5</sub>, PLD<sub>2.5</sub>, and SPECT images. The total scores of the 2 raters were highest for the PLD<sub>1.5</sub> images; this finding suggests a large decrease in CBF. Indeed, these scores were diminished or ambiguous in PLD<sub>2.5</sub> images. SPECT findings were of intermediate severity compared with those for the PLD<sub>1.5</sub> and PLD<sub>2.5</sub> images. These findings appeared to have a profound effect on the diagnostic confidence of AD—that is, for both raters, the positive rate for AD diagnosis was very high (approximately 90%) with a high agreement rate for PLD<sub>1.5</sub> images, while the diagnostic confidence of AD was low for PLD<sub>2.5</sub> images with a low agreement rate. In addition, SPECT images were associated with a moderately high diagnostic confidence and agreement rate. The positive rate of AD diagnosis for the SPECT images in the present investigation was consistent with that of previous studies.<sup>1,2</sup>

In the present study, the PLD<sub>1.5</sub> images often showed marked

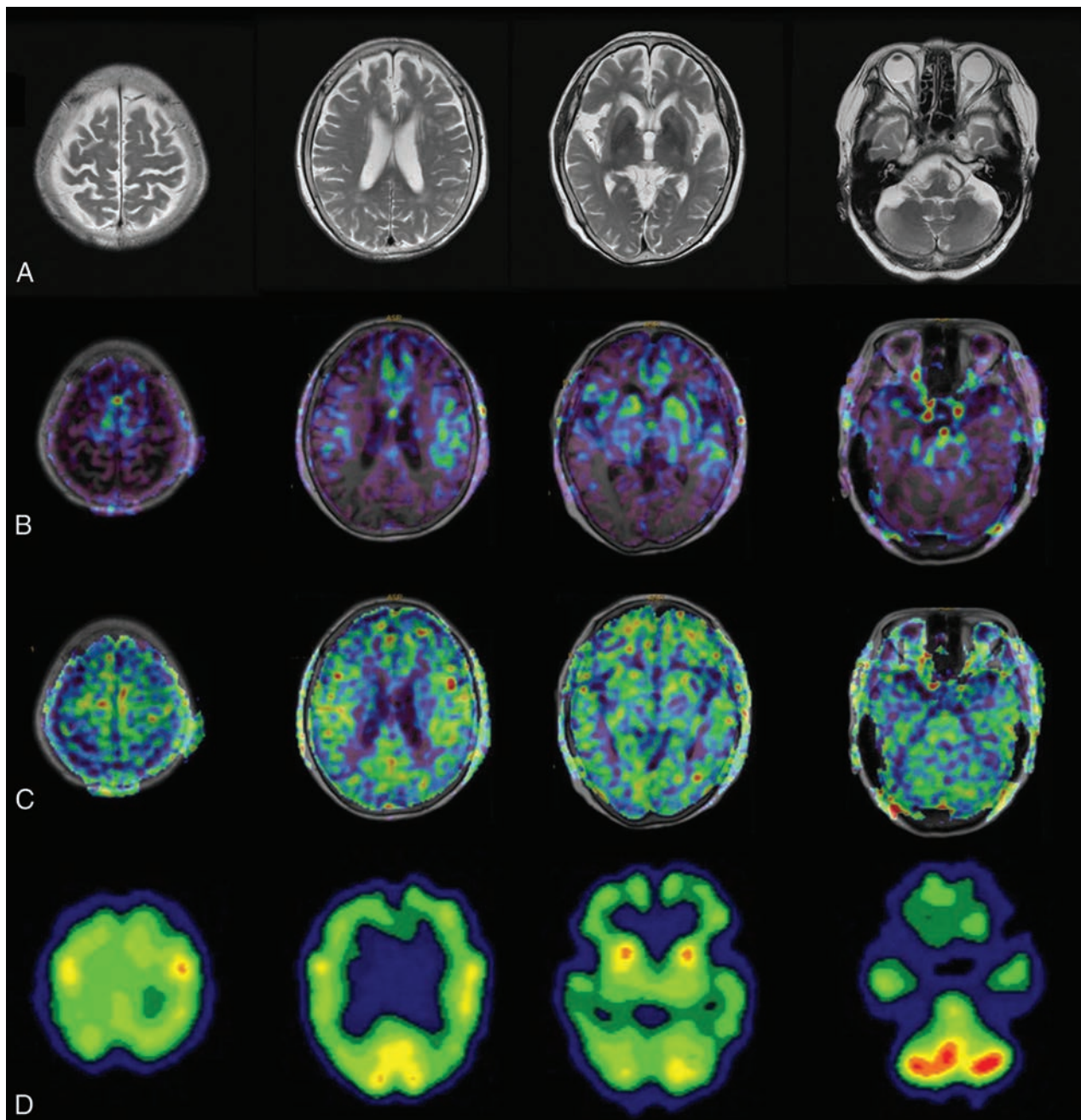


**FIG 3.** An 86-year-old woman with AD. The patient had an MMSE score of 14. Axial images of T2-weighted MR imaging (A), ASL-MR imaging with PLD<sub>1.5</sub> in a color-scale fused with T1-weighted MR imaging (B), ASL-MR imaging with PLD<sub>2.5</sub> in a color-scale fused with T1-weighted MR imaging (C), and brain perfusion SPECT at the level of the parietal lobe, corona radiata, basal ganglia, and cerebellum (D). Both raters indicated a score of 4 (definitely AD) for PLD<sub>1.5</sub> and SPECT and 1 (probably not AD) for PLD<sub>2.5</sub>.

bilateral decreases in signal intensity in the frontal and temporo-parietal lobes, even for patients with AD-induced MCI, but these findings were mostly not present in the PLD<sub>2.5</sub> images (case 3, Fig 5). A previous study using PLD<sub>1.5</sub> for patients with cerebrovascular disease reported a low ASL signal with surrounding cortical areas showing a high signal intensity in the middle cerebral artery–anterior cerebral artery and middle cerebral artery–posterior cerebral artery borderzones. This phenomenon was termed the “borderzone sign”.<sup>17</sup> Another recent study evaluated the performance of PLD<sub>1.5</sub> compared with SPECT in patients with AD and reported that PLD<sub>1.5</sub> images frequently showed the border-

zone sign.<sup>18</sup> Our results suggest the presence of the borderzone sign for PLD<sub>1.5</sub>, but not PLD<sub>2.5</sub>. The presence of the borderzone sign in ASL-MR images with a short PLD, but not in those with a long PLD, could have been due to an early perfusion adjacent to the main cerebral arteries. In fact, our PLD<sub>2.5</sub> images did not frequently show such a broad decrease in CBF, and neither did the SPECT images.

In the present study, the PLD<sub>2.5</sub> images frequently showed only minor pathologic findings with a low image contrast. Generally, a long PLD decreases the signal-to-noise ratio because of T1 relaxation. Thus, we doubled the number of excitations for

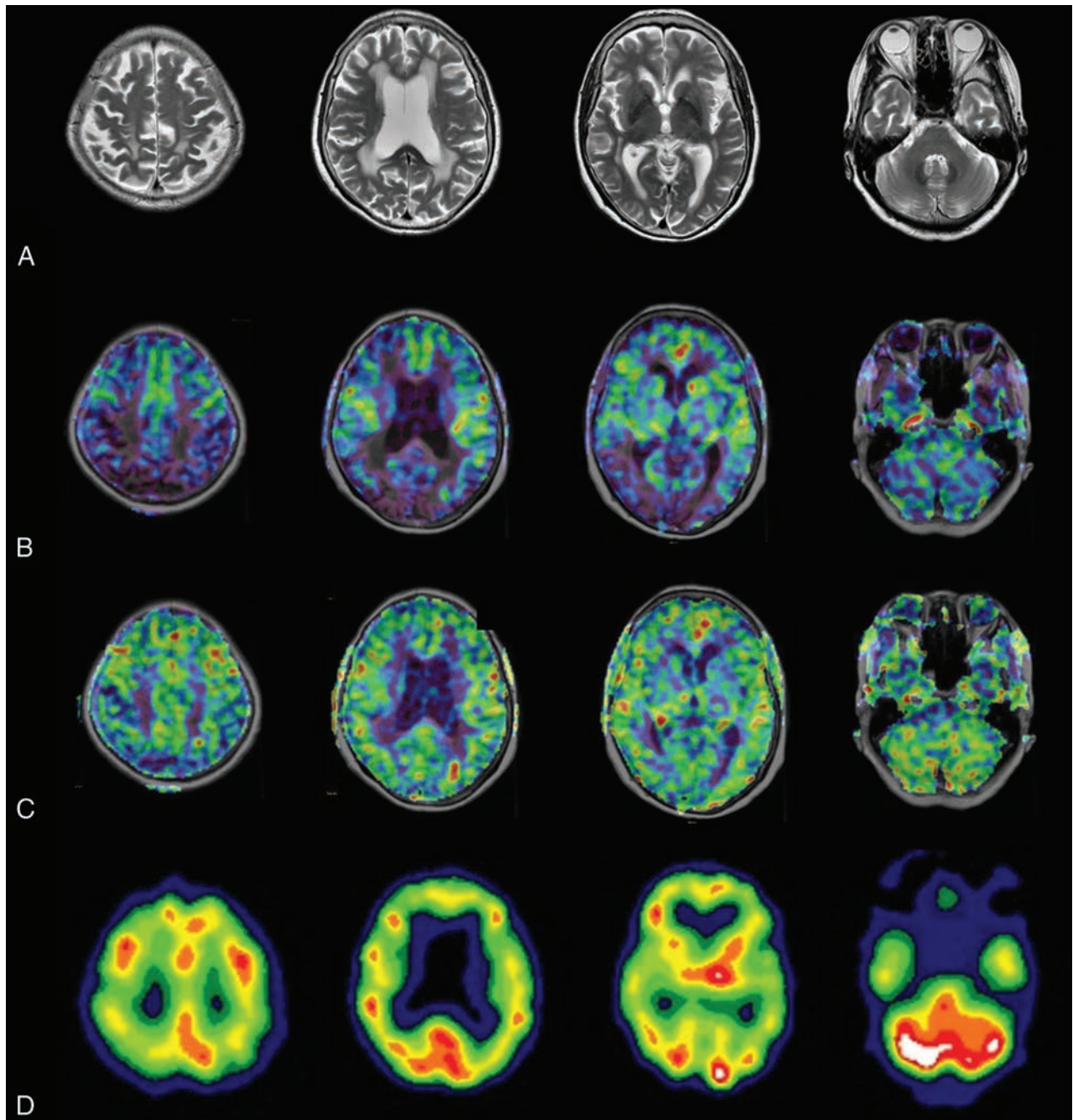


**FIG 4.** An 83-year-old woman with AD. The patient had an MMSE score of 19. Axial images of T2-weighted MR imaging (A), fused T1-weighted and PLD<sub>1.5</sub> ASL-MR imaging (B), fused T1-weighted and PLD<sub>2.5</sub> ASL-MR imaging (C), and brain perfusion SPECT (D). Both raters indicated a score of 4 for PLD<sub>1.5</sub> and 2 (undetermined) for PLD<sub>2.5</sub>. One rater indicated a score of 3 (probably AD) and another rater indicated a score of 4 for SPECT.

PLD<sub>2.5</sub> compared with PLD<sub>1.5</sub>; however, a greater number of excitations or the modification of some other parameter might be necessary to improve image contrast and quality.

A previous study comparing PET using FDG and ASL-MR imaging using PLD<sub>1.5</sub> in patients with AD<sup>19</sup> reported that both methods showed similar regional abnormalities and have comparable diagnostic accuracy in AD. The PLD<sub>1.5</sub> images of this previous study were different from ours, which did not show decreased CBF in the frontal lobes. The findings of this previous study also contradict those in another study that reported decreased CBF in

the frontal lobes of patients with AD.<sup>20</sup> Another study performed multidelay multiparametric ASL for patients with stroke; however, their PLD<sub>1.5</sub> images did not show decreased CBF in the frontal lobes but resembled those of PLD<sub>2.5</sub> images.<sup>21</sup> Such conflicting results between these studies may be due to scanner differences, parameters other than PLD, or other experimental differences.

There is a strong link between brain metabolism and CBF.<sup>22</sup> Thus, SPECT images have been generally interpreted in a manner similar to that of FDG-PET. However, as our results show, ASL-MR images can change depending on the PLD and show

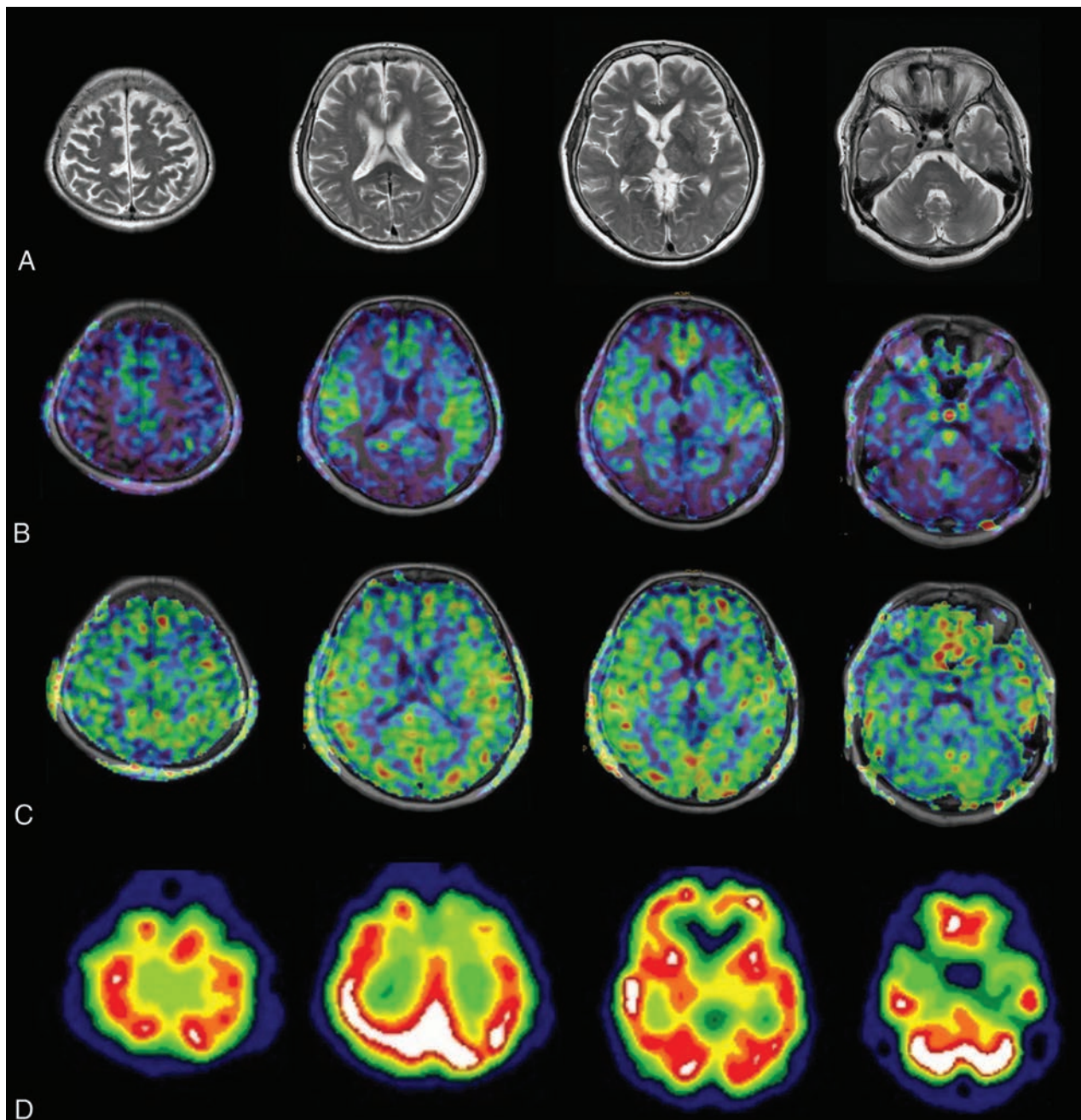


**FIG 5.** A 73-year-old woman with MCI. The patient had an MMSE score of 23. Axial images of T2-weighted MR imaging (A), fused T1-weighted and PLD<sub>1.5</sub> ASL-MR imaging (B), fused T1-weighted and PLD<sub>2.5</sub> ASL-MR imaging (C), and brain perfusion SPECT (D). Both raters scored 4 for PLD<sub>1.5</sub>. However, 1 rater indicated a score of 1 (probably not AD) for PLD<sub>2.5</sub> and 2 for SPECT, while another rater indicated a score of 0 (definitely not AD) for PLD<sub>2.5</sub>, and 1 for SPECT.

significantly different findings from SPECT. The use of FDG criteria for ASL-MR imaging diagnosis of AD increases the risk of over- or underdiagnosis. Further studies will be needed to establish the optimal conditions for ASL-MR imaging in the diagnosis of AD and to define the dynamic temporal patterns of ASL-MR images associated with the development of AD.

Regarding the differentiation of AD and AD-induced MCI, we did not observe significant differences in total scores of the 3 modalities between the AD and AD-induced MCI groups. The positive rates for AD diagnosis for the AD group were slightly higher than those for the AD-induced MCI group; however, the differ-

ences were small. Further studies are required to clarify the usefulness of ASL for the discrimination of AD and AD-induced MCI.

The interrater agreements were low in the present study, even for the 2-alternative scoring method. The participants in our study had relatively high MMSE scores. Only 1 participant had an MMSE score of <10, and 5 of the participants had scores of <15, which could have resulted in a low interrater agreement.

The present study has several limitations. First, the sample size was small; a larger sample would produce more reliable results. Second, we did not perform MR angiography due to tight time

constraints. Third, no images of cognitively healthy participants were used as controls; thus, we could not evaluate the accuracy of the visual-based diagnosis. Finally, an optimal PLD could not be determined in the present study. These limitations should be considered for future research.

## CONCLUSIONS

Significant differences in visual assessments were observed for PLD<sub>1.5</sub>, PLD<sub>2.5</sub>, and SPECT images. PLD<sub>1.5</sub> images showed a robust decrease in CBF, which could have been due to an early perfusion. In contrast, PLD<sub>2.5</sub> did not appear to be influenced by an early perfusion but showed fewer pathologic findings than SPECT. Visual assessment of AD should be performed with attention to these distinctions. Further studies are required to define the dynamic temporal ASL-MR imaging pattern associated with AD.

## ACKNOWLEDGMENTS

We thank Mr. Yuki Koyo for his assistance with data collection and analyses, Dr. Ayako Hino for reading images, and Mr. Naoki Hirata for his advice on the processing of ASL-MR imaging.

## REFERENCES

1. Jagust W, Thisted R, Devous MD Sr, et al. **SPECT perfusion imaging in the diagnosis of Alzheimer's disease: a clinical-pathologic study.** *Neurology* 2001;56:950–56 CrossRef Medline
2. Bonte FJ, Weiner MF, Bigio EH, et al. **Brain blood flow in the dementias: SPECT with histopathologic correlation in 54 patients.** *Radiology* 1997;202:793–97 CrossRef Medline
3. Dai W, Lopez OL, Carmichael OT, et al. **Mild cognitive impairment and Alzheimer disease: patterns of altered cerebral blood flow at MR imaging.** *Radiology* 2009;250:856–66 CrossRef Medline
4. Chao LL, Pa J, Duarte A, et al. **Patterns of cerebral hypoperfusion in amnesic and dysexecutive MCI.** *Alzheimer Dis Assoc Disord* 2009;23:245–52 CrossRef Medline
5. Johnson NA, Jahng GH, Weiner MW, et al. **Pattern of cerebral hypoperfusion in Alzheimer disease and mild cognitive impairment measured with arterial spin-labeling MR imaging: initial experience.** *Radiology* 2005;234:851–59 CrossRef Medline
6. Asllani I, Habeck C, Scarmeas N, et al. **Multivariate and univariate analysis of continuous arterial spin labeling perfusion MRI in Alzheimer's disease.** *J Cereb Blood Flow Metab* 2008;28:725–36 CrossRef Medline
7. Alexopoulos P, Sorg C, Förschler A, et al. **Perfusion abnormalities in mild cognitive impairment and mild dementia in Alzheimer's disease measured by pulsed arterial spin labeling MRI.** *Eur Arch Psychiatry Clin Neurosci* 2012;262:69–77 CrossRef Medline
8. Yoshiura T, Hiwatashi A, Noguchi T, et al. **Arterial spin labelling at 3-T MR imaging for detection of individuals with Alzheimer's disease.** *Eur Radiol* 2009;19:2819–25 CrossRef Medline
9. Mak HK, Chan Q, Zhang Z, et al. **Quantitative assessment of cerebral hemodynamic parameters by QUASAR arterial spin labeling in Alzheimer's disease and cognitively normal elderly adults at 3-Tesla.** *J Alzheimers Dis* 2012;31:33–44 CrossRef Medline
10. Du AT, Jahng GH, Hayasaka S, et al. **Hypoperfusion in frontotemporal dementia and Alzheimer disease by arterial spin labeling MRI.** *Neurology* 2006;67:1215–20 CrossRef Medline
11. Steketee RM, Bron EE, Meijboom R, et al. **Early-stage differentiation between presenile Alzheimer's disease and frontotemporal dementia using arterial spin labeling MRI.** *Eur Radiol* 2016;26:244–53 CrossRef Medline
12. Alsop DC, Detre JA, Golay X, et al. **Recommended implementation of arterial spin-labeled perfusion MRI for clinical applications: a consensus of the ISMRM perfusion study group and the European consortium for ASL in dementia.** *Magn Reson Med* 2015;73:102–16 CrossRef Medline
13. Chen Y, Wolk DA, Reddin JS, et al. **Voxel-level comparison of arterial spin-labeled perfusion MRI and FDG-PET in Alzheimer disease.** *Neurology* 2011;77:1977–85 CrossRef Medline
14. Vercllytte S, Lopes R, Lenfant P, et al. **Cerebral hypoperfusion and hypometabolism detected by arterial spin labeling MRI and FDG-PET in early-onset Alzheimer's disease.** *J Neuroimaging* 2016;26:207–12 CrossRef Medline
15. Binnewijzend MA, Kuijjer JP, Benedictus MR, et al. **Cerebral blood flow measured with 3D pseudocontinuous arterial spin-labeling MR imaging in Alzheimer disease and mild cognitive impairment: a marker for disease severity.** *Radiology* 2013;267:221–30 CrossRef Medline
16. McKhann G, Drachman D, Folstein M, et al. **Clinical diagnosis of Alzheimer disease: report of the NINCDS-ADRDA Work Group under the auspices of Department of Health and Human Service Task Force on Alzheimer Disease.** *Neurology* 1984;34:939–44 CrossRef Medline
17. Zaharchuk G, Bammer R, Straka M, et al. **Arterial spin-label imaging in patients with normal bolus perfusion-weighted MR imaging findings: pilot identification of the borderzone sign.** *Radiology* 2009;252:797–807 CrossRef Medline
18. Takahashi H, Ishii K, Hosokawa C, et al. **Clinical application of 3D arterial spin-labeled brain perfusion imaging for Alzheimer disease: comparison with brain perfusion SPECT.** *AJNR Am J Neuroradiol* 2014;35:906–11 CrossRef Medline
19. Musiek ES, Chen Y, Korczykowski M, et al. **Direct comparison of fluorodeoxyglucose positron emission tomography and arterial spin labeling magnetic resonance imaging in Alzheimer's disease.** *Alzheimers Dement* 2012;8:51–59 CrossRef Medline
20. Raji CA, Lee C, Lopez OL, et al. **Initial experience in using continuous arterial spin-labeled MR imaging for early detection of Alzheimer disease.** *AJNR Am J Neuroradiol* 2010;31:847–55 CrossRef Medline
21. Wang DJ, Alger JR, Qiao JX, et al; UCLA Stroke Investigators. **Multi-delay multi-parametric arterial spin-labeled perfusion MRI in acute ischemic stroke: comparison with dynamic susceptibility contrast enhanced perfusion imaging.** *Neuroimage Clin* 2013;3:1–7 CrossRef Medline
22. Kuschinsky W. **Coupling of function, metabolism, and blood flow in the brain.** *Neurosurg Rev* 1991;14:163–68 CrossRef Medline

# CT Angiography ASPECTS Predicts Outcome Much Better Than Noncontrast CT in Patients with Stroke Treated Endovascularly

F. Sallustio, C. Motta, S. Pizzuto, M. Diomedi, B. Rizzato, M. Panella, F. Alemseged, M. Stefanini, S. Fabiano, R. Gandini, R. Floris, P. Stanzone, and G. Koch



## ABSTRACT

**BACKGROUND AND PURPOSE:** Noncontrast CT ASPECTS has been investigated as a predictor of outcome in patients with acute ischemic stroke. Our purpose was to investigate whether CTA source images are a better predictor of clinical and radiologic outcomes than NCCT ASPECTS in candidates for endovascular stroke therapy.

**MATERIALS AND METHODS:** CT scans of patients ( $n = 124$ ) were independently evaluated by 2 readers for baseline NCCT and CTA source image ASPECTS and for follow-up ASPECTS. An mRS of  $\leq 2$  at 3 months was considered a favorable outcome. Receiver operating characteristic curve analysis was used to assess the ability of NCCT and CTA source image ASPECTS to identify patients with favorable outcomes. A stepwise multiple regression analysis was performed to find independent predictors of outcome.

**RESULTS:** Baseline CTA source image ASPECTS correlated better than NCCT ASPECTS with follow-up ASPECTS ( $r = 0.76$  versus  $r = 0.51$ ;  $P$  for comparison of the 2 coefficients  $< .001$ ). Receiver operating characteristic curve analysis showed that baseline CTA source image ASPECTS compared with NCCT ASPECTS can better identify patients with favorable outcome (CTA source image area under the curve = 0.83; 95% CI, 0.76–0.91; NCCT area under the curve = 0.67; 95% CI, 0.58–0.77;  $P < .001$ ). Finally, the stepwise regression analysis showed that lower age, good recanalization, lower time to recanalization, and good baseline CTA source image ASPECTS, not NCCT ASPECTS, were independent predictors of favorable outcome.

**CONCLUSIONS:** CTA source image ASPECTS predicts outcome better than NCCT ASPECTS; this finding suggests CTA rather than NCCT as a main step in the decision-making process for patients with acute ischemic stroke.

**ABBREVIATIONS:** CTA-SI = CTA source images; ET = endovascular stroke therapy

The Alberta Stroke Program Early CT Score merges the ability of quantifying and describing the topography of brain tissue damage produced by acute ischemic stroke in a semiquantitative way.<sup>1</sup> ASPECTS on noncontrast CT is widely used for the assessment of early ischemic changes, and its prognostic value has already been established,<sup>2</sup> though with poor NCCT sensitivity.<sup>3</sup> Re-

cent randomized controlled trials on endovascular stroke therapy (ET) have been based on strict inclusion criteria, leading to treatment of only those patients with high CT ASPECTS indicating smaller infarct burden.<sup>4–6</sup>

Many attempts have been made to understand which patients are likely to undergo futile reperfusion.<sup>7</sup> For instance, it has been recently demonstrated that patients with poor collaterals and longer time to reperfusion do not achieve good outcomes after ET.<sup>8</sup> Thus, a careful patient selection for ET should be desirable and should be based on a multimodal neuroimaging approach in addition to onset time and stroke severity. Although not as commonly available as NCCT in the acute ischemic stroke setting, CT angiography is useful for confirmation of vessel occlusion in candidates for ET, and hypodensity on CTA source images (CTA-SI) has been shown to reliably correlate with ischemic lesion volume on diffusion-weighted imaging<sup>9</sup> and final infarct size.<sup>10</sup> The superiority of CTA-SI on NCCT in the detection of infarcted areas has been demonstrated for readers of all levels of experience.<sup>11</sup> Few data exist on the value of CTA-SI ASPECTS in patients un-

Received October 14, 2016; accepted after revision March 24, 2017.

From the Department of Neuroscience (F.S., C.M., S.P., M.D., B.R., M.P., F.A., P.S., G.K.), Comprehensive Stroke Center, and Interventional Radiology and Neuroradiology (M.S., S.F., R.G., R.F.), Department of Diagnostic Imaging, University Hospital of Tor Vergata, Rome, Italy; Santa Lucia Foundation (C.M., G.K.), Rome, Italy; and Department of Medicine and Neurology (F.A.), Royal Melbourne Hospital, University of Melbourne, Parkville, Australia.

This work was supported by a grant from the Italian Ministry of Health (RF-2013-02358679).

Ethics approval for this study was obtained from the Tor Vergata Policlinic ethics committee.

Please address correspondence to Fabrizio Sallustio, MD, University Hospital of Tor Vergata, Viale Oxford 81, 00133, Rome, Italy; e-mail: fsall75@gmail.com

Indicates open access to non-subscribers at www.ajnr.org

<http://dx.doi.org/10.3174/ajnr.A5264>

dergoing ET for acute ischemic stroke,<sup>12,13</sup> and this lack of data may explain why only ASPECTS NCCT is currently considered in the guidelines for eligibility for ET. Our purpose was to investigate whether CTA-SI ASPECTS correlate better than NCCT ASPECTS with clinical and radiologic outcome measures in patients with acute ischemic stroke undergoing ET.

## MATERIALS AND METHODS

A retrospective analysis of patients identified from a prospective registry at a comprehensive stroke center (University Hospital of Tor Vergata, Rome, Italy) was performed. Patients with anterior circulation acute ischemic stroke secondary to intracranial proximal arterial occlusion (M1 MCA, M2 MCA, distal internal carotid artery, and proximal ICA plus intracranial proximal arterial occlusion) admitted within 6 hours of symptom onset were included. Due to the study period (between 2009 and 2015) before the publication of recent endovascular stroke trials,<sup>4-6</sup> no exclusion criteria other than the time from symptom onset were adopted. Patients presenting within 4.5 hours of symptom onset were treated with intravenous thrombolysis, which was continued in the angiographic suite during the endovascular procedure. Patients presenting beyond the time window for intravenous thrombolysis or with major contraindications to intravenous thrombolysis (ie, warfarin therapy with an international normalized ratio of 1.7, recent major surgery, or a history of hemorrhage/hematoma) underwent stand-alone thrombectomy. Demographics, vascular risk factors, and baseline and 24-hour NIHSS scores were reported. The modified Rankin Scale was adopted for outcome analysis, and an mRS of  $\leq 2$  at 3 months was considered a favorable outcome. The study was approved by the Tor Vergata Polyclinic Ethical Committee, and informed consent was obtained from all patients or their relatives.

### Image Acquisition

The NCCT and CTA were acquired with a standardized protocol. Axial CT was performed on a multisection scanner (Light Speed VCT; GE Healthcare, Milwaukee, Wisconsin) by using 120 kV and 170 mAs with a 5-mm section thickness. Continuous axial sections parallel to the orbitomeatal line were obtained from the skull base to the vertex. CTA was performed with a 64-detector row scanner. Acquisitions were obtained after single-bolus intravenous contrast injection of 90–120 mL of nonionic contrast media into an antecubital vein at 3–5 mL/s. Imaging was autotriggered by the appearance of contrast media in the ascending aorta. Standard coverage included the area from the arch to the vertex. Source images were reconstructed at a 1.25-mm thickness in the axial planes at half-thickness intervals. NCCT or DWI was performed between 1 and 7 days after stroke onset and used for follow-up ASPECTS.

### Image Processing

NCCT, CTA-SI, and MR imaging (DWI sequences and apparent diffusion coefficient map) scans were independently screened for ASPECTS by 1 neuroradiologist (M.S.) and 1 stroke neurologist (G.K.) who were blinded to the patients' symptoms but aware of acute nonlacunar stroke. The readers performed their evaluation at different time periods to make their assessment blinded as

much as possible. Adequate window and optimal level settings were adopted to maximize the contrast produced by attenuation differences between normal and ischemic tissue. Our ASPECTS reading includes evaluation of all axial sections ([www.aspectsinstroke.com](http://www.aspectsinstroke.com)), and as in previous studies, we excluded isolated cortical swelling from the score.<sup>14</sup> In case of a discrepancy between readers, a third neuroradiologist (R.G.) was involved to achieve a consensus. The interrater reliability was 0.71 for NCCT and 0.75 for CTA-SI, indicating a good interrater agreement for both methods.

### Statistical Analysis

The analysis was performed by using STATA/IC, Version 13 (StataCorp, College Station, Texas) and GraphPad Prism software, Version 6.00 (GraphPad Software, San Diego, California). Continuous variables are summarized as mean  $\pm$  SD or median with interquartile range. Categorical variables are expressed as percentages. To determine differences between the 2 groups, we used a Student *t* test or Mann-Whitney *U* test for continuous variables. Interrater agreement was estimated with the  $\kappa$  statistic. Comparison of frequencies among ASPECTS groups was performed with the Fisher exact test after dichotomization into poor and good ASPECTS. Univariate associations between baseline and follow-up ASPECTS were investigated with the Spearman  $\rho$  analysis, with confidence limits calculated by means of the Fisher *z*-transformation. Bubble plots were used to graphically display correlation analyses, and the area of the bubble has to be read as proportional to the number of observations at each point. A nonparametric receiver operating characteristic curve analysis and the area under the curve were used to assess the ability of NCCT and CTA-SI ASPECTS to identify patients with favorable outcomes (mRS  $\leq 2$ ).

We then calculated the statistical significance of the difference between the area under the curves using the method of DeLong.<sup>15</sup> For both NCCT and CTA-SI ASPECTS, a receiver operating characteristic curve was used to identify the best cutoff point with which to maximize the sensitivity and specificity for discriminating patients with favorable outcomes. A backward and forward stepwise logistic regression analysis was finally performed to determine the independent predictors of good outcome (mRS  $\leq 2$ ), including NCCT and CTA-SI ASPECTS as well as all other variables with a significant association in univariate analysis, to weigh for potentially confounding factors. Odds ratios with standard errors and 95% confidence intervals were provided. A *P* value  $< .05$  was considered statistically significant.

## RESULTS

Of 167 patients with anterior circulation stroke, 124 had complete CT, CTA, and clinical data and were included in the analysis. Baseline characteristics are summarized in Table 1. Single-artery occlusion (ICA, anterior cerebral artery, and middle cerebral artery) was diagnosed in 55.6%, whereas tandem lesions occurred in 44.3% of patients. Correlation analysis showed that baseline CTA-SI ASPECTS correlated better with follow-up ASPECTS ( $r = 0.76$ ; 95% CI, 0.67–0.83;  $P < .001$ ) than baseline NCCT ASPECTS ( $r = 0.51$ ; 95% CI, 0.36–63;  $P < .001$ ; *P* for comparison

of the 2 coefficients  $< .001$ ) (Fig 1). Furthermore, the ability to identify patients with good outcome ( $mRS \leq 2$ ), revealed by receiver operating characteristic curve analysis, was significantly higher for CTA-SI ASPECTS with respect to NCCT ASPECTS (CTA-SI area under the curve, 0.83; 95% CI, 0.76–0.91; NCCT area under the curve, 0.67; 95% CI, 0.58–0.77;  $P < .001$ ). According to each receiver operating characteristic curve, we determined cutoff values (Table 2), on the basis of which we defined a good CTA-SI ASPECTS as  $\geq 5$  and a good NCCT ASPECTS as  $\geq 8$ . Most interesting, a median baseline NCCT ASPECTS of 9 resulted from a recent meta-analysis of 5 endovascular stroke trials.<sup>16</sup> No statistical difference was found in onset-to-imaging acquisition time between good and poor ASPECTS groups (good CTA-SI,  $135 \pm 56$  minutes versus poor CTA-SI,  $137 \pm 52$  minutes;  $P > .05$ ; good NCCT,  $129 \pm 54$  minutes versus poor NCCT,  $131 \pm 54$  minutes;  $P > .05$ ).

Factors predicting favorable outcome ( $mRS \leq 2$ ,  $n = 48$ ) in univariate analysis were both good NCCT ASPECTS and good CTA-SI ASPECTS, as well as age, baseline NIHSS, time to recanalization, and good recanalization (TICI  $\geq 2b$ ) (Table 3). To find the best outcome predictors, we finally constructed backward and forward stepwise regression analyses, including all variables significantly associated with favorable outcome in the univariate

analysis. Both the backward and forward procedures showed that good CTA-SI ASPECTS, age, good recanalization, and time to recanalization remained independent predictors of good clinical outcome, indicating CTA-SI ASPECTS as a better predictor of functional outcome than NCCT ASPECTS (Table 4).

## DISCUSSION

ET seems a safe and effective adjuvant treatment strategy for patients with acute ischemic stroke secondary to large intracranial vessel occlusion in the anterior circulation,<sup>4,17</sup> and many attempts have been made in the recent past to better select those patients who can reliably benefit from ET.<sup>7</sup> One such effort has been in recent randomized endovascular stroke trials that included only patients with small infarct size as defined by an ASPECTS of  $>6-7$  on NCCT.<sup>5,6</sup> Among these trials, the Multicenter Randomized Clinical trial of Endovascular treatment for Acute ischemic stroke in the Netherlands (MR CLEAN) was the only one to include patients on the basis of time from symptom onset and confirmation of occlusion on neuroimaging.<sup>4</sup> Nevertheless, a recent meta-analysis of these trials showed a median baseline CT ASPECTS of 9. Consequently, from all these trials, we have learned that ET works, but we do not know yet whether this kind of reperfusion therapy would be safe and effective in patients with lower ASPECTS.

Regarding these findings, a recent subgroup analysis from the MR CLEAN data showed that patients with NCCT ASPECTS of 5–7, not only those with NCCT ASPECTS of 8–10, may also benefit from ET. This study could not provide further information on patients with NCCT ASPECTS of 0–4 because of a paucity of data.<sup>18</sup> Therefore, there are not thorough data concerning the effects of ET in patients with larger infarct burdens, and we only know that those with lower ASPECTS could be unsuitable for ET<sup>19</sup> but cannot be excluded from treatment. A recent study of 249 patients showed a rate of good outcome of 5% in the CT ASPECTS group of 0–4 and of 38.5% in the CT ASPECTS group of 5–8,<sup>7</sup> suggesting a chance for ET in patients

**Table 1: Patient characteristics**

Variable	Value
Age (yr)	$68 \pm 13.2$
Sex (male)	52.4%
Hypertension	79.8%
Diabetes	16.1%
Atrial fibrillation	32.2%
Smoking	19.3%
Intravenous thrombolysis	60.4%
Baseline NIHSS	19 (IQR, 16–21)
NCCT ASPECTS	8 (IQR, 7–10)
CTA-SI ASPECTS	4 (IQR, 2–6)
Follow-up ASPECTS	3 (IQR, 1–5)

**Note:**—IQR indicates interquartile range.

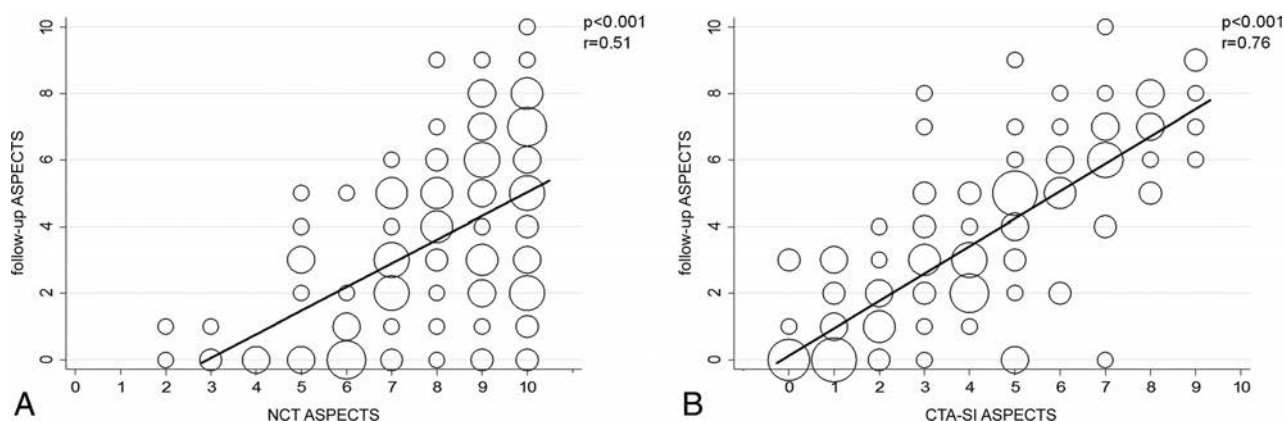


**FIG 1.** Correlation of ASPECTS on NCCT (A) and CTA-SI (B) with follow-up ASPECTS. The area of the bubble is proportional to the number of patient observations at that data point.

**Table 2: ROC curve analysis—CTA-SI ASPECTS and NCCT ASPECTS cutoff values indicating patients with good clinical outcomes**

	AUC (95% CI)	Best Cutoff Value	Sensitivity	Specificity	Correct Classification
CTA-SI ASPECTS	0.83 (0.76–0.91)	5	60.42%	88.16%	77.42%
NCCT ASPECTS	0.67 (0.58–0.77)	8	64.58%	61.84%	62.90%

**Note:**—AUC indicates area under curve; ROC, receiver operating characteristic.

**Table 3: Univariate analysis—variables associated with good clinical outcome**

Variable	mRS 0–2 (n = 48)	mRS 3–6 (n = 76)	P
Age (yr)	63.3 ± 15.3	70.3 ± 11.0	.004
Sex (male)	52%	52%	1.0
Baseline NIHSS	17.6 ± 3.1 (IQR, 11–23)	19.3 ± 3.5 (IQR, 9–25)	.009
Good NCCT ASPECTS	81.2%	50%	.001
Good CTA-SI ASPECTS	79.2%	26.3%	<.001
Onset to recanalization (min)	291.9 ± 86.3 (IQR, 140–635)	322.5 ± 70.3 (IQR, 155–505)	.03
Hypertension	70.8%	85.5%	.07
Diabetes	14.6%	17.3%	.80
Atrial fibrillation	33.3%	31.6%	.84
Smoking	18.7%	19.7%	1.0
Intravenous thrombolysis	93.7%	90.8%	.74
sICH	23.4%	14.7%	.23
TICI 2b–3	79.2%	56.6%	.01

Note:—sICH indicates symptomatic intracranial hemorrhage.

**Table 4: Multivariable regression model—best predictors of good clinical outcome**

	OR	SE	95% CI	P
Good CTA-SI ASPECTS	15.61	8.24	5.54–43.97	<.001
Age	0.95	0.02	0.91–0.99	.011
TICI 2b–3	3.12	1.70	1.07–9.09	.037
Onset to recanalization (min)	0.99	0.01	0.98–0.99	.009

Note:—SE indicates standard error.

with larger infarct burden. Further scientific effort is warranted to identify any markers that could better predict outcome and give useful information for the decision-making process.

Thus, CTA can depict the area of ischemia (though not necessarily infarcted) much better than NCCT, especially when analyzing parenchymal CTA-SI.<sup>12</sup> Hypodensity on CTA-SI provides greater demarcation between normal and abnormal tissue, and this finding could be explained by the ability of CTA to detect alterations in cerebral blood volume, as opposed to cytotoxic edema on NCCT, with a threshold insufficient to produce NCCT changes.<sup>11</sup> In a small previous study, CTA-SI was shown to be more sensitive in the early detection of irreversible ischemia and more accurate in the prediction of final infarct size.<sup>13</sup> Our results confirm those from Bhatia et al,<sup>20</sup> suggesting CTA-SI ASPECTS prior to ET as a better predictor of final infarction. In our study, we also compared CTA-SI ASPECTS and NCCT ASPECTS to evaluate whether the former can improve prediction of clinical outcome. We used receiver operating characteristic curve analysis and found that baseline CTA-SI ASPECTS compared with NCCT ASPECTS can better identify patients with functional independence at 3 months.

Moreover, our study, different from the study of Bhatia et al,<sup>20</sup> also analyzed reperfusion data. In particular, we found that good reperfusion was a predictor of good outcome in univariate analysis and remains a significant and independent predictor of good outcome in a multivariable regression model together with age, time to reperfusion, and CTA-SI ASPECTS, but not NCCT ASPECTS. In line with this finding, good reperfusion has been recently demonstrated to improve the rate of good outcome irrespective of ASPECTS.<sup>21</sup>

### Limitations

Our study has several limitations primarily due to the retrospective methodology of analysis. Moreover, the sample size

was relatively small and may limit the reliability of results. Larger multicenter studies are needed to conclusively demonstrate the utility of CTA-SI in clinical decision-making.

### CONCLUSIONS

Our study shows that CTA-SI ASPECTS can predict final infarct size and outcome better than NCCT ASPECTS. This finding suggests that CTA-SI, rather than NCCT, should be considered a main step of the decision-making process in patients with acute ischemic stroke.

### ACKNOWLEDGMENTS

We thank all stroke neurologists of the Comprehensive Stroke Center at the University of Tor Vergata (Angela Giordano, MD, Vittoria Carla D'Agostino, PhD, Barbara Rizzato, PhD, Simone Napolitano, MD, Domenico Samà, PhD) and interventional radiologists of the Department of Diagnostic Imaging at the University of Tor Vergata (Daniel Konda, MD, Enrico Pampana, MD) for data collection.

Disclosures: Fabrizio Sallustio—RELATED: Grant: Italian Ministry of Health (RF-2013-02358679)\*. Caterina Motta—RELATED: Grant: Italian Ministry of Health (RF-2013-02358679)\*. Marina Diomedi—UNRELATED: Payment for Lectures Including Service on Speakers Bureaus: Italian Society of Neurology (Symposium of Bristol Myers-Squibb and Pfizer), Comments: €1000 for a lecture. Paolo Stanzione—UNRELATED: Board Membership: Union Chimique Belge (UCB), Sandoz, Comments: Advisory Board; Grants/Grants Pending: UCB, Boehringer, Comments: unrestricted grants for sleep disturbances in Parkinson disease, unrestricted grant for a Masters Degree in Neurovascular Disease\*; Payment for Lectures Including Service on Speakers Bureaus: UCB, Chiesi, Comments: Continuous Education in Medicine in Italy. \*Money paid to the institution.

### REFERENCES

- Barber PA, Demchuk AM, Zhang J, et al; ASPECTS Study Group. Validity and reliability of a quantitative computed tomography score in predicting outcome of hyperacute stroke before thrombolytic therapy. *Lancet* 2000;355:1670–74 CrossRef Medline
- Dzialowski I, Hill MD, Coutts SB, et al. Extent of early ischemic changes on computed tomography (CT) before thrombolysis: prognostic value of the Alberta Stroke Program Early CT Score in ECASS II. *Stroke* 2006;37:973–78 CrossRef Medline
- Menon BK, Puetz V, Kochar P, et al. ASPECTS and other neuroimaging scores in the triage and prediction of outcome in acute stroke patients. *Neuroimaging Clin North Am* 2011;21:407–23 CrossRef Medline
- Berkhemer OA, Fransen PS, Beumer D, et al. A randomized trial of intraarterial treatment for acute ischemic stroke. *N Engl J Med* 2015;372:11–20 CrossRef Medline
- Goyal M, Demchuk AM, Menon BK, et al. Randomized assessment of rapid endovascular treatment of ischemic stroke. *N Engl J Med* 2015;372:1019–30 CrossRef Medline
- Jovin TG, Chamorro A, Cobo E, et al. Thrombectomy within 8 hours after symptom onset in ischemic stroke. *N Engl J Med* 2015;372:2296–306 CrossRef Medline
- Yoo AJ, Zaidat OO, Chaudhry ZA, et al. Impact of pretreatment noncontrast CT Alberta Stroke Program Early CT score on clinical outcome after intra-arterial stroke therapy. *Stroke* 2014;45:746–51 CrossRef Medline
- Sallustio F, Motta C, Pizzuto S, et al. CT angiography-based collat-

- eral flow and time to reperfusion are strong predictors of outcome in endovascular treatment of patients with stroke. *J Neurointerv Surg* 2016 Sep 23. [Epub ahead of print] CrossRef Medline
9. Schramm P, Schellinger PD, Fiebich JB, et al. **Comparison of CT and CT angiography source images with diffusion-weighted imaging in patients with acute stroke within 6 hours after onset.** *Stroke* 2002; 33:2426–32 CrossRef Medline
  10. Lev MH, Segal AZ, Farkas J, et al. **Utility of perfusion-weighted CT imaging in acute middle cerebral artery stroke treated with intra-arterial thrombolysis: prediction of final infarct volume and clinical outcome.** *Stroke* 2001;32:2021–28 CrossRef Medline
  11. Aviv RI, Shelef I, Malam S, et al. **Early stroke detection and extent: impact of experience and the role of computed tomography angiography source images.** *Clin Radiol* 2007;62:447–52 CrossRef Medline
  12. Nabavi DG, Kloska SP, Nam EM, et al. **MOSAIC: Multimodal Stroke Assessment Using Computed Tomography—novel diagnostic approach for the prediction of infarction size and clinical outcome.** *Stroke* 2002;33:2819–26 CrossRef Medline
  13. Camargo EC, Furie KL, Singhal AB, et al. **Acute brain infarct: detection and delineation with CT angiographic source images versus nonenhanced CT scans.** *Radiology* 2007;244:541–48 CrossRef Medline
  14. Puetz V, Dzialowski I, Hill MD, et al. **The Alberta Stroke Program Early CT Score in clinical practice: what have we learned?** *Int J Stroke* 2009;4:354–64 CrossRef Medline
  15. DeLong ER, DeLong DM, Clarke-Pearson DL. **Comparing the areas under two or more correlated receiver operating characteristic curves: a nonparametric approach.** *Biometrics* 1988;44:837–45
  16. Goyal M, Menon BK, van Zwam WH, et al; HERMES collaborators. **Endovascular thrombectomy after large-vessel ischaemic stroke: a meta-analysis of individual patient data from five randomised trials.** *Lancet* 2016;387:1723–31 CrossRef Medline
  17. Sallustio F, Koch G, Di Legge S, et al. **Intra-arterial thrombectomy versus standard intravenous thrombolysis in patients with anterior circulation stroke caused by intracranial occlusions: a single-center experience.** *J Stroke Cerebrovasc Dis* 2013;22:e323–31 CrossRef Medline
  18. Yoo AJ, Berkhemer OA, Fransen PS, et al; MR CLEAN investigators. **Effect of baseline Alberta Stroke Program Early CT Score on safety and efficacy of intra-arterial treatment: a subgroup analysis of a randomised phase 3 trial (MR CLEAN).** *Lancet Neurol* 2016;15: 685–94 CrossRef Medline
  19. Wahlgren N, Moreira T, Michel P, et al; ESO-KSU, ESO, ESMINT, ESNR and EAN. **Mechanical thrombectomy in acute ischemic stroke: consensus statement by ESO-Karolinska Stroke Update 2014/2015, supported by ESO, ESMINT, ESNR and EAN.** *Int J Stroke* 2016;11:134–47 CrossRef Medline
  20. Bhatia R, Bal SS, Shobha N, et al; Calgary CTA Group. **CT angiographic source images predict outcome and final infarct volume better than noncontrast CT in proximal vascular occlusions.** *Stroke* 2011;42:1575–80 CrossRef Medline
  21. Noorian AR, Rangaraju S, Sun CH, et al. **Endovascular therapy in strokes with ASPECTS 5–7 may result in smaller infarcts and better outcomes as compared to medical treatment alone.** *Interv Neurol* 2015;4:30–37 CrossRef Medline

# State of Practice: Endovascular Treatment of Acute Aneurysmal SAH in Germany

H. Janssen, A. Berlis, J. Lutz, N. Thon, and H. Brückmann

## ABSTRACT

**BACKGROUND AND PURPOSE:** Acute aneurysmal SAH is a severe disease that requires prompt treatment. Endovascular coiling and neurosurgical clipping are established treatment options. Our intention was to determine the state of current practice in acute aneurysmal SAH treatment in Germany, with emphasis on logistic and temporal aspects.

**MATERIALS AND METHODS:** We interviewed 74 German university and nonuniversity hospitals with an anonymous questionnaire comprising 15 questions concerning the practice of treatment and diagnostics of acute aneurysmal SAH at their respective institutions. The response rate was 74% among all institutions (55/74); among university hospitals, 77%; and among nonuniversity hospitals, 72%.

**RESULTS:** The majority of all aneurysms were treated endovascularly (66% of acute aneurysmal SAH, 66% of unruptured aneurysms). Treatment on weekends was provided by 100% of endovascular and 96% of neurosurgical facilities. Average patients with acute aneurysmal SAH were not treated during the night (98%). Seventy percent of endovascular and 78% of neurosurgical treatments were not started later than 8:00 PM. Fifty-three percent of hospitals would not start a same-day diagnostic angiography in acute aneurysmal SAH if treatment was scheduled for the following day. Eighty-two percent of all centers performed DSA after clipping to evaluate the treatment results.

**CONCLUSIONS:** Our survey gives a detailed summary of the current practice of endovascular treatment and related topics in acute aneurysmal SAH in Germany and also reveals considerable changes in practice in comparison with older data.

**ABBREVIATIONS:** AASAH = acute aneurysmal SAH; ICH = intracranial hemorrhage

Acute aneurysmal SAH (AASAH) is a severe condition. The incidence worldwide is approximately 9 per 100,000 per year, but there are regional differences.<sup>1</sup> In Germany, the incidence is reported to be between 5.9 and 10–13 per 100,000.<sup>1,2</sup> While up to 12% of patients die before getting to the hospital,<sup>3</sup> therapeutic occlusion of the causative aneurysm is one of the most important treatment goals.<sup>4,5</sup> However, because SAH is a complex disease, many other factors also influence clinical outcome.<sup>6</sup> When the aneurysm is left untreated, the mortality rate is >60% within 1 year.<sup>7</sup> The major reason is the high risk of rebleeding after the initial rupture. This risk is time-dependent—up to 15% within the first hours and approximately 4% on the first day and then

declining to 1%–2% per day for the first month.<sup>8–10</sup> Therefore, the timing of the obliterating therapy needs to be adapted to this course of the disease. The German Association of the Scientific Medical Societies recommends, in their SAH guidelines, obliterating aneurysm treatment within 72 hours.<sup>9</sup> The European Stroke Organization recommends the same 72-hour time window but states that the therapy should be performed as early as possible.<sup>11</sup> The American Heart Association and the American Stroke Association, in the latest update of their guidelines, postulate treatment as early as feasible without further specification.<sup>12</sup> According to the quality record by the largest German health insurance provider, Allgemeine Ortskrankenkasse (AOK), 7213 aneurysms were treated in 2008 in Germany.<sup>13,14</sup> To our knowledge, no published data are available that describe current clinical practice in Germany concerning the timing and availability of therapy in AASAH. Therefore, a nationwide cross-sectional survey was conducted.

## MATERIALS AND METHODS

We compiled a questionnaire comprising 15 questions concerning the treatment of AASAH. All questionnaires were designed to

Received January 30, 2017; accepted after revision April 6.

From the Departments of Neuroradiology (H.J., J.L., H.B.) and Neurosurgery (N.T.) Ludwig-Maximilians-University Hospital, Munich, Germany; Department of Neuroradiology (H.J.), Paracelsus Medical University, Nuremberg, Germany; and Department of Neuroradiology (A.B.), Klinikum Augsburg, Augsburg, Germany.

Please address correspondence to Hendrik Janssen, MD, Ludwig-Maximilians-University Hospital, Neuroradiology, Marchioninstr 15, 81377 Munich, Germany; e-mail: hendrik.janssen@klinikum-nuernberg.de

<http://dx.doi.org/10.3174/ajnr.A5260>

**Table 1: Distribution of all aneurysms**

	All				SAH (%)	Unruptured (%)
	Mean	Median	Max	Min		
University hospital (n = 24)	147.2	160	250	35	59	41
Maximum care hospital (n = 22)	94.8	80	400	30	47	53
Specialist hospital (n = 9)	89.6	38	420	30	35	65
All (n = 55)	117.3	100			53	47

**Note:**—Max indicates maximum; Min, minimum.

**Table 2: Distribution of aneurysms presenting with SAH (AASAH)**

	All SAH				Endovascularly Treated SAH				
	Mean	Median	Max	Min	%	Mean	Median	Max	Min
University hospital	87.0	80	150	35	62	53.6	50	100	20
Maximum care hospital	45.3	50	100	15	71	32.5	30	75	10
Specialist hospital	30.6	26	63	15	84	25.4	23	57	7
All	61.6	60			66	40.8	24		

**Note:**—Max indicates maximum; Min, minimum.

**Table 3: Distribution of unruptured aneurysms**

	All Unruptured				Endovascularly Treated Unruptured				
	Mean	Median	Max	Min	%	Mean	Median	Max	Min
University hospital	60.2	60	130	0	52	31.3	30	70	0
Maximum care hospital	49.5	30	300	5	75	37.0	21	200	0
Specialist hospital	59.0	18	357	10	88	51.6	15	323	7
All	55.7	62			66	36.6	51		

**Note:**—Max indicates maximum; Min, minimum.

be administered in an anonymous fashion, and no identification of the participating hospital could be inferred. Self-addressed prepaid envelopes were enclosed.

All questions were designed to obtain the current state at the participating institution. Thirteen questions were multiple-choice, and 2 questions were open-ended. Questions concerning neurosurgical services were also surveyed through the addressed neurointerventionalist. Patient data were sought on a population level; no individual patient data were required.

Forty-three nonuniversity neuroendovascular departments in Germany were identified through the membership roster of the German Professional Organization of Neuroradiologists. Beyond these, we sent the questionnaire to all 31 German university departments of neuroradiology. The questionnaires were sent in June 2014 and were addressed to the head of department/neurointerventional services.

All addressees were informed about anonymity and given instructions for completion by a separate cover letter. Participants were asked to answer the questions for “average patients with aneurysm-induced SAH.” Patients with space-occupying intracranial hemorrhage (ICH), recurrent events during the preceding days, and vasospasm-related symptoms were excluded. Responses were received within 6 months.

We performed all statistical analyses by using SPSS Statistics 22 (IBM, Armonk, New York). Comparison between groups was evaluated with the  $\chi^2$  test. Statistical significance was assumed at  $P < .05$ .

## RESULTS

### Characterization of Participating Hospitals

Question 1 asked for the type of hospital, with choices among university hospital, maximum care hospital, or specialist hospital/other. A maximum care hospital provides all medical specializa-

tions. It differs from a university hospital mainly by not having an affiliation with a medical school. However, aneurysm treatment in Germany is not necessarily exclusively provided in the largest hospitals. Centers might have a focus on the treatment of neurologic disorders while not providing the full range of medical specializations. Also, many hospitals provide only a limited number of medical specializations for other reasons. Therefore, the category “specialist hospital/other” was introduced in the questionnaire. Questions 2 and 3 were the only open-ended questions in the questionnaire and asked for the number of aneurysms treated per year, on average, at the institution, with patients presenting with and without AASAH in total and by endovascular services, respectively. Question 4 asked about neurosurgical clipping as a treatment option at the institution.

The overall response rate was 74% through 55 completed questionnaires.

The response rate of university hospitals was 77% (24/31) and of nonuniversity hospitals, 72% (31/43).

The group of participating nonuniversity hospitals consisted of 22 maximum care hospitals and 9 specialist/other hospitals. In 4/9 of specialist hospitals, endovascular treatment but no neurosurgical clipping was available. In the remaining institutions, both options were routinely performed.

The sum of all reported aneurysms treated neurosurgically and endovascularly per year by the participating hospitals in the survey was 6335.

The median number of treated aneurysms per year in total (AASAH + unruptured) was 100 per hospital (range, 30–420). Patients with AASAH compose, on average, 53% of all patients. The median number of treated patients with SAH in all hospitals was 60 (range, 15–150) (Table 1).

In the group of specialist hospitals, 1 center reported 420 aneurysm treatments per year, while the other 8 hospitals in this group only had 30–70 aneurysm treatments in total.

Sixty-six percent of all aneurysm treatments (SAH and unruptured, respectively;  $P < .001$ ) were treated endovascularly. At university hospitals, the rate was 62%; at maximum care hospitals, 71%; and in specialist hospitals, 86%. Corrected for the 4 institutions that did not provide aneurysm clipping, the rate was 84% in specialist hospitals (Tables 2 and 3).

Quartiles for the total number of aneurysm treatments and endovascular treatments according to hospital type are provided in Table 4.

Questions 5 and 6 dealt with the process flow at the participating hospital. While question 5 asked for the total number of neurointerventionalists at the institution, question 6 asked for the decision-making process in SAH aneurysm treatment concerning the decider of the treatment strategy. The multiple-

**Table 4: Institutional characteristics by quartiles of all aneurysms and endovascularly treated aneurysms**

Quartile	Q All (No.)	Q Ev (No.)	University (No.)		MaxCare (No.)		Special (No.)	
			All	Ev	All	Ev	All	Ev
1	<48.8	<31	1	2	7	7	6	4
2	48.8	31	6	5	7	5	2	4
3	100	58	6	8	7	6	0	0
4	162.5	110	11	9	1	4	1	1

**Note:**—Q, quartiles; Ev, endovascular; University, university hospital; MaxCare, maximum care hospital; Special, specialist hospital.

**Table 5: Interventionalists per hospital**

	No. of Interventionalists					
	1	2	3	4	>4	M
University hospital	0	4	8	9	3	4
Maximum care hospital	4	9	4	4	1	2
Specialist hospital	0	7	1	0	1	2
All	4	20	13	13	5	3

**Note:**—M indicates median.

**Table 6: Last time of day when treatments are started**

	Starting Time				
	6 PM	7 PM	8 PM	9 PM	After 9 PM
Endovascular					
University hospital	3 (13%)	0	13 (54%)	5 (21%)	3 (13%)
Maximum care hospital	3 (14%)	2 (9%)	10 (45%)	4 (18%)	3 (14%)
Specialist hospital	3 (33%)	1 (11%)	4 (44%)	0	1 (11%)
All	8 (16%)	3 (5%)	27 (49%)	9 (16%)	7 (13%)
Neurosurgery					
University hospital	7 (29%)	1 (4%)	12 (50%)	2 (8%)	2 (8%)
Maximum care hospital	8 (36%)	2 (9%)	7 (32%)	2 (9%)	3 (14%)
Specialist hospital	2 (40%)	0	2 (40%)	0	1 (20%)
All	17 (35%)	3 (5%)	21 (38%)	4 (7%)	6 (11%)

choice options were either a decision by the neurointerventionalist or neurosurgeon alone or by a conjoint interdisciplinary decision.

In 85% of all hospitals, the mode of treatment was routinely decided by a consensus of both neurointerventionalists and neurosurgeons. In 9% and 5% of hospitals, treatment decisions were made alone either by the neurointerventionalists or the neurosurgeons, respectively. Differences were seen between types of hospitals: An interdisciplinary treatment consideration was preferred by 88% of the university hospitals. In the remaining 12%, the neurosurgeons were responsible. In nonuniversity hospitals, an interdisciplinary approach was pursued in 84%. In contrast, in the remaining 16% of hospitals, the neurointerventionalist decided alone.

The number of neurointerventionalists capable of treating AASAH is, on average, higher in university hospitals compared with nonuniversity hospitals (Table 5).

### Management Considerations

Questions 7 and 8 asked whether aneurysms were treated at any time during the night by endovascular or neurosurgical services, respectively. Questions 9 and 10 asked for the last time of day when aneurysm treatment is started at the institution by neurointerventionalists or neurosurgeons, respectively (Table 6). Questions 11 and 12 asked whether aneurysms are treated on weekends

**Table 7: Grouped starting times**

	% to Start Until					
	7 PM	P <sup>a</sup>	8 PM	P <sup>a</sup>	9 PM	P <sup>a</sup>
Endovascular						
University hospital	13	.15	67	.55	88	.97
Nonuniversity hospital	29		74		87	
All	21		70		86	
Neurosurgery						
University hospital	33	.38	83	.43	91	.26
Nonuniversity hospital	51		84		91	
All	40		78		85	

<sup>a</sup>  $\chi^2$  test.

**Table 8: Grouped mean number of interventionalists for treatment starting times**

	No.
All until 7 PM	2.4
All until 8 PM	2.8
All until 9 PM	2.8
After 9 PM	3.7

at the institution by neurointerventionalists or neurosurgeons, respectively.

Of all 55 participants, only 1 university hospital reported providing endovascular and neurosurgical aneurysm treatment throughout the entire night on a regular basis for average SAH cases. All other hospitals did not consider routine treatment at night. However, 13% of the university and nonuniversity hospitals did start endovascular treatment after 9:00 PM. In both groups, most set the timeline at 8:00 PM (university, 54%; nonuniversity, 45%) (Table 7).

The share of institutions starting neurosurgical clipping up to 8:00 PM was 83% (university) and 84% (nonuniversity), respectively. Particularly, institutions that set the timeline for treatment before 7:00 PM were more frequent in neurosurgery (university, 33%; nonuniversity, 51%) than in endovascular therapy.

The later treatments are started, the more interventionalists are available at the hospitals (Table 8).

All hospitals (100%) provide endovascular aneurysm treatment for SAH on weekends, and 96% of all hospitals with a neurosurgical unit provide clipping on weekends for SAH. One university hospital and 1 maximum care hospital reported not providing neurosurgical treatment on weekends.

### Diagnostics in AASAH

Finally, questions 13–15 dealt with aneurysm treatment–related diagnostics. Question 13 asked whether a DSA was performed at any time during the night after admission of a patient with AASAH, even if treatment would not take place during the night. Moreover, question 14 asked for the last time of day that a DSA would be started, even if treatment would take place only on the following day. While multiple-choice answers offered times from “6:00 PM” to “after 9:00 PM” by the hour, a possible answer was also “DSA is not performed on the day of admission, only directly preceding treatment” if treatment takes place on the following day. Question 15 asked for the modalities used for imaging control following neurosurgical clipping.

Seven percent of all participants answered that DSA is always performed immediately at any time throughout the night, even if

**Table 9: Time of day to start diagnostic DSA if treatment is scheduled for the following day**

	% Started						
	At Night	Not at All	6 PM	7 PM	8 PM	9 PM	After 9 PM
University hospital	13	58	4	0	13	8	17
Maximum care hospital	5	50	9	5	9	14	14
Specialist hospital	0	44	11	11	22	0	11
All	7	53	7	4	13	9	15

**Table 10: Imaging control of clipped aneurysms<sup>a</sup>**

	% of Controls			
	No Control	CTA	DSA	MRA
University hospital	13	21	88	4
Maximum care hospital	14	18	82	14
Specialist hospital	20	0	60	20
All	14	18	82	10

<sup>a</sup>Multiple answers possible.

treatment is performed only on the following day. Four of these are university hospitals (13% of all university hospitals), and 1 is a maximum care hospital (3% of all nonuniversity hospitals).

Most responders in all 3 hospital groups stated that a DSA is performed only in the context of treatment (all, 53%; university, 58%; maximum care, 50%; specialist hospital, 44%). If the time of day led to a postponement of treatment to the following day, DSA would also only be performed the next day (Table 9).

DSA is the most commonly used technique (all, 82%; university, 88%; nonuniversity, 78%) to control treatment results after neurosurgical clipping (Table 10). Some institutions gave multiple answers to this question. CTA was used in 18% (all); and MRA, in 10% (all). Fourteen percent reported not performing any imaging control after neurosurgical treatment (university, 13%; nonuniversity, 15%). Responses to this question were corrected for the 4 institutions that did not provide neurosurgical clipping.

## DISCUSSION

Our survey was performed with the intention of documenting current clinical practice in diagnostic- and treatment-related aspects of acute aneurysmal SAH in Germany. With the high response rate of 74% including 77% of all German university hospitals, the survey is considered representative. Particularly, the comparison of all reported aneurysms in our survey with the total aneurysm treatment number in Germany<sup>13,14</sup> shows that about 88% of all aneurysm treatments in Germany are represented by this survey. Ten years ago, Sakowitz et al<sup>2</sup> published a German neurosurgical survey mainly emphasizing the clinical aspects of SAH management. To our knowledge, our article is the first survey to report the status quo with a focus on treatment-logistics of AASAH.

Indications are that the treatment volume of hospitals might have relevance for outcome parameters.<sup>15-17</sup> Such data were not included in our analysis, but the correlation of case load and hospital type is analyzed (Table 4) by our quartile calculation. In our study, more than half of all aneurysm cases (56%; AASAH + unruptured) were reported by university hospitals, though nonuniversity institutions were represented more frequently (31 versus 43 institutions;  $P = .017$ ). Accordingly, 11 university hospitals and only 2 nonuniversity hospitals belonged to the upper quartile

(quartile 4) of treatment providers. Moreover, the number of neurointerventionalists capable of endovascular AASAH treatment was also higher in university hospitals. Overall, most (88%) aneurysm treatments took place in university facilities or maximum care hospitals. Only a minor portion (12%) of patients seemed to be treated in specialist or other hospitals. We believe this finding is because cerebral aneurysm treatment demands a very high level of specialization and equipment, even beyond the core disciplines of neuroradiology and neurosurgery. Also, intensive care and departments for neurology and physiotherapy need to be equipped for patients with SAH.

Apparently, only a few hospitals (9 in the survey) in Germany fall into the category “specialist hospital/other,” meeting all these requirements. However, 1 hospital in this group reported 420 aneurysm treatments per year and is, thereby, the center with the highest case volume in the survey. The high treatment number in this center causes heterogeneity in the group “Specialist hospital/other” because the treatment number of the other 8 hospitals in this group ranged in the lower 3 quartiles (Table 4). Nevertheless, this 1 center shows that a high case volume is not necessarily restricted to a university or university-like hospital.

Today more aneurysms are treated endovascularly in Germany than by neurosurgical clipping ( $P < .001$ ). Our data show a coiling rate of 66% for AASAH and unruptured aneurysms (Tables 2 and 3). Ten years ago, endovascular treatment accounted for 46% of patients with AASAH.<sup>2</sup> Our numbers are in concordance with current guidelines, which also favor coiling over clipping if both procedures are considered equally applicable.<sup>9,11,12</sup> Comparing hospital categories, we observed that the share of clipped aneurysms is larger in university hospitals than in nonuniversity hospitals (Tables 2 and 3). An explanation could possibly be the role of university hospitals in the training of fellows. The share of clipped aneurysms could be larger to achieve sufficient training capacity for both specializations. Another possible explanation could be a higher grade of subspecialization of staff in university hospitals. The likelihood that vascular neurosurgery is not a key focus in nonuniversity hospitals could be greater.

Incomplete obliteration of the aneurysm is strongly associated with the risk of rebleeding.<sup>18</sup> While a final imaging control by DSA is immanent to the endovascular treatment method, imaging strategies to control the degree of occlusion after clipping are not consistent. While almost 82% (88% of universities) conduct control DSA after clipping, 14% still do not perform any imaging control at all after clipping. The number of centers that do not perform this imaging control has declined dramatically during the past 10 years.<sup>2</sup> This surprising paradigm shift can possibly be explained by the growing importance of quality assurance and legal considerations, owing to increasing numbers of malpractice lawsuits. It could also be the result of evolved and improved endovascular techniques today that open a spectrum of retreatment options for insufficient obliteration after neurosurgical clipping that did not exist in the past. MRA is the least used technique for clipping controls. This might be due to the artifacts caused by clip material resulting in limited imaging quality.<sup>19</sup>

All guidelines<sup>9,11,12</sup> recommend an interdisciplinary decision-making process for aneurysm treatment, with critical involvement of both endovascular interventionalists and vascular neuro-

surgeons. On this point, almost (85%) all hospitals followed this recommendation.

One of the main intentions of this survey was to document the status quo in temporal aspects of AASAH treatment. Remarkably, all participating institutions, even those with only 1 or 2 interventionalists, also provide full endovascular treatment on weekends. Weekend coverage in neurosurgery is almost as high (96%), with 2 hospitals not providing clipping on weekends.

The overwhelming majority (98% each,  $P < .001$ ) do not treat patients with AASAH during the night, either endovascularly or neurosurgically. Not treating “average patients with AASAH” at night is the standard in Germany.

We believe that the explanation for this finding is the fear of higher complication rates when neurosurgeons and interventionalists perform the delicate procedure of aneurysm repair under difficult circumstances. The literature strongly supports this belief. Different reports show that complication rates in medical procedures are higher at night.<sup>20–22</sup> Furthermore, in many studies of aircraft pilots, it has been proved that fatigue has a negative effect on their error probability and error management.<sup>23–26</sup> Both are crucial determinants in aneurysm treatment as well, and these data can probably also be applied to neurosurgeons and interventionalists, though so far the possibility has never been studied explicitly for aneurysm treatment, to our knowledge.

Most hospitals do not start AASAH treatment later than 8:00 PM. Universities tend to start later than nonuniversity hospitals. This finding seems to be because more interventionalists are available at the hospital when treatments are started later (Table 8). It seems comprehensible that more staff resources allow a higher flexibility in interventions late in the evening because it is easier to respect rest periods on the following day. Neurosurgical treatment tended to be postponed to somewhat earlier the following day. The postponement might be explained by longer procedure times and limited availability of intraoperative neuromonitoring in the evening hours.

Divergent from the policy of not treating ruptured aneurysms at night, a minority of 7% performed diagnostic DSAs at night even if the treatment was not until the following day. The largest group (53%, all; 58%, universities) stated, however, that they do not perform DSA if treatment is scheduled for the following day, regardless of time of day. To us, this approach makes the most sense because it supports minimal movement of untreated patients with AASAH and avoids an additional transport of patients between the intensive care unit and the angiography suite, particularly if the patient is finally treated endovascularly. Only 24% of all centers would start a diagnostic DSA after 8:00 PM.

### Limitations

The questionnaire was sent to the leading neurointerventionalist at each hospital. Whether the answers were given separately or in consensus by the neurointerventionalist and the neurosurgeon was not surveyed. The lack of information about the manner of answering is considered a potential source of bias.

Twenty-six percent of all addressed hospitals did not respond. Comparison of the number of all reported aneurysms in our survey with the total number of all treated cerebral aneurysms in Germany shows that the 26% of nonresponding hospitals account

for approximately 12% of all aneurysms in Germany. The management practice in AASAH in these hospitals remains unknown in this survey.

The questionnaire did not allow evaluation of average time intervals between aneurysm rupture and treatment. A substantially higher effort would have been necessary by the participating hospitals to survey this information, and the authors expected a relevant decline in the willingness to participate in the survey if this information were sought.

### CONCLUSIONS

Our survey gives a detailed summary of the current practice in endovascular treatment of acute aneurysmal SAH and related topics in Germany. It reveals both similarities and differences in AASAH management among treatment-providing hospitals. Today most aneurysms in Germany are treated endovascularly, and university hospitals have a key role in AASAH treatment.

Disclosures: Hendrik Janssen—UNRELATED: Consultancy: Sequent Medical.\* Ansgar Berlis—UNRELATED: Consultancy: Sequent Medical, MicroVent, Medtronic, Stryker; Payment for Lectures Including Service on Speakers Bureaus: Penumbra.\*Money paid to the institution.

### REFERENCES

1. de Rooij NK, Linn FH, van der Plas JA, et al. **Incidence of subarachnoid haemorrhage: a systematic review with emphasis on region, age, gender and time trends.** *J Neurol Neurosurg Psychiatry* 2007;78:1365–72 CrossRef Medline
2. Sakowitz OW, Raabe A, Vucak D, et al. **Contemporary management of aneurysmal subarachnoid hemorrhage in Germany: results of a survey among 100 neurosurgical departments.** *Neurosurgery* 2006;58:137–45; discussion 137–45 CrossRef Medline
3. Huang J, van Gelder JM. **The probability of sudden death from rupture of intracranial aneurysms: a meta-analysis.** *Neurosurgery* 2002;51:1101–05; discussion 1105–07 CrossRef Medline
4. de Gans K, Nieuwkamp DJ, Rinkel GJ, et al. **Timing of aneurysm surgery in subarachnoid hemorrhage: a systematic review of the literature.** *Neurosurgery* 2002;50:336–40; discussion 340–42 Medline
5. Kassell NF, Torner JC, Jane JA, et al. **The International Cooperative Study on the Timing of Aneurysm Surgery, Part 2: surgical results.** *J Neurosurg* 1990;73:37–47 CrossRef Medline
6. Vermeij FH, Hasan D, Bijvoet HW, et al. **Impact of medical treatment on the outcome of patients after aneurysmal subarachnoid hemorrhage.** *Stroke* 1998;29:924–30 CrossRef Medline
7. Hop JW, Rinkel GJ, Algra A, et al. **Case-fatality rates and functional outcome after subarachnoid hemorrhage: a systematic review.** *Stroke* 1997;28:660–64 CrossRef Medline
8. Ohkuma H, Tsurutani H, Suzuki S. **Incidence and significance of early aneurysmal rebleeding before neurosurgical or neurological management.** *Stroke* 2001;32:1176–80 CrossRef Medline
9. Steinmetz H, Berkefeld J, Forsting M, et al. **S1-Leitlinie. Subarachnoidalblutung Arbeitsgemeinschaft der Wissenschaftlichen Medizinischen Fachgesellschaften.** <http://www.awmf.org/leitlinien/detail/II/030-073.html>. Accessed June 1, 2017
10. Kassell NF, Torner JC. **Aneurysmal rebleeding: a preliminary report from the Cooperative Aneurysm Study.** *Neurosurgery* 1983;13:479–81 CrossRef Medline
11. Steiner T, Juvela S, Unterberg A, et al; European Stroke Organization. **European Stroke Organization guidelines for the management of intracranial aneurysms and subarachnoid haemorrhage.** *Cerebrovasc Dis* 2013;35:93–112 CrossRef Medline
12. Connolly ES Jr, Rabinstein AA, Carhuapoma JR, et al; American Heart Association Stroke Council; Council on Cardiovascular Radiology and Intervention; Council on Cardiovascular Nursing; Council on Cardiovascular Surgery and Anesthesia; Council on Clinical Car-

- diology. **Guidelines for the management of aneurysmal subarachnoid hemorrhage: a guideline for healthcare professionals from the American Heart Association/American Stroke Association.** *Stroke* 2012;43:1711–37 CrossRef Medline
13. Berlis A. **Endovascular interventions in neuroradiology: new aspects** [in German]. *Anaesthesist* 2013;62:692–706 CrossRef Medline
  14. Gefährliche Kinderwerbung für Lebensmittel im Netzhttp. Allgemeine Ortskrankenkasse. <http://www.aok-bv.de/>. Accessed March 29, 2017
  15. Solomon RA, Mayer SA, Tarmey JJ. **Relationship between the volume of craniotomies for cerebral aneurysm performed at New York state hospitals and in-hospital mortality.** *Stroke* 1996;27:13–17 CrossRef Medline
  16. Taylor CL, Yuan Z, Selman WR, et al. **Mortality rates, hospital length of stay, and the cost of treating subarachnoid hemorrhage in older patients: institutional and geographical differences.** *J Neurosurg* 1997;86:583–88 CrossRef Medline
  17. Johnston SC. **Effect of endovascular services and hospital volume on cerebral aneurysm treatment outcomes.** *Stroke* 2000;31:111–17 CrossRef Medline
  18. Johnston SC, Dowd CF, Higashida RT, et al; CARAT Investigators. **Predictors of rehemorrhage after treatment of ruptured intracranial aneurysms: the Cerebral Aneurysm Rerupture After Treatment (CARAT) study.** *Stroke* 2008;39:120–25 CrossRef Medline
  19. Grieve JP, Stacey R, Moore E, et al. **Artefact on MRA following aneurysm clipping: an in vitro study and prospective comparison with conventional angiography.** *Neuroradiology* 1999;41:680–86 CrossRef Medline
  20. Rothschild JM, Keohane CA, Rogers S, et al. **Risks of complications by attending physicians after performing nighttime procedures.** *JAMA* 2009;302:1565–72 CrossRef Medline
  21. Schliemann B, Seybold D, Gessmann J, et al. **Bipolar hemiarthroplasty in femoral neck fractures: impact of duration of surgery, time of day and the surgeon's experience on the complication rate** [in German]. *Z Orthop Unfall* 2009;147:689–93 CrossRef Medline
  22. Elshove-Bolk J, Ellensen VS, Baatrup G. **Logistics and outcome in urgent and emergency colorectal surgery.** *Colorectal Dis* 2010;12:e255–259 CrossRef Medline
  23. Caldwell JA. **Fatigue in aviation.** *Travel Med Infect Dis* 2005;3:85–96 CrossRef Medline
  24. Van Dongen HP, Caldwell JA Jr, Caldwell JL. **Investigating systematic individual differences in sleep-deprived performance on a high-fidelity flight simulator.** *Behavior Res Methods* 2006;38:333–43 CrossRef Medline
  25. Thomas MJ, Ferguson SA. **Prior sleep, prior wake, and crew performance during normal flight operations.** *Aviat Space Environ Med* 2010;81:665–70 CrossRef Medline
  26. Drury DA, Ferguson SA, Thomas MJ. **Restricted sleep and negative affective states in commercial pilots during short haul operations.** *Accid Anal Prev* 2012;45(suppl):80–84 CrossRef Medline

# The Impact of Conscious Sedation versus General Anesthesia for Stroke Thrombectomy on the Predictive Value of Collateral Status: A Post Hoc Analysis of the SIESTA Trial

S. Schönenberger, J. Pfaff, L. Uhlmann, C. Klose, S. Nagel, P.A. Ringleb, W. Hacke, M. Kieser, M. Bendszus, M.A. Möhlenbruch, and J. Bösel



## ABSTRACT

**BACKGROUND AND PURPOSE:** Radiologic selection criteria to identify patients likely to benefit from endovascular stroke treatment are still controversial. In this post hoc analysis of the recent randomized Sedation versus Intubation for Endovascular Stroke Treatment (SIESTA) trial, we aimed to investigate the impact of sedation mode (conscious sedation versus general anesthesia) on the predictive value of collateral status.

**MATERIALS AND METHODS:** Using imaging data from SIESTA, we assessed collateral status with the collateral score of Tan et al and graded it from absent to good collaterals (0–3). We examined the association of collateral status with 24-hour improvement of the NIHSS score, infarct volume, and mRS at 3 months according to the sedation regimen.

**RESULTS:** In a cohort of 104 patients, the NIHSS score improved significantly in patients with moderate or good collaterals (2–3) compared with patients with no or poor collaterals (0–1) ( $P = .011$ ; mean,  $-5.8 \pm 7.6$  versus  $-1.1 \pm 10.7$ ). Tan 2–3 was also associated with significantly higher ASPECTS before endovascular stroke treatment (median, 9 versus 7;  $P < .001$ ) and smaller mean infarct size after endovascular stroke treatment (median, 35.0 versus 107.4;  $P < .001$ ). When we differentiated the population according to collateral status (0.1 versus 2.3), the sedation modes conscious sedation and general anesthesia were not associated with significant differences in the predictive value of collateral status regarding infarction size or functional outcome.

**CONCLUSIONS:** The sedation mode, conscious sedation or general anesthesia, did not influence the predictive value of collaterals in patients with large-vessel occlusion anterior circulation stroke undergoing thrombectomy in the SIESTA trial.

**ABBREVIATIONS:** EST = endovascular stroke treatment; CS = conscious sedation; GA = general anesthesia; RCT = randomized trial; SIESTA = Sedation versus Intubation for Endovascular Stroke Treatment; Tan = collateral score of Tan et al<sup>16</sup>

Endovascular stroke treatment (EST) is now the first choice for acute ischemic stroke in the anterior circulation caused by large-vessel occlusion.<sup>1,2</sup> However, selection criteria to identify patients likely to benefit from EST outside highly selective randomized trials (RCTs) are still controversial. It is also important to establish practicable selection criteria for thrombectomy failure to exclude patients prone to futility and save financial, facility,

and personnel resources and, above all, avoid complications like cerebral reperfusion injuries.

Current data suggest that collateral blood flow status is a strong independent predictor of therapeutic success and functional outcome after EST.<sup>3–5</sup> By a network of pre-existing anastomoses, compensatory cerebral collateral blood flow supplies oxygen-deprived brain areas to which the primary flow path is blocked due to large-vessel occlusion. The recently published post hoc analysis on the collateralization status from the seminal thrombectomy trial MR CLEAN (Multicenter Randomized Clinical Trial of Endovascular Treatment of Acute Ischemic Stroke in the Netherlands) showed the highest interventional therapeutic effect in patients with moderate-to-good collateral blood flow.<sup>6</sup>

Why should the chosen sedation/airway regimen influence the impact of collateralization during EST? Collateral effects depend on cerebral perfusion pressure and vasomotor regulation of the vessel diameter. On the one hand, intubation and general anesthesia (GA) are often associated with a substantial drop in blood pressure<sup>7</sup> as was shown in previous EST studies.<sup>8–10</sup> It is quite

Received March 2, 2017; accepted March 17.

From the Departments of Neurology (S.S., S.N., P.A.R., W.H., J.B.) and Neuroradiology (J.P., M.B., M.A.M.), Heidelberg University Hospital, Heidelberg, Germany; and Institute of Medical Biometry and Informatics (L.U., C.K., M.K.), University of Heidelberg, Heidelberg, Germany.

S. Schönenberger and J. Pfaff contributed equally to this work.

The study was performed with departmental funding only.

Please address correspondence to Silvia Schönenberger, MD, Im Neuenheimer Feld 400, 69120 Heidelberg, Germany; e-mail: silvia.schoenenberger@med.uni-heidelberg.de

 Indicates article with supplemental on-line tables.

<http://dx.doi.org/10.3174/ajnr.A5243>

likely that hypotension may compromise even patients with a good collateral status, particularly if their cerebral autoregulation is impaired as is often the case in severe acute ischemic stroke. Moreover, inadvertent mechanical hyperventilation and subsequent hypocarbia can lead to cerebral vasoconstriction.<sup>8,11</sup> Both hypotension and hypocarbia associated with GA may have disadvantageous effects on the insufficiently supplied penumbra. Indeed, many retrospective studies have suggested worse outcome and mortality associated with GA in EST.<sup>12</sup> On the other hand, steering GA in ways that stabilize circulation and aim for normocarbia may theoretically serve to improve collateralization.

We recently conducted the Sedation versus Intubation for Endovascular Stroke Treatment (SIESTA) study to compare GA with conscious sedation (CS) during EST.<sup>13</sup> In that first RCT on peri-interventional management, strict target values for physiologic parameters, including blood pressure and CO<sub>2</sub>, were predefined for both treatment groups, mainly to avoid hypocarbia and hypotension. SIESTA showed no difference between GA and CS with regard to early neurologic improvement measured by the NIHSS after 24 hours,<sup>14</sup> and unadjusted long-term outcome was even better in patients in the GA group. Of note, SIESTA was not powered and designed to primarily investigate long-term functional outcome, and slight imbalances in reperfusion grades, for example, may still have influenced that result even though the results were not statistically significant. This result was in strong contrast to most previous, yet retrospective, studies on the subject.

Why was GA not inferior in SIESTA? We hypothesized that the protocolized way GA was conducted may not have compromised or even improved collateralization. In this post hoc analysis of imaging data from the SIESTA study, we mainly aimed to investigate whether the predictive value of collateral status for infarct volume and outcome is affected by the applied sedation mode (CS versus GA) and, more specifically, whether patients under a very standardized GA may have shown a favorable course despite a suboptimal collateral status at baseline.

## MATERIALS AND METHODS

### Design of the SIESTA Trial

Patient eligibility and the methods, including the study protocol, were previously published.<sup>13</sup>

Briefly, SIESTA was a monocentric, prospective, randomized, parallel-group, open-label treatment trial with blinded end point evaluation. Patients with an NIHSS score of >10 and isolated or combined occlusion of the internal carotid artery or middle cerebral artery selected for EST were randomized 1:1 to either the nonintubated state in CS or to the intubated state in GA. The trial was approved by our institutional review board (Ethikkommission Medizinische Fakultät Heidelberg, ID S-650/2013).

### Main Outcomes of the SIESTA Trial

The main finding of SIESTA was no superiority of CS versus GA with regard to early neurologic improvement (change in the NIHSS score from admission to 24 hours thereafter).<sup>14</sup> There were no differences in most secondary outcomes between the groups either (including in-hospital and 3-month mortality, and variables of peri-interventional safety and feasibility).

Secondary radiologic outcomes relevant to the present analysis included the ASPECTS,<sup>15</sup> the collateral status based on CTA on admission described by Tan et al,<sup>16</sup> the modified TIC1<sup>17</sup> score based on DSA at the end of EST, and the final infarct volume on follow-up CT at 18–24 hours after EST.<sup>18</sup> Only patients with a full dataset (baseline CT including CTA, ASPECTS before EST, and follow-up CT within 18–24 hours after onset) were included in this post hoc analysis. More details and definitions can be found in the earlier publication of the SIESTA protocol.<sup>13</sup>

### Imaging Data Assessment and Analysis

All CT and CTA data were evaluated by 2 independent, experienced neuroradiologists who were blinded to clinical findings, type of anesthesia, and infarction side (J.P., M.A.M.). The ASPECTS score, which ranges from 0 to 10, was used as a quantitative measure of areas with early infarction signs, with higher scores indicating fewer ischemic changes.<sup>15</sup>

Collaterals of the CTA source images were evaluated with the collateral score of Tan et al<sup>16</sup> and divided into the 4 categories: 0 (no collaterals; no filling of the occluded area), 1 (poor collaterals; >0% but <50% filling of the occluded area), 2 (moderate collaterals; >50% but <100% filling of the occluded area), and 3 (good collaterals; 100% filling of the occluded area), yielding the 2 groups with scores of 0–1 and 2–3. CTA was mostly performed in combination with noncontrast CT as part of our in-house protocol for stroke imaging but was sometimes repeated in patients transferred from other hospitals after external CTA. The latter was then used as a baseline for EST. Patients without a baseline CTA and ASPECTS were excluded from this analysis.

### Statistical Analysis

For continuous data, mean ( $\pm$ SD) and median (interquartile range) values are presented. Absolute and relative frequencies are given for categorical and ordinal variables. In a first explorative analysis, patients were divided into 2 Tan groups: good-to-moderate versus poor collaterals (0–1 versus 2–3). To test for differences between the groups, we applied *t* tests,  $\chi^2$  tests, and Mann-Whitney *U* tests, as appropriate. In a second step, we divided the 2 groups into subgroups according to treatment arm in the SIESTA trial (CS or GA). Again, a descriptive analysis and tests were applied to look for any differences within the subgroups. In a third step, we applied linear and logistic regression analyses to examine the predictive value of Tan, ASPECTS, and the randomization arm on the NIHSS score after 24 hours; the mRS after 3 months; and final infarct volume. In addition, we added an interaction term between Tan and the randomization variable that was only included in the final model if it showed a significant influence on the outcome value. In a final step, Pearson or Spearman correlations of improvement of NIHSS, Tan, final infarct volume, and ASPECTS were estimated. We also conducted post hoc power analyses.

A *P* value < .05 was considered statistically significant. Because this was an explorative study, no adjustment for multiple testing was performed. For statistical analyses, we used SAS software (SAS Institute, Cary, North Carolina), Version 9.4, and R, Version 3.3.1.<sup>19</sup>

## RESULTS

### Patient Characteristics

For the present analysis, 104 of 150 patients in SIESTA fulfilled the study-specific inclusion criteria. Of the 46 excluded patients, 43 had not received a baseline CTA before EST, and in 3, the final infarct volume after EST could not be determined due to symptomatic hemorrhage. The group with Tan 2–3 had a significantly better ASPECTS ( $P < .001$ ); 83.9% had an ASPECTS of 8–10 compared with only 50% with Tan 0–1. The group with Tan 2–3 had a significantly poorer pre-mRS ( $P = .02$ ) compared with Tan 0–1. Eight patients had to be converted from CS to GA (5 Tan 0–1 and 3 Tan 2–3). Further baseline, demographic, and clinical characteristics of the 2 collateral groups are shown in Table 1.

### Outcomes According to Collateral Status

Tan 0–1 was associated with a significantly higher mean final infarct size (107.4 versus 35.0  $\text{cm}^3$ ;  $P < .001$ ) compared with Tan 2–3. A statistically significant improvement in the mean NIHSS score after 24 hours was found in patients with Tan 2–3 (mean,  $-5.8 \pm 7.6$  versus  $-1.1 \pm 10.7$ ;  $P = .01$ ). Functional independence after 3 months measured by mRS 0–2 was not significantly different. Significantly lower in-house mortality (14.6% versus 1.8%,  $P = .02$ ), but no higher 3-month mortality (26.8% versus 25%,  $P = .84$ ) was found in Tan 2–3. Finally, the mean length of stay of patients with Tan 2–3 in the neuro-intensive care unit was significantly shorter (mean values, 2.7 versus 8.2 days;  $P < .001$ ). The post hoc power analysis comparing Tan 0–1 versus 2–3 showed a power of 73.4% for the improvement of the NIHSS score after 24 hours, 99.6% for infarct size, and 68.5% for in-house mortality. There were no significant differences in the analysis of short-term peri-interventional safety and feasibility parameters between the collateral groups (Table 2).

### Impact of Collateralization According to Sedation Mode

When the 2 collateralization groups were further subdivided according to the applied sedation mode used in SIESTA (CS versus GA), the only baseline difference was that patients with Tan 0–1 treated with GA were younger (mean, 75.5 versus 68.8 years;  $P < .005$ ). Most outcomes were not different in comparison.

In the subgroup with Tan 0–1, the only significant differences were more long-term functional independence (mRS after 3 months dichotomized to 0–2 and 3–6, CS 8.7% versus GA 32%;  $P = .05$ ) and more delayed extubations (17.4% versus 52%;  $P = .01$ ) in GA.

In the group with Tan 2–3, the GA subgroup was associated with a significantly longer mean time to treatment (104.3 versus 152.0 minutes;  $P = .01$ ), higher ASPECTS ( $P = .05$ ), a higher rate of hypothermia (10.3% versus 33%,  $P = .04$ ), and a higher rate of delayed extubation (3.4% versus 40.7%,  $P < .001$ ). The post hoc power to detect differences between CS and GA was 51% for Tan 0–1 versus 28.5% for Tan 2–3 regarding mRS 0–2 after 3 months (On-line Table 1).

### Association of Sedation Modes with Outcome Prediction by Radiologic Scores

Correlation analysis for the entire cohort showed only an association between infarct volume and NIHSS change after 24 hours

**Table 1: Baseline demographic and clinical characteristics according to no or poor (Tan 0–1) and moderate or good collaterals (Tan 2–3)**

	Tan 0–1 (n = 48)	Tan 2–3 (n = 56)	P Value
Demographic characteristics			
Age (mean) (SD) (yr)	72.0 (11.7)	73.7 (4.3)	.52 <sup>a</sup>
Female sex (No.) (%)	17 (35.4)	23 (41.1)	.56 <sup>b</sup>
Premedication (No.) (%)			
Antiplatelets			
No	33 (71.7)	38 (69.1)	.5 <sup>b</sup>
Aspirin	12 (26.1)	13 (23.6)	
Dual	1 (2.2)	4 (7.3)	
Missing	2	1	
Oral anticoagulants			
No	42 (89.4)	36 (65.5)	.01 <sup>b</sup>
Missing	1	1	
Statins			
No	37 (80.4)	30 (56.6)	.01 <sup>b</sup>
Missing	2	3	
Vascular risk factors (No.) (%)			
Hypertension	37 (77.1)	37 (66.1)	.22 <sup>b</sup>
Diabetes mellitus	13 (27.1)	10 (17.9)	.26 <sup>b</sup>
Hyperlipidemia	12 (25.0)	17 (30.4)	.54 <sup>b</sup>
Smoking <sup>c</sup>	11 (23.4)	4 (7.1)	.02 <sup>b</sup>
Heart failure	10 (20.8)	19 (27.9)	.14 <sup>b</sup>
Atrial fibrillation	24 (50)	30 (53.6)	.72 <sup>b</sup>
Peripheral artery occlusive disease <sup>d</sup>	1 (2.1)	4 (7.4)	.22 <sup>b</sup>
Pretreatment imaging (No.) (%)			
ASPECTS			
10–8	24 (50)	47 (83.9)	<.001 <sup>b</sup>
7–6	22 (45.8)	7 (12.5)	
<6	2 (4.2)	2 (3.6)	
Median (IQR)	7 (6–9)	9 (8–10)	
Infarct volume (mean) (SD) ( $\text{cm}^3$ )	107.4 (99.1)	35.0 (55.1)	<.001 <sup>a</sup>
Scores on admission (No.) (%)			
Premorbid mRS			
0	30 (62.5)	24 (42.9)	.02 <sup>a</sup>
1	11 (22.9)	10 (17.9)	
2	4 (8.3)	14 (25)	
>2	3 (6.3)	8 (14.3)	
NIHSS on admission	17.9 (3.6)	16.9 (3.7)	.14 <sup>a</sup>
GCS on admission			
12	6 (12.5)	2 (3.6)	.8 <sup>e</sup>
13	21 (43.8)	31 (55.4)	
15–14	21 (43.8)	23 (41.2)	
Occlusion (No.) (%)			
MCA	26 (54.2)	39 (69.6)	.08 <sup>b</sup>
ICA	3 (6.3)	0 (0)	
ICA + MCA	19 (39.6)	17 (30.4)	
Occlusion side right	22 (45.8)	23 (44.1)	.63 <sup>b</sup>
Treatment of stroke			
IV tPA + EST	32 (66.7)	31 (55.4)	.24 <sup>b</sup>
EST	16 (33.3)	25 (44.6)	

**Note:**—GCS indicates Glasgow Coma Scale; IQR, interquartile range.

<sup>a</sup> *t* test, 2-sided.

<sup>b</sup>  $\chi^2$  test, 3-sided.

<sup>c</sup> Lower sample size in Tan group 0–1 ( $n = 47$ ).

<sup>d</sup> Lower sample size in Tan group 0–1 ( $n = 47$ ) and Tan group 2–3 ( $n = 54$ ).

<sup>e</sup> Mann-Whitney *U* test, 2-sided.

( $r = 0.58$ ) and between infarct volume and ASPECTS ( $\rho = -0.6$ ). An additional correlation analysis according to the applied sedation mode showed a moderate correlation between early NIHSS improvement and infarct volume ( $r = 0.71$ ) and ASPECTS and infarct volume ( $\rho = -0.62$ ) in the GA treatment group (On-line Table 2). Correlation analysis in the CS treatment group showed only a correlation between early NIHSS improvement and the mRS after 3 months ( $\rho = 0.61$ ).

Regression analysis revealed that the presence of a moderate or good collateral status and favorable ASPECTS were strong predictors for smaller final mean infarct volume (coefficients:  $-51.75$ ;

**Table 2: SIESTA primary and secondary outcome results according to no or poor (Tan 0–1) and moderate or good collaterals (Tan 2–3)**

	Tan 0–1 (n = 48)	Tan 2–3 (n = 56)	P Value
Primary outcome			
Improvement in NIHSS (mean) (SD)	−1.1 (10.7)	−5.8 (7.6)	.01 <sup>a</sup>
Secondary outcomes			
Clinical (No.) (%)			
mRS 0–2 after 3 mo	10 (20.8)	14 (25.0)	.82 <sup>b</sup>
In-house mortality	7 (14.6)	1 (1.8)	.02 <sup>b</sup>
Mortality after 3 mo	12 (25.0)	15 (26.8)	.84 <sup>b</sup>
Logistics (mean) (SD)			
Length of stay in hospital (days)	6.0 (3.7)	4.6 (2.6)	.06 <sup>c</sup>
Length of stay in ICU (half-days) <sup>e</sup>	8.2 (9.2)	2.7 (2.2)	<.001 <sup>c</sup>
Length of ventilation (hr)	30.1 (5.9)	3.8 (5.4)	.11 <sup>c</sup>
Length of stay on stroke unit (half-days) <sup>f</sup>	7.6 (4.3)	7.0 (4.3)	.5 <sup>c</sup>
Onset-to-treatment (IV or IA) (min) <sup>g</sup>	122.8 (64.8)	129.6 (60.9)	.61 <sup>b</sup>
Door-to-groin (min)	71.5 (32.1)	66.1 (21.4)	.52 <sup>c</sup>
Door-to-reperfusion (min) <sup>h</sup>	174.8 (57.1)	165.6 (60.5)	.32 <sup>c</sup>
Feasibility of EST (No.) (%)			
Degree of reperfusion (TICI)			.97 <sup>d</sup>
0–1	3 (6.3)	5 (9)	
2a	4 (8.3)	3 (5.4)	
2b	24 (50.0)	25 (44.6)	
3	17 (35.4)	23 (41.1)	
Substantial patient movement	1 (2.1)	2 (3.6)	.65 <sup>b</sup>
Difficult vascular approach	3 (6.3)	7 (12.5)	.28 <sup>b</sup>
Other	3 (6.3)	8 (14.3)	.18 <sup>b</sup>
Safety (No.) (%)			
Complications before EST			
Impaired monitor installation	0 (0.0)	1 (1.8)	.35 <sup>b</sup>
Other	1 (2.1)	0 (0.0)	.27 <sup>b</sup>
Complications during EST			
Critical ventilation or oxygenation disturbance	2 (4.2)	1 (1.8)	.47 <sup>b</sup>
Intervention-associated complications	0 (0.0)	2 (3.6)	.19 <sup>b</sup>
Vessel perforation with ICH and/or SAH complications after EST	0 (0.0)	2 (3.6)	.19 <sup>b</sup>
Hyper- or hypothermia	12 (25.0)	12 (21.4)	.67 <sup>b</sup>
Delayed extubation	17 (35.4)	12 (21.4)	.11 <sup>b</sup>
Ventilation-associated complications	6 (12.5)	3 (5.4)	.2 <sup>b</sup>
Ventilation-associated pneumonia	6 (12.5)	3 (5.4)	.2 <sup>b</sup>

**Note:**—IA indicates intra-arterial; min, minimum; max, maximum; ICH, intracerebral hemorrhage; ICU, intensive care unit.

<sup>a</sup> ANCOVA, NIHSS as baseline covariate.

<sup>b</sup>  $\chi^2$  test, 2-sided.

<sup>c</sup> *t* test, 2-sided.

<sup>d</sup> Mann-Whitney *U* test, 2-sided.

<sup>e</sup> Lower sample size (41 and 46).

<sup>f</sup> Lower sample size (31 and 51).

<sup>g</sup> Lower sample size (41 and 47).

<sup>h</sup> Lower sample size (45 and 49).

95% CI, −81.58 to −21.92; *P* = .0008; and −2.36; 95% CI, −3.58 to −1.14; *P* < .0002, respectively) (On-line Tables 3 and 4).

However, when we tested the interaction between the Tan group and sedation mode, no significant associations with any of the outcome measures were observed.

## DISCUSSION

This post hoc analysis of the SIESTA trial showed a strong association of moderate-to-good collateral status with several surrogates of thrombectomy success in the entire cohort. Subdividing the cohort into 2 collateral status categories and those divided further according to the chosen sedation mode (CS or GA) did not show a relevant impact of either sedation mode on most associations.

The strong impact of collateral status is consistent with the

results published in other recent studies.<sup>3,4,20</sup> Our study adds to this evidence that the strong predictive value of the collateral score of Tan can be found even in a broad-practice RCT stroke population without rigid clinical or radiologic selection criteria. Although recent studies have suggested that collateral status is very variable in patients and that a good collateralization is strongly associated with smaller resulting infarcts and a better functional outcome,<sup>20,21</sup> none of these studies reported data about the peri-interventional management or the sedation concept. Collateral status appears to be a very robust predictor not vulnerable to sedation mode with regard to most parameters.

We found, however, a few exceptions for patients treated with GA: In both collateral categories, these patients were more likely to experience delayed extubation than those started in CS and intubated during the intervention. Delayed extubation was often a consequence of spontaneous hypothermia after GA. Those with moderate or good collaterals, in particular, had a higher prevalence of postinterventional hypothermia and more delayed extubation. These patients also had a longer mean time-to-treatment (IV or intra-arterial). This delay of treatment initiation in GA Tan 2–3 may have been caused by these patients having presented with fluctuating symptoms, which may have postponed the indication for EST.

Most interesting and relevant to our initial hypothesis, those with poor or no collaterals if treated under GA were more often independent (mRS

0–2) at 3 months compared with the same collateral status group treated in CS, even though the results were only of marginal significance.

Our post hoc analysis is the first study to suggest that the predictive value of the Tan collateralization score and the ASPECTS on outcome does not appear to be influenced by the choice of peri-interventional CS or GA. Either such an influence does not exist or, more likely, SIESTA's protocols with strict target values for blood pressure and CO<sub>2</sub> may have prevented compromising effects. As outlined above, an optimally performed GA may have its advantages compared with CS. The marginal significance for a favorable outcome after 3 months in the GA treatment arm of patients with poor collaterals may indicate such an advantage. Relative hypoventilation with slight hyper-

carbia and cerebral vasodilation or at least stabilization of normocarbia may have improved the function of the few collaterals that remained. Alternative mechanisms may have been the potential neuroprotective effects of the applied sedatives<sup>22</sup> or the significantly higher rate of hypothermia under GA. These speculations, however, demand further prospectively mechanistically designed studies to assess how GA is best conducted during EST.

Our study has several limitations. First, SIESTA was a single-center study, and its findings are difficult to generalize; the same is true for post hoc analyses. Second, very small sample sizes of the subgroups limit insights from this explorative study. Third, in SIESTA, exclusively single-phase CTAs were conducted, which could have led to insufficient categorization of collateralization concerning temporal collaterals. Finally, interpretation of the CTAs may have been influenced by high-grade stenoses of the ICA or a pre-existent congestive heart failure for which we had not controlled.

## CONCLUSIONS

Our results suggest that the benefit from thrombectomy can be expected in patients with moderate and, especially, good collaterals largely irrespective of the chosen sedation mode, if both general anesthesia and conscious sedation are performed according to protocols involving physiology parameter targets. It is still possible that a suboptimally performed GA during EST may eliminate the advantages of a good collateral status.

More prospective, multicenter studies with higher numbers of patients are necessary to clarify whether patients, particularly those with poor collateral statuses, may benefit from certain neuroprotective effects of GA or other sedation modes during thrombectomy.

Disclosures: Johannes Pfaff—UNRELATED: Payment for Lectures Including Service on Speakers Bureaus: Siemens; Travel/Accommodations/Meeting Expenses Unrelated to Activities Listed: Stryker. Simon Nagel—UNRELATED: Consultancy: Brainomix; Grants/Grants Pending: Brainomix\*; Payment for Lectures Including Service on Speakers Bureaus: Medtronic, Pfizer, Bayer; Travel/Accommodations/Meeting Expenses Unrelated to Activities Listed: Bayer, Boehringer Ingelheim, Medtronic, Pfizer. Peter A. Ringleb—UNRELATED: Consultancy: Bayer, Boehringer Ingelheim, Covidien, Comments: Advisory Board member; Payment for Lectures Including Service on Speakers Bureaus: Bayer, Bristol-Myers Squibb, Boehringer Ingelheim, Daiichi Sankyo, Pfizer. Werner Hacke—UNRELATED: Consultancy: Boehringer Ingelheim, Medtronic, Neuravi; Grants/Grants Pending: Boehringer Ingelheim, Comments: grant for ECASS 4 study\*; Payment for Lectures Including Service on Speakers Bureaus: Boehringer Ingelheim, Medtronic, Daiichi Sanyo, Neuravi. Martin Bendszus—UNRELATED: Board Membership: Data and Safety Monitoring Board for Vascular Dynamics, Guerbet, Boehringer Ingelheim; Consultancy: Codman, Hoffmann-La Roche, Guerbet, Boehringer Ingelheim; Grants/Grants Pending: Deutsche Forschungsgemeinschaft, Hopp Foundation, Novartis, Siemens, Guerbet, Stryker, Covidien\*; Payment for Lectures Including Service on Speakers Bureaus: Novartis, Hoffmann-La Roche, Guerbet, Teva Pharmaceutical Industries, Bayer, Codman. Markus A. Möhlenbruch—UNRELATED: Payment for Lectures Including Service on Speakers Bureaus: Codman, Medtronic, Microvention, Stryker, phenox. Julian Bösel—UNRELATED: Grants/Grants Pending: Patient-Centered Outcomes Research Institute, Comments: award SETPOINT2 study\*; Payment for Lectures Including Service on Speakers Bureaus: C.R. BARD, ZOLL, Seiratherm, Boehringer Ingelheim, Sedana Medical, Comments: speaker honoraria and travel support; Travel/Accommodations/Meeting Expenses Unrelated to Activities Listed: C.R. BARD, ZOLL, Seiratherm, Boehringer Ingelheim, Sedana Medical. \*Money paid to the institution.

## REFERENCES

- Goyal M, Menon BK, van Zwam WH, et al; HERMES collaborators. **Endovascular thrombectomy after large-vessel ischaemic stroke: a meta-analysis of individual patient data from five randomised trials.** *Lancet* 2016;387:1723–31 CrossRef Medline
- Saver JL, Goyal M, van der Lugt A, et al; HERMES Collaborators. **Time to treatment with endovascular thrombectomy and outcomes from ischemic stroke: a meta-analysis.** *JAMA* 2016;316:1279–88 CrossRef Medline
- Bang OY, Saver JL, Kim SJ, et al. **Collateral flow predicts response to endovascular therapy for acute ischemic stroke.** *Stroke* 2011;42:693–99 CrossRef Medline
- Liebeskind DS. **Collateral circulation.** *Stroke* 2003;34:2279–84
- Liebeskind DS, Tomsick TA, Foster LD, et al; IMS III Investigators. **Collaterals at angiography and outcomes in the Interventional Management of Stroke (IMS) III trial.** *Stroke* 2014;45:759–64 CrossRef Medline
- Berkhemer OA, Jansen IG, Beumer D, et al; MR CLEAN Investigators. **Collateral status on baseline computed tomographic angiography and intra-arterial treatment effect in patients with proximal anterior circulation stroke.** *Stroke* 2016;47:768–76 CrossRef Medline
- Reich DL, Hossain S, Krol M, et al. **Predictors of hypotension after induction of general anesthesia.** *Anesth Analg* 2005;101:622–28 Medline
- Mundiyanapurath S, Stehr A, Wolf M, et al. **Pulmonary and circulatory parameter guided anesthesia in patients with ischemic stroke undergoing endovascular recanalization.** *J Neurointerv Surg* 2016;8:335–41 CrossRef Medline
- Lowhagen Hendén P, Rentzos A, Karlsson JE, et al. **Hypotension during endovascular treatment of ischemic stroke is a risk factor for poor neurological outcome.** *Stroke* 2015;46:2678–80 CrossRef Medline
- Davis MJ, Menon BK, Baghirzada LB, et al; Calgary Stroke Program. **Anesthetic management and outcome in patients during endovascular therapy for acute stroke.** *Anesthesiology* 2012;116:396–405 CrossRef Medline
- Takahashi CE, Brambrink AM, Aziz MF, et al. **Association of intraprocedural blood pressure and end tidal carbon dioxide with outcome after acute stroke intervention.** *Neurocrit Care* 2014;20:202–08 CrossRef Medline
- Brinjikji W, Murad MH, Rabinstein AA, et al. **Conscious sedation versus general anesthesia during endovascular acute ischemic stroke treatment: a systematic review and meta-analysis.** *AJNR Am J Neuroradiol* 2015;36:525–29 CrossRef Medline
- Schönenberger S, Möhlenbruch M, Pfaff J, et al. **Sedation vs. Intubation for Endovascular Stroke Treatment (SIESTA): a randomized monocentric trial.** *Int J Stroke* 2015;10:969–78 CrossRef Medline
- Schönenberger S, Uhlmann L, Hacke W, et al. **Effect of conscious sedation vs general anesthesia on early neurological improvement among patients with ischemic stroke undergoing endovascular thrombectomy: a randomized clinical trial.** *JAMA* 2016;316:1986–96 CrossRef Medline
- Menon BK, Puetz V, Kochar P, et al. **ASPECTS and other neuroimaging scores in the triage and prediction of outcome in acute stroke patients.** *Neuroimaging Clin N Am* 2011;21:407–23, xii CrossRef Medline
- Tan IY, Demchuk AM, Hopyan J, et al. **CT angiography clot burden score and collateral score: correlation with clinical and radiologic outcomes in acute middle cerebral artery infarct.** *AJNR Am J Neuroradiol* 2009;30:525–31 Medline
- Tomsick T, Broderick J, Carrozella J, et al; Interventional Management of Stroke II Investigators. **Revascularization results in the Interventional Management of Stroke II trial.** *AJNR Am J Neuroradiol* 2008;29:582–87 Medline
- Zaidat OO, Yoo AJ, Khatri P, et al; Cerebral Angiographic Revascularization Grading (CARG) Collaborators, STIR Revascularization working group, STIR Thrombolysis in Cerebral Infarction (TICI) Task Force. **Recommendations on angiographic revascularization grading standards for acute ischemic stroke: a consensus statement.** *Stroke* 2013;44:2650–63 CrossRef Medline
- The R Core Team. *A Language and Environment for Statistical Com-*

- puting. R Vienna: Foundation for Statistical Computing, Vienna, Austria; 2016
20. Liebeskind DS. **Collateral lessons from recent acute ischemic stroke trials.** *Neurol Res* 2014;36:397–402 CrossRef Medline
  21. Menon BK, Smith EE, Modi J, et al. **Regional leptomeningeal score on CT angiography predicts clinical and imaging outcomes in patients with acute anterior circulation occlusions.** *AJNR Am J Neuroradiol* 2011;32:1640–45 CrossRef Medline
  22. Sivasankar C, Stiefel M, Miano TA, et al. **Anesthetic variation and potential impact of anesthetics used during endovascular management of acute ischemic stroke.** *J Neurointerv Surg* 2016;8:1101–06 CrossRef Medline

# Effect of Retrievable Stent Size on Endovascular Treatment of Acute Ischemic Stroke: A Multicenter Study

D. Yang, Y. Hao, W. Zi, H. Wang, D. Zheng, H. Li, M. Tu, Y. Wan, P. Jin, G. Xiao, Y. Xiong, G. Xu, and X. Liu



## ABSTRACT

**BACKGROUND AND PURPOSE:** In clinical practice, stent diameter is one of the variable properties important for endovascular treatment. A consensus guideline for stent retriever size selection has yet to be established. The aim of this study was to investigate the effects of different diameters of Solitaire retrievers on outcomes.

**MATERIALS AND METHODS:** Of 628 patients enrolled from the Endovascular Treatment for Acute Anterior Circulation Ischemic Stroke Registry, 256 were treated with the Solitaire 4-mm device and 372, with the 6-mm device. We matched patients treated with the 2 stent sizes using propensity score analysis. The successful outcome was reperfusion as measured by the modified Thrombolysis in Cerebral Infarction score immediately postprocedure and the dichotomized modified Rankin Scale score at 90 days. Symptomatic intracerebral hemorrhage and in-hospital mortality were also recorded.

**RESULTS:** After propensity score analysis, group outcomes did not differ. In addition, in patients with atherosclerosis-related occlusion, a higher reperfusion rate ( $P = .021$ ) was observed in the Solitaire 4 group, as well as a shorter time interval ( $P = .002$ ) and fewer passes ( $P = .025$ ). Independent predictors of successful reperfusion in patients with atherosclerotic disease on logistic analysis were the small stent (OR, 3.217; 95% CI, 1.129–9.162;  $P = .029$ ) and the propensity score acting as a covariate (OR, 52.84; 95% CI, 3.468–805.018;  $P = .004$ ).

**CONCLUSIONS:** We found no evidence of a differential effect of intra-arterial therapy based on the size of Solitaire retrievers. In patients with atherosclerotic disease, favorable reperfusion was associated with deployment of a small stent.

**ABBREVIATIONS:** ACTUAL = Endovascular Treatment for Acute Anterior Circulation Ischemic Stroke Registry; IQR = interquartile range; mTICI = modified TICI; ST 4 = 4-mm Solitaire stent retriever; ST 6 = 6-mm Solitaire stent retriever

Large-vessel occlusion accounts for 28%–46% of all ischemic strokes and leads to poor prognosis and high mortality.<sup>1</sup> Since 2015, the results of several clinical randomized trials have suggested that intra-arterial treatment is safe and effective for anterior circulation large-vessel occlusion.<sup>2–7</sup> The success also demon-

strated the benefit of newer stent devices in endovascular recanalization therapies because most patients were treated with retrievable stents in these trials.

In these trials, most devices used for mechanical thrombectomy were retrievable stents such as the Solitaire FR (Covidien, Irvine, California)<sup>8</sup> or the Trevo retriever (Stryker, Kalamazoo, Michigan).<sup>9</sup> The Solitaire is a self-expanding and retrievable stentlike device that restores blood flow immediately by thrombus entrapment between the stent struts and the vessel wall,<sup>10</sup> achieving substantially better safety and efficacy outcomes than former

Received January 11, 2017; accepted after revision March 24.

From the Department of Neurology (D.Y., H.W., X.L.), Jinling Hospital, Second Military Medical University, Nanjing, Jiangsu Province, China; Department of Neurology (Y.H., G.Xu, X.L.), Jinling Hospital, Southern Medical University, Nanjing, Jiangsu Province, China; Department of Neurology (W.Z., Y.X., G.Xu, X.L.), Jinling Hospital, Medical School of Nanjing University, Nanjing, Jiangsu Province, China; Department of Emergency Medicine (Y.H.), First Affiliated Hospital of Soochow University, Suzhou, Jiangsu Province, China; Department of Neurology (H.W.), 89th Hospital of the People's Liberation Army, Weifang, Shandong Province, China; Department of Neurology (D.Z.), 175th Hospital of the People's Liberation Army, Affiliated Southeast Hospital of Xiamen University, Zhangzhou, Fujian Province, China; Department of Neurology (H.L.), 476th Hospital of the People's Liberation Army, Fuzhou, Fujian Province, China; Department of Neurology (M.T.), Hubei Wuchang Hospital, Wuhan, Hubei Province, China; Department of Neurology (Y.W.), Hubei Zhongshan Hospital, Wuhan, Hubei Province, China; Department of Neurology (P.J.), Lu'an Affiliated Hospital of Anhui Medical University, Lu'an, Anhui Province, China; and Department of Neurology (G.Xiao), Second Affiliated Hospital of Soochow University, Suzhou, Jiangsu Province, China.

Dong Yang and Yonggang Hao contributed equally to this work.

The project is supported by the National Natural Science Foundation of China (No. 81400898, 81400993, 81571143 and 81671172) and the Chinese Postdoctoral Science Fund (No. 2015M572815).

Please address correspondence to Gelin Xu, MD, PhD, Department of Neurology, Jinling Hospital, Southern Medical University, 305 East Zhongshan Rd, Nanjing, 210002, Jiangsu, China; e-mail: gelinxu@nju.edu.cn; and Xinfeng Liu, MD, PhD, Department of Neurology, Jinling Hospital, Second Military Medical University, 305 East Zhongshan Rd, Nanjing, 210002, Jiangsu, China; e-mail: xfliu2@vip.163.com

Indicates open access to non-subscribers at [www.ajnr.org](http://www.ajnr.org)

Indicates article with supplemental on-line tables.

<http://dx.doi.org/10.3174/ajnr.A5232>

devices.<sup>11</sup> This device was at first designed for aneurysms, with a variety of diameters made available to meet the needs of different sizes of intracranial vessels.<sup>12</sup> For mechanical thrombectomy, stents with 4- and 6-mm diameters delivered through 0.021- and 0.027-inch microcatheters, respectively, optimize performance in intracranial large vessels in present day interventional therapy. The Trevo retriever is structurally similar to the Solitaire FR, with a stent cell geometry designed to integrate the clot into the stent for retrieval.<sup>13,14</sup>

It has been reported that a difference in stent size potentially influences stent properties, including radial force, flexibility, and deliverability.<sup>15-17</sup> The radial force represents the supporting action of the stent on the vessel wall to prevent elastic retraction, while flexibility and deliverability exemplify the ability to pass through the occluded site. Several studies have found that a stent with a large radial force is suitable for proximal vessels and atherosclerotic modified vessels with hardened or calcified plaque, while a more flexible stent should be used in a tortuous or distant vessel.<sup>16,18</sup>

In addition, extensive evidence shows that the stent diameter is associated with in-stent restenosis<sup>19</sup> and change in blood flow after intracranial stent implantation,<sup>20</sup> as well as adverse events after percutaneous coronary intervention.<sup>21,22</sup> These results demonstrated the impact of stent size on vascular interventional therapy and also showed the importance and necessity of research on device size in mechanical thrombectomy. However, as yet there is no established guideline for stent selection, with the choice being left entirely to the interventionist. Hence, uncertainties remain about the benefit and risk of endovascular intervention in relation to different sizes of stents. This study addresses the uncertainties regarding stent size for thrombectomy.

## **MATERIALS AND METHODS**

### **Study Design and Participants**

This is a retrospective observational study on the efficacy and safety of endovascular treatment of acute ischemic stroke in real-world practice. We aimed to evaluate the impact of the sizes of stentlike thrombectomy devices on the outcome of treated patients with ischemic stroke due to large-vessel occlusion of the anterior circulation. Patients were those registered in the Endovascular Treatment for Acute Anterior Circulation Ischemic Stroke Registry (ACTUAL) from January 2014, to June 2016. ACTUAL was a multicenter registry program involving 21 comprehensive stroke centers across 10 provinces in China. All patients with acute ischemic stroke who underwent intra-arterial treatment were registered in ACTUAL. The local ethics committees approved the use of retrospective patient data. The procedure protocol was standardized in each center.

Generally, patients would receive endovascular treatment under the following conditions: 1) They were diagnosed with acute ischemic stroke; 2) had large-artery occlusion in the anterior circulation, including the internal carotid artery, middle cerebral artery (MCA M1 or M2), or anterior cerebral artery A1 or A2; 3) had evidence obtained by CTA, MR angiography, or digital subtraction angiography; 4) were 18 years of age or older; 5) had a pre-morbid modified Rankin Scale score of <2; 6) had a pretreatment National Institutes of Health Stroke Scale score of >5; and

7) could be treated within 6 hours of stroke onset. For selected patients who did not meet these criteria, endovascular treatment was still performed on the basis of a favorable benefit-risk ratio estimate.

To retain the homogeneity of the enrolled patients, we excluded patients treated with intra-arterial thrombolysis alone, or diagnosed with concomitant aneurysm or arteriovenous malformations. For the present study, we selected patients treated with retrievable stents.

### **Patients**

Of 698 patients from ACTUAL, 44 accepted angioplasty therapy and/or stent placement alone, 5 were treated with a thrombus aspiration device alone, 17 were treated with a microguidewire to disrupt clots alone, and 4 were fitted with the Trevo retriever rather than the Solitaire retriever. To maintain consistency of device type, we excluded patients treated with the Trevo retriever. Ultimately, a study cohort of 628 patients treated with the Solitaire stent retriever was enrolled.

### **Procedures**

If they met the criteria for intravenous thrombolytic therapy, patients received intravenous therapy with alteplase within 4.5 hours after the onset of stroke before mechanical treatment. Patients beyond a time window of 4.5 hours or with a contraindication to intravenous thrombolysis were treated directly with mechanical treatment.

Regarding mechanical therapy, patients were treated via femoral access. Under roadmap guidance, a microcatheter was advanced over a guidewire placed through the thrombus, after which the guidewire was removed and DSA was performed to confirm the occlusion. Next, the Solitaire retriever was advanced through the microcatheter across the occluded segment. The stent was unsheathed simultaneous to the microcatheter being pulled back. After 3–5 minutes to allow full expansion, the stent was withdrawn along with the microcatheter. If occlusion persisted, the sequence was repeated (Fig 1).

Choices of anesthesia and rescue therapy were left to the discretion of the interventionist. Stent selection depended on vascular tortuous morphology and sites of occluded vessels in general. A large stent was preferred in a proximal or straight artery, while a small stent was usually chosen for tortuous or distant arteries. The preference of the operator was also important for stent selection.

### **Outcomes**

Successful outcome was defined as achieving a modified TICI (mTICI) score of 2b–3 immediately postprocedure and a functional outcome at 90 days evaluated with the dichotomized modified Rankin Scale score (0–2 versus 3–6). Rates of in-hospital mortality and symptomatic intracerebral hemorrhage within 72 hours after endovascular treatment were recorded. Symptomatic intracerebral hemorrhage was diagnosed according to the Heidelberg Bleeding Classification.<sup>23</sup> Technical complications with the device were also recorded, including vessel perforation, vessel dissection, subarachnoid hemorrhage, stent fracture, and failure to deploy. Outpatient or telephone follow-up was performed to assess the functional outcome by mRS score at each institution.

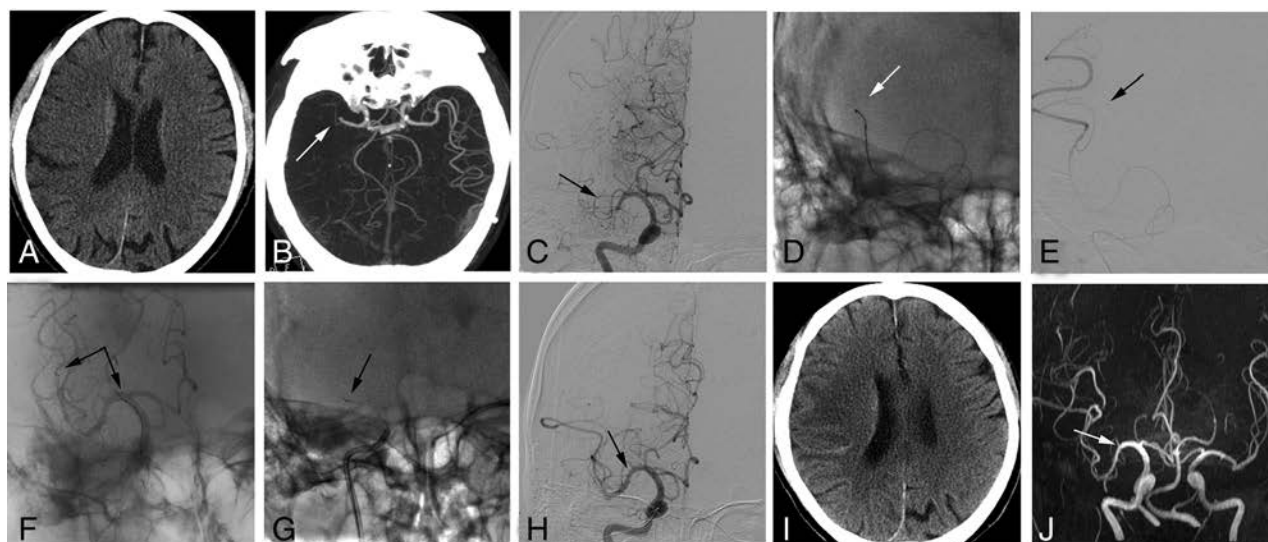


**FIG 1.** A 72-year-old male patient who presented with weakness of the left limb for 4 hours. *A*, CT on admission does not show a large-territory infarct. *B*, CTA shows right MCA segment occlusion (arrow). *C*, DSA confirms occlusion of the right MCA segment (arrow). *D*, A microguidewire crosses the occluded artery. *E*, A microcatheter crosses the thrombus to the distal segment through the microguidewire. *F*, Angiogram after deployment of the Solitaire 6 × 30 mm stent retriever shows restoration immediately in the MCA. Arrows show proximal and distal markers of the Solitaire device. *G*, The stent retriever is unsheathed with the microcatheter being pulled back simultaneously (arrow). *H*, After 3 passes of thrombectomy, the final angiography shows a mTICI flow of grade 2B in the right MCA with favorable perfusion (arrow). *I*, CT postprocedure at 24 hours shows no obvious intracerebral hemorrhage. *J*, MRA postprocedure at 7 days shows good recanalization (arrow).

### Statistical Analysis

Univariate analysis of baseline characteristics was compared between 2 groups according to stent diameter (4-mm Solitaire stent retriever [ST 4] versus 6 mm [ST 6]) with the Student *t* test (normal distribution) or the Mann-Whitney test (non-normal distribution) for continuous variables and a  $\chi^2$  test for categorical variables. In primary analysis, baseline variables differed statistically between the 2 groups. To control bias and minimize imbalance of baseline characteristics, we performed a 1:1 matched model based on the propensity score with the nearest neighbor matching algorithm without replacement. We compared patients treated with ST 4 and ST 6 using the Wilcoxon signed rank test and the McNemar test after matching. In addition, matched models of stroke subtype and vessel occlusion site were performed to conduct subgroup analysis. Furthermore, a logistic regression model with the propensity score as a covariate was computed to evaluate the effect of device choice.

The data were analyzed by SPSS Statistics, Version 22.0 (IBM, Armonk, New York), R statistical and computing software (Version 2.153; <http://www.r-project.org/>), SPSS Statistics–Essentials for R 22 (<https://sourceforge.net/projects/ibmspsstat/>), and PS-MATCHING 3.03 (SPSS Statistics extension bundle document; <https://sourceforge.net/projects/psmssps/>). Two-sided *P* values < .05 were statistically significant.

## RESULTS

### Study Population

Of the 628 enrolled patients, 59.2% (372/628) were treated with 4-mm, and 40.6% (256/628), with 6-mm Solitaire retrievers. There were 58.3% (366/628) men, and the average age was 66 years (range, 56–74 years). The median baseline NIHSS score was 17 (range, 12–21). Delay from symptom onset to door of the emergency department was 125 minutes (60–222

minutes). Delay from stroke onset to groin puncture was 270 minutes (205–350 minutes). When successful recanalization was defined as an mTICI score of 2b or 3, 84.4% (530/628) of the enrolled patients obtained successful recanalization of the targeting artery after endovascular treatment. In these patients who were recanalized (84.4%), the median time from puncture to reperfusion was 102 minutes (75–144 minutes). The proportion of patients with an mRS score of 0–2 at 90 days was 41.7% (262/628). Symptomatic intracerebral hemorrhage occurred in 16.1% (101/628) of patients within 24 hours after endovascular treatment, and death occurred in 24.2% (152/628) of patients. Device-related complications included vessel perforation, 1.3% (8/628); vessel dissection, 1.4% (9/628); subarachnoid hemorrhage, 2.1% (13/628); stent fracture, 0.2% (1/628); and failure to deploy, 0.2% (1/628).

### Baseline Characteristics

Univariate analysis of baseline data suggested that no difference existed between the 2 groups except for the following: age (ST 6, 68 years; interquartile range [IQR], 58–75 years; ST 4, 64 years; IQR, 53–73 years; *P* = .003); atrial fibrillation (ST 6, 51.2%; ST 4, 37.2%; *P* < .001); ASPECTS (ST 6, 9; IQR, 7–10; ST 4, 9; IQR, 8–10; *P* < .001); NIHSS (ST 6, 17; IQR, 13–21; ST 4, 16; IQR, 12–20; *P* = .029); atherosclerotic occlusions (ST 6, 37.1%; ST 4, 46%; *P* = .027); cardiac embolism occlusions (ST 6, 57%; ST 4, 47.5%; *P* = .02); ICA occlusions (ST 6, 60.5%; ST 4, 23.1%; *P* < .001); MCA occlusions (ST 6, 39.1%; ST 4, 76.3%; *P* < .001); and favorable collateral flow (American Society of Interventional and Therapeutic Neuroradiology, Society of Interventional Radiology grade), 2–3 (ST 6, 38.8%; ST 4, 57.8%; *P* < .001). Baseline characteristics are summarized in Table 1.

**Table 1: Baseline characteristics before and after matching<sup>a</sup>**

	Before Matching			After Matching		
	ST 6 (n = 256)	ST 4 (n = 372)	P	ST 6 (n = 169)	ST 4 (n = 169)	P
Age (median) (IQR) (yr)	68 (58–75)	64 (53–73)	.003	67 (56–75)	64 (53–73)	.103
Women (No.) (%)	112 (43.8%)	150 (40.3%)	.392	71 (42%)	64 (37.9%)	.505
AF (No.) (%)	131 (51.2%)	138 (37.2%)	.001	80 (47.3%)	67 (39.6%)	.160
Hypertension (No.) (%)	158 (61.7%)	231 (62.1%)	.924	112 (66.3%)	105 (62.1%)	.500
Diabetes mellitus (No.) (%)	45 (17.6%)	66 (17.7%)	.958	35 (20.7%)	29 (17.2%)	.488
Current smoker (No.) (%)	69 (27%)	92 (24.7%)	.531	49 (29%)	41 (24.3%)	.389
SBP (median) (IQR) (mm Hg)	145 (130–161)	144 (130–160)	.537	148 (129–163)	148 (130–160)	.393
GLU (median) (IQR) (mmol/L)	6.9 (5.83–8.9)	6.7 (5.77–8.38)	.173	6.83 (5.6–9.25)	6.9 (5.81–8.69)	1.000
ASPECTS (median) (IQR)	9 (7–10)	9 (8–10)	.001	9 (7–10)	9 (8–10)	.784
NIHSS (median) (IQR)	17 (13–21)	16 (12–20)	.029	17 (13–21)	17 (13–21)	1.000
IV (No.) (%)	81 (31.6%)	119 (32%)	.927	56 (33.1%)	61 (36.1%)	.657
Time from onset to visit (median) (IQR) (min)	130 (75–230)	120 (60–214)	.058	138 (64–224)	120 (58–214)	.316
Time from onset to puncture (median) (IQR) (min)	280 (210–350)	270 (205–347)	.692	279 (202–345)	270 (195–346)	.589
Stroke subtype						
Atherosclerotic (No.) (%)	95 (37.1%)	171 (46%)	.027	68 (40.2%)	73 (43.2%)	.644
Cardiac embolism (No.) (%)	146 (57%)	177 (47.5%)	.02	90 (53.3%)	85 (50.3%)	.657
Undetermined etiology (No.) (%)	15 (5.9%)	24 (6.5%)	.763	11 (6.5%)	11 (6.5%)	1.000
Artery occlusion site						
ICA (No.) (%)	155 (60.5%)	86 (23.1%)	<.001	78 (46.2%)	76 (45%)	.791
MCA (No.) (%)	100 (39.1%)	284 (76.3%)	<.001	90 (53.3%)	93 (55%)	.607
ACA (No.) (%)	1 (0.4%)	2 (0.5%)	1.000	1 (0.6%)	0	1.000
Collateral flow grade (ASITN/SIR)			<.001			.261
0–1 (No.) (%)	156 (61.2%)	156 (42.2%)		93 (55%)	83 (49.1%)	
2–3 (No.) (%)	99 (38.8%)	214 (57.8%)		76 (45%)	86 (50.9%)	

**Note:**—ASITN/SIR indicates American Society of Interventional and Therapeutic Neuroradiology, Society of Interventional Radiology; AF, atrial fibrillation; GLU, glucose; ACA, anterior cerebral artery; SBP, systolic blood pressure.

<sup>a</sup> The logistic regression model used for the determination of the propensity score included the following factors: age, sex, atrial fibrillation, hypertension, diabetes, time from onset to groin puncture, NIHSS score, ASPECTS, stroke subtype, site of vessel occlusion, and collateral blood flow.

**Table 2: Clinical outcomes before and after matching**

	Before Matching			After Matching		
	ST 6 (n = 256)	ST 4 (n = 372)	P	ST 6 (n = 169)	ST 4 (n = 169)	P
mTICI			.013			.532
0–2a (No.) (%)	51 (19.9%)	47 (12.6%)		31 (18.3%)	26 (15.4%)	
2b–3 (No.) (%)	205 (80.1%)	325 (87.4%)		138 (81.7%)	143 (84.6%)	
Workflow time						
Time from puncture to reperfusion (median) (IQR) (min)	111.5 (80–153)	97 (72–140)	.007	108 (75–147)	100 (75–156)	1.000
Time from stent deployment to reperfusion (median) (IQR) (min)	61 (30–94)	44 (20–75)	<.001	58 (30–87)	45 (21–82)	.021
Passes (median) (IQR)	2 (1–3)	2 (1–3)	.001	2 (1–3)	2 (1–3)	.375
≤3 (No.) (%)	210 (82%)	323 (86.8%)	.099	106 (62.7%)	119 (70.4%)	.154
Rescue therapy (No.) (%)	134 (52.3%)	184 (49.5%)	.478	85 (50.3%)	84 (49.7%)	1.000
Complications						
Vessel dissection (No.) (%)	3 (1.2%)	6 (1.6%)	.744	2 (1.2%)	5 (3.0%)	.453
Arterial perforation (No.) (%)	2 (0.8%)	6 (1.6%)	.482	2 (1.2%)	2 (1.2%)	1.000
Stent failure to deploy (No.) (%)	1 (0.4%)	0	.408	1 (0.6%)	0	1.000
Isolated SAH (No.) (%)	4 (1.6%)	9 (2.4%)	.459	3 (1.8%)	1 (0.6%)	.625
Symptomatic ICH (No.) (%)	41 (16%)	60 (16.1%)	.970	22 (13%)	27 (16%)	.511
Asymptomatic ICH (No.) (%)	92 (35.9%)	118 (31.7%)	.271	56 (33.1%)	67 (39.6%)	.248
mRS 90 days			.003			.087
0–2 (No.) (%)	89 (34.8%)	173 (46.5%)		64 (37.9%)	79 (46.7%)	
3–6 (No.) (%)	167 (65.2%)	199 (53.5%)		105 (62.1%)	90 (53.3%)	
In-hospital mortality (No.) (%)	74 (28.9%)	78 (21%)	.022	38 (22.5%)	39 (23.1%)	1.000

**Note:**—ICH indicates intracerebral hemorrhage.

### Outcomes before and after Matching

Table 2 shows the outcomes before and after matching. Primary results of outcomes before matching suggested that the ST 4 group had a higher rate of reperfusion postprocedure ( $P = .013$ ) and a favorable independent outcome at 90 days ( $P = .003$ ), as well as lower in-hospital mortality ( $P = .022$ ). Efficacy with regard to time was also observed in the ST 4 group, including reduced

time of the procedure ( $P = .007$ ) and time from stent deployment to reperfusion ( $P < .001$ ), as well as fewer passes of thrombectomy ( $P = .001$ ).

However, primary univariate analysis of baseline characteristics showed an imbalance between the 2 groups (Table 1). To minimize the impact of unbalanced factors, we matched a 1:1 model based on the propensity score in which unbalanced base-

**Table 3: Baseline characteristics of atherosclerotic-related occlusion before and after matching<sup>a</sup>**

	Before Matching			After Matching		
	ST 6 (n = 95)	ST 4 (n = 171)	P	ST 6 (n = 66)	ST 4 (n = 66)	P
Age (mean) (SD) (yr)	65 (11)	63 (13)	.086	64 (11.4)	62 (11.7)	.249
Women (No.) (%)	28 (29.5%)	47 (27.5%)	.730	16 (24.2%)	16 (24.2%)	1.000
Hypertension (No.) (%)	65 (68.4%)	115 (67.3%)	.845	48 (72.7%)	42 (63.6%)	.307
Diabetes mellitus (No.) (%)	21 (22.1%)	30 (17.5%)	.365	16 (24.2%)	7 (10.6%)	.078
Current smoker (No.) (%)	34 (35.8%)	56 (32.7%)	.615	25 (37.9%)	25 (37.9%)	1.000
SBP (median) (IQR) (mm Hg)	148 (135–163)	147 (130–160)	.351	148 (135–162)	140 (129–160)	.268
GLU (median) (IQR) (mmol/L)	6.54 (5.46–9.00)	6.70 (5.68–8.32)	.812	6.41 (5.2–8.95)	6.62 (5.7–8.34)	.538
ASPECTS (median) (IQR)	9 (7–10)	9 (8–10)	.012	9 (8–10)	10 (8–10)	.233
NIHSS (median) (IQR)	16 (12–20)	16 (11–19)	.154	16 (12–19)	16 (11–19)	.873
IV (No.) (%)	30 (31.6%)	61 (35.7%)	.500	25 (37.9%)	24 (36.4%)	1.000
Time from onset to visit (median) (IQR) (min)	153 (90–232)	120 (60–216)	.032	152 (90–220)	122 (49–242)	.450
Time from onset to treatment (median) (IQR) (min)	293 (225–364)	280 (210–356)	.352	289 (224–351)	275 (206–355)	.532
Artery occlusion site						
ICA (No.) (%)	55 (57.9%)	33 (19.3%)	<.001	32 (48.5%)	29 (43.9%)	.375
MCA (No.) (%)	39 (41.1%)	136 (79.5%)	<.001	33 (50%)	36 (54.5%)	.375
ACA (No.) (%)	1 (1.1%)	2 (1.2%)	.931	1 (1.5%)	1 (1.5%)	1.000
Collateral flow grade (ASITN/SIR)			.023			1.000
0–1 (No.) (%)	50 (52.6%)	65 (38.2%)		32 (48.5%)	31 (47%)	
2–3 (No.) (%)	45 (47.4%)	105 (61.8%)		99 (51.5%)	214 (53%)	

**Note:**—ASITN/SIR indicates American Society of Interventional and Therapeutic Neuroradiology, Society of Interventional Radiology; GLU, glucose; ACA, anterior cerebral artery; SBP, systolic blood pressure.

<sup>a</sup> The logistic regression model used for the determination of the propensity score included the following factors: age, time from onset symptom to visit, time from onset to groin puncture, NIHSS score, ASPECTS, site of vessel occlusion, and collateral blood flow.

**Table 4: Clinical outcomes of atherosclerotic-related occlusion before and after matching**

	Before Matching			After Matching		
	ST 6 (n = 95)	ST 4 (n = 171)	P	ST 6 (n = 66)	ST 4 (n = 66)	P
mTICI			.012			.021
0–2a (No.) (%)	20 (21.1%)	17 (9.9%)		16 (24.2%)	6 (9.1%)	
2b–3 (No.) (%)	75 (78.9%)	154 (90.1%)		50 (75.8%)	60 (90.9%)	
Workflow time						
Time from puncture to reperfusion (median) (IQR) (min)	125 (90–180)	103 (75–145)	.001	120 (89–170)	95 (65–136)	.013
Time from stent deployment to reperfusion (median) (IQR) (min)	69 (32–117)	45 (23.5–79)	.001	67 (33–114)	46 (19–68)	.002
Passes (median) (IQR)	2 (1–3)	2 (1–2)	.042	2 (1–3)	1 (1–2)	.025
≤3 (No.) (%)	75 (78.9%)	151 (88.3%)	.041	51 (77.3%)	60 (90.9%)	.064
Rescue therapy (No.) (%)	68 (71.6%)	99 (57.9%)	.027	47 (71.2%)	38 (57.6%)	.164
Complications						
Arterial perforation (No.) (%)	0	4 (2.3%)	.300	0	2 (3.0%)	.500
Vessel dissection (No.) (%)	1 (1.1%)	2 (1.2%)	1.000	0	2 (3.0%)	.500
Stent failure to deploy (No.) (%)	1 (1.1%)	0	.357	1 (1.5%)	0	1.000
Isolated SAH (No.) (%)	0	6 (3.5%)	.092	0	1 (1.5%)	1.000
Symptomatic ICH (No.) (%)	13 (13.7%)	18 (10.5%)	.442	6 (9.1%)	4 (6.1%)	.754
Asymptomatic ICH (No.) (%)	29 (30.5%)	52 (30.4%)	.984	19 (28.8%)	24 (36.4%)	.405
mRS 90 days			.032			.486
0–2 (No.) (%)	37 (38.9%)	90 (52.6%)		28 (42.4%)	33 (50%)	
3–6 (No.) (%)	58 (61.1%)	81 (47.4%)		38 (57.6%)	33 (50%)	
In-hospital mortality (No.) (%)	19 (20%)	29 (17%)	.537	13 (19.7%)	15 (22.7%)	.832

**Note:**—ICH indicates intracerebral hemorrhage.

line characteristics and other variables influencing outcomes were taken into account (Table 1).

After propensity score matching, baseline variables were equally distributed in the 2 groups (Table 1). Outcomes of efficacy and safety did not differ between the groups, except for a shorter time from stent deployment to reperfusion in the ST 4 group ( $P = .021$ ).

### Subgroup Analysis

Primary analysis of baseline data also revealed that selection bias was present in the stroke type and occluded vessels. ST 4 was used more than ST 6 for patients with atherosclerotic disease (46%

versus 37.1%,  $P = .027$ ) and MCA occlusion (76.3% versus 39.1%,  $P < .001$ ), while ST 6 was more frequently used than ST 4 in patients with cardiogenic stroke (57% versus 47.5%,  $P = .02$ ) and ICA occlusion (60.5% versus 23.1%,  $P < .001$ ). To explore the effect of device choice on stroke type and vessel occlusion site, we performed subgroup analyses of models of atherosclerotic disease, cardiac embolism, ICA, and MCA (Tables 3 and 4 and Online Tables 1–3).

Results suggested better outcomes for the ST 4 group in stroke classification models. In the atherosclerotic disease model, the ST 4 group demonstrated favorable reperfusion ( $P = .012$ , Table 4)

and better independent outcomes at 90 days ( $P = .032$ ). In addition, increased time efficacy ( $P = .001$ ), fewer attempts ( $P = .042$ ), and lower frequency of rescue therapy ( $P = .027$ ) were also observed in the ST 4 group. In the cardiac embolism model, lower mortality was reported in the ST 4 group ( $P = .035$ , On-line Table 1). When patients were stratified into those with ICA and MCA occlusions, the effects of the stent diameter size on functional outcomes did not show differences in the 2 patient groups (On-line Tables 2 and 3).

Propensity score analysis was also performed in these 4 models, the results of which showed a difference after matching in only the atherosclerotic disease model. Matched analysis of the atherosclerotic disease model showed favorable recanalization ( $P = .021$ ) and time efficacy ( $P = .013$ ) and fewer attempts ( $P = .025$ ) in the ST 4 group (Table 4).

Finally, a logistic regression model was conducted to assess potential predictors of mTICI postprocedure, in which the propensity score acted as a covariate. As a result, ST 4 (OR, 3.217; 95% CI, 1.129–9.162;  $P = .029$ ) and the propensity score (OR, 52.84; 95% CI, 3.468–805.018;  $P = .004$ ) were identified as independent predictors of favorable reperfusion for patients with atherosclerotic disease (On-line Tables 4 and 5).

## DISCUSSION

To the best of our knowledge, this is the first study to investigate the effect of different diameter sizes of stent retrievers on endovascular treatment. Whereas in the primary analysis, we found that patients in the small-stent group obtained better outcomes of efficacy and safety, after we adjusted the imbalance of baseline data, no difference was apparent. In patients with atherosclerotic disease, propensity score matching analysis suggested that a small stent was an independent predictor of successful reperfusion.

Our study aimed to describe the relationship between stent size and outcomes. Although the outcomes did not differ, the time interval between stent deployment and reperfusion was shorter when a small stent was used. Because this interval represents the validity time of stent action, the result suggests greater deliverability with a smaller stent. Consequently, a small stent may be a better choice, especially for tortuous vessels. Also, as is well-known, any delay in the time before reperfusion can lead to worse outcomes, and the prognosis improves the sooner endovascular reperfusion is achieved.<sup>24–26</sup> Hence, choosing a small stent with excellent deliverability could achieve quicker lesion location and thus avoid wasting time.

Selection bias of stent choice exists in the real world. In this study, a small stent was mainly used for patients with MCA occlusion, while the large stent was used mainly for large-vessel occlusion attributable to ICA occlusion and cardiac embolism. This approach appears reasonable, and results of our primary analysis suggested a difference in outcomes for the cardiac embolism model. However, after adjusting for imbalance and bias, propensity score analysis revealed no difference in the outcomes of both the ST 4 and ST 6 groups in the cardiac embolism and MCA and ICA models. It seems that in these cases, outcomes do not rely on stent size, and both choices may thus be equally feasible.

The most interesting finding was that the small stent was associated with better reperfusion in patients with atherosclerotic

disease (On-line Table 4). Large vessels occluded with atherosclerotic lesions, accompanied by in situ stenosis to some extent, result in tortuous and complicated vascular morphology. When one uses thrombectomy via a stent retriever, the vessels tend to be reoccluded after initial reperfusion because of subsequent platelet aggregation.<sup>27</sup> A small stent advanced through a thinner microcatheter is more flexible<sup>15</sup> and can pass through lesions in complex pathways comfortably and rapidly, with better deliverability. The small size is also associated with a low stent-release force,<sup>15</sup> making the release of the stent smoother and safer with greater accuracy. On the other hand, the radial force decreases incrementally with increasing stent diameter,<sup>16,17</sup> so a small stent with a large radial force could maintain vessel wall stability during the procedure. These stent characteristics help to increase time efficiency and recanalization. Another interesting finding was that attempted passes observed with the small stent were fewer. The endovascular procedure unavoidably injures the arterial wall and induces local inflammation and proliferation of smooth-muscle cells, resulting in intimal hyperplasia and restenosis.<sup>19</sup> Loh et al<sup>28</sup> and Angermaier et al<sup>29</sup> reported that  $>3$  attempts would not only be futile with a low additional successful revascularization but also increase the risk of vascular injury and other complications. Hence, a smaller stent with fewer passes could reduce the risk of restenosis and mechanical injury, providing practical clinical value.

It was reported that long stents were an independent predictor of major adverse cardiac events after acute myocardial infarction.<sup>21</sup> Postprocedural new DWI lesions occurred after carotid artery stent placement more often in patients with longer stents.<sup>30</sup> In this study, stent retrievers of 4 mm in diameter included lengths of 15 and 20 mm; stent retrievers of 6 mm in diameter included lengths of 20 and 30 mm. The retrievers with larger diameters are longer. Therefore, it is highly possible that the stent length influences the effects of interventional therapy.

Our study illustrates that both sizes of the Solitaire stent retriever for thrombectomy appear clinically applicable, providing efficacy and safety. The small stent is associated with better recanalization in large-vessel occlusion caused by intracranial atherosclerotic disease. In Asia, atherosclerotic disease is the main cause of acute ischemic stroke, unlike in Western countries.<sup>31</sup> In China, the incidence of atherosclerotic disease accounts for 33%–50% of strokes, higher than in the West (8%–10%).<sup>32,33</sup> Therefore, a small stent may be a better choice for this type of patient. However, these results cannot be generalized until a multicenter randomized controlled trial is designed to test and verify the assumption.

This is the first study to explore the influence of choosing different-sized stents on the effect of endovascular therapy for large-vessel occlusion in China. Our data came from a multicenter study, the samples of which were representative, reflecting real-world clinical practice. We also used a statistical method, namely propensity score matching analysis, which could control bias effectively and minimize the imbalance among groups in observational studies.<sup>34</sup>

Our research also has several limitations. The study was a retrospective, multicenter program, and the data were self-reported by the site investigator, which included selection bias. The registry

did not include CTA or MRA scans at 24 hours after the operation, so the value of mTICI only represented the immediate reperfusion postprocedure. Thrombus burden was not evaluated before treatment based on CTA because not all patients underwent preprocedural CTA examination. Vessel stenoses at 3 months were not assessed in this study due to lack of vascular image results. Some values were also missing from the original reporting data.

## CONCLUSIONS

In this analysis of patients with acute large-vessel ischemic stroke, no differences in efficacy and safety were observed in patients treated with Solitaire retrievable stents of differing diameters. Using smaller retrievers was associated with improved recanalization for occlusion of atherosclerotic etiology. With a 4-mm stent, procedure times were shortened and pass attempts were reduced.

## APPENDIX

ACTUAL investigators are as follows: Xinfeng Liu, Gelin Xu, Yuyun Xiong, Wenjie Zi, Dong Yang, Huaiming Wang, Yonggang Hao, Department of Neurology, Jinling Hospital, Medical School of Nanjing University, Second Military Medical University, Southern Medical University, Nanjing, China; Yuxiu Liu, Department of Medical Statistics, Jinling Hospital, Medical School of Nanjing University; Meng Zhang, Chengchun Liu, Department of Neurology, Research Institute of Surgery, Daping Hospital, Third Military Medical University; Yu Geng, Zongjie Shi, Jinhua Zhang, Department of Neurology, Zhejiang Provincial People's Hospital; Hang Lin, Min Lin, Zhen Hu, Department of Neurology, Fuzhou General Hospital of Nanjing Military Region; Xiaorong Deng, Yue Wan, Department of Neurology, Hubei Zhongshan Hospital; Jiandong Zhang, Zhonghua Shi, Mirui Qu, Department of Neurosurgery, 101st Hospital of the People's Liberation Army; Zhiming Zhou, Xianjun Huang, Department of Neurology, Yijishan Hospital of Wannan Medical College; Wei Wang, Department of Radiology, First People's Hospital of Yangzhou, Yangzhou University; Haowen Xu, Tao Quan, Sheng Guan, Department of Neurology, the First Affiliated Hospital of Zhengzhou University; Xiguang Tian, Lin Chen, Department of Neurology, Chinese Armed Police Force Guangdong Armed Police Corps Hospital; Penghua Lv, Xiaobo Li, Department of Neurology, Northern Jiangsu People's Hospital; Shuiping Wang, Shiquan Yang, Department of Neurology, 123rd Hospital of the People's Liberation Army; Wenhua Liu, Dan Wei, Department of Neurology, Wuhan No. 1 Hospital; Zhen Wang, Department of Neurology, Changsha Central Hospital; Xintong Liu, Department of Neurology, Guangdong Provincial No. 2 People's Hospital; Fuqiang Guo, Shu Yang, Department of Neurology, Sichuan Provincial People's Hospital; Dequan Zheng, Xinyu Wu, Youfu Zeng, Department of Neurology, 175th Hospital of the People's Liberation Army, Affiliated Southeast Hospital of Xiamen University; Mingyi Tu, Department of Neurology, Hubei Wuchang Hospital; Ping Jin, Yong Liu, Department of Neurology, Lu'an Affiliated Hospital of Anhui Medical University; Hua Li, Jiayang Fang, Department of Neurology, 476th Hospital of the People's Liberation Army; and Guo-

dong Xiao, Department of Neurology, the Second Affiliated Hospital of Soochow University.

## ACKNOWLEDGMENTS

The authors acknowledge Yibin Guo, PhD, for his assistance in statistical work.

## REFERENCES

1. Smith WS, Lev MH, English JD, et al. **Significance of large vessel intracranial occlusion causing acute ischemic stroke and TIA.** *Stroke* 2009;40:3834–40 CrossRef Medline
2. Saver JL, Goyal M, Bonafe A, et al; SWIFT PRIME Investigators. **Stent-retriever thrombectomy after intravenous t-PA vs. t-PA alone in stroke.** *N Engl J Med* 2015;372:2285–95 CrossRef Medline
3. Jovin TG, Chamorro A, Cobo E, et al; REVASCAT Trial Investigators. **Thrombectomy within 8 hours after symptom onset in ischemic stroke.** *N Engl J Med* 2015;372:2296–306 CrossRef Medline
4. Goyal M, Demchuk AM, Menon BK, et al; ESCAPE Trial Investigators. **Randomized assessment of rapid endovascular treatment of ischemic stroke.** *N Engl J Med* 2015;372:1019–30 CrossRef Medline
5. Campbell BC, Mitchell PJ, Kleinig TJ, et al; EXTEND-IA Investigators. **Endovascular therapy for ischemic stroke with perfusion-imaging selection.** *N Engl J Med* 2015;372:1009–18 CrossRef Medline
6. Berkhemer OA, Fransen PS, Beumer D, et al. **A randomized trial of intraarterial treatment for acute ischemic stroke.** *N Engl J Med* 2015;372:11–20 CrossRef Medline
7. Bracard S, Ducrocq X, Mas JL, et al; THRACE investigators. **Mechanical thrombectomy after intravenous alteplase versus alteplase alone after stroke (THRACE): a randomised controlled trial.** *Lancet Neurol* 2016;15:1138–47 CrossRef Medline
8. Saver JL, Jahan R, Levy EI, et al; SWIFT Trialists. **Solitaire flow restoration device versus the Merci retriever in patients with acute ischaemic stroke (SWIFT): a randomised, parallel-group, non-inferiority trial.** *Lancet* 2012;380:1241–49 CrossRef Medline
9. Nogueira RG, Lutsep HL, Gupta R, et al; TREVO 2 Trialists. **Trevo versus Merci retrievers for thrombectomy revascularisation of large vessel occlusions in acute ischaemic stroke (TREVO 2): a randomised trial.** *Lancet* 2012;380:1231–40 CrossRef Medline
10. Papanagiotou P, Roth C, Walter S, et al. **Treatment of acute cerebral artery occlusion with a fully recoverable intracranial stent: a new technique.** *Circulation* 2010;121:2605–06 CrossRef Medline
11. Almekhlafi MA, Menon BK, Freiheit EA, et al. **A meta-analysis of observational intra-arterial stroke therapy studies using the Merci device, Penumbra system, and retrievable stents.** *AJNR Am J Neuroradiol* 2013;34:140–45 CrossRef Medline
12. Henkes H, Flessler A, Brew S, et al. **A novel microcatheter-delivered, highly-flexible and fully-retrievable stent, specifically designed for intracranial use: technical note.** *Interv Neuroradiol* 2003;9:391–93 CrossRef Medline
13. Broussalis E, Trinka E, Hitzl W, et al. **Comparison of stent-retriever devices versus the Merci retriever for endovascular treatment of acute stroke.** *AJNR Am J Neuroradiol* 2013;34:366–72 CrossRef Medline
14. Gill R, Schneck MJ. **The use of stent retrievers in acute ischemic stroke.** *Expert Rev Neurother* 2016;16:969–81 CrossRef Medline
15. Schmidt W, Wissgott C, Andresen R, et al. **Performance characteristics of modern self-expanding nitinol stents indicated for SFA.** *Rofa* 2011;183:818–25 CrossRef Medline
16. Voûte MT, Hendriks JM, van Laanen JH, et al. **Radial force measurements in carotid stents: influence of stent design and length of the lesion.** *J Vasc Interv Radiol* 2011;22:661–66 CrossRef Medline
17. Matsumoto T, Inoue K, Tanaka S, et al. **Radial forces of stents used in thoracic endovascular aortic repair and bare self-expanding nitinol stents measured ex vivo: rapid rescue for obstruction of the innominate artery using bare self-expanding nitinol stents.** *Vascular* 2017;25:36–41 CrossRef Medline
18. Bosiers M, de Donato G, Delooste K, et al. **Does free cell area influence**

- the outcome in carotid artery stenting?** *Eur J Vasc Endovasc Surg* 2007;33:135–41; discussion 142–43 CrossRef Medline
19. Zhou Z, Yin Q, Xu G, et al. **Influence of vessel size and tortuosity on in-stent restenosis after stent implantation in the vertebral artery ostium.** *Cardiovasc Intervent Radiol* 2011;34:481–87 CrossRef Medline
  20. Csobay-Novak C, Bárány T, Zima E, et al. **Role of stent selection in the incidence of persisting hemodynamic depression after carotid artery stenting.** *J Endovasc Ther* 2015;22:122–29 CrossRef Medline
  21. Hur SH, Won KB, Kim IC, et al; DIAMOND investigators. **Comparison of 2-year clinical outcomes between diabetic versus nondiabetic patients with acute myocardial infarction after 1-month stabilization: analysis of the prospective registry of DIAMOND (Diabetic Acute Myocardial infarctiON Disease) in Korea: an observational registry study.** *Medicine* 2016;95:e3882 CrossRef Medline
  22. Kitahara H, Okada K, Kobayashi Y, et al. **TCT-555 impact of stent size selection on acute and long-term outcomes after drug-eluting stent implantation in de novo coronary lesions.** *J Am Col Cardiol* 2015;66:B225 CrossRef
  23. von Kummer R, Broderick JP, Campbell BC, et al. **The Heidelberg Bleeding Classification: classification of bleeding events after ischemic stroke and reperfusion therapy.** *Stroke* 2015;46:2981–86 CrossRef Medline
  24. Saver JL, Goyal M, van der Lugt A, et al; HERMES Collaborators. **Time to treatment with endovascular thrombectomy and outcomes from ischemic stroke: a meta-analysis.** *JAMA* 2016;316:1279 CrossRef Medline
  25. Sun CH, Ribo M, Goyal M, et al. **Door-to-puncture: a practical metric for capturing and enhancing system processes associated with endovascular stroke care, preliminary results from the rapid reperfusion registry.** *J Am Heart Assoc* 2014;3:e000859 CrossRef Medline
  26. Mehta BP, Leslie-Mazwi TM, Chandra RV, et al. **Reducing door-to-puncture times for intra-arterial stroke therapy: a pilot quality improvement project.** *J Am Heart Assoc* 2014;3:e000963 CrossRef Medline
  27. Kang DH, Kim YW, Hwang YH, et al. **Instant reocclusion following mechanical thrombectomy of in situ thromboocclusion and the role of low-dose intra-arterial tirofiban.** *Cerebrovasc Dis* 2014;37:350–55 CrossRef Medline
  28. Loh Y, Jahan R, McArthur DL, et al. **Recanalization rates decrease with increasing thrombectomy attempts.** *AJNR Am J Neuroradiol* 2010;31:935–39 CrossRef Medline
  29. Angermaier A, Michel P, Khaw AV, et al. **Intravenous thrombolysis and passes of thrombectomy as predictors for endovascular revascularization in ischemic stroke.** *J Stroke Cerebrovasc Dis* 2016;25:2488–95 CrossRef Medline
  30. Gröschel K, Schnaudigel S, Ernemann U, et al. **Size matters! Stent-length is associated with thromboembolic complications after carotid artery stenting.** *Stroke* 2008;39:e131–32; author reply e133 CrossRef Medline
  31. Lee JS, Hong JM, Lee KS, et al. **Endovascular therapy of cerebral arterial occlusions: intracranial atherosclerosis versus embolism.** *J Stroke Cerebrovasc Dis* 2015;24:2074–80 CrossRef Medline
  32. Wong L. **Global burden of intracranial atherosclerosis.** *Int J Stroke* 2006;1:158–59 CrossRef Medline
  33. Sacco RL, Kargman DE, Gu Q, et al. **Race-ethnicity and determinants of intracranial atherosclerotic cerebral infarction: the Northern Manhattan Stroke Study.** *Stroke* 1995;26:14–20 CrossRef Medline
  34. Baek S, Park SH, Won E, et al. **Propensity score matching: a conceptual review for radiology researchers.** *Korean J Radiology* 2015;16:286–96 CrossRef Medline

# e-ASPECTS Correlates with and Is Predictive of Outcome after Mechanical Thrombectomy

J. Pfaff, C. Herweh, S. Schieber, S. Schönenberger, J. Bösel, P.A. Ringleb, M. Möhlenbruch, M. Bendszus, and S. Nagel



## ABSTRACT

**BACKGROUND AND PURPOSE:** The e-ASPECTS software is a tool for the automated use of ASPECTS. Our aim was to analyze whether baseline e-ASPECT scores correlate with outcome after mechanical thrombectomy.

**MATERIALS AND METHODS:** Patients with ischemic strokes in the anterior circulation who were admitted between 2010 and 2015, diagnosed by CT, and received mechanical thrombectomy were included. The ASPECTS on baseline CT was scored by e-ASPECTS and 3 expert raters, and interclass correlation coefficients were calculated. The e-ASPECTS was correlated with functional outcome (modified Rankin Scale) at 3 months by using the Spearman rank correlation coefficient. Unfavorable outcome was defined as mRS 4–6 at 3 months, and a poor scan was defined as e-ASPECTS 0–5.

**RESULTS:** Two hundred twenty patients were included, and 147 (67%) were treated with bridging protocols. The median e-ASPECTS was 9 (interquartile range, 8–10). Intraclass correlation coefficients between e-ASPECTS and raters were 0.72, 0.74, and 0.76 (all,  $P < .001$ ). e-ASPECTS (Spearman rank correlation coefficient =  $-0.15$ ,  $P = .027$ ) correlated with mRS at 3 months. Patients with unfavorable outcome had lower e-ASPECTS (median, 8; interquartile range, 7–10 versus median, 9; interquartile range, 8–10;  $P = .014$ ). Sixteen patients (7.4%) had a poor scan, which was associated with unfavorable outcome (OR, 13.6; 95% CI, 1.8–104). Independent predictors of unfavorable outcome were e-ASPECTS (OR, 0.79; 95% CI, 0.63–0.99), blood sugar (OR, 1.01; 95% CI, 1.004–1.02), atrial fibrillation (OR, 2.64; 95% CI, 1.22–5.69), premorbid mRS (OR, 1.77; 95% CI, 1.21–2.58), NIHSS (OR, 1.11; 95% CI, 1.04–1.19), general anesthesia (OR, 0.24; 95% CI, 0.07–0.84), failed recanalization (OR, 8.47; 95% CI, 3.5–20.2), and symptomatic intracerebral hemorrhage (OR, 25.8; 95% CI, 2.5–268).

**CONCLUSIONS:** The e-ASPECTS correlated with mRS at 3 months and was predictive of unfavorable outcome after mechanical thrombectomy, but further studies in patients with poor scan are needed.

**ABBREVIATIONS:** AIS = acute ischemic stroke; MT = mechanical thrombectomy; sICH = symptomatic intracranial hemorrhage

Mechanical thrombectomy (MT) in acute ischemic stroke (AIS) due to a large intracranial vessel occlusion in the anterior circulation has been proven to be an effective therapy.<sup>1–5</sup> With the success of the recent trials, an increasing number of patients with AIS will be evaluated for eligibility for this therapy. However, because there are no strict ex-/inclusion guidelines,<sup>6</sup> patient selection for MT remains a challenging process. In the

end, this evaluation process should not withhold therapy from patients who might benefit from MT but should preclude patients who will not benefit. During the evaluation process, multiple factors need to be cautiously reviewed. Noncontrast CT is still the most available imaging tool worldwide. Early signs of infarction on NCCT scans are a potent predictor of clinical outcome in patients with AIS.<sup>7</sup> In 2000, Barber et al<sup>8</sup> introduced the Alberta Stroke Program Early CT Score. ASPECTS divides the middle cerebral artery territory into 10 predefined anatomic areas and grades the presence of early infarct signs by parenchymal hypodensity on NCCT. This increasingly used score has already proved a reliable predictor of clinical outcome in patients with AIS treated with intravenous rtPA and/or MT.<sup>8–10</sup>

Unfortunately, the determination of early signs of ischemia and their translation into the ASPECTS have a considerable inter-rater variability, which is, among other factors, influenced by rater experience.<sup>11–13</sup> However, during the evaluation process for per-

Received January 12, 2017; accepted after revision March 22.

From the Departments of Neuroradiology (J.P., C.H., M.M., M.B.) and Neurology (S. Schieber, S. Schönenberger, J.B., P.A.R., S.N.), University of Heidelberg, Heidelberg, Germany.

Please address correspondence to Simon Nagel, MD, Universität Heidelberg, Abteilung für Neurologie, Im Neuenheimer Feld 400, 69120 Heidelberg, Germany; e-mail: simon.nagel@med.uni-heidelberg.de

Indicates open access to non-subscribers at [www.ajnr.org](http://www.ajnr.org)

Indicates article with supplemental on-line table.

<http://dx.doi.org/10.3174/ajnr.A5236>

forming MT or before transfer of a patient to a comprehensive stroke center performing MT, scoring variability could negatively influence the decision-making process and lead to false patient in-/exclusion. The e-ASPECTS software (Brainomix, Oxford, UK; www.brainomix.com) is a standardized, fully automated, CE mark–approved ASPECTS scoring tool for NCCT, which has previously demonstrated scoring on an expert level.<sup>14,15</sup> We analyzed whether e-ASPECT scores correlate with outcome after mechanical thrombectomy and whether low scores are predictors of unfavorable outcome. In particular, we were interested in whether patients with low e-ASPECTS (0–5, poor scans) were very likely to have a bad outcome.

## MATERIALS AND METHODS

From a prospectively collected stroke data base, we identified 430 patients with AIS in the anterior circulation who underwent MT between May 2010 and May 2015. All patients were treated with endovascular revascularization therapy and, in case of eligibility, with intravenous thrombolysis after an interdisciplinary decision by the neurologist and neurointerventionalist on call. Historically, during MT, patients were treated under general anesthesia; and since 2009, we have been following a strict standardized operating procedure. In September 2013, an additional standardized operating procedure for conscious sedation was introduced, and selected patients were treated following this procedure with MT. Since April 2014, eligible patients were included in our single-center randomized sedation trial, Sedation vs. Intubation for Endovascular Stroke Treatment (SIESTA).<sup>16</sup> After the procedure, all patients were treated according to in-house standardized operating procedures in our neurointensive care unit and/or our stroke unit. In our data base, clinical data at baseline and during the hospital stay as well as radiologic and laboratory information are prospectively entered and used for analysis when appropriate.

Recanalization was assessed with the Thrombolysis in Cerebral Infarction Score by a blinded investigator (J.P.). TICI 0–2a was scored as failed, and TICI 2b–3 was scored as successful recanalization. The outcome was measured with the modified Rankin Scale after 3 months and was obtained through rehabilitation reports, outpatient assessments, or a standardized interview by an unblinded investigator. Unfavorable outcome was defined as a modified Rankin Scale score between 4 and 6; favorable outcome, as mRS 0–3; and good outcome, as mRS 0–2. Symptomatic intracranial hemorrhage (sICH) was defined according to the European Cooperative Acute Stroke Study II (blood at any site in the brain and clinical deterioration with an increase in the NIHSS score of at least 4 points compared with the lowest value within the first 7 days or any intracranial hemorrhage leading to death).

NCCT scans of the included patients were obtained from the same multisection CT scanners. Between May 2010 and January 2014, images were acquired from a Somatom Volume Zoom (Siemens, Erlangen, Germany,  $n = 150$ ). Incremental sections had a thickness of 6 mm with an in-plane resolution of  $512 \times 512$  mm. Between February 2014 and May 2015, NCCTs were acquired from a Somatom Definition AS (Siemens,  $n = 70$ ) with a section thickness of 4 mm and an in-plane resolution of  $512 \times 512$  mm. NCCT scans were retrospectively scored by e-ASPECTS (Version 5.0), as well as by 3 stroke experts, and software and experts were

blinded to any patient data and clinical information except for the side of the unilateral ischemic stroke. The experts had 6–12 years of extensive experience in neurovascular imaging interpretation (J.P. and C.H., board-certified neuroradiologists; S.N., board-certified neurologist). e-ASPECTS is based on a combination of advanced image-processing and machine-learning algorithms. Several image-enhancement filters are applied to the input DICOM CT image to deal with noise, differences between scanners, and image artifacts. A 3D registration module corrects for any tilt, rotation, and other transformations. The ASPECTS regions are then segmented; this segmentation provides a standardized reference for the cortical regions. The scoring module operates on the standardized 3D images, classifying signs of ischemic damage and assigning them to ASPECTS regions. It applies statistical learning methods to image features to determine whether a region is likely to be damaged.<sup>14,15</sup> An e-ASPECTS score between 0 and 5 was considered a poor scan.

## Statistical Analysis

Our primary end point was defined as unfavorable outcome as opposed to good outcome because we wanted to test the hypothesis that patients with low e-ASPECTS are indeed under a higher risk of futile treatment. Nominal data are presented as frequencies; ordinal data, as median with interquartile range; and metric data, as mean  $\pm$  SD. To show univariate differences in outcome groups, we used the Fisher exact test, the  $\chi^2$  test, the Mann-Whitney  $U$ , or unpaired  $t$  test when appropriate according to data category. For multivariate analysis to show predictors of unfavorable and good outcome, we used a stepwise forward binary logistic regression model with correction for all significant variables ( $P \leq .05$ ) in univariate analyses. Odds ratios are presented as values with 95% confident intervals. For the agreement between e-ASPECTS with each expert we used the intraclass correlation coefficient. For correlation of the e-ASPECTS and the mRS at 3 months, we used the Spearman rank correlation coefficient.

## Ethics Approval

Our local ethics committee approved the prospective data base and retrospective analysis herein. Due to its monocentric and retrospective character, the requirement for subsequent written patient informed consent was waived.

## RESULTS

Two hundred twenty patients of 430 met the inclusion criteria for this analysis (ie, in-house NCCT with no or minor motion artifacts before MT; Fig 1). Patients' baseline characteristics are shown in the On-line Table. This shows that our cohort is very typical for patients with acute large intracranial vessel occlusion. The median NIHSS at baseline was 18 (interquartile range, 15–21), but in contrast to previous randomized controlled trials, we also included around 9% of patients with a premorbid mRS of  $>2$  (ie, 14 patients with an mRS of 3 and 6 with an mRS of 4). Most patients had either an M1 occlusion or a carotid-T occlusion. One hundred forty-seven (67%) patients were treated with rtPA-based bridging protocols. After prior exclusion of 43 (10%) patients due to severe motion artifacts rendering ASPECTS scoring for the

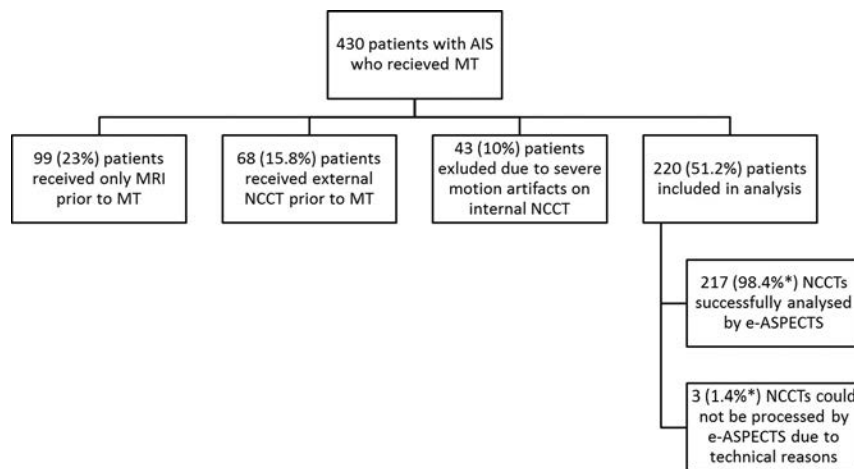


**FIG 1.** Exclusion criteria for patients with AIS who received MT entering this analysis. Severe motion artifacts were defined as artifacts that impair differentiation of anatomic structures (eg, basal ganglia, subarachnoid space) and/or clear identification of intracranial hemorrhage by the human rater. The asterisk indicates percentage regarding included patients.

human rater impossible, an additional 3 (1.4%) scans could not be processed by e-ASPECTS due to technical reasons (upload or processing of the DICOM data). The median e-ASPECTS was 9 (interquartile range, 8–10). The distribution of e-ASPECTS and human raters' scores are shown in Fig 2. Only 16 patients (7.4%) had a poor scan, which was strongly associated with unfavorable outcome (OR, 13.6; 95% CI, 1.8–104;  $P = .012$ ). Overall, after 3 months, the primary end point of unfavorable outcome was met by 123 (55.9%) patients, and 61 (27.7%) patients reached the secondary end point of good outcome.

The intraclass correlation coefficients between e-ASPECTS and each rater were 0.72, 0.74, and 0.76, respectively (all,  $P < .001$ ). The agreement within the human raters was very robust as well (intraclass correlation coefficients, 0.7, 0.77, and 0.75; all,  $P < .001$ ). Although the overall agreement of raters and e-ASPECTS was good, in some cases, considerably different scoring results occurred and an example with a low e-ASPECTS (4) is presented in Fig 3. Only e-ASPECTS (Spearman rank correlation coefficient =  $-0.15$ ,  $P = .027$ ) and the expert's scoring with the highest agreement with e-ASPECTS (Spearman rank correlation coefficient =  $-0.19$ ,  $P = .004$ ) correlated inversely but significantly with mRS at 3 months, indicating that a lower ASPECTS is associated with a higher mRS after 3 months. ASPECTS scoring of the other 2 readers differed from the e-ASPECTS scores to the extent that a significant statistical correlation between their ASPECTS scores and clinical outcome could not be detected. Spearman rank correlation coefficient for e-ASPECTS and mRS in our analysis differed from the Spearman rank correlation coefficient in the study of Barber et al ( $-0.69$ )<sup>8</sup> because Barber et al used only 3 categories of the mRS for correlation and their cohort consisted of consecutive patients with suspected stroke in the anterior circulation, whereas our patients all had proved large-vessel occlusion.

One hundred ninety-eight (90%) patients were treated with modern stent retrievers (mostly Solitaire; Covidien, Irvine, California), and 195 (88.6%) patients underwent thrombectomy under general anesthesia. In the univariate analysis for the primary end point, among other significant differences, patients with unfavorable outcome had lower e-ASPECTS (median, 8; interquar-

tile range, 7–10 versus median, 9; interquartile range, 8–10;  $P = .014$ ; On-line Table). Bridging therapy or treatment and procedural times, however, were not significantly different in patients with unfavorable outcome versus patients with favorable outcome (mRS, 0–3). For multivariate analysis, we included the variables age, premorbid mRS, atrial fibrillation, previous stroke, baseline blood sugar, and hemoglobin A1c, as well as NIHSS, hyperdense vessel sign, e-ASPECTS, general anesthesia, recanalization, and sICH (all  $P < .05$  in univariate analysis). Independent predictors of unfavorable outcome were e-ASPECTS (OR, 0.79; 95% CI, 0.63–0.99;  $P = .049$ ) but also blood sugar (OR, 1.01; 95% CI, 1.004–1.02;  $P = .005$ ), atrial fibrillation (OR, 2.64; 95% CI,

1.22–5.69;  $P = .013$ ), premorbid mRS (OR, 1.77; 95% CI, 1.21–2.58;  $P = .003$ ), NIHSS (OR, 1.11; 95% CI, 1.04–1.19;  $P = .003$ ), general anesthesia (OR, 0.24; 95% CI, 0.07–0.84;  $P = .007$ ), failed recanalization (OR, 8.47; 95% CI, 3.5–20.2;  $P < .001$ ), and sICH (OR, 25.8; 95% CI, 2.5–268;  $P = .007$ ).

In the analysis of the secondary end point, factors associated with good outcome were mean age ( $66 \pm 12$  versus  $74 \pm 11$  years;  $P < .001$ ), premorbid mRS (median, 0; interquartile range, 0–1 versus median, 1; interquartile range, 0–2;  $P = .002$ ), atrial fibrillation (34.4% versus 52.2%;  $P = .023$ ), blood sugar ( $118 \pm 33$  versus  $139 \pm 57$  mg/dL;  $P = .015$ ), creatinine ( $0.89 \pm 0.25$  versus  $1.1 \pm 0.78$  mg/dL;  $P = .03$ ), general anesthesia (80.3% versus 91.8%;  $P = .03$ ), NIHSS (median, 16; interquartile range, 11–19 versus median, 19; interquartile range, 15–22;  $P < .001$ ), successful recanalization (88.5% versus 58.9%,  $P < .001$ ) and sICH (0% versus 8.8%,  $P = .012$ ). The e-ASPECTS, however, was not associated with good outcome (median, 9; interquartile range, 8–10 versus median, 9; interquartile range, 7–10;  $P = .249$ ). After multivariate analysis (sICH was not included in the model because no patient with good outcome had sICH), only age (OR, 0.96; 95% CI, 0.93–0.98), blood sugar levels (OR, 0.99; 95% CI, 0.99–1.0), NIHSS (OR, 0.91; 95% CI, 0.86–0.97), and successful recanalization (OR, 5.45; 95% CI, 2.18–13.61) remained independent predictors of good outcome.

## DISCUSSION

Our study confirmed that the e-ASPECTS software performs in a manner similar to that of stroke experts in detecting early ischemic damage in the MCA territory. Furthermore, we could demonstrate for the first time that fully automatically derived e-ASPECT scores correlated inversely with patient outcome 3 months after MT (Spearman rank correlation coefficient =  $-0.15$ ,  $P = .027$ ). Patients with poor scans (ASPECTS 0–5) at baseline had a significantly high probability of unfavorable outcome (OR, 13.6; 95% CI, 1.8–104). On the basis of the multivariate regression analysis, a 1-point decrease in the e-ASPECTS increases the risk for an unfavorable clinical outcome by 20%. Most important, indicating the robustness of our results, we could also confirm

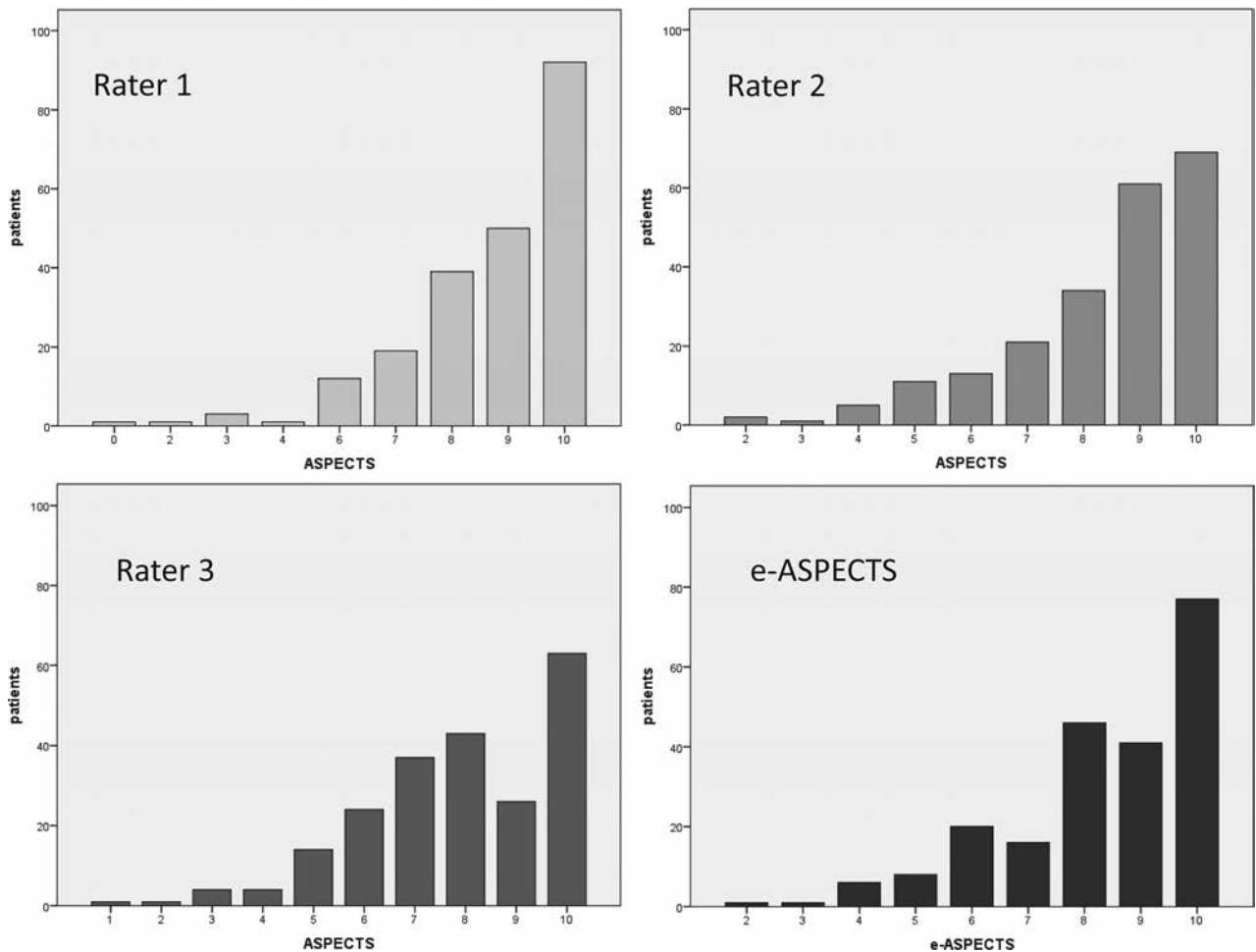


**FIG 2.** Distribution of ASPECTSs according to the 3 human raters and e-ASPECTS.

other known predictors of outcome after acute ischemic stroke, such as recanalization, sICH, atrial fibrillation, NIHSS, pre-morbid functionality, and blood sugar levels.

The ASPECTS is a validated, reliable, and reproducible grading system to assess early ischemic changes on noncontrast CT studies in patients with acute ischemic stroke of the anterior circulation.<sup>8</sup> The Highly Effective Reperfusion evaluated in Multiple Endovascular Stroke trials (HERMES) collaboration has recently shown a clear association between favorable clinical outcome after MT and ASPECTS of  $\geq 6$ .<sup>17</sup> Additionally, a subgroup analysis of the Multicenter Randomized Clinical trial of Endovascular treatment for Acute ischemic stroke in the Netherlands (MR CLEAN) also demonstrated that patients with moderate early ischemic changes (ASPECTS 5–7) benefit from mechanical thrombectomy.<sup>18</sup> On the other hand, there are other studies that could not show a correlation between ASPECTS 5–7 and clinical outcome after 3 months,<sup>19</sup> and the HERMES data revealed that there is no clear benefit for patients with an ASPECTS of 0–5. Another study found that patients with ASPECTS 0–4 before mechanical thrombectomy had higher rates of serious adverse events and hemicraniectomy. Furthermore, death within 1 week and 30 days after treatment was more frequent.<sup>18</sup> Therefore, the effect of endovascular treatment for patients with a poor scan (ASPECTS 0–5) is unclear, with perhaps only a slim margin for benefit. Ad-

ditionally, multivariate regression analysis to show the independent prognostic effects of the ASPECTS has not been performed in these previous trials.

Because the probability of achieving functional independence declines and the risk of severe disability and death rises with lower ASPECTS, this scoring system appears important for patient evaluation for endovascular stroke treatment. Our data indicate that e-ASPECTS can provide important technical support in estimating a patient's prognosis. Furthermore, in the present analysis, 2 of 3 expert raters' scores did not correlate with the clinical outcome, whereas e-ASPECT scores did. This nicely illustrates 2 features: First, as already shown by others, the ASPECTS has considerable variability even among experts. This may be even more pronounced in the acute treatment decision for understandable reasons, such as emotional issues and stress. Second, an automated scoring tool can be advantageous here due to its "objectivity." Hence, e-ASPECTS could contribute to decision-making for patient selection in the community hospital or telemedicine services and/or patient transfer into a comprehensive stroke center for MT. Other important imaging variables derived from CT angiography and CT perfusion have also been shown to carry prognostic information that can inform treatment decision-making,<sup>20</sup> but NCCT is still the most commonly used imaging tool in acute stroke.

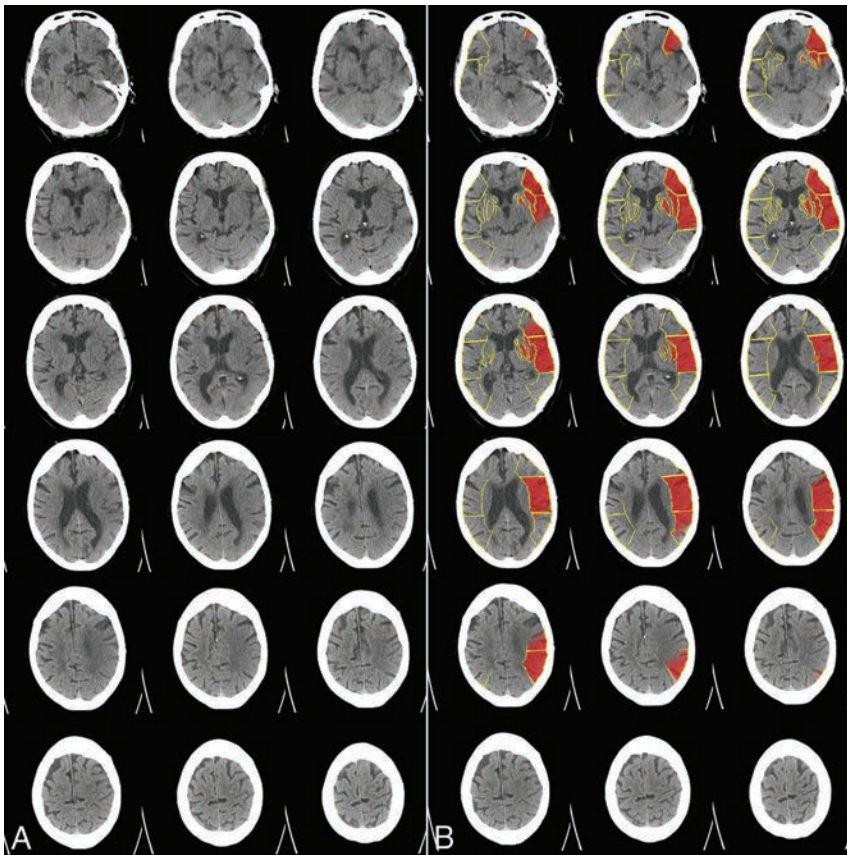


**FIG 3.** Example of a patient with extensive early signs of ischemic damage on the baseline NCCT (A). The processed e-ASPECTS results is a score of 4. The human raters scored an ASPECTS of 6, 8, and 9, respectively, highlighting considerable disagreement in this particular case (B). An MI occlusion was present, onset to treatment time was 143 minutes, TIC1 2a was achieved, and no sICH occurred. Unfortunately, this patient had died within 3 months.

Our analysis focused on the prognostic value of ASPECTS, specifically e-ASPECTS for unfavorable outcome, as opposed to good outcome. According to current guidelines considering endovascular stroke therapy, a favorable ASPECTS is not an unconditional prerequisite, especially within 6 hours from onset (American Heart Association guidelines/European Stroke Organisation–European Foundation of Minimally Invasive Neurological Therapy guidelines).<sup>21,22</sup> The question does not seem to be whom to treat but for whom treatment could be disadvantageous due to missing success or the increased likelihood of complications because patients with ASPECTS  $\leq 5$  have a lower chance of independent living or even survival. The e-ASPECTS was not a predictor of good outcome in this analysis, which indicates that patients with low scores still have a considerable probability of achieving clinical improvement through therapy; therefore, this analysis reinforces the need for a prospective controlled trial to investigate the potential benefit of thrombectomy in patients with a low initial ASPECTS.

Our study has several limitations: 1) Because we treated patients with broad inclusion criteria (ie, higher premorbid mRS and so forth), one cannot expect outcome results similar to those in the recent seminal MT trials, but rather similar to real-life data. 2) This analysis was based on a prospective single-center cohort data base, and data were analyzed retrospectively; therefore, caution should be exercised when generalizing the results. Our data

regarding the mode of sedation need to be interpreted with caution. Most (88.6%) patients were treated under general anesthesia; and only a minority, with conscious sedation. We only introduced this mode of sedation in September 2013, and until April 2014, a selection bias in our cohort was present. The results of the SIESTA trial, however, indicated that in our center, general anesthesia is not associated with impaired outcome.<sup>16</sup> 3) The performance of e-ASPECTS might have been compromised due to the available section thicknesses of 4 and 6 mm; the optimal thickness for analysis is 1 mm. Moreover, there was no ground truth (ie, diffusion-weighted imaging or CT perfusion) defined for ASPECTS scoring for this analysis. However, the e-ASPECTS software has previously shown similar and noninferior performance to that of stroke experts,<sup>14,15</sup> and most centers do not have sophisticated imaging tools and rely on NCCT, which makes this an important analysis. 4) Additionally, the number of patients with a poor scan of  $\leq 5$  ASPECTS points was low, and our results need to be confirmed by analysis of large registries of patients undergoing MT, at best by randomized controlled trials including those patients in whom considerable uncertainty still exists with

respect to the efficacy and safety of MT (ie, patients with extensive ischemic brain damage at baseline). The e-ASPECTS software could be a suitable tool for patient stratification in such trials.

The strengths of this study were that our cohort was very typical for patients undergoing MT and that we included numerous clinical, laboratory, and radiologic data in our analysis. The multivariate model confirmed many previously described prognostic factors, while the predictive value of e-ASPECTS prevailed, thereby indicating the robustness of our results.

## CONCLUSIONS

The e-ASPECTS correlated with outcome overall and was predictive of unfavorable outcome after mechanical thrombectomy. e-ASPECTS might facilitate treatment decision-making, especially in centers without modern imaging tools for tissue perfusion and collateral status. It is easy to use, has a robust and reliable performance, and removes intra- and interrater variability. Because there are few patients with poor initial CT scans who improve after treatment, further prospective studies in those patients are needed and individual decision-making remains necessary.

Disclosures: Johannes Pfaff—UNRELATED: Payment for Lectures Including Service on Speakers Bureaus: Siemens; Travel/Accommodations/Meeting Expenses Unre-

lated to Activities Listed: Stryker. Christian Herweh—UNRELATED: Consultancy: Brainomix, Comments: temporary consultancy related to a project different from the one from which the current article originated; *Payment for Lectures Including Service on Speakers Bureaus*: Bristol-Myers Squibb, Brainomix: once in 2016; *Travel/Accommodations/Meeting Expenses Unrelated to Activities Listed*: Stryker, Brainomix: travel expenses for attending a national meeting in 2016. Julian Bösel—UNRELATED: *Grants/Grants Pending*: Patient-Centered Outcomes Research Institute, Brainomix Ltd: award pending for SETPOINT2 Trial; *Travel/Accommodations/Meeting Expenses Unrelated to Activities Listed*: Zoll, Bard Medical, Sedana Medical, Seiratherm, Boehringer Ingelheim, Brainomix Ltd: speaker's honoraria and travel support. Peter A. Ringleb—UNRELATED: *Consultancy*: advisory board member for Boehringer Ingelheim, Covidien; *Payment for Lectures Including Service on Speakers Bureaus*: lecture fee from Boehringer Ingelheim, Bayer, Pfizer, Daichii Sanyo. Markus Möhlenbruch—UNRELATED: *Payment for Lectures Including Service on Speakers Bureaus*: Codman, MicroVenton, phenox, Stryker. Martin Bendszus—UNRELATED: *Board Membership*: Data and Safety Monitoring Board for Vascular Dynamics; *Consultancy*: Codman, Roche, Guerbet, Boehringer Ingelheim; *Grants/Grants Pending*: Deutsche Forschungsgemeinschaft, Hopp Foundation, Novartis, Siemens, Guerbet, Stryker, Covidien\*; *Payment for Lectures Including Service on Speakers Bureaus*: Novartis, Roche, Guerbet, Teva Pharmaceutical Industries, Bayer, Codman. Simon Nagel—UNRELATED: *Consultancy*: Brainomix; S.N. has had an ongoing consultancy appointment with Brainomix since 2015 independent from the current study; *Grants/Grants Pending*: Brainomix; The University Hospital Heidelberg received grants from Brainomix for prior studies\*; *Payment for Lectures Including Service on Speakers Bureaus*: Bayer, Medtronic, Pfizer; *Travel/Accommodations/Meeting Expenses Unrelated to Activities Listed*: Boehringer Ingelheim, Brainomix. \*Money paid to the institution.

## REFERENCES

- Berkhemer OA, Fransen PSS, Beumer D, et al. **A randomized trial of intraarterial treatment for acute ischemic stroke.** *N Engl J Med* 2015; 372:11–20 CrossRef Medline
- Campbell BC, Mitchell PJ, Kleinig TJ, et al; EXTEND-IA Investigators. **Endovascular therapy for ischemic stroke with perfusion-imaging selection.** *N Engl J Med* 2015;372:1009–18 CrossRef Medline
- Goyal M, Fargen KM, Turk AS, et al. **2C or not 2C: defining an improved revascularization grading scale and the need for standardization of angiography outcomes in stroke trials.** *J Neurointerv Surg* 2014;6:83–86 CrossRef Medline
- Jovin TG, Chamorro A, Cobo E, et al; REVASCAT Trial Investigators. **Thrombectomy within 8 hours after symptom onset in ischemic stroke.** *N Engl J Med* 2015;372:2296–306 CrossRef Medline
- Saver JL, Goyal M, Bonafe A, et al; SWIFT PRIME Investigators. **Stent-retriever thrombectomy after intravenous t-PA vs. t-PA alone in stroke.** *N Engl J Med* 2015;372:2285–95 CrossRef Medline
- A collaboration of the European Stroke Organisation–Karolinska Stroke Update, European Society for Minimally Invasive Neurological Therapy, and European Society of Neuroradiology. **Consensus statement on mechanical thrombectomy in acute ischemic stroke.** In: *Proceedings of the European Stroke Organisation–Karolinska Stroke Update*, Stockholm, Sweden. November 16–18, 2014
- Wardlaw JM, Mielke O. **Early signs of brain infarction at CT: observer reliability and outcome after thrombolytic treatment—systematic review.** *Radiology* 2005;235:444–53 CrossRef Medline
- Barber PA, Demchuk AM, Zhang J, et al. **Validity and reliability of a quantitative computed tomography score in predicting outcome of hyperacute stroke before thrombolytic therapy: ASPECTS Study Group—Alberta Stroke Programme Early CT Score.** *Lancet* 2000; 355:1670–74 CrossRef Medline
- Menon BK, Puetz V, Kochar P, et al. **ASPECTS and other neuroimaging scores in the triage and prediction of outcome in acute stroke patients.** *Neuroimaging Clin N Am* 2011;21:407–23, xii CrossRef Medline
- Liebeskind DS, Jahan R, Nogueira RG, et al; SWIFT Investigators. **Serial Alberta Stroke Program Early CT score from baseline to 24 hours in Solitaire Flow Restoration with the Intention for Thrombectomy study: a novel surrogate end point for revascularization in acute stroke.** *Stroke* 2014;45:723–27 CrossRef Medline
- Demaerschalk BM, Silver B, Wong E, et al. **ASPECT scoring to estimate > 1/3 middle cerebral artery territory infarction.** *Can J Neurol Sci* 2006;33:200–04 CrossRef Medline
- Mak HK, Yau KK, Khong PL, et al; Alberta Stroke Programme Early CT Score. **Hypodensity of > 1/3 middle cerebral artery territory versus Alberta Stroke Programme Early CT Score (ASPECTS): comparison of two methods of quantitative evaluation of early CT changes in hyperacute ischemic stroke in the community setting.** *Stroke* 2003;34:1194–96 CrossRef Medline
- Finlayson O, John V, Yeung R, et al. **Interobserver agreement of ASPECT score distribution for noncontrast CT, CT angiography, and CT perfusion in acute stroke.** *Stroke* 2013;44:234–36 CrossRef Medline
- Herweh C, Ringleb PA, Rauch G, et al. **Performance of e-ASPECTS software in comparison to that of stroke physicians on assessing CT scans of acute ischemic stroke patients.** *Int J Stroke* 2016;11:438–45 CrossRef Medline
- Nagel S, Sinha D, Day D, et al. **e-ASPECTS software is non-inferior to neuroradiologists in applying the ASPECTS score to CT scans of acute ischemic stroke patients.** In: *Proceedings of the 2nd European Stroke Organisation Conference*, Barcelona, Spain. May 10–12, 2016
- Schonenberger S, Uhlmann L, Hacke W, et al. **Effect of conscious sedation vs general anesthesia on early neurological improvement among patients with ischemic stroke undergoing endovascular thrombectomy: a randomized clinical trial.** *JAMA* 2016;316:1986–96 CrossRef Medline
- Goyal M, Menon BK, van Zwam WH, et al; HERMES collaborators. **Endovascular thrombectomy after large-vessel ischaemic stroke: a meta-analysis of individual patient data from five randomised trials.** *Lancet* 2016;387:1723–31 CrossRef Medline
- Yoo AJ, Berkhemer OA, Fransen PS, et al; MR CLEAN investigators. **Effect of baseline Alberta Stroke Program Early CT Score on safety and efficacy of intra-arterial treatment: a subgroup analysis of a randomised phase 3 trial (MR CLEAN).** *Lancet Neurol* 2016;15:685–94 CrossRef Medline
- Costalat V, Lobotesis K, Machi P, et al. **Prognostic factors related to clinical outcome following thrombectomy in ischemic stroke (RECOSt study): 50 patients prospective study.** *Eur J Radiol* 2012; 81:4075–82 CrossRef Medline
- Turk AS, Magarick JA, Frei D, et al. **CT perfusion-guided patient selection for endovascular recanalization in acute ischemic stroke: a multicenter study.** *J Neurointerv Surg* 2013;5:523–27 CrossRef Medline
- Powers WJ, Derdeyn CP, Biller J, et al; American Heart Association Stroke Council. **2015 American Heart Association/American Stroke Association Focused Update of the 2013 Guidelines for the Early Management of Patients with Acute Ischemic Stroke Regarding Endovascular Treatment: A Guideline for Healthcare Professionals from the American Heart Association/American Stroke Association.** *Stroke* 2015;46:3020–35 CrossRef Medline
- Wahlgren N, Moreira T, Michel P, et al; ESO-KSU, ESO, ESMINT, ESNR and EAN. **Mechanical thrombectomy in acute ischemic stroke: consensus statement by ESO-Karolinska Stroke Update 2014/2015, supported by ESO, ESMINT, ESNR and EAN.** *Int J Stroke* 2016;11:134–47 CrossRef Medline

# Acute Basilar Artery Occlusion: Differences in Characteristics and Outcomes after Endovascular Therapy between Patients with and without Underlying Severe Atherosclerotic Stenosis

Y.Y. Lee, W. Yoon, S.K. Kim, B.H. Baek, G.S. Kim, J.T. Kim, and M.S. Park



## ABSTRACT

**BACKGROUND AND PURPOSE:** Prediction of underlying intracranial atherosclerotic stenosis before endovascular therapy might be helpful for appropriate therapeutic planning in patients with acute ischemic stroke. This study aimed to compare the characteristics and treatment outcomes in patients with acute basilar artery occlusion relative to the existence or nonexistence of underlying intracranial atherosclerotic stenosis.

**MATERIALS AND METHODS:** Sixty-two patients with acute basilar artery occlusion underwent multimodal endovascular therapy. All patients underwent stent-retriever thrombectomy as a first-line endovascular therapy. Patients with underlying intracranial atherosclerotic stenosis underwent additional intracranial angioplasty and stent placement. The clinical and imaging characteristics and treatment outcomes were retrospectively analyzed and compared between patients with and without intracranial atherosclerotic stenosis.

**RESULTS:** Underlying intracranial atherosclerotic stenosis was identified at the occlusion site in 15 patients (24.1%). Occlusion in the proximal segment of the basilar artery was more common in patients with intracranial atherosclerotic stenosis (60% versus 6.4%,  $P < .001$ ), whereas occlusion in the distal segment was more common in those without it (91.5% versus 26.7%,  $P < .001$ ). Bilateral thalamic infarction on a pretreatment DWI was less common in patients with intracranial atherosclerotic stenosis (0% versus 27.7%,  $P = .027$ ) compared with those without it. There were no significant differences in the rates of successful revascularization, favorable outcome, symptomatic hemorrhage, and mortality between the 2 groups.

**CONCLUSIONS:** Underlying intracranial atherosclerotic stenosis was not uncommon in patients with acute basilar artery occlusion. The occlusion segment of the basilar artery and the presence or absence of bilateral thalamic infarction on a pretreatment DWI might be helpful for predicting underlying intracranial atherosclerotic stenosis in patients with acute basilar artery occlusion. Patients with and without underlying intracranial atherosclerotic stenosis who underwent endovascular therapy had similar outcomes.

**ABBREVIATIONS:** BAO = basilar artery occlusion; ICAS = intracranial atherosclerotic stenosis

Acute ischemic stroke due to basilar artery occlusion (BAO) is associated with the highest mortality and morbidity among strokes attributable to intracranial large-vessel occlusions.<sup>1,2</sup> Morbidity and mortality rates have been reported to be up to 95%, and the chances for good outcome are extremely low without active treatment.<sup>2,3</sup> The rates of death or dependency have been 76%–78%, even when patients with acute BAO were treated with intravenous or intra-arterial thrombolysis.<sup>3</sup> Stent-retriever

thrombectomy is increasingly being used in patients with acute BAO and shows a high recanalization rate.<sup>4</sup> Many case series have shown that stent-retriever thrombectomy is a safe and feasible treatment technique in patients with acute BAO.<sup>4–7</sup>

Embolism from cardiac or proximal large-artery sources and in situ thrombosis superimposed on underlying intracranial atherosclerotic stenosis (ICAS) have been identified as major causes of acute BAO.<sup>8</sup> ICAS is one of the most common causes of ischemic stroke worldwide and is particularly prevalent in Asian, black, Hispanic, and Indian populations.<sup>9</sup> Strategies for endovascular therapy in patients with acute stroke with underlying ICAS should be different from those without it. In this regard, prediction of underlying ICAS before endovascular therapy might be important and helpful to neurointerventionalists in the planning of endovascular therapy in patients with acute BAO; however, this has not yet been systematically studied, to our knowledge. In ad-

Received February 9, 2017; accepted after revision March 24.

From the Departments of Radiology (Y.Y.L., W.Y., S.K.K., B.H.B., G.S.K.) and Neurology (J.T.K., M.S.P.), Chonnam National University Medical School, Chonnam National University Hospital, Gwangju, Republic of Korea.

Please address correspondence to Woong Yoon, MD, Department of Radiology, Chonnam National University Hospital, 42 Jebong-ro, Dong-gu, Gwangju, 61469, Republic of Korea; e-mail: radyoon@jnu.ac.kr

<http://dx.doi.org/10.3174/ajnr.A5233>

dition, very few studies have investigated outcomes after endovascular therapy in patients with acute BAO due to underlying ICAS.<sup>10,11</sup> Accordingly, this study aimed to investigate the imaging and clinical characteristics for predicting underlying ICAS in patients with acute BAO and to compare the clinical outcomes of endovascular therapy in those patients relative to the existence or nonexistence of underlying ICAS.

## MATERIALS AND METHODS

### Patients

From December 2010 to February 2016, 62 patients with acute stroke due to BAO received stent-retriever thrombectomy at a regional comprehensive stroke center. We retrospectively analyzed clinical and radiologic data of these 62 patients, including age, sex, stroke risk factors, intravenous thrombolysis, time to procedure, procedural time, time to revascularization, and etiology of stroke according to the Trial of Org 10172 in Acute Stroke Treatment (TOAST) classification.<sup>12</sup>

On admission, all patients were assessed with the NIHSS by a stroke neurologist. Patients underwent nonenhanced CT and MR imaging before endovascular therapy. The inclusion criteria for stent-retriever thrombectomy were as follows: 1) presentation within 12 hours of stroke onset, 2) baseline NIHSS score of  $\geq 4$ , 3) no intracranial hemorrhage detected on cranial CT or MR imaging, 4) BAO detected with MR angiography and conventional angiography, 5) no bilateral diffuse pontine ischemia on DWI, and 6) a premorbid mRS score of  $\leq 2$ . The institutional ethics committee approved this retrospective analysis and waived the requirements for informed consent on the basis of study design.

### Endovascular Therapy

All endovascular therapy was performed by one interventional neuroradiologist with 14 years of experience in neurovascular intervention. Written informed consent for endovascular therapy was obtained from a family member for all patients. Cerebral angiography and endovascular therapy were performed with the patient under conscious sedation. In cases of agitation, an IV bolus of midazolam was given and repeated if necessary. After detecting arterial occlusion on diagnostic angiography, we used stent-retriever thrombectomy with a Solitaire stent (Covidien, Irvine, California) or Trevo stent (Stryker, Kalamazoo, Michigan) as the first-line endovascular therapy method. When stent-retriever thrombectomy was unsuccessful, manual aspiration thrombectomy with intermediate catheters was performed as a rescue treatment. The details of the techniques used for stent-retriever thrombectomy and manual aspiration thrombectomy were described previously.<sup>6,13</sup>

Underlying ICAS was determined when severe ( $\geq 70\%$ ) stenosis of the basilar artery was seen on the initial diagnostic angiography or on the follow-up angiography after a mechanical thrombectomy procedure.<sup>14</sup> The degree of arterial stenosis was determined with the Warfarin Aspirin Symptomatic Intracranial Disease criteria.<sup>15</sup> If underlying ICAS was revealed, intracranial angioplasty was performed with a Gateway PTA balloon catheter (Stryker). The diameter of the balloon was undersized to 80% of the normal vessel diameter just distal to the stenosis. The balloon was inflated slowly 1 or 2 times with a screw-type pressure inflation device at

4–6 atm for 60 seconds. After balloon angioplasty, intracranial stent placement with the Wingspan stent system (Stryker) was performed whenever possible. The stent diameter was sized to exceed the diameter of the normal vessel by 0.5 mm. The stent length was selected to cover the entire stenotic segment. All patients who underwent intracranial angioplasty or stent placement received aspirin and clopidogrel (Plavix) orally or via a nasogastric tube for at least 3 months after the procedure.

BAO was classified according to Archer and Horenstein<sup>16</sup> into proximal (from the vertebrobasilar junction to the origin of the anterior inferior cerebellar artery), middle (from the origin of the anterior inferior cerebellar artery to the origin of the superior cerebellar artery), and distal occlusion (distal to the origin of the superior cerebellar artery). Revascularization status was assessed on the final angiogram and was classified according to the modified TICI scale<sup>17</sup>; successful revascularization was defined as modified TICI grades 2b or 3. All patients underwent nonenhanced CT immediately after and 24 hours after endovascular therapy for detection of intracranial hemorrhage.

### Outcome Measures

For all patients, we assessed posterior circulation ASPECTS on pretreatment DWI, according to Tei et al.<sup>18</sup> The presence or absence of thalamic infarction and its involved territory was also evaluated. The territory of thalamic infarctions was classified into anterior, posteromedial, ventrolateral, and posterolateral according to their arterial supply.<sup>19</sup> Classification of BAO, revascularization status, posttreatment CT findings, posterior circulation ASPECTS, and thalamic infarction on pretreatment DWI were assessed by 2 neuroradiologists (with 3 and 5 years of experience, respectively) who were blinded to any clinical information. Conclusions were reached by consensus.

Neurologic evaluation was performed by a stroke neurologist immediately and 24 hours and 3 months after treatment; when any change occurred in clinical symptoms; and before the patient was discharged. Clinical outcome was assessed with the mRS by a stroke neurologist 3 months after treatment. When patients could not visit for neurologic evaluation, they were assessed via phone call. Good clinical outcome was defined as an mRS score of  $\leq 2$ . Symptomatic hemorrhage was defined as a documented hemorrhage associated with a decline of  $\geq 4$  points in the NIHSS score or 1-point deterioration in the level of consciousness.

### Statistical Analysis

Sixty-two patients were divided into 2 groups for comparison, namely the ICAS group and the non-ICAS group. The baseline characteristics and clinical outcomes of the 2 groups were compared. Statistical analyses were performed with the use of SPSS software (Version 21.0; IBM, Armonk, New York). The  $\chi^2$  test or Fisher exact test was used for categorical and binary variables, and the Mann-Whitney *U* test, for continuous variables.  $P < .05$  was considered significant.

## RESULTS

Baseline patient characteristics are shown in Table 1. The mean age was 69 years, and 36 (58.1%) were men. The etiology of ischemic stroke was cardioembolism in 32 patients (51.6%), large-

**Table 1: Baseline characteristics of the study population**

	All Patients (n = 62)	Patients with ICAS (n = 15)	Patients without ICAS (n = 47)	P Value
Age (mean) (yr)	69.6 ± 11.95	67.1 ± 10.03	70.3 ± 12.50	.205
Male sex (No.) (%)	36 (58.1)	12 (80.0)	24 (51.1)	.048
Risk factor (No.) (%)				
Hypertension	37 (59.7)	11 (73.3)	26 (55.3)	.216
Diabetes mellitus	14 (22.6)	4 (26.7)	10 (21.3)	.727
Dyslipidemia	16 (25.8)	6 (40.0)	10 (21.3)	.182
Smoking	15 (24.2)	5 (33.3)	10 (21.3)	.489
Coronary artery disease	5 (8.1)	0 (0.0)	5 (10.6)	.323
IV thrombolysis (No.) (%)	17 (27.4)	7 (46.7)	10 (21.3)	.094
Occlusion sites (No.) (%)				
Proximal	12 (19.4)	9 (60.0)	3 (6.4)	<.001
Middle	3 (4.8)	2 (13.3)	1 (2.1)	.143
Distal	47 (75.8)	4 (26.7)	43 (91.5)	<.001
Bilateral thalamic infarction (No.) (%)	13 (21.0)	0 (0.0)	13 (27.7)	.027
Baseline NIHSS score (mean)	12.4 ± 6.23	12.7 ± 5.95	12.3 ± 6.37	.773
pc-ASPECTS (median) (IQR)	7 (6–8)	7 (6–8)	7 (6–8)	.794
Time to procedure (mean) (min)	289.6 ± 129.68	309.3 ± 139.65	283.3 ± 127.60	.532
Procedure time (mean) (min)	30.9 ± 17.76	39.0 ± 19.47	28.3 ± 16.56	.006
Time to revascularization (mean) (min)	321.0 ± 136.22	348.3 ± 143.84	312.2 ± 134.12	.459

**Note:**—IQR indicates interquartile range; pc-ASPECTS, posterior circulation ASPECTS.

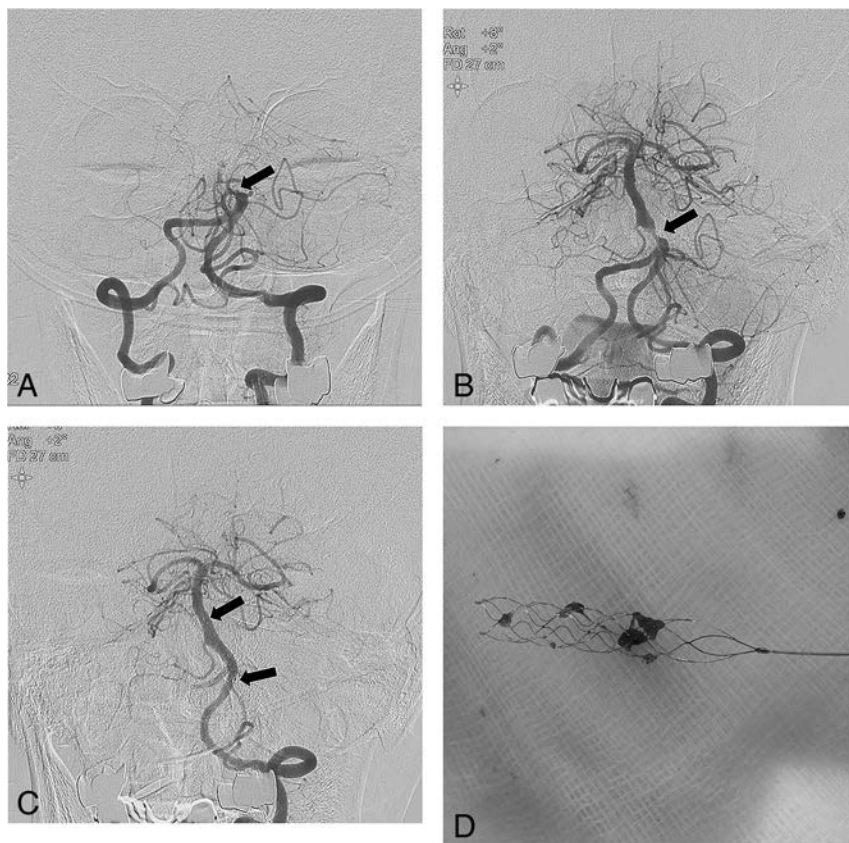


**FIG 1.** A 74-year-old male patient with acute stroke due to acute basilar artery occlusion. A, Left vertebral artery angiogram shows an occlusion (arrow) at the proximal segment of the basilar artery. B, Angiogram obtained after 1 passage of the stent retriever reveals a severe underlying atherosclerotic stenosis (arrow) at the proximal segment of the basilar artery. C, Left vertebral artery angiogram obtained after intracranial angioplasty and stent placement shows complete recanalization of the basilar artery with good distal perfusion. Arrows indicate the proximal and distal ends of the Wingspan stent. D, Photograph shows small fragmented thrombi retrieved with a Solitaire stent.

artery atherosclerosis in 21 patients (33.9%), and undetermined etiology in 9 patients (14.5%). IV rtPA was administered in 17 patients (27.4%). The mean NIHSS score on admission was 12, with scores ranging from 4 to 25.

Of the 62 patients, 15 (24.2%) had underlying ICAS at the occlusion site. Of these 15 patients, 1 had preocclusive severe stenosis on diagnostic angiography and 14 had occlusion on initial diagnostic angiography. These 14 patients had stenosis of  $\geq 70\%$  on follow-up angiography after first-line stent-retriever thrombectomy. Of 15 patients with underlying ICAS, 5 underwent intracranial angioplasty alone and 8 received angioplasty with stent placement (Fig 1). Two patients did not undergo angioplasty or stent placement due to device inaccessibility. Overall, 17.7% (11/62) of patients were treated by additional manual aspiration thrombectomy after failure of first-line stent-retriever thrombectomy.

The mean procedural time was longer in the ICAS group than in the non-ICAS group (39 minutes versus 28 minutes,  $P = .006$ ). Occlusion in the proximal segment of the basilar artery was more frequent in the ICAS group (9/15, 60%) than in the non-ICAS group (3/47, 6.4%) ( $P < .001$ ). In contrast, occlusion in the distal segment of the basilar artery was more frequent in the non-ICAS group (43/47, 91.5%) than in the ICAS group (4/15, 26.7%) ( $P < .001$ ). Otherwise, there were no significant differences between the 2 groups in age, sex, stroke risk factors, intravenous thrombolysis, time to procedure, time to revascularization, baseline NIHSS score, and DWI posterior circulation ASPECTS.

On a pretreatment DWI, thalamic infarction was seen in 24 patients (38.7%). Of the 24 patients with thalamic infarctions, 13 had bilateral thalamic infarctions and 11 had unilateral thalamic infarctions. All bilateral thalamic infarctions occurred in paramedian regions. Five patients in the ICAS group had thalamic infarctions, and all of these 5 patients showed unilateral thalamic infarction. Nineteen patients in the non-ICAS group had thalamic infarction. Of these 19 patients, 13 had bilateral thalamic infarctions and 6 had unilateral thalamic infarction. There was no significant difference in the rate of thalamic infarction between the 2 groups, but the rate of bilateral thalamic infarction was significantly lower in the ICAS group (0/15, 0%) compared with the non-ICAS group (13/47, 27.7%) ( $P = .027$ ).

**Table 2: Outcomes after endovascular therapy in 62 patients with acute stroke due to BAO**

	All Patients (n = 62)	Patients with ICAS (n = 15)	Patients without ICAS (n = 47)	P Value
mTICI 2b or 3 (No.) (%)	60 (96.8)	15 (100.0)	45 (95.7)	NS
mRS 0–2 (No.) (%)	33 (53.2)	9 (60.0)	24 (51.1)	NS
Symptomatic hemorrhage (No.) (%)	1 (1.6)	0 (0.0)	1 (2.1)	NS
Mortality (No.) (%)	10 (16.1)	2 (13.3)	8 (17.0)	NS

**Note:**—mTICI indicates modified TICI; NS, nonsignificant.

The clinical outcomes of 62 patients are summarized in Table 2. Overall, successful revascularization (modified TICI grades 2b or 3) was achieved in 96.8% (60/62) of the patients, and favorable outcomes (mRS 0–2), in 53.2% (33/62) of the patients. There was 1 patient (1.6%) with symptomatic hemorrhage, and the mortality rate was 16.1% (10/62). There was no significant difference between the 2 groups in the rates of successful revascularization, favorable outcome, symptomatic hemorrhage, and mortality.

## DISCUSSION

The main findings of our study are as follows: 1) Underlying ICAS of  $\geq 70\%$  was identified in 24.2% of the patients with acute ischemic stroke due to BAO; 2) occlusion in the proximal segment was more frequently seen in patients with BAO with underlying ICAS, whereas occlusion in the distal segment was more frequently observed in those without underlying ICAS; and 3) bilateral thalamic infarction on pretreatment DWI was seen only in patients without underlying ICAS.

The incidence of underlying ICAS in acute ischemic stroke caused by intracranial large-artery occlusion has been reported to be 17%–60%.<sup>10,11,14</sup> It is well-known that ICAS is more prevalent in Asian countries, and accordingly, the highest incidence was reported by a Chinese center.<sup>10</sup> The results of our study are in line with those reports; 24% of patients with acute BAO had underlying ICAS of  $\geq 70\%$ . The possibility of underlying ICAS should be considered when performing endovascular therapy in patients with acute BAO, especially when encountering a difficulty during mechanical thrombectomy in regions where ICAS is more prevalent. The primary revascularization rate of stent-retriever thrombectomy in patients with acute stroke due to large-vessel occlusions was reported to be up to 70%–80%.<sup>13</sup> Underlying ICAS in the occluded artery can be an important cause of failed stent-retriever thrombectomy, especially in Asian patients.<sup>13,14</sup>

Predicting the presence of underlying ICAS before and during stent-retriever thrombectomy will be helpful for neurointerventionists for appropriate therapeutic planning. Our study suggested that the occlusion site can be a useful marker in predicting underlying ICAS in patients with acute BAO. In our study, 73% of patients with underlying ICAS had occlusions in the proximal and middle segments of the basilar artery, while 92% of those without underlying ICAS had occlusions in distal segment of the basilar artery. The results from our study are in accordance with those in a recently published study by Kim et al,<sup>11</sup> which included 51 patients with acute vertebrobasilar artery occlusion. They found that 69.3% of patients with ICAS had occlusions in the proximal and middle segments of the basilar artery, while 87.5% of those with embolism had occlusions in the distal segment.

Thalamic infarctions are often detected on a pretreatment DWI in patients with acute BAO.<sup>7</sup> However, to our knowledge,

there have been no reports regarding the association between thalamic infarction on a pretreatment DWI and underlying ICAS. In our study, there was no significant difference between the ICAS group and the non-ICAS group in the incidence of thalamic infarction; however, the incidence of bilateral thalamic infarctions differed significantly between patients with underlying ICAS and those without it. No patients with underlying ICAS showed bilateral thalamic infarctions on pretreatment DWI. This difference might be related to the occlusion segment of the basilar artery. In this study, all bilateral thalamic infarction occurred in the bilateral paramedian region, which is supplied by a single thalamoperforating artery (the artery of Percheron).<sup>20,21</sup> The artery of Percheron arises from the proximal P1 segment of the posterior cerebral artery. In case of occlusion in the distal basilar artery, the emboli may easily extend to the P1 segment of the posterior cerebral artery, which would result in occlusion of the artery of Percheron and cause bilateral paramedian thalamic infarction. In contrast, patients with ICAS are not likely to have paramedian thalamic infarctions because occlusions of the proximal and middle segment are more common and the P1 segments are usually preserved in patients with ICAS. Our study suggested that if bilateral paramedian thalamic infarctions are seen on pretreatment DWI in patients with BAO, the possibility of the presence of underlying ICAS would be low.

The optimal treatment for patients with acute BAO with underlying ICAS remains unclear. In the present study, 86.7% of patients (13/15) with underlying ICAS were treated with intracranial angioplasty with or without stent placement after first-line mechanical thrombectomy. We achieved high rates of successful revascularization (100%) and favorable outcome (60%), no symptomatic hemorrhage, and a low mortality rate (13.3%) in these 15 patients. Recently, Yoon et al<sup>14</sup> reported the results of emergent angioplasty and stent placement in 40 patients with acute ischemic stroke due to underlying ICAS. They reported high rates of successful revascularization (95%) and favorable outcome (62.5%) and low rates of symptomatic hemorrhage (7.5%) and mortality (15%). They suggested that intracranial angioplasty with or without stent placement is safe and feasible in hyperacute stroke secondary to underlying ICAS. Gao et al<sup>10</sup> also reported a 100% successful revascularization rate and a favorable 3-month outcome rate of 46% in a series of 13 patients with acute BAO and underlying ICAS who were treated with stent-retriever thrombectomy and intracranial stent placement.

In contrast to our study, Kim et al<sup>11</sup> recently reported a low rate of good outcome (10.5% with mRS 0–2 at 3 months) and a high mortality rate (21.1%) after endovascular therapy in 19 patients with acute vertebrobasilar occlusion due to ICAS. The main reasons for the poor outcomes after endovascular therapy in the study of Kim et al may be heterogeneity of the rescue treatment after primary mechanical thrombectomy, the low rate of angioplasty/stent placement as a rescue treatment, and long procedural time. In their study, one-third of patients received intra-arterial infusion of tirofiban, one-third of patients underwent angioplasty alone, and another one-third of patients underwent stent place-

ment. The results of our study together with previous reports suggest that intracranial angioplasty with or without stent placement is promising in patients with acute BAO due to underlying ICAS. In addition, the procedural time was much longer in the study of Kim et al (96 versus 39 minutes in patients with ICAS and 61 versus 28 minutes in those without ICAS) than in our study.

Our study had several limitations, including a retrospective, noncontrolled study design and a limited number of patients. Prospective, multicenter studies are needed to further determine the clinical and radiologic characteristics of patients with BAO with underlying ICAS. In addition, prospective clinical trials are also needed to confirm the efficacy and safety of intracranial angioplasty and stent placement in patients with BAO with underlying ICAS compared with other treatment options such as intra-arterial infusion of antiplatelet drugs.

## CONCLUSIONS

Underlying ICAS is common in patients with acute stroke due to BAO. The occlusion site can be used as a useful marker for predicting underlying ICAS in patients with acute BAO. There was no difference in treatment outcomes after endovascular therapy between patients with underlying ICAS and those without it.

## REFERENCES

1. Schonewille WJ, Wijman CA, Michel P, et al; BASICS study group. **Treatment and outcomes of acute basilar artery occlusion in the Basilar Artery International Cooperation Study (BASICS): a prospective registry study.** *Lancet Neurol* 2009;8:724–30 CrossRef Medline
2. Mortimer AM, Bradley M, Renowden SA. **Endovascular therapy for acute basilar artery occlusion: a review of the literature.** *J Neurointerv Surg* 2012;4:266–73 CrossRef Medline
3. Yeung JT, Matouk CC, Bulsara KR, et al. **Endovascular revascularization for basilar artery occlusion.** *Interv Neurol* 2015;3:31–40 CrossRef Medline
4. Gory B, Eldesouky I, Sivan-Hoffmann R, et al. **Outcomes of stent retriever thrombectomy in basilar artery occlusion: an observational study and systematic review.** *J Neurol Neurosurg Psychiatry* 2016;87:520–25 CrossRef Medline
5. Möhlenbruch M, Stampfl S, Behrens L, et al. **Mechanical thrombectomy with stent retrievers in acute basilar artery occlusion.** *AJNR Am J Neuroradiol* 2014;35:959–64 CrossRef Medline
6. Baek JM, Yoon W, Kim SK, et al. **Acute basilar artery occlusion: outcome of mechanical thrombectomy with Solitaire stent within 8 hours of stroke onset.** *AJNR Am J Neuroradiol* 2014;35:989–93 CrossRef Medline
7. Yoon W, Kim SK, Heo TW, et al. **Predictors of good outcome after stent-retriever thrombectomy in acute basilar artery occlusion.** *Stroke* 2015;46:2972–75 CrossRef Medline
8. Mattle HP, Arnold M, Lindsberg PJ, et al. **Basilar artery occlusion.** *Lancet Neurol* 2011;10:1002–14 CrossRef Medline
9. Bang OY. **Intracranial atherosclerosis: current understanding and perspectives.** *J Stroke* 2014;16:27–35 CrossRef Medline
10. Gao F, Lo WT, Sun X, et al. **Combined use of mechanical thrombectomy with angioplasty and stenting for acute basilar occlusions with underlying severe intracranial vertebrobasilar stenosis: preliminary experience from a single Chinese center.** *AJNR Am J Neuroradiol* 2015;36:1947–52 CrossRef Medline
11. Kim YW, Hong JM, Park DG, et al. **Effect of intracranial atherosclerotic disease on endovascular treatment for patients with acute vertebrobasilar occlusion.** *AJNR Am J Neuroradiol* 2016;37:2072–78 CrossRef Medline
12. Adams HP Jr, Bendixen BH, Kappelle LJ, et al. **Classification of subtype of acute ischemic stroke. Definitions for use in a multicenter clinical trial. TOAST. Trial of Org 10172 in Acute Stroke Treatment.** *Stroke* 1993;24:35–41 Medline
13. Kim SK, Yoon W, Moon SM, et al. **Outcomes of manual aspiration thrombectomy for acute ischemic stroke refractory to stent-based thrombectomy.** *J Neurointerv Surg* 2015;7:473–77 CrossRef Medline
14. Yoon W, Kim SK, Park MS, et al. **Endovascular treatment and the outcomes of atherosclerotic intracranial stenosis in patients with hyperacute stroke.** *Neurosurgery* 2015;76:680–86 discussion 686 CrossRef Medline
15. Samuels OB, Joseph GJ, Lynn MJ, et al. **A standardized method for measuring intracranial arterial stenosis.** *AJNR Am J Neuroradiol* 2000;21:643–46 Medline
16. Archer CR, Horenstein S. **Basilar artery occlusion: clinical and radiological correlation.** *Stroke* 1977;8:383–90 CrossRef Medline
17. Zaidat OO, Yoo AJ, Khatri P, et al; STIR Revascularization working group, STIR Thrombolysis in Cerebral Infarction (TICI) Task Force. **Recommendations on angiographic revascularization grading standards for acute ischemic stroke: a consensus statement.** *Stroke* 2013;44:2650–63 CrossRef Medline
18. Tei H, Uchiyama S, Usui T, et al. **Posterior circulation ASPECTS on diffusion-weighted MRI can be a powerful marker for predicting functional outcome.** *J Neurol* 2010;257:767–73 CrossRef Medline
19. Song YM. **Topographic patterns of thalamic infarcts in association with stroke syndromes and aetiologies.** *J Neurol Neurosurg Psychiatry* 2011;82:1083–86 CrossRef Medline
20. Lazzaro NA, Wright B, Castillo M, et al. **Artery of percheron infarction: imaging patterns and clinical spectrum.** *AJNR Am J Neuroradiol* 2010;31:1283–89 CrossRef Medline
21. Li X, Agarwal N, Hansberry DR, et al. **Contemporary therapeutic strategies for occlusion of the artery of Percheron: a review of the literature.** *J Neurointerv Surg* 2015;7:95–98 CrossRef Medline

# Treatment of Tandem Internal Carotid Artery Aneurysms Using a Single Pipeline Embolization Device: Evaluation of Safety and Efficacy

 N. Adeeb,  J.M. Moore,  C.J. Griessenauer,  P.M. Foreman,  H. Shallwani,  A.A. Dmytriw,  H. Shakir,  A.H. Siddiqui,  E.I. Levy,  J.M. Davies,  M.R. Harrigan,  A.J. Thomas, and  C.S. Ogilvy

## ABSTRACT

**BACKGROUND AND PURPOSE:** Tandem aneurysms are defined as multiple aneurysms located in close proximity on the same parent vessel. Endovascular treatment of these aneurysms has rarely been reported. Our aim was to evaluate the safety and efficacy of a single Pipeline Embolization Device for the treatment of tandem aneurysms of the internal carotid artery.

**MATERIALS AND METHODS:** A retrospective analysis of consecutive aneurysms treated with the Pipeline Embolization Device between 2009 and 2016 at 3 institutions in the United States was performed. Cases included aneurysms of the ICA treated with a single Pipeline Embolization Device, and they were divided into tandem versus solitary. Angiographic and clinical outcomes were compared.

**RESULTS:** The solitary group (median age, 58 years) underwent 184 Pipeline Embolization Device procedures for 184 aneurysms. The tandem group (median age, 50.5 years) underwent 34 procedures for 78 aneurysms. Aneurysms were primarily located along the paraophthalmic segment of the ICA in both the single and tandem groups (72.3% versus 78.2%, respectively,  $P = .53$ ). The median maximal diameters in the solitary and tandem groups were 6.2 and 6.7 mm, respectively. Complete occlusion on the last angiographic follow-up was achieved in 75.1% of aneurysms in the single compared with 88.6% in the tandem group ( $P = .06$ ). Symptomatic thromboembolic complications were encountered in 2.7% and 8.8% of procedures in the single and tandem groups, respectively ( $P = .08$ ).

**CONCLUSIONS:** Tandem aneurysms of the ICA can be treated with a single Pipeline Embolization Device with high rates of complete occlusion. While there appeared to be a trend toward higher thromboembolic complication rates, this did not reach statistical significance.

**ABBREVIATION:** PED = Pipeline Embolization Device

Multiple intracranial aneurysms account for 14%–34% of the distribution of all intracranial aneurysms.<sup>1–5</sup> When these aneurysms are located in close proximity to each another on the same parent vessel, they are referred to as “tandem aneurysms.” The treatment of tandem aneurysms has rarely been reported in the literature. These aneurysms are most commonly found along the internal carotid artery and may arise within the same anatomic segment or involve adjacent segments. Rarely, they are identified in the posterior circulation.<sup>1,6–9</sup> Flow diversion with the Pipeline Embolization Device (PED; Covidien, Irvine, California) was initially approved by the US Food and Drug Administration

for treatment of large or giant, wide-neck cerebral aneurysms of the ICA from the petrous to superior hypophyseal segments.<sup>10</sup> Numerous studies have since demonstrated the safety and efficacy of the PED in the treatment of aneurysms with varying morphologies and anatomic locations.<sup>11–16</sup> Currently, only a few studies with small numbers of patients have evaluated endovascular treatment of tandem aneurysms with coil embolization,<sup>8</sup> stent-assisted coiling,<sup>9</sup> or flow diversion.<sup>9</sup> In this study, we compare the outcomes following deployment of a single PED in 2 groups of patients, those with solitary ICA aneurysms and those with tandem ICA aneurysms.

## MATERIALS AND METHODS

A retrospective analysis of consecutive aneurysms treated with PED deployment between 2009 and 2016 at 3 academic institutions in United States was performed. Inclusion criteria consisted of all adult patients with saccular intracranial ICA aneurysms treated with a single PED. Both ruptured and unruptured aneurysms were included. Patients were then divided into 2 groups: solitary aneurysms and tandem aneurysms. Tandem aneurysms

Received February 6, 2017; accepted after revision March 13.

From the Neurosurgical Service (N.A., J.M.M., C.J.G., A.A.D., A.J.T., C.S.O.), Beth Israel Deaconess Medical Center, Harvard Medical School, Boston, Massachusetts; Department of Neurosurgery (P.M.F., M.R.H.), University of Alabama at Birmingham, Birmingham, Alabama; and Department of Neurosurgery (H. Shallwani, H. Shakir, A.H.S., E.I.L., J.M.D.), State University of New York at Buffalo, Buffalo, New York.

Please address correspondence to Christopher S. Ogilvy, MD, Neurosurgical Service, Beth Israel Deaconess Medical Center, 110 Francis St, Suite 3B, Boston, MA 02215-5501; e-mail: cogilvy@bidmc.harvard.edu

<http://dx.doi.org/10.3174/ajnr.A5221>

consisted of >1 intracranial ICA aneurysm within the same anatomic segment or involving adjacent anatomic segments. We collected the following information: patient demographics, aneurysm and PED characteristics, procedural complications, and angiographic and functional outcomes. Institutional review board approval was obtained at all 3 centers before commencement of the study.

### **Procedural Details**

Patients undergoing elective aneurysm treatment received aspirin, 325 mg, and clopidogrel, 75 mg, daily for 3–14 days before the intervention. Platelet function testing was routinely performed with whole-blood lumi-aggregometry, light transmission aggregometry, or the VerifyNow P2Y12 assay (Accumetrics, San Diego, California). Clopidogrel nonresponders were identified on the basis of established cutoff values at the individual institutions and were guided by manufacturer's recommendations. If a patient was identified as a clopidogrel responder, clopidogrel was continued. If a patient was identified as a clopidogrel nonresponder, the choice to continue the same dose of clopidogrel, administer a 1-time 600-mg clopidogrel boost within 24 hours of the procedure, or switch to ticagrelor was at the discretion of the interventionalist performing the procedure. Patients undergoing treatment of a ruptured aneurysm received a loading dose of aspirin, 650 mg, and clopidogrel, 600 mg, immediately before the intervention. Patients underwent local anesthesia with sedation or general anesthesia at the discretion of the individual institutions, and all patients were anticoagulated with heparin throughout the procedure, with an activated clotting time target of 250–300 seconds. The type of the guide catheter and microcatheter used for PED deployment was at the discretion of the individual institutions. The deployment and apposition of the PED to the ICA wall was documented by fluoroscopy. Dual antiplatelet therapy was continued for at least 3 months after the procedure, and aspirin, indefinitely thereafter.

### **Angiographic and Clinical Outcome**

Angiographic outcome was assessed with digital subtraction angiography or MR angiography based on follow-up protocols used at each individual institution. Aneurysm occlusion on follow-up DSA imaging was assessed by the treating interventionalist. Follow-up MRAs were assessed by a diagnostic radiologist and the treating interventionalist. Occlusion was categorized as complete occlusion (100%), near-complete occlusion (90%–100%), and partial occlusion (< 90%). Functional outcomes were assessed by using the modified Rankin Scale at last follow-up.

### **Statistical Analysis**

Statistical analysis was performed by using SPSS, Version V 21.0 (IBM, Armonk, New York). In univariate analysis, variables were compared between groups with the Mann-Whitney *U* test for nonparametric numeric variables and the  $\chi^2$  test for categorical variables. Statistical significance was defined as  $P < .05$ . Multivariate logistic regression was performed on candidate predictor variables to identify independent differences in outcome between both groups.

## **RESULTS**

### **Baseline Characteristics**

The solitary aneurysm group (median age, 58 years) underwent 184 PED placement procedures for the treatment of 184 aneurysms, and the tandem aneurysm group (median age, 50.5 years) underwent 34 PED placement procedures for the treatment of 78 aneurysms. Current smoking was identified in 22.8% and 52.9% of patients undergoing procedures in the solitary and tandem groups, respectively ( $P < .001$ ). The pretreatment mRS was 0–2 in 97.8% and 94.1% of procedures in the solitary and tandem aneurysm groups, respectively ( $P = .23$ ). Treatment of acute aneurysmal subarachnoid hemorrhage occurred in 2.2% and 8.8% of procedures in the solitary and tandem aneurysm groups, respectively ( $P = .11$ ).

### **Aneurysm Characteristics**

Aneurysms were primarily located along the paraophthalmic segment of the ICA in both the solitary and tandem aneurysm groups (72.3% versus 78.2%, respectively,  $P = .53$ ). The median maximal diameter of the aneurysm was 6.2 mm in the solitary aneurysm group and 6.7 mm in the tandem aneurysm group. The median neck diameter of the aneurysm was 4 mm in the solitary group and 3.9 mm in the tandem group (Table 1). Aneurysms other than the largest aneurysm in the tandem aneurysm group had a median maximal diameter of 3 mm (range, 1–12 mm) and a median neck width of 2.4 mm (range, 1–6 mm). This finding was significantly different from the respective measurements of the largest treated aneurysm in the tandem aneurysm group and the solitary aneurysm group ( $P < .001$  and  $P < .001$ , respectively) (Table 2). A daughter sac was present in 25.1% and 15.4% of aneurysms in the single and tandem aneurysm groups, respectively ( $P = .08$ ).

### **Treatment Outcome**

There was no significant difference in the length of the procedure in the treatment of solitary aneurysms compared with tandem aneurysms (69.5 versus 76 minutes, respectively,  $P = .52$ ). Similarly, there was no significant difference in the length ( $P = .42$ ) or diameter ( $P = .26$ ) of PEDs used in either group. The median length of angiographic follow-up was significantly longer in the tandem aneurysm group compared with the solitary aneurysm group, 18 months (mean, 19.2 months) versus 12 months (mean, 15.4 months), respectively ( $P = .008$ ). On the last angiographic follow-up, complete occlusion was achieved in 75.1% of aneurysms in the solitary aneurysm group compared with 88.6% in the tandem aneurysm group ( $P = .06$ ). After stratifying the tandem aneurysm group into the largest aneurysm and other aneurysms within the tandem group, the rate of complete occlusion was not significantly higher compared with solitary aneurysms ( $P = .21$ ) (Table 3). Retreatment was performed in 4.9% and 5.7% of the solitary and tandem aneurysm groups, respectively ( $P = .81$ ). At last follow-up, the mRS improved in 27.5% and 27.3% of patients and worsened in 7% and 0% of the solitary and tandem aneurysm groups, respectively ( $P = .33$ ). Symptomatic thromboembolic complications were encountered in 2.7% and 8.8% of procedures in the solitary and tandem aneurysm groups, respectively ( $P = .08$ ). Symptoms were permanent (lasting >30

**Table 1: Baseline characteristics**

Parameter	Solitary Aneurysm	Tandem Aneurysms	P Value
No. of PEDs placed	184	34	—
Aneurysms treated with single PED	184	78	—
1	184	—	—
2	—	28	—
3	—	3	—
4	—	2	—
5	—	1	—
Sex			
Female	166 (90.2%)	31 (91.2%)	.86
Male	18 (9.8%)	3 (8.8%)	
Median age (median) (range) (yr)	58 (24–82)	50.5 (19–75)	.006
Smoking (No.)	42 (22.8%)	18 (52.9%)	<.001
Pretreatment mRS (No.)			
0–2	180 (97.8%)	32 (94.1%)	.23
3–5	4 (2.2%)	2 (5.9%)	
Aneurysm location			
Cavernous	25 (13.6%)	7 (9%)	.53
Paraophthalmic	133 (72.3%)	61 (78.2%)	
Posterior communicating	26 (14.1%)	10 (12.8%)	
Aneurysm measurements (median) (range) (mm)			
Maximal diameter	6.2 (1.6–28.3) <sup>a</sup>	6.7 (2–40)	.48
Neck size	4 (1–14.3) <sup>b</sup>	3.9 (1.8–8.5) <sup>c</sup>	.14
Daughter sac (No.)	46 (25.1%)	12 (15.4%)	.08
Subarachnoid hemorrhage (No.)			
Acute (<2 weeks)	4 (2.2%)	3 (8.8%)	.11
Remote (>2 weeks)	19 (10.3%)	2 (5.9%)	
Prior treatment (No.)			
Endovascular	23 (12.5%)	2 (2.6%)	.031
Surgery	6 (3.3%)	0	
Both	2 (1.1%)	1 (1.3%)	
Clopidogrel responders (No.)			
Yes	123 (68.7%) <sup>d</sup>	24 (75%) <sup>e</sup>	.48
No	56 (31.3%)	8 (25%)	

<sup>a</sup> Data are missing for 25 aneurysms.<sup>b</sup> Data are missing for 50 aneurysms.<sup>c</sup> Data are missing for 2 aneurysms.<sup>d</sup> Data are missing for 5 procedures.<sup>e</sup> Data are missing for 2 procedures.**Table 2: Aneurysm size**

Parameter	Solitary Aneurysm	Tandem Aneurysms	
		Largest Aneurysm	Other Aneurysms
Median maximal diameter (range) (mm)	6.2 (1.6–28.3) <sup>a,b</sup>	6.7 (2–40) <sup>b</sup>	3 (1–12) <sup>b</sup>

<sup>a</sup> Data are missing for 25 aneurysms.<sup>b</sup>  $P < .001$ .**Table 3: Occlusion rate**

Occlusion Rate	Solitary Aneurysm	Tandem Aneurysms		P Value
		Largest Aneurysm	Other Aneurysms	
Complete (100%)	109 (75.1%) <sup>a</sup>	36 (90%) <sup>b</sup>	26 (86.6%) <sup>b</sup>	.21
Near-complete (90%–99%)	12 (8.3%)	2 (5%)	2 (6.7%)	
Partial (<90%)	24 (16.6%)	2 (5%)	2 (6.7%)	

<sup>a</sup> Data are missing for 39 aneurysms.<sup>b</sup> Data are missing for 4 aneurysms.

days) in 1.6% and 2.9% of procedures, respectively ( $P = .60$ ). One procedure for the treatment of a solitary aneurysm was complicated by both an ischemic stroke and an intraparenchy-

mal hemorrhage. There were no mortalities in either group (Table 4).

## DISCUSSION

In this study, we report a multicenter experience with single PED placement for the treatment of tandem intracranial aneurysms of the internal carotid artery. Factors that influenced the decision to attempt treatment of tandem aneurysms with a single flow diverter included close proximity of the aneurysms, a favorable local angioarchitecture of the parent vessel, and small aneurysm size. Tandem aneurysms were compared with solitary aneurysms with respect to rates of aneurysm occlusion and complications. Complete occlusion rates were higher in the tandem aneurysms group compared with solitary aneurysms, with a trend toward statistical significance. A potential confounder was the small size of the adjacent aneurysms in the tandem group when the largest aneurysm was excluded. Therefore, after stratifying tandem aneurysms based on size, the difference was not statistically significant (Table 3). Despite a trend toward higher symptomatic thromboembolic complication rates in the tandem group, no statistically significant difference was identified. These findings mirror a prior study that associated a higher aneurysm occlusion rate but also procedural complications with simultaneous treatment of multiple aneurysms with the PED.<sup>13</sup>

### Endovascular Treatment of Tandem Aneurysms

The surgical management of tandem aneurysms can be challenging, especially when paraophthalmic or posterior circulation sites are involved.<sup>6</sup> Endovascular treatment is therefore a favorable alternative for these subgroups. Fang et al<sup>6</sup> reported on the use of stent-assisted coiling in the treatment of 21 patients with 42 tandem aneurysms, most of which were located within the ICA or middle cerebral artery; 1 patient had tandem aneurysms located within the posterior circulation.<sup>6</sup> Of these, 57.1% of patients presented with a ruptured aneurysm. At last angiographic follow-up (mean, 25.4 months), complete occlusion was achieved in 76.5%. There were no symptomatic thromboembolic complications. The authors concluded that stent-assisted coiling may have an advantage over the PED in the treatment of ruptured and posterior circulation aneurysms. However, there was no direct comparison within the study.

Lin et al<sup>8</sup> reported on endovascular treatment of 13 patients with 28 tandem aneurysms. In 1 case, the aneurysms were located within the posterior circulation. Seven patients were treated with stent-assisted coiling, while the remaining 6 patients were

**Table 4: Outcome measures**

Parameter	Solitary Aneurysm	Tandem Aneurysms	P Value
Length of procedure (median) (range) (min)	69.5 (16–192) <sup>a</sup>	76 (19–194) <sup>b</sup>	.52
PED dimensions (median) (range) (mm)			
PED length	19 (12–35)	20 (6–30)	.42
PED diameter	4 (2.5–5.5)	4 (3.5–5)	.26
Last angiographic follow-up (median) (range) (mo)	12 (1–79) <sup>c</sup>	18 (4.8–51) <sup>d</sup>	.008
Follow-up occlusion rate (No.)			
Complete (100%)	109 (75.1%) <sup>c</sup>	62 (88.6%) <sup>d</sup>	.06
Near-complete (90%–99%)	12 (8.3%)	4 (5.7%)	
Partial (<90%)	24 (16.6%)	4 (5.7%)	
Retreatment (No.)			
Endovascular	7 (4.9%)	4 (5.7%)	.81
Posttreatment mRS (No.)			
0–2	169 (98.8%) <sup>e</sup>	32 (97%) <sup>f</sup>	.42
3–5	2 (1.2%)	1 (3%)	
Follow-up mRS (No.)			
Improved	47 (27.5%) <sup>e</sup>	9 (27.3%) <sup>f</sup>	.33
No change	112 (65.5)	24 (72.7%)	
Worsened	12 (7%)	0	
Neurologic complications (No.)			
Symptomatic thromboembolic	5 (2.7%)	3 (8.8%)	.08
Permanent	3 (1.6%)	1 (2.9%)	.60
Symptomatic hemorrhagic	2 (1.1%)	1 (2.9%)	.39

<sup>a</sup> Data are missing for 32 procedures.

<sup>b</sup> Data are missing for 15 procedures.

<sup>c</sup> Data are missing for 39 aneurysms.

<sup>d</sup> Data are missing for 8 aneurysms.

<sup>e</sup> Data are missing for 13 procedures.

<sup>f</sup> Data are missing for 1 procedure.

treated with the PED. At last angiographic follow-up (mean, 20.3 months), complete occlusion was achieved in 90% of PED-treated aneurysms compared with 72.7% of those treated with stent-assisted coiling. Two patients (28.6%) treated with stent-assisted coiling required retreatment.

The high rate of complete occlusion following PED placement compared with stent-assisted coiling is likely due to the larger surface area coverage provided by the PED, leading to better reconstruction and endothelialization of the aneurysm neck. The PED can also theoretically induce repair of a dysplastic parent vessel and therefore potentially offer more durable treatment of adjacent tandem intracranial aneurysms.<sup>9</sup> The PED has also proved effective in small aneurysms,<sup>13</sup> which often make up the adjacent aneurysms in patients with tandem aneurysms and in whom there is a particularly high risk of rupture when treated with traditional stent-coiling techniques following deployment of the stent. Moreover, in the treatment of tandem aneurysms, the PED is often technically preferred because placement of a single PED can be sufficient to achieve complete occlusion of all aneurysms, compared with stent-assisted coiling, in which each aneurysm has to be catheterized and treated separately.

### Hemodynamics of Tandem Aneurysm Occlusion

Mut et al<sup>9</sup> examined the hemodynamics of tandem aneurysm occlusion following PED placement. They proposed that aneurysms located on the convex side of the parent artery wall have an inflow stream entering the aneurysm through the proximal aspect of the neck, while the aneurysms located in the concave part of the wall have an inflow through the distal aspect. Following PED placement, the aneurysms on the concave side of the parent artery have a larger reduction in aneurysm inflow, mean velocity, shear rate,

and wall shear stress and smoother flow patterns, leading to faster occlusion compared with their convexity counterparts. They also reported that the energy content in the aneurysm (total kinetic energy calculated over the aneurysm sac) at the convex side changed from 30% of the energy of the parent artery to 13%, while in the aneurysm at the concave side, it changed from 18% to approximately 3%. When the energy content (or energy loss) approaches zero, the blood flow is expected to cease with subsequent blood coagulation and obliteration of the aneurysm.

In the present study, the side of the aneurysm orifice in respect to the parent artery geometry had no correlation with complete occlusion because 4 of 8 (50%) aneurysms with incomplete occlusion were located on the concave portion of the parent artery. However, in 5 of 8 (62.5%) cases of incomplete occlusion, the aneurysm was part of a tandem sequence of 2 aneurysms that were separated by at least 1 ICA segment. For example, 1 aneurysm was located in the cavernous segment of the ICA, while the second was located along the ophthalmic segment. Moreover, complete occlusion occurred in the proximal aneurysm in all cases, while the distal aneurysm failed to occlude. In the remaining 3 cases, all aneurysms within the tandem sequence along the ophthalmic segment remained patent. Another factor that may explain the failure to occlude in tandem aneurysms is the size of aneurysm because in 5 of 8 (62.5%) aneurysms, it was the larger aneurysm that failed to occlude. However, due to the limited number of cases, further studies with greater numbers of patients are required to investigate this hypothesis.

### Complications

The natural history of tandem aneurysms is not well-understood. Kaminogo et al<sup>2</sup> reported no significant difference in the rate of acute SAH between single and multiple aneurysms at the time of presentation, which is supported by the present study. Inagawa,<sup>1</sup> on the other hand, reported a positive correlation between the multiplicity of the aneurysms and a risk of aneurysm rupture.

Following endovascular procedures, Lin et al<sup>8</sup> reported no significant difference in the rate of complications between stent-assisted coiling and the PED for the treatment of tandem aneurysms. However, in their study, the number of PEDs placed for aneurysm treatment was variable. Moreover, no previous study has compared the outcomes following PED placement in the treatment of tandem-versus-solitary aneurysms.

In the present study, symptomatic thromboembolic complications were encountered following 3 procedures (8.8%) for PED placement in the treatment of tandem aneurysms compared with 2.7% in the treatment of solitary aneurysms ( $P = .08$ ). Permanent

symptoms (lasting >30 days) as a result of ischemic stroke were encountered in 1.6% and 2.9% of procedures for the treatment of solitary and tandem aneurysms, respectively ( $P = .6$ ). Although there was a tendency for tandem aneurysms to occur in smokers, smoking per se had no significant correlation with thromboembolic complications.

### Limitations

We acknowledge that our study is limited by its retrospective nature. Although the inclusion of multiple institutions improves the generalizability of the findings, it introduces variability in patient management, follow-up protocols, imaging studies, and evaluation of aneurysm occlusion. There was also variation in patient characteristics and aneurysm size between both comparison groups, and only a relatively small number of complications were observed in each group, limiting the power of the study to detect small differences between groups. However, this is the largest comparison of tandem and single aneurysms treated by the PED in the literature, to our knowledge, and there were attempts to control for significant differences between comparison groups during analysis of outcomes.

### CONCLUSIONS

Tandem aneurysms of the internal carotid artery can be treated with a single PED with high rates of complete aneurysm occlusion. The higher rates of aneurysm occlusion in the tandem group compared with the solitary group could be confounded by differences in aneurysm size. While there did appear to be a trend toward higher thromboembolic complication rates in the tandem group, this did not reach statistical significance.

Disclosures: Adnan H. Siddiqui—UNRELATED: Board Membership: Intersocietal Accreditation Commission; Consultancy: Codman, Medtronic, Guidepoint Global Consulting, Penumbra, Stryker Neurovascular, MicroVention, W.L. Gore and Associates, Three Rivers Medical Inc, Corindus Inc, Amnis Therapeutics Ltd, CereVasc LLC, Pulsar Vascular, The Stroke Project Inc, Cerebrotech Medical Systems Inc, Rapid Medical, Neuravi, Silk Road Medical, Rebound Therapeutics Corp, Claret Medical Inc, Comments: also Principal Investigator/National Steering Committees: Penumbra: 3D Separator Trial, COMPASS Trial, INVEST Trial; Covidien (now Medtronic): SWIFT PRIME and SWIFT DIRECT Trials; MicroVention: FRED Trial, CONFIDENCE Study; Codman & Shurtleff: LARGE Trial; MUSC: POSITIVE Trial; Stock/Stock Options: StimMed, Valor Medical, Neuro Technology Investors, Cardinal Health, Medina Medical Systems, Buffalo Technology Partners LLC, International Medical Distribution Partners. Elad I. Levy—UNRELATED: Board Membership: Stryker Neurovascular, NeXtGen Biologics, and MEDX, Comments: served on acute ischemic stroke Clinical Advisory Board for Stryker Neurovascular, serve on Advisory Board for NeXtGen Biologics and MEDX; no money; Consultancy: Pulsar Vascular; Payment for Development of Educational Presentations: Covidien, Comments: honorarium for training and lectures; Stock/Stock Options: Intratech Medical Ltd and NeXtGen Biologics, Comments: shareholder/ownership interest; Other: Abbott Vascular, Comments: carotid training sessions for physicians. Ajith J. Thomas—UNRELATED: Consultancy: Stryker

Neurovascular, Comments: data safety monitoring board\*; Expert Testimony: CRICO, Comments: expert witness, neurovascular. \*Money paid to the institution.

### REFERENCES

1. Inagawa T. **Incidence and risk factors for multiple intracranial saccular aneurysms in patients with subarachnoid hemorrhage in Izumo City, Japan.** *Acta Neurochir (Wien)* 2009;151:1623–30 CrossRef Medline
2. Kaminogo M, Yonekura M, Shibata S. **Incidence and outcome of multiple intracranial aneurysms in a defined population.** *Stroke* 2003;34:16–21 CrossRef Medline
3. Ostergaard JR, Hög E. **Incidence of multiple intracranial aneurysms: influence of arterial hypertension and gender.** *J Neurosurg* 1985;63:49–55 CrossRef Medline
4. Rinne J, Hernesniemi J, Puranen M, et al. **Multiple intracranial aneurysms in a defined population: prospective angiographic and clinical study.** *Neurosurgery* 1994;35:803–08 CrossRef Medline
5. Vajda J **Multiple intracranial aneurysms: a high risk condition.** *Acta Neurochir (Wien)* 1992;118:59–75 CrossRef Medline
6. Fang YB, Zhang ZL, Yang PF, et al. **Stepwise stent deployment technique for tandem intracranial aneurysms: a review of 21 cases.** *Eur Radiol* 2016;26:351–58 CrossRef Medline
7. Ichikawa T, Miyachi S, Izumi T, et al. **Fenestration of a supraclinoid internal carotid artery associated with dual aneurysms: case report.** *Neurosurgery* 2011;69:E1005–08; discussion E1009 CrossRef Medline
8. Lin N, Brouillard AM, Xiang J, et al. **Endovascular management of adjacent tandem intracranial aneurysms: utilization of stent-assisted coiling and flow diversion.** *Acta Neurochir (Wien)* 2015;157:379–87 CrossRef Medline
9. Mut F, Scrivano E, Bleise C, et al. **Hemodynamics in two tandem aneurysms treated with flow diverters.** *Int J Numer Methods Biomed Eng* 2014;30:517–24 CrossRef Medline
10. Adeeb N, Griessenauer CJ, Moore J, et al. **Pipeline embolization device for recurrent cerebral aneurysms after microsurgical clipping.** *World Neurosurg* 2016;93:341–45 CrossRef Medline
11. Becske T, Kallmes DF, Saatci I, et al. **Pipeline for uncoilable or failed aneurysms: results from a multicenter clinical trial.** *Radiology* 2013;267:858–68 CrossRef Medline
12. Griessenauer CJ, Ogilvy CS, Foreman PM, et al. **Pipeline embolization device for small intracranial aneurysms: evaluation of safety and efficacy in a multicenter cohort.** *Neurosurgery* 2017;80:579–87 CrossRef Medline
13. Kühn AL, Hou SY, Perras M, et al. **Flow diverter stents for unruptured saccular anterior circulation perforating artery aneurysms: safety, efficacy, and short-term follow-up.** *J Neurointerv Surg* 2015;7:634–40 CrossRef Medline
14. Lin N, Brouillard AM, Keigher KM, et al. **Utilization of Pipeline embolization device for treatment of ruptured intracranial aneurysms: US multicenter experience.** *J Neurointerv Surg* 2015;7:808–15 CrossRef Medline
15. Nelson PK, Lylyk P, Szikora I, et al. **The Pipeline embolization device for the intracranial treatment of aneurysms trial.** *AJNR Am J Neuroradiol* 2011;32:34–40 CrossRef Medline
16. Li TF, Shui SF, Han XW, et al. **One-stage endovascular embolization for multiple intracranial aneurysms.** *Turk Neurosurg* 2016 Jul 25. [Epub ahead of print] CrossRef Medline

# Non-Contrast-Enhanced Silent Scan MR Angiography of Intracranial Anterior Circulation Aneurysms Treated with a Low-Profile Visualized Intraluminal Support Device

 N. Takano,  M. Suzuki,  R. Irie,  M. Yamamoto,  K. Teranishi,  K. Yatomi,  N. Hamasaki,  K.K. Kumamaru,  M. Hori,  H. Oishi, and  S. Aoki



## ABSTRACT

**BACKGROUND AND PURPOSE:** The Low-Profile Visualized Intraluminal Support Device comprises a small-cell nitinol structure and a single-wire braided stent that provides greater metal coverage than previously reported intracranial stents, as well as assumed strong susceptibility artifacts. This study aimed to assess the benefits of non-contrast-enhanced MRA by using a Silent Scan (Silent MRA) for intracranial anterior circulation aneurysms treated with Low-Profile Visualized Intraluminal Support Device stents.

**MATERIALS AND METHODS:** Thirty-one aneurysms treated with Low-Profile Visualized Intraluminal Support Device stents were assessed by using Silent MRA, 3D TOF-MRA, and x-ray DSA. The quality of MRA visualization of the reconstructed artery was graded on a 4-point scale from 1 (not visible) to 4 (excellent). Aneurysm occlusion status was evaluated by using a 2-grade scale (total occlusion/remnant [neck or aneurysm]). Weighted  $\kappa$  statistics were used to evaluate interobserver and intermodality agreement.

**RESULTS:** The mean scores  $\pm$  SDs for Silent MRA and 3D TOF-MRA were  $3.16 \pm 0.79$  and  $1.48 \pm 0.67$  ( $P < .05$ ), respectively, with substantial interobserver agreement ( $\kappa = 0.66$ ). The aneurysm occlusion rates of the 2-grade scale (total occlusion/remnant [neck or aneurysm]) were 69%/31% for DSA, 65%/35% for Silent MRA, and 92%/8% for 3D TOF-MRA, respectively. The intermodality agreements were 0.88 and 0.30 for DSA/Silent MRA and DSA/3D TOF-MRA, respectively.

**CONCLUSIONS:** Silent MRA seems to be useful for visualizing intracranial anterior circulation aneurysms treated with Low-Profile Visualized Intraluminal Support Device stents.

**ABBREVIATIONS:** CE = contrast-enhanced; LVIS Jr. = Low-Profile Visualized Intraluminal Support Device; UTE = ultrashort TE

Endovascular treatment involving coil embolization is commonly used to manage both ruptured and unruptured intracranial aneurysms.<sup>1,2</sup> In recent years, intracranial stents, including the Neuroform<sup>3,4</sup> (Stryker, Kalamazoo, Michigan) and Enterprise stents<sup>5,6</sup> (Codman & Shurtleff, Raynham, Massachusetts), have been implemented for the stent-assisted coil embolization of wide-neck

aneurysms. Both types of stents comprise nitinol and are self-expandable. The Neuroform stent features an open-cell design with stainless steel and platinum markers,<sup>7,8</sup> whereas the Enterprise stent is a closed-cell design with tantalum markers.<sup>9,10</sup>

This study implemented the Low-Profile Visualized Intraluminal Support Device<sup>11-14</sup> (LVIS Jr. stent; MicroVention, Tustin, California), a self-expandable nitinol single-wire braided stent comprising 1.5-mm cells. The LVIS Jr. stent contains 3 radiopaque tantalum markers on the proximal and distal tines and 3 tantalum helical strands in the stent body<sup>13,14</sup>; thus, it provides higher metal coverage (12%–21%)<sup>11-13</sup> relative to previously reported stents. Accordingly, stent-related magnetic susceptibility during MR imaging is a topic of research interest.

Despite reports of the use of 3D TOF-MRA after stent-assisted coil embolization,<sup>9</sup> the radiofrequency shielding and susceptibility artifacts make it difficult to visualize flow in an intracranial stent with this technique. Because the LVIS Jr. stent is composed of nitinol and features a braided component and higher metal coverage relative to earlier stents, this device may not facilitate depiction of an intracranial stent with 3D TOF-MRA for radiofrequency shielding and susceptibility artifacts.

Received December 15, 2016; accepted after revision March 14, 2017.

From the Department of Radiology (N.T., M.S., K.K.K., M.H., S.A.), Graduate School of Medicine, Juntendo University, Tokyo, Japan; Department of Radiology (N.T., M.S., R.I., N.H., K.K.K., M.H., S.A.), Juntendo University Hospital, Tokyo, Japan; and Departments of Neurosurgery (M.Y., K.T., K.Y., H.O.) and Neuroendovascular Therapy (H.O.), Juntendo University School of Medicine, Tokyo, Japan.

This work was funded by the Impulsing Paradigm Change through disruptive Technologies Program of the Council for Science, Technology, and Innovation (Cabinet Office, Government of Japan). This work was also supported by the Japan Society for the Promotion of Science Grants-in-Aid for Scientific Research Grant No. JP16H06280 and Grant-in-Aid for Scientific Research on Innovative Areas, resource and technical support platforms for promoting research “Advanced Bioimaging Support.”

Please address correspondence to Nao Takano, RT, MMSc, Department of Radiology, Graduate School of Medicine, Juntendo University, 2-1-1 Hongo, Bunkyo-ku, Tokyo 113-8421, Japan; e-mail: ntakano@juntendo.ac.jp

 Indicates open access to non-subscribers at [www.ajnr.org](http://www.ajnr.org)

<http://dx.doi.org/10.3174/ajnr.A5223>

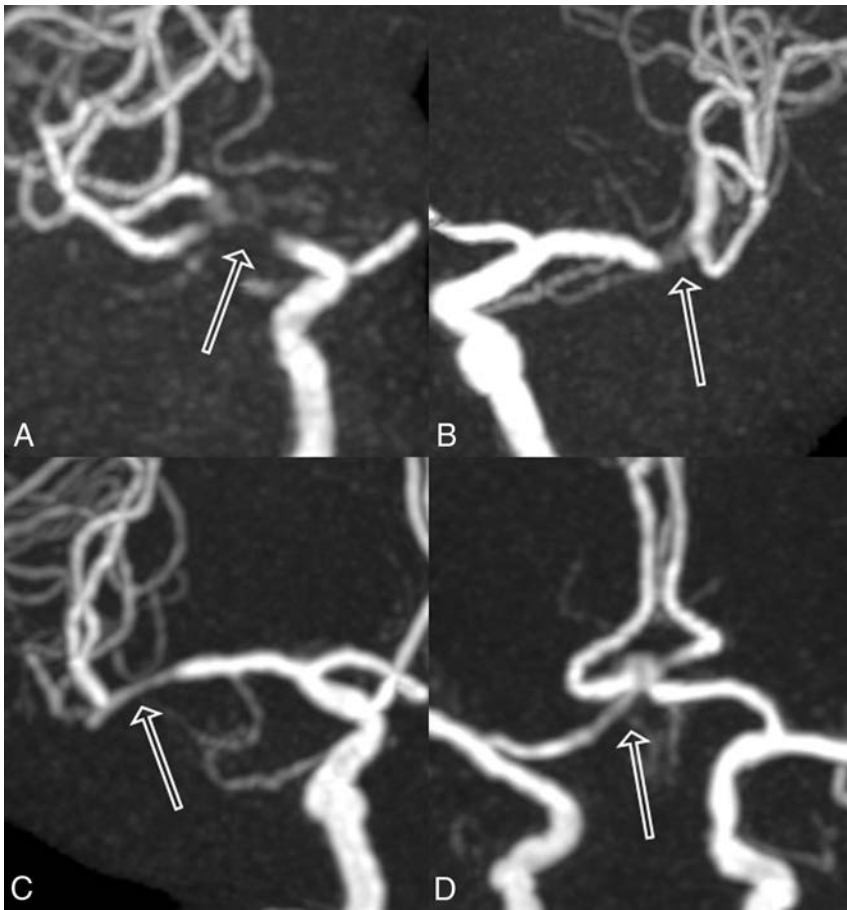


**FIG 1.** Examples of MRA scoring. The MRA scores by 2 observers were classified on a 4-point scale as follows: 1, (A); 2, (B); 3, (C); 4, (D). Outlined arrows are the stented segment.

Silent Scan (GE Healthcare, Milwaukee, Wisconsin) MRA (Silent MRA) is a non-contrast-enhanced MRA technique that uses an ultrashort TE (UTE) combined with arterial spin-labeling,<sup>15</sup> which is used as a preparation pulse to visualize blood flow. Subsequent data acquisition is based on 3D radial sampling.<sup>15,16</sup> Because UTE decreases the susceptibility artifacts associated with metallic devices, Silent MRA could potentially reduce the artifacts associated with braided, high-metal-coverage stents. Accordingly, we evaluated the efficacy of Silent MRA versus 3D TOF-MRA for intracranial anterior circulation aneurysms treated with LVIS Jr. stent-assisted coil embolization.

## MATERIALS AND METHODS

### Patient and Aneurysm Characteristics

Between July 2015 and September 2016, 32 aneurysms in 29 patients treated with LVIS Jr. stent-assisted coil embolization for anterior circulation aneurysms were retrospectively examined. We obtained approval for this study from the ethics review board. Written informed consent was not required because of the retrospective nature of this study. One patient was excluded from the study due to postoperative deep brain stimulation with an MR imaging-unsafe device. The remaining 28 patients with 31 aneurysms comprised 13 men and 15 women with a mean age of  $60.8 \pm 11.3$  years (range, 41–77 years). Twenty-one aneurysms were treated with a single stent, and 10 were treated with 2 stents (ie, 41 LVIS Jr. stents were

used in 31 aneurysms). We deployed the following stent sizes (diameter  $\times$  length):  $2.5 \times 13$  mm ( $n = 21$ );  $2.5 \times 17$  mm ( $n = 14$ );  $2.5 \times 23$  mm ( $n = 3$ ); and  $3.5 \times 18$  mm,  $3.5 \times 23$  mm, and  $3.5 \times 28$  mm ( $n = 1$  each). The distribution of aneurysm locations was as follows: anterior communicating artery ( $n = 15$ ), internal carotid artery ( $n = 3$ ), and middle cerebral artery ( $n = 13$ ).

For all patients, Silent MRA and 3D TOF-MRA were performed in a single scanning session. The average interval between aneurysm treatment and both MRA evaluations was 5.6 days (range, 1–83 days; median, 1 day). The average interval between the most recent DSA evaluation and both MRA evaluations was 1.6 days (range, 1–9 days; median, 1 day).

### Silent MRA

Silent MRA was performed with a Silent Scan. However, the details of the Silent Scan algorithm were undisclosed. Silent Scan is a combination of a 3D acquisition and reconstruction technology. This technique requires highly stable system power electronics (gradients and radiofrequency) and fast radiofrequency switching capability within the radiofrequency coil structure.

This process slowly steps the gradients while collecting data during a 3D acquisition. The data acquisition is based on a 3D radial sampling, and an arterial spin-labeling technique is used as a preparation pulse to visualize blood flow. In Silent MRA, control images (nonlabelled images) are scanned before the labeling pulse. Labeled images are scanned after the labeling pulse, and the labeled blood exhibits low signal intensity. The angiographic images of blood flow are the result of subtraction of labeled images from control images.

### Intra-Arterial DSA Technique

X-ray catheter-based intra-arterial cerebral DSA was performed with the following biplane angiographic system: Artis Q BA Twin (Siemens, Erlangen, Germany). The image matrix and FOV were  $1024 \times 1024$  and  $170 \times 170$  mm, respectively. The temporal resolution was 3 frames per second. Selective manual internal carotid artery injections were administered according to the aneurysm location. Rotational 3D angiography was performed for additional confirmation of the findings. Additional selected working angles were obtained to clarify the aneurysmal anatomy at the discretion of the neurosurgical interventionist.

### MRA Scan Parameters

Silent MRA and 3D TOF-MRA were performed on a 3T MR imaging unit (Discovery MR750w; GE Healthcare) with a 12-channel

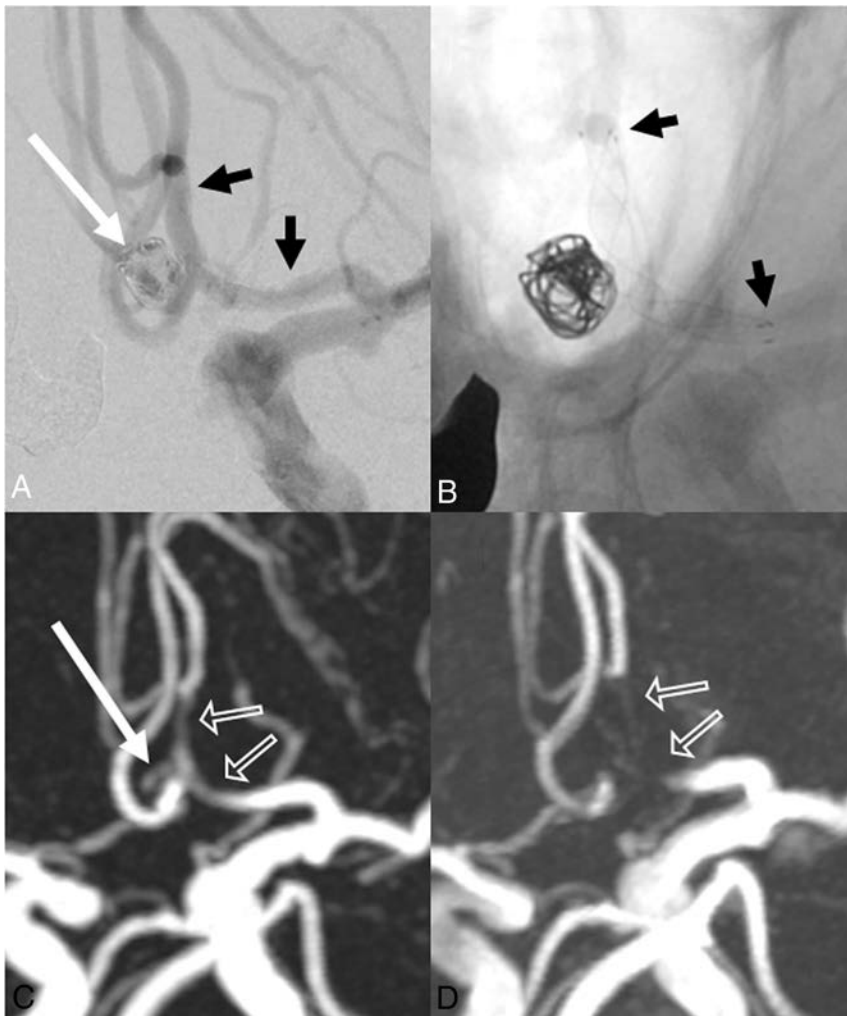


**FIG 2.** A 73-year-old woman. A, Stent-assisted coil embolization of the anterior communicating artery was performed with a LVIS Jr. stent ( $2.5 \times 17$  mm). The aneurysm remnant is indicated by the long white arrow. Short black arrows indicate stent edges. B, X-ray digital angiography reveals stent edges (short black arrows). C, Silent MRA shows minimal signal loss at the stented segment (outlined arrows). The aneurysm remnant is visible (long white arrow). D, 3D time-of-flight MRA shows complete signal losses at the stented segments (outlined arrows). The aneurysm remnant is not depicted. The scores of Silent MRA by 2 observers are 4 and 4. The scores of 3D TOF-MRA are 1 and 1.

head-neck coil system. The following scan parameters were used for Silent MRA: TR/TE, 642.8/0.016 ms; flip angle,  $5^\circ$ ; FOV,  $180 \times 180$  mm; matrix,  $180 \times 180$ ; section thickness, 1.0 mm (with section interpolation); NEX, 1.4; bandwidth,  $\pm 31.2$  kHz; acquisition time, 12 minutes 13 seconds; and reconstructed voxel size,  $1.0 \times 1.0 \times 0.5$  mm.

The 3D TOF-MRA scan parameters were as follows: TR/TE, 20/2.9 ms; flip angle,  $18^\circ$ ; FOV,  $200 \times 200$  mm; acquisition matrix,  $416 \times 224$ ; section thickness, 1.0 mm (with section interpolation); NEX, 1; bandwidth,  $\pm 41.7$  kHz; acquisition time, 4 minutes 45 seconds (3 slabs, overlap between a slab: 14 sections, 1 slab: 38 sections); reconstruction matrix, 512; and reconstructed voxel size,  $0.39 \times 0.39 \times 0.5$  mm.

### Image Analysis

Each DSA, Silent MRA, and 3D TOF-MRA series was anonymized by random number assignment. We evaluated DSA images and the 2 types of MRA images. The 2 types of MRA images were

assessed separately to minimize bias due to knowledge of the results of the other MRA image. We used MIP and source images. All images were independently evaluated in random order by 2 neuro-radiologists (M.S. and R.I., who have 15 and 6 years of experience in neuroradiology, respectively) on the PACS. In all images, the window-width and window-level could be modified for evaluation. The locations of the treated aneurysms to be evaluated were provided to the 2 observers because the pretreatment x-ray DSA images were unavailable.

The quality of Silent MRA- and 3D TOF-MRA-based visualization of the reconstructed arteries was evaluated. Two neuro-radiologists independently reviewed both types of MRAs and rated visualization of the flow in each stent subjectively on a 4-point scale as follows: 1, not visible (near-complete signal loss or no signal); 2, poor (structures are slightly visible but with substantial artifacts or blurring); 3, acceptable (acceptable diagnostic quality with medium artifacts or blurring); 4, excellent (good diagnostic quality with minimal artifacts or blurring). Figure 1 shows a sample of the 4-point scale. Aneurysm occlusion was evaluated by using a 2-grade scale (total occlusion/remnant [neck or aneurysm]). The most recent DSA images were used as a reference standard.

### Statistical Analysis

The scores of MIP images from the 2 observers were averaged, and the scores were compared between techniques by using the Wilcoxon signed rank test. A

$P$  value  $< .05$  was statistically significant. Weighted  $\kappa$  statistics were used to evaluate interobserver and intermodality agreement. According to Landis and Koch,<sup>17</sup>  $\kappa$  was interpreted as follows:  $<0$ , no agreement; 0–0.19, poor agreement; 0.20–0.39, fair agreement; 0.40–0.59, moderate agreement; 0.60–0.79, substantial agreement; and 0.80–1.00, almost perfect agreement. All statistical analyses were performed by using SPSS software, Version 22 (IBM, Armonk, New York).

### RESULTS

The mean scores ( $\pm$  SDs) for Silent MRA and 3D TOF-MRA differed significantly, with respective values of  $3.16 \pm 0.79$  and  $1.48 \pm 0.67$  ( $P < .05$ ), and substantial interobserver agreement was observed ( $\kappa = 0.66$ ). The aneurysm occlusion rates of the 2-grade scale (total occlusion/remnant [neck or aneurysm]) were 69%/31% for DSA, 65%/35% for Silent MRA, and 92%/8% for 3D TOF-MRA. Intermodality agreement values of 0.88 and 0.30 were obtained for DSA/Silent MRA and DSA/3D TOF-MRA, respectively. Figures 2–4 are representative images.

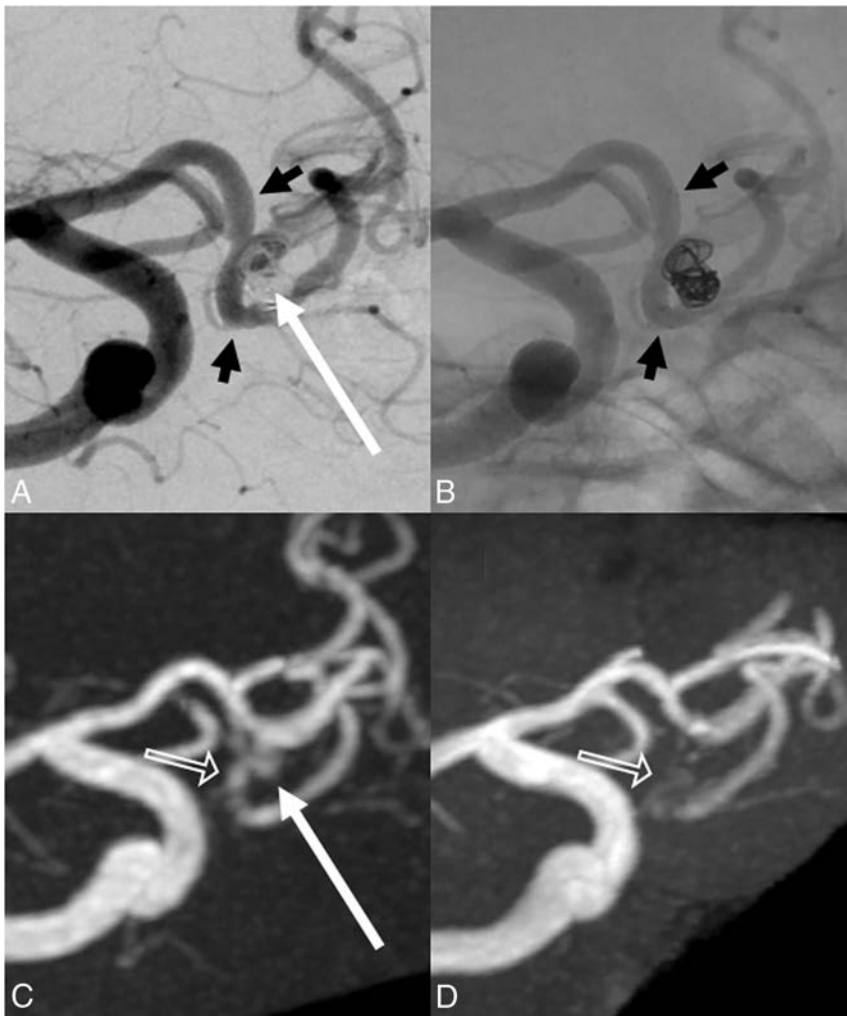


**FIG 3.** A 71-year-old man. A, Stent-assisted coil embolization of the anterior communicating artery is performed with a LVIS Jr. stent (2.5 × 17 mm). The neck remnant is indicated by the long white arrow. Short black arrows indicate stent edges. B, X-ray digital angiography shows the stent edges (short black arrows). C, Silent MRA shows minimal signal loss at the stented segment (outlined arrow). The neck remnant is depicted almost equally well as with digital subtraction angiography (long white arrow). D, 3D time-of-flight MRA shows almost complete signal loss in the stented segment (outlined arrow). The neck remnant is not depicted. The scores of Silent MRA by 2 observers are 4 and 4. The scores of 3D TOF-MRA are 1 and 1.

## DISCUSSION

This study demonstrated superior visualization of the reconstructed artery with Silent MRA compared with 3D TOF-MRA in patients treated with LVIS Jr. stents. With consensual x-ray DSA as a reference standard, the intermodality agreement was better with Silent MRA than with 3D TOF-MRA. Moreover, Silent MRA showed strong concordance with DSA for the detection of occluded aneurysms, despite the small diameter of the LVIS Jr. stent.

Several studies have evaluated LVIS Jr. stent-assisted coil embolization<sup>11-14</sup>; however, none have used MRA for follow-up evaluations after treatment with LVIS Jr. stents, though 3D TOF-MRA, Silent MRA, and contrast-enhanced (CE)-MRA have been used to follow up patients who underwent other stent-assisted coil embolizations.<sup>7,9,10,15,18</sup> Cho et al<sup>9</sup> reported a good correlation between 3D rotational angiography and 3D TOF-MRA, which was attributed to the very small voxel size, whereas Irie et al<sup>15</sup> reported the efficacy of Silent MRA in stent-assisted coil embolization. Although the authors reported superior visualization of neck remnants with Silent MRA

versus 3D TOF-MRA, they assessed only closed-cell Enterprise stents. Takano et al<sup>19</sup> reported on a Silent MRA study in Y-configuration stent-assisted coil embolization. The visualization ability of Silent MRA was superior to that of 3D TOF-MRA in a study that included Neuroform, Enterprise, and LVIS Jr. stents. In this study, Silent MRA showed neck remnants more precisely than did 3D TOF-MRA. In contrast, Agid et al<sup>7</sup> reported that CE-MRA better depicted flow in a stent, compared with 3D TOF-MRA, in a study that included Neuroform, Enterprise, and LEO (Balt Extrusion, Montmorency, France) stents. CE-MRA and DSA had similar visualization abilities; however, CE-MRA was associated with several complications such as nephrogenic systemic fibrosis,<sup>20</sup> gadolinium accumulation,<sup>21</sup> and anaphylactic shock.

In this study, although Silent MRA had a larger matrix size than 3D TOF-MRA, it yielded superior visualization of the reconstructed artery. This outcome was attributed to the use of a UTE, which minimizes phase dispersion of the labeled blood flow signal and reduces magnetic susceptibility artifacts. Specifically, the TE was 2.9 ms during 3D TOF-MRA, but only 0.016 ms during Silent MRA. Choi et al<sup>8</sup> reported that a short TE could increase signal intensity while optimizing the stent-visualization parameter. Similarly, Yamada et al<sup>22</sup> reported that a TE of 1.54–1.60 ms was used in their 3D TOF-MRA study, and Ikushima et al<sup>23</sup> reported that a wide bandwidth (short TE) could increase the in-stent signal intensity and in-coil signal intensity during a CE-MRA phantom study. Furthermore, Irie et al<sup>15</sup> reported a TE of 0.016 ms during Silent MRA. In our study, Silent MRA with a UTE allowed the precise visualization of in-stent flow.

A LVIS Jr. stent diameter of 2.5 mm was used for 38 stent placements in 28 patients (93%). During 3D TOF-MRA, the in-stent signal in this type of stent is affected by susceptibility artifacts caused by stents and coils. Therefore, the use of a small-diameter stent is more likely to reduce the in-stent signal. In contrast, Silent MRA allows precise visualization of the in-stent signal. The UTE used with this technique can minimize phase dispersion of the labeled blood flow signal in the voxel and reduce the magnetic susceptibility artifacts. Accordingly, artifacts caused by stents or coils are reduced.

Notably, Silent MRA yields better detection of aneurysm occlusions compared with 3D TOF-MRA. Because 3D TOF-MRA uses the inflow effect to visualize blood flow signal, a higher flip

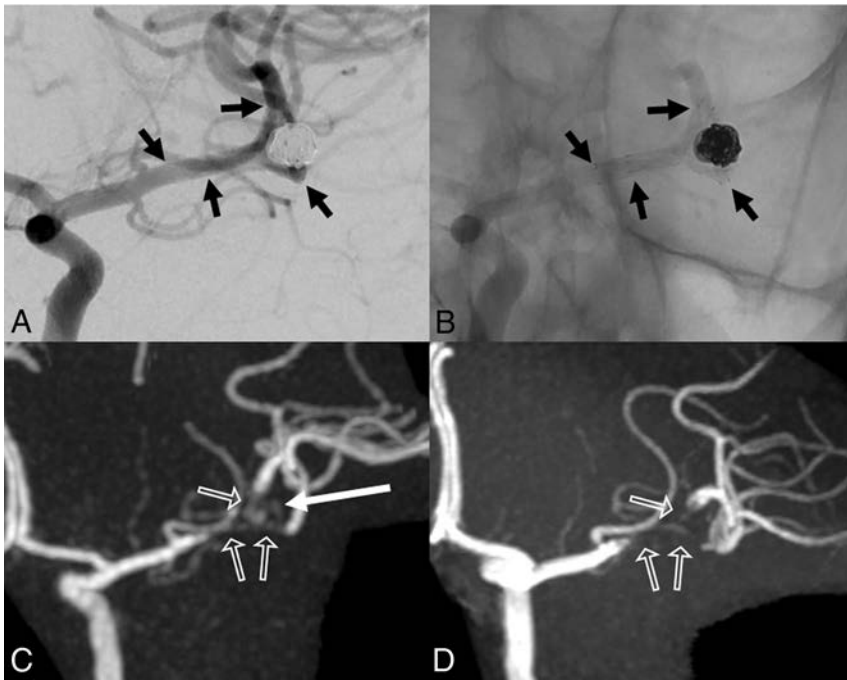


**FIG 4.** A 45-year-old woman. *A*, Stent-assisted coil embolization is performed with LVIS Jr. stents ( $2.5 \times 13$  mm and  $2.5 \times 17$  mm) for a left middle cerebral artery bifurcation. The neck or aneurysm remnant is not depicted. *Short black arrows* indicate stent edges. *B*, X-ray digital angiography indicates stent edges (*short black arrows*). *C*, Silent MRA depicts the aneurysm remnant (*long white arrow*). Stented segments are slightly visible, and moderate signal loss is apparent on Silent MRA (*outlined arrows*). *D*, 3D time-of-flight MRA does not depict the neck or aneurysm remnant and yields a complete signal loss at the stented segment (*outlined arrows*). The scores of Silent MRA by 2 observers are 3 and 2. The scores of 3D TOF-MRA are 1 and 1.

angle is needed to increase the signal intensity<sup>8,24,25</sup>; however, in areas of slow or turbulent flow, the saturation effect caused by a high flip angle decreases the signal intensity. Therefore, visualization of the neck remnant is difficult, even if the higher flip angle increases the signal intensity in the stent. In contrast, Silent MRA yields good visualization of the neck remnant because it uses arterial spin-labeling and UTE for blood flow depiction and phase dispersion, respectively.

Most interesting, in our series, a helmet-type remnant<sup>26</sup> was detected in 3 patients by Silent MRA. This remnant type is caused by a lack of x-ray penetration of the coil mass itself. According to Agid et al,<sup>26</sup> CE-MRA is superior to x-ray DSA for the detection of helmet-type remnants. Notably, Silent MRA may similarly detect helmet-type remnants and has the advantage of being a non-contrast-enhanced technique. Figure 4 demonstrates a helmet-type remnant.

The self-expandable, single-wire braided nature of the LVIS Jr. stent allows greater metal coverage of the blood vessel, compared with conventional open-cell and closed-cell stents. The open-cell Neuroform stent and closed-cell Enterprise stent yield 11% and 10% coverage, respectively,<sup>14</sup> and flow-diverter stents yield approximately 30%–35%<sup>27</sup> coverage. In contrast, the LVIS Jr. stent yields approximately 12%–21% coverage.<sup>11–13</sup> Furthermore, the adaptation blood vessel diameter is smaller with the LVIS Jr. stent compared with the Neuroform and Enterprise stents. Because the metal quantity per unit blood vessel area increases with the LVIS Jr. stent, 3D TOF-

MRA depictions of the neck remnants of aneurysms are thought to be more difficult following LVIS Jr. stent placement, compared with Neuroform and Enterprise stent placement.

Nevertheless, our study observed a good intermodality agreement between DSA and Silent MRA during an evaluation of aneurysm occlusion. In particular, Silent MRA and x-ray DSA yielded results of similar quality, a finding that was attributed to the reduction in susceptibility artifacts as a result of using a UTE during Silent MRA. In addition, the blood flow saturation effect was reduced when using arterial spin-labeling for blood flow depiction. Thus, Silent MRA might be useful for follow-ups of patients treated with LVIS Jr. stents.

Silent MRA can be used to visualize the in-stent flow. Moreover, it can depict a neck remnant also shown with x-ray DSA. Therefore, Silent MRA can be used as a substitute for the x-ray DSA.

One of the disadvantages of Silent MRA is motion artifacts due to the long scanning duration. However, only a few cases showed severe motion artifacts. In many cases, the artifacts were caused by

an oral motion, so there was not much influence on the depiction of intracranial blood vessels. The acquisition time required for Silent MRA is very long for clinical use, but it offers advantages in the visualization of in-stent flow.

Our study had some limitations. First, the sample size was small; preferably, we would add additional cases. Second, we did not evaluate CE-MRA, which is known to be useful for follow-ups after stent-assisted coil embolization<sup>7,18,24</sup> and depiction of helmet-type remnants.<sup>26</sup> Therefore, comparative evaluations with CE-MRA are also required. Third, in this study, we evaluated only anterior circulation aneurysm cases. Additional study is needed because posterior circulation aneurysm cases may yield different results. Fourth, a Pointwise Encoding Time Reduction with Radial Acquisition (PETRA) MRA sequence (Siemens) with similarities to Silent MRA has been reported,<sup>28,29</sup> and this sequence may yield results similar to those of the present study. A comparison of these sequences should be performed in the future.

We did not set the time interval between the MRA readings. This study may be biased by a neuroradiologist's recognition of previous MRA images. Experienced neuroradiologists might recognize 2 types of MRA images of the same subject. Therefore, this evaluation may, in effect, be nonblinded. Moreover, in this study, there are some of cases of differences in the duration of the period between the evaluation of DSA and MRA images (average, 1.6 days; range, 1–9 days; median, 1 day). These differences may lead to changes in remnant size.

## CONCLUSIONS

Silent MRA is superior to 3D TOF-MRA in the quality of visualization of a reconstructed artery and has strong concordance with DSA for the detection of aneurysm occlusions. Moreover, Silent MRA may detect helmet-type remnants, thus eliminating the need for gadolinium contrast agents. Silent MRA might therefore be useful for intracranial anterior circulation aneurysms treated with LVIS Jr. stent-assisted coil embolization.

## ACKNOWLEDGMENTS

The authors thank Shuji Sato, Hideo Kawasaki, Issei Fukunaga, Tomoya Muroi, and Haruyoshi Hoshito (Radiologic Technologists, Department of Radiology) for their technical advice.

Disclosures: Nao Takano—*RELATED: Grant:* Impulsing Paradigm Change through disruptive Technologies Program of the Council for Science, Technology, and Innovation (Cabinet Office, Government of Japan) and Grant-in-Aid for Scientific Research on Innovative Areas, resource and technical support platforms for promoting research “Advanced Bioimaging Support.” *Comments:* This work was funded by the Impulsing Paradigm Change through disruptive Technologies Program of the Council for Science, Technology, and Innovation (Cabinet Office, Government of Japan). This work was also supported by the Japan Society for the Promotion of Science Grants-in-Aid for Scientific Research Grant No. JP16H06280, Grant-in-Aid for Scientific Research on Innovative Areas, resource and technical support platforms for promoting research “Advanced Bioimaging Support”\*; *UNRELATED: Payment for Lectures Including Service on Speakers Bureaus:* GE Healthcare Japan, *Comments:* 42nd Japanese Society of Radiological Technology Autumn Scientific Congress, October 9–11, 2014, Sapporo, Hokkaido, Japan, and luncheon seminar, “Experience of MR angiography (Silent MRA) using Silenz sequence.” Shigeki Aoki—*UNRELATED: Board Membership:* Bayer Yakuhin; *Consulting Fee or Honorarium:* GE Healthcare, *Comments:* luncheon lecture; *Grants/Grants Pending:* Bayer Yakuhin, Daiich-Sankyo, Eisai, Fuji Seiyaku; *Payment for Lectures Including Service on Speakers Bureaus:* Bayer Yakuhin, Daiich-Sankyo, Eisai, Fuji Seiyaku, Toshiba, GE Healthcare, Hitachi, Siemens. \*Money paid to the institution.

## REFERENCES

1. Molyneux AJ, Kerr RS, Yu LM, et al. **International Subarachnoid Aneurysm Trial (ISAT) of neurosurgical clipping versus endovascular coiling in 2143 patients with ruptured intracranial aneurysms: a randomised comparison of effects on survival, dependency, seizures, rebleeding, subgroups, and aneurysm occlusion.** *Lancet* 2005;366:809–17 Medline
2. Pierot L, Spelle L, Vitry F, et al; ATENA Investigators. **Immediate clinical outcome of patients harboring unruptured intracranial aneurysms treated by endovascular approach: results of the ATENA study.** *Stroke* 2008;39:2497–504 CrossRef Medline
3. Benitez RP, Silva MT, Klem J, et al. **Endovascular occlusion of wide-necked aneurysms with a new intracranial microstent (Neuroform) and detachable coils.** *Neurosurgery* 2004;54:1359–67; discussion 1368 CrossRef Medline
4. Fiorella D, Albuquerque FC, Deshmukh VR, et al. **Usefulness of the Neuroform stent for the treatment of cerebral aneurysms: results at initial (3–6 mo) follow up.** *Neurosurgery* 2005;56:1191–201; discussion 1201–02 CrossRef Medline
5. Mocco J, Snyder KV, Albuquerque FC, et al. **Treatment of intracranial aneurysms with the Enterprise stent: a multicenter registry.** *J Neurosurg* 2009;110:35–39 CrossRef Medline
6. Higashida RT, Halbach VV, Dowd CF, et al. **Initial clinical experience with a new self-expanding nitinol stent for the treatment of intracranial cerebral aneurysms: the Cordis Enterprise stent.** *AJNR Am J Neuroradiol* 2005;26:1751–56 Medline
7. Agid R, Schaaf M, Farb R. **CE-MRA for follow-up of aneurysms post stent-assisted coiling.** *Interv Neuroradiol* 2012;18:275–83 CrossRef Medline
8. Choi JW, Roh HG, Moon WJ, et al. **Optimization of MR parameters of 3D TOF-MRA for various intracranial stents at 3.0T MRI.** *Neurointervention* 2011;6:71 CrossRef Medline
9. Cho WS, Kim SS, Lee SJ, et al. **The effectiveness of 3T time-of-flight magnetic resonance angiography for follow-up evaluations after the stent-assisted coil embolization of cerebral aneurysms.** *Acta Radiol* 2014;55:604–13 CrossRef Medline
10. Takayama K, Taoka T, Nakagawa H, et al. **Usefulness of contrast-enhanced magnetic resonance angiography for follow-up of coil embolization with the Enterprise stent for cerebral aneurysms.** *J Comput Assist Tomogr* 2011;35:568–72 CrossRef Medline
11. Spiotta AM, Miranpuri A, Chaudry MI, et al. **Combined balloon stent technique with the Scepter C balloon and low-profile visualized intraluminal stent for the treatment of intracranial aneurysms.** *J Neurointerv Surg* 2013;5:iii79–82 CrossRef Medline
12. Möhlenbruch M, Herweh C, Behrens L, et al. **The LVIS Jr. microstent to assist coil embolization of wide-neck intracranial aneurysms: clinical study to assess safety and efficacy.** *Neuroradiology*. 2014;56:389–95 CrossRef Medline
13. Behme D, Weber A, Kowoll A, et al. **Low-Profile Visualized Intraluminal Support device (LVIS Jr) as a novel tool in the treatment of wide-necked intracranial aneurysms: initial experience in 32 cases.** *J Neurointerv Surg* 2015;7:281–85 CrossRef Medline
14. Ge H, Lv X, Yang X, et al. **LVIS stent versus Enterprise Stent for the treatment of unruptured intracranial aneurysms.** *World Neurosurg* 2016;91:365–70 CrossRef Medline
15. Irie R, Suzuki M, Yamamoto M, et al. **Assessing blood flow in an intracranial stent: a feasibility study of MR angiography using a Silent Scan after stent-assisted coil embolization for anterior circulation aneurysms.** *AJNR Am J Neuroradiol* 2015;36:967–70 CrossRef Medline
16. Alibek S, Vogel M, Sun W, et al. **Acoustic noise reduction in MRI using Silent Scan: an initial experience.** *Diagn Interv Radiol* 2014;20:360–63 CrossRef Medline
17. Landis JR, Koch GG. **The measurement of observer agreement for categorical data.** *Biometrics* 1977;33:159–74 CrossRef Medline
18. Choi JW, Roh HG, Moon WJ, et al. **Time-resolved 3D contrast-enhanced MRA on 3.0T: a non-invasive follow-up technique after stent-assisted coil embolization of the intracranial aneurysm.** *Korean J Radiol* 2011;12:662–70 CrossRef Medline
19. Takano N, Suzuki M, Irie R, et al. **Usefulness of non-contrast-enhanced MR angiography using a Silent Scan for follow-up after Y-configuration stent-assisted coil embolization for basilar tip aneurysms.** *AJNR Am J Neuroradiol* 2017;38:577–81 CrossRef Medline
20. Penfield JG, Reilly RF. **Nephrogenic systemic fibrosis risk: is there a difference between gadolinium-based contrast agents?** *Semin Dial* 2008;21:129–34 CrossRef Medline
21. Kanda T, Ishii K, Kawaguchi H, et al. **High signal intensity in the dentate nucleus and globus pallidus on unenhanced T1-weighted MR images: relationship with increasing cumulative dose of a gadolinium-based contrast material.** *Radiology* 2014;270:834–41 CrossRef Medline
22. Yamada N, Hayashi K, Murao K, et al. **Time-of-flight MR angiography targeted to coiled intracranial aneurysms is more sensitive to residual flow than is digital subtraction angiography.** *AJNR Am J Neuroradiol* 2004;25:1154–57 Medline
23. Ikushima Y, Hashido T, Watanabe Y, et al. **Effects of imaging parameters on the quality of contrast-enhanced MR angiography of cerebral aneurysms treated using stent-assisted coiling: a phantom study.** *Magn Reson Med Sci* 2017;16:146–51 CrossRef Medline
24. Wang Y, Truong TN, Yen C, et al. **Quantitative evaluation of susceptibility and shielding effects of nitinol, platinum, cobalt-alloy, and stainless steel stents.** *Magn Reson Med* 2003;49:972–76 CrossRef Medline
25. van Holten J, Wielopolski P, Brück E, et al. **High flip angle imaging of metallic stents: implications for MR angiography and intraluminal signal interpretation.** *Magn Reson Med* 2003;50:879–83 CrossRef Medline
26. Agid R, Willinsky RA, Lee SK, et al. **Characterization of aneurysm remnants after endovascular treatment: contrast-enhanced MR an-**

- giography versus catheter digital subtraction angiography. *AJNR Am J Neuroradiol* 2008;29:1570–74 CrossRef Medline
27. Boddu SR, Tong FC, Dehkarghani S, et al. **Contrast-enhanced time-resolved MRA for follow-up of intracranial aneurysms treated with the Pipeline embolization device.** *AJNR Am J Neuroradiol* 2014;35:2112–18 CrossRef Medline
28. Koktzoglou I, Giri S, Piccini D, et al. **Arterial spin-labeled carotid MR angiography: a phantom study examining the impact of technical and hemodynamic factors.** *Magn Reson Med* 2016;75:295–301 CrossRef Medline
29. Grodzki DM, Jakob PM, Heismann B. **Ultrashort echo time imaging using Pointwise Encoding Time reduction with Radial Acquisition (PETRA).** *Magn Reson Med* 2012;67:510–18 CrossRef Medline

# Jugular Anomalies in Multiple Sclerosis Are Associated with Increased Collateral Venous Flow

 S.K. Sethi,  A.M. Daugherty,  G. Gadda,  D.T. Utraiainen,  J. Jiang,  N. Raz, and  E.M. Haacke



## ABSTRACT

**BACKGROUND AND PURPOSE:** To date, research on extracranial venous collaterals has been focused on structure, with relatively little attention paid to hemodynamics. We addressed this limitation by quantitatively comparing collateral flow in patients with multiple sclerosis and healthy controls by using phase-contrast MR imaging. We hypothesize that patients with MS with structurally anomalous internal jugular veins will have elevated collateral venous flow compared with healthy controls.

**MATERIALS AND METHODS:** The sample consisted of 276 patients with MS and 106 healthy controls. We used MRV to classify internal jugular veins as stenotic and nonstenotic based on an absolute cross-sectional area threshold in 276 patients with MS and 60 healthy controls; 46 healthy controls lacked this imaging. Individual and total vessel flows were quantified by using phase-contrast MR imaging on all patients. Veins were classified by extracranial drainage type: internal jugular veins (I), paraspinal (II), and superficial (III). Differences among healthy controls, patients with MS, nonstenotic patients, and stenotic subgroups in total venous flow by vessel type were evaluated in a general linear model for statistical analysis.

**RESULTS:** In the MS group, 153 patients (55%) evidenced stenosis, whereas 12 (20%) healthy controls were classified as stenotic ( $P < .001$ ). Compared with healthy controls, the MS group showed lower type I flow and increased type II flow. Stenosis was associated with reduced flow in the type I vessels [ $F(1272) = 68$ ;  $P < .001$ ]. The stenotic MS group had increased flow in the type II vessels compared with the nonstenotic MS group [ $F(1272) = 67$ ;  $P < .001$ ].

**CONCLUSIONS:** Compared with healthy controls, patients with MS exhibit reduced venous flow in the main extracerebral drainage vein (internal jugular vein). In contrast, flow in the paraspinal venous collaterals is elevated in patients with MS and exacerbated by venous stenosis. Collateral drainage may be a compensatory response to internal jugular vein flow reduction.

**ABBREVIATIONS:** CSA = cross-sectional area; HC = healthy control; IJV = internal jugular vein; PC = phase-contrast

Multiple sclerosis is an inflammatory, demyelinating disease of the CNS. The exact origin remains elusive, though epidemiologic studies have shown that it is multifactorial and likely caused by an interaction between environmental and genetic factors.<sup>1</sup> Although autoimmune etiology is the current consensus, a recent vascular hypothesis of MS suggested chronic cerebrospinal venous insufficiency as a major culprit. The chronic cerebrospinal

venous insufficiency hypothesis postulates that abnormalities in the structure and hemodynamics of intracranial and extracranial veins may induce MS symptoms. Initial research on chronic cerebrospinal venous insufficiency used Doppler sonography and catheter venography to quantify flow and visualize vascular anatomy, respectively. Since then, however, several attempts to validate the initial findings yielded mixed results. The lack of standardized image modalities and analytic methods, as well as low statistical power, may explain the discrepant conclusions.<sup>2,3</sup>

MR imaging, unlike ultrasonography, is an operator-independent method that can detect demyelinating and iron-laden lesions in the brain parenchyma and confirm the MS diagnosis. The advantages of MR imaging, in addition to lesion detection, are the abilities to rapidly generate a 3D map of the vasculature by using venography and to quantify blood flow in large and small extracranial blood vessels by using phase-contrast (PC) flow quantification. These methods have been already successfully applied

Received January 15, 2017; accepted after revision March 13.

From The MRI Institute for Biomedical Research (S.K.S., D.T.U., J.J., E.M.H.), Detroit, Michigan; Institute of Gerontology (A.M.D., N.R.) and Departments of Psychology (N.R.) and Radiology (E.M.H.), Wayne State University, Detroit, Michigan; and Department of Physics and Earth Sciences (G.G.), University of Ferrara, Ferrara, Italy.

This work was supported in part by a grant from the National Institute on Aging, R37-AG011230 to Dr. Naftali Raz.

Please address correspondence to Sean K. Sethi, MS, 440 E. Ferry St #1, The MRI Institute for Biomedical Research, Detroit, MI 48202; e-mail: sethisea@gmail.com

 Indicates open access to non-subscribers at [www.ajnr.org](http://www.ajnr.org)

<http://dx.doi.org/10.3174/ajnr.A5219>

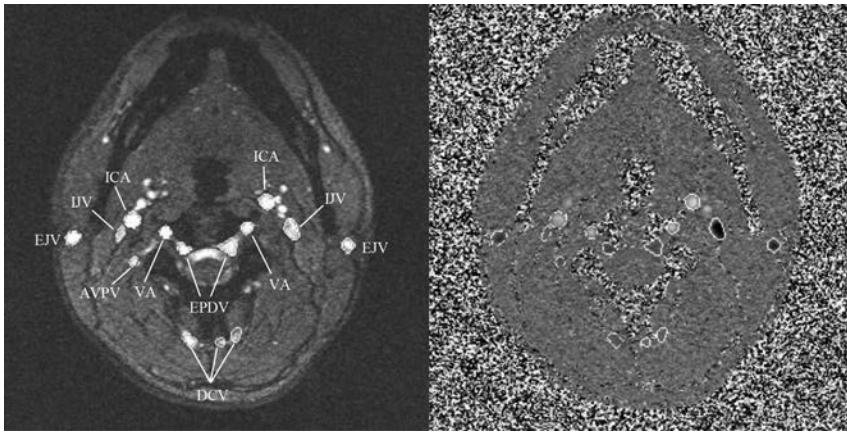


**FIG 1.** PC-MR imaging magnitude (*left*) and phase (*right*) images showing the neck level for a healthy patient. Artery and vein contours were traced on the images semiautomatically; arteries appear bright, whereas veins appear dark on phase images. Type I veins: IJV; type II veins: AVPV; anterior venous plexus vein; EPDV: epidural vein; DCV, deep cervical vein; type III veins: EJV, external jugular vein. Arteries: ICA; VA, vertebral artery.

to detecting vascular and flow abnormalities in the internal jugular vein (IJV) in healthy older adults<sup>4</sup> and within a subset of patients with MS.<sup>3,5-7</sup>

Research on venous abnormalities in MS thus far has been limited to the IJV, and little is known about extracranial venous collateralization. The extrajugular drainage system consists of the vertebral venous system; the deep cervical veins, which anatomically are paraspinous toward the heart; and the anterior and external jugular veins, which receive blood from facial and superficial areas.<sup>8</sup> Although the presence and structure of collateral veins have been assessed by using time-resolved imaging of contrast kinetics venography, flow values were not quantitatively evaluated.<sup>9-11</sup> The purpose of this work was to examine the relation of extracranial venous anatomy and flow in a large cohort of patients with MS and healthy controls (HCs) taken from our neuroimaging data base.<sup>12</sup> Because of the complexity of the extracranial venous system, we have classified these vessels into 3 groups based on anatomic MR information and their drainage path: primary (ie, IJV), paraspinous, and superficial. We hypothesized that increased venous paraspinous and superficial flow will also be observed for cases that evidence abnormal IJV structure and flow. In contrast, a subset of patients with MS may have a distinct collateral venous flow pattern compared with patients with MS and HCs without structural venous anomalies.

## MATERIALS AND METHODS

### Participants

The sample consisted of 276 patients with MS (194 women; mean, 48.8 years; SD, 10.9 years) and 106 HCs (58 women; M, 42.4 years; SD, 15.4 years). The patients with MS were classified into 3 types: relapsing-remitting ( $n = 157$ ), primary-progressive ( $n = 30$ ), and secondary-progressive ( $n = 39$ ), whereas 50 patients did not have a known subtype. Patients with MS were excluded if they had a history of hypertension, previous vascular intervention, or presence of hypercoagulable state. Pregnant women and patients with cognitive impairment who were incapable of signing an informed consent form were also excluded. HCs were excluded if they had a history of diabetes, chronic renal disease, psychiatric or neuro-

logic disorder, or substance abuse. All patients with MS and HCs with any contraindicated implant(s) were not included in this study.

### Data Acquisition

All data were collected under Health Insurance Portability and Accountability Act guidelines and institutional review board approval. 3D contrast-enhanced MRV and 2D TOF MRV were used to assess the anatomy of the extracranial vessels on all patients with MS and 60 HCs because 46 of the 106 HCs lacked this imaging. Blood flow was quantified with PC-MR imaging at the C2–C3 cervical level for all patients with MS and HCs. Data from patients with MS were collected from 2 sites by using a 3T Trio

Scanner (Siemens, Erlangen, Germany),<sup>3,7</sup> and HC images were acquired on a 3T Verio scanner (Siemens)<sup>4</sup> at the MR Research Facility at Wayne State University. On both scanners, a 16-channel head/neck coil arrangement was used. Imaging parameters and inclusion/exclusion criteria have been described in a previous publication.<sup>7</sup>

### Image Processing and Analysis

All data were processed and reviewed retrospectively with Signal Processing In Nuclear MR software (SPIN; MR Imaging Institute for Biomedical Research, Detroit, Michigan). Two raters evaluated MRV (3D time-resolved imaging of contrast kinetics or 2D TOF MRV if available) to assess stenosis of the IJVs in all samples by using established methods.<sup>7</sup> Patients were classified as stenotic if the IJV met the following stenosis criteria: if the cross-sectional area (CSA) was less than 25 mm<sup>2</sup> at the segment caudal to the C3 vertebral level and less than 12.5 mm<sup>2</sup> at the segment cranial to the C3 vertebral level.<sup>3,7</sup> Atretic or aplastic IJVs that showed no signal on venography were also categorized as stenotic. The cutoff of 25 mm<sup>2</sup> was chosen assuming 70% stenosis in an IJV diameter of 1 cm.<sup>13,14</sup> Discernable arterial and venous structures that flow to and from the cerebrum were identified and subtyped by using venography and PC flow sequences.

PC flow sequences were processed by 3 raters who were blinded to participants' characteristics. Vessels were demarcated by using an intensity threshold-based method, with manual tracing if necessary (Fig 1). Boundaries for each vessel were checked on the PC magnitude and phase maps. A list of vessels that were traced for each cervical level is given in the Table. Flow rates (mL/s) were calculated based on integrated flow velocities within the vessel lumen. Velocities that exceeded 50 cm/s were unwrapped by SPIN software by using a robust automatic unwrapping algorithm that compares pixel-wise phase values in the x, y, and z directions and ensures that only pixels that are aliased are unwrapped.<sup>15</sup>

Venous structures were classified by drainage mode into 3 types (Table): type I, IJV; type II, paraspinous veins; and type III, superficial veins. For all statistical analyses, total venous flows,

### List of vessels classified by flow direction and drainage type

Venous Type I (Primary)	Venous Type II (Paraspinal)	Venous Type III (Superficial)	Arteries
Internal jugular veins	Deep cervical veins Vertebral veins Epidural veins Anterior vertebral venous plexus veins Posterior vertebral venous plexus veins	External jugular veins Anterior jugular veins Posterior external jugular veins	Vertebral arteries Internal carotid arteries

which is the bilateral sum of all included vessels within a vessel type, were used for each type.

### Statistical Methods

Individual and group differences in flow measured in the 3 vessel types were assessed within a general linear model framework. Flow at the C2–C3 cervical level served as the dependent variable; age and sex were entered as covariates. First, we gauged the differences in flow between 2 diagnostic groups (group, patients with MS versus HCs) across 3 vessel types, with vessel type being a within-patient variable and group being a between-patient variable. A full model that included all interactions was tested first, and nonsignificant interactions were removed before evaluating a reduced model. All significant interactions were decomposed by using post hoc analyses of simple effects. For all statistical analyses, we used SYSTAT 13.0 (Systat Software, San Jose, California).

Before data processing, interrater reliability in assessing flow volume per cardiac cycle (mL/CDC) was tested by using an intraclass correlation coefficient–2 statistic that assumes random raters.<sup>16</sup> Total vessel flow for the ICA, vertebral artery, and IJV, as well as their sum (right + left) vessel flow, were tested in prior studies of patients with MS<sup>3</sup> and healthy adults.<sup>4</sup> For this study, we evaluated the reliability of total cerebral blood flow values (ICA + vertebral artery for the C2–C3 neck level), as well as total type II and III venous flow indicators. All rater pairs met a reliability of intraclass correlation coefficient–2 > 0.9 for vessel totals. Agreement between raters for anatomic assessment was calculated by using a Cohen  $\kappa$  statistic from a sample of 15 patients with MS and 15 HCs. The raters had an agreement of 0.87. For Cohen  $\kappa$ , we considered values above 0.75 as excellent, values of 0.40–0.75 as modest, and values below 0.40 as low.

## RESULTS

### Anatomic Assessment

Among patients with MS, 153 (60%) had venous stenosis. No age differences between the groups were found ( $P = .84$ ). Stenosis was more prevalent among men (59/82; 72%) than women (94/194; 48%;  $P < .001$ ). Among HCs, only 60 (M, 37.9 years; SD, 10.9 years) were evaluated for stenosis because of a lack of anatomic venography imaging data (2D TOF MRV and 3D contrast enhanced MRA) on the remaining 46 HCs. Stenosis was identified in 12 HCs (20%, 5 men and 7 women;  $P = .24$ ).

### Differences in Flow between Diagnostic Groups and among Vessel Types

Small age differences were noted in venous flow [ $F(1378) = 15.92$ ;  $P < .001$ ]; significance was reached only for type 1 vessels ( $r = -0.13$ ;  $P = .015$ ). Neither sex- nor group-related differences were found (both main effects,  $F < 1$ ). However, a significant vessel  $\times$  group interaction was observed [ $F(2756) = 23$ ;  $P < .001$ ]. De-

composition of that interaction into simple effects revealed greater flow in type I vessels among HCs compared with patients with MS [ $8.43 \pm .27$  mL/s versus  $7.32 \pm 0.18$  mL/s;  $F(1378) = 12$ ;  $P = .001$ ] and lesser flow in type II vessels for HCs compared with patients with MS [ $0.70 \pm .17$  mL/s versus  $2.11 \pm 0.11$  mL/s;  $F(1378) = 49$ ;  $P < .001$ ]. No flow differences in type III vessels were observed between the HCs and the patients with MS [ $1.22 \pm 0.70$  mL/s versus  $1.40 \pm 0.11$  mL/s;  $F(1378) = 2.0$ ; no significance]. Fig 2 shows the mean total flows by venous drainage type plotted for the MS and HC groups.

### Venous Stenosis and Venous Flow in Patients with MS

Among patients with MS, mild age differences in flow were observed [ $F(1272) = 11$ ;  $P = .001$ ;  $r = -.18$ ,  $P = .03$  for type II vessels, with the effect for type I and type III being nonsignificant]. The presence of stenosis was associated with a significant overall reduction in venous flow [ $F(1272) = 4$ ;  $P = .038$ ]. However, the main effect was qualified by a significant vessel type  $\times$  stenosis interaction [ $F(2544) = 71.23$ ;  $P < .001$ ].

Decomposition of the interaction revealed that stenosis was associated with reduced flow in the type I vessels compared with the nonstenotic cohort [ $6.20 \pm 0.21$  mL/s versus  $8.86 \pm 0.26$  mL/s;  $F(1272) = 68$ ;  $P < .001$ ]. In contrast, patients with MS with stenosis had increased flow in the type II vessels [ $2.79 \pm 0.14$  mL/s versus  $1.08 \pm 0.17$  mL/s;  $F(1272) = 67$ ;  $P < .001$ ]. A smaller but significant increase in flow was observed in type III vessels of patients with stenosis [ $1.37 \pm 0.089$  versus  $0.99 \pm 0.11$ ;  $F(1272) = 8$ ;  $P = .005$ ]. No effects of MS subtype were observed [main effect  $F(2221) = 1$ , nonsignificant; all interactions  $F < 1$ ]. Fig 3 details the mean total flows for nonstenotic-MS, stenotic-MS, and HC groups.

## DISCUSSION

The main finding in this study is that in patients with MS compared with HCs, venous flow is reduced in the IJV but increased in the paraspinal and other collateral veins. Moreover, in patients with MS, the presence of visible structural abnormalities, such as venous stenosis, is associated with a further decrease in jugular flow and an increase in drainage through the collateral veins.

Under normal physiologic conditions, encephalic drainage depends on body position. In the supine position, the IJVs drain most of the venous blood,<sup>17–20</sup> whereas in the upright position, the paraspinal vessels assume more of this role.<sup>21–23</sup> The IJVs merge with the subclavian vein to form the brachiocephalic vein, which drains the venous blood back to the heart. Along the way, several tributaries may enter the IJVs at the cervical level. The collateral veins' primary function is to augment venous drainage. The findings in this study suggest that blood may be draining via anastomosis through such structures as the anterior

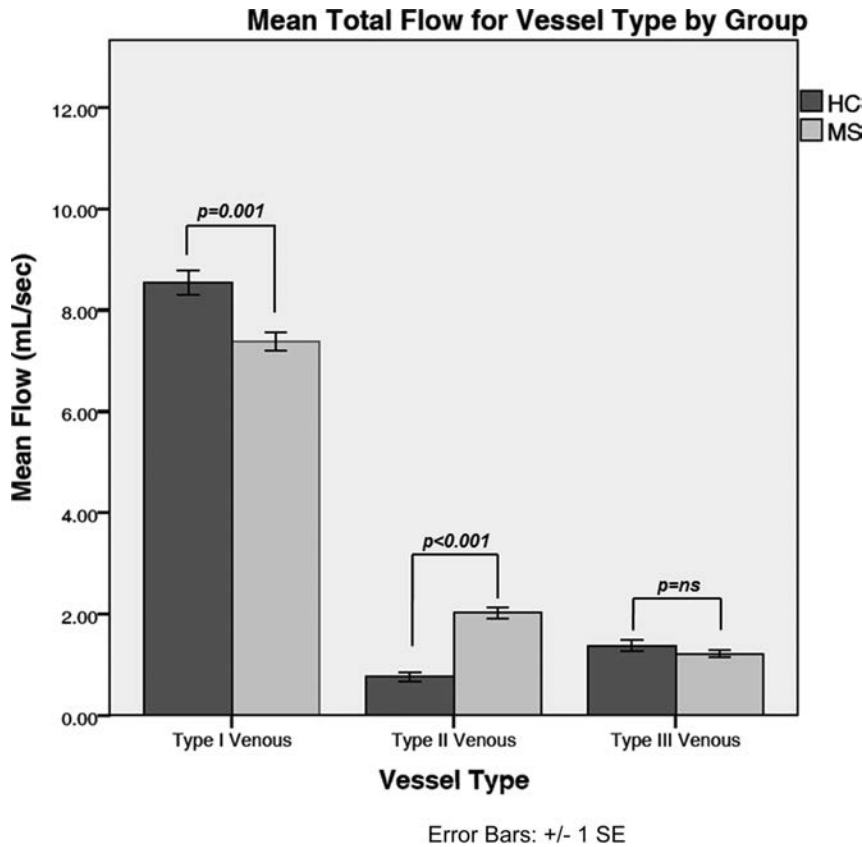


**FIG 2.** Comparison of total mean flows (mL/s) for vessel types between diagnostic groups. The error bars represent standard errors of the mean.

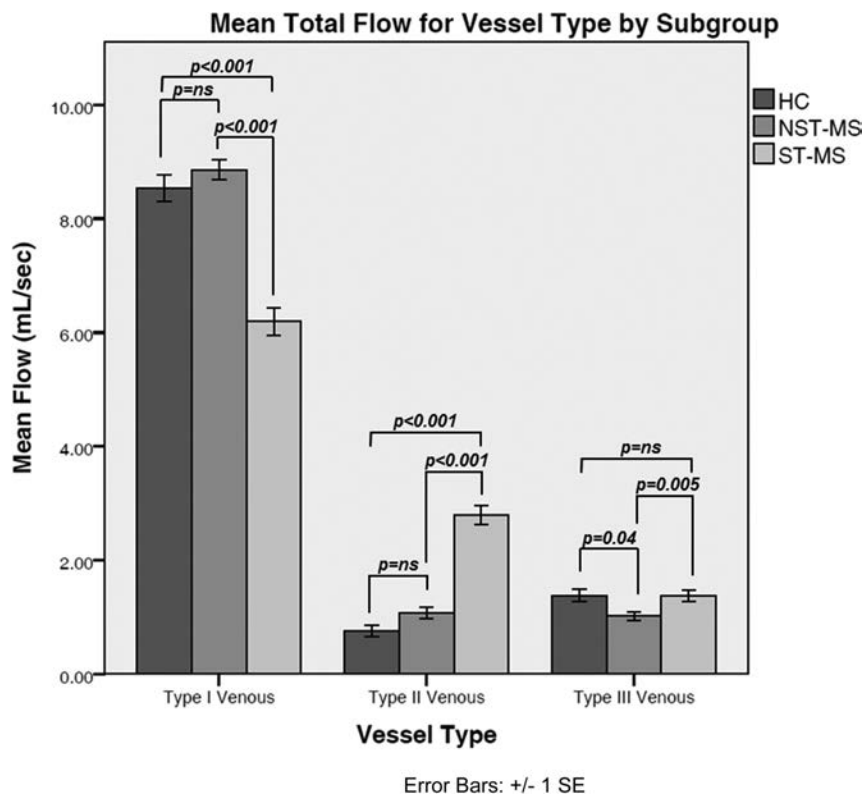


**FIG 3.** Comparison of total mean venous flow (mL/s) by vessel type among nonstenotic-MS (NST-MS), stenotic-MS (ST-MS), and HC groups. The error bars represent standard errors of the mean.

condylar confluence and into the vertebral venous system.<sup>24</sup> Increased intra-abdominal and intrathoracic pressures have also been known to shunt blood through the vertebral and epidural networks.<sup>25</sup> Although HCs are not exempt from having stenosis, and variations have been reported in non-disease states,<sup>11</sup> the percentage of stenotic HCs is far less (20%) than the percentage of stenotic patients with MS (55%;  $P < .001$ ). Of note, flow in nonstenotic patients with MS is similar to HCs for all venous types, whereas stenotic patients with MS show markedly reduced IJV flow and elevated type II and III venous flow compared with nonstenotic counterparts and control patients. Although our method has been consistent in predicting jugular stenosis and resultant outflows, it is uncertain whether altered venous outflow stems from the disease or some other cause.

Our results are in accord with the findings of McTaggart et al,<sup>9</sup> who showed greater IJV flattening and a trend toward venous collaterals specifically in MS compared with HCs. They have, however, used TOF and time-resolved imaging of contrast kinetics MRV without quantifying the flow. Using a fixed CSA as well as quantitative flow measurement, as reported here, removes the subjectivity of a nominal assessment. A pilot study by Zamboni et al<sup>26</sup> also showed that HCs tend to drain blood via the IJVs as opposed to collaterals. Torres et al,<sup>11</sup> however, found that the recruitment of extracranial veins as collaterals was a common finding in patients without MS by using contrast-enhanced MR angiography and venography imaging. Zivadinov et al<sup>27</sup> reported no evidence of increased collaterals in MS by using TOF and time-resolved imaging of contrast kinetics. Their method for evaluating collaterals was ordinal: any collaterals that were  $>5$  mm in diameter (or 7 mm for the segment of the inferior segment of the external jugular vein) were noted as prominent. This shows that anatomic assessment alone is not enough to show differences between patients with MS and HCs and may provide an incomplete picture of the cerebral hemodynamics.

In contrast with recent studies that used a percentage method for assessing jugular stenosis, we used an absolute threshold for the CSA measurement.<sup>28,29</sup> We posit that the percentage method is limited because of the variation in IJV size and shape and its venous tributaries, as well as its compliance, sometimes manifesting as pinpoint, elliptic, or crescentic shapes.<sup>27</sup> In our previous work,<sup>3</sup> we have shown differences between the 2 methods and how using a percentage stenosis method leads to higher rates of stenosis in both HC and MS groups compared with an absolute method. A CT-based analysis of CSA that used a percentage method revealed high variability of the IJV and increasing mean CSA values along the caudal direction of the IJV.<sup>30</sup> This vessel property served as the rationale for using absolute CSA thresholds for both the upper and lower neck levels.

An investigation of structural and functional alterations in the veins of patients with MS based on postcontrast 3D volumetric interpolated brain examination data<sup>31</sup> revealed a high prevalence of stenosis when using a nominal assessment method.<sup>10</sup> PC-MR imaging analysis of blood flow velocity demonstrated reflux. Although the authors claimed that 6 of the 28 patients had nearly completely occluded IJVs, they reported that the flow was not abnormal in these cases. This is an unusual finding given that a completely occluded vessel should have no flow. Their findings differ from ours, which suggest that the IJV morphology analysis method may affect the conclusion pertaining to the effects of morphology on venous flow.

Our findings should be interpreted in the context of several limitations. The imperfect resolution of MR imaging methods may affect the prediction of stenosis and flow. TOF and time-resolved imaging of contrast kinetics venography have been shown to have lower specificity and positive predictive value relative to catheter venography.<sup>32</sup> The latter, while remaining the “gold standard” for assessing stenosis, is invasive, and it does not provide global and quantifiable functional information about the venous system. Moreover, MR venography methods are in good agreement with contrast venography, though MRV may have the tendency to overestimate vessel stenosis.<sup>10</sup>

The 2D PC-MR imaging flow sequence in this study is limited to capturing velocities only in the cranial and caudal directions because the data are collected in the plane perpendicular to the major arteries and veins of the neck. Advanced MR techniques such as 4D flow can successfully capture the spiral/vortexed flow property at the jugular bulb in persons with and without luminal irregularities.<sup>33</sup> In a recent study,<sup>34</sup> the application of a 4D flow technique combined with 3D contrast-enhanced MRA and Doppler sonography was used to evaluate venous structure and function in MS and other neurologic diseases. In that study, only a small group of participants met the criterion of chronic cerebrospinal venous insufficiency, with patients and HCs equally represented. The authors also concluded that a small amount of reflux in the cerebrospinal venous system may be a normal variant.<sup>34</sup> Although these findings are discordant with ours, the study suffers from 2 notable drawbacks: the low intraobserver agreement when using 3D MRA to assess venous stenosis and the large age ranges used in their group comparisons yielding high variability in the flow estimates. Although 4D flow MR imaging enables diverse velocity field–based analyses, it is limited by low spatial and

temporal resolution, systematic errors and noise, and the inability to resolve instantaneous and small-scale velocities.<sup>33</sup> Further improvements in the reliability and validity of this promising approach are needed before these discrepancies can be resolved.

Morphologic IJV changes may also be due to several other factors: head and neck position, intrathoracic pressure, extrinsic compression from the coil, and swallowing movement artifacts.<sup>27</sup> Small arteries and venules are difficult to measure when using PC-MR imaging, so it is not certain how the microvasculature is affected by a primary venous stenosis. Moreover, age, sex, hand side, and body mass index have been shown to affect IJV CSA<sup>35,36</sup>; our stenosis criteria measurement did not account for those factors. Recent semiautomatic estimation of IJV calibers at all neck levels reported  $37.47 \pm 19.00$  mm<sup>2</sup> for the left IJV and  $45.03 \pm 21.86$  mm<sup>2</sup> for the right IJV at the C2 level.<sup>37</sup> At 70% stenosis, this would be a CSA of 11.24 mm<sup>2</sup> and 13.5 mm<sup>2</sup>, respectively, which lends further credence to our initial upper neck level threshold of 12.5 mm<sup>2</sup>. Buch et al,<sup>30</sup> while reporting normal variations in the caliber of IJVs in patients with MS and HCs, noted a C1 neck level average CSA of  $47.7 \pm 24.8$  mm<sup>2</sup> and  $66.0 \pm 29.7$  mm<sup>2</sup> for the left and right IJVs, respectively; 70% of these values would be 14.3 mm<sup>2</sup> and 19.8 mm<sup>2</sup>, which lends further credence to our initial upper neck level threshold of 12.5 mm<sup>2</sup>. Future studies should use the aforementioned indices when diagnosing for venous stenosis. Because the HC data were pooled from multiple studies at the same imaging center, 46 of the HCs lacked anatomic venographic imaging because it was not included for that particular study. On the other hand, the flow measurements from that study helped increase the statistical power of the analysis. Future studies should include additional HCs to allow for the comparison of a higher percentage of stenotic cases with the other subgroups. Last, the comparison of MRV findings should be interpreted with caution because the groups that did have venography were not age-matched, which may skew the results because of the younger age of the HC group because age has been correlated with CSA for all cervical levels.<sup>35,36</sup>

## CONCLUSIONS

PC-MR imaging is a viable method for quantifying the extent of compensation in the extracranial venous system in MS and has demonstrated an increase in collateral flow caused by the presence of jugular stenosis. It is possible that this increase in collateral drainage is a compensatory response in the MS-affected brain to reduction of the IJV flow.

## ACKNOWLEDGMENTS

The authors would like to thank Magnetic Resonance Innovations, Inc. - India for their assistance in data processing and Dr. Phillip Levy for usage of healthy control data.

Disclosures: Sean K. Sethi—UNRELATED: Employment: Magnetic Resonance Innovations, Inc., Comments: part-time employment for MR sequence and software development. David T. Utraiainen—UNRELATED: Employment: Magnetic Resonance Innovations, Inc., Comments: half-time employee. Jing Jiang—UNRELATED: Employment: Full-time employment at Magnetic Resonance Innovations, Inc. as a software developer. Naftali Raz—RELATED: Grant: National Institutes of Health/National Institute on Aging\*; Consulting Fee or Honorarium: National Institutes of Health, Comments: study section (grant reviews); Other: National Institutes of Health, Comments: grant review panel. E. Mark Haacke—UNRELATED: Board Membership: Magnetic Reso-

## REFERENCES

1. Compston A, Coles A. **Multiple sclerosis.** *Lancet* 2008;372:1502–17 CrossRef Medline
2. Haacke EM, Sethi SK, Jiang J, et al. **The role of magnetic resonance imaging in assessing venous vascular abnormalities in the head and neck: a demonstration of cerebrospinal venous insufficiency in a subset of multiple sclerosis patients.** *Veins Lymphatics* 2015;4:5012–20 CrossRef
3. Sethi SK, Utraiainen DT, Daugherty AM, et al. **Jugular venous flow abnormalities in multiple sclerosis patients compared to normal controls.** *J Neuroimaging* 2015;25:600–07 CrossRef Medline
4. Raz N, Daugherty AM, Sethi SK, et al. **Age differences in arterial and venous extra-cerebral blood flow in healthy adults: contributions of vascular risk factors and genetic variants.** *Brain Struct Funct* 2017 Jan 24. [Epub ahead of print] CrossRef Medline
5. Feng W, Utraiainen D, Trifan G, et al. **Characteristics of flow through the internal jugular veins at cervical C2/C3 and C5/C6 levels for multiple sclerosis patients using MR phase contrast imaging.** *Neurorol Res* 2012;34:802–09 CrossRef Medline
6. Feng W, Utraiainen D, Trifan G, et al. **Quantitative flow measurements in the internal jugular veins of multiple sclerosis patients using magnetic resonance imaging.** *Rev Recent Clin Trials* 2012;7:117–26 CrossRef Medline
7. Haacke EM, Feng W, Utraiainen D, et al. **Patients with multiple sclerosis with structural venous abnormalities on MR imaging exhibit an abnormal flow distribution of the internal jugular veins.** *J Vasc Interv Radiol* 2012;23:60–68.e1–3 CrossRef Medline
8. Zivadinov R, Chung CP. **Potential involvement of the extracranial venous system in central nervous system disorders and aging.** *BMC Med* 2013;11:260 CrossRef Medline
9. McTaggart RA, Fischbein NJ, Elkins CJ, et al. **Extracranial venous drainage patterns in patients with multiple sclerosis and healthy controls.** *AJNR Am J Neuroradiol* 2012;33:1615–20 CrossRef Medline
10. Zaharchuk G, Fischbein NJ, Rosenberg J, et al. **Comparison of MR and contrast venography of the cervical venous system in multiple sclerosis.** *AJNR Am J Neuroradiol* 2011;32:1482–89 CrossRef Medline
11. Torres C, Hogan M, Patro S, et al. **Extracranial venous abnormalities: a true pathological finding in patients with multiple sclerosis or an anatomical variant?** *Eur Radiol* 2017;27:239–46 CrossRef Medline
12. Pacurar EE, Sethi SK, Habib C, et al. **Database integration of protocol-specific neurological imaging datasets.** *Neuroimage* 2016;124:1220–24 CrossRef Medline
13. Furukawa S, Nakagawa T, Sakaguchi I, et al. **The diameter of the internal jugular vein studied by autopsy.** *Rom J Legal Med* 2010;18:125–28 CrossRef
14. Tartière D, Seguin P, Juhel C, et al. **Estimation of the diameter and cross-sectional area of the internal jugular veins in adult patients.** *Crit Care* 2009;13:R197 CrossRef Medline
15. Jiang J, Kokeny P, Ying W, et al. **Quantifying errors in flow measurement using phase contrast magnetic resonance imaging: comparison of several boundary detection methods.** *Magn Reson Imaging* 2015;33:185–93 CrossRef Medline
16. Shrout PE, Fleiss JL. **Intraclass correlations: uses in assessing rater reliability.** *Psychol Bull* 1979;86:420–28 CrossRef Medline
17. Schreiber SJ, Lurtzing F, Gotze R, et al. **Extrajugular pathways of human cerebral venous blood drainage assessed by duplex ultrasound.** *J Appl Physiol (1985)* 2003;94:1802–05 CrossRef Medline
18. Nylin G, Hedlund S, Regnstrom O. **Studies of the cerebral circulation with labeled erythrocytes in healthy man.** *Circ Res* 1961;9:664–74 CrossRef Medline
19. Shenkin HA, Scheurman WG, Spitz EB, et al. **The effects of change of position upon the cerebral circulation of man.** *Am J Med Sci* 1948;216:714 Medline
20. Wilson EM, Halsey JH Jr., Vitek JJ. **Validation of jugular venous flow as an index of total cerebral blood flow.** *Stroke* 1972;3:300–21 CrossRef Medline
21. Valdueza JM, von Munster T, Hoffman O, et al. **Postural dependency of the cerebral venous outflow.** *Lancet* 2000;355:200–01 CrossRef Medline
22. Doepp F, Schreiber SJ, von Münster T, et al. **How does the blood leave the brain? A systematic ultrasound analysis of cerebral venous drainage patterns.** *Neuroradiology* 2004;46:565–70 CrossRef Medline
23. Menegatti E, Zamboni P. **Doppler haemodynamics of cerebral venous return.** *Curr Neurovasc Res* 2008;5:260–65 CrossRef Medline
24. San Millán Ruiz D, Gailloud P, Rüfenacht DA, et al. **The craniocervical venous system in relation to cerebral venous drainage.** *AJNR Am J Neuroradiol* 2002;23:1500–08 Medline
25. Schaller B. **Physiology of cerebral venous blood flow: from experimental data in animals to normal function in humans.** *Brain Res Brain Res Dev* 2004;46:243–60 CrossRef Medline
26. Zamboni P, Sisini F, Menegatti E, et al. **An ultrasound model to calculate the brain blood outflow through collateral vessels: a pilot study.** *BMC Neurol* 2013;13:81 CrossRef Medline
27. Zivadinov R, Lopez-Soriano A, Weinstock-Guttman B, et al. **Use of MR venography for characterization of the extracranial venous system in patients with multiple sclerosis and healthy control subjects.** *Radiology* 2011;258:562–70 CrossRef Medline
28. Traboulsee AL, Knox KB, Machan L, et al. **Prevalence of extracranial venous narrowing on catheter venography in people with multiple sclerosis, their siblings, and unrelated healthy controls: a blinded, case-control study.** *Lancet* 2014;383:138–45 CrossRef Medline
29. Martin N, Traboulsee AL, Machan L, et al. **Prevalence of extracranial venous narrowing on magnetic resonance venography is similar in people with multiple sclerosis, their siblings, and unrelated healthy controls: a blinded, case-control study.** *Can Assoc Radiol J* 2017;68:202–09 CrossRef Medline
30. Buch K, Groller R, Nadgir RN, et al. **Variability in the cross-sectional area and narrowing of the internal jugular vein in patients without multiple sclerosis.** *AJR Am J Roentgenol* 2016;206:1082–86 CrossRef Medline
31. Raz E, Pontecorvo S, Barra V, et al. **MR venography in patients with multiple sclerosis and correlation with clinical and MRI parameters.** *J Neuroimaging* 2014;24:492–97 CrossRef Medline
32. Zivadinov R, Galeotti R, Hojnacki D, et al. **Value of MR venography for detection of internal jugular vein anomalies in multiple sclerosis: a pilot longitudinal study.** *AJNR Am J Neuroradiol* 2011;32:938–46 CrossRef Medline
33. Kefayati S, Amans M, Faraji F, et al. **The manifestation of vortical and secondary flow in the cerebral venous outflow tract: an in vivo MR velocimetry study.** *J Biomech* 2017;50:180–87 CrossRef Medline
34. Schrauben EM, Kohn S, Macdonald J, et al. **Four-dimensional flow magnetic resonance imaging and ultrasound assessment of cerebrospinal venous flow in multiple sclerosis patients and controls.** *J Cereb Blood Flow Metab* 2017;37:1483–93 CrossRef Medline
35. Magnano C, Belov P, Krawiecki J, et al. **Internal jugular vein narrowing and body mass index in healthy individuals and multiple sclerosis patients.** *Veins Lymphatics* 2014;3:89–92
36. Magnano C, Belov P, Krawiecki J, et al. **Internal jugular vein cross-sectional area enlargement is associated with aging in healthy individuals.** *PLoS One* 2016;11:e0149532 CrossRef Medline
37. Laganà MM, Pelizzari L, Scaccianoce E, et al. **Assessment of internal jugular vein size in healthy subjects with magnetic resonance and semiautomatic processing.** *Behav Neurol* 2016;2016:9717210 CrossRef Medline

# Functional Connectivity in Virally Suppressed Patients with HIV-Associated Neurocognitive Disorder: A Resting-State Analysis

J.R. Chaganti, A. Heinecke, T.M. Gates, K.J. Moffat, and B.J. Brew



## ABSTRACT

**BACKGROUND AND PURPOSE:** HIV-associated neurocognitive disorder still occurs despite virally suppressive combination antiretroviral therapy. In the pre-combination antiretroviral era and in patients without HIV suppression, HIV-associated neurocognitive disorder was caused by synaptodendritic injury resulting in impairment of neural networks, characterized by decreased attention, psychomotor slowing, and working memory deficits. Whether similar pathogenesis is true for HIV-associated neurocognitive disorder in the context of viral suppression is not clear. Resting-state fMRI has been shown to be efficient in detecting impaired neural networks in various neurologic illnesses. This pilot study aimed to assess resting-state functional connectivity of the brain in patients with active HIV-associated neurocognitive disorder in the context of HIV viral suppression in both blood and CSF.

**MATERIALS AND METHODS:** Eighteen patients with active HIV-associated neurocognitive disorder (recent diagnosis with progressing symptoms) on combination antiretroviral therapy with viral suppression in both blood and CSF and 9 demographically matched control subjects underwent resting-state functional MR imaging. The connectivity in the 6 known neural networks was assessed. To localize significant ROIs within the HIV and control group, we performed a seed-based correlation for each known resting-state network.

**RESULTS:** There were significant group differences between the control and HIV-associated neurocognitive disorder groups in the salience (0.26 versus 0.14,  $t = 2.6978$ ,  $df = 25$ ,  $P = .0123$ ) and executive networks (0.52 versus 0.32,  $t = 2.2372$ ,  $df = 25$ ,  $P = .034$ ). The covariate analysis with neuropsychological scores yielded statistically significant correlations in all 6 studied functional networks, with the most conspicuous correlation in salience networks.

**CONCLUSIONS:** Active HIV-associated neurocognitive disorder in virally suppressed patients is associated with significantly decreased connectivity in the salience and executive networks, thereby making it potentially useful as a biomarker.

**ABBREVIATIONS:** cART = combination antiretroviral therapy; HAND = HIV-associated neurocognitive disorder; NC = neurocognitive; rs-fMRI = resting-state fMRI

HIV-associated neurocognitive disorder (HAND) persists in the era of potent combination antiretroviral therapy (cART), even when confounding conditions are excluded and patients are virally suppressed.<sup>1,2</sup> HAND is a broad term to encompass neurocognitive disorders including asymptomatic neurocognitive impairment, mild neurocognitive impairment, and HIV-associated dementia with prevalence ranging from 18% to 52%. The diagnosis of different stages of HAND is based on the recommen-

datations from updated research nosology for HIV-associated neurocognitive disorders<sup>1</sup> and includes neuropsychological testing and neurologic evaluation. The variation in the prevalence depends on whether patients with confounding conditions and unsuppressed HIV viral load are included. Nonetheless, even in the absence of confounds and the presence of viral suppression in both blood and CSF, HAND still occurs and may develop for reasons that are unclear.<sup>3,4</sup>

HAND is characterized by decreased attention, psychomotor slowing, and working memory deficits.<sup>5,6</sup> While HAND in the pre-cART era was characterized as subcortical, the advent of cART has shifted the impairment to include higher order cognitive abilities such as executive functioning.<sup>3,5</sup> The higher order cognitive dysfunction was substantiated by a number of task-based functional MR imaging studies that demonstrated increased use of reserve brain regions during working memory tasks in patients with HIV with mild dementia and in those

Received July 11, 2016; accepted after revision March 29, 2017.

From the Departments of Radiology (J.R.C., K.J.M.) and Neurology (B.J.B.), St Vincent's Hospital, Darlinghurst, Sydney, New South Wales, Australia; Brain Innovation B.V. (A.H.), Maastricht, the Netherlands; Department of Neurology, Clinical Research Program (T.M.J.) and Neurosciences Program, Peter Duncan Neurosciences Unit (B.J.B.), St Vincent's Centre for Applied Medical Research, University of New South Wales, Sydney, Australia.

Please address correspondence to Joga Chaganti, MD, St Vincent's Hospital, Victoria Street, Darlinghurst, Sydney 2100, Australia; e-mail: joga.chaganti@svha.org.au

<http://dx.doi.org/10.3174/ajnr.A5246>

who were neuroasymptomatic.<sup>7,8</sup> These studies showed that there are abnormal levels (initial increase and later reduced activity) of activation in the dorsolateral prefrontal cortex and parietal cortices. However, these studies did not include patients who were virally suppressed in both blood and CSF.

Resting-state fMRI (rs-fMRI) has been established as a powerful tool to measure the brain networks, which are implicated in cognitive disorders. Currently, there are only 5 studies that have examined resting-state networks in HAND.<sup>9-13</sup> These studies have noted abnormalities, especially early in the course of HIV infection.<sup>9</sup> Some studies have shown conflicting results (Ipser et al<sup>11</sup> and Guha et al<sup>12</sup>). However, no studies have been specifically designed to address the pathogenesis of HAND in the cART era. Thus, additional criteria are required. Patients with HAND must be virally suppressed in both blood and CSF and should demonstrate symptoms of HAND that are recent and progressive and are not related to the legacy effect from the past (cognitive abnormalities that reflect “burn-out” disease).

Consequently, the aim of this study was to analyze the effect of HIV infection on various resting networks in virally controlled patients with active HAND as a means of understanding the pathogenesis in the cART era.

## MATERIALS AND METHODS

Eighteen patients with HIV with HAND were enrolled. All had been on a stable cART regimen for at least the previous 12 months, and all had HIV RNA levels of <20 copies per mL in both blood and CSF. All had recent onset of symptoms within the past 6 months. All were assessed by a neurologist, and all had blood and CSF analyses to exclude other causes of cognitive impairment. All had  $\beta$ -2 microglobulin and neopterin measured in both blood and CSF. (Both  $\beta$ -2 microglobulin and neopterin are markers of immune activation and inflammation and are known to be elevated in many neuroinflammatory conditions and are shown to be mildly elevated in patients who have suppressed plasma and CSF HIV RNA to below the detection limits of clinical assays). All were diagnosed with HAND by the American Academy of Neurology criteria,<sup>14</sup> with a full neuropsychological assessment.<sup>15,16</sup> Of these 18 patients with HAND, 12 were identified with mild neurocognitive impairment (12/18); 4 patients, with asymptomatic neurocognitive impairment; and 2, with HIV-associated dementia (2/18). Individuals with a prior history of drug abuse, significant head injury, psychiatric illness, and Hepatitis C co-infection were excluded. Nine HIV seronegative matched controls were included in the study. None of the patients had any white matter abnormalities or microhemorrhages on anatomic MR imaging protocols. Local ethics approval was obtained from the St Vincent’s Hospital Human Research Ethics Committee, and all the participants provided written informed consent before enrollment (Table 1).

### Neurocognitive Evaluation

Neurocognitive testing was performed with a brief research test battery described previously, which has been validated for use in the HIV-positive population.<sup>14,15</sup> Briefly, the test battery consisted of a brief computerized battery (CogState) supplemented with a small selection of standardized pencil-and-paper tests to

**Table 1: Demographic, HIV, and neurocognitive characteristics of the study sample**

	HIV+ (n = 18)	Control (n = 9)	P
Age (mean) (SD) (yr)	53.7 (7.5)	55 (4.0)	.6897
Male sex (%)	100	100	
Ethnicity (% white)	100	100	
Education (mean) (SD) (yr)	13.0 (3.0)	15 (2.0)	.0043
Duration stable on cART (median) (IQR) (yr)	2 (2)	NA	
CD4 cell count (median) (IQR) (cells/mm <sup>3</sup> )	657 (550)		
Nadir CD4 (median) (IQR)	194.5 (263.5)		
Composite neurocognitive z score (median) (IQR)	−0.69 (0.75)		

**Note:**—NA indicates not applicable; IQR, interquartile range; +, positive.

**Table 2: Tests included in the brief neurocognitive research battery**

Cognitive Domain	Tests
Speed of information processing	CogState Detection Task CogState Identification Task Trail-Making Test: Parts A and B WAIS-III Digit Symbol Coding
Attention/working memory	CogState One Back Task CogState Two Back Task
Motor functioning	Grooved Pegboard: Dominant and Non-Dominant Hand
Verbal learning	CogState International Shopping List Task: Learning
Verbal memory	CogState International Shopping List Task: Delayed Recall

**Note:**—WAIS-III indicates Wechsler Adult Intelligence Scale-III.

cover 5 cognitive domains: 1) speed of information processing, 2) attention/working memory, 3) motor coordination, 4) verbal learning, and 5) verbal memory (Table 2). CogState is sensitive to HAND<sup>17</sup> and uses playing cards as stimuli to minimize the influences of culture and education on testing. Other tests were selected to provide greater coverage of other cognitive domains affected by HAND (psychomotor speed and motor coordination). Additionally, premorbid intellectual functioning was estimated with the National Adult Reading Test or a demographic-based regression equation when the National Adult Reading Test could not be validly administered. Psychological measures included the Depression, Anxiety, and Stress Scales and the Mini-International Psychiatric Interview (Version 5.0.). Functional decline for HAND status classification was measured via a standard Independence of Activities of Daily Living questionnaire.<sup>18</sup>

### Image Acquisition

All imaging was performed with a 3T MR imaging scanner (Ingenia; Philips Healthcare, Best, the Netherlands) with a 24-channel head coil. High-resolution 3D T1-weighted volume and rs-fMRI scans were obtained. Volumetric scanning was performed with T1 fast-field echo (TR, 7600 ms [shortest]; TE, 3.5 ms; bandwidth, 191.5 Hz/per pixel; flip angle, 7°; acquisition matrix, 256/256; section thickness, 1-mm isometric voxel [3D encoding] with an acceleration of 2× sensitivity encoding).

We used a resting-state scan sequence in which participants were instructed to focus on a white cross presented on a screen

during the scan. They were also asked not to think of anything in particular. The parameters were the following: total duration, 7.39 minutes; TR/TE, 3000/35 ms; flip angle, 90°; 150 dynamics with the shortest dynamic scan time; acquisition matrix, 230/230/94; section thickness, 4 mm acquired parallel to the anterior/posterior commissure plane.

**Preprocessing.** The data processing was performed on BrainVoyager QX, Version 2.8.4 (Brain Innovation, Maastricht, the Netherlands). Anatomic images were corrected for inhomogeneity with an automatic intensity-based approach (which included a brain extraction). The functional data were corrected for the differences in section scan-time acquisition, motion in 3 planes (with the first volume as reference), and linear and nonlinear temporal drifts with a high-pass filter based on a general linear model with a Fourier basis set (1 linear, 2 sine, and 2 cosine functions). Native functional and anatomic data were coregistered in 2 steps with first, the header-based positioning information and, second, an intensity-based alignment algorithm.

**Image Analysis.** Subsequently both the anatomic and functional data were normalized with affine transformation into the anterior/posterior commissural planes and finally to Talairach space with an inbuilt function of BrainVoyager, which uses a piecewise linear approach.<sup>19,20</sup>

On the basis of the standardized (Talairach) 3D anatomic dataset, white matter and ventricle voxels were defined for each subject. From both anatomic areas, the average time courses were extracted and used in combination with motion confounds (6 parameters) to regress out specific sources of noise within the functional data.<sup>21</sup> ROI time-series were computed by selecting a seed location based on predefined coordinates in the Talairach Atlas (based on the Brodmann file available in the BrainVoyager standard installation) and taking the average of all voxels from the following ROIs: Brodmann areas 2 (somatosensory cortex-network), 8 (intraparietal sulcus-dorsal attentional networks), 9 (dorsolateral prefrontal cortex-executive network), 13 (anterior insular cortex-salience network), 17 (primary visual cortex-visual network), and 31 (posterior cingulate-default mode network) based on a predefined/standard ROI file in Talairach space.

**Postprocessing and Statistical Analysis.** To localize significant ROIs within the HIV and control groups, we performed a seed-based correlation for each of the 6 mentioned resting-state networks. On the basis of subject-specific correlation maps, an independent *t* test was performed to show up the differences between the HIV and control groups. The analysis of the comparison of interregional connectivity between the HIV and control group included the following steps: Consistent regions between both the groups were defined for each resting-state network on the basis of the anatomic conjunction (overlap) of functional maps. From these overlapping ROIs in each resting-state network, the signal time courses were extracted for each subject. Pair-wise correlations were calculated from within each network, and the average correlations were computed at the subject level. On the basis of the subject-specific inter-region correlations, an independent *t* test was used to assess the differences between the HIV and con-

trol groups. All statistical analysis was performed with SPSS (Version: 1.2; IBM, Armonk, New York).

### **Inclusion of External Covariates**

A single composite neurocognitive *z* score was generated through 2 steps. First, CogState normative data raw scores were converted to age-corrected *z* scores ( $M = 0$ ,  $SD = 1$ ) with CogState normative data, and raw scores on other tests were converted to age-adjusted scaled scores with published normative data<sup>14</sup> before being transformed into *z* scores. (*Z* scores are standardized scores, ie, transformed to fit in a normal curve after being adjusted for variables such as age and sex. In healthy individuals, the distribution of standardized cognitive scores, after adjustments, is centered at zero [mean and median] with an SD of 1. Cognitively impaired individuals may have a cognitive score lower than that of healthy individuals, so the average *z* score for cognitively impaired individuals is much lower). Second, the average of each subset *z* score was taken to derive a composite neurocognitive score for each patient (Table 1).

The neurocognitive (NC) scores of all the 18 patients were plotted, and a median split was performed. On the basis of the median split of the NC score, a 1-way analysis of variance was performed with the seed-based resting-state data as a dependent variable.

Within the resulting *F*-maps, a contrast checking of the difference between group 2 (NC score > median) and group 1 (NC score < median) was performed. All resulting *t* maps were corrected for multiple comparison problems with the cluster-correction approach (Forman et al, 1995<sup>22</sup>) based on an uncorrected starting threshold of  $P = .05$  (a classic Forman cluster-correction approach to 3D statistical maps is implemented in BrainVoyager; [http://support.brainvoyager.com/documents/Functional\\_Statistics/ClusterThreshPluginHelp/](http://support.brainvoyager.com/documents/Functional_Statistics/ClusterThreshPluginHelp/)).<sup>21</sup>

## **RESULTS**

rs-fMRI data were obtained from 27 subjects (18 seropositive and 9 seronegative controls). All the participants were included in the final analysis. The controls were of similar age, sex, and ethnicity (Table 1).

### **Comparisons of Connectivity in Different Seed Region Networks**

There were significant group differences between the average intercluster correlation in the control and patient groups in the executive network (0.26 versus 0.14,  $t = 2.6978$ ,  $df = 25$ ,  $P = .0123$ ) and salience network (0.52 versus 0.32,  $t = 2.2372$ ,  $df = 25$ ,  $P = .034$ ), indicating that there is significantly reduced synchronicity within these 2 networks (salience and attentional networks) (Figs 1 and 2; Table 3).

The difference between controls and patients was trending toward being significant in the dorsal attention network (0.37 versus 0.24,  $t = 1.83$ ,  $df = 25$ ,  $P = .07$ ).

The group differences in the somatosensory network (0.29 versus 0.36,  $t = 0.179$ ), ventral attentional network (0.37 versus 0.24,  $t = 0.06$ ), and default mode network (0.21 versus 0.21,  $t = 0.91$ ) did not reach statistical significance.

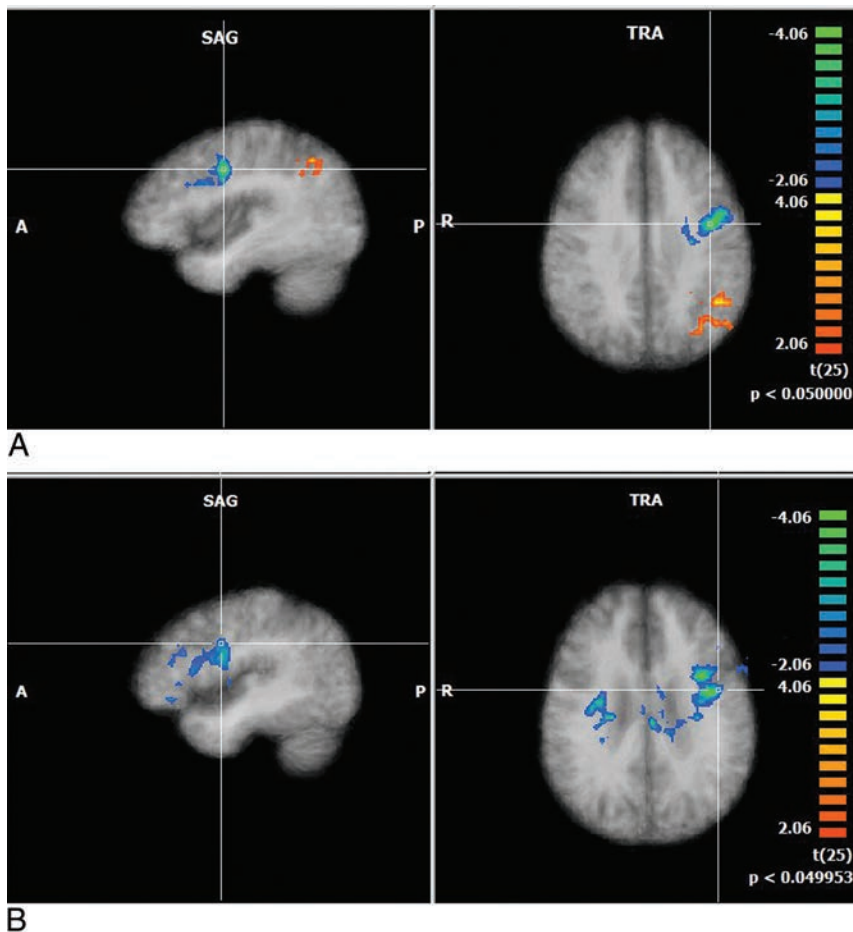


**FIG 1.** Multiplanar and axial depictions of differences between patients with HIV and control subjects in Brodmann area 9 (executive networks) and Brodmann area 13 (salience networks). Positive values represent higher correlation, and negative values depict lower correlation in patients with HIV relative to control subjects. (All the resultant maps are cluster-corrected). *A*, Brodmann area 9: patients-controls. *B*, Brodmann area 13: patients-controls.

### Correlations between Network Connectivity Analysis and Clinical Measures

We assessed whether observed changes in brain networks were associated with neuroinflammatory markers (namely CSF and plasma neopterin and  $\beta$ -2 microglobulin) and NC scores. None of the networks demonstrated any significant positive or negative correlations with plasma/CSF biomarkers. However, neurocognitive scores showed significant correlations with all 6 mentioned networks. Within these networks, the salience networks demonstrated the most significant correlations with reduced neurocognitive scores (Figs 3 and 4).

### DISCUSSION

Our study showed that there is significant attenuation in the salience and executive networks in patients with HAND with active disease despite viral suppression in both plasma and CSF. The network changes correlated with the degree of neuropsychological impairment but not with markers of neuroinflammation in the blood or CSF.

The salience network is considered important for monitoring the salience of external inputs and internal brain events, and the central executive network is engaged in higher order cognitive and attentional control. The salience networks comprise cortical areas of the

anterior insula and anterior cingulate and subcortical areas, including the amygdala, substantia nigra, and thalamus. The central executive networks connect the dorso-lateral prefrontal cortex to the striatum and posterior inferior parietal areas and have subcortical networks distinct from those in the salience networks.<sup>23</sup>

Only 5 studies examined the effect of HIV and secondarily HAND on rs-fMRI. Foryt et al<sup>9</sup> in their study on HIV-positive subjects in their first year of infection showed diminished connectivity within the lateral occipital network (visual attention or visuospatial attention), but there were no patients with HAND. Ipser et al<sup>11</sup> had a cohort of 15 HIV-positive patients, 11 of whom were on cART. There were 4 patients with HAND. Reduced fronto-striatal connectivity was noted, especially in relation to the executive network. Thomas et al<sup>10</sup> had a heterogeneous cohort of 52 HIV-positive patients (23 were on cART but the number who were virally suppressed was not clear and only 12 had HAND). They were evaluated for the effect of aging in HIV compared with seronegative controls. They found attenuation in the default mode and salience networks, similar to that which occurs with age, and inferred that there is premature aging in HIV. This study did not find any correlation with neurocognitive scores or plasma markers.

Guha et al<sup>12</sup> evaluated resting networks in HIV-infected individuals older than 60 years of age (HIV-positive,  $n = 52$ , and controls,  $n = 29$ ). Most were on cART (94%) but not all were virally suppressed (35 of 50 patients) and 27 had HAND, though none appeared to have active disease. Those with detectable plasma HIV-RNA had reduced connectivity in the salience networks. No significant relationship between the neuropsychiatric performance and rs-fMRI was observed.

Ann et al<sup>13</sup> tested the differences in connectivity in seropositive patients with and without HAND, using seed-based connectivity in the default mode network with seed in the precuneus, and demonstrated that there was reduced connectivity between the precuneus and prefrontal regions in the HAND group versus the non-HAND group (10 patients in HAND and 13 in non-HAND). The group separation was not based on CSF viral suppression. The whole-brain networks were not evaluated in this study. It is, therefore, a targeted deterministic seed-based study assessing 1 domain only (default mode network). It is also unclear whether there were any white matter lesions associated with age in this cohort and how much the effect of aging and vascular disease influenced the results.

As previously mentioned, none of the above-mentioned studies included patients with HAND with viral suppression in both

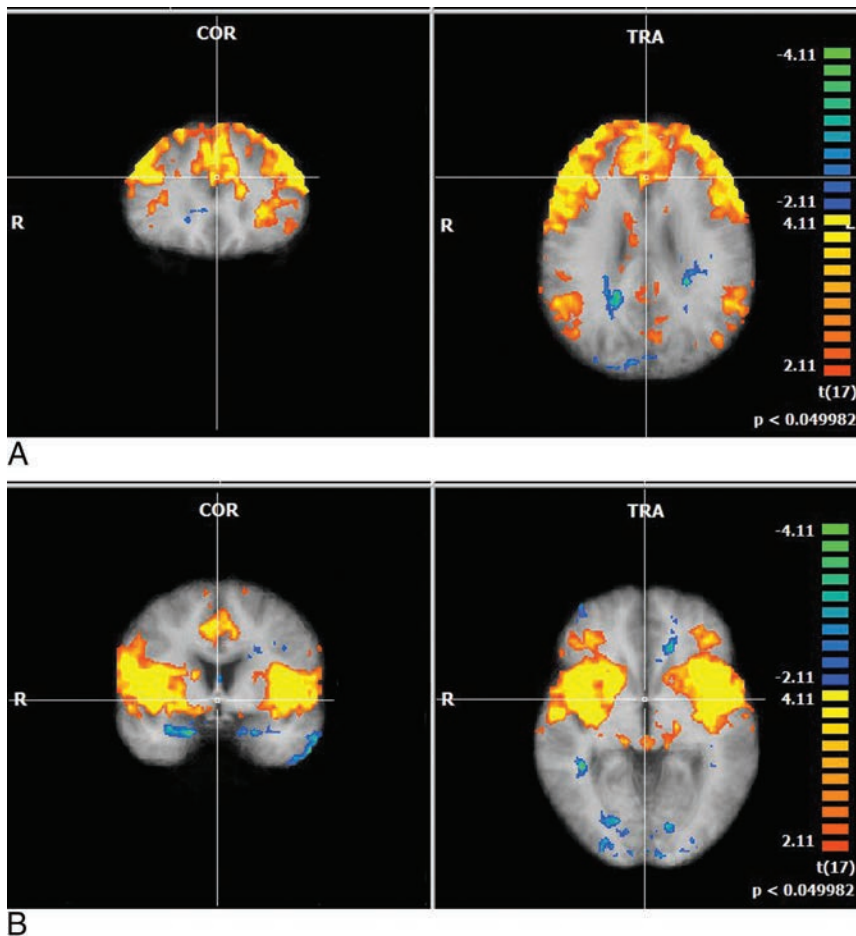


**FIG 2.** A, Multiplanar depictions of group effect in subjects with HIV in the executive networks with the seed region in Brodmann area 9. Note large consistently activated voxels in the entire group, with activation in the dorsolateral frontal cortex and posterior inferoparietal regions and in the striatum. B, Multiplanar depictions of group effect in subjects with HIV in the executive networks with seed regions in Brodmann area 13. Large consistently activated voxels in the group with activation in the anterior insula, anterior cingulate, and thalamus.

**Table 3: Mean Talairach coordinates of the center-of-gravity coordinates in X, Y, and Z axes and SD and number of voxels (1-mm resolution of each cluster) in Brodmann area 9 (control executive networks) and 13 (salience networks) seed region networks<sup>a</sup>**

	Mean X	Mean Y	Mean Z	SD X	SD Y	SD Z	Voxel No.
BA 9							
Cluster1_conjunction	5.98	25.50	34.01	35.43	23.28	11.16	78,154
Cluster2_conjunction	37.79	-39.71	46.68	3.68	6.20	3.33	1149
Cluster3_conjunction	2.67	7.61	22.38	7.57	9.84	2.31	824
Cluster4_conjunction	-2.32	-65.50	37.52	4.02	3.44	5.86	1437
Cluster5_conjunction	-32.92	-61.66	49.64	6.30	5.04	3.92	1540
BA 13							
Cluster1_conjunction	-30.81	10.97	12.36	14.87	15.63	13.75	16,021
Cluster2_conjunction	42.25	13.22	8.38	8.56	11.14	8.12	13,973
Cluster3_conjunction	-43.21	-17.40	8.17	10.22	12.70	8.91	4252
Cluster4_conjunction	52.63	-20.30	12.93	6.53	17.32	11.82	6609

**Note:**—BA indicates Brodmann area.

<sup>a</sup> The clusters are defined on the basis of conjointly activated voxels in patients and control subjects.

blood and CSF, and the activity of HAND was not mentioned. Nonetheless, in those studies with patients with HAND, 2 of 3 found a relationship to attenuation of the salience network.<sup>10,12</sup> Ipser et al<sup>11</sup> noted a relationship only with the central executive control network, but the study included patients with substance misuse and only 4 patients had HAND. Of potential additional importance is the finding by Guha et al<sup>12</sup> of a reduction in

the salience network with an elevated plasma viral load. This may be relevant to our findings: it suggests that active HAND, at least in our study, is associated with viral replication in the brain at a level not reflected in the blood or the CSF.

Our study also identified significant correlations between neuropsychological scores and significant attenuation in all 6 networks, but especially in the salience, default mode, and executive control networks. These could be due to global injury associated with HIV.<sup>24,25</sup>

Our findings may have specificity for HAND. The frontostriatal networks have been found to be attenuated in Parkinson disease, and attenuation of these executive networks along with default mode networks is said to occur when there is coexistent cognitive impairment associated with Parkinson disease.<sup>26</sup> However, salience network involvement is not known to occur in Parkinson disease. In healthy aging and Alzheimer disease, there is some uniformity in the involvement of default mode networks. In healthy aging, it was found that there is a decline in the connectivity in the default mode networks. It was also found that there is some evidence of increased connectivity with age, possibly as a compensatory mechanism due to changing neural strategies in most of the other networks. Similarly, in Alzheimer disease, there is a decline in connectivity in most of the networks, but this decline is exaggerated with the default mode network being affected most and much more pronounced than in individuals with healthy aging.<sup>27</sup> Studies in vascular dementia with rs-fMRI showed involvement of multiple domains, with most pronounced changes in the prefrontal posterior cingulate loop, which is not a typical feature in Alzheimer dementia or HAND.<sup>28,29</sup> Therefore, the demonstration of attenuation of both the executive and salience networks could be useful as a specific biomarker for active HAND.

There are several limitations in interpreting the results of our study. The study group only included white males. Sample sizes used in this study were small; this small size limited the power to detect between-group differences in the salience and attentional networks. Our cohort had a smaller number of controls who did not undergo formal neuropsychological testing though they were entirely asymptomatic. However, the test we used was not a factorial ANOVA and

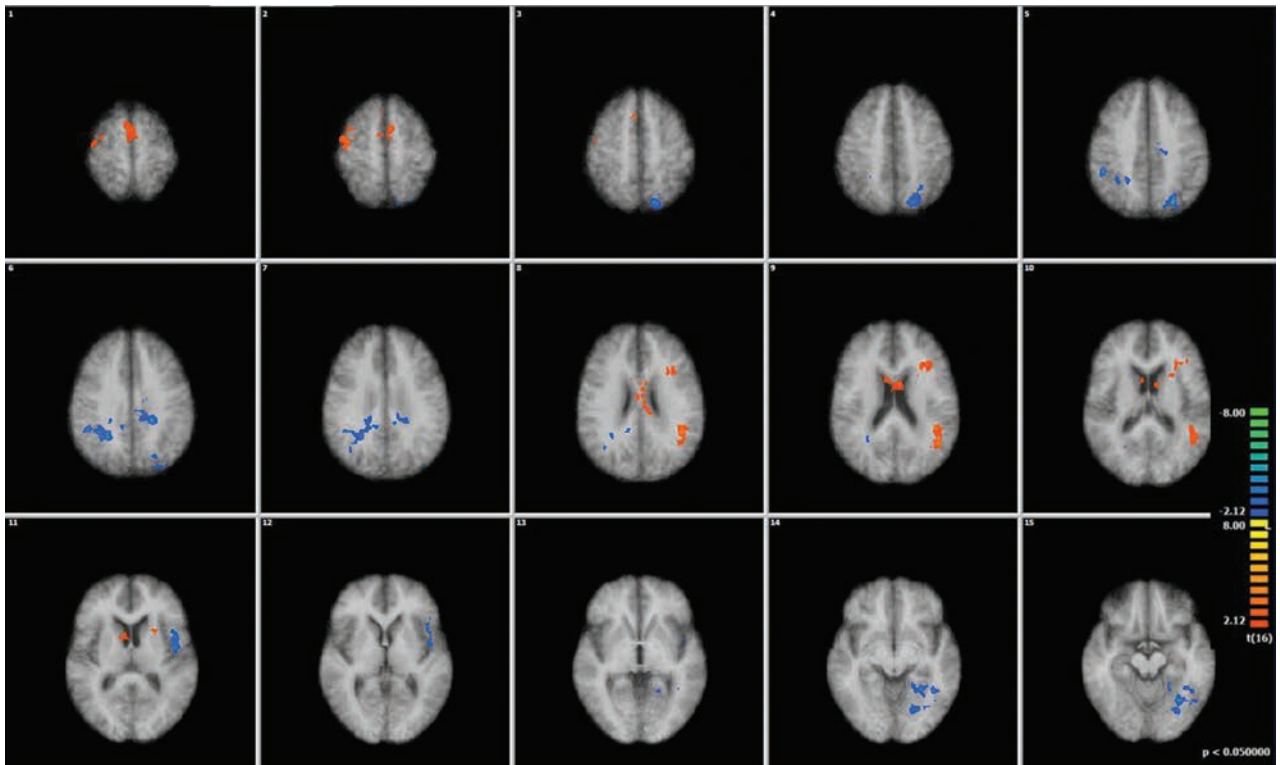


**FIG 3.** Salience networks. Difference in correlation of the salience network with neurocognitive score (NCS): (Correlation Value in NCS > Median) – (Correlation Value in NCS < median). Orange denotes areas showing larger correlation values in patients with larger neurocognitive values, while blue shows the opposite. Each of the maps is corrected with the cluster-correction approach.

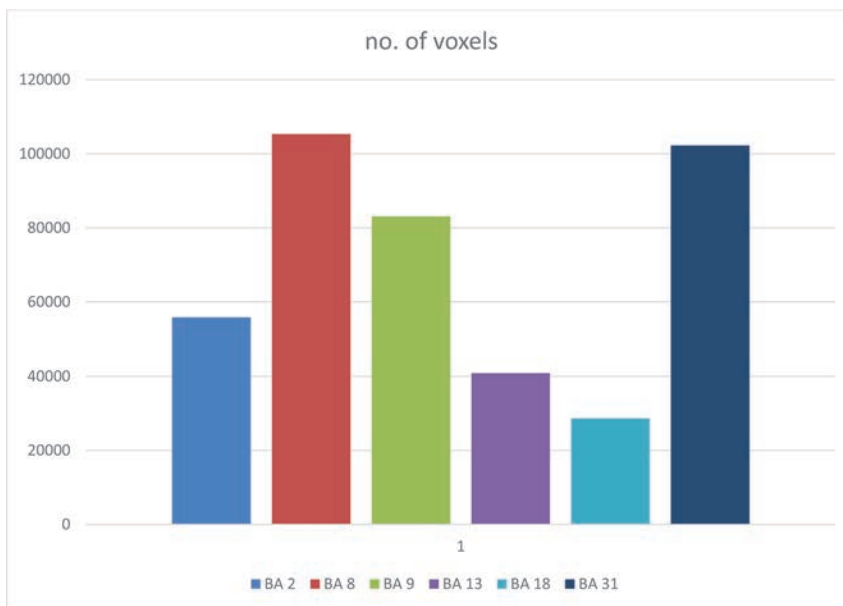


**FIG 4.** Covariate analysis with neurocognitive scores demonstrating surviving voxels in each of the 6 networks.

hence probably would have a limited effect on the results (we used a *t* test with heterogeneous variances). In addition, the inherent ambiguities and pitfalls of rs-fMRI could have influenced the outcome of the results through residual effects of noise and inherent blood oxygenation-associated confounds. However, we think these noise effects are not significant because of preprocessing. Last, we cannot exclude the importance of neurotoxicity from cART as opposed to

observed that there was no effect on either blood flow or connectivity in a small cohort.<sup>30,31</sup>

### CONCLUSIONS

We found significantly decreased connectivity in the executive and salience networks in active HAND, suggesting that it could be used as a biomarker. Furthermore, the association with the sa-

HIV, given that all the patients in our group were on long-term (>4 years) cART, though the effect of neurotoxicity-associated cognitive impairment appears to be inconclusive. The persistence of the minor cognitive impairment after widespread implementation of cART raised questions about the possible role of the antiretrovirals, particularly nucleoside reverse transcriptase inhibitors.<sup>30,31</sup> However, several studies have demonstrated the neuroprotective effectiveness of the cART regimen on neurocognitive function.<sup>31,32</sup> Using MR spectroscopy, investigators have shown that there is marked improvement in both clinical measures and metabolite concentrations.<sup>8</sup> One recent study used the metrics derived from arterial spin-labeling and rs-fMRI to measure the blood flow and connectivity in HIV-negative individuals before and after using 2 common antiretroviral medications (efavirenz and ritonavir) and ob-

lience network and its relationship with HIV replication in the blood<sup>12</sup> raises a further testable and plausible hypothesis: Active HAND in the context of viral suppression in blood and CSF is driven by very low-level brain replication. Future studies will need to validate these findings with larger patient numbers and correlate the findings with CSF single-copy assays of HIV.

Disclosures: Thomas M. Gates—UNRELATED: Travel/Accommodations/Meeting Expenses Unrelated to Activities Listed: Viiv Healthcare Australia, Comments: paid for conference registration: 2014 Association for Psychological Science's College of Clinical Neuropsychologists conference.

## REFERENCES

1. Heaton RK, Clifford DB, Franklin DR Jr, et al; CHARTER Group. **HIV-associated neurocognitive disorders persist in the era of potent antiretroviral therapy: CHARTER Study.** *Neurology* 2010;75:2087–96 CrossRef Medline
2. Heaton RK, Franklin DR, Ellis RJ, et al; CHARTER Group; HNRC Group. **HIV-associated neurocognitive disorders before and during the era of combination antiretroviral therapy: differences in rates, nature, and predictors.** *J Neurovirol* 2011;17:3–16 CrossRef Medline
3. Mothobi NZ, Brew BJ. **Neurocognitive dysfunction in the highly active antiretroviral therapy era.** *Curr Opin Infect Dis* 2012;25:4–9 CrossRef Medline
4. Cysique LA, Brew BJ. **Prevalence of non-confounded HIV-associated neurocognitive impairment in the context of plasma HIV RNA suppression.** *J Neurovirol* 2011;17:176–83 CrossRef Medline
5. Brew BJ. **Evidence for a change in AIDS dementia complex in the era of highly active antiretroviral therapy and the possibility of new forms of AIDS dementia complex.** *AIDS* 2004;18(suppl 1):S75–78 Medline
6. Woods SP, Moore DJ, Weber E, et al. **Cognitive neuropsychology of HIV-associated neurocognitive disorders.** *Neuropsychol Rev* 2009;19:152–168 CrossRef Medline
7. Chang L, Tomasi D, Yakupov R, et al. **Adaptation of the attention network in human immunodeficiency virus brain injury.** *Ann Neurol* 2004;56:259–72 CrossRef Medline
8. Chang L, Yakupov R, Nakama H, et al. **Antiretroviral treatment is associated with increased attentional load-dependent brain activation in HIV patients.** *J Neuroimmune Pharmacol* 2008;3:95–104 CrossRef Medline
9. Foryt P, Wang X, Ochs R, et al. **Diminished resting-state functional connectivity in lateral occipital cortex in early HIV infection.** In: *Proceedings of the Annual Meeting of the International Society for Magnetic Resonance in Medicine*, Montreal, Quebec, Canada. May 6–13, 2011;19:4163
10. Thomas JB, Brier MR, Snyder AZ, et al. **Pathways to neurodegeneration: effects of HIV and aging on resting-state functional connectivity.** *Neurology* 2013;80:1186–93 CrossRef Medline
11. Ipser JC, Brown GG, Bischoff-Grethe A, et al; Translational Methamphetamine AIDS Research Center (TMARC) Group. **HIV infection is associated with attenuated frontostriatal intrinsic connectivity: a preliminary study.** *J Int Neuropsychol Soc* 2015;21:203–13 CrossRef Medline
12. Guha A, Wang L, Tanenbaum A, et al. **Intrinsic network connectivity abnormalities in HIV-infected individuals over age 60.** *J Neurovirol* 2016;22:80–87 CrossRef Medline
13. Ann HW, Jun S, Shin NY, et al. **Characteristics of resting-state functional connectivity in HIV-associated neurocognitive disorder.** *PLoS One* 2016;11:e0153493 CrossRef Medline
14. Antinori A, Arendt G, Becker, et al. **Updated research nosology for HIV-associated neurocognitive disorders.** *Neurology* 2007;69:1789–99 CrossRef Medline
15. Heaton RK. *Revised Comprehensive Norms for an Expanded Halstead-Reitan Battery: Demographically Adjusted Neuropsychological Norms for African American and Caucasian Adults, Professional Manual.* Lutz, Florida: Psychological Assessment Resources; 2004
16. Gates TM, Cysique LA, Siefried, KJ, et al. **Maraviroc-intensified combined antiretroviral therapy improves cognition in virally suppressed HIV-associated neurocognitive disorder.** *AIDS* 2016;30:591–600 CrossRef Medline
17. Cysique LA, Maruff P, Darby D, et al. **The assessment of cognitive function in advanced HIV-1 infection and AIDS dementia complex using a new computerised cognitive test battery.** *Arch Clin Neuropsychol* 2006;21:185–94 CrossRef Medline
18. Lane T, Moore D, Batchelor J, et al. **Facial emotional processing in HIV infection: relation to neurocognitive and neuropsychiatric status.** *Neuropsychology* 2012;26:713–22 CrossRef Medline
19. Goebel R, Esposito, F, Formisano E. **Analysis of functional image analysis contest (FIAC) data with BrainVoyager QX: from single-subject to cortically aligned group general linear model analysis and self-organizing group independent component analysis.** *Hum Brain Mapp* 2006;27:392–401 CrossRef Medline
20. Goshtasby A. **Piecewise linear mapping functions for image registration.** *Pattern Recog* 1986;19:459–66 CrossRef
21. Weissenbacher A, Kasess C, Gerstl F, et al. **Correlations and anticorrelations in resting-state functional connectivity MRI: a quantitative comparison of preprocessing strategies.** *Neuroimage* 2009;47:1408–16 CrossRef Medline
22. Forman SD, Cohen JD, Fitzgerald M, et al. **Improved assessment of significant activation in functional magnetic resonance imaging (fMRI): use of a cluster-size threshold.** *Magn Reson Med* 1995;33:636–47 CrossRef Medline
23. Bressler SL, Menon V. **Large-scale brain networks in cognition: emerging methods and principles.** *Trends Cogn Sci* 2010;14:277–90 CrossRef Medline
24. Kallianpur KJ, Kirk GR, Sailasuta N, et al. **Regional cortical thinning associated with detectable levels of HIV DNA.** *Cereb Cortex* 2012;22:2065–75 CrossRef Medline
25. Gongvatana A, Harezlak J, Buchthal S, et al; HIV Neuroimaging Consortium. **Progressive cerebral injury in the setting of chronic HIV infection and antiretroviral therapy.** *J Neurovirol* 2013;19:209–18 CrossRef Medline
26. Amboni M, Tessitore A, Esposito F, et al. **Resting-state functional connectivity associated with mild cognitive impairment in Parkinson's disease.** *J Neurol* 2015;262:425–34 CrossRef Medline
27. Dennis EL, Thompson MP. **Functional brain connectivity using fMRI in aging and Alzheimer's disease.** *Neuropsychol Rev* 2014;24:49–62 CrossRef Medline
28. Liu C, Li C, Yin X, et al. **Abnormal intrinsic brain activity patterns in patients with subcortical ischemic vascular dementia.** *PLoS One* 2014;9:e87880 CrossRef Medline
29. Castellazzi, G, Palesi, Casiraghi L, et al. **Patterns of altered functional connectivity in Alzheimer disease and vascular dementia.** In: *Proceedings of the Annual Meeting and Exhibition of the International Society for Magnetic Resonance in Medicine*, Toronto, Ontario, Canada. May 30–June 5, 2015
30. Brier MR, Wu Q, Tanenbaum AB, et al. **Effect of HAART on brain organization and function in HIV-negative subjects.** *J Neuroimmune Pharmacol* 2015;10:517–21 CrossRef Medline
31. Marra CM, Zhao Y, Clifford DB, et al; Clinical Trials Group 736 Study Team. **Impact of combination antiretroviral therapy on cerebrospinal fluid HIV RNA and neurocognitive performance.** *AIDS* 2009;23:1359–66 CrossRef Medline
32. Bogoch II, Davis BT, Venna N. **Reversible dementia in a patient with central nervous system escape of human immunodeficiency virus.** *J Infect* 2011;63:236–39 CrossRef Medline

# Influence of Ultra-Low-Dose and Iterative Reconstructions on the Visualization of Orbital Soft Tissues on Maxillofacial CT

G. Widmann, D. Juranek, F. Waldenberger, P. Schullian, A. Dennhardt, R. Hoermann, M. Steurer, E.-M. Gassner, and W. Puelacher

## ABSTRACT

**BACKGROUND AND PURPOSE:** Dose reduction on CT scans for surgical planning and postoperative evaluation of midface and orbital fractures is an important concern. The purpose of this study was to evaluate the variability of various low-dose and iterative reconstruction techniques on the visualization of orbital soft tissues.

**MATERIALS AND METHODS:** Contrast-to-noise ratios of the optic nerve and inferior rectus muscle and subjective scores of a human cadaver were calculated from CT with a reference dose protocol (CT dose index volume = 36.69 mGy) and a subsequent series of low-dose protocols (LDPs I–4: CT dose index volume = 4.18, 2.64, 0.99, and 0.53 mGy) with filtered back-projection (FBP) and adaptive statistical iterative reconstruction (ASIR)-50, ASIR-100, and model-based iterative reconstruction. The Dunn Multiple Comparison Test was used to compare each combination of protocols ( $\alpha = .05$ ).

**RESULTS:** Compared with the reference dose protocol with FBP, the following statistically significant differences in contrast-to-noise ratios were shown (all,  $P \leq .012$ ) for the following: 1) optic nerve: LDP-I with FBP; LDP-II with FBP and ASIR-50; LDP-III with FBP, ASIR-50, and ASIR-100; and LDP-IV with FBP, ASIR-50, and ASIR-100; and 2) inferior rectus muscle: LDP-II with FBP, LDP-III with FBP and ASIR-50, and LDP-IV with FBP, ASIR-50, and ASIR-100. Model-based iterative reconstruction showed the best contrast-to-noise ratio in all images and provided similar subjective scores for LDP-II. ASIR-50 had no remarkable effect, and ASIR-100, a small effect on subjective scores.

**CONCLUSIONS:** Compared with a reference dose protocol with FBP, model-based iterative reconstruction may show similar diagnostic visibility of orbital soft tissues at a CT dose index volume of 2.64 mGy. Low-dose technology and iterative reconstruction technology may redefine current reference dose levels in maxillofacial CT.

**ABBREVIATIONS:** ALADA = As Low As Diagnostically Achievable; ALARA = As Low As Reasonably Achievable; ASIR = adaptive statistical iterative reconstruction; CNR = contrast-to-noise ratio; CTDI<sub>vol</sub> = CT dose index volume; FBP = filtered back-projection; HU = Hounsfield unit; IRM = inferior rectus muscle; LDP = low-dose protocol; MBIR = model-based iterative reconstruction; ON = optic nerve

The success of modern maxillofacial surgery is undoubtedly related to the increased use of multisection CT. Image data are used for diagnosis and treatment, including software planning, fabrication of rapid prototyping models, customized surgical plate modeling, and computer-guided surgery.

However, the increasing use of CT has been cited as a cause for the increasing collective dose of ionizing radiation to populations.<sup>1</sup> The

public awareness of cumulative radiation exposure from medical imaging is strongly reflected by legislative authorities and radiologic societies, leading to recent awareness campaigns such as the Image Gently and Image Wisely Campaigns and the American College of Radiology Dose Index Registry Initiatives.<sup>2</sup>

In the field of maxillofacial imaging, the eye lenses and thyroid gland are the most critical organs affected by direct or scattered radiation.<sup>3</sup> Available CT technology has to be optimized to assure that the examination adheres to the As Low As Reasonably Achievable (ALARA)/As Low As Diagnostically Achievable (ALADA) principles to reduce the potential risks from ionizing radiation. Protection from ionizing radiation is critical in young and middle-aged patients who frequently have sports-related midface and orbital fractures.<sup>4</sup> One has to take into account that most patients have already had an initial CT scan during the emergency diagnostic evaluation and may require repeat CT scans for treatment planning, guided surgery, and postoperative evaluation.<sup>5</sup>

Modern CT technology is able to substantially reduce the

Received February 10, 2017; accepted March 19.

From the Departments of Radiology (G.W., P.S., E.-M.G.) and Craniomaxillofacial Surgery (D.J., F.W., A.D., W.P.) and Division of Functional and Clinical Anatomy (R.H.), Innsbruck Medical University, Innsbruck, Austria.

Paper previously presented in abstract form at: Computer-Assisted Radiology and Surgery 30th International Congress and Exhibition, June 21–25, 2016; Heidelberg, Germany.

Please address correspondence to Gerlig Widmann, MD, Department of Radiology, Innsbruck Medical University, A-6020 Innsbruck, Anichstr 35, Austria; e-mail: gerlig.widmann@i-med.ac.at

<http://dx.doi.org/10.3174/ajnr.A5239>

**Table 1: Scan protocols and parameters used including CTDI<sub>vol</sub>, DLP, and effective dose**

Dose Protocol	Reconstruction		kV	mAs	Pitch	Rotation Time (s)	CTDI <sub>vol</sub> (mGy)	DLP (mG × cm)	Effective Dose (mSv)
	Technique	Kernel							
Emergency protocol head	ASIR-50	Bone	120	314–488	1	0.6	47.55	1141.26	4.9
Reference dose protocol	FBP	Bone, std	120	100	0.5	1	36.69	930.78	3.5
Low-dose protocol I	ASIR-50	Bone, std							
	ASIR-100	Bone, std							
	MBIR	std							
	FBP	Bone, std	100	35	0.5	0.5	4.18	106.18	0.4
Low-dose protocol II	ASIR-50	Bone, std							
	ASIR-100	Bone, std							
	MBIR	std							
	FBP	Bone, std	80	40	0.5	0.5	2.64	66.69	0.3
Low-dose protocol III	ASIR-50	Bone, std							
	ASIR-100	Bone, std							
	MBIR	std							
	FBP	Bone, std	80	15	0.5	0.5	0.99	25.13	0.1
Low-dose protocol IV	ASIR-50	Bone, std							
	ASIR-100	Bone, std							
	MBIR	std							
	FBP	Bone, std	80	10	0.5	0.4	0.53	13.39	0.1

**Note:**—DLP indicates dose-length product; std, standard.

dose.<sup>6–10</sup> Furthermore, dose reduction may not significantly influence registration and navigation accuracy for computer-aided surgery.<sup>11–13</sup> However, the associated increase in noise may significantly influence the diagnostic image quality of soft-tissue structures such as the optical nerve and orbital muscles. The recent implementation of iterative reconstruction techniques such as adaptive statistical iterative reconstruction (ASIR) and model-based iterative reconstruction (MBIR) may improve image quality with reduced radiation doses compared with the traditionally used filtered back-projection (FBP) technique.<sup>14,15</sup>

The aim of the present study was to evaluate the influence of various low-dose protocols and iterative reconstructions on the visualization of orbital soft tissues.

## MATERIALS AND METHODS

We used 1 cadaver head preserved with an arterial injection of a formaldehyde-phenol solution/an alcohol-glycerin solution and immersion in phenolic acid in water for 1–3 months.<sup>16</sup> The bodies were donated by individuals who had given their informed consent before death for their use for scientific and educational purposes.<sup>17,18</sup>

The entire cadaver head including the mandible was scanned by using the Discovery CT750 HD (GE Healthcare, Milwaukee, Wisconsin) and the following protocols: the standard emergency protocol of the head (as used during initial cranial CT in the emergency setting), a high-resolution reference dose protocol (as used for surgical planning and navigated surgery), and a subsequent series of low-dose protocols (LDPs) with various iterative reconstruction techniques and bone and standard kernels (protocol details can be found in Table 1). The images were exported in a DICOM format with Impax EE (Agfa-Gevaert, Mortsel, Belgium) PACS.

### Dose Estimation

CT dose index volume (CTDI<sub>vol</sub>) and dose-length product were obtained from the DICOM tags. In addition, CT-Expol, Version 2.1 (Medical University Hannover, Hannover, Ger-

many), an Excel (Microsoft, Redmond, Washington) application for assessing the radiation doses delivered to patients undergoing CT examinations based on the scan parameters of the used scanner type, was used to calculate effective doses (International Commission of Radiation Protection: ICRP 103; [http://apps.snm.org/docs/CME/PresenterItems/EventID\\_85/PresenterItemTypeID\\_1/3.%20Eckerman%20-%201050.pdf](http://apps.snm.org/docs/CME/PresenterItems/EventID_85/PresenterItemTypeID_1/3.%20Eckerman%20-%201050.pdf)) (Table 1).<sup>19</sup>

### Analysis of Hounsfield Unit Values and Contrast-to-Noise Ratios of Orbital Soft Tissues

All images were evaluated by 2 readers with AW Server 2.0 (GE Healthcare). The readers were trained for image reformation and volumetric segmentation.

Images were reformatted in axial, coronal, and sagittal views. The window/level was adjusted to obtain the best subjective contrast. The paint-on-slices tool of the AW Server 2.0 software was used to segment the optical nerve (ON) and inferior rectus muscle (IRM) on both sides.

The anterior border of the segmented structures was the horizontal line at the posterior margin of the orbital bulb, and the posterior border was the horizontal line at the foramen of the posterior ethmoid artery. Average Hounsfield units (HUs) and SDs of the segmented volumes were recorded.

In addition, the average Hounsfield unit and SD of the orbital fat lateral to the optic nerve posterior to the horizontal line at the posterior margin of the orbital bulb was measured with a spheric ROI with a 6-mm diameter.

The contrast-to-noise ratio (CNR) for each anatomic structure (ON and IRM) was calculated with the following formula:

$$CNR_a = \frac{|MHU_a - MHU_{fat}|}{\sqrt{(SD_a^2 + SD_{fat}^2)}}$$

with *MHU* indicating the mean Hounsfield unit value, and *SD*, the standard deviation of Hounsfield unit values.

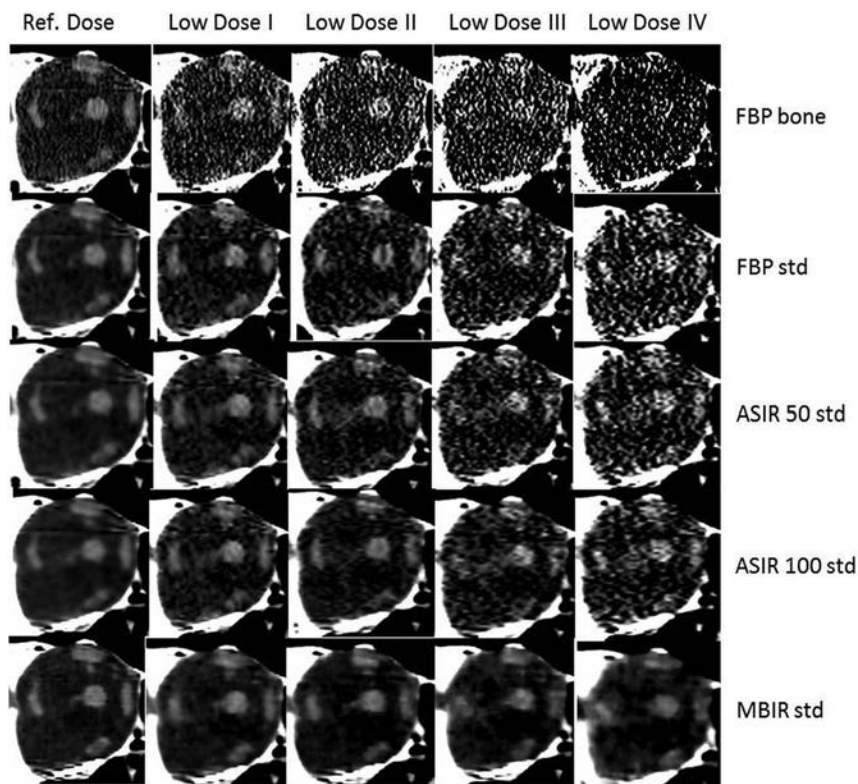


**FIG 1.** Images of the right orbit with different protocols (vertical columns), reconstructions, and kernels (horizontal columns). Std indicates standard.

**Table 2: Mean CNR and SD of ON and IRM for each combination of protocol and reconstruction technique<sup>a</sup>**

Dose Protocol	Reconstruction Technique	ON		IRM		Score Bone Kernel	Score Std Kernel
		CNR (SD)	SD	CNR (SD)	SD		
Emergency protocol head	ASIR-50	2.75 (0.62)		1.82 (0.26)		4.0	
Reference dose protocol	FBP	3.80 (2.07)		2.39 (1.22)		3.0	4.0
	ASIR-50	4.28 (2.04)		2.71 (1.24)		3.0	4.0
	ASIR-100	4.37 (1.39)		2.99 (1.01)		3.0	4.0
	MBIR	5.68 (0.17)		3.60 (0.54)			5.0
Low-dose protocol I	FBP	1.57 (1.07) <sup>b</sup>		1.11 (0.79)		2.0	3.0
	ASIR-50	2.15 (1.27)		1.22 (0.81)		2.0	3.0
	ASIR-100	2.49 (0.98)		1.65 (0.59)		2.0	3.0
	MBIR	4.12 (0.85)		3.05 (0.46)			4.0
Low-dose protocol II	FBP	1.05 (0.75) <sup>b</sup>		0.74 (0.46) <sup>b</sup>		1.0	2.0
	ASIR-50	1.41 (0.94) <sup>b</sup>		0.91 (0.43)		1.0	2.0
	ASIR-100	2.16 (1.15)		1.34 (0.40)		1.0	3.0
	MBIR	4.11 (0.66)		2.81 (0.77)			4.0
Low-dose protocol III	FBP	0.63 (0.44) <sup>b</sup>		0.23 (0.30) <sup>b</sup>		1.0	1.0
	ASIR-50	0.87 (0.57) <sup>b</sup>		0.50 (0.44) <sup>b</sup>		1.0	1.0
	ASIR-100	1.29 (0.65) <sup>b</sup>		0.92 (0.60)		1.0	1.0
	MBIR	3.08 (0.63)		2.32 (0.44)			2.0
Low-dose protocol IV	FBP	0.44 (0.36) <sup>b</sup>		0.10 (0.16) <sup>b</sup>		1.0	1.0
	ASIR-50	0.52 (0.57) <sup>b</sup>		0.31 (0.34) <sup>b</sup>		1.0	1.0
	ASIR-100	0.93 (0.63) <sup>b</sup>		0.62 (0.56) <sup>b</sup>		1.0	1.0
	MBIR	2.62 (0.52)		3.14 (2.71)			2.0

**Note:**—Std indicates standard.

<sup>a</sup> Subjective scores are given separately for images with a bone and standard kernel: 1 indicates very poor/not sufficient; 2, suboptimal but sufficient; 3, average = equal to reference; 4, above average; and 5, excellent.

<sup>b</sup> Statistically significant difference compared with the reference dose protocol with FBP ( $P < .05$ ).

### Analysis of Subjective Image Quality

Subjective image quality of the orbital soft tissues was assessed by consensus of 3 readers with a 5-scale system: 1, very poor/not sufficient; 2, suboptimal but sufficient; 3, average = equal to ref-

erence; 4, above average; and 5, excellent. As a “reference,” the image of the reference dose protocol with FBP and the bone kernel was used, which referred to images usually provided by maxillofacial and sinus CT. Subjective scores were evaluated for each combination of dose, reconstruction technique, and kernel.

### Statistical Analysis

Data analysis and descriptive statistics were performed with PASW Statistics (Version 15.0; IBM, Armonk, New York). Interobserver agreement was assessed with weighted  $\kappa$  statistics. The Dunn Multiple Comparison Test and the Bonferroni-corrected test were used to compare each combination of protocols ( $\alpha = .05$ ). The analysis of variance for dependent variables was used to test between-subject effects: protocol, reconstruction, and kernel.

### RESULTS

Using the 6 protocols, 4 reconstruction techniques, and 2 convolution kernels, we generated 36 CT datasets.  $CTDI_{vol}$ , dose-length product, and effective doses can be found in Table 1.

Compared with the reference dose protocol, LDP I–IV showed dose reductions of about 88.7%, 92.8%, 97.3%, and 98.6%. The effective doses for LDP I–IV, which include the scan of the entire head and mandible, were 0.4, 0.3, 0.1, and 0.1 mSv.

Figure 1 shows images including the reference dose protocol with FBP using the bone and standard kernels, and all low-dose protocols with FBP, ASIR-50, ASIR-100, and MBIR with the standard kernel. The mean CNR and SDs of the ON and IRM for each protocol and reconstruction technique can be found in Table 2.

### Influence of Dose

With the bone kernel, the reference dose protocol showed statistically significantly better CNR than all LDPs for both the ON and IRM (all  $P < .001$ ). Compared with the reference standard, no statistically significant difference from the emergency protocol head ( $P = 1.000$

for the ON,  $P = .951$  for IRM) was found. LDP-I was statistically significantly better than LDP II–IV for the ON ( $P = .011$ ,  $P < .001$ ,  $P < .001$ ), and LDP-III and IV, for the IRM (all,  $P < .001$ ).

LDP-I was not statistically significantly better than LDP-II for the IRM ( $P = 1.000$ ). LDP-II was statistically significantly better than LDP-III and IV for the ON ( $P = .010$ ,  $P < .001$ ) and IRM (all  $P < .001$ ). LDP-III did not show statistically significant differences from LDP-IV for the ON ( $P = .112$ ) and IRM ( $P = .126$ ).

With the standard kernel, the reference dose protocol showed statistically significantly better CNR than all LDPs (all  $P < .001$ ). LDP-I was statistically significantly better than LDP III–IV for the ON (all,  $P < .001$ ) and IRM (all  $P = .004$ ). LDP-I was not statistically significantly better than LDP-II for the ON ( $P = .057$ ) and IRM ( $P = .611$ ). LDP-II was statistically significantly better than LDP III and IV for the ON (all,  $P < .001$ ) but not for the IRM ( $P = .676$ ,  $P = .759$ ). LDP-III did not show statistically significant differences compared with LDP-IV for the ON ( $P = .565$ ) and IRM ( $P = 1.000$ ).

### **Influence of Reconstruction**

With the bone kernel, ASIR-50 and ASIR-100 showed statistically significantly better CNR than FBP for the ON and IRM (all  $P < .001$ ). ASIR-100 had a statistically significantly better CNR than ASIR-50 for the ON ( $P = .007$ ) and IRM ( $P < .001$ ).

With the standard kernel, ASIR-50 had a statistically significantly better CNR than FBP for the ON ( $P = .037$ ) but not for the IRM ( $P = 1.000$ ). ASIR-100 and MBIR showed statistically significantly better CNR than FBP for the ON (all,  $P < .001$ ) and IRM ( $P = .036$ ,  $P < .001$ ). ASIR-100 did not show a statistically significantly better CNR than ASIR-50 ( $P = .745$ ). MBIR showed a statistically significantly better CNR than both ASIR-50 and ASIR-100 for the ON (all  $P < .001$ ) and IRM ( $P < .001$ ,  $P = .001$ ).

### **Influence of the Convolution Kernel**

The standard kernel showed a statistically significantly higher CNR than the bone kernel for the ON and IRM (all  $P < .001$ ). The convolution kernel influenced the effect of iterative reconstructions (see previous sections).

### **Interobserver Agreement**

Interobserver agreement between both readers showed a Pearson correlation coefficient of 0.638 for the CNR measurements of the ON and 0.914 for the CNR measurements of the IRM. The Test of Between-Subjects Effects showed no statistically significant difference ( $P = .950$ ).

### **Comparison with the Reference Dose Protocol with FBP**

Compared with the reference dose protocol with FBP, statistically significant differences of the CNR for the ON were shown with LDP-I with FBP ( $P = .010$ ); LDP-II with FBP ( $P < .001$ ) and ASIR-50 ( $P = .003$ ); LDP-III with FBP ( $P < .001$ ), ASIR-50 ( $P < .001$ ), and ASIR-100 ( $P = .001$ ); and LDP-IV with FBP ( $P < .001$ ), ASIR-50 ( $P < .001$ ), and ASIR-100 ( $P < .001$ ) (Table 2).

For the IRM, statistically significant differences from the reference dose protocol with FBP were shown with LDP-II with FBP ( $P = .012$ ); LDP-III with FBP ( $P < .001$ ) and ASIR-50 ( $P = .001$ ); and LDP-IV with FBP ( $P < .001$ ), ASIR-50 ( $P < .001$ ), and ASIR-100 ( $P = .004$ ) (Table 2).

### **Subjective Scoring**

Compared with the reference dose protocol with FBP bone, which was given the reference score of 3 (average = equal to reference), scores decreased progressively during dose reduction (see Table 2 and the comparison of the images in Fig 1). Images with a standard kernel showed a higher score than with the bone kernel. The reference dose protocol with FBP standard showed a score of 4. In LDP-II, the standard kernel could retain a score of 2 (suboptimal but sufficient) in contrast to the bone kernel, which was insufficient. ASIR-50 had no remarkable effect over FBP on subjective scores. ASIR-100 showed a small effect. MBIR showed the best subjective score in all images. MBIR obtained a score of 4 for LDP I and II and retained a score of 2 for LDP III and IV. ON showed better subjective visibility than IRM.

### **DISCUSSION**

Various iterative reconstruction technologies have been implemented to reduce image noise and improve the quality of low-dose images.<sup>20,21</sup> Adaptive statistical iterative reconstruction uses information obtained from the FBP algorithm but integrates a comparison of the pixel values with an ideal value to selectively identify and then subtract noise from an image at adaptive blend levels freely selectable typically from 10% to 100%.<sup>22</sup> Model-based iterative reconstruction does not rely on the FBP as a starting point but instead uses a more complex system of prediction models, including noise and the spatial and geometric features of the x-ray beam and detector technology.<sup>23</sup> In a cadaver, ASIR-100 at a  $CTDI_{vol} = 3.48$  and  $2.19$  mGy and MBIR at a  $CTDI_{vol} = 0.82$  mGy provided similar subjective cross-sectional and 3D bone image quality compared with the FBP reference at  $CTDI_{vol} = 30.48$  mGy.<sup>24</sup> At a  $CTDI_{vol} = 2.19$  mGy, ASIR-50 reduced noise by 22%; ASIR-100, by 35%; and MBIR, by 67%.<sup>24</sup> When we compared contrast-to-noise ratios of the different reconstructions using a reference dose protocol at a  $CTDI_{vol} = 36.58$  mGy and several ultra-low doses in a phantom study with a customized polymethyl methacrylate phantom, MBIR demonstrated the highest CNR throughout, followed by ASIR-100, ASIR-50, and FBP.<sup>25</sup> With MBIR, ultra-low-dose protocols at  $CTDI_{vol} = 4.14$  and  $2.63$  mGy may show comparable scores for spatial resolution, which may allow a dose-reduction potential of up to 93%.<sup>26</sup> Compared with FBP, ASIR was not able to significantly improve spatial resolution.<sup>26</sup> In a more recent human cadaver study evaluating the influence of various low-dose protocols and IRTs on the detectability of midfacial fractures, ultra-low-dose protocols at  $CTDI_{vol} = 1.0$  and  $2.6$  mGy were diagnostic for dislocated and nondislocated fractures, respectively.<sup>14</sup> However, due to smoothing effects, ASIR and MBIR could not improve fracture detection.<sup>14</sup> MBIR does not evaluate thin bony structures well; this evaluation may be important in surgical planning and postoperative evaluation. Unfortunately, MBIR cannot be reconstructed in bone kernels.<sup>14,27</sup>

Following the fracture study, the aim of the present study was to evaluate the variability of the CNR of orbital soft tissues with low-dose protocols and IRTs. The measures were based on 3D volume-segmented HU evaluations of the ON, IRM, and orbital fat. Compared with the reference dose protocol ( $CTDI_{vol} = 36.69$  mGy), LDP I–IV ( $CTDI_{vol} = 4.18$ ,  $2.64$ ,  $0.99$ , and  $0.53$  mGy) showed a dose reduction of up to 98.6%. For comparison, the

current reference dose of the German Federal Office for Radiation Protection for diagnostic sinus CT is  $CTDI_{vol} = 9$  mGy. The presented doses described above were equal or lower than those of previous CT techniques and also most dentomaxillofacial conebeam CT devices.<sup>8-10,28,29</sup> Unlike CT, an important limitation of conebeam CT is the insufficient soft-tissue contrast from which orbital soft tissues cannot be discriminated.

As expected, the reference dose protocol showed a statistically significantly better CNR than all LDPs for both the ON and IRM. The standard kernel had a statistically significantly higher CNR than the bone kernel, and the convolution kernel influenced the effect of iterative reconstructions. LDP-I showed a statistically significantly higher CNR than LDP-III and IV with both kernels. However, with a standard kernel, the CNR of LDP-I did not significantly differ from that of LDP-II. ASIR-50 showed significantly better CNR than FBP for both the ON and IRM with the bone kernel but only for the ON with the standard kernel. ASIR-100 was statistically significantly better than ASIR-50 with the bone kernel but not if the standard kernel was used. Schulz et al<sup>21</sup> reported that iterative reconstructions with a soft-tissue kernel were more efficient at 120 kV than the 100-kV series, and at the lowest dose settings, use of the soft-tissue kernel reduced the benefit of iterative reconstructions. In the present study, MBIR achieved a statistically significantly better CNR compared with all other reconstruction techniques, which is in line with previously published results with a phantom.<sup>25</sup> Hoxworth et al<sup>27</sup> reported a significant improvement in the evaluation of soft-tissue structures with MBIR. Compared with the reference dose protocol with FBP, CNR of both the ON and IRM showed no statistically significant difference from the following: 1) LDP-I with ASIR-50, ASIR-100, and MBIR; 2) LDP-II with ASIR-100 and MBIR; 3) LDP-III with MBIR; and 4) LDP-IV with MBIR.

The CNR change was also supported by the subjective scoring. Scores were lower with a decreasing dose and higher for the standard kernel than for the bone kernel. The ON showed better subjective visibility than the IRM. On maxillofacial CT, images are usually provided in only the bone kernel. With the bone kernel, the orbital soft tissues were highly visible with the reference dose. However, they were blurred and invisible with ultra-low doses. The standard kernel, which is typically used only for soft-tissue imaging, such as in oncology, significantly improved visibility. ASIR-50 had no remarkable effect over FBP on subjective scores, and ASIR-100 showed only a small effect. In agreement with other researchers, an insufficient number of photons may not be compensated for by simply increasing the iterative reconstruction strength.<sup>21</sup> MBIR showed the best subjective score in all images. Compared with the reference dose protocol with FBP bone, which was given a score of 3 (average = equal to reference) and the reference dose protocol with FBP standard, which obtained a score of 4 (above average), use of MBIR obtained a score of 4 for LDP-I and II and was able to retain a score of 2 (suboptimal but sufficient) for LDP-III and IV. Previous studies also indicated the high subjective image quality with iterative reconstructions in low-dose protocols, which may reach equivalent or even superior levels compared with non-dose-reduced CT scans with conventional FBP.<sup>15,24</sup>

The study has several limitations. It was performed with a

human cadaver. The results may thus not be comparable in living humans. Only 1 cadaver head was used; however, the relative differences in CNR may be very similar. Intraorbital bleeding may impair the CNR of orbital soft tissues. The influence of artifacts from surgical screws and plates has not been investigated.

## CONCLUSIONS

Application of optimally tailored CT protocols with the lowest acceptable diagnostic dose is imperative in modern radiology. High-resolution ultra-low-dose CT protocols capable of being used for surgical planning and image-guided maxillofacial surgery may retain similar diagnostic visibility of orbital soft tissues at  $CTDI_{vol} = 2.64$  mGy with MBIR compared with a reference protocol at  $CTDI_{vol} = 36.69$  mGy with FBP. Reconstructions with a standard kernel may improve orbital soft-tissue visibility and should be provided in addition to the bone kernel. The achieved diagnostic dose levels in modern CT may be far lower than current reference levels for sinus CT. Application of low-dose technology and iterative reconstructions should be tested in clinical practice and may lead to redefinition of the ALARA/ALADA criteria for maxillofacial CT.

## ACKNOWLEDGMENTS

The authors wish to thank individuals who donated their bodies and tissues for the advancement of education and research.

Disclosures: Wolfgang Puelacher—UNRELATED: Employment: University Clinic for Craniomaxillofacial Surgery, Innsbruck, Austria.

## REFERENCES

1. United Nations Scientific Committee on the Effects of Atomic Radiation. **Sources and effects of ionizing radiation.** Official Records of the General Assembly, Sixty-third Session, Supplement No. 46. New York: United Nations; 2008 [http://www.unscear.org/docs/reports/2008/09-86753\\_Report\\_2008\\_GA\\_Report\\_corr2.pdf](http://www.unscear.org/docs/reports/2008/09-86753_Report_2008_GA_Report_corr2.pdf). Accessed May 1, 2017
2. Kalra MK, Sodickson AD, Mayo-Smith WW. **CT radiation: key concepts for gentle and wise use.** *Radiographics* 2015;35:1706–21 CrossRef Medline
3. Stewart FA, Akleyev AV, Hauer-Jensen M, et al; Authors on behalf of ICRP. **ICRP publication 118: ICRP statement on tissue reactions and early and late effects of radiation in normal tissues and organs: threshold doses for tissue reactions in a radiation protection context.** *Ann ICRP* 2012;41:1–322 CrossRef Medline
4. Kraft A, Abermann E, Stigler R, et al. **Craniomaxillofacial trauma: synopsis of 14,654 cases with 35,129 injuries in 15 years.** *Cranio-maxillofac Trauma Reconstr* 2012;5:41–50 CrossRef Medline
5. Wick MC, Weiss RJ, Lill M, et al. **The “Innsbruck Emergency Algorithm” avoids the underdiagnosis of blunt cervical vascular injuries.** *Arch Orthop Trauma Surg* 2010;130:1269–74 CrossRef Medline
6. Jeong DK, Lee SC, Huh KH, et al. **Comparison of effective dose for imaging of mandible between multi-detector CT and cone-beam CT.** *Imaging Sci Dent* 2012;42:65–70 CrossRef Medline
7. Cordasco G, Portelli M, Militi A, et al. **Low-dose protocol of the spiral CT in orthodontics: comparative evaluation of entrance skin dose with traditional x-ray techniques.** *Prog Orthod* 2013;14:24 CrossRef Medline
8. Bodelle B, Wichmann JL, Klotz N, et al. **Seventy kilovolt ultra-low dose CT of the paranasal sinus: first clinical results.** *Clin Radiol* 2015;70:711–15 CrossRef Medline
9. Lell MM, May MS, Brand M, et al. **Imaging the paranasal region with a third-generation dual-source CT and the effect of tin filtration on**

- image quality and radiation dose.** *AJNR Am J Neuroradiol* 2015;36:1225–30 CrossRef Medline
10. Schell B, Bauer RW, Lehnert T, et al. **Low-dose computed tomography of the paranasal sinus and facial skull using a high-pitch dual-source system: first clinical results.** *Eur Radiol* 2011;21:107–12 CrossRef Medline
  11. Widmann G, Fasser M, Schullian P, et al. **Substantial dose reduction in modern multi-slice spiral computed tomography (MSCT)-guided craniofacial and skull base surgery.** *Rofo* 2012;184:136–42 CrossRef Medline
  12. Dubach P, Eichenberger A, Caversaccio M. **Radiation dose reduction in computer assisted navigation for functional endoscopic sinus surgery: cadaver head experiments and clinical implementation.** *Rhinology* 2010;48:339–43 CrossRef Medline
  13. Nauer CB, Eichenberger A, Dubach P, et al. **CT radiation dose for computer-assisted endoscopic sinus surgery: dose survey and determination of dose-reduction limits.** *AJNR Am J Neuroradiol* 2009;30:617–22 CrossRef Medline
  14. Widmann G, Dalla Torre D, Hoermann R, et al. **Ultralow-dose computed tomography imaging for surgery of midfacial and orbital fractures using ASIR and MBIR.** *Int J Oral Maxillofac Surg* 2015;44:441–46 CrossRef Medline
  15. Bulla S, Blanke P, Hassepas F, et al. **Reducing the radiation dose for low-dose CT of the paranasal sinuses using iterative reconstruction: feasibility and image quality.** *Eur J Radiol* 2012;81:2246–50 CrossRef Medline
  16. Platzer W, Putz R, Poisel S. **New system for the preservation and storage of anatomical matter** [in German]. *Acta Anat (Basel)* 1978;102:60–67 CrossRef Medline
  17. McHanwell S, Brenner E, Chirculescu AR, et al. **The legal and ethical framework governing body donation in Europe: a review of current practice and recommendations for good practice.** *Eur J Anat* 2008;12:12
  18. Riederer BM, Bolt S, Brenner E, et al. **The legal and ethical framework governing body donation in Europe: 1st update on current practice.** *Eur J Anat* 2012;16:21
  19. Stamm G, Nagel HD. **CT-expo: a novel program for dose evaluation in CT** [in German]. *Rofo* 2002;174:1570–76 CrossRef Medline
  20. Padole A, Ali Khawaja RD, Kalra MK, et al. **CT radiation dose and iterative reconstruction techniques.** *AJR Am J Roentgenol* 2015;204:W384–92 CrossRef Medline
  21. Schulz B, Beerers M, Bodelle B, et al. **Performance of iterative image reconstruction in CT of the paranasal sinuses: a phantom study.** *AJNR Am J Neuroradiol* 2013;34:1072–76 CrossRef Medline
  22. Silva AC, Lawder HJ, Hara A, et al. **Innovations in CT dose reduction strategy: application of the adaptive statistical iterative reconstruction algorithm.** *AJR Am J Roentgenol* 2010;194:191–99 CrossRef Medline
  23. Fleischmann D, Boas FE. **Computed tomography: old ideas and new technology.** *Eur Radiol* 2011;21:510–17 CrossRef Medline
  24. Widmann G, Schullian P, Gassner EM, et al. **Ultralow-dose CT of the craniofacial bone for navigated surgery using adaptive statistical iterative reconstruction and model-based iterative reconstruction: 2D and 3D image quality.** *AJR Am J Roentgenol* 2015;204:563–69 CrossRef Medline
  25. Widmann G, Bischel A, Stratis A, et al. **Ultralow dose dentomaxillofacial CT imaging and iterative reconstruction techniques: variability of Hounsfield units and contrast-to-noise ratio.** *Br J Radiol* 2016;89:20151055 CrossRef Medline
  26. Widmann G, Bischel A, Stratis A, et al. **Spatial and contrast resolution of ultralow dose dentomaxillofacial CT imaging using iterative reconstruction technology.** *Dentomaxillofac Radiol* 2017 Feb 17. [Epub ahead of print] CrossRef Medline
  27. Hoxworth JM, Lal D, Fletcher GP, et al. **Radiation dose reduction in paranasal sinus CT using model-based iterative reconstruction.** *AJNR Am J Neuroradiol* 2014;35:644–49 CrossRef Medline
  28. Pauwels R, Beinsberger J, Collaert B, et al; SEDENTEXCT Project Consortium. **Effective dose range for dental cone beam computed tomography scanners.** *Eur J Radiol* 2012;81:267–71 CrossRef Medline
  29. Bornstein MM, Scarfe WC, Vaughn VM, et al. **Cone beam computed tomography in implant dentistry: a systematic review focusing on guidelines, indications, and radiation dose risks.** *Int J Oral Maxillofac Implants* 2014;29(suppl):55–77 CrossRef Medline

# Does 3T Fetal MRI Improve Image Resolution of Normal Brain Structures between 20 and 24 Weeks' Gestational Age?

G. Priego, N.J. Barrowman, J. Hurteau-Miller, and E. Miller



## ABSTRACT

**BACKGROUND AND PURPOSE:** Stronger magnetic fields have the potential to improve fetal image resolution. Our objective was to detect whether there was better anatomic resolution of brain structures in fetuses imaged with a 3T magnet compared with a 1.5T magnet.

**MATERIALS AND METHODS:** Multiple cerebral and facial anatomic structures were retrospectively assessed in 28 fetal MR imaging scans with normal findings (12 at 3T and 16 at 1.5T) with a 0–3 grading score. Fetuses were assessed during the second trimesters (gestational age, 20–24 weeks). The association between the quality ratings and magnetic field strengths (1.5T versus 3T) was evaluated by a linear mixed-effects model. A quantitative assessment of the signal intensity was also performed in the different layers of the developing brain. Comparative log-ratios were calculated across the different layers of the fetal brain.

**RESULTS:** There was a statistically significant interaction between location and magnetic field strength ( $P < .001$ ). The cerebral structures of the cerebellum, pons, venous system, semicircular canal, and cochlea showed statistically significant higher values on the 3T magnet. Similarly, statistical significance was also obtained on the quantitative assessment of the multilayer appearance of the brain; the 3T magnet had a median factor of 8.38 higher than the 1.5T magnet (95% CI, 4.73–14.82). Other anatomic structures assessed in the supratentorial compartment of the brain showed higher values on the 3T magnet with no statistical significance.

**CONCLUSIONS:** Both magnets depict cerebral and facial normal anatomic structures; however, our data indicates better anatomic detail on the 3T than on the 1.5T magnet.

**ABBREVIATIONS:** feMRI = fetal MR imaging; GA = gestational age; SAR = specific absorption rate

Since the first fetal MR imaging was performed in 1983,<sup>1</sup> the technique has developed vastly in the past 3 decades with the use of ultrafast sequences, which minimize motion artifacts<sup>2</sup> and improve the image quality of the mobile fetus. In addition, the higher magnet strength has already demonstrated superior anatomic contrast resolution in neuroradiology and has been an outstanding diagnostic tool.<sup>3–6</sup>

Recent literature has shown an advantage of 3T magnets in fetal body pathology imaging<sup>7,8</sup> and in fetal brain resolution.<sup>9</sup>

Other advanced techniques such as MR spectroscopy and diffusion tensor imaging have begun to be applied in fetal imaging with promising results.<sup>10,11</sup> In addition, the use of stronger magnets has the potential to improve the SNR, which can be used to attain higher image quality, or can be traded for increased temporal resolution (decreased acquisition time) or a combination of both. In the case of fetal imaging, in which the fetus is usually very small and highly mobile, this gain can represent a substantial advantage. The gain in SNR can also allow implementation of SNR applications such as parallel imaging with multichannel coils to speed up single-shot MR imaging protocols, to reduce TE, to mitigate susceptibility, and to decrease radiofrequency heating by minimizing the number of pulses.

As could be anticipated, the main challenge when performing fetal MR imaging at 3T was imaging artifacts. With single-shot FSE sequences, the main artifacts were secondary to B1 inhomogeneity, which is noted as diffuse areas of image shading but did not limit diagnostic interpretation. On the other hand, an increase in the SNR can eliminate the image noise or interference at

Received January 13, 2017; accepted after revision March 29.

From the Department of Medical Imaging (G.P., J.H.-M., E.M.) and Research Institute (N.J.B.), Children's Hospital of Eastern Ontario, University of Ottawa, Ottawa, Ontario, Canada. Dr Priego is now with Department of Medical Imaging, Queen's Hospital, London, UK.

Please address correspondence to Elka Miller, MD, FRCPC, Children's Hospital of Eastern Ontario, Department of Medical Imaging, 401 Smyth Rd, Ottawa, ON K1H 8L1, Canada; e-mail: emiller@cheo.on.ca



Indicates article with supplemental on-line table.



Indicates article with supplemental on-line photo.

<http://dx.doi.org/10.3174/ajnr.A5251>

1.5T, which results in improvement of the image quality at 3T. Motion artifacts were not thought to be different between the 2 magnets. The only perceptible difference is that planning between sequences in the 3T magnet took a few seconds longer, which might result in fetal motion.

Small centers with only 1 magnet may prefer to choose the higher field magnet for their clinical practice, which must then fulfill all their imaging requirements, including fetal imaging. Re-evaluation of the availability of fetal imaging with 3T magnets can be beneficial in this or other specific instances.

In this study, we aimed to compare the normal anatomy of the fetal brain in the second trimester between images acquired on 1.5T and 3T magnets. The normal anatomy reference of the fetal brain is essential for the interpretation of normal and abnormal fetal MR imaging (feMRI) findings. Our objective was to detect whether there was better anatomic resolution of brain and facial structures in fetuses between the gestational ages (GAs) of 20–24 weeks that were imaged with a 3T magnet compared with a 1.5T magnet. Improved anatomic resolution has the potential of a more detailed assessment and an accurate diagnosis and prognosis.<sup>12</sup>

## MATERIALS AND METHODS

### Demographic Data

This retrospective study was approved by the institutional review board of the Children's Hospital of Eastern Ontario, Canada. All referrals for feMRI followed a dedicated fetal neurosonographic study. No written informed consent was obtained at the Medical Imaging Department, but feMRI requisitions are discussed with a multidisciplinary team prior to booking the MR imaging, as per departmental practice. A search of the Medical Imaging Department data base was performed to identify feMRI studies performed with a 3T system (Magnetom Skyra; Siemens, Erlangen, Germany) and a 1.5T MR imaging system (Sigma HD; GE Healthcare, Milwaukee, Wisconsin) from July 2010 to January 2016. Patients were identified by searching for the term "normal fetal brain" in the final report and having a gestational age between 20 and 24 weeks.

A total of 305 feMRIs (51 performed on the 3T and 254 performed on the 1.5T MR imaging scanner) were reviewed. Twenty-eight feMRI scans met the criteria for the term "normal fetal brain" in the final report and had a gestational age between 20 and 24 weeks (12 on 3T and 16 on 1.5T). Patients were excluded if they did not have normal brain MR imaging findings. Indications for the feMRI of the study group included the following: previous abnormal fetus, mild ventriculomegaly, or other fetal malformation not affecting the brain. No oligo- or polyhydramnios was present in the selected study group.

### Sequence Selection

Every sequence of the selected feMRI studies was reviewed by the pediatric radiology fellow (G.P.), who selected the best diagnostic sequences in each plane. The criteria for selection of the sequences included the following: no or minimal motion artifacts and the presence of the 3 standard brain planes. The sagittal plane included the entire corpus callosum and vermis in the same image.

**Table 1: Parameters for 1.5T and 3T fetal MRIs**

Fetal Sequences
1.5T, 3 planes, T2WI SSFSE
Free-breathing
TR/TE, 3000/87.8 ms, ST = 4 mm
FOV, 340 × 340 mm <sup>2</sup>
Matrix, 320 × 224 px <sup>2</sup>
Time, 22.4 seconds
1.5T, 3 planes, steady-state FIESTA
Free-breathing
TR/TE, 3700/160 ms, ST = 4 mm
FOV, 34 × 34 mm <sup>2</sup>
Matrix, 320 × 224 px <sup>2</sup>
Time, 25 seconds
3T, 3 planes, T2WI SSFSE
Free-breathing
TR/TE, 1400/96 ms, ST = 3 mm
FOV, 280 × 280 mm <sup>2</sup>
Matrix, 320 × 288 px <sup>2</sup>
Time, 22.4 seconds

**Note:**—SSFSE indicates single-shot FSE; px, pixel; ST, section thickness.

Axial and coronal images needed to display a symmetric appearance of the cerebral and cerebellar hemispheres and of the ventricles. In the infratentorial region, the axial plane needed to demonstrate the entire cerebellum and the middle cerebellar peduncles. Angulated or tilted sequences were excluded. Readers were provided with the best preselected sequences. The structures were evaluated with a single-shot FSE sequence obtained with both magnet strengths and with a steady-state acquisition (FIESTA) pulse sequence from the 1.5T magnet.

### Imaging Data Acquisition

Pregnant patients were positioned in the supine or lateral decubitus position. No anesthesia was used. MR images obtained with a 3T MR imaging scanner used a spine matrix coil with 24 elements in the table and a light weight 18-channel phased coil on the surface of the mother. The MR images obtained with a 1.5T MR imaging scanner were acquired with an 8-channel phased array cardiac coil. Imaging parameters for both magnets followed our institutional standard protocol (Table 1).

### Image Analysis

All MR images were evaluated by 2 pediatric neuroradiologists with 16 and 10 years of experience in fetal imaging (E.M., J.H.-M.). Readers were blinded to all clinical information, gestational age, selection of the sequences, and magnet strength. Before starting to read cases, the readers interpreted 4 examinations in consensus to familiarize themselves with the qualitative grading and reach a consensus on the evaluation of the different brain structures and the planes needed for the evaluation. These 4 feMRIs were randomly chosen from both magnet strengths and outside the study group. A mini-atlas was also created for reference by the readers during the independent interpretation. The results of the readers' interpretations were documented in a Research Electronic Data Capture (RedCap; <https://catalyst.harvard.edu/services/redcap/>) by each investigator.

### Qualitative Assessment

The following structures were evaluated in the coronal and axial images: the multilayered appearance of the brain parenchyma, the

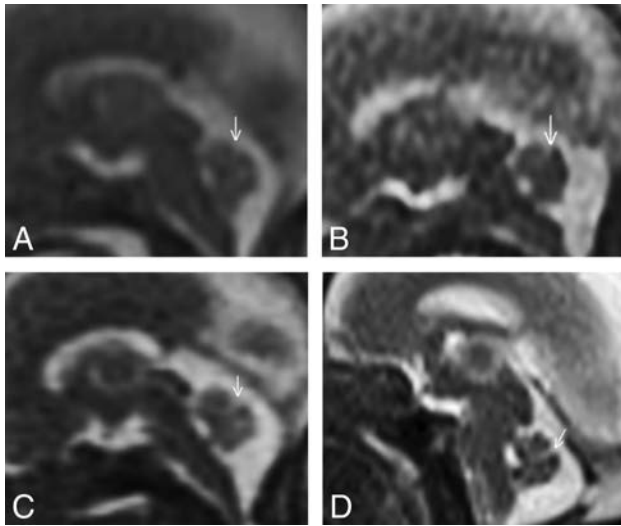


**FIG 1.** Sagittal T2 midline images of fetuses. Examples provide the qualitative assessment of the primary fissure of the cerebellum (arrows). A, Gestational age (GA), 21 weeks 1 day; 1.5T; score 0: no visible structure. B, GA, 21 weeks; 1.5T; score 1: partially visible structure. C, GA, 22 weeks; 1.5T; score 2: entirely visible structure, but ill-defined contour. D, GA, 20 weeks; 3T; score 3: entirely visible and sharp margins.

septum pellucidum, the cerebellar shape, optic (eye globes, optic nerves, optic chiasm) and ear structures (pinnae, cochlea, semi-circular canals), and the choanae. In the sagittal plane, structures were the following: the corpus callosum, vermis and fissures, the belly of the pons, myelination of the midbrain, fastigial point, aqueduct of Sylvius, pituitary stalk, and face profile. In the axial plane, the cerebral peduncles and posterior walls of the optic globe were evaluated. The cerebral venous sinuses were assessed in all 3 planes. The qualitative assessments of the selected structures were rated as follows: 0 represented a structure that was not visible; 1 represented a partially visible structure; 2 represented an entirely visible structure; and 3 represented an excellent resolution of the structure with sharp margins (Fig 1). Approximately 9 months after the initial readings, each reader repeated the image interpretation separated for assessment of the intrarater agreement.

To assess intra- and interrater agreement of the diagnostic quality ratings, the readers used the Cohen weighted  $\kappa$ . To evaluate the association between diagnostic quality ratings and magnetic field strength, they used a linear mixed-effects model. The model treated fetus as a random effect and reader, location, and magnetic field strength as fixed effects. A third-order interaction among location, magnet strength, and gestational age was initially included, together with all lower order interactions and main effects, in particular, an interaction between location and magnet strength. Because the third-order interaction was not statistically significant, it was removed and the model was refitted. At each location, we calculated the estimated average effect of magnetic field strength on diagnostic quality ratings, with a 95% confidence interval, adjusted for multiple testing.<sup>13</sup> Two-sided  $P$  values  $< .05$  were considered statistically significant.

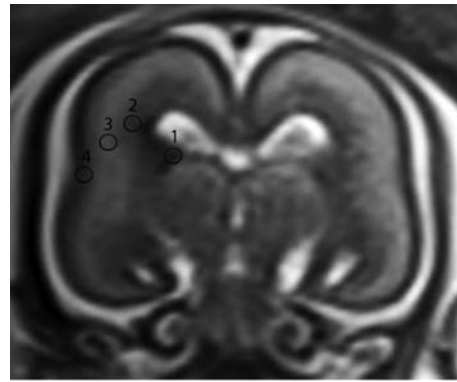


**FIG 2.** A coronal image was selected from each scan at the level of the third ventricle. One-millimeter ROIs were drawn in the developing brain layers: 1) germinal matrix, 2) periventricular, 3) subplate, and 4) cortical plate. These values were compared with an ROI outside the patient (air). This fetus had a GA of 20 weeks, scanned at 3T.

### Quantitative Assessment

A quantitative assessment by the ROI of the supratentorial brain layers was obtained by a pediatric radiology fellow (G.P.). An ROI of 1 mm was manually placed on the different layers of the brain (Fig 2): germinal matrix, periventricular layer, subplate layer, and cortical layer. The mean signal intensity for each layer was collected, and a comparative ratio between the different layers and air was calculated. The contrast resolution of each layer was analyzed to compare the different magnet strengths.

The ratios of signal intensity between paired ROIs were compared between the 2 magnetic-field-strength groups. The ratios were log-transformed so that their distributions were approximately normal. A linear mixed-effects model was used to evaluate the association between the log-ratios and magnet strength across different ROIs. The model treated fetus as a random effect, with magnet strength and ROI treated as fixed effects.

## RESULTS

### Study Group

The gestational age range of the 12 fetuses in the group that underwent 3T MR imaging was 20.0–23.9 weeks (median, 21.8 weeks; interquartile range, 21.0–22.2 weeks). The gestational age range of the 16 fetuses in the group that underwent 1.5T MR imaging scans was 20.3–24.7 weeks (median, 21.1 weeks; interquartile range, 20.7–22.7 weeks). The maternal age range was 17.0–39.0 years (median, 32.5 years; interquartile range, 29.5–34.2 years).

Indications for MR imaging included mild ventriculomegaly ( $n = 7$ ), body malformation ( $n = 11$ ), and abnormality of a fetus in a previous pregnancy ( $n = 10$ ). The cases with mild ventriculomegaly on sonography that were not confirmed on MR imaging were classified as normal fmMRI studies. The remaining fetal brain cases were considered normal.

### Qualitative Results

As presented in Table 2, the scores of both readers for all locations demonstrated an increased frequency of score 3 (excellent resolution of the structure with sharp margins) on the 3T

MR imaging scanner ( $n = 309, 56\%$ ) compared with the 1.5T MR imaging scanner ( $n = 108, 15\%$ ) and a larger number of score 0 for the 1.5T scanner ( $n = 74, 10\%$ ) than for the 3T scanner ( $n = 20, 4\%$ ).

In the linear mixed-effects model, the interaction among location, magnet strength, and gestational age was not statistically significant. On removing the interaction and refitting the model, all 2-way interactions were statistically significant, namely location by magnet strength ( $P < .001$ ), location by gestational age ( $P < .001$ ), and gestational age by magnet strength ( $P = .03$ ). Confidence intervals for the interaction of location and magnet strength, adjusted for multiple testing, revealed that 12 structures had a significantly higher diagnostic quality with the 3T magnet and none had a significantly lower diagnostic quality. The 3T magnet showed significantly higher diagnostic quality ratings for the following: semicircular canal, cochlea, primary and secondary fissure of the cerebellum, pituitary stalk, fastigial point, pinnae,

belly of the pons, optic chiasm, and the straight, transverse, and superior sagittal venous sinuses (On-line Table 1). The largest statistically significant difference was for the semicircular canal for which it was estimated that the 3T magnet yielded 1.6 points in higher diagnostic quality ratings (95% CI, 1.0–2.2). Other structures had higher values on the 3T scanner than on the 1.5T scanner, but with no statistical significance: septum pellucidum, choanae, optic nerves, face, corpus callosum, globes, cerebellar shape, cerebellar peduncles, posterior myelination of the pons, and the multilayer appearance of the brain. The only structure that did not show better values on 3T was the aqueduct of Sylvius (Fig 3).

The Cohen weighted  $\kappa$  for the 2 sets of readings by reader 1 was 0.75; for reader 2, it was 0.76. The Cohen weighted  $\kappa$  between readers was 0.71. The linear mixed-effects model for the diagnostic quality ratings showed a significant reader effect. Compared with the first reader, the second reader's scores were lower by 0.35 points (95% CI, 0.28–0.42).

**Table 2: Frequency of scores within magnet type, including both readers**

	Magnet Score			
	0	1	2	3
1.5T	74 10.1%	237 32.2%	317 43.1%	108 14.7%
3T	20 3.6%	71 12.9%	152 27.5%	309 56.0%

### Quantitative Results

Comparative ratios were calculated between germinal matrix/air, periventricular layer/air, subplate layer/air, and cortical layer/air for each fetal MR imaging scan. The median ratios were higher on the 3T scanner than on the 1.5T scanner (Table 3). Across all ROIs, compared with the 1.5T magnet, the signal-intensity ratios from the 3T magnet were higher by a median factor of 8.38 (95% CI, 4.73–14.82) (Fig 4).

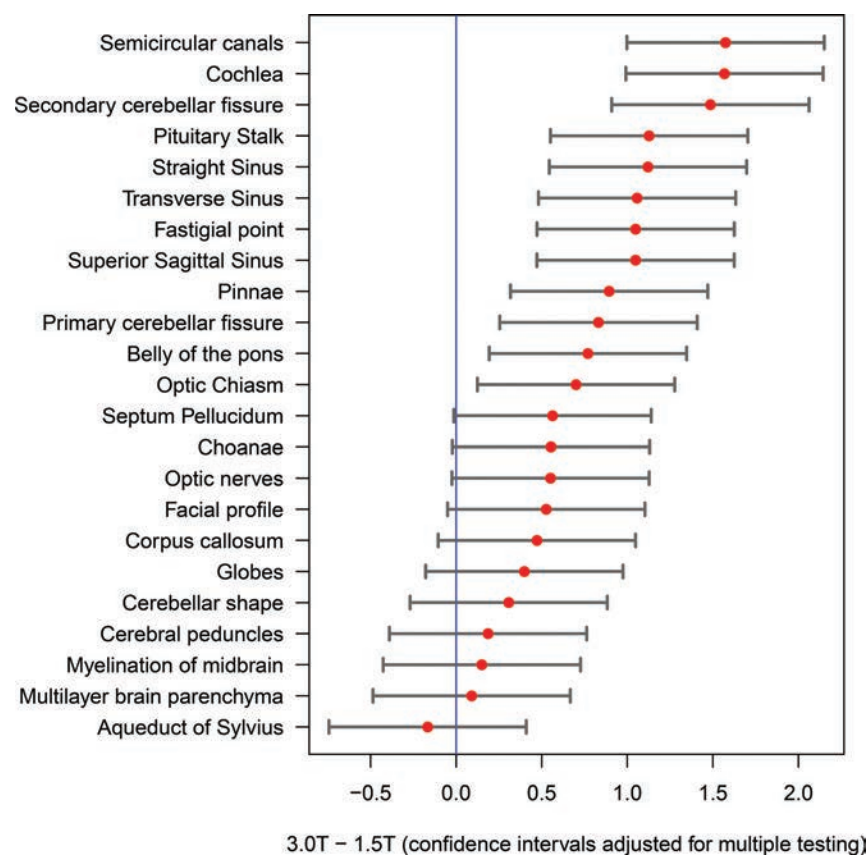


**FIG 3.** Estimated differences in the mean score between magnet types at each location from a linear mixed-effects model. Estimates are accompanied by 95% confidence intervals, adjusted for multiple testing.

### DISCUSSION

MR imaging is a noninvasive technique increasingly used to scan pregnant patients. Imaging performed with higher strength magnets has been proven superior in clinical practice<sup>3-6</sup> due to their high signal intensity, resolution, reduced scanning times, and overall improved diagnostic ability. Imaging of the fetus has been evaluated with 3T, but studies were mainly focused on body imaging and not the brain and head anatomy.<sup>8</sup> Our aim was to demonstrate the difference in spatial resolution between 1.5 and 3T magnets in fetal brain anatomy. Fetal MR images were selected between 20 and 24 weeks of gestation to ensure a similar fetal sulcation age and anatomy.<sup>14</sup> This choice has resulted in a relatively homogeneous sample for our trial, with similar gyration patterns. In addition, the early second trimester is a crucial time in pregnancy development, counseling, and decision-making. The second trimester feMRI has been demonstrated to be safe and helpful for the diagnosis of brain anomalies when there is a sonography concern, adding valuable information and changing management in approximately 30% of cases.<sup>15</sup>

The classification into 4 categories for each structure was carefully considered to be a good representation of the variety of qualitative imaging acquired on the scans and also an acceptable pathway for agreement between readers. The locations selected in our study are an extensive representation of the neuroanatomy in the fetus and key structures in the assessment of anomalies. The results of the analyzed brain structures demonstrated higher values on 3T magnets than on the 1.5T magnets, meaning better qualitative assessment with a stronger magnetic field. In particular, all the structures involving the auditory system showed exponential statistical significance (semicircular canals, cochleae, and pinnae). Inner ear structures have already been shown to have higher resolution on 3T than on 1.5T magnets in healthy adult volunteers.<sup>16</sup> In addition, the 3T magnet is often chosen as the preferred technique for volumetric assessment of adult inner ear structures,<sup>17</sup> particularly in the quantification of volumes for inner ear pathologies. The observation from the assessment with our grading also confirms that the stronger field can be used as a tool in

prenatal diagnosis to reassure normal anatomic development of the major structures of the inner ear.

On the other hand, the optic chiasm and many of the posterior fossa structures such as the belly of the pons, fastigial point, and primary and secondary fissures of the vermis revealed statistically significant differences in the qualitative assessment. Because a normal biometry of posterior fossa structures rules out many of the concerning anomalies in neurofetal imaging, it is essential to appropriately visualize and assess these structures. These structures are often critical and an area of challenge when performing neurofetal sonography; therefore, the fMRI becomes a tool of trustworthiness.<sup>18</sup>

The flow void of cerebral venous vessels, including the superior sagittal, transverse, and straight venous sinuses, also revealed better resolution on the 3T magnet than on the 1.5T magnet with statistical significance. Anomalies of the cerebral venous sinus in the fetus are very rare but may present as congenital anomalies, such as the persistence of the falcine sinus or agenesis of the straight sinus, or as acquired disorders, most commonly a thrombotic occlusion.<sup>19</sup> Prenatal sonography is an effective method for diagnosing and monitoring thrombosis, but fMRI serves as a complementary technique to evaluate the full extent of the cerebral venous sinuses and extension of thrombus and to rule out cerebral parenchymal lesions secondary to hypoperfusion of the associated malformation.<sup>20</sup>

The remainder of the evaluated structures did not show statistically significant values, but the multi-layering appearance of the brain on a 3T magnet demonstrated higher comparative quantitative ratios than on the 1.5T magnet.

These quantitative differences in the signal intensity of the brain layers has been demonstrated to reflect different histologic patterns.<sup>21</sup> The visualization of a normal transient laminar organization in the fetal brain is a relevant finding related to the normal development of the white matter in the neonate.<sup>21</sup> Detection and characterization of malformation of cortical development have already been demonstrated to be better with a 3T than with a 1.5T magnet.<sup>22</sup> The lack of statistical significance in our study group might be because only fetal studies with normal findings were included in this trial. Future studies with a combination of normal and pathologic fetal cases might enhance differences in the multilayered appearance of the fetal brain and could demonstrate the better image resolution of stronger magnets when pathology is present.

fMRI has shown no reproducible harmful effects on pregnant women and their fetuses at a magnetic field strength of  $\leq 3T$ .<sup>7,8</sup> The major concern of fMRI is thermal exposure to the mother and

**Table 3: Median IQR signal intensity ratio by location and magnet**

Location	1.5T	3T
Germinal	7.3 (4.8–19.4)	72.3 (49.5–100.6)
Periventricular layer	10.7 (6.2–21.1)	103.8 (54.9–181.7)
Subplate	12.0 (8.4–25.4)	165.2 (97.2–270.1)
Cortical	9.7 (5.5–19.5)	90.1 (61.7–119.4)

Note:—IQR indicates interquartile range.

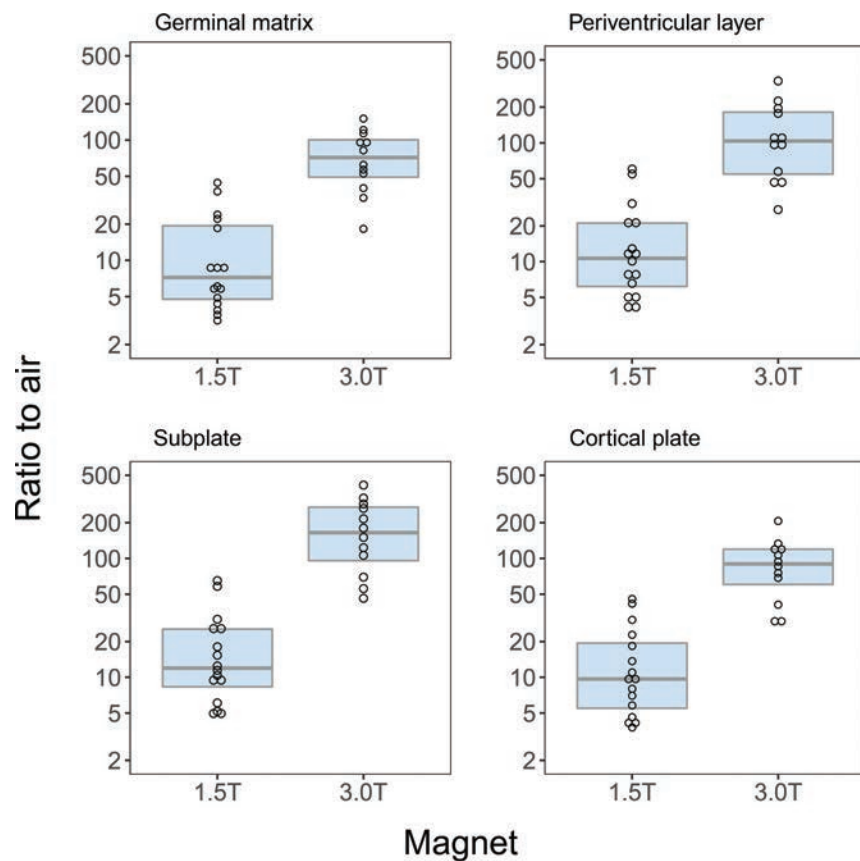


**FIG 4.** The ratio between signal intensity and air at each location for each magnet. Each estimated ratio is shown as a *small circle*. Each superimposed box indicates the 25th percentile (*lower part of the box*), median (*heavy horizontal line*), and 75th percentile (*upper part of the box*). Note that the vertical axis has a logarithmic scale.

fetus because of the potential biologic damage. In fact, the main reason to avoid fMRI during the first trimester is the thermal risk. The heating caused by the radiofrequency energy is measured by the specific absorption rate (SAR), which is fixed by the appropriate authorities. In the United States, the Food and Drug Administration mandates that the SAR not exceed 4 W/kg of the mother's body weight for all magnet strengths.<sup>7</sup> The SAR is also limited by manufacturers to ensure that the increase in body temperature is <0.5°C. Experimental evidence proposes that SAR deposition to the fetus in utero is higher at 3T<sup>4,6,7</sup> but remains within accepted limits for clinical practice. There are recommendations to reduce the fetal SAR between 2 and 3 times with circularly polarized B1 fields instead of linear-horizontal polarization mode 2-port radiofrequency shimming.<sup>2,3</sup> The ability to decrease magnet time with faster sequences at 3T also has the potential to decrease the SAR. In addition, the acoustic effect has also been raised as a hypothetical concern, but the literature has shown it to be a theoretic risk rather than a real practical issue.<sup>4-7</sup>

The advantages of a stronger magnet are primarily an increase in the signal-to-noise ratio,<sup>2,5</sup> meaning a higher image quality, with an increased spatial-temporal resolution and a decreased acquisition time per sequence. The principal disadvantage is artifacts from a higher magnet strength (On-line Figure) (ie, susceptibility and magnetic field heterogeneity)<sup>2</sup> because there is stronger radiofrequency penetration, which results in more unpaired hydrogen proton spin-up.

Limitations of this study include the small sample size, the retrospective design, and the lack of prospective follow-up to ensure that each fetus is entirely neurologically normal in childhood. Another limitation is the difference between the technique and parameters applied on the 3T and 1.5T magnets, including the difference in section thickness between the 1.5T magnet (4 mm) and the 3T magnet (3 mm), particularly important in the assessment of small structures. The combination of T2-weighted single-shot FSE and steady-state FIESTA was used on the 1.5T magnet compared with single T2-weighted single-shot FSE on the 3T magnet. The 3D and 2D FIESTA sequences have been useful in the assessment of brain and body abnormalities in the second trimester, primarily because the FIESTA sequence provides better motion artifact-free imaging.<sup>24,25</sup> Motion artifacts of the images were also eliminated from the sample by selectively including the best sequence from each study in the 3 different planes.

## CONCLUSIONS

Both magnet strengths can examine brain and facial anatomic structures for diagnostic purposes. However, our research demonstrates a better qualitative and quantitative resolution of the evaluated structures and images with the 3T magnet. This seems especially noticeable in the posterior fossa structures, venous system, and inner ears. Future studies comparing normal and abnormal fetal brains at different gestational ages may enhance the practical impact of using higher strength magnets as long as the safety of the fetus and mother are guaranteed or assured.

## ACKNOWLEDGMENTS

We thank Cassandra Kapoor for administrative and editorial support and Barry Smith, MRT, for the collaboration with the MR imaging studies.

## REFERENCES

1. Smith FW, Adam AH, Phillips WD. NMR imaging in pregnancy. *Lancet* 1983;1:61–62 Medline
2. Levine D, Barnes PD, Sher S, et al. Fetal fast MR imaging: reproducibility, technical quality, and conspicuity of anatomy. *Radiology* 1998;206:549–54 CrossRef Medline
3. Mack A, Wolff R, Scheib S, et al. Analyzing 3-Tesla magnetic resonance imaging units for implementation in radiosurgery. *J Neurosurg* 2005;102(suppl):158–64 CrossRef Medline
4. De Marzi R, Seppi K, Högl B, et al. Loss of dorsolateral nigral hyperintensity on 3.0 Tesla susceptibility-weighted imaging in idiopathic rapid eye movement sleep behavior disorder. *Ann Neurol* 2016;79:1026–30 CrossRef Medline
5. Peng L, Xiao Y, Liu L, et al. Evaluation of cochlear nerve diameter and cross-sectional area in ANSD patients by 3.0-Tesla MRI. *Acta Otolaryngol* 2016;136:792–99 CrossRef Medline
6. Schwarz ST, Afzal M, Morgan PS, et al. The 'swallow tail' appearance of the healthy nigrosome: a new accurate test of Parkinson's disease—a case-control and retrospective cross-sectional MRI study at 3T. *PLoS One* 2014;9:e93814 CrossRef Medline
7. Victoria T, Jaramillo D, Roberts T, et al. Fetal magnetic resonance imaging: jumping from 1.5 to 3 Tesla (preliminary experience). *Pediatr Radiol* 2014;44:376–86; quiz 373–75 CrossRef Medline
8. Victoria T, Johnson A, Edgar J, et al. Comparison between 1.5 T and 3 T MRI for fetal imaging: is there an advantage to imaging with a higher field strength? *AJR Am J Reontgenol* 2016;206:195–201 CrossRef Medline
9. Krishnamurthy U, Neelavalli J, Mody S, et al. MR imaging of the fetal brain at 1.5T and 3.0T field strengths: comparing specific absorption rate (SAR) and image quality. *J Perinat Med* 2015;43:209–20 CrossRef Medline
10. Qiu AL, Mori S, Miller MI. Diffusion tensor imaging for understanding brain development in early life. *Annu Rev Psychol* 2015;66:853–76 CrossRef Medline
11. Cetin I, Barberis B, Brusati V, et al. Lactate detection in the brain of growth-restricted fetuses with magnetic resonance spectroscopy. *Am J Obstet Gynecol* 2011;205:350.e1–7 CrossRef
12. Glenn OA. MR imaging of the fetal brain. *Pediatr Radiol* 2009;40:68–81 CrossRef
13. Hothorn T, Bretz F, Westfall P. Simultaneous inference in general parametric models. *Biom J* 2008;50:346–63 CrossRef Medline
14. Garel C, Chantrel E, Brisse H, et al. Fetal cerebral cortex: normal gestational landmarks identified using prenatal MR imaging. *AJNR Am J Neuroradiol* 2001;22:184–89 Medline
15. Rossi AC, Prefumo F. Additional value of fetal magnetic resonance imaging in the prenatal diagnosis of central nervous system anomalies: a systematic review of the literature. *Ultrasound Obstet Gynecol* 2014;44:388–93 CrossRef Medline
16. Graf H, Schick F, Claussen CD, et al. MR visualization of the inner ear structures: comparison of 1.5 Tesla and 3 Tesla images. *Rofo* 2004;176:17–20 CrossRef Medline
17. Inui H, Sakamoto T, Ito T, et al. Volumetric measurements of the inner ear in patients with Meniere's disease using three-dimensional magnetic resonance imaging. *Acta Otolaryngol* 2016;136:888–93 CrossRef Medline
18. Katorza E, Bertucci E, Perlman S, et al. Development of the fetal vermis: new biometry reference data and comparison of 3 diagnostic modalities: 3D ultrasound, 2D ultrasound, and MR imaging. *AJNR Am J Neuroradiol* 2016;37:1359–66 CrossRef Medline
19. Komiya M, Ishiguro T, Kitano S, et al. Serial antenatal sonographic observation of cerebral dural sinus malformation. *AJNR Am J Neuroradiol* 2004;25:1446–48 Medline

20. McInnes M, Fong K, Grin A, et al. **Malformations of the fetal dural sinuses.** *Can J Neurol Sci* 2009;36:72–77 CrossRef Medline
21. Widjaja E, Geibprasert S, Mahmoodabadi SZ, et al. **Alteration of human fetal subplate layer and intermediate zone during normal development on MR and diffusion tensor imaging.** *AJNR Am J Neuro-radiol* 2010;31:1091–99 CrossRef Medline
22. Mellerio C, Labeyrie MA, Chassoux F, et al. **3T MRI improves the detection of transmantle sign in type 2 focal cortical dysplasia.** *Epilepsia* 2014;55:117–22 CrossRef Medline
23. Murbach M, Neufeld E, Samaras T, et al. **Pregnant women models analyzed for RF exposure and temperature increase in 3T RF shimmed birdcages.** *Magn Reson Med* 2017;77:2048–56 CrossRef Medline
24. Shen SH, Guo WY, Hung JH. **Two-dimensional fast imaging employing steady-state acquisition (FIESTA) cine acquisition of fetal non-central nervous system abnormalities.** *J Magn Reson Imaging* 2007;26:672–77 CrossRef Medline
25. Griffiths PD, Jarvis D, McQuillan H, et al. **MRI of the foetal brain using a rapid 3D steady-state sequence.** *Br J Radiol* 2013;86:20130168 CrossRef

# MR Imaging Diagnosis of Diencephalic-Mesencephalic Junction Dysplasia in Fetuses with Developmental Ventriculomegaly

 M. Severino,  A. Righini,  D. Tortora,  L. Pinelli,  C. Parazzini,  G. Morana,  P. Accorsi,  V. Capra,  D. Paladini, and  A. Rossi



## ABSTRACT

**SUMMARY:** Diencephalic-mesencephalic junction dysplasia is a rare malformation characterized by a poorly defined junction between the diencephalon and the mesencephalon, associated with a characteristic butterfly-like contour of the midbrain (butterfly sign). This condition may be variably associated with other brain malformations, including callosal abnormalities and supratentorial ventricular dilation, and is a potential cause of developmental hydrocephalus. Here, we have reported 13 fetuses with second-trimester obstructive ventriculomegaly and MR features of diencephalic-mesencephalic junction dysplasia, correlating the fetal imaging with available pathology and/or postnatal data. The butterfly sign can be clearly detected on axial images on fetal MR imaging, thus allowing for the prenatal diagnosis of diencephalic-mesencephalic junction dysplasia, with possible implications for the surgical management of hydrocephalus and parental counseling.

**ABBREVIATION:** DMJ = diencephalic-mesencephalic junction

**D**iencephalic-mesencephalic junction (DMJ) dysplasia is a rare malformation characterized by a poorly defined junction between the diencephalon and the mesencephalon and associated with a characteristic butterfly-shaped contour of the midbrain on axial sections on MR imaging.<sup>1-3</sup> This condition is included in a larger spectrum of DMJ anomalies, comprising forms that are recognizable in the axial (type A-DMJ anomalies, including DMJ dysplasia) or sagittal planes (type B-DMJ anomalies).<sup>3</sup> DMJ anomalies may be variably associated with other brain malformations, including callosal abnormalities and supratentorial ventricular dilation. In the original report, massively enlarged lateral ventricles were appreciated in 2 patients with DMJ dysplasia.<sup>1</sup> Thereafter, partial aqueductal stenosis was identified in 1 patient with DMJ dysplasia and prenatal onset of severe ventriculomegaly, suggesting a mixed obstructive and malfor-

native cause of the hydrocephalus.<sup>3</sup> The prenatal imaging features of DMJ have not been reported. Moreover, the relationship between DMJ anomalies and early developmental hydrocephalus remains unclear.

Several causes of developmental hydrocephalus have been described in fetuses and children, mostly associated with myelomeningocele, aqueductal obstruction, posterior fossa crowding, and cysts or cephaloceles.<sup>4-6</sup> To the best of our knowledge, no imaging features of DMJ dysplasia have been described in fetuses with developmental ventriculomegaly. Here, we have reported the second-trimester prenatal MR imaging of 13 fetuses with moderate-to-severe obstructive ventriculomegaly presenting unequivocal features of DMJ dysplasia, and we correlated the imaging with available pathology and/or postnatal data.

## CASE SERIES

This case series included 13 fetuses, referred to 3 pediatric institutions over a 10-year period (2005–2015) for fetal MR imaging because of second-trimester ultrasound findings of obstructive ventriculomegaly, in whom clear MR features of DMJ dysplasia were retrospectively detected. These cases were found by searching the fetal MR imaging data bases of the 3 centers for reports indicating obstructive ventriculomegaly, defined as bilateral atrial width > 12 mm with the hemisphere convexity reaching or almost reaching the skull inner surface, and with downward displacement of the fornix, without enlargement of the fourth ventricle. The DMJ dysplasia was not detected in the sonography examinations.

Received February 14, 2017; accepted after revision March 29.

From the Neuroradiology Unit (M.S., D.T., G.M., A. Rossi), Genetic Unit, Department of Neurosurgery (V.C.), and Fetal Medicine and Surgery Unit (D.P.), Istituto Giannina Gaslini, Genoa, Italy; Radiology and Neuroradiology Department (A. Righini, C.P.), Ospedale dei Bambini V Buzzi, Milano, Italy; and Neuroradiology (L.P.) and Neuropsychiatry Units (P.A.), Azienda Ospedaliera Spedali Civili di Brescia, Brescia, Italy.

Paper previously presented at: XX Symposium Neuroradiologicum, September 7–12, 2014; Istanbul, Turkey.

Please address correspondence to Mariasavina Severino, MD, Neuroradiology Unit, Istituto Giannina Gaslini, via Gaslini 5, Genoa 16147, Italy; e-mail: mariasavinaseverino@gaslini.org; @MSavinaSeverino; @TortoraDomenico

 Indicates article with supplemental on-line table.

 Indicates article with supplemental on-line photo.

<http://dx.doi.org/10.3174/ajnr.A5245>



**FIG 1.** DMJ dysplasia in a 28-week-old fetus (case #9). *A*, Axial T2-weighted image reveals fusion of the hypothalamus and midbrain (*asterisk*), enlargement of the dorsoventral axis of the midbrain, and a ventral midbrain cleft (*arrow*) resulting in a butterfly-like appearance. *B*, Sagittal T2-weighted image demonstrates partial callosal agenesis (*black arrow*) associated with hypoplasia of the pons (*empty arrow*) and vermis and mild kinking of the cervicomedullary junction (*white arrowhead*). Note that the cerebral aqueduct is not visible. The interthalamic adhesion is enlarged and ventrally located (*black arrowhead*). *C*, Coronal T2-weighted image shows fusion between the midbrain and thalami (*asterisks*) as well as moderate supratentorial ventriculomegaly.

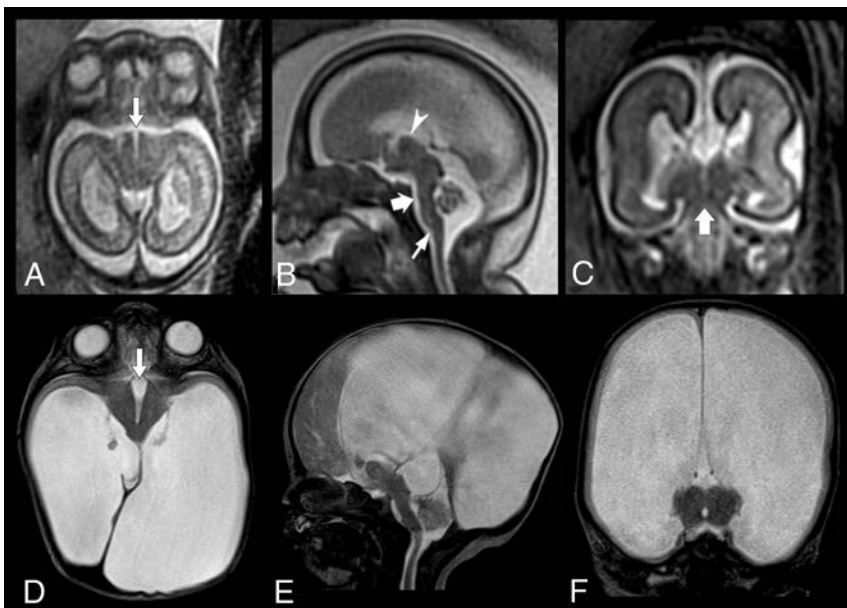


**FIG 2.** Prenatal and postnatal MR findings of DMJ dysplasia in a 23-week-old fetus (case #7). *A*, Axial T2-weighted image reveals abnormal contour of the midbrain with a deep ventral cleft (*arrow*), resulting in a butterfly-like appearance. *B*, Sagittal T2-weighted image demonstrates marked hypoplasia of the pons (*thick arrow*) and vermis, aqueductal stenosis, and mild kinking of the cervicomedullary junction (*thin arrow*). The interthalamic adhesion is enlarged and ventrally located (*arrowhead*). *C*, Coronal T2-weighted image shows fusion between the midbrain and thalami (*thick arrow*) and complete callosal agenesis. Corresponding axial (*D*), sagittal (*E*) and coronal (*F*) T2-weighted images obtained on day 5 after birth confirm the prenatal findings, including the DMJ dysplasia (*arrow*, *D*) and brain stem anomalies, and reveal severe supratentorial hydrocephalus.

The MR imaging studies were performed for clinical purposes on 1.5T scanners (Achieva, Philips Healthcare, Best, the Netherlands; Ingenia, Philips Healthcare; Magnetom Avanto, Siemens, Erlangen, Germany) with a phased array abdominal or cardiac coil after an expert neurosonography study. All studies included 3 mm-thick single-shot fast spin-echo multiplanar T2-weighted images. The mothers had signed a specific consent form for fetal MR imaging, and the study complied with the internal guidelines for retrospective studies of the 3 institutions.

The On-line Table summarizes the clinical radiologic data of all fetuses. The mean gestational age at first fetal MR imaging was 23.8 weeks (range, 20–31 weeks). All fetuses were

males. The mean maternal age was 32.9 years. Congenital infections and alcohol abuse were excluded in all pregnancies. No karyotype anomalies were reported in the 11/13 cases with available testing.

The mean atrial width was 20.6 mm (range, 12–38 mm). Supratentorial brain mantle thinning was noted in all fetuses, with the brain surface reaching or almost reaching the inner skull surface. Complete or partial agenesis of the corpus callosum was noted in 9/13 fetuses, and marked callosal thinning caused by the underlying ventriculomegaly was seen in the remaining 4 cases. In all cases, on prenatal MR imaging, the butterfly sign was detected on axial sections, and on sagittal images, a poorly defined DMJ was noticeable, with the thalamic mass sitting in an abnormal anterior position with respect to the midbrain (Fig 1 and On-line Figure). On coronal sections, a merger between the midbrain and thalami was detected in all cases. Ventral dislocation of an enlarged interthalamic adhesion was noted in 9/13 fetuses, and the aqueduct was poorly defined in 10/13 cases. Pontine hypoplasia was identified in 6/13 fetuses and cerebellar hypoplasia in 3 cases. A moderate brain stem kinking was present in 11/13 cases.

In 9/13 cases, the parents elected for termination of pregnancy after prenatal counseling. Two fetuses had a second antenatal MR imaging performed 1 and 10 weeks after the first examination, respectively. Postnatal MR imaging was available in 4 patients (Fig 2), and MR autopsy was performed in 1 fetus. DTI was performed in 2 patients on a 1.5T scanner along 34 noncolinear directions by using an axial single-shot spin-echo echo-planar sequence, with b-values of 0 and 1000 s/mm<sup>2</sup>; TR, 9203 ms; TE, 71 ms; section thickness, 2 mm; FOV, 240 × 240 mm; matrix size, 128 × 128. The corticospinal tracts were reconstructed with a deterministic algorithm by using the IntelliSpace Portal 8.0 (Philips Healthcare). Interestingly, no tracking of corticospinal tracts was obtained below the level of the midbrain (Fig 3). Neuropathologic data were available in 2 fetuses, confirming the altered DMJ segmentation with deep ventral midbrain cleft and the level and etiology of the obstruction. In 1 fetus, there was a trifurcation of the cerebral aqueduct, and the olivary nuclei were small and anteriorly dislocated. Moreover, an incomplete lobulation of the right lung and right-sided moderate hydronephrosis were noted. Overall, the prenatal diagno-

ness, 2 mm; FOV, 240 × 240 mm; matrix size, 128 × 128. The corticospinal tracts were reconstructed with a deterministic algorithm by using the IntelliSpace Portal 8.0 (Philips Healthcare). Interestingly, no tracking of corticospinal tracts was obtained below the level of the midbrain (Fig 3). Neuropathologic data were available in 2 fetuses, confirming the altered DMJ segmentation with deep ventral midbrain cleft and the level and etiology of the obstruction. In 1 fetus, there was a trifurcation of the cerebral aqueduct, and the olivary nuclei were small and anteriorly dislocated. Moreover, an incomplete lobulation of the right lung and right-sided moderate hydronephrosis were noted. Overall, the prenatal diagno-

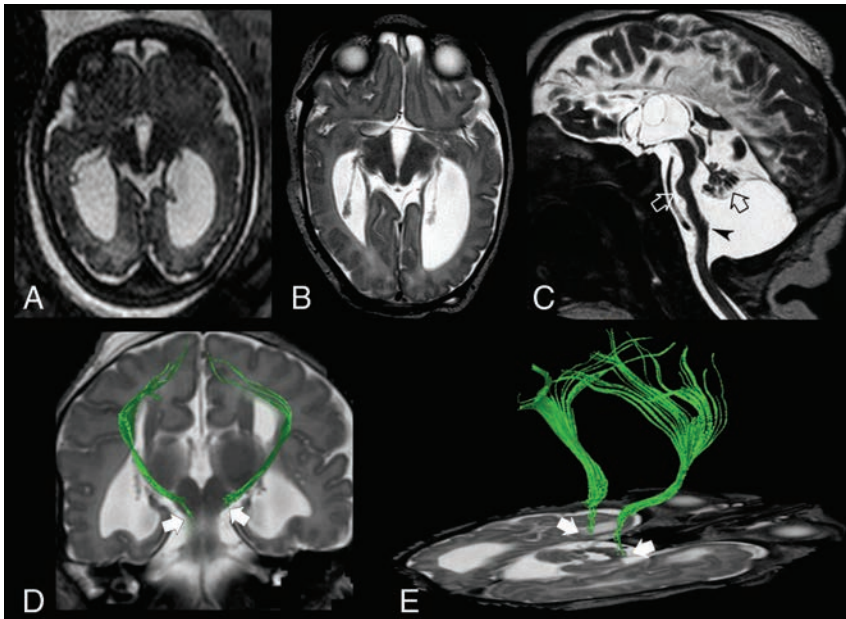


**FIG 3.** Prenatal and postnatal MR findings with DTI in a 31-week-old fetus with DMJ dysplasia (case #13). *A*, Axial T2-weighted image shows the typical “butterfly” appearance of the DMJ. *B*, Axial T2-weighted image obtained at age 7 days confirms the abnormal contour of the midbrain. *C*, Sagittal T2-weighted driven equilibrium pulse image demonstrates complete callosal agenesis, marked hypoplasia of the pons (*white empty arrow*) and vermis (*black empty arrow*), elongated midbrain, and kinked cervicomedullary junction (*arrowhead*). Coronal (*D*) and oblique axial (*E*) T2-weighted images fused with motor tractography reveal no tracking of the corticospinal tracts below the level of the midbrain (*thick arrows*). Color version available on-line.

sis of DMJ dysplasia was confirmed postnatally or *ex vivo* in 6/13 cases of this series.

## DISCUSSION

We described a relatively large series of fetuses with second-trimester obstructive ventriculomegaly associated with clear features of DMJ dysplasia. Our cohort demonstrates that DMJ dysplasia could already be detected before gestational week 24 and that it has to be included among the causes of early developmental hydrocephalus. Fetal ventriculomegaly is a relatively common finding, occurring in approximately 1% of fetuses on sonography and in 1 of 1000 live born neonates.<sup>4</sup> Conversely, DMJ dysplasia is probably rare, though it may be underestimated in cases without ventriculomegaly. The role of MR imaging in detecting brain anomalies in fetuses with ventriculomegaly is well established. Griffiths et al<sup>7</sup> demonstrated a 17% risk of finding other brain abnormalities in fetuses with a confident sonography diagnosis of isolated ventriculomegaly. More recently, Barzilay et al<sup>8</sup> showed that in fetuses with ventriculomegaly, the MR detection rate of minor and major brain findings increases with each millimeter increase in ventricle width. Various etiologies of fetal ventriculomegaly have been demonstrated, including acquired causes such as intraventricular hemorrhage, infection, or neoplasms.<sup>4,5</sup> When these have been excluded, radiologists must carefully assess MR images to identify additional brain abnormalities that may suggest a developmental/malformative cause of the hydrocephalus.<sup>9</sup>

DMJ dysplasia is a rare malformation first described in 6 children born from 3 consanguineous Egyptian families, with facial dysmorphisms, severe cognitive impairment, axial hypotonia, spastic quadriplegia, vasomotor instability, unexplained fever,

and seizures.<sup>1</sup> So far, no causative genes have been linked to this condition. On imaging, DMJ dysplasia is characterized by a poorly defined junction between the diencephalon and the mesencephalon and by a ventral cleft contiguous with the third ventricle, producing a characteristic butterfly-shaped contour of the midbrain on axial images.<sup>1–3</sup> Notably, MR imaging identified the butterfly sign and the abnormal relation between the midbrain and thalamic mass already at 20–21 gestational weeks in 6 fetuses of this series. Nonetheless, if not carefully sought, this finding may be overlooked, especially in the early gestational weeks. Therefore, to improve the detection rate of DMJ anomalies in earlier gestational stages, fetal MR imaging must be technically adequate, with perfectly oriented axial planes, and should not be hampered by fetal motion artifacts.

Developmental forms of hydrocephalus often have multiple points of obstruction.<sup>4</sup> In the present series, cerebral aqueduct stenosis was confirmed in all cases with postnatal MR imaging or autopsy. Moreover, the cerebral aqueduct

was scarcely visible in most fetuses of our series, suggesting that aqueductal stenosis could be the main cause of obstructive ventriculomegaly. Of note, the identification of the lumen of the cerebral aqueduct on MR imaging may not always be reliable in the early gestational weeks, often requiring follow-up studies for confirmation. Interestingly, in most of the present fetuses, the interthalamic adhesion was additionally enlarged and caudally displaced. The location of the interthalamic adhesion is highly variable in humans, but in most people, it lies at the center or in the anterior upper quadrant of the third ventricle, whereas it is located in the posterior inferior quadrant in fewer than 1% of cases.<sup>10</sup> A recent computational study on CSF dynamics demonstrated that pressure in the third ventricle is higher when the interthalamic adhesion is located close to the cerebral aqueduct.<sup>11</sup> Partial or complete aqueductal stenosis associated with alterations of CSF flow dynamics within the third ventricle and abnormal WM development might thus explain the ventriculomegaly in these fetuses. In addition, the interthalamic adhesion hypertrophy is an important dysmorphic feature reported in several brain malformations, including Chiari II malformation, L1 syndrome with X-linked hydrocephalus,<sup>12</sup> and 6q terminal deletion syndrome.<sup>13</sup> Notably, marked interthalamic adhesion hypertrophy may overlap with diencephalosynapsis, a rare malformation designating a complete or partial fusion of the thalami associated with secondary reduction of the lumen of the third ventricle,<sup>14,15</sup> and with rhombencephalosynapsis.<sup>6</sup>

Interestingly, all our presented fetuses were males, suggesting a possible X-linked inheritance pattern. Neuropathologic data from 138 fetuses and neonates genetically tested for X-linked

hydrocephalus showed that 56 subjects (42%) harbored *LICAM* gene mutations, and the remaining fetuses (58%) were classified into 4 distinct subgroups: 1) “L1-like” syndrome, including fetuses with no *LICAM* mutations, but exhibiting characteristics of L1 syndrome (20%); 2) aqueductal atresia/forking spectrum, often associated with midbrain-hindbrain dorsoventral patterning defects (27%); 3) hydrocephalus associated with polymalformative syndromes, such as VACTERL-H (9%); and 4) hydrocephalus associated with isolated CNS malformations (44%).<sup>16</sup> The *LICAM* gene (Xq28) encodes a highly conserved type 1 transmembrane protein of the immunoglobulin superfamily that plays important roles in neuronal adhesion, neuronal migration, axonal growth, pathfinding, and fasciculation as well as in the development of the ventricular system and cerebellum. On imaging, L1 syndrome with X-linked hydrocephalus is usually characterized by bi- or triventricular dilation, aqueductal stenosis, enlarged quadrigeminal plate, interthalamic adhesion hypertrophy, and vermian hypoplasia.<sup>12,17</sup> Intriguingly, most of the fetuses in our series showed phenotypic and imaging characteristics similar to *LICAM*-mutated fetuses. Moreover, postnatal MR imaging with DTI revealed corticospinal tract abnormalities in 2 cases, likely corresponding to the agenesis/fragmentation of the corticospinal tracts described in neuropathology cases of L1 and L1-like syndromes. Unfortunately, because of the lack of *LICAM* genetic analysis in the present cases, we cannot establish whether DMJ dysplasia is caused by *LICAM* mutations or if it belongs to the L1-like spectrum. Moreover, data on fetal MR features of L1 or L1-like syndrome are not available in the literature. DMJ features are likely to occur on a different genetic basis, and studies on genotype-phenotype correlation are definitively needed.

Finally, we observed pontine hypoplasia and small cerebellar vermis in most of the present fetuses, variably associated with moderate brain stem kinking. The differential diagnosis of prenatal ventriculomegaly and brain stem kinking has been recently widened to include several brain malformations, such as congenital muscular dystrophies, X-linked hydrocephalus caused by *LICAM* mutations, microcephaly with lissencephaly and mid-hindbrain involvement, and tubulinopathies.<sup>18,19</sup> Taken together, these data indicate that a kinked brain stem is not a pathognomonic finding, but more likely an indicator of severe neurodysgenesis arising early in gestation and often associated with developmental hydrocephalus.<sup>18</sup>

The main limitation of our report is the lack of extensive genetic testing and histology investigation in all cases with pregnancy termination. Moreover, the possibility that fetal DMJ dysplasia cases without developmental obstructive ventriculomegaly may have been missed in our prenatal imaging search has to be taken into account.

In conclusion, a butterfly-shaped contour of the midbrain along with an abnormal spatial relation between the midbrain and thalamic mass may be detected on axial and sagittal sections, respectively, thus allowing an early prenatal diagnosis of DMJ dysplasia in fetuses with proximal obstructive ventriculomegaly. Among the rare causes of developmental hydrocephalus, DMJ dysplasia is likely to be an underestimated condition and seems to share several phenotypic features with the L1 and L1-like syndromes. Further studies on larger fetal populations with genotype-phenotype correlations are needed

to clarify the causes, pathophysiology, and prevalence of DMJ dysplasia in the fetal population.

Disclosures: Andrea Rossi—UNRELATED: Consultancy: Bracco Imaging Italia Srl.

## REFERENCES

- Zaki MS, Saleem SN, Dobyns WB, et al. **Diencephalic-mesencephalic junction dysplasia: a novel recessive brain malformation.** *Brain* 2012;135:2416–27 CrossRef Medline
- Jissendi-Tchofo P, Severino M, Nguema-Edzang B, et al. **Update on neuroimaging phenotypes of mid-hindbrain malformations.** *Neuroradiology* 2015;57:113–38 CrossRef Medline
- Severino M, Tortora D, Pistorio A, et al. **Expanding the spectrum of congenital anomalies of the diencephalic-mesencephalic junction.** *Neuroradiology* 2016;58:33–44 CrossRef Medline
- Tully HM, Dobyns WB. **Infantile hydrocephalus: a review of epidemiology, classification and causes.** *Eur J Med Genet* 2014;57:359–68 CrossRef Medline
- Tully HM, Ishak GE, Rue TC, et al. **Two hundred thirty-six children with developmental hydrocephalus: causes and clinical consequences.** *J Child Neurol* 2016;31:309–20 CrossRef Medline
- Cagneaux M, Vasiljevic A, Massoud M, et al. **Severe second-trimester obstructive ventriculomegaly related to disorders of diencephalic, mesencephalic and rhombencephalic differentiation.** *Ultrasound Obstet Gynecol* 2013;42:596–602 CrossRef Medline
- Griffiths PD, Reeves MJ, Morris JE, et al. **A prospective study of fetuses with isolated ventriculomegaly investigated by antenatal sonography and in utero MR imaging.** *AJNR Am J Neuroradiol* 2010;31:106–11 CrossRef Medline
- Barzilay E, Bar-Yosef O, Dorembus S, et al. **Fetal brain anomalies associated with ventriculomegaly or asymmetry: an MRI-based study.** *AJNR Am J Neuroradiol* 2017;38:371–75 CrossRef Medline
- Huisman TAGM, Tekes A, Poretti A. **Brain malformations and fetal ventriculomegaly: what to look for?** *J Pediatr Neuroradiol* 2012;1:185–95 CrossRef
- Samra KA, Cooper IS. **Radiology of the massa intermedia.** *Radiology* 1968;91:1124–28 CrossRef Medline
- Cheng S, Tan K, Bilston LE. **The effects of the interthalamic adhesion position on cerebrospinal fluid dynamics in the cerebral ventricles.** *J Biomech* 2010;43:579–82 CrossRef Medline
- Kanemura Y, Okamoto N, Sakamoto H, et al. **Molecular mechanisms and neuroimaging criteria for severe L1 syndrome with X-linked hydrocephalus.** *J Neurosurg* 2006;105(5 suppl):403–12 CrossRef Medline
- Elia M, Striano P, Fichera M, et al. **6q terminal deletion syndrome associated with a distinctive EEG and clinical pattern: a report of five cases.** *Epilepsia* 2006;47:830–38 CrossRef Medline
- De France I, Saada P, Jouannic JM, et al. **Ultrasonographic and pathological correlation in a fetal intracranial cyst: a case of “diencephalo-synapsis”** [in French]. *J Gynecol Obstet Biol Reprod (Paris)* 2002;31:600–03 Medline
- Kepes JJ, Clough C, Villanueva A. **Congenital fusion of the thalami (atresia of the third ventricle) and associated anomalies in a 6-month-old infant.** *Acta Neuropathol* 1969;13:97–104 CrossRef Medline
- Adle-Biassette H, Saugier-Verber P, Fallet-Bianco C, et al. **Neuropathological review of 138 cases genetically tested for X-linked hydrocephalus: evidence for closely related clinical entities of unknown molecular bases.** *Acta Neuropathol* 2013;126:427–42 CrossRef Medline
- Yamasaki M, Kanemura Y. **Molecular biology of pediatric hydrocephalus and hydrocephalus-related diseases.** *Neurol Med Chir (Tokyo)* 2015;55:640–46 CrossRef Medline
- Stroustrup Smith A, Levine D, Barnes PD, et al. **Magnetic resonance imaging of the kinked fetal brain stem: a sign of severe dysgenesis.** *J Ultrasound Med* 2005;24:1697–709 CrossRef Medline
- Amir T, Poretti A, Boltshauser E, et al. **Differential diagnosis of ventriculomegaly and brainstem kinking on fetal MRI.** *Brain Dev* 2016;38:103–08 CrossRef Medline

# Temporal Evolution of Disc in Young Patients with Low Back Pain and Stress Reaction in Lumbar Vertebrae

A. Sharma, K. Sargar, and A. Salter

## ABSTRACT

**BACKGROUND AND PURPOSE:** Although stress-induced bony changes often resolve with conservative treatment, the long-term effects of such mechanical stresses on intervertebral discs have not been studied. We aimed to assess the differences in the temporal evolution of disc in segments of the lumbar spine with and without signs of increased mechanical stresses.

**MATERIALS AND METHODS:** Using MR imaging performed >6 months apart, 2 radiologists evaluated lumbar intervertebral discs for degenerative changes affecting the annulus fibrosus, the nucleus pulposus, and the endplates in 42 patients (22 male, 20 female; mean age,  $16.0 \pm 3.7$  years [range, 7–25 years]) with low back pain and imaging evidence of stress reaction/fracture in the lumbar spine. Data were analyzed for differences in the presence and progression of disc degeneration in stressed versus nonstressed segments.

**RESULTS:** At baseline, stressed discs had a higher burden of annular fissures, radial fissures, herniation, and nuclear degeneration. Endplate defect burden was comparable in stressed and control discs. At follow-up, the burden of new annular fissures and endplate defects was comparable for stressed and control discs. However, a higher proportion of stressed discs showed worsening nuclear signal intensity grade (14.3% versus 0% control discs;  $P = .008$ ) and worsening nuclear degeneration grade (11.9% versus 0% control discs;  $P = .02$ ). An increased risk of progressive nuclear degeneration of stressed discs was observed irrespective of the outcome of bony changes.

**CONCLUSIONS:** Stressed discs exhibit a higher burden of nuclear and annular degeneration at baseline. These discs have a higher risk of progressive nuclear degeneration irrespective of improvement or worsening of stress-related bony changes.

**S**tress reaction in posterior elements of the lumbar spine is a common cause for low back pain in young athletes.<sup>1–11</sup> Whereas ongoing mechanical stresses can cause overt stress fractures and eventually spondylolisthesis, an initial microtraabecular bony injury within an affected pedicle or pars interarticularis manifests either as edema on MR imaging or as increased uptake on a bone scan.<sup>2–5,12,13</sup> Intervertebral discs attached to stressed vertebrae experience higher mechanical stresses, and even at a young age, these stressed discs demonstrate a higher burden of annular fissures, herniation, and loss of normal hyperintensity of the nucleus pulposus on T2WI.<sup>14</sup> The stressed bone often heals with conservative management, allowing patients to resume their

athletic activities.<sup>12,15,16</sup> In contrast to the ability of bone to heal itself, there is little evidence to support disc regeneration after the initiation of the degenerative cascade, wherein an insult to the disc may initiate a chain of chemical or inflammatory events that can further damage the disc.<sup>17</sup> Although cross-sectional studies have highlighted a higher prevalence of disc degeneration in patients with spondylolysis and spondylolisthesis in adults,<sup>18–21</sup> there is a paucity of information about the risk of progressive disc degeneration in young patients presenting with clinical and imaging evidence for bony stresses in the lumbar spine. We aimed to study the longitudinal evolution of degeneration in the individual components of stressed discs, hypothesizing that the stressed discs would demonstrate a higher burden of progressive degeneration relative to control discs.

Received February 8, 2017; accepted after revision March 17.

From the Mallinckrodt Institute of Radiology (A. Sharma, K.S.) and Department of Biostatistics (A. Salter), Washington University School of Medicine, St. Louis, Missouri; Department of Radiology (A. Sharma), Barnes-Jewish Hospital South, St. Louis, Missouri; and Department of Radiology (A. Sharma), St. Louis Children's Hospital, St. Louis, Missouri.

Please address correspondence to Aseem Sharma, MD, Mallinckrodt Institute of Radiology, Washington University School of Medicine, Campus Box 8131, 510 S. Kingshighway Blvd, St. Louis, MO 63110; e-mail: sharmaa@mir.wustl.edu

<http://dx.doi.org/10.3174/ajnr.A5237>

## MATERIALS AND METHODS

Our institutional review board at Washington University School of Medicine approved this retrospective longitudinal observational study, waiving the need for consent.

### Patient Selection

We identified consecutive patients diagnosed with a stress reaction or fracture in the posterior elements of the lumbar spine over

an 8-year period ending in 2015. Inclusion criteria were age <25 years and the availability of lumbar spine MR images obtained first at presentation and then >6 months later. All patients presented with low back pain without any history of acute injury. Diagnosis was confirmed by the senior author, a board-certified neuroradiologist with >15 years of experience. Patients with spinal infection and neoplasms were excluded. Forty-two patients (22 male, 20 female; mean age, 16.0 ± 3.7 years [range, 7–25 years]) were included. Bony stresses involved the L5 segment in 29 (69.0%) patients and the L4 segment in 9 (21.4%). Four patients (9.6%) had bony stresses at 2 segments (L3 and L4 in 2; L4 and L5 in 2). Thirty-nine of 46 (84.8%) stressed segments showed bilateral changes. Anterolisthesis (grade 1 in all) was present in 15 (35.7%) cases. The mean duration between 2 studies was 19.8 months (range, 6–51 months). On the Hollenberg grading system,<sup>2</sup> which categorizes stress injury into grades 1 through 4 (corresponding to edema without fracture line, incomplete fracture, complete fracture with edema, and fracture nonunion without associated edema, respectively), 18 of 42 (42.9%) patients were graded 1 or 2, indicating a lack of complete fracture.

### Imaging Analysis

MR imaging was performed on 1.5T or 3T scanners (Sonata, Vision, Avanto, Magnetom Aera, and Trio; Siemens, Erlangen, Germany) and included sagittal T1WI (TR, 448–640 ms; TE, 11–29 ms; thickness, 3 mm), sagittal T2WI (TR, 3110–5390 ms; TE, 99–164 ms; thickness, 3 mm), sagittal STIR (TR, 4300–6359 ms; TE, 18–100 ms; TI, 135–160 ms; thickness, 3 mm), and axial T2WI (TR, 2280–4820 ms; TE, 102–120 ms; thickness, 3–4 mm).

Two radiologists (K.S., a neuroradiology fellow, and A. Sharma, the senior author) evaluated MR images in a consensus read. Each component of the intervertebral discs between the T12 and S1 segments was evaluated on baseline scans as reported previously.<sup>22</sup> The annulus fibrosus was assessed for annular fissure, radial fissure (annular fissure with its hyperintensity in continuity with that of the nucleus pulposus), and herniation. The nucleus pulposus was graded according to the Pfirrmann classification<sup>23</sup> and on a 6-point signal intensity–based scale.<sup>24</sup> The presence or absence of endplate defects was noted. The reliability of these scales had been tested earlier and was reported to range from moderate to almost perfect ( $\kappa = 0.57–0.86$ ).<sup>24,25</sup> To assess the longitudinal temporal evolution of disc degeneration and bony changes, the initial and follow-up scans were viewed simultaneously.

### Stressed Discs and Control Discs

Both intervertebral discs adjacent to the stressed bony segments were considered stressed (Table 1). The lumbar spine was divided into cranial (T12 through L3) and caudal (L3 through S1) segments. To account for the effects of axial loading, control discs were chosen from the same (cranial or caudal) segment to which the stressed discs belonged (Table 1).<sup>14</sup>

### Statistical Analysis

For the initial scan, the burden of individual degenerative changes was calculated on a per-disc basis.<sup>14</sup> For example, if 1 of the 2

**Table 1: Definitions of stressed discs and control discs for each vertebral segment showing bony stress**

Location of Bony Stress Changes	Stressed Discs	Control Discs
T12	T12–L1	L1–2, L2–3
L1	T12–L1, L1–2	L2–3
L2	L1–2, L2–3	T12–L1
L3	L2–3, L3–4	T12–L1, L1–2, L4–5, L5–S1
L4	L3–4, L4–5	L5–S1
L5	L4–5, L5–S1	L3–4
S1	L5–S1	L3–4, L4–5

stressed discs demonstrated annular fissure, the burden of annular fissures in stressed discs was 0.5. Similarly, if the only control disc had nuclear degeneration, the burden of nuclear degeneration for the control disc was 1. For meeting the binary definition of nuclear degeneration, the disc had to be graded III or higher on the Pfirrmann scale. The baseline degenerative burden in stressed and control discs was compared. Differences between stressed and control discs for various parameters were assessed by using a non-parametric paired test, the Wilcoxon signed rank test, and the McNemar test. Correlation was sought between baseline disc degeneration, the presence of spondylolisthesis, and the grade of bony stress. Differences between scans were used to assess the burden of new degeneration by using similar tests. In cases where no new changes were observed in the discs of all patients, a binomial test of proportions was calculated. The Fisher exact test was used to test differences between patients with persistent bony stresses and those with improvement. A *P*-value < .05 was considered significant. All tests were 2-sided.

### RESULTS

At baseline, the burdens of annular fissures, radial fissures, and herniation were higher in stressed discs compared with control discs ( $P < .0001$ ,  $P < .0001$ , and  $P = .024$ , respectively) (Table 2; Fig 1). Median [25th, 75th percentiles] signal intensity rating for stressed discs was 1.39 [1, 2], significantly higher than control discs (1 [1, 1];  $P < .0001$  [Table 2]). A higher percentage (52.4%) of patients showed at least 1 stressed disc with signal intensity grade >1 compared with those with a similar change in control discs (11.9%;  $P < .0001$ ). Although the mean Pfirrmann grade in the 2 groups was comparable, a higher percentage of patients had nuclear degeneration (Pfirrmann grade >II) in stressed segments (19.1% versus 4.8% for control segments;  $P = .031$ ). The endplate defect burden in stressed and control discs was comparable (Table 2).

No significant Spearman correlation was observed between various parameters of disc degeneration in stressed discs and spondylolisthesis at baseline. No significant Spearman correlation was present between annular fissure or radial fissure burdens in stressed discs and bony stress reaction grade (Wilcoxon signed rank,  $P = .37$  and  $P = .29$ ). However, there was a significant difference in the median stress grade for stressed discs showing nuclear degeneration compared with those without such indications (Wilcoxon signed rank,  $P = .034$ ). For control discs, none of the parameters demonstrated any correlation with the grade of bony stress reaction.

At follow-up, the burdens of new annular fissures, new radial

**Table 2: Disc degeneration in stressed and nonstressed segments of lumbar spine**

	Baseline Degeneration		Progressive Degeneration	
	Stressed Discs	Control Discs	Stressed Discs	Control Discs
Annular fissure <sup>a,b</sup>	0.76 ± 0.35 37 (88.1)	0.37 ± 0.48 16 (38.1)	0.07 ± 0.18 6 (14.3)	0.05 ± 0.22 2 (4.9)
Radial fissure <sup>a,b</sup>	0.59 ± 0.43 30 (71.4)	0.17 ± 0.38 8 (19.1)	0.07 ± 0.18 6 (14.3)	0.05 ± 0.22 2 (4.9)
Herniation <sup>a,b</sup>	0.07 ± 0.20 5 (11.9)	0.00 ± 0.00 0 (0.0)	0.01 ± 0.08 1 (2.4)	0.00 ± 0.00 0 (0.0)
Nuclear degeneration <sup>a,b,c</sup>	0.13 ± 0.30 8 (19.1)	0.05 ± 0.22 2 (4.8)	0.10 ± 0.28 5 (11.9)	0.00 ± 0.00 0 (0.0)
Nuclear SI loss <sup>a,b,d</sup>	0.39 ± 0.42 22 (52.4)	0.12 ± 0.33 5 (11.9)	0.17 ± 0.48 6 (14.3)	0.00 ± 0.00 0 (0.0)
EPD <sup>a,b</sup>	0.11 ± 0.24 8 (19.1)	0.12 ± 0.33 5 (11.9)	0.00 ± 0.00 0 (0.0)	0.00 ± 0.00 0 (0.0)

**Note:**—EPD indicates endplate burden; SI, signal intensity.

<sup>a</sup> Burden (mean ± SD) of degenerative parameter calculated on per disc basis.

<sup>b</sup> Number (%) of patients with specified degenerative parameters in stressed or control segments of lumbar spine; “Baseline Degeneration” refers to changes on MR scan obtained at the time of presentation and “Progressive Degeneration” refers to appearance of new changes noted on a follow-up MR scan obtained >6 months later.

<sup>c</sup> Defined as discs graded higher than 2 on Pfirrmann grading system.

<sup>d</sup> Discs graded higher than 1 on a 6-point scale based on SI on T2-weighted images indicating any loss of normal hyperintense signal.

fissures, and new herniation in stressed discs ( $0.06 \pm 0.17$ ,  $0.07 \pm 0.18$ , and  $0.01 \pm 0.08$ , respectively; Table 2; Fig 2) and control discs ( $0.05 \pm 0.22$ ,  $0.05 \pm 0.22$ , and  $0.00 \pm 0.00$ , respectively; Table 2; Fig 2) were not significantly different. Similarly, the percentages of stressed and control discs demonstrating new annular fissure, radial fissure, or herniation were also comparable ( $P = .375$ ,  $P = .219$ , and not available). Worsened signal intensity and Pfirrmann grade were present in 6 (14.3%) and 5 (11.9%) stressed discs, respectively (Figs 3–5). Control discs had no shift in their signal intensity or Pfirrmann rating. The binomial test of proportions indicates that stressed discs had a statistically different proportion with signal intensity ( $P = .008$ ) and Pfirrmann rating ( $P = .017$ ). No new endplate defects were

## Burden of Baseline Degeneration

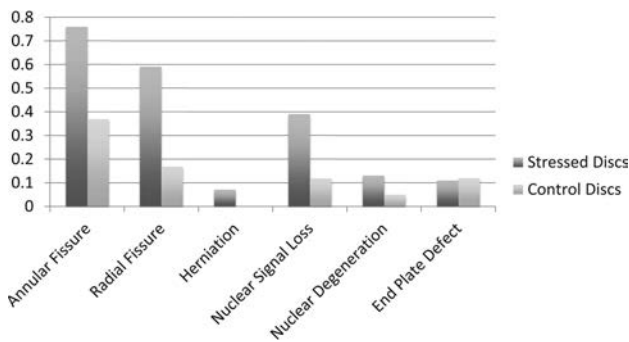


**FIG 1.** A bar diagram demonstrating the baseline burden of degenerative parameters in the individual components of the lumbar intervertebral discs of patients <25 years old and presenting with low back pain caused by stress reaction in the posterior elements of the lumbar vertebrae. Stressed discs refer to intervertebral discs attached to the vertebra with increased bony stresses. Control discs refer to discs not in contact with stressed vertebra, but with otherwise equivalent axial loading.

## Burden of Progressive Degeneration

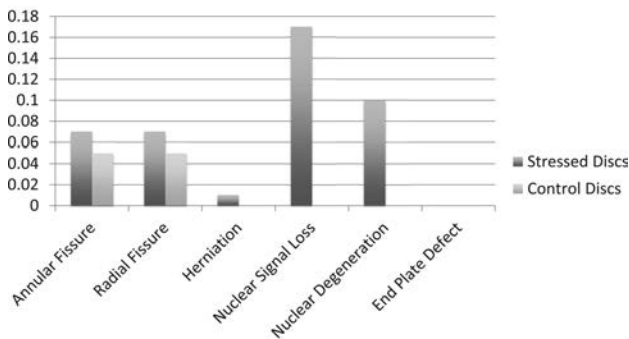


**FIG 2.** A bar diagram demonstrating the burden of new degenerative changes in stressed and control discs as observed on follow-up MR imaging acquired >6 months after the baseline scan.

found for either stressed or control discs (Table 2; Fig 2).

Fisher exact test did not reveal any differences in the parameters of progressive disc degeneration in patients with improved (8 patients; Fig 5) and those with persistent/worsening bony stress reaction (34 patients) on follow-up imaging.

## DISCUSSION

Previous studies have reported a high prevalence of disc degeneration in adults with spondylolysis, with or without spondylolisthesis.<sup>18–20</sup> Degeneration of discs at the level of spondylolisthesis has been documented in adolescents.<sup>21,26</sup> It has also been demonstrated that early degenerative changes in the form of annular fissures, radial fissures, and nuclear degeneration can be seen around stressed vertebral segments in young patients with a stress reaction detected on MR imaging before complete stress fracture.<sup>14</sup> By showing a relatively higher overall rate of worsened disc degeneration in stressed discs in follow-up studies, our results demonstrate, for the first time, the progressive nature of degenerative changes initiated in association with bony stress reaction/fractures at a young age.<sup>14</sup>

Although disc degeneration progresses relatively slowly, the long life expectancy of patients included in our study makes these results particularly noteworthy. It should be noted that most outcome studies in this patient population are limited to 1–3 years of follow-up, a rather short time span compared with the life expectancy of these patients.<sup>8,27,28</sup> Based on the progressive disc degeneration seen in our study, it is likely that the advanced disc degeneration documented in many adults with spondylolytic spondylolisthesis<sup>18,19</sup> reflects the sequela of a mechanical process that initiated degenerative cascade in discs at the same time it induced stress fractures in the vertebral elements.

Outcome studies in young patients with back pain caused by stress reaction have focused on either clinical symptoms or the evolution of stressed bone, with relatively few studies exploring the effects of such stresses on associated intervertebral

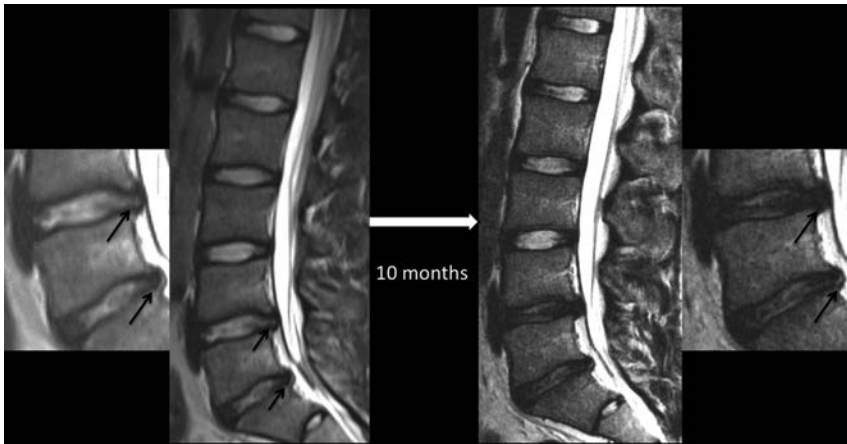


**FIG 3.** Sequential MR images of the lumbar spine showing the evolution of lumbar disc degeneration in a 16-year-old female patient presenting with low back pain and evidence for stress reaction in both L5 pedicles (not shown) at the time of presentation. Both intervertebral discs (L4–5 and L5–S1; also shown in magnified images) around the stressed segment demonstrated the presence of annular fissures (arrows), disc herniation, and nuclear degeneration at baseline. The control disc in the lower half of the lumbar spine (L3–4) had an intact annulus and preserved nuclear signal intensity at baseline. Follow-up MR imaging 10 months later reveals stability in the appearance of the control disc, but interval loss of signal intensity, signifying progressive nuclear degeneration of both stressed discs. The annular fissure at the L4–5 level has become less conspicuous, but one at the L5–S1 level is more easily recognizable on a follow-up scan.



**FIG 4.** Sequential lumbar MR imaging over a 47-month period in a 12-year-old female patient presenting with low back pain caused by a partial L4 stress fracture as indicated by edema in the right pedicle (arrow) on a parasagittal STIR image. Initial and follow-up midsagittal T2-weighted images highlight marked progressive nuclear degeneration in the inferior stressed disc at the L4–5 level, but preserved appearance of a more caudally located control disc at the L5–S1 level.

discs around the time of presentation.<sup>8,12,15,27,29,30</sup> Conservative treatment is often successful in alleviating patients' symptoms, allowing a high proportion of these patients to resume the offending physical activity. Follow-up imaging in our patients was done based on clinical need, and thus, our study fails to document the evolution of disc degeneration in patients who become asymptomatic. However, given the propensity of disc degeneration to remain asymptomatic and a higher baseline burden of annular pathology that is associated with progressive nuclear degeneration, it is possible that progressive disc degeneration also occurs in some patients despite their becoming asymptomatic.<sup>22,24</sup>

stressed discs with annular pathology at baseline would undergo progressive nuclear degeneration on follow-up imaging irrespective of how the bony changes evolve, likely explaining the progressive disc degeneration in patients with improved bony stress reaction.

Although stressed discs showed a higher baseline burden of both annular and nuclear degeneration, progressive changes were mainly seen in the nucleus pulposus. Lack of a higher burden of new annular fissures in stressed discs could potentially be attributed to activity modifications induced by persistent symptoms in our patients. Alternatively, because the annulus may be the first component of the intervertebral discs to

Progressive degeneration was observed in stressed discs irrespective of bone healing on follow-up imaging. It implies that in some patients, long-term sequelae of high segmental spinal stresses may be left in the form of disc degeneration rather than a stress fracture (Fig 5). Studies in asymptomatic athletes have demonstrated a high prevalence of both bony stress reaction and disc degeneration in the lumbar spine,<sup>31,32</sup> indicating that mechanical stress-induced bony fractures as well as accompanying disc degeneration can take place in the absence of overt pain. The role of mechanical factors in disc degeneration is well established.<sup>14,33–38</sup> The previously reported higher burden of degeneration in stressed discs on both sides of the stressed vertebral segment<sup>14,18</sup> suggests that in patients with a bony stress reaction, increased mechanical stresses are conveyed to the disc through the vertebral body to whichever disc components are attached. Whether, and to what extent, a similar mechanism may be responsible for initiating disc degeneration in the general population is unclear. Our results do suggest that in patients with advanced disc degeneration, intact posterior vertebral elements in the vertebrae around the degenerated disc do not exclude the possibility of a similar mechanism for the initiation of disc degeneration.

At baseline, the pattern of disc degeneration observed was similar to what has been previously reported, with a higher burden of annular fissures, radial fissures, and herniation as well as nuclear degeneration.<sup>14</sup> Previous studies have highlighted the association between radial annular fissures and progressive nuclear degeneration.<sup>22,24,39–44</sup>

Therefore, it is to be expected that some

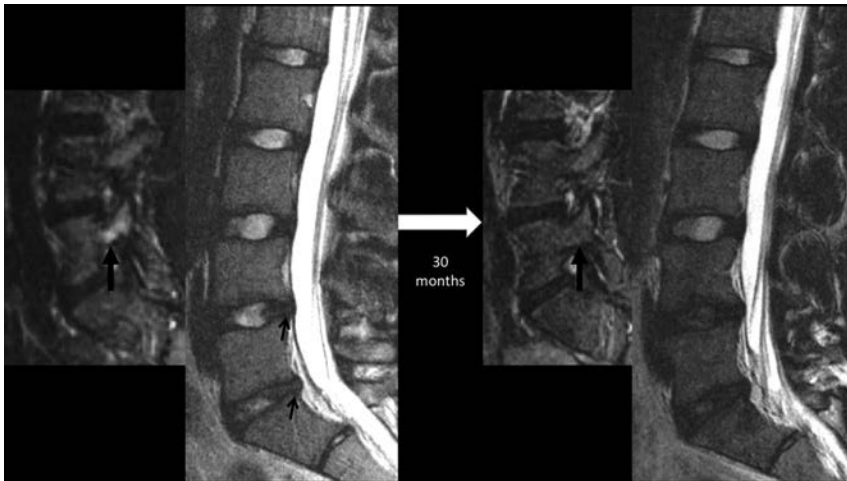


**FIG 5.** Sequential lumbar MR images obtained 30 months apart in a 15-year-old male patient with back pain, highlighting progressive disc degeneration despite the resolution of bony stress reaction. Initial MR imaging revealed edema in the right L5 pedicle (*thick arrow*) as shown here on a parasagittal STIR image, consistent with a stress reaction. Sagittal T2WI at this time revealed subtle annular fissures at the L4–5 and L5–S1 discs (*small arrows*) and signs of nuclear degeneration at the L5–S1 level. Follow-up MR imaging obtained 30 months later reveals the resolution of pedicular edema (*thick arrow*), but progressive loss of nuclear signal intensity of both stressed discs at the L4–5 and L5–S1 levels. Note that the control disc at the L3–4 level remains normal.

be affected in the degenerative process,<sup>14,22,24,25</sup> it is possible that patients in whom the annulus was prone to stress-induced injury had already developed annular fissures by the time of presentation. A similar explanation could also be used to explain why only nuclear degeneration correlated with the bony stress grade. The Hollenberg grading system progressing from bony edema to fracture nonunion can be viewed as an indirect proxy for the duration and/or the degree of mechanical stresses.<sup>2</sup> Accordingly, even the baseline imaging in these patients may provide a sense of the timeline of associated disc degeneration. Again, it is possible that any annulus fibrosus predisposed to rupture in the face of increased mechanical stresses did so early in the process, thereby inciting ongoing nuclear degeneration that became more evident as the disease progressed.

Stressed discs did not exhibit a higher burden of endplate defects. These results are concordant with those previously reported.<sup>14</sup> Apparent discordance from other studies showing a strong association between Schmorl nodes and disc degeneration<sup>45</sup> may simply reflect differences in the population being studied and the hypothesis being tested. Despite a strong correlation between endplate defects and nuclear degeneration,<sup>22,45</sup> their segmental distributions differ. Endplate defects are more prevalent at the thoracolumbar junction with inherently weaker endplates, whereas nuclear degeneration preferentially affects caudal segments of the lumbar spine.<sup>14,22,45-47</sup> Stressed discs in our study were mainly seen in the caudal half of the lumbar spine, likely explaining a low burden of endplate defects in both stressed and control discs.

The retrospective nature of our study imposes some limitations. Very few segments from the upper lumbar spine were represented in our study. We did not take into consideration the weight of patients or activity level between the 2 studies. Although both of these factors can influence the risk of disc degeneration,

these factors would have affected both the stressed and control discs. A longer follow-up duration could have further exaggerated the differences in the progression of disc degeneration of stressed versus control discs. Similarly, the overall burden of disc degeneration could have been different had we restricted the study to higher-strength MR imaging. Despite these limitations, the selection of stressed and control discs from the same patients allowed us to conclusively demonstrate a higher burden of both the baseline and the progressive degeneration of discs in lumbar spinal segments experiencing higher mechanical stress.

## CONCLUSIONS

Intervertebral discs in stressed segments of the lumbar spine demonstrate a higher burden of disc degeneration at baseline and an increased risk of progressive degeneration irrespective of the outcome of bony changes. The progres-

sion of disc degeneration occurs mainly in the form of worsening nuclear degeneration.

## REFERENCES

- Dunn AJ, Campbell RS, Mayor PE, et al. **Radiological findings and healing patterns of incomplete stress fractures of the pars interarticularis.** *Skeletal Radiol* 2008;37:443–50 CrossRef Medline
- Hollenberg GM, Beattie PF, Meyers SP, et al. **Stress reactions of the lumbar pars interarticularis: the development of a new MRI classification system.** *Spine (Phila Pa 1976)* 2002;27:181–86 CrossRef Medline
- Motley G, Nyland J, Jacobs J, et al. **The pars interarticularis stress reaction, spondylolysis, and spondylolisthesis progression.** *J Athl Train* 1998;33:351–58 Medline
- Pennell RG, Maurer AH, Bonakdarpour A. **Stress injuries of the pars interarticularis: radiologic classification and indications for scintigraphy.** *AJR Am J Roentgenol* 1985;145:763–66 CrossRef Medline
- Tofte JN, CarlLee TL, Holte AJ, et al. **Imaging pediatric spondylolysis: a systematic review.** *Spine (Phila Pa 1976)* 2017;42:777–82 CrossRef Medline
- Nitta A, Sakai T, Goda Y, et al. **Prevalence of symptomatic lumbar spondylolysis in pediatric patients.** *Orthopedics* 2016;39:e434–37 CrossRef Medline
- Changstrom BG, Brou L, Khodae M, et al. **Epidemiology of stress fracture injuries among US high school athletes, 2005–2006 through 2012–2013.** *Am J Sports Med* 2015;43:26–33 CrossRef Medline
- Bouras T, Korovessis P. **Management of spondylolysis and low-grade spondylolisthesis in fine athletes. A comprehensive review.** *Eur J Orthop Surg Traumatol* 2015;25(suppl 1):S167–75 CrossRef Medline
- Mora-de Sambricio A, Garrido-Stratenwerth E. **Spondylolysis and spondylolisthesis in children and adolescents [in Spanish].** *Rev Esp Cir Ortop Traumatol* 2014;58:395–406 CrossRef Medline
- Donaldson LD. **Spondylolysis in elite junior-level ice hockey players.** *Sports Health* 2014;6:356–59 CrossRef Medline
- Barrack MT, Gibbs JC, De Souza MJ, et al. **Higher incidence of bone stress injuries with increasing female athlete triad-related risk**

- factors: a prospective multisite study of exercising girls and women.** *Am J Sports Med* 2014;42:949–58 CrossRef Medline
12. Morita T, Ikata T, Katoh S, et al. **Lumbar spondylolysis in children and adolescents.** *J Bone Joint Surg Br* 1995;77:620–25 Medline
  13. Papanicolaou N, Wilkinson RH, Emans JB, et al. **Bone scintigraphy and radiography in young athletes with low back pain.** *AJR Am J Roentgenol* 1985;145:1039–44 CrossRef Medline
  14. Sharma A, Lancaster S, Bagade S, et al. **Early pattern of degenerative changes in individual components of intervertebral discs in stressed and nonstressed segments of lumbar spine: an in vivo magnetic resonance imaging study.** *Spine (Phila Pa 1976)* 2014;39:1084–90 CrossRef Medline
  15. Iwamoto J, Sato Y, Takeda T, et al. **Return to sports activity by athletes after treatment of spondylolysis.** *World J Orthop* 2010;1:26–30 CrossRef Medline
  16. Pizzutillo PD, Hummer CD 3rd. **Nonoperative treatment for painful adolescent spondylolysis or spondylolisthesis.** *J Pediatr Orthop* 1989;9:538–40 CrossRef Medline
  17. Modic MT, Ross JS. **Lumbar degenerative disk disease.** *Radiology* 2007;245:43–61 CrossRef Medline
  18. Jeong HY, You JW, Sohn HM, et al. **Radiologic evaluation of degeneration in isthmic and degenerative spondylolisthesis.** *Asian Spine J* 2013;7:25–33 CrossRef Medline
  19. Dai LY. **Disc degeneration in patients with lumbar spondylolysis.** *J Spinal Disord* 2000;13:478–86 CrossRef Medline
  20. Szypryt EP, Twining P, Mulholland RC, et al. **The prevalence of disc degeneration associated with neural arch defects of the lumbar spine assessed by magnetic resonance imaging.** *Spine (Phila Pa 1976)* 1989;14:977–81 CrossRef Medline
  21. Schlenzka D, Poussa M, Seitsalo S, et al. **Intervertebral disc changes in adolescents with isthmic spondylolisthesis.** *J Spinal Disord* 1991;4:344–52 CrossRef Medline
  22. Sharma A, Parsons M, Pilgram T. **Temporal interactions of degenerative changes in individual components of the lumbar intervertebral discs: a sequential magnetic resonance imaging study in patients less than 40 years of age.** *Spine (Phila Pa 1976)* 2011;36:1794–800 CrossRef Medline
  23. Pfirrmann CW, Metzendorf A, Zanetti M, et al. **Magnetic resonance classification of lumbar intervertebral disc degeneration.** *Spine (Phila Pa 1976)* 2001;26:1873–78 CrossRef Medline
  24. Sharma A, Pilgram T, Wippold FJ 2nd. **Association between annular tears and disk degeneration: a longitudinal study.** *AJNR Am J Neuroradiol* 2009;30:500–06 CrossRef Medline
  25. Sharma A, Parsons MS, Pilgram TK. **Temporal association of annular tears and nuclear degeneration: lessons from the pediatric population.** *AJNR Am J Neuroradiol* 2009;30:1541–45 CrossRef Medline
  26. Paaanjanen H, Tertti M. **Association of incipient disc degeneration and instability in spondylolisthesis. A magnetic resonance and flexion-extension radiographic study of 20-year-old low back pain patients.** *Arch Orthop Trauma Surg* 1991;111:16–19 CrossRef Medline
  27. Lee GW, Lee SM, Ahn MW, et al. **Comparison of surgical treatment with direct repair versus conservative treatment in young patients with spondylolysis: a prospective, comparative, clinical trial.** *Spine J* 2015;15:1545–53 CrossRef Medline
  28. Menga EN, Kebaish KM, Jain A, et al. **Clinical results and functional outcomes after direct intralaminar screw repair of spondylolysis.** *Spine* 2014;39:104–10 CrossRef Medline
  29. Mohriak R, Vargas Silva PD, Trandafilov M, Jr., et al. **Spondylolysis and spondylolisthesis in young gymnasts.** *Rev Bras Ortop* 2010;45:79–83 CrossRef Medline
  30. Scheepers MS, Streak Gomersall J, Munn Z. **The effectiveness of surgical versus conservative treatment for symptomatic unilateral spondylolysis of the lumbar spine in athletes: a systematic review.** *JBI Database System Rev Implement Rep* 2015;13:137–73 CrossRef Medline
  31. Rajeswaran G, Turner M, Gissane C, et al. **MRI findings in the lumbar spines of asymptomatic elite junior tennis players.** *Skeletal Radiol* 2014;43:925–32 CrossRef Medline
  32. Alyas F, Turner M, Connell D. **MRI findings in the lumbar spines of asymptomatic, adolescent, elite tennis players.** *Br J Sports Med* 2007;41:836–41; discussion 841 CrossRef Medline
  33. Rajasekaran S, Vidyadhara S, Subbiah M, et al. **ISSLS prize winner: a study of effects of in vivo mechanical forces on human lumbar discs with scoliotic disc as a biological model: results from serial post-contrast diffusion studies, histopathology and biochemical analysis of twenty-one human lumbar scoliotic discs.** *Spine (Phila Pa 1976)* 2010;35:1930–43 CrossRef Medline
  34. Ariga K, Yonenobu K, Nakase T, et al. **Mechanical stress-induced apoptosis of endplate chondrocytes in organ-cultured mouse intervertebral discs: an ex vivo study.** *Spine (Phila Pa 1976)* 2003;28:1528–33 CrossRef Medline
  35. Adams MA, Freeman BJ, Morrison HP, et al. **Mechanical initiation of intervertebral disc degeneration.** *Spine (Phila Pa 1976)* 2000;25:1625–36 CrossRef Medline
  36. Lotz JC, Colliou OK, Chin JR, et al. **Compression-induced degeneration of the intervertebral disc: an in vivo mouse model and finite-element study.** *Spine* 1998;23:2493–506 CrossRef Medline
  37. Natarajan RN, Ke JH, Andersson GB. **A model to study the disc degeneration process.** *Spine (Phila Pa 1976)* 1994;19:259–65 CrossRef Medline
  38. Adams MA, Hutton WC. **Prolapsed intervertebral disc. A hyperflexion injury 1981 Volvo Award in Basic Science.** *Spine* 1982;7:184–91 CrossRef Medline
  39. Moore RJ, Latham JM, Vernon-Roberts B, et al. **Does plate fixation prevent disc degeneration after a lateral annulus tear?** *Spine* 1994;19:2787–90 CrossRef Medline
  40. Osti OL, Vernon-Roberts B, Fraser RD. **1990 Volvo Award in experimental studies. Annulus tears and intervertebral disc degeneration. An experimental study using an animal model.** *Spine (Phila Pa 1976)* 1990;15:762–67 CrossRef Medline
  41. Yu SW, Sether LA, Ho PS, et al. **Tears of the annulus fibrosus: correlation between MR and pathologic findings in cadavers.** *AJNR Am J Neuroradiol* 1988;9:367–70 Medline
  42. Milette PC, Fontaine S, Lepanto L, et al. **Differentiating lumbar disc protrusions, disc bulges, and discs with normal contour but abnormal signal intensity. Magnetic resonance imaging with discographic correlations.** *Spine (Phila Pa 1976)* 1999;24:44–53 CrossRef Medline
  43. Olsewski JM, Schendel MJ, Wallace LJ, et al. **Magnetic resonance imaging and biological changes in injured intervertebral discs under normal and increased mechanical demands.** *Spine (Phila Pa 1976)* 1996;21:1945–51 CrossRef Medline
  44. Dullerud R, Johansen JG. **CT-diskography in patients with sciatica. Comparison with plain CT and MR imaging.** *Acta Radiol* 1995;36:497–504 CrossRef Medline
  45. Mok FP, Samartzis D, Karppinen J, et al. **ISSLS prize winner: prevalence, determinants, and association of Schmorl nodes of the lumbar spine with disc degeneration: a population-based study of 2449 individuals.** *Spine (Phila Pa 1976)* 2010;35:1944–52 CrossRef Medline
  46. Hou Y, Luo Z. **A study on the structural properties of the lumbar endplate: histological structure, the effect of bone density, and spinal level.** *Spine (Phila Pa 1976)* 2009;34:E427–33 CrossRef Medline
  47. Miller JA, Schmatz C, Schultz AB. **Lumbar disc degeneration: correlation with age, sex, and spine level in 600 autopsy specimens.** *Spine (Phila Pa 1976)* 1988;13:173–78 CrossRef Medline

# Percutaneous Spinal Ablation in a Sheep Model: Protective Capacity of an Intact Cortex, Correlation of Ablation Parameters with Ablation Zone Size, and Correlation of Postablation MRI and Pathologic Findings

A.N. Wallace, T.J. Hillen, M.V. Friedman, Z.S. Zohny, B.H. Stephens, S.C. Greco, M.R. Talcott, and J.W. Jennings

## ABSTRACT

**BACKGROUND AND PURPOSE:** Despite the growing use of percutaneous ablation therapy for the treatment of metastatic spine disease, several issues have yet to be fully addressed. Our aims were to determine whether the vertebral body cortex protects against ablation-induced spinal cord injury; correlate radiofrequency, cryo-, and microwave ablation parameters with resulting spinal ablation zone dimensions and describe normal spinal marrow postablation changes on MR imaging.

**MATERIALS AND METHODS:** Ten thoracolumbar vertebrae in 3 sheep were treated with radiofrequency ablation, cryoablation, or microwave ablation under fluoroscopic guidance. Technique parameters were chosen to produce ablation zones that exceeded the volume of the vertebral bodies in sheep 1 and were confined to the vertebrae in sheep 2 and 3. Expected ablation zone dimensions were based on data provided by the device manufacturers. Postablation MR imaging was performed at 48 hours (sheep 1) or 7 days (sheep 2 and 3).

**RESULTS:** In sheep 1, cryoablation and microwave ablations extended into the spinal canal and caused histologically confirmed neurologic injury, but radiofrequency ablation did not. The mean difference between the lengths of the radiofrequency ablation zone dimensions measured on gross pathology compared with those expected was  $9.6 \pm 4.1$  mm. The gross pathologic cryo- and microwave ablation zone dimensions were within 1 mm of those expected. All modalities produced a nonenhancing ablation zone with a rim of enhancement, corresponding histologically to marrow necrosis and hemorrhagic congestion.

**CONCLUSIONS:** An intact cortex appears to protect against radiofrequency ablation-induced spinal cord injury, but not against non-impedance-based modalities. Ablation dimensions produced by microwave and cryoablation are similar to those expected, while radiofrequency ablation dimensions are smaller. Ablation of normal marrow produces a rim of enhancement at the margin of the ablation zone on MR imaging.

**ABBREVIATIONS:** MWA = microwave ablation; RFA = radiofrequency ablation

Percutaneous, image-guided ablation is a minimally invasive therapy for metastatic spine disease. Several ablation modalities are commercially available, including radiofrequency ablation (RFA), cryoablation, and microwave ablation (MWA). RFA and MWA heat the tumor to temperatures above 60°C, at which

point protein denaturation, immediate cell death, and coagulative necrosis occur.<sup>1</sup> Mechanisms of cryoablation-induced cell death include osmotic bursting, intracellular ice formation, coagulative necrosis, free radical release and apoptosis in response to biochemical stress, and stimulated immunologic targeting of tumor cells.<sup>2</sup> For patients with painful spinal metastases who do not respond or have a contraindication to radiation therapy, ablation may produce clinically significant pain palliation.<sup>3-7</sup> Additionally, Wallace et al<sup>8</sup> recently reported a 1-year radiologic local control rate of 70% (21/30) after RFA of spinal metastases, and Tomasián et al<sup>5</sup> achieved a 97% (30/31) radiologic local control rate of spinal metastases treated with cryoablation after a median follow-up of 10 months (range, 1–24 months). As a result, recent treatment algorithms for metastatic spine disease have incorporated ablation as an alternative option for pain palliation and local tumor control.<sup>9</sup>

Received December 28, 2016; accepted after revision March 17, 2017.

From the Mallinckrodt Institute of Radiology (A.N.W., T.J.H., M.V.F., J.W.J.), Department of Neurosurgery (Z.S.Z., B.H.S.), and Division of Comparative Medicine (S.C.G., M.R.T.), Washington University, St Louis, Missouri.

The authors received ablation probes from DFINE, Galil Medical, and Medtronic for this study.

Please address correspondence to Adam N. Wallace, MD, Mallinckrodt Institute of Radiology, Washington University, 510 South Kingshighway Blvd, St Louis, MO 63141; e-mail: wallacea@mir.wustl.edu

<http://dx.doi.org/10.3174/ajnr.A5228>

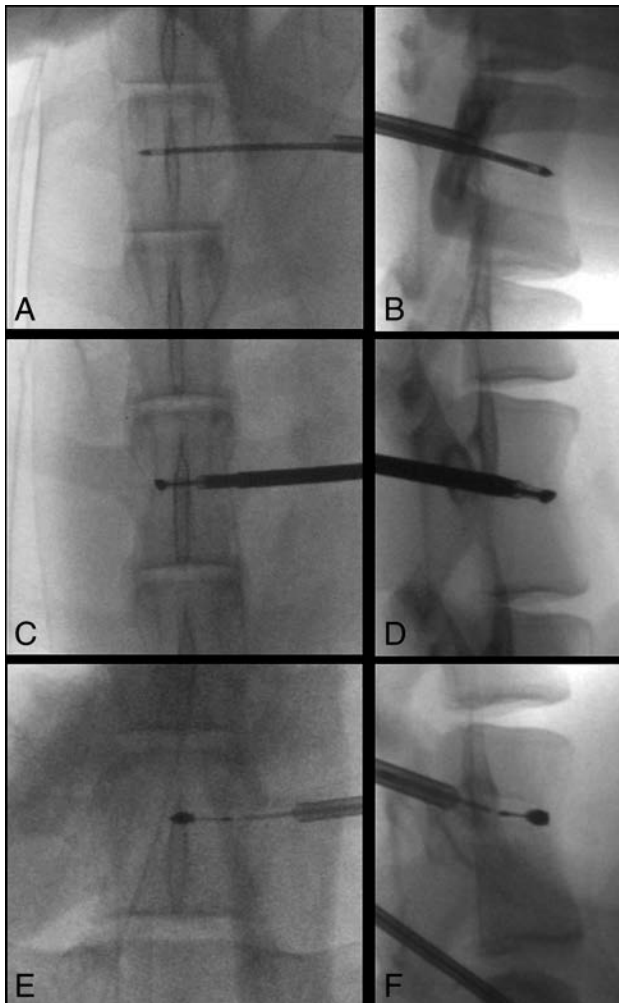


**FIG 1.** Fluoroscopic documentation of ablation probe placement in sheep. Anteroposterior (A, C, and E) and lateral (B, D, and F) fluoroscopic images show transpedicular placement of the cryoablation probe within the T14 vertebra (A and B), the radiofrequency ablation probe within the L3 vertebra (C and D), and the microwave ablation probe within the L6 vertebra (E and F).

**Table 1: Technical parameters used for radiofrequency ablation, expected minor-axis diameter of the ablation zones based on nonanimal models, and measured ablation zone diameters on MRI and gross pathology**

Watts	Thermocouple Temperatures (°C)		Ablation Time (sec)	Diameter of Ablation Zone Orthogonal to Ablation Probe (mm)		
	Proximal	Distal		Expected	MRI	Gross Pathology
10	72	51	92	20.0	13.4	13.8
5	58	42	107	16.6	9.2	10.0
5	51	40	42	13.0	7.3	8.0

**Table 2: Technical parameters used for cryoablation, expected minor-axis diameter of the ablation zones based on nonanimal models, and measured ablation zone diameters on MRI and gross pathology**

Probe	Intensity (%)	Freeze Cycles (min)	Thaw (min)	Diameter of Ablation Zone Orthogonal to Ablation Probe (mm)		
				Expected	MRI	Gross Pathology
IceSphere	60	6.0	7.0	20.0	19.2	20.1
IceSeed	50	4.0	5.0	6.0	6.6	7.4
IceSeed	50	3.5	5.0	6.0	6.4	7.0
IceSeed	50	3.0	5.0	5.0	5.5	6.8

Despite the growing use of percutaneous ablation therapy for the treatment of metastatic spine disease, several important issues have yet to be fully addressed. First, most spinal metastases involve the posterior vertebral body where complete tumor ablation is essential to prevent localized epidural invasion and spinal cord compression.<sup>10,11</sup> However, it is unclear whether intact cortex acts as a protective barrier for the spinal cord and exiting nerve roots during ablation of the posterior vertebral body.<sup>12,13</sup> Second, adequate tumor ablation requires accurate correlations between technique parameters and the resulting ablation zone dimensions. However, existing correlations derived from the manufacturers' preclinical data are based on soft-tissue and artificial models that have different thermal and electrical conductive properties to bone.<sup>14</sup> Last, although MR imaging is typically used to assess for local tumor control after ablation of spinal metastases,<sup>15</sup> diagnosis of residual tumor is limited by a paucity of literature describing ablation-induced MR imaging findings in normal spinal marrow.

The purposes of this study were to determine whether intact posterior vertebral body cortex protects the spinal cord against radiofrequency-, cryo-, or microwave ablation-induced injury, to correlate the technical parameters of each ablation technique with the resulting dimensions of the ablation zone, and to describe normal spinal marrow postablation changes on MR imaging.

## MATERIALS AND METHODS

The protocol of this study was approved by our institutional animal care and use committee.

### Ablation Technique

Ablations were performed under fluoroscopic guidance by 4 radiologists (A.N.W., T.J.H., M.V.F., J.W.J.) with 1–9 years of experience performing musculoskeletal tumor ablation. Ten vertebral bodies in 3 healthy living adult female sheep (weight range, 55–60 kg) were ablated. All 3 sheep were sedated by a veterinarian

staff member with an intramuscular injection of ketamine hydrochloride (2–10 mg/kg) and xylazine (0.2 mg/kg), intubated, and maintained under inhaled isoflurane (1%–5%) for general anesthesia. Mechanical ventilation was used throughout the procedure. The target vertebrae were localized by using a single-plane fluoroscopy unit, and the planned skin entry sites were sterilized with betadine scrubs and draped. Five- to 10-mm incisions were made at each skin entry site with a No. 11 blade to accommodate the percutaneous instruments. Unilateral transpedicular osseous channels into the vertebral bodies were created for ablation probe placement by using the OnControl system (Vidacare, Shavano Park, Texas), which consists of a 10-ga outer can-

**Table 3: Technical parameters used for microwave ablation, expected minor-axis diameter of the ablation zones based on nonanimal models, and measured ablation zone diameters on MRI and gross pathology**

Watts	Ablation Time (sec)	Diameter of Ablation Zone Orthogonal to Ablation Probe (mm)		
		Expected	MRI	Gross Pathology
100	50	20.0	17.4	20.0
100	15	9.5	7.9	9.0
100	10	6.0	5.9	6.5

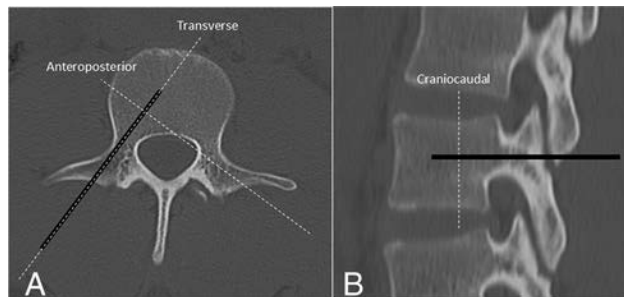


**FIG 2.** Anteroposterior (A) and lateral (B) CT images of a normal lumbar vertebra. The *thick black line* represents the unilateral transpedicular trajectory of the ablation probe. By definition, the transverse and anteroposterior dimensions of the ablation zone are parallel and perpendicular to the ablation probe in the axial plane, respectively, and the craniocaudal dimension of the ablation zone is perpendicular to the ablation probe in the sagittal plane.

nula and 12-ga inner osteotome. The locations of each probe were documented fluoroscopically (Fig 1).

### Ablation Parameters

The technical parameters and expected dimensions of each ablation zone based on preclinical data provided by the manufacturers are detailed in Tables 1–3. In sheep 1, cryoablation, RFA, and MWA were performed in the T14, L3, and L6 vertebral bodies, respectively. Sheep most commonly have 14 rib-bearing thoracic and 6 lumbar vertebrae, and the spinal cord terminates caudal to the sacrum. Each ablation probe tip was placed 5 mm from the posterior vertebral body cortex on a true lateral fluoroscopic projection. The parameters of radiofrequency, cryo-, and microwave ablation were chosen to produce ablation zones with anteroposterior, transverse, and craniocaudal dimensions of  $30 \times 20 \times 20$  mm,  $25 \times 20 \times 20$  mm, and  $20 \times 20 \times 20$  mm, respectively. The orientation of each dimension of the ablation zone with respect to the ablation probe was defined as depicted in Fig 2. Thus, for each ablation, the radius of the ablation zone extending from the probe tip toward the posterior vertebral body cortex was expected to be 10 mm. Every third vertebra was treated to ensure correct localization of histologic ablation-induced spinal cord injury.

In sheep 2 and 3, each ablation probe was placed in the center of the vertebral body, and the parameters of each ablation were chosen to produce an ablation volume that would be confined to the vertebra on the basis of preclinical data provided by the manufacturers. In sheep 2, RFA was performed at T14; MWA, at L3; and cryoablation, at L6. In sheep 3, RFA was performed at T14; MWA, at L2; and cryoablation, at L4 and L6.

RFA was performed with the STAR Tumor Ablation System

(DFINE, San Jose, California). Ablations can be performed at power settings of 5 or 10 W. Two thermocouples located on the shaft of the probe enable real-time monitoring of temperatures 10 and 15 mm from the center of the ablation zone, and the dimensions of the ablation zone are estimated from these maximum temperature readings. The expected diameter of each RFA zone orthogonal to the probe is based on the manufacturer's thermal distribution curves derived from ex vivo porcine liver models.

Cryoablations were performed with the Visual-ICE Cryoablation System (Galil Medical, Arden Hills, Minnesota) with either the IceSeed 1.5 or IceSphere 1.5 cryoprobe. For a given cryoprobe, the volume of the ablation zone is controlled by changing the intensity (percentage maximum) and the duration of the freeze cycle. In the present study, 2 freeze cycles were performed and the probe was actively heated to thaw the tissue between cycles. The expected diameter of each ablation zone orthogonal to the cryoprobe was based on the  $-40^{\circ}\text{C}$  isotherm dimensions produced in a  $37^{\circ}\text{C}$  gel bath.

MWAs were performed by using the Emprint Ablation System (Medtronic, Minneapolis, Minnesota). Ablations were performed at a power setting of 100 W for 10, 15, and 50 seconds. Power settings of 45 and 75 W are also available. The expected diameter of each MWA zone was based on an ex vivo porcine kidney model.

### Postablation Evaluation

The sheep were clinically evaluated by a veterinarian immediately after each procedure for signs of pain or ablation-induced nerve injury, including lameness or abnormal movement. Subcutaneous buprenorphine, 0.005–0.01 mg/kg, was administered every 10–12 hours, and carprofen, 2–4 mg/kg, was administered every 12–24 hours for 2 days postoperatively. The sheep were then periodically monitored by veterinary staff before sacrifice for evidence of procedure-related complications.

### MR Imaging

In sheep 1, MR imaging was performed 48 hours after treatment owing to clinical signs of spinal cord injury and the ethical necessity for euthanasia earlier than the planned 7-day time point. MR imaging was performed 7 days after treatment of sheep 2 and 3. Images were obtained on a Magnetom Trio 3T scanner (Siemens, Erlangen, Germany) using the spine coil within the table of the scanner. The protocol included T1-weighted conventional spin-echo images (TR, 783 ms; TE, 10 ms), T2-weighted fast spin-echo images with fat suppression (TR, 3500 ms; TE, 94 ms), and post-contrast conventional spin-echo T1-weighted images with fat suppression obtained after the intravenous bolus administration of 0.1 mmol/kg of gadoversetamide (Optimark; Covidien, Irvine, California). All images were acquired with a 2.5-mm section thickness with 1-mm intersection spacing,  $30 \times 30$  cm FOV, and  $288 \times 384$  matrix. On MR imaging, the ablation zone was defined as the volume of nonenhancement on contrast-enhanced T1-weighted images with fat suppression.<sup>15</sup> The measurements of MR imaging ablation zones were performed on high-resolution MR imaging workstation monitors. The anteroposterior, transverse, and craniocaudal ablation zone dimensions were measured for sheep 2 and 3. Only the transverse and craniocaudal dimen-

sions of each ablation zone were measured in sheep 1, because the anteroposterior dimensions was not confined to the vertebral body marrow. MR signal and enhancement characteristics of the ablation zones of each technique were also subjectively reviewed by the first and senior authors. No interpretations were discrepant.

### Pathology

Following MR imaging, the sheep were euthanized by barbiturate overdose (intravenous pentobarbital, 150 mg/kg) and the vertebral bodies and spinal cord were harvested by senior neurosurgery residents (B.H.S., Z.S.Z.). Tissues were fixed in 10% neutral buffered formalin. After fixation, the vertebral bodies were decalcified in hydrochloric acid–ethylenediaminetetraacetic acid decalcifier (EKI, Joliet, Illinois) to permit cross-sectioning of the bones for gross examination of the ablation sites and trimming of tissues for histopathology. The diameters of the pale tan necrosis orthogonal probe tract were measured once by the first author and a veteri-

nary pathologist with a Westcott 6" Clear Plastic Acrylic Ruler (Acme United Corporation, Fairfield, Connecticut). Because the vertebral bodies could be sectioned in only 1 plane, only the transverse and craniocaudal diameters of the ablation zones could be measured. Tissues were then paraffin-embedded, sectioned at 5  $\mu\text{m}$ , and stained with hematoxylin-eosin for histopathologic evaluation.

### RESULTS

Immediately after recovering from anesthesia, sheep 1 demonstrated bilateral lower extremity weakness, which did not improve during 48 hours of observation. MR imaging showed intramedullary T2 hyperintensity and enhancement involving the ventral spinal cord at the level of the cryoablated vertebra consistent with ablation-induced injury. Similar findings were seen along the ventrolateral aspect of the spinal cord at the level of the microwave-ablated vertebra, likely due to a slightly more oblique angulation of the MWA probe relative to the coronal plane. Histologically, the ablation zone was characterized by white matter necrosis with cavitation and axonal swelling and degeneration (Fig 3). The RFA zone measured 13.8 mm in the craniocaudal dimension. Because the RFA probe was placed only 5 mm from the posterior vertebral body cortex, the RFA zone should have extended into the spinal canal. Yet, histologic evaluation of the spinal cord at this level showed no evidence of ablation-induced injury.

Tables 1–3 summarize the correlations between the technical parameters of each technique and the resulting dimensions of the gross pathologic ablation zones. The mean differences in millimeters among the anteroposterior, transverse, and craniocaudal ablation zone dimensions expected on the basis of the manufacturers' preclinical data and those measured on MR imaging and gross pathology are presented in Table 4. The dimensions of the RFA zones measured on gross pathology were smaller than those expected on the basis of correlations provided by the manufacturer. The mean differences between the lengths of the transverse and craniocau-

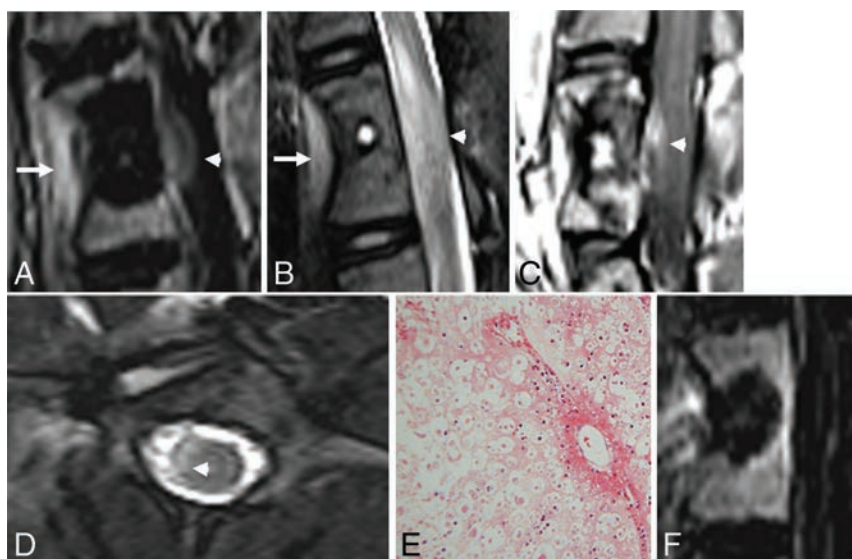


**FIG 3.** Sagittal postcontrast T1-weighted image with fat suppression (A) and a T2-weighted image (B) of the vertebral level treated with cryoablation show the ablation zone extending beyond the posterior vertebral body into the spinal canal. There is enhancement and intramedullary T2 signal hyperintensity in the ventral aspect of the edematous spinal cord (white arrowheads). There is also inflammation in the soft tissues ventral to the spine where the ablation zone extended beyond the anterior vertebral body cortex (white arrows). Sagittal postcontrast T1-weighted image (C) and axial T2-weighted image (D) of the vertebral level treated with microwave ablation similarly show extension of the ablation zone into the spinal canal (white arrowheads). E, Hematoxylin-eosin staining of the spinal cord at the level of the cryoablated vertebra at  $\times 100$  total magnification shows axonal necrosis and edema. Similar findings were seen at the microwave-ablated level (not shown). F, Sagittal postcontrast T1-weighted image with fat suppression of the radiofrequency-ablated vertebra shows the posterior margin of the ablation zone confined to the vertebral body.

**Table 4: Mean differences among the anteroposterior, transverse, and craniocaudal ablation zone dimensions expected on the basis of manufacturers' preclinical data and those measured on MRI and gross pathology<sup>a</sup>**

	Expected vs MRI (mm)			Expected vs Pathology (mm)		MRI vs Pathology (mm)	
	AP	TV	CC	TV	CC	TV	CC
Radiofrequency ablation	6.7 $\pm$ 0.9	11.0 $\pm$ 2.5	6.6 $\pm$ 0.7	13.4 $\pm$ 2.1	5.9 $\pm$ 0.7	-1.2 $\pm$ 0.7	-0.8 $\pm$ 0.1
Cryoablation	-0.5 $\pm$ 0.3	0.1 $\pm$ 0.7	-0.1 $\pm$ 0.7	-0.4 $\pm$ 0.6	-1.0 $\pm$ 0.5	-3.4 $\pm$ 0.2	-0.9 $\pm$ 0.3
Microwave ablation	0.9 $\pm$ 0.4	0.3 $\pm$ 0.5	1.4 $\pm$ 1.0	0.1 $\pm$ 0.5	0 $\pm$ 0.4	-0.8 $\pm$ 0.2	-0.9 $\pm$ 0.3

**Note:**—AP indicates anteroposterior; TV, transverse; CC, craniocaudal.

<sup>a</sup> A positive value indicates that the value listed first in the upper row was larger than the value listed second. For example, a positive value under the "Expected vs MRI" column indicates that the expected ablation zone dimension was larger than that measured on MRI. Orientations of the ablation zone dimensions with respect to the ablation probe are defined in Fig 2.

**Table 5: MRI, gross, and histopathologic findings produced by all 3 ablation modalities**

	T1WI	T2WI	CE-T1WI	Histopathology
Probe track	Hyperintense	Hyperintense	Enhancement	Hemorrhage, trabecular fragments, serum exudate, granulation tissue
Center	Slightly hyperintense	Slightly hypointense	No enhancement	Marrow necrosis, granulation tissue, intact trabeculae
Rim	Hyperintense	Hyperintense	Enhancement	Hemorrhagic congestion

**Note:**—CE indicates contrast-enhanced.

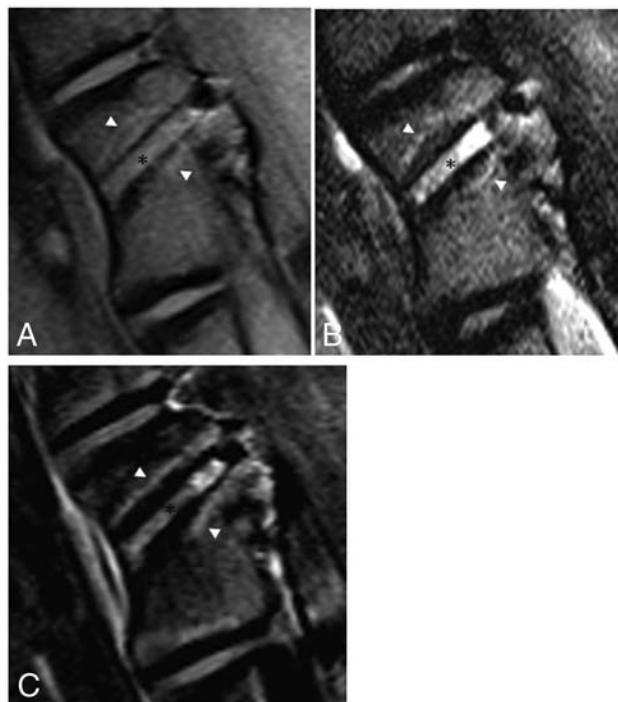


**FIG 4.** MR imaging findings 7 days after RFA of an L2 vertebral body in a sheep model. *A*, T1-weighted oblique sagittal MR imaging (*left*, anterior; *right*, posterior) shows T1 hyperintense soft tissue within the probe tract (*black asterisk*) outlined by a signal void. The surrounding ablation zone is isointense to normal marrow and outlined by a thin hyperintense rim (*white arrowheads*). *B*, T2-weighted oblique sagittal MR imaging with fat suppression shows the hyperintense probe tract (*black asterisk*) and slightly hypointense ablation zone surrounded by a hyperintense rim (*white arrowheads*). *C*, T1-weighted, postcontrast subtraction images show enhancement along the probe tract (*black asterisk*) and the nonenhancing ablation zone surrounded by a rim of enhancement (*white arrowheads*).

dal RFA zone dimensions measured on gross pathology compared with those expected were  $13.4 \pm 2.1$  and  $5.9 \pm 0.7$  mm, respectively. In contrast, the cryo- and microwave ablation zone dimensions measured on gross pathology were within 1 mm of those expected.

All ablation modalities produced the same subjective signal and enhancement characteristics on MR imaging (Table 5). Relative to normal marrow, the probe tracts demonstrated T1 isointense, T2 hyperintense, and enhancing tissue outlined by signal void. The ablation zones were defined by nonenhancing tissue that was slightly T1 hyperintense and T2 isointense and delineated by a thin rim of T1 and T2 hyperintensity and enhancement (Fig 4). The gross and histologic findings seen with all modalities were qualitatively similar (Table 5). Gross examination revealed discrete pale tan ablation zones. Histologically, the ablation zones were characterized by widespread marrow necrosis with areas of granulation tissue and edematous stroma.

Surrounding the ablation zones were rims of hemorrhagic congestion (Fig 5).

## DISCUSSION

In the present study, we used a bipolar RFA system in an attempt to produce an ablation zone with a minor-axis diameter greater than the distance from the probe tip to the posterior vertebral body cortex, but caused no histologic evidence of spinal cord injury due to the insulating effect of the posterior cortex. Previous animal experiments assessing the safety of RFA in close proximity to the spinal cord have been inconclusive. Dupuy et al<sup>12</sup> safely performed monopolar RFA of the posterior vertebral body for 10 minutes, but the maximum temperature generated within the bone was only 48°C, which is below the cytotoxic threshold. In a subsequent porcine study, monopolar RFA performed flush with the posterior vertebral body cortex for 10 minutes at a constant temperature of 90°C at the probe tip caused paraplegia with histologically confirmed spinal cord injury.<sup>13</sup> However, this latter experiment does not reflect clinical practice because adequate ablation of tumor within the posterior vertebral body only requires that the periphery of the ablation zone reach 60°C for a matter of seconds.<sup>1</sup>

In contrast with these previous studies, the ablation system used in the present experiment has several features that facilitate its safe use in the spine. First, the distal segment of the probe articulates up to 90°, enabling accurate placement of the tip with respect to the posterior vertebral body cortex. Second, the 2 active thermocouples incorporated into the shaft of the probe allow real-time estimation of the dimensions of the ablation zone. Last, monopolar systems require placement of a skin-grounding pad, which, if placed incorrectly, can cause a skin burn. This risk is eliminated with the use of a bipolar probe.<sup>16</sup> The RFA zones measured on gross pathology were smaller than those predicted from the manufacturer's preclinical data derived from a soft-tissue model.<sup>14</sup> Potential reasons for this discrepancy include the higher impedance and lower thermal conductivity of bone compared with soft tissue and a heat sink effect from blood flow in the vertebrae and epidural space, as well as circulating CSF.<sup>1,12</sup>

In contrast to RFA, when we produced a cryoablation zone with a diameter greater than the distance from the probe tip to the posterior vertebral body cortex, histologic evaluation of the spinal cord at the treated level showed white matter necrosis with cavitation and axonal swelling and degeneration consistent with ablation-induced injury. Although there are no prior studies assessing the safety of cryoablation within the posterior vertebral body, this result is expected because increased bone density does not limit the propagation of the cryoablation zone.<sup>17</sup> Several measures may be taken to minimize the risk of this complication clinically. First, the distance between the probe tip and the spinal

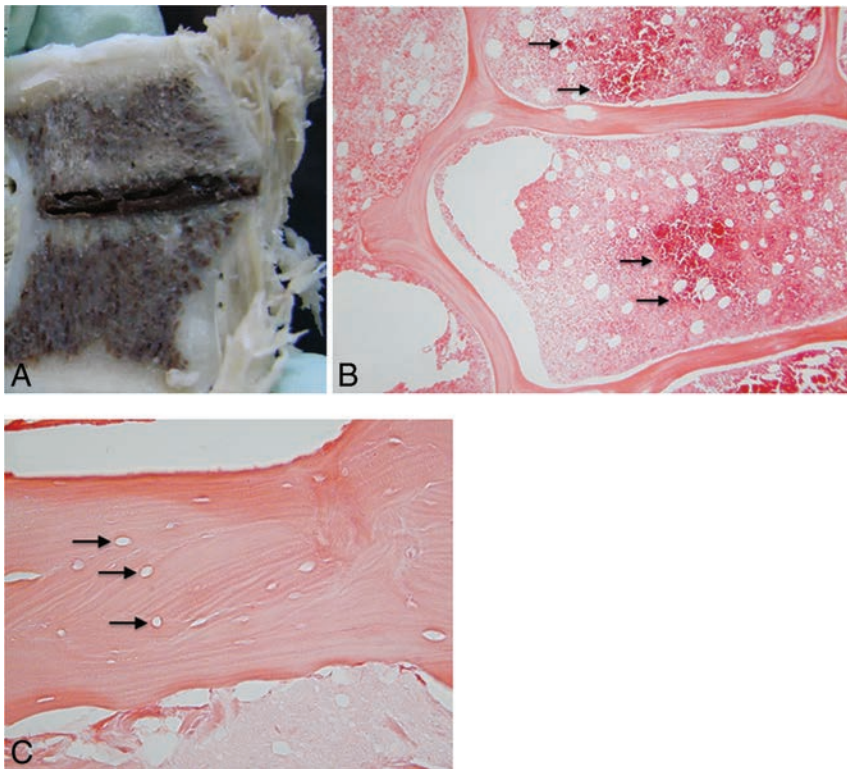


**FIG 5.** A, Gross pathology of the vertebral body shown in Fig 2 cut along the plane of the radiofrequency ablation probe tract. The tract is filled with hemorrhagic debris and is surrounded by a pale, tan zone of necrosis. B, Hematoxylin-eosin staining of the margin of the ablation zone at  $\times 40$  total magnification shows a dense band of red blood cells (black arrows), which demarcate necrotic marrow on the left from the intact region on the right. C, At  $\times 200$  magnification, the ablation zone shows empty lacunae (black arrows), representing a loss of osteocytes, within an intact trabecula.

canal must be accurately measured, and the cryoprobe and intensity and duration of the freeze cycles can then be chosen to ensure that the ablation zone does not exceed this distance. The dimensions of the cryoablation zones measured on gross pathology were within 1 mm of those predicted from the manufacturer's preclinical data derived from a  $37^{\circ}\text{C}$  gel bath model. Second, a coaxial needle with an inner thermocouple can be placed through the neural foramen to monitor the temperature in the epidural space, while the outer cannula is used to inject carbon dioxide for neural insulation and room temperature 5% dextrose in water to warm the epidural space.<sup>18</sup> Last, the use of motor-evoked potential monitoring and peripheral motor nerve electrostimulation to prevent iatrogenic cryoablation nerve injury have been described.<sup>19,20</sup>

The present experiment also showed that the posterior vertebral body cortex is not a barrier to MWA because this ablation zone also extended into the spinal canal and caused histologically evident spinal cord injury. Like cryoablation, this result is expected because MWA is also non-impedance-based. However, the efficiency with which tissue absorbs microwave energy is proportional to its water content, and soft tissue is  $>70\%$  water compared with the approximately 20% water content of bone.<sup>21,22</sup> Therefore, one would expect the MWA zones in the spine to be smaller than those expected from preclinical data derived from an ex vivo soft-tissue model. Yet, such a discrepancy was not observed. Accurate sizing of the MWA zone to remain confined to

the vertebral body and injection of carbon dioxide and room temperature 5% dextrose in water into the epidural space may increase the safety of the procedure.

The ablation-induced marrow changes on MR imaging, gross pathology, and histopathology were consistent across all 3 modalities. The necrotic ablation zone was depicted on postcontrast T1-weighted MR imaging with fat suppression as a nonenhancing area surrounded by a thin, enhancing rim of granulation tissue. T2 hyperintense enhancing residual tumor can appear similar to the rim of the ablation cavity. In some cases, FDG PET/CT or biopsy may be needed to differentiate residual tumor from postablation change.<sup>15</sup> The ablation zone dimensions of all 3 modalities measured on gross pathology were slightly larger than those measured on MR imaging. In the absence of a plausible physiologic explanation, the discrepancy is likely related to the resolution limitations of MR imaging.

A limitation of this study is that the correlations between technical ablation parameters and ablation zone dimensions were derived in normal bone, and these correlations may be altered by the presence of tumor. Also, the derived correlations are specific to the ablation

systems used in this experiment and cannot be extrapolated to other devices.

## CONCLUSIONS

Intact posterior vertebral body cortex in normal sheep may protect the spinal cord from radiofrequency ablation-induced injury, but not against microwave or cryoablation injury. Ablation dimensions produced by microwave and cryoablation are similar to those expected, while RFA volumes are smaller. Postablation marrow changes in normal spinal marrow include a rim of enhancement at the margin of the ablation zone.

Disclosures: Adam N. Wallace—RELATED: Grant: Medtronic, Galil, DFINE, Comments: received donated ablation probes from these companies.\* Travis J. Hillen—UNRELATED: Consultancy: Merit Medical, Comments: honorarium for proctoring physician education courses. Jack W. Jennings—UNRELATED: Consultancy: Galil, Medtronic, Merit Medical, Bard Medical; Payment for Lectures Including Service on Speakers Bureaus: Merit Medical and Medtronic Speaker Panels; Travel/Accommodations/Meeting Expenses Unrelated to Activities Listed: Comments: for meetings in which Speaker Panel duties were performed. \*Money paid to the institution.

## REFERENCES

1. Brace CL. Radiofrequency and microwave ablation of the liver, lung, kidney, and bone: what are the differences? *Curr Probl Diagn Radiol* 2009;38:135–43 CrossRef Medline
2. Rybak LD. Fire and ice: thermal ablation of musculoskeletal tumors. *Radiol Clin North Am* 2009;47:455–69 CrossRef Medline

3. Wallace AN, Greenwood TJ, Jennings JW. **Radiofrequency ablation and vertebral augmentation for palliation of painful spinal metastases.** *J Neurooncol* 2015;124:111–18 CrossRef Medline
4. Anchala PR, Irving WD, Hillen TJ, et al. **Treatment of metastatic spinal lesions with a navigational bipolar radiofrequency ablation device: a multicenter retrospective study.** *Pain Physician* 2014;17:317–27 Medline
5. Tomasian A, Wallace A, Northrup B, et al. **Spine cryoablation: pain palliation and local tumor control for vertebral metastases.** *AJNR Am J Neuroradiol* 2016;37:189–95 CrossRef Medline
6. Kastler A, Alnassan H, Aubry S, et al. **Microwave thermal ablation of spinal metastatic bone tumors.** *J Vasc Interv Radiol* 2014;25:1470–75 CrossRef Medline
7. Pusceddu C, Sotgia B, Fele RM, et al. **Combined microwave ablation and cementoplasty in patients with painful bone metastases at high risk of fracture.** *Cardiovasc Intervent Radiol* 2016;39:74–80 CrossRef Medline
8. Wallace AN, Tomasian A, Vaswani D, et al. **Radiographic local control of spinal metastases with percutaneous radiofrequency ablation and vertebral augmentation.** *AJNR Am J Neuroradiol* 2016;37:759–65 CrossRef Medline
9. Wallace AN, Robinson CG, Meyer J, et al. **The metastatic spine disease multidisciplinary working group algorithms.** *Oncologist* 2015;20:1205–15 CrossRef Medline
10. Algra PR, Heimans JJ, Valk J, et al. **Do metastases in vertebrae begin in the body or the pedicles? Imaging study in 45 patients.** *AJR Am J Roentgenol* 1992;158:1275–79 CrossRef Medline
11. Klimo P Jr, Thompson CJ, Kestle JR, et al. **A meta-analysis of surgery versus conventional radiotherapy for the treatment of metastatic spinal epidural disease.** *Neuro Oncol* 2005;7:64–76 CrossRef Medline
12. Dupuy DE, Hong R, Oliver B, et al. **Radiofrequency ablation of spinal tumors: temperature distribution in the spinal canal.** *AJR Am J Roentgenol* 2000;175:1263–66 CrossRef Medline
13. Nour SG, Aschoff AJ, Mitchell IC, et al. **MR imaging-guided radiofrequency thermal ablation of the lumbar vertebrae in porcine models.** *Radiology* 2002;224:452–62 CrossRef Medline
14. Singh S, Saha S. **Electrical properties of bone: a review.** *Clinl Orthop Relat Res* 1984;186:249–71
15. Wallace AN, Greenwood TJ, Jennings JW. **Use of imaging in the management of metastatic spine disease with percutaneous ablation and vertebral augmentation.** *AJR Am J Roentgenol* 2015;205:434–41 CrossRef Medline
16. Wallace AN, Tomasian A, Chang RO, et al. **Treatment of osteoid osteomas using a navigational bipolar radiofrequency ablation system.** *Cardiovasc Intervent Radiol* 2016;39:768–72 CrossRef Medline
17. Gangi A, Buy X. **Percutaneous bone tumor management.** *Semin Intervent Radiol* 2010;27:124–36 CrossRef Medline
18. Buy X, Tok CH, Szwarc D, et al. **Thermal protection during percutaneous thermal ablation procedures: interest of carbon dioxide dissection and temperature monitoring.** *Cardiovasc Intervent Radiol* 2009;32:529–34 CrossRef Medline
19. Kurup AN, Morris JM, Boon AJ, et al. **Motor evoked potential monitoring during cryoablation of musculoskeletal tumors.** *J Vasc Intervent Radiol* 2014;25:1657–64 CrossRef Medline
20. Tsoumakidou G, Garnon J, Ramamurthy N, et al. **Interest of electrostimulation of peripheral motor nerves during percutaneous thermal ablation.** *Cardiovasc Intervent Radiol* 2013;36:1624–28 CrossRef Medline
21. Emery JL, Finch E. **The fat and water content of the left and right liver before and after birth.** *Arch Dis Child* 1954;29:242–47 Medline
22. Smith JW. **Observations on the water content of bone.** *J Bone Joint Surg Br* 1964;46:553–62 Medline

## Is an Intact Posterior Vertebral Body Cortex Protective for Percutaneous Ablation?

**A**fter the lung and liver, bone is the most common site for metastatic disease and the spine is the most common site of bony metastases.<sup>1</sup> Roughly 70% of patients with cancer will develop metastatic disease. Of these, 40% develop spinal metastatic disease and 10%–20% of these will develop metastatic spinal cord compression.<sup>2</sup>

Treatment of spinal metastases is usually palliative, with the goals of therapy including timely control of pain, local tumor control to prevent neurologic deficits, and mechanical stabilization to preserve function.<sup>2</sup> Traditional treatment has been noninvasive, using analgesics, chemotherapy, and radiation therapy. Surgery is considered for radiation-resistant tumors, spinal instability, symptomatic neural compression, or intractable pain unresponsive to nonoperative measures. Recent studies have demonstrated image-guided invasive techniques of radiofrequency ablation (RFA), cryoablation, microwave ablation (MWA), and vertebral augmentation to be safe and effective in treating symptomatic metastatic osseous disease.<sup>3–8</sup> The effects of different ablation modalities on the vertebral body and spinal cord are not completely understood.

The authors presented a study showing the ablation effects of bipolar RFA, cryoablation, and MWA on a normal sheep vertebral body and the adjacent spinal cord and nerve roots.<sup>9</sup> The study addressed whether an intact posterior cortex of the vertebral body will be a protective barrier of the spinal cord and exiting nerve roots during the ablation. Second, the authors determined ablation zone dimensions for the 3 ablation modalities included in the study and correlated these with manufacturer's data. This is important because bone has different thermal and electrical conductive properties than a 37°C gel bath model used by the manufacturers to derive the ablation zones. Finally, the authors described the bone marrow changes seen after ablation on MR imaging and correlated these with pathologic specimens.

The study addressed the important point of whether a posterior intact cortex of the vertebral body will act as an insulator during ablation to prevent injury to the spinal cord. The authors showed that an intact posterior vertebral body cortex acts as an insulator when using a bipolar radiofrequency system; however, with cryoablation and MWA, this effect is not present and cord

damage may occur. The results of previous animal experiments assessing the safety of RFA in proximity to the spinal cord have been inconclusive.<sup>10,11</sup> However, these were monopolar RFA systems, whereas the current study used a bipolar system. There are no prior studies assessing the safety of cryoablation or MWA within the posterior vertebral body. This study showed that for cryoablation and MWA, the posterior vertebral body cortex does not act as an insulating barrier. For these 2 modalities, the ablation probes must be accurately placed in the vertebral body and the ablation zone must not extend past the posterior wall of the vertebral body to avoid injury to the spinal cord and nerve roots. Motor-evoked potential monitoring and peripheral motor nerve electrostimulation can be performed only with cryoablation and may prevent iatrogenic injury to the spinal cord and nerve roots.<sup>12,13</sup>

The RFA zones measured on gross pathology were smaller than those predicted from the manufacturer's 37°C gel bath model. However, the cryoablation and MWA zones were within 1 mm of those predicted from the manufacturer's preclinical data derived from the gel bath model. Awareness of this information is important for operators when performing ablation of a vertebral body.

Furthermore, the authors showed that ablation-induced marrow changes were similar on MR imaging, gross pathology, and histopathology across all 3 different ablation modalities. MR imaging showed the ablation area to be slightly hyperintense on T1-weighted imaging, slightly hypointense on T2-weighted imaging, with a central area of nonenhancement and a peripheral rim of enhancement on the contrast-enhanced T1-weighted images. The ablation zone dimensions of all 3 modalities measured on gross pathology were larger than those measured on MR imaging. These findings are helpful for the diagnostic neuroradiologist and interventionalist interpreting the posttreatment images to determine whether there is residual tumor.

The main limitation of the experiment is that all ablations were performed in a normal vertebral body, which is not the same scenario as in the clinical setting. The ablation zone volumes obtained from the experiment may not correlate with vertebral bodies with tumor involvement, given the different impedance and

thermal conductive properties of specific tumor types versus normal bone. Furthermore, the ablation zones derived from the experiment are specific to each manufacturer and cannot be generalized to other manufacturers of similar equipment.

The authors are to be commended for performing this in vitro experiment in a sheep model with the 3 most common ablation modalities. This report provides valuable information for operators performing vertebral body ablation with augmentation in patients with metastatic disease to the spine. With any palliative treatment, it is important to limit morbidity and maintain or improve quality of life. This information will help operators prevent injury to the adjacent spinal cord and nerve roots.

## REFERENCES

1. Aaron AD. **The management of cancer metastatic to bone.** *JAMA* 1994;272:1206–09 Medline
2. Klimo P Jr, Schmidt MH. **Surgical management of spinal metastases.** *Oncologist* 2004;9:188–96 CrossRef Medline
3. Anchala PR, Irving WD, Hillen TJ, et al. **Treatment of metastatic spinal lesions with a navigational bipolar radiofrequency ablation device: a multicenter retrospective study.** *Pain Physician* 2014;17:317–27 Medline
4. Hillen TJ, Anchala P, Friedman MV, et al. **Treatment of metastatic posterior vertebral body osseous tumors by using a targeted bipolar radiofrequency ablation device: technical note.** *Radiology* 2014;273:261–67 CrossRef Medline
5. Kastler A, Almassan H, Aubry S, et al. **Microwave thermal ablation of spinal metastatic bone tumors.** *J Vasc Interv Radiol* 2014;25:1470–75 CrossRef Medline
6. Tomasian A, Wallace A, Northrup B, et al. **Spine cryoablation: pain palliation and local tumor control for vertebral metastases.** *AJNR Am J Neuroradiol* 2016;37:189–95 CrossRef Medline
7. Wallace AN, Greenwood TJ, Jennings JW. **Radiofrequency ablation and vertebral augmentation for palliation of painful spinal metastases.** *J Neurooncol* 2015;124:111–18 CrossRef Medline
8. Wallace AN, Tomasian A, Vaswani D, et al. **Radiographic local control of spinal metastases with percutaneous radiofrequency ablation and vertebral augmentation.** *AJNR Am J Neuroradiol* 2016;37:759–65 CrossRef Medline
9. Wallace AN, Hillen TJ, Friedman MV, et al. **Percutaneous spinal ablation in a sheep model: protective capacity of an intact cortex, correlation of ablation parameters with ablation zone size, and correlation of postablation MRI and pathologic findings.** *AJNR Am J Neurodiol* 2017;38:1653–59 CrossRef
10. Dupuy DE, Hong R, Oliver B, et al. **Radiofrequency ablation of spinal tumors: temperature distribution in the spinal canal.** *AJR Am J Roentgenol* 2000;175:1263–66 CrossRef Medline
11. Nour SG, Aschoff AJ, Mitchell IC, et al. **MR imaging-guided radiofrequency thermal ablation of the lumbar vertebrae in porcine models.** *Radiology* 2002;224:452–62 CrossRef Medline
12. Kurup AN, Morris JM, Boon AJ, et al. **Motor evoked potential monitoring during cryoablation of musculoskeletal tumors.** *J Vasc Interv Radiol* 2014;25:1657–64 CrossRef Medline
13. Franceschi F, Koutbi L, Gitenay E, et al. **Electromyographic monitoring for prevention of phrenic nerve palsy in second-generation cryoballoon procedures.** *Circ Arrhythm Electrophysiol* 2015;8:303–07 CrossRef Medline

J.J. Gemmete

University of Michigan Hospitals  
Ann Arbor, Michigan

<http://dx.doi.org/10.3174/ajnr.A5235>

## Regarding “Differences in Hemodynamics and Rupture Rate of Aneurysms at the Bifurcation of the Basilar and Internal Carotid Arteries”

With great interest and appreciation, we have read the article by Doddasomayajula et al<sup>1</sup> entitled “Differences in Hemodynamics and Rupture Rate of Aneurysms at the Bifurcation of the Basilar and Internal Carotid Arteries.” They analyzed the differences in hemodynamics at the bifurcation of the basilar and internal carotid arteries to explain why posterior circulation aneurysms have a higher rupture risk than those in the anterior circulation, and they found that higher-flow conditions in basilar tip aneurysms could explain their high rupture risk compared with internal carotid bifurcation aneurysms.

In their article, the typical inlet flow boundary conditions were used for all models. However, the inlet flow boundary conditions of the basilar artery (the posterior circulation) and internal carotid artery (the anterior circulation) could be an obvious difference for the diameter and flow of the inlet artery. Such settings with the same inlet flow boundary conditions of the basilar and internal carotid arteries may disrupt the hemodynamic results markedly in this study, and the conclusions might involve significant bias without considering this factor. To avoid such biases, mirror aneurysms may be an ideal within-patient disease model to provide an internal control for the analysis of possible factors linked to aneurysm rupture.<sup>2,3</sup> Moreover, patient-specific

inflow boundary conditions may avoid biases in the calculation of hemodynamics when using the computational fluid dynamics techniques.<sup>4</sup>

The authors should be commended for their meticulous in-study design using state-of-the-art methodology. We look forward to future research and discussion.

### REFERENCES

1. Doddasomayajula R, Chung B, Hamzei-Sichani F, et al. **Differences in hemodynamics and rupture rate of aneurysms at the bifurcation of the basilar and internal carotid arteries.** *AJNR Am J Neuroradiol* 2017; 38:570–76 CrossRef Medline
2. Tian Z, Zhang Y, Jing L, et al. **Rupture risk assessment for mirror aneurysms with different outcomes in the same patient.** *Front Neurol* 2016;7:219 CrossRef Medline
3. Fan J, Wang Y, Liu J, et al. **Morphological-hemodynamic characteristics of intracranial bifurcation mirror aneurysms.** *World Neurosurg* 2015;84:114–20.e2 CrossRef Medline
4. Jansen IG, Schneiders JJ, Potters WV, et al. **Generalized versus patient-specific inflow boundary conditions in computational fluid dynamics simulations of cerebral aneurysmal hemodynamics.** *AJNR Am J Neuroradiol* 2014;35:1543–48 CrossRef Medline

W. Li

Y. Wang

Department of Neurosurgery  
The First Affiliated Hospital of Nanchang University  
Nanchang University  
Nanchang, China

<http://dx.doi.org/10.3174/ajnr.A5224>

## REPLY:

We appreciate the interest and comments on our paper entitled “Differences in Hemodynamics and Rupture Rate of Aneurysms at the Bifurcation of the Basilar and Internal Carotid Arteries.”

There are a few points that we would like to clarify.

In our models, we do not use the same flow conditions for all patients. The inflow boundary conditions are scaled with the size of each person’s anatomy based on a relationship determined experimentally with MR measurements<sup>1</sup> and consistent with flows reported in other studies.<sup>2</sup> In the absence of direct patient-specific measurements, this is, in our opinion, a reasonable approximation. In addition, our sensitivity analyses lead us to believe that relatively small variations in the boundary conditions (of approximately 30%) do not have an important effect on the conclusions drawn from the computational fluid dynamics (CFD) analysis that we are doing.<sup>3</sup>

We agree that our results should be confirmed with studies that use direct patient-specific flow conditions and large sample sizes.

On the other hand, using mirror aneurysms, as suggested, would not solve the problem because in those cases, the aneurysms are located at the same anatomic location on each side. In our study, we compared basilar tip and internal carotid terminus aneurysms, which are fed by different arteries. Furthermore, even if only patients with aneurysms at the basilar tip and the internal carotid bifurcation were considered, there is still the uncertainty of the relative flow conditions in the feeding arteries. Only in

ipsilateral multiple aneurysms fed by the same parent artery one can be sure that the inflow conditions are the same. In fact, we are submitting a new paper entitled “Hemodynamic Characteristics of Ruptured and Unruptured Multiple Aneurysms at Mirror and Ipsilateral Locations” that focuses on this issue. The results of that paper are consistent with the results presented in the current article.

We look forward to further discussions and exchanges of ideas.

## REFERENCES

1. Cebal JR, Castro MA, Putman CM, et al. **Flow-area relationship in internal carotid and vertebral arteries.** *Physiol Meas* 2008;29:585–94 CrossRef Medline
2. Oktar SO, Yücel C, Karaosmanoglu D, et al. **Blood-flow volume quantification in internal carotid and vertebral arteries: comparison of 3 different ultrasound techniques with phase-contrast MR imaging.** *AJNR Am J Neuroradiol* 2006;27:363–69 Medline
3. Cebal JR, Mut F, Weir J, et al. **Quantitative characterization of the hemodynamic environment in ruptured and unruptured brain aneurysms.** *AJNR Am J Neuroradiol* 2011;32:145–51 CrossRef Medline

● **R. Doddasomayajula**

Department of Bioengineering  
Volgenau School of Engineering  
George Mason University  
Fairfax, Virginia

● **C. Putman**

Department of Interventional Neuroradiology  
Inova Fairfax Hospital  
Falls Church, Virginia

● **J.R. Cebal**

Department of Bioengineering  
Volgenau School of Engineering  
George Mason University  
Fairfax, Virginia

<http://dx.doi.org/10.3174/ajnr.A5240>

## Regarding “What Is the Ideal Core Number for Ultrasonography-Guided Thyroid Biopsy of Cytologically Inconclusive Nodules?”

We read with great interest the article “What Is the Ideal Core Number for Ultrasonography-Guided Thyroid Biopsy of Cytologically Inconclusive Nodules?” by Hahn et al.<sup>1</sup> In that study, the authors evaluated the correct number of core-needle specimens for patients with previously inconclusive fine-needle aspiration cytology (FNA) results and suggested that at least 2 core specimens containing intranodular and capsular tissue are necessary for a proper diagnosis. In their results, the diagnostic ability of 2 specimens was found to be higher than that of 1 specimen and was similar to that of 3 specimens. This concept is concordant with that of the recent core-needle biopsy (CNB) guidelines published by the Korean Society of Thyroid Radiology.<sup>2</sup> Application of the results of Hahn et al<sup>1</sup> will help patients to avoid repeated FNAs or diagnostic surgery. Thanks to the valuable results in CNB skills and pathologic evaluation of core specimens. This study explained comprehensive aspects of the number of core specimens, and this concept had not been reported to date. The authors revealed several important aspects of core biopsy after previously inconclusive FNA results: 1) CNB achieved no nondiagnostic results; 2) the rate of inconclusive results was just 6.7% (4 of 60); 3) the final surgical pathology was well correlated with the core biopsy results; and 4) CNB procedures were tolerable in all patients. Thus, CNB is an effective and safe procedure for patients with previously inconclusive results, and these findings are concordant with those of previous CNB studies.

Although the study of Hahn et al<sup>1</sup> obtained informative results, there are 3 points to be considered. The first is the relationship between the number of core specimens and the size of the specimen notch of the core device. Second, capsule information is necessary, especially for diagnosing follicular neoplasm; however, a core technique including the capsule is not recommended in all patients, especially those with suspected papillary thyroid cancers. Finally, to justify 2 core specimens, the complications of the 3 groups should be compared. Regarding the relationship between the core specimen number and the size of the specimen notch of the core device, a core device with a large specimen notch requires fewer core specimens. The authors used a 1.1-cm excursion core

device, which has a 0.7-cm specimen notch. This obtains a core specimen of approximately 0.7 cm in length. A 1.6-cm excursion core device can obtain a 1.2-cm specimen length, whereas a 2-cm excursion device can obtain a 1.6-cm specimen length. Therefore, 2 specimens obtained by a 1.1-cm device are similar to 1 specimen obtained by a 1.6- or 2-cm core device. In addition, an 18-gauge core device can obtain larger-bore tissue than a 20- or 21-gauge core device. However, complications should be compared among devices with different lengths or thicknesses. Regarding capsule information, capsules can help to diagnose follicular neoplasms. Current CNB guidelines recommend that a nodule capsule be obtained during core biopsy.<sup>2</sup> However, capsule information is unnecessary for the diagnosis of papillary thyroid cancers. Therefore, the use of an extra core biopsy should be restricted to certain types of thyroid nodules. Suh et al<sup>3</sup> performed less than 2 core biopsy, but inconclusive results is not high in their factor analysis. Multiple biopsies can cause more complications; this issue should be considered during CNB procedures. To minimize complications, the operators performing CNB should understand the basic techniques and perithyroidal structures.<sup>4</sup>

In conclusion, Hahn et al<sup>1</sup> have reported valuable results on the number of core specimens needed for patients with previously inconclusive FNA results in thyroid biopsy. Although these data are practically important, knowledge of the core device, the relationship between specimen notch and specimen length, the type of thyroid nodule, and possible complications is essential for operators to perform thyroid CNB.

Disclosures: Jung Hwan Baek—UNRELATED: Consultancy: RFA Company, ATARmed and RF Medical, Comments: since 2017, \$2700/year.

### REFERENCES

1. Hahn SY, Shin JH, Oh YL. **What is the ideal core number for ultrasonography-guided thyroid biopsy of cytologically inconclusive nodules?** *AJNR Am J Neuroradiol* 2017;38:777–81 CrossRef Medline
2. Na DG, Baek JH, Jung SL, et al. **Core needle biopsy of the thyroid: 2016 consensus statement and recommendations from Korean Society of Thyroid Radiology.** *Korean J Radiol* 2017;18:217–37 CrossRef Medline
3. Suh CH, Baek JH, Lee JH, et al. **The role of core-needle biopsy as a**

**first-line diagnostic tool for initially detected thyroid nodules.** *Thyroid* 2016;26:395–403 CrossRef Medline

4. Ha EJ, Baek JH, Lee JH. **Ultrasonography-based thyroïdal and perithyroidal anatomy and its clinical significance.** *Korean J Radiol* 2015; 16:749–66 CrossRef Medline

✉ **H.S. Park**

✉ **J.H. Baek**

Department of Radiology and Research Institute of Radiology  
University of Ulsan College of Medicine

Asan Medical Center  
Seoul, Korea

✉ **N.D. Gyu**

Department of Radiology  
GangNeung Asan Hospital  
Seoul, Korea

Department of Radiology

Human Medical Imaging and Intervention Center  
Seoul, Korea

## Regarding “Measured Head CT/CTA Skin Dose and Intensive Care Unit Patient Cumulative Exposure”

We thank Nawfel and Young<sup>1</sup> for their thoughtful article, “Measured Head CT/CTA Skin Dose and Intensive Care Unit Patient Cumulative Exposure.” Nawfel and Young<sup>1</sup> have published a timely study in the midst of recent positive neurointerventional stroke trials and the resultant increased volume of CT angiographic imaging. Radiation exposure from medical imaging is always part of the risk-benefit analysis for critically ill patients. Accurate radiation dosimetry has been a topic of much debate in recent years, both from a scientific standpoint and from patient concerns sparked by the lay press. We would like to discuss the conclusions from Nawfel and Young<sup>1</sup> regarding radiation exposure from head CT/CTA in the context of the current medical literature and the potential future directions for research.

The authors did not find a statistically significant correlation between patient head size and peak skin dose. The peak skin dose was found to be consistently lower than the volumetric CT dose index (CTDI<sub>vol</sub>), citing the use of a “correction factor” with no additional variable. However, McCollough et al<sup>2</sup> summarized an exponential relationship between patient size (sum of anteroposterior [AP] and lateral diameters) and patient dose at other sites such as the abdomen. Perhaps the patient sample size was not sufficient to include enough variability to make an exponential relationship apparent. In addition, adult head size does not vary as widely as abdominal girth. The homogeneity of adult head size in the available cohort of patients may not sufficiently power for accurate statistical analysis. Perhaps either a much larger cohort or the inclusion of a pediatric patient population would have introduced the size heterogeneity necessary to make clear whether the exponential relationship between patient size and dose applies to head imaging as it does for the abdomen.

Whereas the authors used the geometric mean to represent head size, other surrogates for size have been cited in the literature, such as weight, body mass index, single AP or single lateral diameter from either the localizer image or an axial cross-

sectional image, summative AP and lateral diameters, and effective diameters.<sup>3</sup> Work by the American Association of Physicists in Medicine<sup>3</sup> has also identified water-equivalent diameter ( $D_w$ ) as a surrogate for patient size in thoracic and abdominal imaging. In addition to measuring patient size, the application of  $D_w$  in the head would also take into account the variable attenuation properties ranging from air within paranasal sinuses to sclerotic calvaria. In fact, recent work by Anam et al<sup>4</sup> has demonstrated an exponential relationship between a normalized size-specific dose estimate and  $D_w$  for head CT, including automation of the  $D_w$  calculation as others have previously described. Perhaps  $D_w$  or one of the other surrogates of patient size might have been useful in the study by Nawfel and Young<sup>1</sup> to elucidate the exponential relationship with size-specific dose estimate.

Disclosures: Michele Johnson—UNRELATED: Board Membership: Continuum Health, Comments: nonprofit board with no compensation.

### REFERENCES

1. Nawfel RD, Young GS. **Measured head CT/CTA skin dose and intensive care unit patient cumulative exposure.** *AJNR Am J Neuroradiol* 2017;38:455–61 CrossRef Medline
2. McCollough CH, Leng S, Yu L, et al. **CT dose index and patient dose: they are not the same thing.** *Radiology* 2011;259:311–16 CrossRef Medline
3. American Association of Physicists in Medicine. *Use of Water Equivalent Diameter for Calculating Patient Size and Size-Specific Dose Estimates (SSDE) in CT. The Report of AAPM Task Group 220.* College Park, Maryland: American Association of Physicists in Medicine; 2014. AAPM report no. 220
4. Anam C, Haryanto F, Widita R, et al. **Automated calculation of water-equivalent diameter (DW) based on AAPM Task Group 220.** *J Appl Clin Med Phys* 2016;17:320–33 CrossRef Medline

● I. Ikuta

● A. Mustafa

● M.H. Johnson

Department of Radiology & Biomedical Imaging  
Yale University School of Medicine  
New Haven, Connecticut

## REPLY:

We would like to thank Dr. Ikuta et al for their interest in our paper and comments on the data underlying Fig 4, which illustrates the variation in peak skin dose with patient head size.<sup>1</sup>

In our study, the effective diameter of adults undergoing head CT/CTA ranged from 14.9–18.7 cm. As Ikuta et al note, prior studies have demonstrated an exponential relationship between patient size and patient dose. McCollough et al<sup>2</sup> demonstrated this in a study showing substantially more variation in abdomen size (20–80 cm) than the head size variation in our study. Anam et al<sup>3</sup> reported that the normalized dose/100 mAs over a range of head sizes was only approximately 4 mGy. As such, we agree with Ikuta et al that the small range of head sizes encountered in our study, as compared with variation in abdominal girth, likely accounts for the absence of an exponential relationship between head size and dose in our data.

We believe that our use of effective diameter to represent head size, following the method of AAPM Reports 204 and 220, is appropriate because body mass index and weight are not necessarily well correlated with head size.<sup>4,5</sup> AAPM Report 220 reports only a slight change in size-specific dose estimate when using water equivalent diameter ( $D_w$ ) as compared with effective diameter as a conversion factor. Hence, we doubt that using  $D_w$  as a surrogate for head size would have changed our results significantly or demonstrated an exponential relationship between head size and peak skin dose.

To the contrary, our data provide support for the recommendation by Huda et al<sup>6</sup> that a standard head size is appropriate for adult dose assessment because of the minimal variation in adult patient dose related to head size.

<http://dx.doi.org/10.3174/ajnr.A5242>

## REFERENCES

1. Nawfel RD, Young GS. **Measured head CT/CTA skin dose and intensive care unit patient cumulative exposure.** *AJNR Am J Neuroradiol* 2017;38:455–61 CrossRef Medline
2. McCollough CH, Leng S, Yu L, et al. **CT dose index and patient dose: they are not the same thing.** *Radiology* 2011;259:311–16 CrossRef Medline
3. Anam C, Haryanto F, Widita R, et al. **Automated calculation of water-equivalent diameter (DW) based on AAPM Task Group 220.** *J Appl Clin Med Phys* 2016;17:320–33 CrossRef Medline
4. Boone JM, Strauss KJ, Cody DD, et al. *Size-Specific Dose Estimates (SSDE) in Pediatric and Adult Body CT Examinations: Report of AAPM Task Group 204.* College Park, Maryland: American Association of Physicists in Medicine; 2011
5. McCollough C, Bakalyar DM, Bostani M, et al. *Use of Water Equivalent Diameter for Calculating Patient Size and Size-Specific Dose Estimates (SSDE) in CT: The Report of AAPM Task Group 220.* College Park, Maryland: American Association of Physicists in Medicine; 2014
6. Huda W, Lieberman KA, Chang J, et al. **Patient size and x-ray technique factors in head computed tomography examinations, I: radiation doses.** *Med Phys* 2004;31:588–94 CrossRef Medline

✉ **R.D. Nawfel**

Department of Radiology  
Brigham and Women's Hospital  
Boston, Massachusetts  
Department of Radiology  
Harvard Medical School  
Boston, Massachusetts

✉ **G.S. Young**

Department of Radiology  
Brigham and Women's Hospital  
Boston, Massachusetts  
Department of Radiology  
Dana Farber Cancer Institute  
Boston, Massachusetts  
Department of Radiology  
Harvard Medical School  
Boston, Massachusetts

The authors regret that in the October 2013 article “Widespread White Matter Alterations in Patients with End-Stage Renal Disease: A Voxelwise Diffusion Tensor Imaging Study” (*AJNR Am J Neuroradiol* 2013;34:1945–51), the MNI coordinates of brain regions shown in Tables 2–6 were incorrect. The MNI coordinates in Tables 2–6 should be corrected by shifting  $-20$  in Y direction and  $+20$  in Z direction. The tables are reproduced below with the corrected segments shown in bold.

**Table 2: MNI coordinates of major areas with significant AD differences along with their means and standard deviations**

Brain Regions	MNI Coordinate (mm)			AD (Mean $\pm$ SD) $\times 10^{-3}$ mm <sup>2</sup> /s	
	X	Y	Z	ESRD	Healthy
	Rt. RLIC	25	<b>-36</b>	<b>8</b>	1.43 $\pm$ 0.17
Lt. RLIC	-27	<b>-34</b>	<b>6</b>	1.66 $\pm$ 0.21	1.57 $\pm$ 0.13
Lt. Fminor	-21	<b>32</b>	<b>8</b>	1.43 $\pm$ 0.07	1.33 $\pm$ 0.07
Pons	1	<b>-34</b>	<b>-36</b>	1.85 $\pm$ 0.18	1.73 $\pm$ 0.11

**Table 3: MNI coordinates of major areas with significant RD differences along with their means and standard deviations**

Brain Regions	MNI Coordinate (mm)			RD (Mean $\pm$ SD) $\times 10^{-3}$ mm <sup>2</sup> /s	
	X	Y	Z	ESRD	Healthy
	GCC	1	<b>19</b>	<b>19</b>	0.94 $\pm$ 0.2
SCC	1	<b>-34</b>	<b>25</b>	0.65 $\pm$ 0.15	0.56 $\pm$ 0.08
Rt. Fmajor	24	<b>-74</b>	<b>12</b>	0.66 $\pm$ 0.11	0.62 $\pm$ 0.09
Lt. Fmajor	-28	<b>-62</b>	<b>12</b>	0.67 $\pm$ 0.09	0.61 $\pm$ 0.11
Rt. PCR	25	<b>-43</b>	<b>27</b>	0.64 $\pm$ 0.09	0.63 $\pm$ 0.04
Lt. PCR	-28	<b>-40</b>	<b>27</b>	0.66 $\pm$ 0.09	0.65 $\pm$ 0.04
Rt. ACR	17	<b>31</b>	<b>14</b>	0.64 $\pm$ 0.06	0.62 $\pm$ 0.05
Lt. ACR	-20	<b>36</b>	<b>12</b>	0.63 $\pm$ 0.06	0.59 $\pm$ 0.05
Pons	3	<b>-33</b>	<b>-34</b>	0.82 $\pm$ 0.19	0.71 $\pm$ 0.12

**Table 4: MNI coordinates of major areas with significant MD differences along with their means and standard deviations**

Brain Regions	MNI Coordinate (mm)			MD (Mean $\pm$ SD) $\times 10^{-3}$ mm <sup>2</sup> /s	
	X	Y	Z	ESRD	Healthy
	GCC	1	<b>19</b>	<b>12</b>	1.16 $\pm$ 0.07
SCC	1	<b>-33</b>	<b>25</b>	1.12 $\pm$ 0.13	1.02 $\pm$ 0.06
Rt. SS	31	<b>-51</b>	<b>11</b>	1.27 $\pm$ 0.22	1.21 $\pm$ 0.15
Lt. SS	-39	<b>-44</b>	<b>5</b>	1.07 $\pm$ 0.12	1.04 $\pm$ 0.08
Rt. Fmajor	25	<b>-62</b>	<b>17</b>	0.96 $\pm$ 0.11	0.89 $\pm$ 0.04
Lt. Fmajor	-30	<b>-54</b>	<b>17</b>	1.15 $\pm$ 0.11	0.99 $\pm$ 0.09
Rt. PCR	27	<b>-45</b>	<b>24</b>	1.07 $\pm$ 0.12	0.92 $\pm$ 0.06
Lt. PCR	-29	<b>-45</b>	<b>21</b>	1.21 $\pm$ 0.18	1.11 $\pm$ 0.15
Pons	2	<b>-34</b>	<b>-36</b>	1.28 $\pm$ 0.13	1.13 $\pm$ 0.09

**Table 5: MNI coordinates of major areas with significant FA differences along with their means and standard deviations**

Brain Regions	MNI Coordinate (mm)			FA (Mean $\pm$ SD)	
	X	Y	Z	ESRD	Healthy
	GCC	3	<b>20</b>	<b>12</b>	0.6 $\pm$ 0.06
SCC	3	<b>-34</b>	<b>25</b>	0.65 $\pm$ 0.05	0.72 $\pm$ 0.05
Rt. SS	31	<b>-48</b>	<b>14</b>	0.50 $\pm$ 0.04	0.56 $\pm$ 0.04
Lt. SS	-27	<b>-59</b>	<b>14</b>	0.46 $\pm$ 0.05	0.56 $\pm$ 0.07
Rt. MCP	13	<b>-38</b>	<b>-38</b>	0.45 $\pm$ 0.03	0.53 $\pm$ 0.04

**Table 6: MNI coordinates of areas with significant correlations along with their correlation coefficients**

Brain Regions	MNI Coordinate (mm)			Correlation Coefficient
	X	Y	Z	
RD and duration				
Lt. Pons	-16	<b>-23</b>	<b>-26</b>	0.7093
RD and CASI				
Lt. ACR	-28	<b>33</b>	<b>39</b>	-0.7442
Rt. SCR	31	<b>-13</b>	<b>41</b>	-0.6154
MD and duration				
Rt. RLIC	33	<b>-40</b>	<b>14</b>	0.6009
Lt. FWM	-21	<b>43</b>	<b>15</b>	0.6287
Lt. Pons	-12	<b>-23</b>	<b>-26</b>	0.6675
MD and CASI				
Lt. ACR	-28	<b>13</b>	<b>39</b>	-0.7657
Rt. SCR	31	<b>-13</b>	<b>41</b>	-0.5463
FA and CASI				
Lt. ACR	-17	<b>20</b>	<b>38</b>	0.7067
Lt. PCR	-20	<b>-49</b>	<b>44</b>	0.6117
Rt. SCR	33	<b>-14</b>	<b>46</b>	0.6815